Boundary shear stress distribution for a converging compound channel

B. Naik & Kishanjit K. Khatua

Taylor & Francis
Taylor & Francis Group

Boundary shear stress distribution for a converging compound channel

B. Naik and Kishanjit K. Khatua

Department of Civil Engineering, National Institute of Technology Rourkela, Rourkela, India

ABSTRACT
The boundary shear force distribution in open channel flow is needed for various purposes such as the flow resistance relationship, for designing stable channels. During floods, river overtops the main channel and flows over the flood plain located to its sides. For such compound channels the flow structure becomes complicated due to the transfer of momentum between the deep main channel and the adjoining flood plains that magnificently affects the shear stress distribution in flood plain and main channel subsections. Due to the rapidly growing population and the consequent demand for food and accommodation, more and more land on floodplain regions of a river system has been used for agriculture and settlement. This also causes flood plain geometry to vary along the length of the flow called converging compound channel. In this paper an experimental investigation concerning the distribution of shear stress in the main channel and flood plain of the converging compound channels are presented. Based on the experimental results of boundary shear, a new equation is developed for predicting boundary shear stress distribution in terms of non-dimensional geometric and flow variables.

1. Introduction

Accurate determination of the distribution of boundary shear stress on and near the banks of natural channels is essential for addressing a variety of problems in fluvial geomorphology and stream restoration. So it is very essential to study the flow mechanism of rivers both in in-bank and overbank conditions due to the velocity difference between the main channel and flood plains. Sellin (1964) first investigated through laboratory investigations the momentum transfer phenomena. After that several investigators found that the momentum transfer was responsible for the non-uniformity in the boundary shear stress distribution across the section perimeter (e.g. Ghosh and Jena (1971), Knight and Hamed (1984), Patra et al. (2004). Knight and Hamed (1984) developed a model for boundary shear tress distribution of homogeneous compound channel of width ratio (α = flood plain width (B)/main channel width (b)) value up to 4. Khatua and Patra (2007) based on more experimental observations carried forward the study and developed a model for channels of width ratio (α) value up to 5.25. Mohanty and Khatua (2014) again developed a new model for channel with $6.67 \leq \alpha \leq 11.96$. Both prismatic and meandering compound channels' geometries were extensively investigated in laboratory flumes. However, when the compound section data of prismatic compound channels were compared with non-prismatic compound channels significant errors in estimation of %S_{fp} were noticed due to non-inclusion of extra mass and momentum transfer as explained by Bousmar and Zech (1999), Bousmar et al. (2004), and Proust et al. (2006). Where %$S_{fp} = 100 \times S_{fp}/SF$, S_{fp} = the boundary shear carried by the flood plains and SF the total shear force of the compound channel. This extra momentum exchange should be taken into account in the flow modeling for non-prismatic compound channel. Distribution of boundary shear stress mainly depends

upon the shape of the cross-section and the structure of the secondary flow cells. So new models are necessary to be developed for the non-prismatic compound sections. New experiments on compound channels with converging flood plains were conducted to develop new expression for %S_{fp}.

2. Experimental works

2.1. Experimental setup

Experiments have been conducted at the Hydraulics and Fluid mechanics Laboratory of Civil Engineering Department of National Institute of Technology, Rourkela, India. Three sets of non-prismatic compound channels with varying cross-sections were built inside a concrete flume with Perspex sheet measuring 15 m long × 0.90 m width × 0.5 m depth. The width ratio (α) of the channel was 1.8 and the aspect ratio (δ = main channel width (b)/main channel depth (h)) was 5. Keeping the geometry constant, the converging angles of the channels were varied as 12.38°, 9°, and 5°, respectively. Converging length of the channels fabricated were found to be 0.84, 1.26, and 2.28 m, respectively. Longitudinal bed slope of the channel was 0.0011, it was satisfying subcritical flow conditions at different sections of the non-prismatic compound channels. Roughness of the flood plain and main channel was taken identical. From the in-bank flow measurements of the channel of same surface materials (used in the main channel and flood plains) and using the back calculations of Manning's equations, Manning's n value of 0.011 has been estimated. The flow conditions in the converging section were turbulent. A recirculating system of water supply was established with pumping of water from an underground sump to an overhead tank from where water flows under gravity to the experimental channel. Adjustable vertical gates along with flow strengtheners were provided in

---

upstream section sufficiently ahead of rectangular notch to reduce turbulence and velocity of approach in the flow near the notch section. An adjustable tailgate at the downstream end of the flume helps to maintain uniform flow over the test reach. Water from the channel was collected in a volumetric tank that helps to measure the discharge rate. From the volumetric tank water runs back to the underground sump. Figure 1a shows the plan view of experimental setup. Figure 1b shows the plan view of different test reaches with cross-sectional dimensions of both NITR & Rezaei (2006) channels. Figure 1c shows the typical grid showing the arrangement of velocity measurement points along horizontal and vertical directions at the test section.

A movable bridge was provided across the flume for both span wise and stream wise movements over the channel area so that each location on the plan of compound channel could be accessed for taking measurements. The broad parameters of this channel are aspect ratio of main channel (δ), width-ratio (α). A micro-Pitot tube of 4.77-mm external diameter in conjunction with suitable inclined manometer was used to measure velocity at these points of the flow grid. The Pitot tube was physically rotated with respect to the main stream direction till it gave maximum deflection of the manometer reading. A flow

direction finder having a least count of 0.1° was used to get the direction of maximum velocity with respect to the longitudinal flow direction. The angle of limb of Pitot tube with longitudinal direction of the channel was noted by the circular scale and pointer arrangement attached to the flow direction meter. The overall discharge obtained from integrating the longitudinal velocity plot and from the volumetric tank collection was found to be within ±3% of the observed values. Using the velocity data, the boundary shear at various points on the channel beds and walls were evaluated from a semi log plot of velocity distribution. Boundary shear stresses were also obtained from the manometer readings of the head differences of Preston tube techniques using Patel's (1965) relationship. Error adjustments to the shear value were done by comparing the corresponding shear values obtained from the energy gradient approach. The results so obtained were found to be consistently within ±3% the value. According to the laboratory data analysis, shear stress from a Pitot tube is the most appropriate shear stress calculation method as compared to ADV. Because near the boundary velocity measurement ADV is never accurate. Further, ADV has some limitations of velocity measurements. It can measure 5 cm below its top edge. So in down probe of micro-ADV it
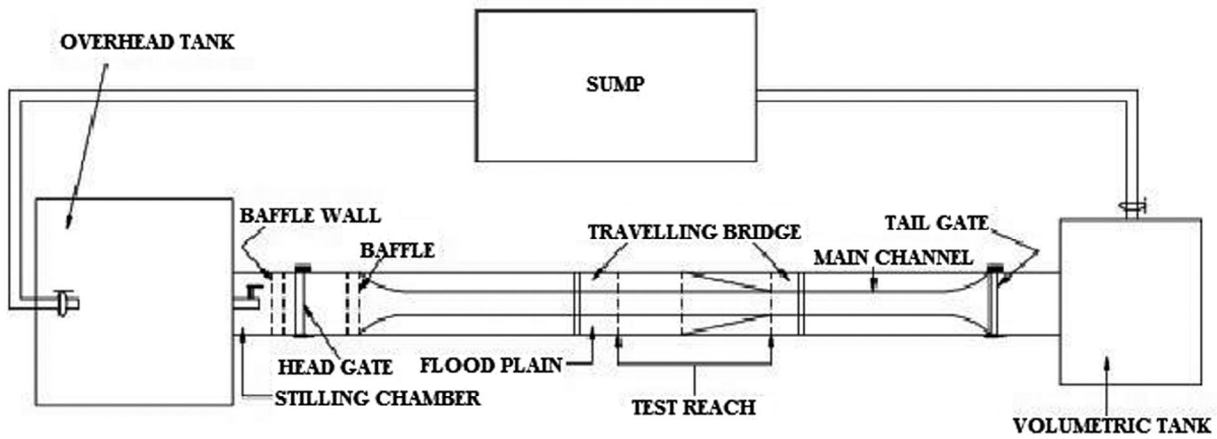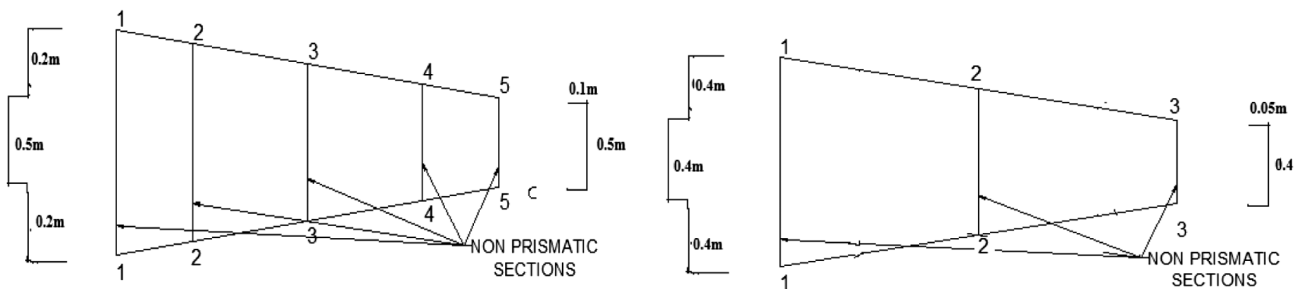

Figure 1a. Plan view of experimental setup.

Figure 1b. Plan view of different test reaches with cross-sectional dimensions of both NITR & Rezaei (2006) channels.
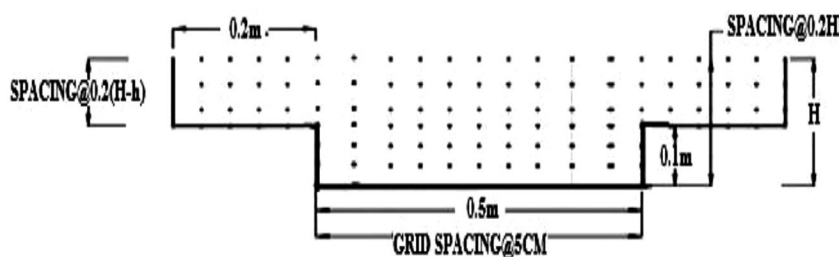

Figure 1c. Typical grid showing the arrangement of velocity measurement points at the test section.

could not measure 5 cm near the free surface. So Pitot tube has been utilized to measure the short fall. The accuracy of this method has been verified from the energy gradient approach i.e. weight component of the flow.

3. Experimental results

The results of boundary shear stress distributions for the converging flood plain of angle 12.38° and 11.31° of Rezaei (2006) for different cross-sections of relative depth 0.15 and 0.5 are shown in Figures 2a and 2b. These figures indicate that the boundary shear stress distributions are reasonably symmetric in all sections and gradually increase from sec-1 to sec-5. In all sections the boundary shear value is found to be the maximum at the middle of main channel and gradually decreases towards the interface between the main channel and the flood plain. At the interface, the boundary shear suddenly falls then it decreases and reaches the minimum at both the ends of flood plains. This may be due to momentum transfer phenomena between the main channel and flood plains. Similarly this

happens to the converging channel of Rezaei (2006) with angle 11.31°. However, at the last section of Rezaei (2006) maximum boundary shear is found to occur at the two ends of the main channel instead of the middle of main channel. Because the last section is the single channel with higher aspect ratio as compared to the present experimental channel. To analyze the boundary shear stress distributions, various boundary elements of the non-prismatic compound channels comprising the wetted parameters are labeled as (1), (2), (3), and (4) as shown in Figure (3). Label (1) denotes the two vertical walls of flood plain of length $[2(H–h)]$, and (2) denotes flood plain beds of length $(B–b)$. Label (3) denotes the two main channel walls of length $(2h)$ and the bed of the main channel of length b is represented by label (4) (where H is the total depth of the compound channel, h is the main channel height, and B is the total width of the compound channel). Experimental shear stress distributions at each point of the wetted perimeter are numerically integrated over the respective sublengths of each boundary element (l), (2), (3), and (4) to obtain the respective boundary shear force per unit length for each element. Sum
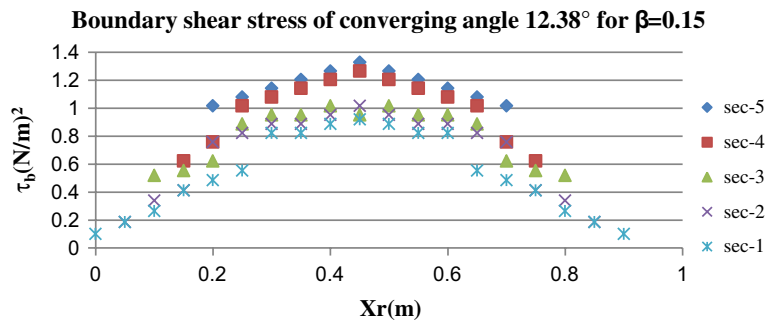

Boundary shear stress of converging angle 12.38° for β=0.15

Figure 2a. Boundary shear distribution for the present experimental channel of relative depth 0.15 (for converging angle 12.38°).

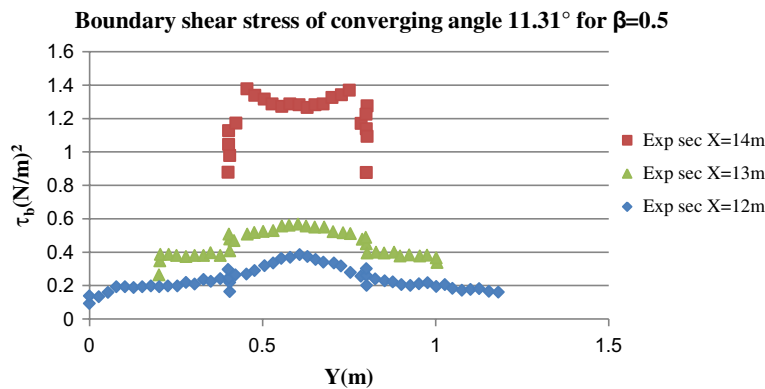**Boundary shear stress of converging angle 11.31° for β=0.5**

Figure 2b. Boundary shear distribution for the Rezaei (2006) experimental channel of relative depth 0.5 (for converging angle 11.31°).
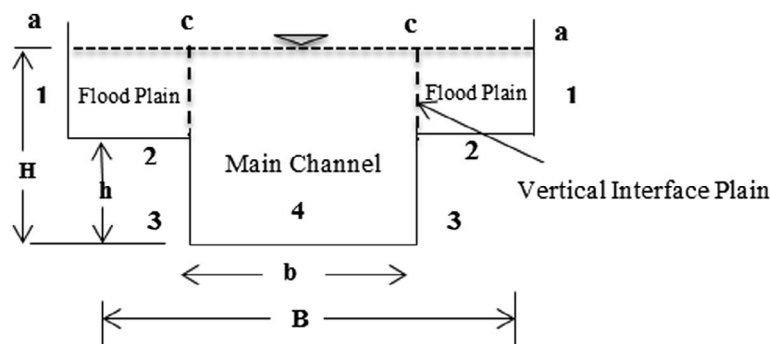

Figure 3. Interface planes dividing a compound section into subareas.

of the boundary shear forces for all the beds and walls of the compound channel is used as a divisor to calculate the shear force percentages carried by the boundary elements. Percentage of shear force carried by flood plains comprising elements (1) and (2) is represented as $\%S_{\text{fp}}$.

4. The boundary shear stress distribution model

In a simple open channel flow the boundary shear per unit length (SF) is generally assumed to be uniform and is expressed as $SF = \rho gAS$, where ρ is density of water and g is acceleration due to gravity. The parameters ρ, g, and S are assumed constant for a given channel. Only the flow area (A) varies with flow depth. So it can be stated that SF is a function of A. The percentage of the area occupied by the flood plain subsections obtained by vertical interfaces (Figure 3), is denoted by $\%A_{\text{fp}} = 100 \times A_{\text{fp}}/A$, where A_{fp} is the corresponding area by flood plain and A is the total area of the compound channel. Therefore, a functional relationship between $\%S_{\text{fp}}$ and $\%A_{\text{fp}}$ has been derived. This equation has been obtained by curve fitting between $\%A_{\text{fp}}$ and $\%S_{\text{fp}}$ which gave the highest regression coefficient. We have attempted to develop an equation of $\%S_{\text{fp}}$ with α and β for compound channels with converging flood plains. Previously different investigators have presented their model for $\%S_{\text{fp}}$. Knight and Demetriou (1983) presented an equation for the percentage of total shear force carried by the flood plain as $\%S_{\text{fp}}$

$$\%S_{\text{fp}} = 48(\alpha - 0.8)^{0.289}(2\beta)^m \tag{1}$$

where α = width ratio = B/b, β = relative depth = $(H–h)/H$, b = width of main channel, B = total width of compound channel, h = bank full depth, and H = total depth of flow. The exponent m is evaluated from the relation

$$m = 1/[0.75e^{0.38\alpha}] \tag{2}$$

Equation (1) is applicable for homogeneous compound channels. For non-homogeneous compound channels Equation (1) is improved by Knight and Hamed (1984) as

$$\%S_{\text{fp}} = 48(\alpha - 0.8)^{0.289}(2\beta)^m[1 + 1.02\sqrt{\beta}\log\gamma] \tag{3}$$

where γ = the ratio of Manning's roughness of the flood plain (n_{fp}) to that for the main channel (n_{mc}).

Equation (1) is good for $\alpha \leq 4$. Khatua and Patra (2007) further improved Equation (2) and proposed an equation for $\%S_{\text{fp}}$ as

$$\%S_{\text{fp}} = 1.23(\beta)^{0.1833}(38\text{Ln}\alpha + 3.6262)[1 + 1.02\sqrt{\beta}\log\gamma] \tag{4}$$

Khatua and Patra (2007) have shown the validity of Equation (4) for α up to = 5.25. Again for α = 6.67, Khatua et al. (2012) obtained a new relation for percentage shear carried by the flood plain as

$$\%S_{\text{fp}} = 4.1045(\%A_{\text{fp}})^{0.691} \tag{5}$$

In terms of β and α, Equation (5) is simplified as

$$\%S_{\text{fp}} = 4.105\left[\frac{100\beta(\alpha - 1)}{1 + \beta(\alpha - 1)}\right]^{0.691} \tag{6}$$

For width ratio up to 12, from regression analysis, Equation (5) is further modified by Mohanty and Khatua (2014).

$$\%S_{\text{fp}} = 3.3254(\%A_{\text{fp}})^{0.746} \tag{7}$$

Looking equations of different investigators i.e. Equations (1), (5), and (7) etc. it is seen that $\%S_{\text{fp}} = F(\alpha, \beta, \delta)$ for prismatic compound channel, where F is the functional symbol. But when all the equations are tested against compound channels with converging sections significant errors are found. So an attempt has been made here to investigate the variation in $\%S_{\text{fp}}$ with respect to different non-dimensional parameters of a non-prismatic compound channel. The percentage of shear carried by flood plain ($\%S_{\text{fp}}$) for non-prismatic sections have been derived from a wide range of experimental data-sets i.e. from three different types of converging compound channels of NIT, Rourkela, India and three series of converging compound channels data of Rezaei (2006) (details of the data-sets are given in Table 1). These compound channels have homogeneous roughness both in the main channel and flood plain subsections. Manning's n values for all these smooth surfaces are taken as 0.01. For a compound channel with converging flood plain the boundary shear distribution changes from section to section. So two additional parameters with the above three are considered for modeling of the boundary shear stress distribution of such compound channels. Therefore, a multiple variable regression model is attempted by taking all the five most influencing dimensionless parameters.

The possible functional relationships is in the form

$$\%S_{\text{fp}} = F\left(\alpha, \beta, \delta, \theta, X_r\right) \tag{8}$$

where θ = Converging angle, X_r = Relative distance (x/L), and L = Non-prismatic length.

The possible dependency of $\%S_{\text{fp}}$ and the best functional relationships with each non-dimensional variable have been found out from the Figures 4–6 described below. The variation in $\%S_{\text{fp}}$ has been plotted for six converging compound

Table 1. Hydraulic parameters for the experimental channel data.

Verified test channel	Types of channel	Angle of convergent (θ)	Longitudinal slope (S)	Cross-sectional geometry	Total channel width (B) (m)	Main channel width (b) (m)	Main channel depth (h) (m)	Width ratio (sec-1) B/b (α)	Converging length (X_r) (m)	Aspect Ratio b/h (δ)
Rezaei (2006)	Converging (CV2)	11.31°	0.002	Rectangular	1.2	0.398	0.05	3	2	7.96
Rezaei (2006)	Converging (CV6)	3.81°	0.002	Rectangular	1.2	0.398	0.05	3	6	7.96
Rezaei (2006)	Converging (CV6)	1.91°	0.002	Rectangular	1.2	0.398	0.05	3	6	7.96
N.I.T. Rkl	Converging	5°	0.0011	Rectangular	0.9	0.5	0.1	1.8	2.28	5
N.I.T. Rkl	Converging	9°	0.0011	Rectangular	0.9	0.5	0.1	1.8	1.26	5
N.I.T. Rkl	Converging	12.38°	0.0011	Rectangular	0.9	0.5	0.1	1.8	0.84	5

%S$_{fp}$ vs β for Different Converging Angles

$$\%S_{fp} = 81\beta^{0.6318}$$
$$R^2 = 0.9992$$

Legend: 11.31, 3.81, 1.91, 12.38, 5, 9
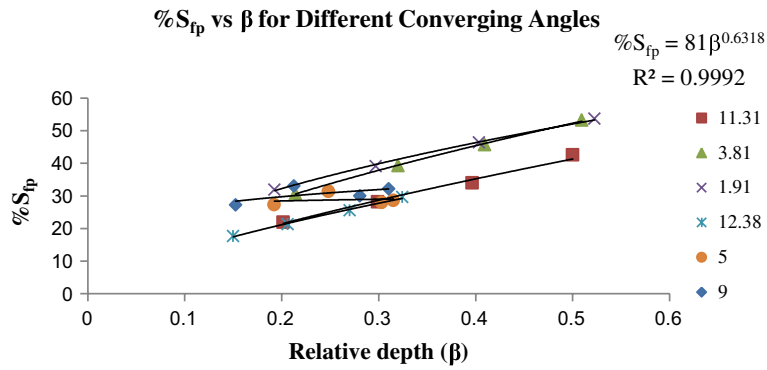
Figure 4. Variation in %S_{fp} of non-prismatic compound channel at typical sections.

%S$_{fp}$ vs X$_r$ of different Relative Depth

$$\%S_{fp} = -27.154X_r + 28.23$$
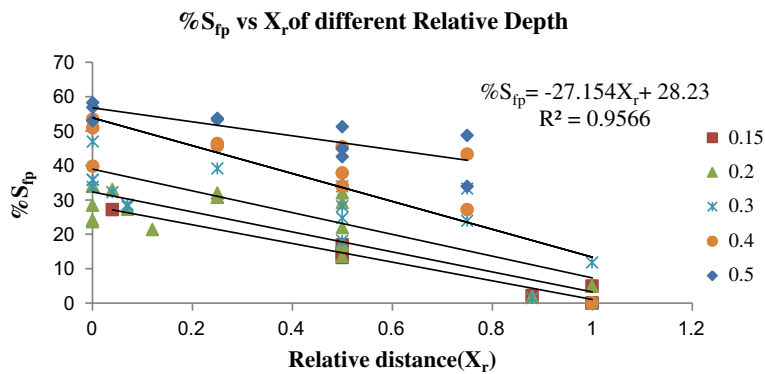$$R^2 = 0.9566$$

Legend: 0.15, 0.2, 0.3, 0.4, 0.5

Figure 5. Variation in %S_{fp} of flood plain shear with section to section along the converging angle and prismatic channel width.

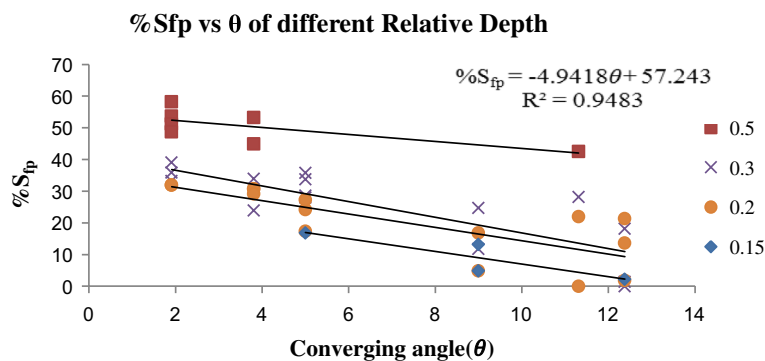**%Sfp vs θ of different Relative Depth**

$$\%S_{fp} = -4.9418\theta + 57.243$$
$$R^2 = 0.9483$$

Legend: 0.5, 0.3, 0.2, 0.15

Figure 6. Variation in %S_{fp} of flood plain shear with converging angles for constant relative depth.

Actual %S$_{fp}$ vs Predicted %S$_{fp}$

Legend: New Method, Knight et al Method(1984), Khatua et al Method(2012), Mohanty et al Method(2014)
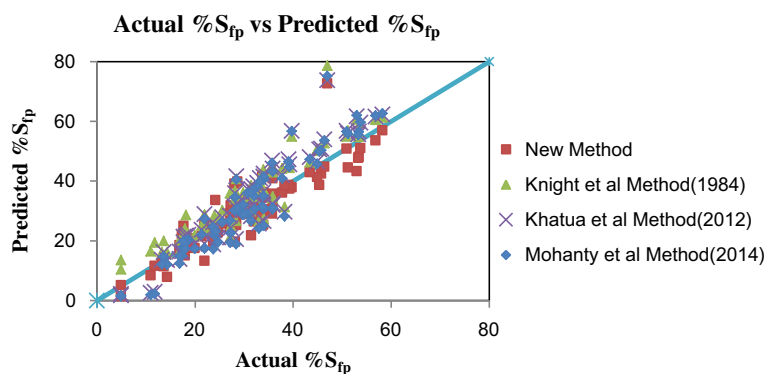
Figure 7. Scatter plot for observed and modeled value of %S_{fp}.

channels. Figure (4) shows the variation in %S_{fp} with relative flow depths β for each channel for different converging angles θ. From the figure it is seen that %S_{fp} increases with increase in relative flow depth. Similarly, the variations in %S_{fp} with relative distance X_r are plotted for different relative depths in Figure (5). From the Figure (5) it is seen that the shear force percentage carried by flood plains (%S_{fp}) is found to decrease from section to section of all the converging compound channels

Table 2. Unstandardized coefficient and regression statistics.

	Coefficients		Regression statistics	
Intercept	−22.985	Multiple R		0.911
β	0.767	R Square		0.831
X_r	0.899	Adjusted R Square		0.826
θ	0.281	Standard error		7.154
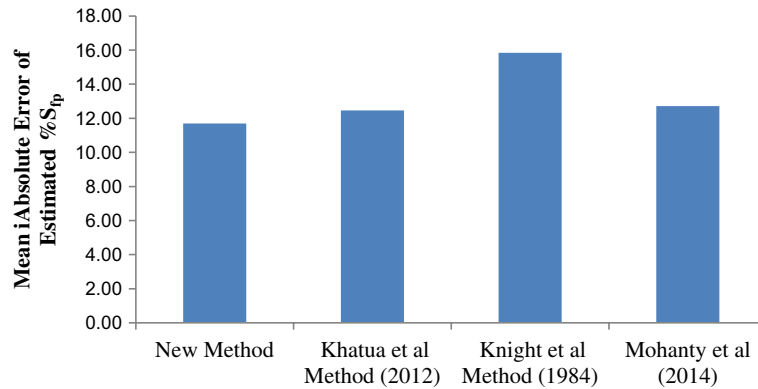
Figure 8. Mean Absolute Error by standard approaches applied to Present experimental channel data.

for all converging channels. The variation in $\%S_{fp}$ with different converging angles θ for different relative depths are also shown in Figure (6), showing an increase of shear force percentage carried by flood plains with increase in the overbank flow depth. From these graphs we observed that the $\%S_{fp}$ has power function with depth ratio (β), linear function with relative distance (X_r), and converging angle (θ), respectively, as presented in Equations (9–11).

By analyzing the above plots, percentages of boundary shear stress carried by flood plain region i.e. $\%S_{fp}$ with different non-dimensional geometric and hydraulic parameters of compound channel with converging flood plain are found to be

$$\%S_{fp} = F_1(\beta) = A(\beta)^{0.63} \tag{9}$$

$$\%S_{fp} = F_2(X_r) = B(X_r) + C \tag{10}$$

$$\%S_{fp} = F_3(\theta) = D(\theta) + E \tag{11}$$

These equations (Equations 9–11) show the relation between $\%S_{fp}$ with relative depth, converging angle, and relative distance. From the above graphs (Figure 4–6) it is also seen that R^2 value is very high and varies from 0.95 to 0.99 for each chosen functional relationships. Using the above relationships we compiled to develop a mathematical model using the regression analysis software in Micro Excel tool.

Table 2 represents the result of regression statistics, coefficients, and intercept from the linear regression analysis. After compiling all the equations (Equation 9–11) and unstandardized coefficients of Table 2, a generalized mathematical empirical relation is created and is shown in Equation 12.

$$\%S_{fp} = -22.985 + 0.767\left(F_1(\beta)\right) + 0.899(F_2(X_r)) + 0.281(F_3(\theta)) \tag{12}$$

After simplifying the above equation,

$$\%S_{fp} = 18.505 + 62.140(\beta)^{0.631} - 24.42(X_r) + 1.38(\theta) \tag{13}$$

Equation (13) represents the final expression of the model.

The variation between the calculated values of ($\%S_{fp}$) for compound channel with converging flood plain using Equations (1), (5), and (7) and the corresponding observed values for all the six types of channels are shown in Figure 7. The percentage error in the estimation of ($\%S_{fp}$) is less for model II when compared to the previous models for both Present experimental channel as well as Rezaei (2006) channels.

Using the new equation, various conventional methods are estimated for the flow cases considered in Present experimental channel of Rourkela and Rezaei (2006) channel. The methods considered are Khatua et al. (2012), Knight and Hamed (1984), Mohanty et al. (2014). The percentage of error in estimating the discharge is computed as

$$\text{Mean Absolute Error}(\%) = \frac{100\%}{N}\left|\frac{S_{fpcal} - S_{fpact}}{S_{fpact}}\right| \tag{14}$$

where S_{fpcalc} is the estimated discharge, S_{fpact} is the actual discharge, and N is the total number of data. Figure (8) shows the comparison among various methods in Present experimental channel of Rourkela and Rezaei (2006) channel cases. In Figure 8, the New Method appears to be the best method.

5. Results and discussion

5.1. Error analysis

To check the strength of the model, error analyses have been done. Mean absolute error (MAE), the mean absolute percentage error (MAPE), mean squared error (MSE), and the root mean squared error (RMSE) for all the converging compound channels for different flow conditions have been estimated. The definitions of error terms are described below. The detailed results of the error analysis have been presented in Table 3. The expression used to estimate errors in different forms are

5.1.1. Mean Absolute Error (MAE)
The Mean Absolute Error has been evaluated as,

$$\text{MAE} = \frac{1}{n}\sum_{i}^{n}\left|\frac{P_i - O_i}{O_i}\right| \tag{15}$$

Table 3. Statistical error analysis of different methods.

Statistical parameters	Methods			
	New Method	Khatua et al.	Knight et al. method	Mohanty et al. method
MSE	28.78119	35.62421	45.33	39.95373
RMSE	5.364811	5.968602	6.73	6.320896
MAE	3.734498	4.759234	5.31	4.746045
MAPE	13.43366	17.19923	21.63	17.4745

where P_i = predicted values, O_i = observed values.

5.1.2. Mean Absolute Percentage Error (MAPE)

MAPE also known as Mean absolute Percentage Deviation. It was usually expressed as a percentage, and was defined by the formula

$$\text{MAPE} = \frac{1}{n} \sum_{i}^{n} \left| \frac{O_i - P_i}{O_i} \right| \qquad (16)$$

5.1.3. Mean Squared Error (MSE)

MSE measures the average of the squares of the errors. It is computed as

$$\text{MSE} = \frac{1}{n} \sum_{i}^{n} (P_i - O_i)^2 \qquad (17)$$

5.1.4. Root Mean Squared Error (RMSE)

RMSE or Root Mean Squared Deviation is also a measure of the differences between values predicted by model or an estimator and the actually observed values. These individual differences are called as residuals when the calculations are performed over the data sample that is used for estimation, and are known as estimation errors when computed out of the sample. The RMSE is defined as,

$$\text{RMSE} = \sqrt{\text{MSE}} \qquad (18)$$

6. Conclusions

The following conclusions can be derived from the above research presented in this work.

(1) From the experimental results on converging compound channels, the boundary shear from point to point along the wetted perimeter for different sections along the converging compound channels are measured and the distribution of shear force carried by flood plains and in main channel perimeters were presented.

(2) In all sections the boundary shear is found to be maximum at the middle of main channel and gradually decreases towards the interface between the main channel and flood plain. At the interface, the boundary shear suddenly falls then it decreases and reaches minimum at both the ends of floodplain. This may be due to momentum transfer phenomena occurring between the main channel and the flood plain.

(3) The dependency of shear force percentage carried by flood plains with five most influencing non-dimensional geometric and hydraulic parameters of a converging compound channel are evaluated and modeled. The %S_{fp} in converging compound channel is found to be a non-linear function of all these non-dimensional parameters.

(4) Different standard models to predict the shear force percentage carried by flood plains are applied to the present channel and the channels of other investigators. The present mathematical model presented for %S_{fp} of a converging compound channel gives least error when compared with other models applied at different reaches of the channels.

(5) Error analysis in terms of MSE, RMSE, MAE, and MAPE are performed for all data series by all the models to predict the shear force percentage carried by converging flood plains showing the efficacy of the present model.

References

Bousmar, D., and Zech, Y. (1999). "Momentum transfer for practical flow computation in compound channels." *J. Hydraul. Eng.*, 125(7), 696–706.

Bousmar, D., Wilkin, N., Jacquemart, J.H., and Zech, Y. (2004). "Overbank flow in symmetrically narrowing floodplains." *J. Hydraul. Eng.*, 130(4), 305–312.

Ghosh, S., and Jena, S.B. (1971). "Boundary shear stress distribution in open channel compound Proc." *Inst. Civil Eng.*, 49, 417–430.

Khatua, K.K., and Patra, K.C. (2007). "Boundary shear stress distribution in compound open channel flow." *ISH J. Hydraul. Eng.*, 13(3), 39–54.

Khatua, K.K., Patra, K.C., and Mohanty, P.K. (2012). "Stage-discharge prediction for straight and smooth compound channels with wide floodplains." *J. Hydraul. Eng.*, 138(1), 93–99.

Knight, D.W., and Demetriou, J.D. (1983). "Flood plain and main channel flow interaction." *J. Hydraul. Eng.*, 109(8), 1073–1092.

Knight, D.W., and Hamed, M.E. (1984). "Boundary shear in symmetrical compound channels." *J. Hydraul. Eng.*, 110(10), 1412–1430.

Mohanty, P.K., Khatua, K.K., and Dash, S.S. (2014). "Flow prediction in two stage wide compound channels." *ISH J. Hydraul. Eng.*

Mohanty, P. K., & Khatua, K. K. (2014). "Estimation of discharge and its distribution in compound channels." *Journal of Hydrodynamics, Ser. B*, 26(1), 144–154.

Patel, V.C. (1965). "Calibration of the Preston tube and limitations on its use in pressure gradients." *J. Fluid Mech.*, 231, 85–208. Cambridge University Press.

Patra, K.C., Kar, S.K., and Bhattacharya, A.K. (2004). "Flow and velocity distribution in meandering compound channels." *J. Hydraul. Eng.*, 130(5), 398–411.

Proust, S., Rivière, N., Bousmar, D., Paquier, A., and Zech, Y. (2006). "Flow in compound channel with abrupt floodplain contraction." *J. Hydraul. Eng.*, 132(9), 958–970.

Rezaei, B. (2006). "Overbank flow in compound channels with prismatic and non-prismatic floodplains." PhD thesis, Univ. of Birmingham, UK.

Sellin, R.H.J. (1964). "A laboratory investigation into the interaction between the flow in the channel of a river and that over its flood plain." *La Houille Blanche*, 7, 793–802.

Adaptive Contrast Enhancement and White Balancing Integration for Image Enhancement Based on Non-linear Generalized Equalization Model

Chiruvella Suresh[1], K. Amith Bansal[2]

[1]Research Scholar, Department of Electronics and Communication Engineering, University of Allahabad, Allahabad, U.P India

[2]Professor, Department of Electronics and Communication Engineering, University of Allahabad, Allahabad, U.P India

Abstract: *The digital image processing has introduced revolutionary developments in research fields like medicine, military, security, biometrics, robotics, satellite image processing, digital image compression, digital image enhancement, digital video processing, etc. Image enhancement is the predominant fundamental step in the image processing and digital image enhancement creates an image which is perceived by human visual system (HVS) in pleasant way. Although tremendous progress has been made in the past years on digital image enhancement process but still digital image enhancement is area of concern in the field of digital image processing. In the proposed method a non-linear generalized equalization model for image enhancement has proposed by integrating the non linear contrast enhancement and white balancing to form a unified algorithm based on the different parameter configurations into considerations. An adaptive image enhancement algorithm has been derived which yields good theoretical results based on two important histogram transform properties namely contrast gain and non linearity. Finally experimental results shows proposed method achieves good performance and low complexity over traditional state of art methods and proposed model is successful in achieving better efficiency in terms of tone correction as well as white balancing.*

Keywords: Image enhancement, white balancing, non-linear contrast enhancement, transformation, non linearity

1. Introduction

The invention of the computers is the pillar for the modern science and technology and digital image is the predominant area is also a technology based on computer. Digital image processing supports wide range of applications ranging from daily needs like mobiles, laptops, photography to high level research fields like medicine, satellites, radars, remote sensing, Etc. Digital image processing has ability to process the information visualized by human visual system (HVS) and daily trillions of new images are generated which needs automatic processing, manipulation.

Acquiring the sensory information using the digital sensors is called as digital images, mostly all image acquisition devices namely satellites, radars, cameras has one thing in common i.e. sensors. As shown in following figure 1.1 the acquisition of the object by digital sensors is the initial step in the image processing and then digital sensors acquired with great speed results in the abnormal content in some scenarios which needs processing to perceive the visual content by th human visual system in pleasant way.
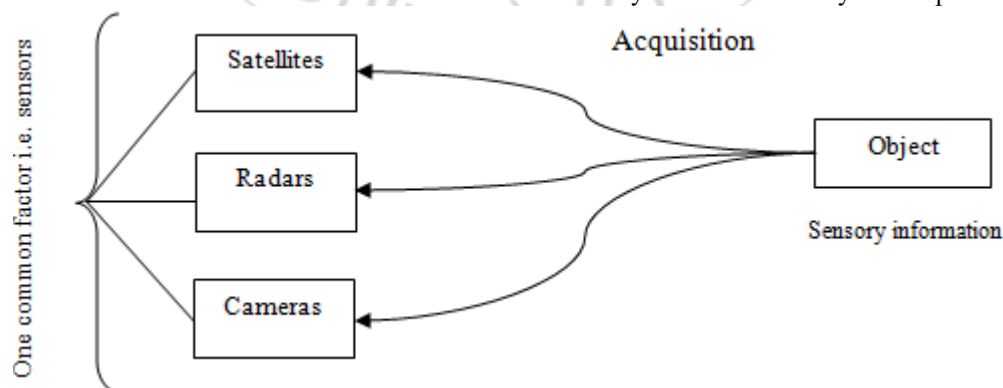

Figure 1: Acquisition of sensory information by digital sensors (Digital image)

In 1960's the processing of the digital image is consider to be expensive affair because of the expensive hardware included and digital image sensors has witnessed revolutionary changes from past few decades and the hardware cost has drastically reduced which makes digital image processing applicable to wide range of applications belongs to different research fields. Digital image processing has various advantages over the analog image processing which results in the high quality digital images with better quality.

A. Adaptive Image enhancement

Acquisition of the digital image is the initial step where the quality is decided and the key factor which decides the image quality is the environment in which it has acquired. If the image has acquired at abnormal lighting conditions then it results in the low quality image, if the hand shake has occur while acquiring the image then it results in the distorted and noisy image. Conversion of the acquired image content to better visualized content is technically called as adaptive image enhancement.
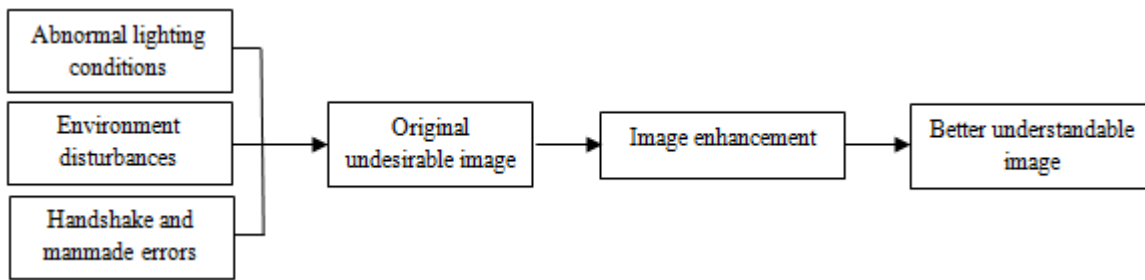

Figure 2: Adaptive image enhancement

Digital images acquired by the digital sensors are considered as the original images and the content in the acquired original images may be in degraded or better visualized. The process of transforming the degrade mode of content in acquired original image to better understandable image is called as image enhancement and image enhancement process uses different approaches as filtering approaches, frameworks, algorithms in order to get the clarity in the images which are often corrupted by the noise, blur and artifacts.

The digital image examination is done in accurate manner by histogram and enhancement process first uses the histogram before perform any task of image enhancement which helps in yielding the better quality image. The X-axis and Y-axis of the histogram represents the 0 to 255 (on X-axis) and number of pixels (Y-axis). The most popular enhancement schemes are contrast enhancement and filtering.

The satisfactory factors which predicts the quality of the image relies on adverse factors like abnormal lighting conditions as seen in the evening time, capturing device failure etc. These types of conditions results in the low quality image and in some conditions degraded image will be the outcome. So the undesirable image content either by environmental issues or manmade errors which is technically called as aesthetic and pragmatic needs enhancement process to make the undesirable form of content to understandable form of content. Image enhancement schemes are already in usage in various imaging devices for better tone mapping and in the end all this process is performing to provide better visualized content to the human visual system.

When the image is acquired by using digital sensors then the resultant raw image with big bit length makes it incompatible to be displayed in normal displays and this problem is analyzed in early ages of digital image processing. After research for decades the problem is resolved by using popular techniques namely gamma correction which makes raw format of image to display on the normal displays by using suitable dynamic range.

2. Problem Statement

Adaptive image enhancement is an important digital image processing aspect which helps to solve various issues occurs in the real time in many research fields. Although tremendous has been registered in the past two decades to get high quality images but still acquiring the original image is a area of concern and image enhancement needs more attention to get suitable image with substantial content which is visualized in better way by human visual system.

In this work generalized image enhancement model is proposed to tackle the drawbacks like color consistency, tone correction, abnormal lighting conditions, imaging system failure, etc.

Traditional image enhancement algorithms are relied on single framework based which fails to meet the practical requirements in terms of producing better quality with good tonal correction for human perception.

An integrated image enhancement model namely generalized image enhancement model is designed by integrate the non-linear white balance and contrast enhancement into unified framework based on the convex programming. The proposed uses different parameters of various enhancement techniques into consideration to create a meaningful joint strategy image enhancement model and finally extensive experimental results show the effectiveness of the proposed over traditional image enhancement techniques. Finally the computational complexity is also analyzed.

3. Aim and Objectives

A. Aim

The main aim of the project is to create adaptive enhanced image content by enhancing the undesirable image using the generalized equalization model

B. Objectives

- Initial step is to establish the generalized equalization model for adaptive image enhancement by properly analyzing the relationship between the image histogram and contrast

- Acquisition of the image by cost effective imaging devices results in undesirable form of images and usage of imaging model along with the linear transform mechanism maps the image into ideal from original (White balancing)
- Restoring the degraded mode information to better visualized information is done by using the contrast enhancement
- A unified model is proposed in this work by taking different parameters such as non linearity, tone distortion, etc belongs to various image enhancement techniques.
- Integration of non-linear contrast enhancement and white balancing approaches are done by using the convex programming

4. Literature Review

In this chapter, a brief description of adaptive image enhancement works by some prominent authors is presented. Finally tabular column is presented to give the information about the parameters and limitations about the works discussed here.

A. A new image enhancement algorithm which deals with dark regions and edges are proposed by ADIN RAMIREZ RIVERA, BYUNGYONG RYU, AND OKSAM CHAE in the year 2012 [1]. Generally when the images are captured in abnormal lighting conditions it results in the dark images which has tiny amount of brightness. The intention of the method is to preserve flat regions information by smoothness, gradient (edge) sharpening and enhancing dark regions. The outcome of this work is to maximum enhancement by adaptively creating mapping functions producing the ad hoc transformation to every individual image.

B. A non linear transform based color image enhancement approach is proposed by DEEPAK GHIMIRE AND JOONWHOAN LEE in the 2011 [2]. RGB color space is the basic color space for color images but RGB color space won't accept any changes in terms of brightness and angle. In this work for processing the image to create th meaningful enhanced image RGB to HSV color space is done. Here the enhancement process is carried on color image and processing of the color image is based on the HSV (hue saturation value) and in this work illuminance component V of the HSV color space is the key component for image enhancement and remaining two components of the H and S are kept unchanged.

C. Multiscale retinex image enhancement scheme based on fusion approach for color restoration is proposed by SUDHARSAN PARTHASARATHY, PRAVEEN SANKARAN in the year 2012 [3]. Generally cost effective imaging systems captured images are low in quality and the display won't display the image in reliable way. Multi scale retinex algorithm has two important steps to enhance the image based on contrast parameter, in the initial step gain values of each and every pixel is taken into consideration and in the latter step the background power consumption is minimized for better visualization of the image. Displays like organic light emitting diode (OLED) uses the multi scale retinex algorithm for good quality of vision and the

entire process is automatically carried on by automatic computer vision system. Adaptive image enhancement is an important step in the situation where the image is captured by cost effective imaging systems results in abnormal images.

5. Proposed Methodology

5.1 Initialization

The image representation is done in two ways (i) Two dimensional image representation where content can be perceived by the human visual system (ii) Representing the digital image content in graphical way for better analysis of pixel statistics in the form of bars (technically called bins). In order to process the digital image which in degraded way both representations are taken into consideration for providing more enhanced image in accurate manner. In literature wide range of works have reported on adaptive image enhancement based on fuzzy, filters, algorithms, and transforms, but hardly these approaches are succeed to attain enhanced image in approximate manner.

An adaptive image enhancement approach is presented in this paper to attain good image enhancement for better perception of content in the digital image. Initially a relationship between the non-linear image contrast and histogram is analyzed to establishing the proposed model namely generalized image enhancement model. In proposed model a series of mathematical functions and definitions are proposed for analyzing non linearity, tone distortion and context free contrast. All parameters relationships are taken into considerations based on the different parameters in the joint model. The proposed non-linear generalized equalization model combines the all histogram based toned mapping algorithms and the generalized algorithm based on convex programming and joint strategy of white balancing and non-linear contrast. Both white balancing image enhancement method and adaptive contrast enhancement are unified for the creation of the generalized equalization model
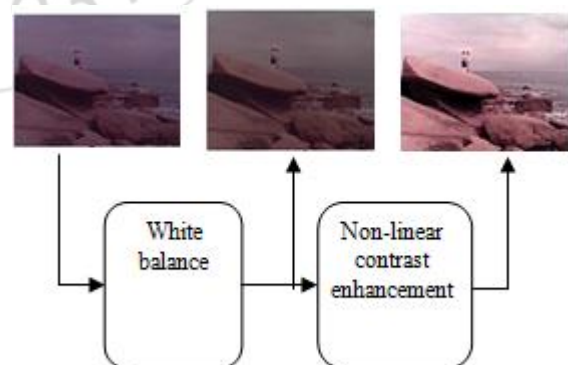

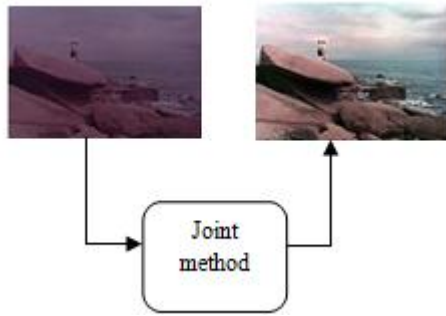**Figure 3:** Representation of Traditional enhancement strategy

Figure 4: Representation of adaptive enhancement strategy

5.2 White balancing

RGB color space is considered as the primary source to notate the color image. The acquisition of the digital image by using cost effective digital sensors in abnormal lighting conditions results in color bias. Color bias is referred as the problem of leaning one of the primary colors into another and when it happens it results in the evolution of the new color i.e. secondary color. To create the good correlations between the primary colors is the primary task accomplished by estimating the light source and once th creation of the good correlation between the primary colors fails then linear transform is vividly applied on the image to map the first image.

5.3 Non-linear contrast enhancement

Digital image processing is combination of many fundamental steps and image restoration is the one of the important which is still considered as the area of concern in the field of digital image processing.

As reported in the literature image restoration process is carried on based on the contrast enhancement algorithms. Restoration process recovers original image information from degraded media. Among all reported contrast enhancement approaches global histogram equalization is the popular choice for image restoration. Other contrast enhancement approaches include as follows
(a) Local histogram equalization
(b) Spatial filtering image enhancement
(c) Texture synthesis approach
(d) Transform based methods

5.4 Histogram Based Analysis (White Balancing)

Image enhancement has prominent role in all image processing applications and white balancing is popular mechanism. The key factors in histogram based analysis in terms of white balancing are color constancy and relationship establishment. Color constancy approach in traditional focus on the leaning based systems while white balancing focus on low level approach.

The digital image expressed by suing Lambertian surface model is as follows

$$f_c = \int r(\lambda)\, l(\lambda)\, m_c(\lambda)\, d\lambda \qquad (1)$$

The above expression consists of for imporatnt parameters which helps in image enhancement process namely visble

light wavelength represented by λ, surface reflectance is represented by. $r(\lambda)$, light source representation is by $l(\lambda)$ and finally (λ) represents the camera sensitivity. The image in the Lambertian surface model is represented in the RGB color space which helps in estimating the light sources which is totally different from the paper work. The RGB color space consist of three channels and another widely acceptance approach for color constancy is gray world hypothesis which assumes average reflectance. Finally both these assumptions are unified as follows

$$\left(\frac{\int |f(x)|^{\alpha} dx}{\int dx}\right)^{\frac{1}{\alpha}} = Ce \qquad (2)$$

The left side of the expression 2 can be rewritten based on the image histogram viewpoint as

$$\left(\frac{\int |f(x)|^{\alpha} dx}{\int dx}\right)^{\frac{1}{\alpha}} = \begin{pmatrix} (P_r^T)^{\frac{1}{\alpha}} \\ (P)^{\frac{T}{g}} \\ ((P)^{\frac{T}{b}}) \end{pmatrix} \qquad (3)$$

The connection between the histogram and white balancing sis notated by the expression 3 and the resultant image is as follows

$$e_C(\alpha) = \frac{(P_C^T h_C^{\alpha})^{\frac{1}{\alpha}}}{\sqrt{\sum_{c=r,g,b}(P_C^T h_C^{\alpha})^{\frac{2}{\alpha}}}} \qquad (4)$$

Finally the resultant of the white balancing in terms of image histogram is denoted by $\hat{h}_C$ and $\hat{h}_C$ is computed as follows

$$\hat{h}_C = \frac{1}{e_C(\alpha)\sqrt{3}}\hat{h}_C \qquad (5)$$

Th white balancing image enhancement process is linear in approach results in the good quality image but fails to give original content as output image. The usage of the linear transformation is the key factor in the white balancing process. In the latter section analytical differences between the contrast enhancement and white balancing are displayed based on the linear transformations

5.5 Histogram Based Analysis (Adaptive Contrast Enhancement)

Contrast and brightness are two key factors for practical visualization 2D signal to human visual system as image. After white balancing in terms of histogram, contrast enhancement is popular image enhancement mechanism which has wide range varieties.

The representation of the context free contrast is as follows

$$C = P_C^T S_C \qquad (6)$$

The contrast enhancement definition allows to achieve maximum contrast levels by binary image, minimizes the contrast as zero when the image is taken as constant. The achieved contrast levels are represented as follows

$$\hat{S}_C = argmax\ P_C^T S_C s.t\ \sum_{i=1}^{K} S_{ci} = L_C\ ,S_{Ci} \geq d \quad (7)$$

Where the first constraint makes sure that the output image still has a suitable dynamic range and the second constraint denotes the minimum distance between adjacent gray levels as d.

$$h_{ci} - C \sum_{j=n}^{i} P_{Ci} \qquad (8)$$

Paper ID: ART20162823

Here C ,is a constant. Eq. (8) also gives a relationship between histogram and the distance between adjacent intensity levels, as following shows

$$\hat{S}_{ci} = \hat{h}_{ci} - \hat{h}_{c,i-1} = \hat{C}_{pci} \qquad (9)$$

According to (8), (9), histogram equalization is equivalent to solving following optimization problem

$$\hat{S_c} = argmax \frac{1}{\|P_C^{-1}S_C\|}, \qquad (10)$$

$$S.t. \sum_{i=1}^{K} S_{ci} = L_C, \qquad S_{ci} \geq d$$

The performance of histogram equalization is not optimal in most situations. The essential reason for its limited performance is the questionable assumption that the histogram of ideal image obeys uniform distribution. To get better equalization result, we need to find a better distribution which is a big challenge. Recently, some adaptive histogram equalization methods are pro-posed but gave neither a clear definition of contrast nor an explicit objective function of contrast enhancement like (7), (10) shows. A common feature of all the enhancement methods mentioned above is that the transform of histogram is non-linear, which is different from white balancing.

5.6 Proposed Method

The aims of establishing the non-linear generalized equalization model include: 1) giving a unified explanation to white balancing problem and contrast enhancement problem; 2) providing an explicit objective function for these two problems and proposing a joint algorithm for them; 3) controlling the performance of the algorithm by as few parameters as possible. The proposed model is inspired by (7), (10). Although (7),(10) seem to be very different, if we regard the order of and

$$\hat{S}_C = argmax \frac{1}{\|P_C^{-\beta}S_C\|n}$$

$$S.t. \sum_{i=1}^{K} S_{ci} = L_C, \qquad S_{ci} \geq d \qquad (11)$$

Both (10) and (7) have interesting relationships with (11)

According to the analysis above, (11) provides a reasonable and unified definition with the objective function of contrast enhancement. We will further take white balancing into the model. Based on (4), (11), we formulate the generalized equalization model mathematically as follows

$$\hat{S_C} = argmax \sum_{c=r,g,b} \|P_C^{-1}S_C\|_n,$$

$$S.t \sum_{i=1}^{K} S_{ci} = \frac{1}{\theta_c(\alpha)\sqrt{3}} \sum_{i=1}^{K} S_{ci}, \qquad S_{ci} \geq (12)$$

$$d$$

$$G = \frac{P_C^T S_C}{P_C^T S_C}, NL = \|\nabla(\hat{S}_C - \hat{S}_C)\|2 \qquad (13)$$

However, separate nonlinear transform of histograms of three channels may cause tone distortion. In the next section, we will theoretically prove that the proposed method, with a suitable configuration of parameters, can achieve a best trade-off between contrast enhancement and tone adjustment.
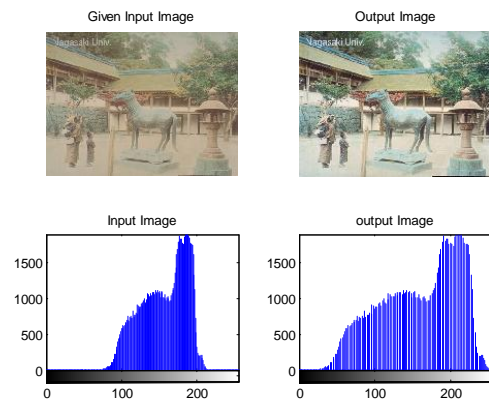
6. Results and Analysis

Figure 2: Adaptive image enhancement by non-linear generalized equalization model (Horse image) Elapsed time is 0.366000 seconds

7. Conclusion

Adaptive image enhancement is the fundamental step in the image processing to get better understandable image from low quality degraded mode. In this paper a novel image enhancement method based on generalized model is proposed based on image histogram and contrast relationship. Finally the experimental results conclude that integration of the non-linear contrast enhancement and white balancing results in the better quality image which can perceived by the human visual system in pleasant way. In this model different adaptive image enhancement methods are unified to yield the better image with low complexity and high performance than the traditional enhancement algorithms.

References

[1] A. R. Rivera, B. Ryu, and O. Chae, "Content-Aware Dark Image Enhancement Through Channel Division" IEEE Transactions On Image Processing, Vol. 21, No. 9, September 2012

[2] D. Ghimire and J. Lee ," Nonlinear Transfer Function-Based Local Approach for Color Image Enhancement," IEEE Transactions on Consumer Electronics, Vol. 57, No. 2, May 2011.

[3] S. Parthasarathy, P. Sankaran," Fusion Based Multi Scale RETINEX with Color Restoration for Image Enhancement," 2012 International Conference on Computer Communication and Informatics (ICCCI - 2012), Jan. 10 – 12, 2012, Coimbatore, India.

[4] S. Bronte, L. M. Bergasa, P. F. Alcantarilla, "Fog Detection System Based on Computer Vision Techniques".

[5] Z. Chaofu, M. Li-ni, J. Lu-na ," Mixed Frequency domain and spatial of enhancement algorithm for infrared image", 2012 9th International Conference on Fuzzy Systems and Knowledge Discovery (FSKD 2012).

[6] A. Poljicak, L. Mandic, M. Strgar Kurecic ," Improvement of the Watermark Detector Performance Using Image Enhancement Filters," IWSSIP 2012,11-13 April 2012,Vienna, Austria.

[7] S. W. Jung, J.Y. Jeong, and S.J. K ," Sharpness Enhancement of Stereo Images Using Binocular Just-Noticeable Difference," IEEE Transactions On Image Processing, Vol. 21, No. 3, March 2012.

[8] H. Zhang, Q. Zhao, Lu Li, Y.c. Li, Y.h. You ," Muti-scale Image Enhancement Based on Properties of Human Visual System," 2011 4th International Congress on Image and Signal Processing.

[9] R. K. Jha, R. Chouhan, P. K. Biswas ," Noise-induced Contrast Enhancement of Dark Images using Non-dynamic Stochastic Resonance," 978-1-4673-0816-8/12S ©2012 IEEE.

[10] K. Hasikin, N. A. Mat Isa ," Enhancement of the low contrast image using fuzzy set theory," 2012 14th International Conference on Modelling and Simulation

NEW VLSI ARCHITECTURE FOR EXPLOITING CARRY-SAVE ARITHMETIC USING VERILOG HDL

Medishetti.vijitha [1]   **Chiruvella Suresh**[2]   **K.Hymavathi**[3]

vijithamedishetti@gmail.com[1]   chiruvellasuresh@gmail.com[2]

[1]PG Scholar, Dept of ECE, Swami Ramananda Thirtha Institute of Science and Technology, Nalgonda, Telangana,

[2]Assistant Professor, Dept of ECE, Swami Ramananda Thirtha Institute of Science and Technology, Nalgonda, Telangana,

[3]Associate Professor, HOD, Dept of ECE, Swami Ramananda Thirtha Institute of Science and Technology, Nalgonda, Telangana

Abstract:- The selective use of carry-save arithmetic, where appropriate, can accelerate a variety of arithmetic-dominated circuits. Carry-save arithmetic occurs naturally in a variety of DSP applications, and further opportunities to exploit it can be exposed through systematic data flow transformations that can be applied by a hardware compiler. Field-programmable gate arrays (FPGAs), however, are not particularly well suited to carry-save arithmetic. To address this concern, we introduce the "field programmable counter array" (FPCA), an accelerator for carry-save arithmetic intended for integration into an FPGA as an alternative to DSP blocks. In addition to multiplication and multiply accumulation, the FPCA can accelerate more general carry-save operations, such as multi-input addition (e.g., add integers) and multipliers that have been fused with other adders. Our experiments show that the FPCA accelerates a widervariety of applications than DSP blocks and improves performance, area utilization, and energy consumption compared with soft FPGA logic.

Index Terms—Carry-save arithmetic, field-programmable gate array (FPGA),

I. INTRODUCTION

Modern embedded systems target high-end application domains requiring efficient implementations of computationally intensive digital signal processing (DSP) functions. The incorporation of heterogeneity through specialized hardware accelerators improves performance and reduces energy consumption [1]. Although application-specific integrated circuits (ASICs) form the ideal acceleration solution in terms of performance and power, their inflexibility leads to increased silicon complexity, as multiple instantiated ASICs are needed to accelerate various kernels. Many researchers have proposed the use of domain-specific coarse-grained reconfigurable accelerators in order to increase ASICs' flexibility without significantly compromising their performance.

High-performance flexible data paths have been proposed to efficiently map primitive or chained operations found in the initial data-flow graph (DFG) of a kernel. The templates of complex chained operations are either extracted directly from the kernel's DFG or specified in a predefined behavioral template library. Design decisions on the accelerator's datapath highly impact its efficiency. Existing works on coarse-grained reconfigurable datapaths mainly exploit architecture-level optimizations, e.g., increased instruction-level parallelism (ILP) . The domain-specific architecture generation algorithms of [5] and [9] vary the type and number of computation units achieving a customized design structure. The flexible architectures were proposed exploiting ILP and operation chaining. Recently aggressive operation chaining is adopted to enable the computation of entire sub expressions using multiple ALUs with heterogeneous arithmetic features.

The aforementioned reconfigurable architectures exclude arithmetic optimizations during the architectural synthesis and consider them only at the internal circuit structure of primitive components, e.g., adders, during the logic synthesis . However, research activities have shown that the arithmetic optimizations at higher abstraction levels than the structural circuit one significantly impact on the datapath performance. In [10], timing-driven optimizations based on carry-save (CS) arithmetic were performed at the post-Register Transfer Level (RTL) design stage. In [11], common subexpression elimination in CS computations is used to optimize linear DSP circuits. Verma *et al.* [12] developed transformation techniques on the application's DFG to maximize the use of CS arithmetic prior the actual datapath synthesis. The aforementioned CS optimization approaches target inflexible datapath, i.e., ASIC, implementations. Recently, a flexible architecture combining the ILP and pipelining techniques with the CS-aware operation chaining has been proposed. However, all the aforementioned solutions feature an inherent limitation, i.e., CS optimization is bounded to merging only additions/subtractions. A CS to binary conversion is inserted before each operation that differs from addition/subtraction, e.g.,multiplication, thus, allocating multiple CS to binary conversions that heavily degrades performance due to time-consuming carry propagations.

In this brief, we propose a high-performance architectural scheme for the synthesis of flexible hardware DSP accelerators by combining optimization techniques from both the architecture and arithmetic levels of abstraction. We introduce a flexible datapath architecture that exploits CS optimized templates of chained operations. The proposed architecture comprises flexible computational units (FCUs), which enable the execution of a large set of operation templates found in DSP kernels. The proposed accelerator architecture delivers average gains in area-delay product and in energy consumption compared to state-of-art flexible datapaths , sustaining efficiency toward scaled technologies.

II. Carry-Save Arithmetic: Motivational Observations and Limitations

CS representation has been widely used to design fast arithmetic circuits due to its inherent advantage of eliminating the large carry-propagation chains. CS arithmetic optimizations rearrange the application's DFG and reveal multiple input additive operations (i.e., chained additions in the initial DFG), which can be mapped onto CS compressors. The goal is to maximize the range that a CS computation is performed within the DFG. However, whenever a multiplication node is interleaved in the DFG, either a CS to binary conversion is invoked or the DFG is transformed using the distributive property . Thus, the aforementioned CS optimization approaches have limited impact on DFGs dominated by multiplications, e.g., filtering DSP applications.

In this brief, we tackle the aforementioned limitation by exploiting the CS to modified Booth (MB) recoding each time a multiplication needs to be performed within a CS-optimized datapath. Thus, the computations throughout the multiplications are processed using CS arithmetic and the operations in the targeted datapath are carried out without using any intermediate carry-propagate adder for CS to binary conversion, thus improving performance.

III. Proposed Flexible Accelerator

The proposed flexible accelerator architecture is shown in Fig. 1. Each FCU operates directly on CS operands and produces data in the same form1 for direct reuse of intermediate results. Each FCU operates on 16-bit operands. Such a bit-length is adequate for the most DSP datapaths , but the architectural concept of the FCU can be straightforwardly adapted for smaller or larger bit-lengths. The

number of FCUs is determined at design time based on the ILP and area constraints imposed by the designer. The CStoBin module is a ripple-carry adder and converts the CS form to the two's complement one.

The register bank consists of scratch registers and is used for storing intermediate results and sharing operands among the FCUs. Different DSP kernels (i.e., different register allocation and data communication patterns per kernel) can be mapped onto the proposed architecture using post-RTL datapath interconnection sharing techniques.

The control unit drives the overall architecture (i.e., communication between the data port and the register bank, configuration words of the FCUs and selection signals for the multiplexers) in each clock cycle.
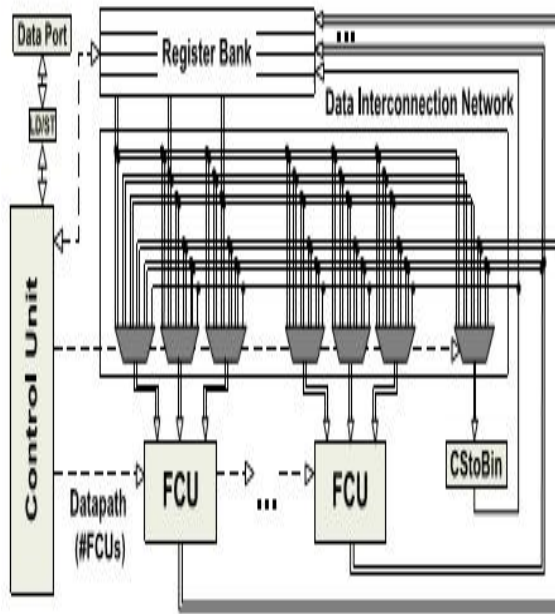
Fig. 1. Abstract form of the flexible datapath.

A. Structure of the Proposed Flexible Computational Unit

The structure of the FCU (Fig. 2) has been designed to enable high-performance flexible operation chaining based on a library of operation templates. Each FCU can be configured to any of the T1–T5 operation templates shown in Fig. 3. The proposed FCU enables intratemplate operation chaining by fusing the additions performed before/after the multiplication &performs any partial operation template of the following complex operations:

$$W^* = A \times (X^* + Y^*) + K^* \qquad (1)$$

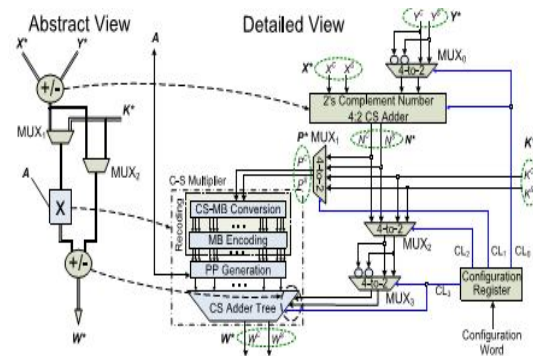$$W^* = A \times K^* + (X^* + Y^*) \qquad (2)$$

Fig. 2. FCU.

The following relation holds for all CS data: $X^* = \{ X^C, X^S \} = X^C + X^S$. The operand A is a two's complement number. The alternative execution paths in each FCU are specified after properly setting the control signals of the multiplexers MUX1 and MUX2 (Fig. 2). The multiplexer MUX0 outputs Y^* when CL0 = 0 (i.e., $X^* + Y^*$ is carried out) or Y^* when $X^* - Y^*$ is required and CL0 = 1. The two's complement 4:2 CS adder produces the $N^* = X^* + Y^*$ when the input carry equals 0 or the $N^* = X^* - Y^*$ when the input carry equals 1. The MUX1 determines if N^* (1) or K^* (2) is multiplied with A. The MUX2 specifies if K^* (1) or N^* (2) is added with the multiplication product. The multiplexer MUX3 accepts the output of MUX2 and its 1's complement and outputs the former one when an addition with the multiplication product is required (i.e., CL3 = 0) or the later one when a subtraction is carried out (i.e., CL3 = 1). The 1-bit ace for the subtraction is added in the CS adder tree.

The multiplier comprises a CS-to-MB module, which adopts a recently proposed technique to recode the 17-bit P* in its respective MB digits with minimal carry propagation. The multiplier's product consists of 17 bits. The multiplier includes a compensation method for reducing the error imposed at the product's accuracy by the truncation technique. However, since all the FCU inputs consist of 16 bits and provided that there are no overflows, the 16 most significant bits of the 17-bit W* (i.e., the output of the Carry-Save Adder (CSA) tree, and thus, of the FCU) are inserted in the appropriate FCU when requested.

B. DFG Mapping Onto the Proposed FCU-Based Architecture

In order to efficiently map DSP kernels onto the proposed FCU-based accelerator, the semiautomatic synthesis methodology has been adapted. At first, a CS-aware transformation is performed onto the original DFG, merging nodes of multiple chained additions/subtractions to 4:2 compressors. A pattern generation on the transformed DFG clusters the CS nodes with the multiplication operations to form FCU template operations (Fig. 3). The designer selects the FCU operations covering the DFG for minimized latency. Given that the number of FCUs is fixed, a resource-constrained scheduling is considered with the available FCUs and CStoBin modules determining the resource constraint set. The clustered DFG is scheduled, so that each FCU operation is assigned to a specific control step. A list-based scheduler has been adopted considering the mobility2 of FCU operations. The FCU operations are scheduled according to descending mobility. The scheduled FCU operations are bound onto FCU instances and proper configuration bits are generated. After completing register allocation, a FSM is generated in order to implement the control unit of the overall architecture.
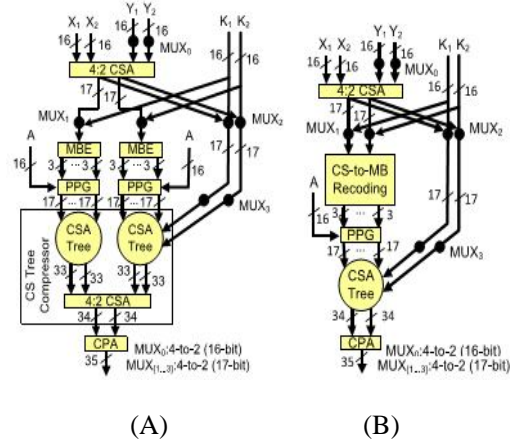

(A)   (B)

Fig.4. Typical chaining of addition–multiplication–addition operations reflecting T1 template of Fig. 3. Its design is based on (A) CS optimizations with multiplication distribution (B) incorporating the CS-to-MB recoding concept.
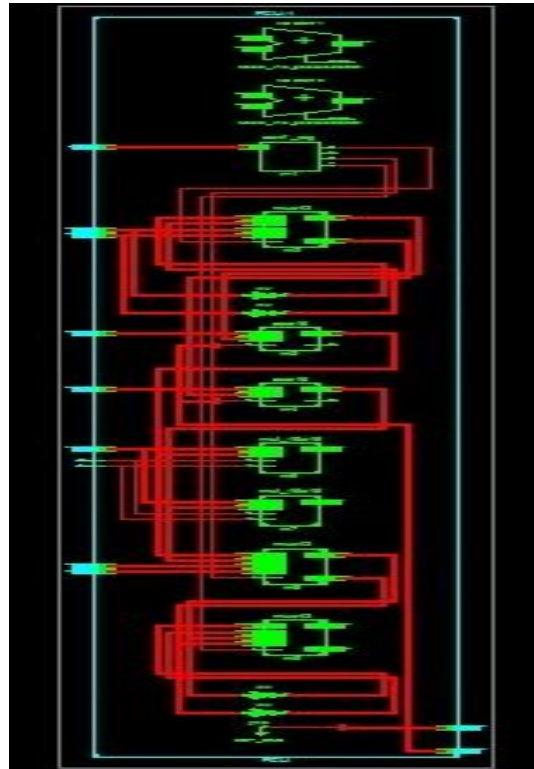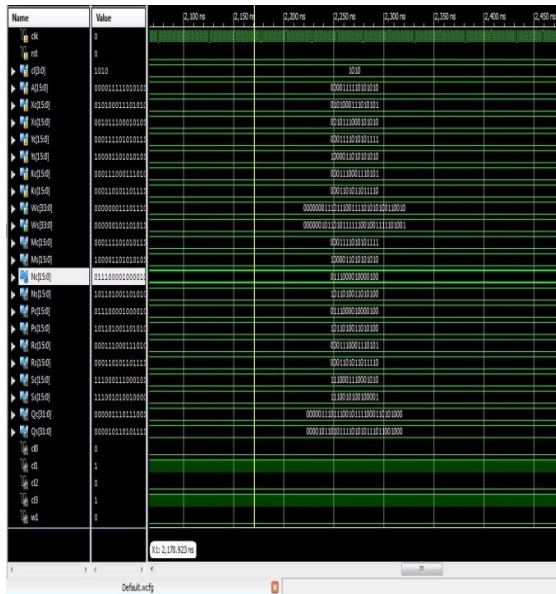
IV. SIMULATION RESULTS

FIG.5 RTL

FIG.6 Output Waveform

V. CONCLUSION

In this brief, we introduced a flexible accelerator architecture that exploits the incorporation of CS arithmetic optimizations to enable fast chaining of additive and multiplicative operations. The proposed flexible accelerator architecture is able to operate on both conventional two's complement and CS-formatted data operands, thus enabling high degrees of computational density to be achieved. Theoretical and experimental analyses have shown that the proposed solution forms an efficient design tradeoff point delivering optimized latency/area and energy implementations.

REFERENCES

[1] P. Ienne and R. Leupers, Customizable Embedded Processors: Design Technologies and Applications. San Francisco, CA, USA: Morgan Kaufmann, 2007.

[2] P. M. Heysters, G. J. M. Smit, and E. Molenkamp, "A flexible and energy-efficient coarse-grained reconfigurable architecture for mobile systems," J. Supercomput., vol. 26, no. 3, pp. 283–308, 2003.

[3] B. Mei, S. Vernalde, D. Verkest, H. D. Man, and R. Lauwereins, "ADRES: An architecture with tightly coupled VLIW processor and coarse-grained reconfigurable matrix," in Proc. 13th Int. Conf. Field Program. Logic Appl., vol. 2778. 2003, pp. 61–70.

[4] M. D. Galanis, G. Theodoridis, S. Tragoudas, and C. E. Goutis, "A high-performance data path for synthesizing DSP kernels," IEEE Trans. Comput.-Aided Design Integr. Circuits Syst., vol. 25, no. 6, pp. 1154–1162, Jun. 2006.

[5] K. Compton and S. Hauck, "Automatic design of reconfigurable domainspecific flexible cores," IEEE Trans. Very Large Scale Integr. (VLSI) Syst., vol. 16, no. 5, pp. 493–503, May 2008.

[6] S. Xydis, G. Economakos, and K. Pekmestzi, "Designing coarse-grain reconfigurable architectures by inlining flexibility into custom arithmetic data-paths,"Integr., VLSI J., vol. 42, no. 4, pp. 486–503, Sep. 2009.

[7] S. Xydis, G. Economakos, D. Soudris, and K. Pekmestzi, "High performance and area efficient flexible DSP datapath synthesis," IEEE Trans. *Very Large Scale Integr. (VLSI) Syst.*, vol. 19, no. 3, pp. 429–442, Mar. 2011.

[8] G. Ansaloni, P. Bonzini, and L. Pozzi, "EGRA: A coarse grained reconfigurable architectural template," *IEEE Trans. Very Large Scale Integr. (VLSI) Syst.*, vol. 19, no. 6, pp. 1062–1074, Jun. 2011.

[9] M. Stojilovic, D. Novo, L. Saranovac, P. Brisk, and P. Ienne, "Selective flexibility: Creating domain-specific reconfigurable arrays," *IEEE Trans. Comput.-Aided Design Integr. Circuits Syst.*, vol. 32, no. 5, pp. 681–694, May 2013.

[10] T. Kim and J. Um, "A practical approach to the synthesis of arithmetic circuits using carry-save-adders," IEEE Trans. Comput.- Aided Design Integr. Circuits Syst., vol. 19, no. 5, pp. 615–624, May 2000.

[11] A. Hosangadi, F. Fallah, and R. Kastner, "Optimizing high speed arithmetic circuits using three-term extraction,"

in Proc. Design, Autom. Test Eur. (DATE), vol. 1. Mar. 2006, pp. 1–6.

[12] A. K. Verma, P. Brisk, and P. Ienne, "Data-flow transformations to maximize the use of carry-save representation in arithmetic circuits," IEEE Trans. Comput.-Aided Design Integr. Circuits Syst., vol. 27, no. 10, pp. 1761–1774, Oct. 2008.

BIOGRAPHIES

Medishetti.vijitha is currently a PG scholar of VLSI System Design in ECE Department. She received B.TECH degree from Madhira Institute of Technology and science, JNTU. Her current research interest includes Analysis & Design of VLSI System Design.

**Chiruvella Suresh** Currently working as Assistant Professor Department of Electronics and Communication Engineering in Swami Ramananda Thirtha Institute of Science and Technology, Nalgonda, Telangana, India. His current research interest includes VLSI Design.

K.Hymavathi Currently working as Associate Professor, Department of Electronics and Communication Engineering in Swami Ramananda Thirtha Institute of Science and Technology, Nalgonda, Telangana, India. Her current research interest includes VLSI Design.
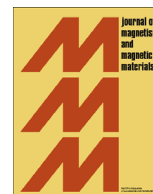
Current Perspectives

Magnetic and dielectric properties of Co doped nano crystalline Li ferrites by auto combustion method

CrossMark

G. Aravind [a], M. Raghasudha [b],*, D. Ravinder [a], R. Vijaya Kumar [c]

[a] Department of Physics, Osmania University, Hyderabad 500007, Telangana State, India
[b] Department of Chemistry, Osmania University, Hyderabad 500007, Telangana State, India
[c] School of Physics, University of Hyderabad, 500046 Telangana State, India

ARTICLE INFO

ABSTRACT

The ultra fine particles of the cobalt substituted lithium ferrites with the formula $[Li_{0.5}Fe_{0.5}]_{1-x}Co_xFe_2O_4$ ($0.0 \leq x \leq 1.0$) were synthesized by low temperature citrate-gel auto combustion method. Structural characterization of the samples was carried out using XRD studies and FESEM (Field Emission Scanning Electron Microscopy) analysis. XRD studies confirms the formation of single phased spinel structure with crystallite size in the range of 36–43 nm. The M–H loops have been traced using Vibrating Sample Magnetometer (VSM) for all the compositions at room temperature and hysteresis parameters were evaluated. The hysteresis loops of the prepared samples show clear saturation at an applied field of ± 20 k Oe and the loops were highly symmetric in nature. The dielectric parameters such as dielectric constant (ε'), dielectric loss tangent ($\tan \delta$) of the samples were studied as a function of frequency in the range of 20 Hz to 2 MHz at room temperature using LCR Meter. The dielectric constant and loss tangent of the samples show a normal dielectric behavior with frequency which reveals that the dispersion is due to the Maxwell-Wagner type interfacial polarization and hopping of electrons between the Fe^{2+} and Fe^{3+} ions.

© 2015 Elsevier B.V. All rights reserved.

1. Introduction

Nano crystalline spinel ferrites have been the subject of interest for many researchers due to their enhanced optical, structural, electrical and magnetic properties, when compared with their bulk counterparts. These properties of nano particles make them desirable for a variety of applications such as in electronics, optical devices, magnetic storage devices, coolants, MLCI applications [1]. Nano crystalline magnetic ferrites are also used as permanent magnets in many devices instead of pure metals because of their high resistivity, low eddy current loss, low magnetic loss and low cost. According to the crystal structure, spinel ferrites possess AB_2O_4 type crystal structure with tetrahedral (A) sites and octahedral (B) sites. They show various magnetic properties depending on their composition and cation distribution on the two sites. Various metal cations occupied in tetrahedral site and octahedral site tune the magnetic and dielectric properties of ferrites. Depending on occupancy of tetrahedral and octahedral sites, ferrites exhibit ferri-magnetic, anti-ferromagnetic, spin clusters and paramagnetic behavior [2]. Hence, many researchers have focused

on investigating the effect of transition metal ion doping in the spinel ferrite crystal lattice.

Various properties of ferrites suchas magnetic and electrical properties depend on their microstructure which is determined by various factors. They are quality of the raw materials used, sintering temperature, sintering time and the materials composition. The microstructure of the material developed during sintering is determined by particle size, shape, porosity, agglomeration, chemical and phase composition which are closely related to the processing technique [3].

Lithium and substituted lithium ferrites are promising materials for the microwave device applications since they are less sensitive to the stress and possess high Curie temperature (T_c). Lithium ferrites are used in microwave devices such as isolators, circulators, gyrators and phase shifters. They play a vital role in microwave latching devices, magnetic switching circuits. They can also be used as cathode materials in lithium batteries. Many researchers have reported the effect of magnetic and non-magnetic substitutions in lithium ferrites on their various properties [4–5].

The applications of lithium ferrites were restricted due to the difficulties experienced in sintering the prepared samples at the high temperatures. The irreversible loss of lithium and oxygen during sintering was the main cause that made lithium ferrites difficult to synthesize [6]. Spinel Ferrites can be synthesized by

---

* Corresponding author.
E-mail address: raghasudha_m@yahoo.co.in (M. Raghasudha).

various techniques viz., standard Ceramic method [7], Chemical co-precipitation method [8], Solid state reaction [9], Hydrothermal process [10], Micro-emulsion method [11] and sol–gel method [12].

The ceramic method has some inherent drawbacks such as, Poor compositional control, Chemical inhomogeneity, Coarse particle size, Introduction of impurities during grinding and requires high temperature ($> 1000\,^\circ$C). By using various wet chemical routes such as co-precipitation, sol–gel, freeze drying, spray drying etc. the particle size can be brought down at lower temperature compared to ceramic technique. These wet chemical methods are reproducible, low cost and requires low temperature. In the recent years, sol–gel method is the most effective method for the synthesis of pure and homogeneous nanoparticles at relatively low temperatures due to its potential to produce relatively large quantities of final product at low cost as compared to other chemical processes [13].

In the sol–gel auto combustion reaction method, if the organic fuel used is Citric acid, the method is called citrate-gel auto combustion method. In this method the citrate precursors decompose at temperature less than 500 °C and hence it has been possible to prepare spinel ferrites at relatively low temperatures by this method [14].

Hence, it is clear that the citrate sol–gel auto combustion method provides an easy alternative for the synthesis of lithium nano crystalline ferrites at low temperature sintering itself [15].

The magnetization studies were useful in understanding the arrangement of spins and the distribution of magnetic cations in the sub-lattice. It is a well known fact that the properties of the spinel ferrites were also sensitive to the presence of doped cations and amount of doping. The substitution of small amount of impurities changes the electrical and magnetic properties of ferrites. The modifications in the properties of lithium ferrites by the substitution of different ions have been studied by various researchers [16–17]. The authors have assumed that the substitution of non-magnetic lithium ion with magnetic cobalt ion may result in improvement of their magnetic and electrical properties. Moreover, there are very few reports on the synthesis and properties of single phased cobalt substituted lithium nano crystalline ferrite particles by the citrate gel auto-combustion method.

The present study reports the synthesis of nano crystalline cobalt substituted lithium ferrites using low temperature citrate-gel auto combustion method. Characterization, magnetic and dielectric properties of the prepared ferrites were also discussed in the present article.

2. Experimental technique

The properties of ferrites are profoundly influenced by the preparation conditions. Nano crystalline cobalt substituted lithium ferrites with the chemical formula $[Li_{0.5}Fe_{0.5}]_{1-x}Co_xFe_2O_4$ ($0.0 \leq x \leq 1.0$) were prepared by low temperature auto-combustion method. The synthesized ferrite samples were characterized by X-ray diffraction studies using Philips X-ray diffractometer (3710). The surface morphology of the samples was studied by Field Emission Scanning Electron Microscope (FE-SEM model-JSM-7610F).

The magnetic properties of the synthesized samples were measured by using Vibrating Sample Magnetometer (VSM, Model-155) and dielectric properties were measured by using Agilent E4980 LCR meter.

The starting materials used for the synthesis of Li–Co ferrites under investigation are Ferric nitrate–$Fe(NO_3)_2 9H_2O$, Cobalt nitrate–$Co(NO_3)_2 6H_2O$, Lithium nitrate–$LiNO_3$, Citric acid $C_6H_8O_7.H_2O$ and Ammonia solution–NH_3. All the raw materials used are 99.0% pure (Sigma Aldrich Company) and are used without any further purification.

Li–Co ferrite samples with desired composition were synthesized using citrate-gel auto combustion method. The detailed flow chart for this method was explained in our earlier publication [18–19]. Calculated quantities of above mentioned metal nitrates were dissolved in double distilled water and required amount of aqueous citric acid solution was added that acts as organic fuel. The mixture was placed on a magnetic stirrer for thorough stirring to get a homogeneous solution. Ammonia solution was added to this nitrate-citrate mixture to adjust the pH to 7. The mixed solution was heated on a magnetic hot plate at about 100 °C with uniform stirring and was evaporated to obtain a highly viscous gel described as precursor. The resultant gel was further heated on a hot plate maintained in a temperature range of 180–200 °C. Finally, when all water molecules were removed from the mixture, the viscous gel began rising with sodt mass. The gel gave a fast flameless self ignited combustion reaction with the evolution of large amounts of gaseous products. It started in the hot portion of the beaker and propagated from the bottom to the top like a volcanic eruption. The reaction was completed in a minute giving rise to dark gray product. The synthesized powders were sintered at 500 °C for 4 h in air at a slow heating rate of 5 °C/min and then furnace was cooled to room temperature. The cooled samples were ground using mortar and pestle for getting fine powdered samples.

The resulting samples were used for structural characterization using x-ray diffraction studies. Part of the prepared samples was x-ray examined by X-ray diffractometer using Cu-K$_\alpha$ radiation of wavelength (λ) 1.5405 Å with a scanning step increment of 0.02 and scanning rate of 2 °/min. The x-ray generator was operated at 40 kV and 30 mA. A specially designed silicon sample was used as the instrumental standard. The crystallite size (D) of the prepared samples has been estimated from the full-width half maxima (FWHM) of the strongest reflection of the plane (311) using Debye Scherer's formula as mentioned below

$$D = \frac{0.91\lambda}{\beta \cos\theta} \tag{1}$$

where β is the full width at half maximum and θ is the diffraction angle.

The disc shaped pellets of the ferrite samples with 13 mm diameter and 2 mm thickness were prepared by applying a pressure about 39.23×10^3 Pa. The measured density 'ρ_m' was calculated by the following expression [20],

$$\rho_m = \frac{M}{V} \tag{2}$$

where 'M' is the mass of the pellet that was determined using a digital balance, and 'V' is the volume of the pellet.

The specific surface area of the prepared samples was calculated from the following relation [21].

$$S = \frac{6000}{D\rho_m} \tag{3}$$

where D is the crystallite size and the ρ_m is the measured density.

The FE scanning electron microscope (FE-SEM) is a very useful tool for high-resolution surface imaging in the fields of nanomaterials science. Electron microscopes use a beam of highly energetic electrons to probe objects on a very fine scale. In standard electron microscopes, electrons are mostly generated by "heating" a tungsten filament (electron gun). On the other hand, in a field emission (FE) electron microscope, no heating but a so-called "cold" source is employed. The FE source reasonably combines with scanning electron microscopes (SEMs) whose development

has been supported by advances in secondary electron detector technology. The electron beam produced by the FE source is about 1000 times smaller than that in a standard microscope with a thermal electron gun. Hence, the image quality of the prepared samples was markedly improved [22].

The magnetic properties of the prepared Li–Co ferrite samples as a function of composition at 300 K were determined using a Vibrating Sample Magnetometer (VSM) at a maximum field of 20 kOe. Various magnetic parameters were measured from the hysteresis loops obtained from the VSM measurements.

The experimental magnetic moment per formula unit m_{exp} expressed in Bohr Magneton (μ_B) can be calculated using the following formula [23].

$$m_{exp} = \frac{M_w M_s}{5585} \tag{4}$$

where M_w is the molecular weight of the sample and M_s is the saturation magnetization in emu/g.

The magnetic anisotropic constant (K) can be related to the saturation magnetization (M_s) and magnetic coercivity (H_c) [24] as,

$$K = \frac{M_s H_c}{0.96} \tag{5}$$

To measure the dielectric properties, samples should be in the form of pellet, and these pellets were silver pasted for good ohmic contact, calcinated at 500 °C for 4 h at a heating rate of 4 °C/min. Using LCR meter, capacitance (c) and $\tan \delta$ (loss tangent) of the pellets were measured directly from the instrument. By using this data, dielectric constant (ε') of the prepared samples can be calculated using the following formula [25].

$$\text{Real part of dielectric constant} = \varepsilon' = \frac{cd}{A\varepsilon_0} \tag{6}$$

$$\text{Imaginary part of dielectric constant} = \varepsilon'' = \varepsilon' \tan \delta \tag{7}$$

Where 'c' is the capacitance, 'd' is the thickness and 'A' is the area of cross section of the pellet, ε_0 is the permittivity of free space. From these values, one can analyze the variation of dielectric constant (ε') and dielectric loss tangent ($\tan \delta$) with respect to frequency and composition.

3. Results and discussions

3.1. XRD studies

The X-ray diffraction analysis is a powerful non-invasive technique for characterizing crystal structure of the materials. Thus, in order to investigate the phase formation and micro structure, the XRD analysis was carried out on the synthesized samples. X-ray diffraction pattern of the prepared samples was shown in Fig. 1.

All Bragg's reflections have been indexed as (111), (220), (311), (400), (511) and (440) which confirmed the formation of well-defined single phased cubic spinel structure that belongs to the space group Fd3m with JCPDS card number 00-013-0207 without any impurity peak. The strongest reflection was observed from the (311) plane that indicates the spinel phase. Crystallite size and specific surface area of the nano crystalline Li–Co ferrite samples were calculated using the relations (1) and (2) and summarized in the Table 1.

From the table, it is observed that the average crystallite size of the prepared samples was in the range of 36–43 nm and specific surface area of the prepared samples was in the range of 31–36 m²/gm which shows the nano crystalline nature of the prepared samples. The specific surface area of the prepared ferrites
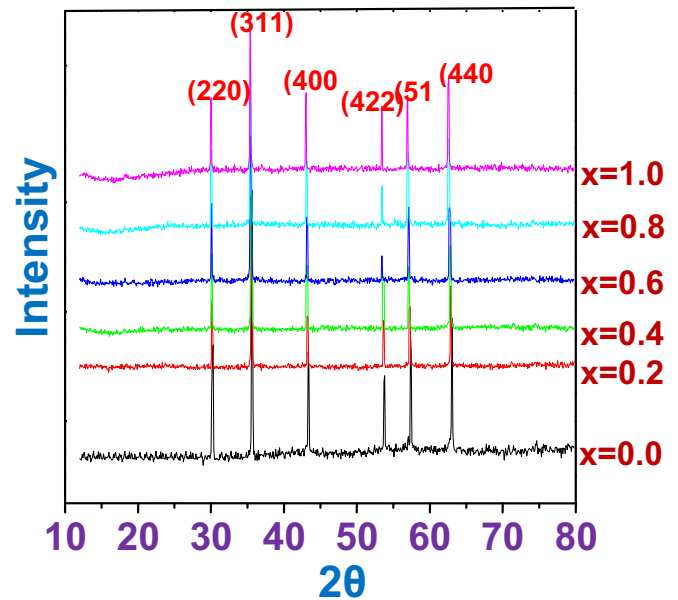

Fig. 1. XRD pattern of [Li$_{0.5}$Fe$_{0.5}$]$_{1-x}$Co$_x$Fe$_2$O$_4$ ferrites with $x = 0.0$–1.0.

Table 1
Crystallite size, Surface area of the prepared nano crystalline Li–Co ferrites.

Composition	Crystallite size (D) (nm)	Average grain size (nm) from FESEM micrograph	Surface area S (m²/gm)
Li$_{0.5}$Fe$_{2.5}$O$_4$	41.90	78	33.45
Li$_{0.4}$Co$_{0.2}$Fe$_{2.4}$O$_4$	43.01	85	31.99
Li$_{0.3}$Co$_{0.4}$Fe$_{2.3}$O$_4$	38.44	79	35.63
Li$_{0.2}$Co$_{0.6}$Fe$_{2.2}$O$_4$	37.57	87	36.05
Li$_{0.1}$Co$_{0.8}$Fe$_{2.1}$O$_4$	37.06	84	35.58
CoFe$_2$O$_4$	36.90	86	34.81

is the aggregation of the areas of the exposed surfaces of the ferrite particles present per unit mass. Crystallite size and the surface area are inversely proportional to each other and is evident from the Table 1. Lesser the crystallite size larger is the surface area of the ferrites which results in the improvement of their properties.

3.2. FE-SEM analysis

The structural morphology of prepared ferrite samples was studied using FE-SEM. The FE-SEM images of the samples were shown in Fig. 2. The average particle size of all the ferrite compositions calculated from FESEM images was in the range of 78–87 nm as depicted in Table 1. It is clear that the average grain size of the various ferrite compositions obtained from FESEM is larger than the crystallite size of the samples as calculated using XRD analysis (Table 2). This fact suggests that each grain is the resultant of agglomeration of number of nanocrystals. The micrographs show the agglomerated grainy structure with clusters of fine particles clinging together. The morphology of surface is almost uniform and regular having cubical to nearly spherical shaped particles. Such morphology of the samples demonstrates the fine particle nature.

3.3. Magnetic measurements

The room temperature magnetization measurements were carried out using Vibrating Sample Magnetometer. For the magnetic measurements, the ferrite samples were made in the form of pellets and were subjected to calcination at 500 °C for 4 h at a
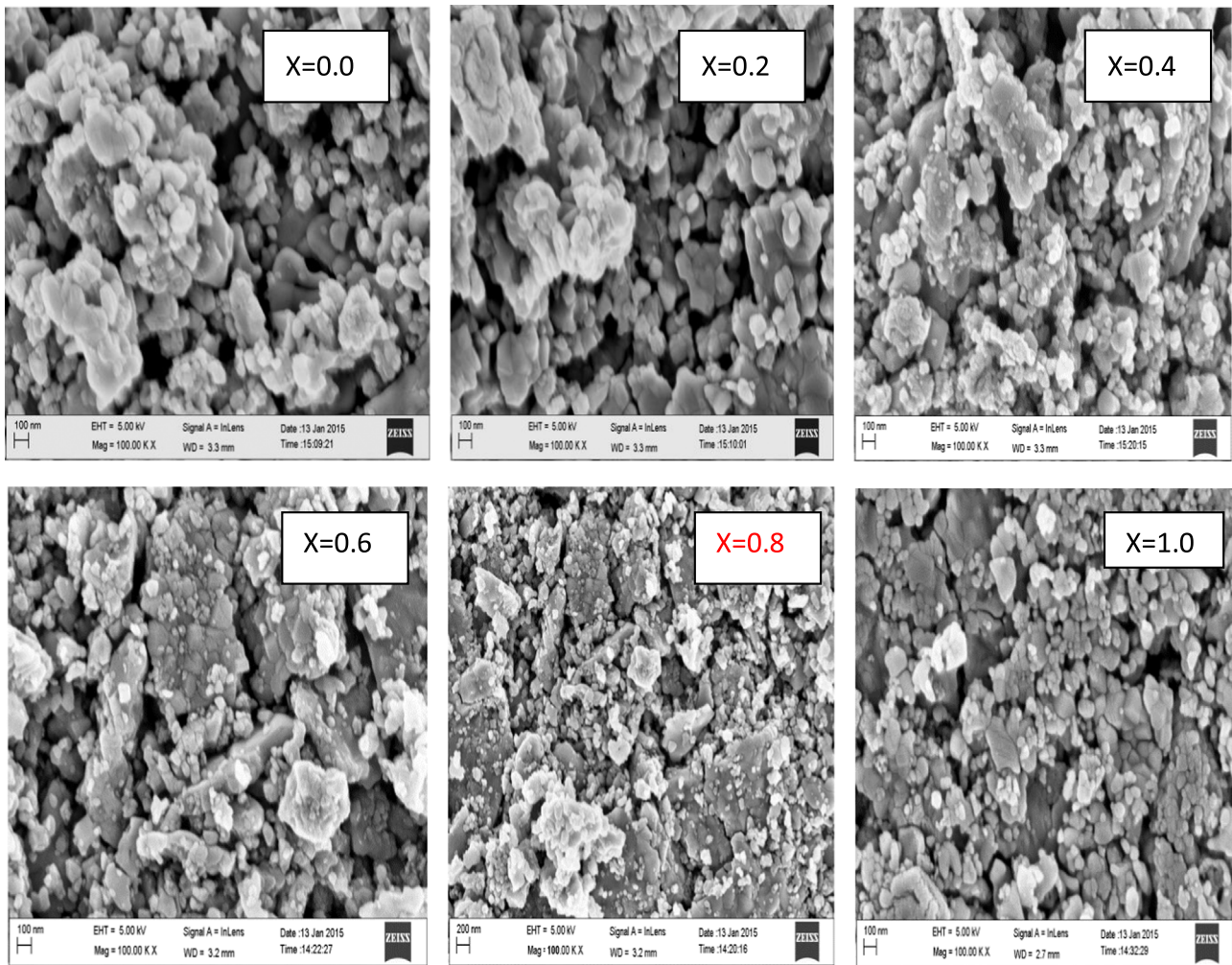
Fig. 2. FE-SEM images of $[Li_{0.5}Fe_{0.5}]_{1-x}Co_xFe_2O_4$ ferrites with x=0.0 to 1.0.

heating rate of 4 °C/min. Hysteresis loops obtained from VSM for all the compositions of Li–Co ferrites were shown in Fig. 3 which show the dependence of Magnetization values (M) on the applied magnetic field (H).

Various magnetic parameters measured from the hysteresis loops are Saturation Magnetization – M_s (Maximum value of magnetization), Remanance Magnetization – M_r (Magnetization at Zero field), Coercivity – H_c (magnetic field required to reduce the magnetization of that material to zero after the magnetization of the sample has been driven to saturation). These Magnetic parameters are used to exemplify the magnetic properties of prepared ferrite materials. The measured magnetic parameters (M_s, M_r and H_c)for the synthesized samples under the applied magnetic field (H) are summarized in Table 2. The measured values show a clear hysteresis loop behavior.

From the figure, one can observe that pure lithium ferrite ($x=0.0$) with least squareness ratio was the soft ferrite and pure cobalt ferrite ($x=1.0$) with maximum squareness ratio was the hard ferrite. Hence, by substituting cobalt in the lithium ferrite, the system changes from soft ferrite into hard ferrite.

The shape and width of the hysteresis loop is influenced by several factors including chemical composition, fabrication method, sintering temperature/time and grain size etc. [new Ref. [15]] [26]. From the figures it is evident that with increase in the cobalt composition in the ferrite system the width of hysteresis loop has increased. This indicates that a very soft magnetic material has changed to hard magnetic material with the introduction of cobalt content in the ferrite system. In spinel ferrites, the magnetic moment of the A-site and B-site were aligned anti-parallel to each other and shows ferri-magnetism with a magnetization M (M_B– M_A).

Table 2
Magnetic parameters (μ_B, K, M_s, H_c and M_r, S) of the prepared nano crystalline Li–Co samples.

| Composition	Molecular weight (gm)	Magnetic moment (μ_B)	Anisotropic constant (K) (erg/Oe)	Saturation Magnetization M_s (emu/gm)	Coercivity H_c (Oe)	Remanent magnetization M_r(emu/gm)	Squareness ratio (S)
$Li_{0.5}Fe_{2.5}O_4$	207.079	2.073	8731	55.93	153	15.15	0.270
$Li_{0.4}Co_{0.2}Fe_{2.4}O_4$	212.587	2.219	52,826	58.30	888	25.20	0.449
$Li_{0.3}Co_{0.4}Fe_{2.3}O_4$	218.095	2.369	26,253	60.68	424	30.08	0.495
$Li_{0.2}Co_{0.6}Fe_{2.2}O_4$	223.603	2.497	88,364	62.39	1388	32.34	0.485
$Li_{0.1}Co_{0.8}Fe_{2.1}O_4$	229.111	2.801	107,521	68.29	1543	34.36	0.503
$CoFe_2O_4$	234.619	2.387	121,742	56.84	2099	31.15	0.548
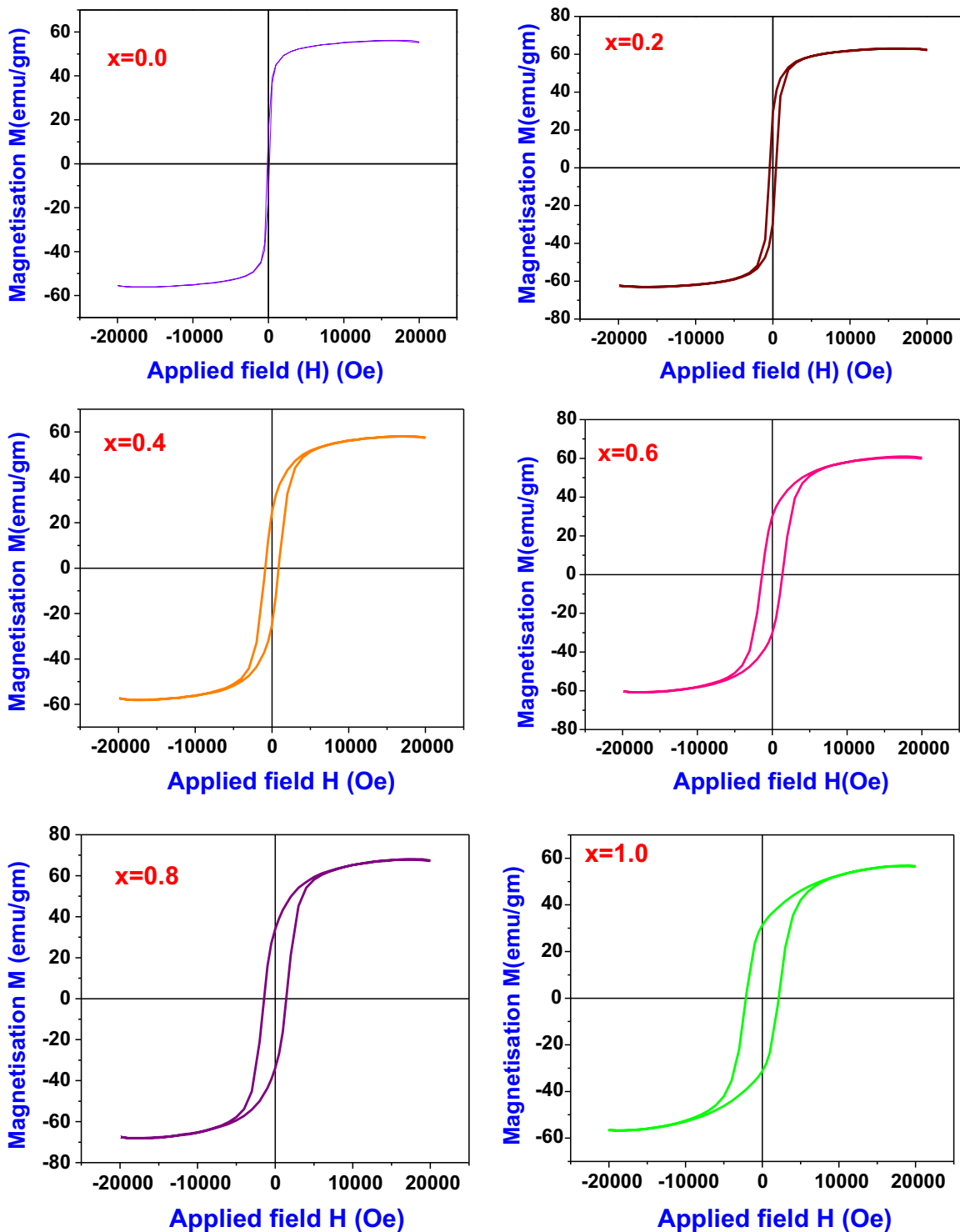
Fig. 3. Hysteresis loops for $[Li_{0.5}Fe_{0.5}]_{1-x}Co_xFe_2O_4$ ferrites with $x=0.0–1.0$.

From measured values one can conclude that in nano crystalline Li–Co ferrites, saturation magnetization (M_s) and remanent magnetization (M_r) values were observed to be increasing with increase in the Co doping until $x \leq 0.8$ beyond which a decrease in the value was observed and is evident from Fig. 4. This observed fact can be explained on the basis of cation distribution. From the literature survey, it is observed that Li^+ ions occupy only B-site whereas Co^{2+} ions can occupy both A and B sites [27]. It is also reported that the magnetic moment of Co^{2+} ions is more (3 μ_B) [28] than that of the Li^+

(0 μ_B i.e. non magnetic ion) and is less than that of Fe^{3+} ion (5 μ_B) [29]. By increasing the cobalt substitution in the Li–Co ferrite system, lithium ions may be replaced by the cobalt ions and iron ions so as to increase the resultant magnetization values but in case of pure cobalt ferrites these cobalt ions replace the iron ions that led to decrease in magnetization. As saturation magnetization got increased, the superexchange interaction in the particles between the octahedral and tetrahedral sites also increases with increase in cobalt content in lithium ferrites.
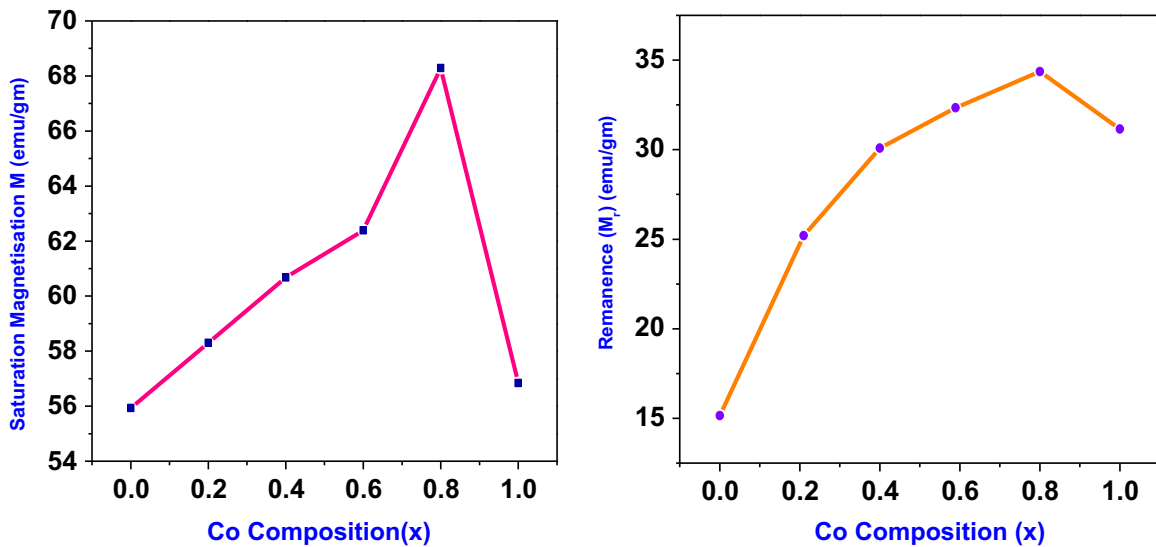
Fig. 4. Compositional variation of Saturation Magnetization (M_s) and Remanence magnetization (M_r) for Li–Co ferrites.

Coercivity is the magnetic field strength required for overcoming anisotropy to flip the magnetic moment which is influenced by the doping of metal ions [30]. The coercivity values were in the range of 153–2099 Oe as clear from Table 2. The magnetic coercivity the materials depends on the magneto-crystalline anisotropic energy, micro-strain, inter-particle interaction, temperature size etc [31]. In cobalt ferrites, the Co^{2+} (3d^7, 4F$_{9/2}$, $L=3, S=3/2, J=9/2$) cations possess 7 D-electrons, three of which are unpaired. Evidently, large magneto crystalline anisotropic energy may be due to the strong L–S coupling on the Co^{2+} cation sites. Energy barriers in the individual constituents was considered and introduced by the magneto crystalline anisotropic energy of the prepared cobalt ferrite [32].

The magnetic moment (m) and anisotropic constant (K) of all the Li–Co ferrites were calculated using the relations (4) and (5) from the saturation magnetization (M_s) and coercivity (H_c). The ratio of M_r to M_s, called as squareness ratio or remanence ratio was calculated and all the values are given in the Table 2. From the values, one can observe that the magnetic moment and squareness ratio are observed to be increasing with the increase in the cobalt concentration in Li–Co ferrites.

From all these results, it is apparent that by increasing the cobalt concentration in the nano crystalline Li–Co ferrite, magnetic property of the ferrite samples were improved and the material is being converted from soft magnetic to hard magnetic. Such materials can be used for the fabrication of hard permanent magnets. It is observed that the magnetization values for Li–Co ferrites synthesized by citrate-gel auto-combustion method were higher than those obtained by standard ceramic method [33].

3.4. Electrical measurements

The dielectric constant (ε') and loss tangent (tan δ) of all prepared samples at room temperature in the frequency range 20 Hz to 2 MHz were measured using LCR meter with the help of relations (6) and (7). The variation of real part of dielectric constant (ε') with frequency was shown in Fig. 5 from which it is clear that the value of ε' decreases with increase in the frequency for all prepared samples, the imaginary part also shows the same variation with frequency (not shown).

Thus, it shows a normal dielectric behavior with frequency. This dielectric dispersion can be explained on the basis of Koop's two layer model [34] and Maxwell-Wagner polarization theory [35–
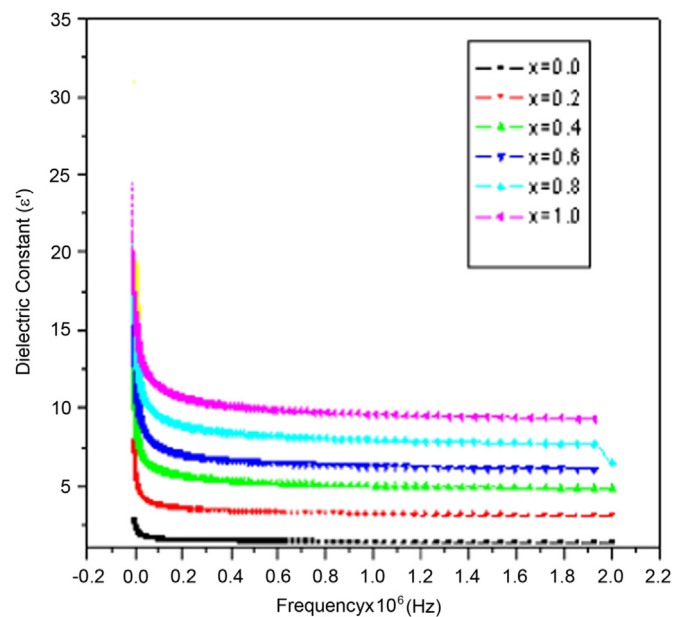

Fig. 5. Variation dielectric constant (ε') with frequency of Li–Co nano ferrites.

36]. The large value of dielectric constant at low frequency was due to the combined effect of interfacial and dipolar polarizations. With increase in the frequency the dielectric constant decreases, because after certain frequency, the hopping frequency no longer follows the frequency of the applied field. From the Fig. (4), it was observed that pure Lithium ferrites and pure Cobalt ferrites have less dielectric constant values compared with that of substituted Li–Co ferrites. This is because, the probability of hopping of charge carriers between the ions in mixed ferrites was more compared to that in pure ferrites. The variation of dielectric loss tangent with frequency was shown in Fig. 6. In low frequency region, where the high resistive grain boundaries are more effective, more energy is required for electron exchange between the Fe^{2+} and Fe^{3+} ions as a result the loss is high. Whereas less resistive grains are active in high frequency region and less energy is needed for hopping. Hence, loss decreases with increase in frequency [37].

The variation of dielectric constant (ε') with cobalt composition is shown in Fig. 7.

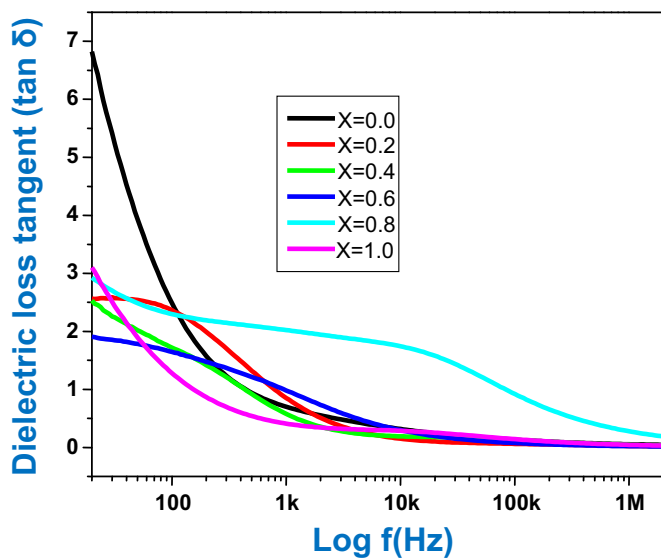From the figure, one can observe that pure lithium ferrites and

Fig. 6. Variation dielectric loss tangent with frequency of Li–Co nano ferrites.
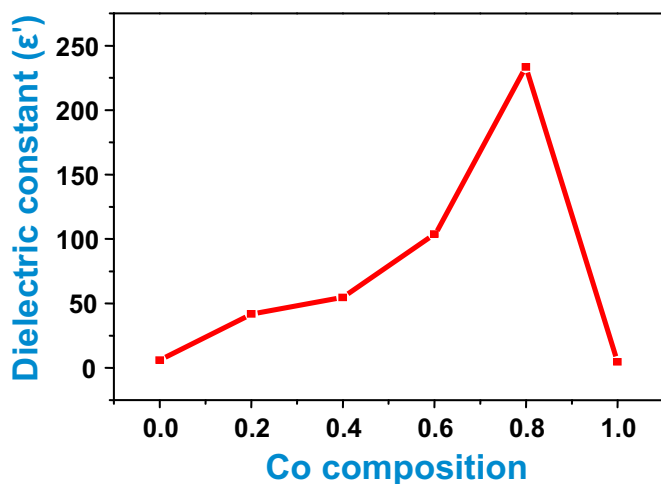

Fig. 7. Variation of dielectric constant with Co composition.

pure cobalt ferrites have less dielectric constant (ε') compared with that of mixed (Li–Co) ferrites. This is because, in mixed ferrites there are more number of charge carriers to increase the polarization effect.

4. Conclusions

Cobalt substituted Lithium ferrites synthesized by auto-combustion method are new materials for the fabrication of hard magnets which is evident from its increased saturation magnetization. The samples prepared were crystalline in nature confirmed by XRD analysis. The crystallite size of the samples was in the range of 36–43 nm. The particles are spherical I shape as studied by FESEM. By increasing the cobalt concentration in the lithium ferrites, the saturation magnetization increased up to $x \leq 0.8$ beyond which it decreased. This is because, Co^{2+} ion with high magnetic moment replaced the non-magnetic Li^+ ion in the prepared Li–Co ferrite samples. But, in case of pure cobalt ferrites, Co^{2+} ions replaced the Fe^{2+} ions only resulting in decrease in magnetization of pure cobalt ferrite. By increasing the cobalt doping in Li–Co ferrites, the material converted from soft to hard magnetic material. The dielectric parameters of the prepared

samples decreased with increasing frequency.

Acknowledgment

References

[1] M. Raghasudha, D. Ravinder, P. Veerasomaiah, Investigation of super-paramagnetism in $MgCr_{0.9}Fe_{1.1}O_4$ nano ferrites synthesized by citrate-gel method, J. Magn. Magn .Mater. 355 (2014) 210–214.

[2] A.K.M. Akther Hussain, M. Seki, T. Kawai, H. Tabala, Colossal magnetoresistance in spinel type $Zn_{1-x} Ni_xFe_2O_4$, J. Appl. Phys. 96 (2004) 1273–1275.

[3] M.A. Ei Hiti, A.I. Ei Shora, S.M. Hammad, Some physical properties of Mg–Zn ferrites, Mater. Sci. Technol. 13 (1997) 625–630.

[4] B.K. Kuanr, Effect of the strong relaxor cobalt on the parallel and perpendicular pumping spin-wave instability threshold of LiTi ferrites, J. Magn. Magn. Mater. 163 (1996) 164–172.

[5] S.C. Watawe, B.D. Sarwade, S.S. Bellad, B.D. Sutar, B.K. Chougule, Microstructure, frequency and temperature-dependent dielectric properties of cobalt-substituted lithium ferrites, J. Magn. Magn. Mater. 214 (1–2) (2000) 55–60.

[6] Mathew George, Swapnw S. Nair, Asha Mary John, P.A. Joy, M.R. Anantharaman, Structural, magnetic and electrical properties of the sol–gel prepared $Li_{0.5}Fe_{2.5}O_4$ fine particles, J. Phys. D: Appl. Phys. 39 (2006) 900–910.

[7] M.U. Rana, T. Abbas, AC susceptibility abd magnetic interaction in Mg–Ni–Fe–O sysem, Mater. Lett. 57 (2002) 925–928.

[8] Qi Chen, A.J. Rondinone, B.C. Chakoumakos, Z.J. Zhang, Synthesis of superparamagnetic $MgFe_2O_4$ nanoparticles by coprecipitation, J. Magn. Magn. Mater. 194 (1999) 1–7.

[9] M.E. Rabanal, A. Várez, B. Levenfeld, J.M. Torralba, Magnetic properties of Mg-ferrite after milling process, J. Mater. Process. Technol. 143 (2003) 470–474.

[10] T. Sasaki, S. Ohara, T. Naka, J. Vejpravova, V. Sechovsky, M. Umetsu, S. Takami, B. Jeyadevan, T. Adschiri, Continuous synthesis of fine $MgFe_2O_4$ nanoparticles by supercritical hydrothermal reaction, J. Supercrit. Fluids 53 (2010) 92–94.

[11] E.J. Choi, Y. Ahn, S. Kim, D.H. An, K.U. Kang, B.G. Lee, K.S. Baek, H.N. Oak, Superpparamagnetic relaxation in $CoFe_2O_4$ nanoparticles, J. Magn. Magn. Mater. 262 (2003) L198–L202.

[12] A. Pradeep, C. Thangasamy, G. Chandrasekaran, Synthesis, structural studies on $Ni_{0.5+x}Zn_{0.5}Cu_xFe_2O_4$, J. Mater. Sci.: Mater. Electron. 15 (2004) 797–802.

[13] B.P. Jacob, S. Thankachan, S. Xavier, E.M. Mohammed, Dielectric behavior and AC conductivity of Tb^{3+} doped $Ni_{0.4}Zn_{0.6}Fe_2O_4$ nanoparticles, J. Alloy. Compd. 541 (2012) 29–35.

[14] A. Verma, T.C. Goel, R.G. Mendiratta, P. Kishan, Magnetic properties of nickel–zinc ferrites prepared by the citrate precursor method, J. Magn. Magn. Mater. 208 (2000) 13–19.

[15] K.V. Manukyan, Y.S. Chen, S. Rouvimov, Peng Li, Xiang Li, Sining Dong, Xinyu Liu, J.K. Furdyna, Alexei Orlov, G.H. Bernstein, W. Porod, S. Roslyakov, A.S. Mukasyan, Ultrasmall α-Fe_2O_3 superparamagnetic nanoparticles with high magnetization prepared by template-assisted combustion process, J. Phys. Chem. C 118 (29) (2014) 16264–16271.

[16] S.A. Saafan, S.T. Assar, B.M. Moharram, M.K. El Nimr, Comparison study of some structural and magnetic properties of nano-structured and bulk Li–Ni–Zn ferrite samples, J. Magn. Magn. Mater. 322 (2010) 628–632.

[17] Mamata Maisnam, Sumitra Phanjoubam, Frequency dependence of electrical and magnetic properties of Li–Ni–Mn–Co ferrites, Solid State Commun. 152 (2012) 320–323.

[18] G. Aravind, D. Ravinder, Preparation and structural properties of aluminium substituted lithium nano ferrites by citrate-gel auto combustion method, Int. J. Eng. Res. Appl. 3 (2013) 1414–1421.

[19] G. Aravind, D. Ravinder, V. Nathanial, Structural and electrical properties of Li–Ni nanoferrites synthesised by citrate gel auto-combustion method, Phys. Res. Int. 2014 (2014), Article ID 672739, 11 pages.

[20] I. Soibam, S. Phanjoubam, C. Prakash, Mössbauer and magnetic studies of cobalt substituted lithium zinc ferrites prepared by citrate precursor method, J. Alloy. Compd. 475 (2009) 328–331.

[21] I.H. Gul, A.Z. Abbasi, F. Amin, M. Anis-ur Rehman, A. Maqsood, Structural, magnetic and electrical properties of $Co_{1-x}Zn_xFe_2O_4$ synthesized by co-precipitation method, J. Magn. Magn. Mater. 311 (2007) 494–499.

[22] H. Yao, K. Kimura, Field emission scanning electron microscopy for structural characterization of 3D gold nanoparticle superlattices, Mod. Res. Educ. Top. Microsc. 2 (2007) 568–575.

[23] M.A. Gabal, Magnetic properties of NiCuZn ferrite nanoparticles synthesized using egg-white, Mater. Res. Bull. 45 (2010) 589–593.

[24] R.C. Kambale, K.M. Song, Y.S. Koo, N. Hur, Low temperature synthesis of

nanocrystalline Dy^{3+} doped cobalt ferrite: structural and magnetic properties, J. Appl. Phys. 110 (2011) 053910–053910-7.

[25] M.M. Hessien, Synthesis and characterization of lithium ferrite by oxalate precursor route, J. Magn. Magn. Mater. 320 (2008) 2800–2807.

[26] M. Ghobeiti-Hasab, Z. Shariati, Magnetic properties of Sr-ferrite nano-powder synthesized by sol–gel auto-combustion method, Int. J. Chem. Mol. Mater. Met. Eng. 8 (2014) 1095–1098.

[27] I. Soibam, S. Phanjoubam, C. Prakash, Magnetic and Mossbauer studies of Ni substituted Li–Zn ferrite, J. Magn. Magn. Mater. 321 (2009) 2779–2782.

[28] S.T. Assar, H.F. Abosheiasha, Structure and magnetic properties of Co–Ni–Li ferrites synthesized by citrate precursor method, J. Magn. Magn. Mater. 324 (2012) 3846–3852.

[29] N. Singh, A. Agarwal, S. Sanghi, P. Singh, Synthesis, microstructure, dielectric and magnetic properties of Cu substituted Ni–Li ferrites, J. Magn. Magn. Mater. 323 (2011) 486–492.

[30] M. Raghasudha, D. Ravinder, P. Veerasomaiah, Magnetic properties of Cr substituted Co- ferrite nano particles synthesized by citrate gel auto combustion method, J. Nanostruct. Chem. 3 (2013) 63.

[31] Q. Zeng, I. Baker, V. Mc Creary, Zh Yan, Soft ferromagnetism in nanostructured mechanical alloying FeCo-based powders, J. Magn. Magn. Mater. 318 (2007) 28–38.

[32] M. Georgescu, J. Viota, M. Klokkenburg, B. Enre, D. Vanmaekelbergh, P. Zeijlmansvan emmichoven, Short-range magnetic order in two-dimensional cobalt-ferrite nanoparticle assemblies, Phys. Rev. B 77 (2008) 024423.

[33] S.C. Watawe, B.D. Sarwade, S.S. Bellad, B.D. Sutar, B.K. Chaugule, Micro-structure and magnetic properties of Li-Co ferrites, Mater. Chem. Phys. 65 (2000) 173–177.

[34] Erum parvez, I.H. Gul, Enhancement of electrical properties due to Cr^{3+} substitution in Co-ferrite nanoparticles synthesized by two chemical techni-ques, J. Magn. Magn. Mater. 324 (2012) 3695–3703.

[35] C.G. Koops, On the dispersion of resistivity and dielectric constant of some semiconductors at audiofrequencies, Phys. Res. 83 (1951) 121–124.

[36] J.C. Maxwell, A Treatise on Electricity and Magnetism, Clarendon Press, Oxford (1982), p. 328.

[37] K.W. Wagner, The theory of heterogeneous dielectric, Ann. Phys. 40 (1913) 817–855.

Optimization technique of digital FIR filter coefficients using Genetic algorithm

[1] Sravan Kumar Talusani , [2]Srikanth Immareddy [3]Suresh.D

[1] *Electronics and Communication Engineering Dept, Methodist College of Engineering and Technology, Hyderabad 500001, India.*

[2]*Electronics and Communication Engineering Dept, Methodist College of Engineering and Technology, Hyderabad 500001, India.*

[3]*Electronics and Communication Engineering Dept, Methodist College of Engineering and Technology, Hyderabad 500001, India*

Abstract— **This research work has been proposed a method to design FIR filter with the optimized filter coefficients using Genetic Algorithm (GA) concept. Generally FIR filters are non recursive filters since the error of FIR filter is non linear. The coefficient is been represented by using Canonical Signed Digit (CSD) format. The CSD format representation is been chosen to reduce the hardware complexity and cost. The aim of this research is to select a best coefficient for the filter design and the wordlength reduction in the coefficient, so that the desirable magnitude response is been met with the hardware complexity. The obtained Genetic Algorithm (GA) results are compared with windowing technique's results. The implementation is done using MATLAB.**

Index Terms— **Canonical Signed Digit (CSD), Equiripple algorithm, Genetic Algorithm(GA), optimization.**

I.INTRODUCTION

In this paper, FIR filters would be favored on account of their features like stability& linear phase. A FIR's usage noise characteristics are easy to model & because of its all zero structure, it has a linear phase response. However for administering this, one must pay those value in the form of vast number of multipliers, due to this vast number for multipliers the speed of the processor will be reduced, thereby expanding the equipment cosset additionally. [1]. To beat this, the coefficients are represented in CSD format. This design need no multipliers so, hardware complexity may be decreased and cosset may be also lessened What's more additionally is high speed requirements are satisfied.

CSD format diminishes the multiplier operation to shift and add operations. Similarly as the multiplier is reduced to a minimum shift and add operations, the hardware complexity is also reduced, thereby reducing the hardware cost and automatically speed will be increased [1]. Therefore, in this paper we utilize CSD format to represent the coefficients. Along with the reduction of hardware complexity & hardware cost, filter coefficients optimization is a critical task. In this paper, for the optimization, a method was proposed, first of all the initial set of coefficients which are given as input to genetic algorithm are optimized filter coefficients obtained from equiripple algorithm because compared to coefficients obtained from windows technique equiripple algorithm results are more optimum according to the results obtained. Equiripple algorithm is used because equiripple outputs and genetic algorithm outputs are practically same if hardware cost & complexity are not taken into

consideration [2] that is where genetic algorithm is needed.

Idea behind the suggested technique is to optimize the filter coefficients simultaneously and also the hardware cost & complexity are taken consideration at the same time guaranteeing high speeds.

II. WINDOW METHOD

The simplest design of FIR filters is attained utilizing the windowing technique. In this technique, the design starts with an ideal desired frequency response which is given by [2]

$$H_d(e^{jw}) = \sum_{n=-\infty}^{\infty} h_d(n)\ e^{-jwn} \quad \text{---------} \ (1)$$

$$h_w(n) = h_d(n)\ w(n) \qquad \text{-----------} \ (2)$$

Where $h_d(n)$ is the impulse response of the filter

w[n] is the window function

$h_w(n)$ is the windowed impulse response

As a result, the frequency response of the windowed impulse response is the periodic convolution of the desired frequency response with the Fourier transform of the window and which is given by

$$H_W(e^{jw}) = \frac{1}{2\Pi} \int_{-\Pi}^{\Pi} Hd(e^{-j\theta})\ D(e^{j(w-\theta)}) d\theta \ \text{------} \ (3)$$

The frequency response of the approximation filter will be
given by

$$H_d(e^{jw}) = e^{-jwnd}\ H_W(e^{jw}) \ \text{----------} (4)$$

where n_d will be the essential time delay to present causality in the approximated filter. The filter designed by windowing technique will have greatest error on either side of the discontinuity of the ideal frequency response [2]. The length of the estimated filter (N) should be as short as possible. Furthermore, the windowing technique doesn't tolerate singular control over the close estimation errors in various bands. Preferred filters result from minimization of maximum error in both, the stop band and the pass band of the filter which leads to equiripple filters[2].

III. EQUIRIPPLE ALGORITHM

Equiripple   algorithm   is   also   known   as Park.Mc.Clellan's algorithm. It is used to optimize the filter coefficients as it provides the optimum result when the hardware cost & complexity are not taken into consideration. In this algorithm the design of linear phase FIR filter is predicated on the min-max error paradigm i.e.., minimizing the maximum error possible [2], which there by produces the optimum result. The method implemented is an iterative numerical algorithm. It converges very rapidly to the optimal solution. This method is very robust and is broadly utilized because of the optimum results (in spite of hardware complexity). In equiripple algorithm N (filter length) w_p, ws, and the ratio $\delta p/\delta s$ are fixed and it is considered as most popular

approach because of its flexibility and computational efficiency [2].

The weighted error function is given by

$$E(w)=(A(w)-D(w)) \quad ------------------ \quad (5)$$

Where N= filter length

A(w)= desired(real valued) amplitude function

D(w)= non negative weighting function

FIR filter's amplitude response can be formulated as

$$A(w) = \sum_{n=0}^{N} a(n)\cos(nw) ------(6)$$

$$D(w) = \begin{cases} 1, 0 < w < wo(passband) \\ 0, wo < w < \prod(stopband) \end{cases}$$

$$W(w) = \begin{cases} kp, 0 \leq w \leq wp \\ 0, wp \leq w \leq ws \\ ks, ws \leq w \leq \pi \end{cases}$$

Where $0 < w_p < w_0 < w_s < \prod$

Maximum error

$$\|E(w)\|_\infty = \max_{w\varepsilon(0,\pi)}|W(w)(A(w)-D(w)| \quad ------ \quad (7)$$

The solution to this quandary is called best weighted approximation to D(ω) , similarly as it provides the optimum result and it also minimizes the maximum value of error (min max solution)[4].

So, for computing this solution alteration theorem is used. Alteration theorem states that, |E(w)| attains its maximum value at a minimum of M+2 points & the weighted error function alternates sign on at least M+2 of those points[4].

Let us say,

R=M+2

Where, R is a reference set

$$E(w_i)= c(-1)^i \quad \|E(w)\|_\infty \quad -------------------- \quad (8)$$

From eqn. (2), we can write the above equation as

$$W(w_i)(A(w_i)- D(w_i))= (-1)^i\delta \quad ------------- \quad (9)$$

$$A(w_i) - D(w_i))= (-1)^i\delta / W(w_i) \quad ---------- \quad (10)$$

The above equation represents interpolation problem, which can be represented in the matrix form as

$$\begin{bmatrix} 1 & cosw_1 \cdots cosM_{w1} & 1/W(w_1) \\ 1 & cosw_2 \ldots cosM_{w2} & -1/W(w2) \\ 1 & cosw_R \ldots cosM_{wR} & -(-1)^R/W(w_R) \end{bmatrix} \begin{bmatrix} a(0) \\ a(1) \\ \vdots \\ \delta \end{bmatrix} = \begin{bmatrix} D(w_1) \\ D(w_2) \\ \vdots \\ D(w_R) \end{bmatrix}$$

There will be an unique solution to this linear system of equations, that solution is taken as optimal minmax solution[4]. This utilization takes excessive amount of computer time and memory, so it is not very useful [3] & we cannot guarantee convergence in equiripple algorithm where as in genetic algorithm convergence is guaranteed.

Algorithm steps are

1. Interpolation can be repeated by taking new set of R points.

2. Updating the reference (R) set till the desired optimized result is met.

Those acquired equiripple coefficients are converted into Canonical Signed Digit (CSD) format. CSD format is used to represent the binary numbers. In this format , binary numbers are encoded in such a way that word has fewest number of non zero digits. This technique maps a tenary system to a binary system [5].

Properties of CSD are:

1. No two consecutive bits in the encoded bit are non zeros.

2. The encoded word should contain a minimum number of non-zero digits.

For example, to represent 23 in CSD, csdigit(23) returns +0-00-. Where cs digit is a in-built function in MATLAB. CSD contains 33% fewer non-zero bits than 2's complement digits [5].

IV.GENETIC ALGORITHM

Offspring can be produced in more number by the organisms and the offspring produced can be similar to the parent organisms but some offspring can have similarities that none of the parent organism have due to mutations (random changes) and some characteristics are inherited through reproduction from parent organisms. The characteristics it has inherited through mutations and reproduction helps it to survive [6] or not to survive while undergoing through natural changes in the environment. To understand this adaptive process of nature and to apply it so that it"ll be desensitized to changes, John Holland (1970) developed algorithm called Genetic Algorithm (GA).It is a heuristic algorithm and it finds the optimal results by decreasing the value of objective function continuously. It provides both efficient & effective techniques for optimization. The major hindrance in the conventional application of GA is about the premature convergence, Whether those body of evidence happens. GA produces a sub-optimal result In there, may be no outside 'strength' or 'instruction' which lead GA out of local optima[7] which is dealt in this method by iterating over population many times and simultaneously iterating different regions of population.

Basic steps of GA are:

A. Population

Encode each bit as a gene and a string of genes are called as chromosome and set of chromosomes is called population. First step to start with is to initialize the population i.e., is called as initial population.

B. Evaluation

Each chromosome has to be assessed and to be assigned a

value called fitness value, larger the fitness value, (that says i.e.., a good gene) probability will be more

to select it for reproduction. Fitness is the measure of goodness of a chromosome.

C. Selection

The individual chromosomes which have best fitness values are selected and proceeded for next step called reproduction where blending of the both guardians would be carried to process new offspring's [8]. Two regularly utilized

methods are 'roulette wheel' & 'tournament' selection Over roulette wheel, every individual will be allocated a sector (slice) size proportional to their fitness evaluated The wheel is then spun and the individual inverse to the marker turns into a standout amongst those as parents[2].In this paper roulette wheel selection is used.

D. Reproduction

Two chromosomes which are selected based on the fitness value [9] from the population undergo a process called reproduction to produce offspring's. Parents who have better fitness values have superior possibilities to be selected for production of finer offsprings.

E. Crossover

Choosing a random point and Splitting the parents at this crossover point and Creating children by trading their tails is called crossover process. Crossover probability is typically in the range (0.6, 0.9) [10]. Fig .1 describes the crossover process. It can be classified as

a. Simple Crossover: The Process we discussed above is a simple crossover process[2].

b. Arithmetic Crossover: It is a process where two complimentary linear combinations of the parents were produced [2].

c. Heuristic Crossover: It gets profit from fitness information with furthermore extrapolation of the two individuals to enhance the offspring [2].

In this paper, simple crossover was used.

E. Mutation

Mutations are random changes done to a chromosome in order to get a good fitness value as shown in Fig. 2. Mutations are random changes which reintroduces the genetic diversity into the population [9].

Mutation can also be classified as

a. Uniform mutation

b. Non uniform mutation

c. Multi-non uniform mutation

In this paper, non uniform method is used where one variable (gene in a chromosome) is selected randomly and its equivalent is set to a non uniform random number.

Then afterward finishing every last one of above steps, if the desired criteria are met by the coefficients, then it will stop, otherwise the process will be continued along with the new generated off springs as a population until the required specifications met.

V. DESIGN PROCEDURE

Here, the aim is to design a FIR filter with desired frequency, magnitude response, and to optimize the filter coefficients this can be achieved by the following methods of proposed technique.

A. Window method

1. On deciding the specifications of the filter that has to be kept constant for equiripple & genetic algorithms
2. Design a filter using any window let's say hamming window
3. Calculate the magnitude response & filter coefficients for particular filter length (in the paper N= 23).

B. Implementation of equiripple algorithm

1. We have to decide the filter specifications and length.
2. After deciding the length, w_p (pass band edge frequency) & w_s (stop band edge frequency), the main idea of equiripple algorithm starts with taking reference set as explain in section II before.
3. The magnitude response of the filter designed is compared with the desired magnitude response and error $E(\omega)$ is calculated.
4. If error is more i.e. magnitude response of filter observed are not coinciding with the desired magnitude response then a new reference set will be taken.
5. Again, the step repeats until error function is less than smallest number defined as SN in the program(i.e. taken SN=1e-8)
6. If it is less than SN i.e. max (err) < SN, then result is displayed as converged.

C. CSD conversion

1. The filter coefficients thus obtained are converted into CSD format.
2. They are converted into CSD format by using the MATLAB built-in function (csdigit)

[a,p,n] = csdigit (num, range, resolution)
    Where; a is the CSD digit
        p is the positive part
        n is the negative part
        num = input number (decimal)
 range = maximum digits to the left of the decimal point
resolution = digits to the right of decimal point for example,
csdigit(.25,2,2) represents xx.xx binary
csdigit(.25,0,4) represents .xxxx binary

D. Genetic algorithm

1. The first step in genetic algorithm is to define the objective Function
    f=max(err)
    err = W(ω)(A(ω)-D(ω))   (12)
2. The coefficients obtained in equiripple method is taken as initial population

3. Then, we have to calculate fitness value for each individual in the population.
4. Fitness value is calculated by the fitness function given below

$$ff = \frac{1}{f} + k(SONZ) \qquad (13)$$

Where, f is the objective function defined at the starting of the algorithm

    k=0.02

  SONZ=sum of non zeros in CSD digit.
5. Two individuals (parents) who have fitness value more are selected for reproduction to produce off springs.

Eg: P1 00+00-
                  P2 0+0000
                  O1 00+00
                  O2 0+00-

where P1, P2 are
parents & O1, O2
are offsprings.
6. After crossover, the next step is mutations (random changes of variables), so that it can produce better fitness value.
7. If this population gives the desired frequency response with optimized filter coefficients, stop the algorithm otherwise include the offspring & create a new generation & repeat all the steps as mentioned above.
Fig1 . Shows the typical flow of the proposed algorithm
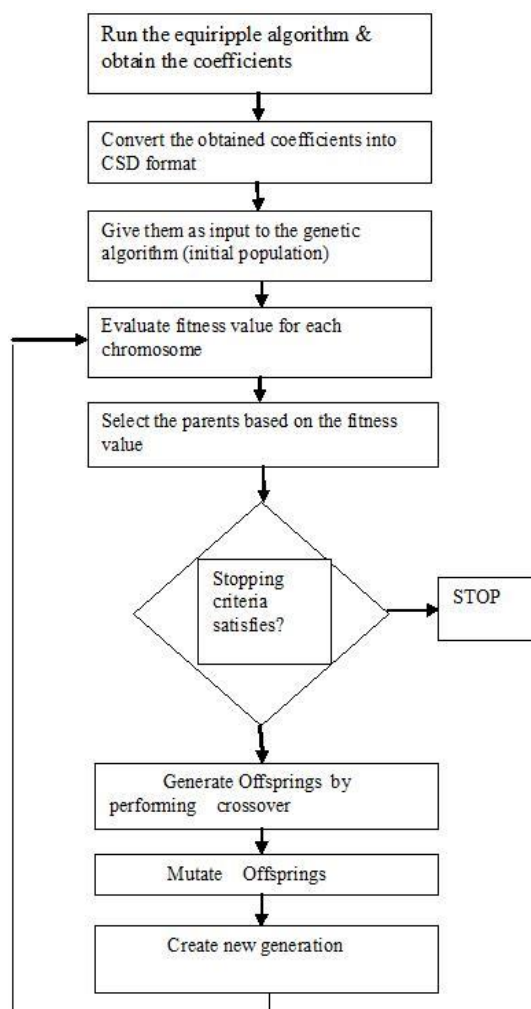
Coefficients	Values
1,19	$2^{-9}+2^{-8}+2^{-14}$
2,18	$2^{-8}+2^{-7}+2^{-15}$
3,17	$2^{-7}+2^{-6}+2^{-13}$
4,16	$2^{-8}+2^{-7}$
5,15	$2^{-4}+2^{-5}+2^{-10}$
6,14	$2^{-8}+2^{-7}+2^{-12}$
7,13	$2^{-7}+2^{-14}$
8,12	$2^{-2}+2^{-4}+2^{-7}+2^{-9}$
9,11	$2^{-2}+2^{-4}+2^{-6}+2^{-8}+2^{-10}$
10	$2^{-1}+2^{-3}+2^{-5}+2^{-7}+2^{-10}$

TABLE I. FILTER COEFFICIENTS USING WINDOWING

Coefficients	Values
1,19	$2^{-9}+2^{-8}$
2,18	0
3,17	$2^{-7}+2^{-6}+2^{-9}$
4,16	0
5,15	0
6,14	0
7,13	$2^{-7}+2^{-9}$
8,12	2^{-2}
9,11	0
10	2^{-4}

TABLE II. FILTER COEFFICIENTS USING EQUIRIPPLE ALGORITHM

Coefficients	Values
1,23	2^{-9}
2,22	0
3,21	$2^{-7}+2^{-6}$
4,20	0
5,19	0
6,18	0
7,17	2^{-7}
8,16	2^{-2}
9,15	0
10,14	0
11,13	$2^{-7}+2^{-9}$
12	2^{-4}

TABLE III. FILTER COEFFICIENTS USING GENETIC ALGORITHM

The TABLE I shows the filter coefficients of FIR filter designed using windowing technique.TABLE II. shows the filter coefficients of FIR filter designed according to the equiripple algorithm. TABLEIII. Shows the filter coefficients of FIR filter designed based on the genetic algorithm concept.On comparision of TABLE I, TABLEII & TABLEIII it can be observed that non zero digits are reduced in coefficients obtained from genetic algorithm than in

the equiripple algorithm coefficients or coefficients obtained in windowing technique. That proves the reduction in hardware complexity.

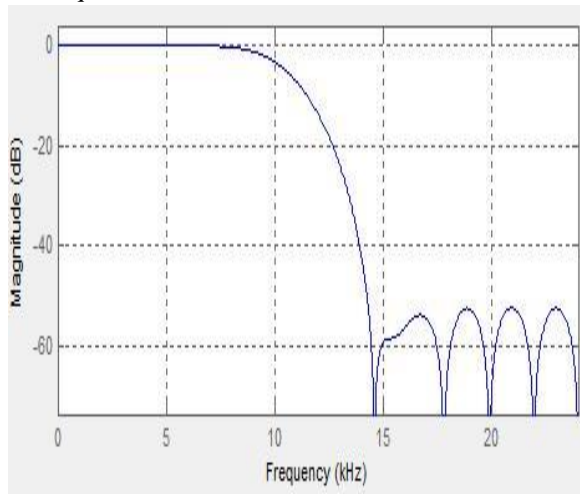Fig 2. Magnitude Response obtained by windowing technique

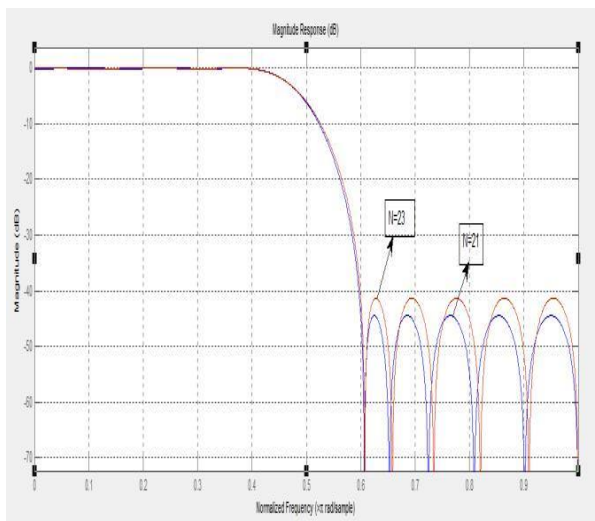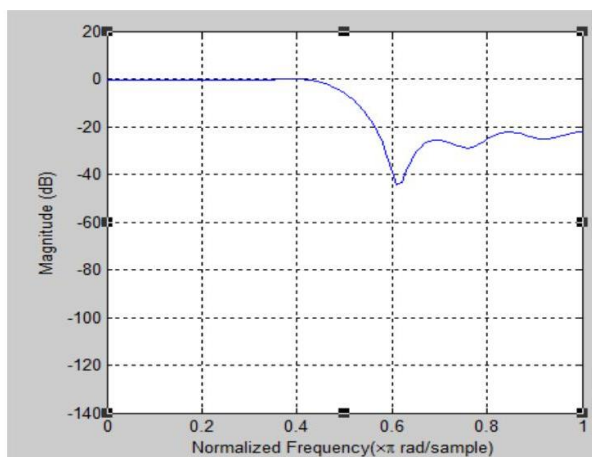Fig 3.Magnitude response obtained by equiripple algorithm

Fig 4.Magnitude response obtained by genetic algorithm

The response shown in Fig 2. indicates the magnitude response of the FIR filter designed by windowing (hamming) method. It can be observed that the response has some fluctuations and pass band is not completely flat. The response shown in Fig 3. indicates the magnitude response of the FIR filter designed by equiripple method. It can be observed that the response is not purely flat in pass band and the Fig. 2. represents the magnitude response of filter designed according to genetic algorithm, in this it is obvious that the error has minimized to complete zero in the pass band i.e., the pass band is totally flat in Fig2. That means the error is completely minimized to zero in the pass band i.e., a flat response for pass band is a desired characteristic.

Using MATLAB software to design a FIR filter by window method, an FIR filter with 23 coefficients and of word length 15 satisfies the given specifications

The same filter to be designed using equiripple algorithm it will cost 19 coefficients and word length 11.

If such a filter is designed using proposed method (GA) an FIR filter with 23 coefficients and word length 8 satisfies the given specifications.

It can be observed that GA has minimum word length so minimum hardware complexity and a desired frequency response. So it can be concluded that of all the three methods GA is the most optimum method.

VII. CONCLUSION

The proposed method required the optimum number of filter coefficients to obtain the desired frequency response with minimum word length. This method results in hardware reduction and cost as compared with windowing method and equiripple methods.

VIII. FUTURE SCOPE

By giving obtained genetic algorithm coefficients as a input to another genetic algorithm procedure to improve the frequency response characteristics of filter.

REFERENCES

[1] A. R. Rezaee,"Using genetic algorithms for designing of fir digital filters," ICTACT journal on soft computing, july 2010, Issue: 01, pp.18-22.

[2] Jehad I.Ababneh, Mohammad H. Bataineh , "Linear phase FIR filter design using particle swarm optimization and genetic algorithms",Elsevier, vol. 18 Issue:4.

[3] P. Janardhan, M. N. Neelakantan, "A fast perturbation method for the design of linear phase fir digital filters of finite wordlength using single frequency filters," springer journal on circuit systems and signal processing, vol. 10,Issue 2, pp. 233-244.

[4] I.Selesnick,"The Remez Algorithm".

[5] A. Rajolia, M. Kaur, "Finite impulse response (fir) filter design using canonical signed digits (csd)," International Journal of science and research (IJSR), india online issn: 2319-7064.

[6] R. Singh, S. K. Arya, " Genetic algorithm for the design of optimal iir digital filters," *Journal of Signal and Information Processing*, 2012, Issue: 3, pp. 286-292.

[7] Ling Cen,"A hybrid genetic algorithm for the design of FIR filters with SPoT coefficients",Elsevier vol.87,, Issue:3.

[8] P. Kaur, S. Kaur, "Optimization of fir filters design using gentic algorithm," IJETTCS, Issue :3, Vol. 1.

[9] S.T.Tzeng, "Genetic algorithm approach for designing 2-D FIR digital filters with 2-D symmetric properties," Elsevier, vol. 84,
Issue: 10.

[10] S. Aggarwal, A. Gagneja, A. panghal, "Design of fir filter using ga and its comparison with hamming window and parks mcclellan optimization techniques," IJARCSSE, vol. 2, Issue: 7.

[11] A. N. Kani, "Digital signal processing", second edition.

[12] A. Lee, M. Ahmadi, G.A. Jullien, W.C. Miller, R.S.Lashkari," Digital filter design using genetic algorithm", in:Proceedings of IEEE Symposium on Advances in Digital Filtering and Signal Processing,June 1998.

[13] E. Hostetter, A.V. Oppenheim, J. Siegel, On optimum nonrecursive digital filters, in: Proc. 9th Allerton Conf. Circuit System Theory, October 1971.

[14]T.W. Parks, J.H. McClellan, Chebyshev approximation for nonrecursive digital filters with linear phase, IEEE Trans. Circuit Theory CT-19(1972) 189–194.

[15] T.W. Parks, J.H. McClellan, A program for the design of linear phase finite impulse response filters, IEEE Trans. Audio Electroacoust. AU-20 (3) (1972) 195–199.

[16] J.H. McClellan, T.W. Parks, A unified approach to the design of optimum FIR linear phase digital filters, IEEE Trans. Circuit Theory CT-20(1973) 697–701.

[17] J.H. McClellan, T.W. Parks, L.R. Rabiner, A computer program for designing optimum FIR linear phase digital filters, IEEE Trans. Audio Electroacoust. AU-21 (1973) 506–526.

[18] A.V.Oppenheim, R.W. Schafer, J.R. Buck, Discrete-Time Signal Processing, Prentice Hall, Englewood Cliffs, NJ, 1999.

[19] J.H. Holland, Adaptation in Natural and Artificial systems,MIT
Press, 1975.

[20] Mitra, Digital Signal Processing: A Computer-Based Approach, McGraw-Hill, 2001.

[21] K.F. Man, K.S. Tang, S. Kwong, Genetic Algorithms:Concepts and Designs, Springer, London, 1999.

[22] M. Srinivas, L.M. Patnaik, Genetic algorithms: a survey,Computer 27(6) (June 1994) 17–26.

SRAVANKUMAR TALUSANI Received the Bachelor degree in Electronics and Communication Engineering (ECE) from Osmania University, India and Master degree in Digital Systems & Computer Electronics from JNTU Ananthapur, India.
He is working as Assistant Professor in ECE Dept at Methodist College of Engineering and Technology, India. His major interests are in the fields of Analog Electronics and Signal Processing.

SRIKANTH IMMAREDDY Received the Bachelor degree in Electronics and Communication Engineering (ECE) from the JNTU Hyderabad India and Master degree in Digital Systems from Osmania University, India in 2009.
He is working as Assistant Professor in ECE Dept at Methodist College of Engineering and Technology, India. His main interests are in the fields of Very Large Scale Integration and Digital Signal Processing.

SURESH.D Received the Bachelor degree in Electronics and Communication Engineering (ECE) from JNTU, India and Master degree in VLSI from KAKATIYA UNIVERSITY, India.
He is working as Assistant Professor in ECE Dept at Methodist College of Engineering and Technology, India. His major interests are in the fields of VLSI.

Significance of Software Testing Methods - Case Driven

Dr. B V Ramana Murthy[1], Dr. V Padmakar[2]

[1]Professor & Principal, Department of CSE, AAMEC, Hyderabad, India
[2]Associate Professor, Department of CSE , MIST, Hyderabad, India

Abstract—*Software Testing is a process of any software development which is used to measure the quality of developed software final product. It finds all errors, bugs and flaws in the developed software final product. In this paper we present software testing techniques for detecting the errors which are described by static testing and dynamic testing.*

Keywords—*Testing, static testing, dynamic testing.*

I. INTRODUCTION

Software Testing Levels
1. Static Testing
2. Dynamic Testing

1. Static Testing:
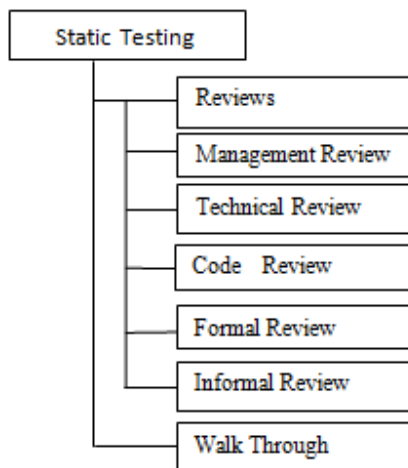
It is the process of verifying or developing the right system or not. This static testing will be carried out with the help of reviews and walkthroughs**.** Verification[1] is to check whether software conforms to the specifications done by the development team at various development phases. During development phase the SRS document, Design document, Code document are reviewed to ensure that product is being developed using the process oriented approach.

- It is an in-house activity of the development organization.
- It is a quality assurance [2] activity which prevents the defects of the product.

i) **Reviews**
Examining a project related work or process related work is called review.

    Types of reviews:
a) Management Review
b) Technical Review
c) Code Review
d) Formal Review
e) Informal Review

a) Management Review: This review will be conducted by top level or middle level management to monitor the project status. Those reviews are helpful for the management to take the necessary actions.

b) Technical Review: Technical Reviews will be conducted among the technical people to decide the best approach of implementation.

c) Code Review: This review will be conducted among the developers to decide the best approach of programming preparation.

d) Formal Review: If a review is carried out with a particular plan by following a systematic procedures and proper documentation then it is called as Formal Review.

e) Informal Review: If a review is conducted without following any procedures and documentation then it is called as Informal Review.

ii) **Walk Through**:
A step by step presentation conducted by the other or by the domain expert about a subject. KT (Knowledge Transfer) is the best example for walk through[1,2]

2. Dynamic Testing
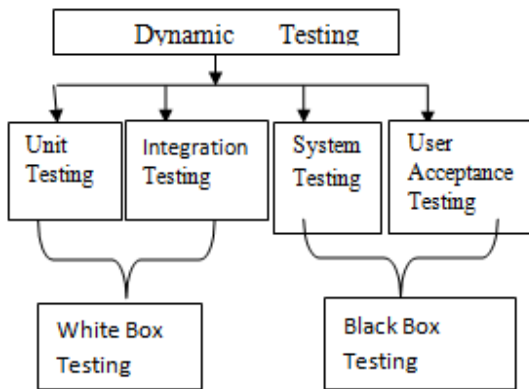
There are two types of methods

  i)   White box testing
  ii) Black box testing

i)   White Box Testing

Testing[3] conducted by the developers on Coding to ensure the code coverage that the code is working as expected or not is called White box testing. Combination of unit & integration testing is called White box testing. White box[10] testing is also as Glass box, Clear box or Structural testing.

Unit Testing :The smallest testable portion in the source code of the application is called Unit Testing.

• Module Testing
• Component Testing (Functions, Procedures, Methods, Objects)

Integration Testing

Integration testing[4] is a software development process in which program units are combined and tested as groups in multiple ways. Once the unit testing is completed developers will integrate all source code units and check interaction among all units. This is called as Integration Testing.

While conducting Integration testing follow the below subtests

i) Top Down Approach
ii) Bottom Up Approach
iii) Hybrid Approach
iv) System Approach / Big Bang Approach

i)   Top Down Approach

Top down integration is primarily considering as an approach where modules are developed and of that modules always starting at the first level of the programming hierarchy and continuing towards the lower levels. Top

down is an incremental approach because we precede one level at a time.
Example: Login Page
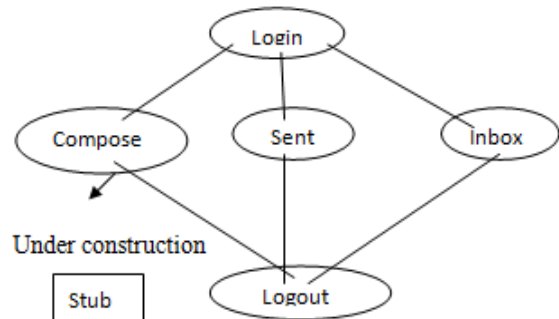
Under construction

Benefits
  1.   Having the framework, we can test major or supreme functions early in the development process.
  2.   Major benefit of this practice is that we include a partially working framework to show to the clients and to the top management too

Drawbacks
  1.   Impose stubs does not permit all the essential upward data flow.
  2.   The top level modules cannot be really tested perfectly and every time the stubs are replaced with the real modules, the modules which are calling should be properly re-tested again for integrity.

ii)   Bottom Up Approach

After unit testing of individual components the components are combined together into a system. Bottom-Up Integration: each component at lower hierarchy is tested individually; then the components that rely upon these are tested.

Component Driver**:** a routine that simulates a test call from parent component to child component
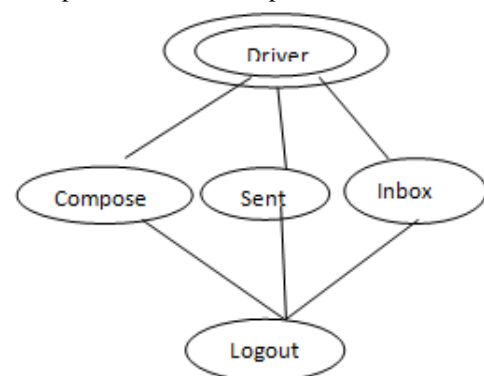
iii)   Hybrid Approach

Combination of top down and bottom up approach is called as Hybrid or Sandwich approach.

iv)   System Approach

System approach [1]is also known as Big Bang Approach. In Big Bang integration testing all components or modules are integrated simultaneously, after which everything is tested as a whole. In this approach individual modules are not integrated until and unless all the modules are ready. This approach is generally executed by the developers. In case any bug arises then the developers has to detach the integrated modules in order to find the actual cause of the bug.
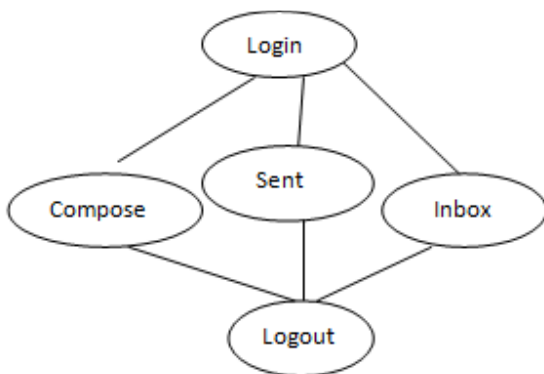
Note: From the above approaches we can follow any one of the approach based on the requirement.

Functional System Testing

In functional system[1,2] testing basically the testing of the functions of component or system is done. It refers to activities that verify a specific action or function of the code. It is a mandatory level testing.

During functional system testing, testers concentrate on below subtests:

i)   Sanity Testing
ii)   Real Testing
iii) Retesting
iv)   Regression
v)   Database Testing

i)   Sanity Testing

Sanity Testing is the surface level testing where QA engineer verifies that all the menus, functions, commands available in the project and project are working fine. Sanity testing is carried out to check whether the bugs reported in previous build are fixed & there is regression introduced due to these fixes i.e. not breaking any previously working functionality[10]. The main aim of Sanity testing to check the planned functionality is working as expected. Sanity tests helps to avoid wasting time and cost involved in testing if the build is failed. After completion of regression

testing the Sanity testing is started to check the defect fixes & changes done in the software application is not breaking the core functionality of the software. Typically this is done nearing end of SDLC i.e. while releasing the software. You can say that sanity testing is a subset of acceptance testing.

Here are the few consolidated points of Sanity testing:

- Sanity testing follows narrow and deep approach with detailed testing of some limited features.
- Sanity testing is typically non-scripted.
- Sanity testing is a sub-set of regression testing.
- Sanity testing is cursory testing to prove software application is working as mention in the specification documents & meets the user needs.
- Sanity testing is used to verify the requirements of end users are meeting or not.
- Sanity testing to check the after minor fixes the small section of code or functionality is working as expected & not breaking related functionality.

During this test, test engineers concentrate on basic functionalities of the Application like:

- Application basically working or not?
- Understandable or not?
- Consistent or not?
- Controllable or not?
- Simplicity

Example for Sanity Testing

There are five modules in a project like

- Login Page
- Home Page
- User details Page
- New User creation
- Task creation

So we have the bug in Login page like **User Name** field accepts less than 6 alpha numeric characters which are against the requirements. It is specified that username should not be below than 6 characters but as user name accepts less than 6 characters it is the **bug.**

- Now the bug is reported by the testing team to the developer team to fix it. When the developing team fixes the bug and passed it to testing team then the testing team checks the other modules of the application

ii)   Real Testing

Checking every functionality of the application is called Real Testing (checking size and type)

iii) Retesting

Retesting is executing a previously failed test against new software to check if the problem is resolved. After a defect has been fixed, retesting is performed to check the scenario under the same environmental conditions. During Retesting[3,4], testers look for granularity details at the changed area of functionality.

iv) Regression Testing

Regression testing is the process of testing changes to computer programs to make sure that the older programming still works with the new changes.

Example:

There are 3 modules in the project:

- Admin module
- Personal information
- Employment module

Suppose bug occurs in the Admin module like existing user is not able to login with valid login credentials (this is the bug).

- Now testing team sends the above mentioned bug to the development team to fix it and when development team fixes the Bug and hand over to testing team then testing team checks the fixed bug does not affect the remaining functionality of the other modules. So this is known as Regression testing.

v) Database Testing

Database testing is one of the major testing which requires tester to expertise in checking tables, writing queries and procedures. Testing can be performed in web application or desktop and database can be used in the application like SQL or Oracle. There are many projects like Banking, Finance, Health insurance which requires extensive database testing. Nowadays database is getting more complex due to the business logic which plays an important role for the applications. Testers should make sure that values have been added correctly after the implementation of the business rules. Database is the spine of the application and tester should make sure to test very carefully. It requires skill, proficiency and sound knowledge.

Example – Login and User Security

The validations of the Login and User security credentials need to take into consideration the   following things:

1. Whether the application prevents the user to proceed further in the application in case of a

- Invalid username but valid password
- Valid username but invalid password
- Invalid username and invalid password
- Valid username and a valid password

2. Whether the user is allowed to perform only those specific operations which are specified by the business requirements.
3. Whether the data secured from unauthorized access[7,8]
4. Whether there are different user roles created with different permissions.
5. Whether all the users have required levels of access on the specified Database as required by the business specifications.
6. Checking that sensitive data like passwords, credit cards numbers are encrypted and not stored as plain text in database.

Non Functional System Testing

After completion of functional system testing, test engineers concentrate on non functionalities of the application like **User Interface**, **Performance, and Compatibility, Security** etc.

i)   User Interface Testing

User interface testing is a technique used to identify the presence of defects in a product/software under test by using Graphical User Interface (GUI)

Graphical User Interface (GUI) testing is the process of testing the system's GUI of the System under Test. GUI testing involves checking the screens with the controls like menus, buttons, icons, and all types of bars - tool bar, menu bar, dialog boxes and windows etc.

The following checklist will ensure detailed GUI Testing.

- Check all the GUI elements for size, position, width, length and acceptance of characters or numbers. For instance, you must be able to provide inputs to the input fields.
- Check you can execute the intended functionality of the application using the GUI
- Check Error Messages are displayed correctly
- Check for Clear demarcation of different sections on screen
- Check Font used in application is readable
- Check the alignment of the text is proper
- Check the Color of the font and warning messages is aesthetically pleasing
- Check that the images have good clarity
- Check that the images are properly aligned
- Check the positioning of GUI elements for different screen resolution.

Example of User Interface Testing for Mobile Application

User Interface Testing is to test the characteristics of a mobile app.

- Device specific characteristics. These are characteristics that are related to the device on which the app is installed.
- Network specific checks
- App checks. These are things to check that have to do with functionality that is frequently used in an app.
- App User interface checks.
- Store specific checks.

ii) Performance Testing

Performance testing is a non-functional testing technique performed to determine the system parameters in terms of responsiveness and stability under various workloads. Performance testing measures the quality attributes of the system, such as scalability, reliability and resource usage

Performance Testing Techniques:

- Load Testing
- Spike Testing
- Stress Testing
- Endurance Testing

a) Load Testing

Load Testing is a type of Non functional testing. It is a type of software testing which is conducted to understand the behavior of the application under a specific expected load. Load testing is performed to determine a system's behavior[9] under both normal and at peak conditions. It helps to identify the maximum operating capacity of an application. The primary goal of a load testing is to define the maximum amount of work a system can handle without significant performance degradation.

Examples of Load Testing:

- Downloading a series of large files from the internet.
- Running multiple applications on a computer simultaneously
- Assigning many jobs to a printer in a queue.
- Writing and reading data to and from a hard disk continuously
- Subjecting a server to a large amount of traffic.

b) Spike Testing

Spike Testing is a mechanism of testing which means when in a web page frequent number of visitor access the page unexpectedly increases to maximum then obviously performance of the page breaks down. Spike testing is usually done by unexpectedly increasing the number of loads generated by users by a very enormous amount and observing the dramatic behavior of the system. The goal of spike testing is to regulate whether performance will deteriorate, the system will always fail, or it will be able to hold dramatic changes in load.   **Example:**

When we check the results on JNTUH site, site is suddenly loaded and unloaded and then the IT squad of JNTUH checks how the site reacts with unexpected increase and decrease of users.

c) Stress Testing

Stress testing is the process of determining the ability of a computer, network, program or device to maintain a certain level of effectiveness under unfavorable conditions.

Example: Handling 25 user login

If there is an application which can handle 25 simultaneous user login at a time.

- In stress testing we will test with more users than 25 and the test will continue to any number.

d) Endurance Testing

Endurance Testing is a type of performance testing which is usually used to determine how much a system can sustain the continuous expected load. During the period of Endurance testing memory utilization is always monitored to detect any potentials leaks.

Example: Banking Application

In closing days of bank we have continuous load on that days so we always test the banking application by keeping in mind the endurance testing.

iii) Compatibility Testing

Compatibility testing is a non functional testing conducted on the application to evaluate the application's compatibility within different environments.

Types of compatibility testing:

- Browser compatibility testing
- Hardware testing
- Networks
- Mobile devices
- Operating System
- Versions

Common Compatibility testing defects

- Changes in UI (look and feel)
- Change in font size
- Alignment related issues
- Change in style and color
- Scroll bar related issues
- Content or Label overlapping

    Example: ebay.com

For example to test the compatibility of site ebay.com. Download different versions of Firefox and install them one by one and test the eBay site.

EBay site should behave equally same in each version.

iv) Security Testing

Security Testing[7,8] is a type of software testing that intends to uncover vulnerabilities of the system and determine that its data and resources are protected from possible intruders. The six basic security concepts that need to be covered by security testing are:

- Confidentiality
- Integrity
- Authentication
- Authorization
- Non repudiation

Example: Web Application

The Security tester should have good knowledge of the HTTP protocol. It is important to have an understanding of how the client and the server communicate using HTTP. The tester should at least know the basics of SQL injection and XSS.

- Password Cracking

The Security testing on a web application can be kicked off by "password cracking". In order to login to the private areas of the application, one can either guess a username /password cracker tool for the same.

v) Data Volume Testing

Volume testing is a Non-functional testing that is performed as part of performance testing where the software is subjected to a huge volume of data. It is also referred as flood testing. If we expect certain database growth, we may want to artificially grow the database to that size and test the performance of the application when using it. System performance can degrade when large amounts of data must be searched or indexed. This kind of testing can determine the amount of data the application can handle before it starts to display errors or even stop responding. During this test, testing team operates software by storing sample data to estimate capacity of the software database.

Volume Testing Characteristics:

- During development phase, only small amount of data is tested.
- The performance of the software deteriorates over time as there is enormous amount of data overtime.
- Test cases are derived from design documents.
- Test data is usually generated using a test data generator.

- Test data need not be logically correct but the data is to assess the system performance.
- Upon completion of testing, results are logged and tracked to bring it to closure.

II. CONCLUSION

Software testing is one of the important phases of software life cycle that aims to make the program error free and ensures product quality. The cost of testing is generally higher than the cost of remaining activities in the software development life cycle. Test planning is carried out before performing a test. There are two types of test cases design strategies black box and white box testing.

REFERENCES

[1] Pressman, R.S. 1997. Software Engineering: A practitioner Approach.4th Edition. Tata McGraw Hill.

[2] Sommerville, I. 1998. Software Engineering. 5th edition. Addison-Wesley.

[3] Myers, G.J. The Art of Software Testing.New York: John Wiley and Sons.

[4] McGraw.Chess,B.Seven pernicious kingdom.2005. A Taxonomy of Software Security Errors.WISST Workshop on Software Security Assurance Tools, Techniques and metrices.

[5] Sarma, M. D,Kundu.Mall, R. 2007. Automatic Test Case Generation from UML Sequence Diagram. International Conference on Advance Computing and Communication. Doi:10.1109/ADCOM:2007.68.

[6] Rina, DCSK, KU,Haryana ,INDIA,Tyagi,Sanjay.DCSA,KU,Haryana.2013.AComp arative Study Of Performance Testing Tools.IJARCSSE. 3,2(May 2013)

[7] Karen Scarfone.2012. Intro to Information Security Testing & Assessment. ScarfonecyberSecurity Csr.nist.gov.(7June 2012).

[8] B,Beizer .1990.Software Testing Techniques. Technology Maturation and Research Strategies Carneige Mellon University Pittsburg,USA.

[9] B.Beizer .1995. Software Testing Techniques.2006.Van Nostrand Reinhold, New York.1990.ISBN.0-442-20672-0.(31.Oct.2006).

[10] Khan,Mohd.Khan,Farmeena.2012. A Comparative Study of White Box, Black Box and Grey Box Testing Techniques.2012. International Journal of Advanced Computer Science and Applications(IJACSA). Vol. 3.No.6.(2012)

[11] Swain,S.k.Mohapatra,D.P.Mall, R.2010.Test Case Generation Based on Use Case and Sequence

Diagram.International journal of Software Engineering (IJSE) .3, 2.(July 2010),(289-321).

[12] hakre, Sheetal. Chavan, savita. Chavan, P.M. 2012.Software Testing Strategies and Techniques. International Journal of Emerging Technology and Advanced Engineering .Website: www.ijetae.com .2,4.(April 2012), (2250-2459).

Dr. B. V.Ramana Murthy has done his PhD from Osmania University, presently he working as Professor in Computer Science and Engineering, has 18 years of experience in Teaching and R&D. His primary area of interest is Software Engineering & Web Engineering.

Dr. V Padmakar has done his PhD in CSE, presently working as Associate Professor in the Department of Computer Science and Engineering has 18 years of experience in Teaching and Industry. His primary area of interests is Software Engineering, Network Security, and Data mining

Empirical Analysis of Function Point Analysis – Research View

Vuppu Padmakar
Department of CSE
Ph D Research Scholar
OPJS University, Rajasthan
padmaker@gmail.com

Dr. B V Ramana Murthy
Department of CSE, Professor
Mahaveer Institute of Science &
Technology, Hyderabad
drbvrm@gmail.com

Dr. Vaibhav Bansal
Department of CSE
Associate Professor
OPJS University, Rajasthan
drvb.cse@gmail.co

Abstract: Software measurement [1], once an obscure and esoteric specialty, has become essential to good software engineering [2, 3, 4]. Many of the best software developers measure characteristics of the software to get some sense of whether the requirements are consistent and complete, whether the design is of high quality, and whether the code is ready to be tested. Effective project manager's measure attributes of process and product to be able to tell when the software will be ready for delivery and whether the budget will be exceeded. Informed customers measure aspects of the final product to determine if it meets the requirements and is of sufficient quality. And maintainers must be able to assess the current product to see what should be upgraded and improved. Here, we present empirical research in two areas, Function Oriented Analysis to find function points and weightages of plan driven vs agile development based on type of project, validations will be carried out using train test procedure for FPA and Ideal Point Analysis for weightages

Keywords: FPA, metrics, size estimations, code estimation.

_____*****_____

I. INTRODUCTION & RELATED WORK.

Metrics for the Analysis Model:- These metrics address various aspects of the analysis model and include:

- Functionality Delivered: Provides an indirect measure of the functionality that is packaged with in the software.
- System Size: measures[5] of the overall size of the system defined in terms of information available as part of the analysis model[7].
- Specification Quality: provides an indication of the specificity and completeness of a requirements specification.

Function-Based Metrics: The Function Point Metric [FP] [7, 8, 9, 10], first proposed by Albrecht, can be used effectively as a means for measuring[6] the functionality delivered by a system. Using historical data, the FP can then be used to

(1) estimate the cost or effort required to design, code, and test the software;

(2) predict the number of errors that will be encountered during testing.

(3) forecast the number of components and/or the number of projected source lines in the implemented system.

Function points are delivered using an empirical relationship based on countable (direct) measures of software's information domain and assessments of software complexity. Information domain values are defined in the following manner:

Number of external inputs (EIs): Each external input originates from a user or is transmitted from another application and provides distinct application-oriented data or control information. Inputs are often used to update internal logical files (ILFs). Inputs should be distinguished from inquiries, which are counted separately.

Number of external outputs (EOs): Each external output is derived within the application and provides information to the user. In this context external output refers to reports, screens, error messages, and so on. Individual data items within a report are not counted separately.

Number of external inquiries (EQs): An external inquiry is defined as an online input that results in the generation of some immediate software response in the form of an on-line output (often retrieved from an ILF).

Number of internal logical files (ILFs): Each internal logical file is a logical grouping of data that resides within the application's boundary and is maintained via external inputs.

Number of external interface files (ELFs): Each external interface file is a logical grouping of data that resides external to the application but provides data that may be of use to the application.

Sample projects of 'C' Source Code
As mentioned fellow the 'C' source code of the 20 projects total number of lines are counted physically.

S.No.	Project ID	Project Name	FP	NLOC
1	P-1	CPA Calculation	21.75	261
2	P-2	Travel AirBase Agency	12.23	159
3.	P-3	Hospital Management System	49.5	693
4	P-4	Banking Management System	47.61	619
5	P-5	Calendar Project	41.07	575
6	P-6	Contact Management System	12.75	153
7	P-7	Cyber Management System	172.5	2415
8	P-8	Department Store Management System	46.5	696
9	P-9	Employee Record System	29.5	354
10	P-10	Library Management system	52.64	737
11	P-11	Medical Store Management System	171.5	2401
12	P-12	Personal Diary Management System	47.42	664
13	P-13	Phonebook Project	23.33	280
14	P-14	School Billing System	73.61	957
15	P-15	Snake Game	34.38	447
16	P-16	Student Record System	41.08	493
17	P-17	Telecom Billing System	51.57	218
18	P-18	Tic-Tac-Toe Game	17.0	221
19	P-19	Modern Periodic Table	27.78	389
20	P-20	Snakes and Ladders Game	56.71	794
			1030.43	13526

Each FP is calculated by the above process and NLOC non commented lines of code is corresponding the each FP.

Empirical validation process

(i)   The aim of the statistical validation is the determine whether the function point metric can be used to predict the size of FO system in terms of LOC.

(ii)   From the data collected we have to perform descriptive analysis of both for the dependent variable LOC and the independent variable FP.
 i.e.,   NLOC = a + b * FP
From the data sets finding metric

Step 1: $\sum$FP =1030.43

Step 2: $\sum$FP² = 1061785.98

Step3: $\sum$LOC=   13526

Step4: $\sum$FP *$\sum$LOC = 13937596.18

Step5: $\sum$LOC = n a + b $\sum$FP
13526 = 20 a + b * 1030.43   ---------- (1)

Step6: $\sum$FP *$\sum$LOC = a * $\sum$FP + b * $\sum$FP²
 13937596.18 = 20 * 1030.43 + b * 1061785.98   -----(2)

$\qquad$ = 20608.6 + b * 1061785.98

b $\qquad$ = 13916987.58 /1061785.98

$\qquad$ = 13.107

13526 = 20 a + 13.107 * 1030.43

$\qquad$ = 20 a + 13505.84

a $\qquad$ = 13526 – 13505.84 / 20

$\qquad$ = 1.08

From   equation (1)   and (2)
 a =   1.08   b = 13.107
We get
NLOC = 1.08 + 13.107 * FP

That is by observation for each FP approximately it (involves the size estimation) 16 lines of code Scatter diagram and least square regression line of FP and NLOC. Process of finding metric of size estimation based on FP independent metric (derived from design) and dependent variable (LOC).
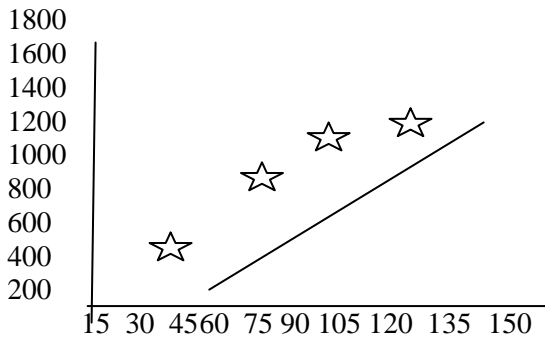
Finding variation (Coefficient of determination)

$$NLOC = \frac{\sum NLOC}{N}$$

Where 'N' is the data sets lie 20

$$NLOC = \frac{13526}{20} = 676.3$$

$$NLOC = a + b * FP$$
$$NLOC = 1.08 + 13.107 * FP$$

Calculating the FP based on the original 'C' source code projects based on the number of line of code.

FP	NLOC	NLOC: NLOC	(LOC: NLOC)²
21.75	261	-415.30	172474.09
12.23	159	-517.30	267599.29
49.5	693	16.70	278.89
47.61	619	-57.30	3283.29
41.07	575	-101.30	10261.69
12.75	153	-523.30	273842.89
172.5	2415	1738.70	3023077.69
46.5	696	19.70	388.09
29.5	354	-322.30	103877.29
52.64	737	60.70	3684.49
171.5	2401	1724.70	2974590.09
47.42	664	-12.30	151.29
23.33	280	-396.30	157053.69
73.61	957	280.70	78792.49
34.38	447	-229.30	52578.49
41.08	493	-183.30	33598.89
51.57	218	-458.30	210038.89
17	221	-455.30	207298.09
27.78	389	-287.30	82541.29
			7655410.91

4.5   Determination of NLOC

LOC	LOC-NLOC	(NLOC-NLOC)²
286.16	25.16	632.89
161.38	2.38	5.66
649.88	-43.12	1859.64
625.10	6.10	37.26
539.38	-35.62	1268.46
168.19	15.19	230.87
2262.04	-152.96	23397.53
610.56	-85.44	7300.76
387.74	33.74	1138.15
691.03	-45.97	2113.01
2248.93	-152.07	23125.13
622.61	-41.39	1712.81
306.87	26.87	721.80
965.89	8.89	78.97
451.70	4.70	22.08
539.52	46.52	2163.70
677.01	459.01	210688.33
223.90	2.90	8.40
365.19	-23.81	566.80
		277072.25

The coefficient of determination

$$= \frac{7655410.91 - 277072.25}{7655410.90}$$

$$= 0.96$$

	Sample1	Sample2	Sample3	Sample4	Sample5	Sample6	Sample7	Sample8	Sample9	Sample10
SLA	0.15	0.20	0.16	0.15	0.13	0.15	0.15	0.15	0.14	0.15
ITBA	1.24	1.19	1.88	1.33	1.25	0.90	1.28	0.72	0.96	0.73
ECS	1.72	2.48	1.39	1.51	1.16	1.22	1.43	1.17	1.14	0.98
BPS	1.73	1.50	1.31	1.77	1.00	1.29	1.09	1.00	1.40	1.67
ES	0.29	0.34	0.59	0.84	0.81	0.98	1.19	1.61	1.30	1.35
SMSSIS	1.34	1.14	1.14	1.11	1.71	1.47	0.50	0.66	1.04	1.13
DCS	1.06	0.64	0.97	0.70	1.07	1.20	1.65	1.37	0.68	0.74
S&S	0.46	0.51	1.51	0.59	0.86	0.79	0.71	1.31	1.33	1.25
	7.99	8.00	8.95	8.00	7.99	8.00	8.00	7.99	7.99	8.00

weights of 'C' different projects of 10 samples

The value of r² = 0.96 shows that the regression equation LOC = 1.08 + FP * 13.107 explains about 96.205 percent of the total navigation observed in the dependent variable. Thus, only 3.795 percent of the total variation in the dependent variable NLOC MC certy * Lecernt – chose

Weights of the 10 sample projects data of graphs for different projects

weights of 'C' different projects of sample 10

Different projects 10 sample graphs

	SLA	ITBA	ECS	BPS	ES	SMSIS	DCS	S&S	
Sample1	39	8.53	7.2	8.09	24.33	8.23	11.25	19.58	126.21
Sample2	40	8.51	2.82	10.12	28.33	10.58	13.95	19.45	133.76
Sample3	39	9.28	8.98	6.81	13.5	9.78	18.89	21.64	127.88
Sample4	38	7.29	9.08	8.98	21.64	10.78	12.33	18.45	126.55
Sample5	40	12.37	7.75	15.07	14	10.87	12.41	14.83	127.3
Sample6	39	16.5	5.9	14.33	12	11.92	7.84	16.17	123.66
Sample7	38	13.74	7.42	12.23	15.59	14.33	12.06	19.58	132.95
Sample8	38	15.92	10.65	15.14	13.01	16.08	12.49	13.87	135.16
Sample9	39	12.23	11	11.45	10.83	11.33	14.48	13.93	124.25
Sample10	37	13.95	13	10.9	10.73	10.89	24.4	15.95	136.82
	387	118.32	83.8	113.12	163.96	114.79	140.1	173.45	

weights of sample 10 for 'C' different projects

weights of sample 10 for 'C' different projects

II. CONCLUSION

The work described in this thesis combined the research areas, size estimation of the Software projects and empirical analysis of software projects. Area1: The objective of size estimation of software projects is to estimate size of LOC for given class diagram. The data collection is made at a macro level, Programming Language source code and class diagram were taken to derive metric. For estimating lines of code of Software Projects, we have considered a linear regression between class point and lines of code. The FP values are obtained from a given class diagram, when subjected to FP calculation process, the lines of code is a dependent variable which is estimated as follows,

$$LOC = a + b * FP,$$

Where a , b, are extracted from Research Work. We have shaped the metric for size estimation of entire application as well as the components of the application like Problem Domain Type, Human Interaction Type, and Data Management Type. The validation of the metric can be better tested by using empirical validation; we used techniques like variances and Productivity Analysis for success rate depending upon the threshold value. To fix the metric (LOC = a + b * FP) we have used train and test method, in which the data is divided into two sets , one set is used to find the size metric and another set is used to validate size metric. This is repeated for 'i' items and its average is taken to fix the equation. The results of the study are found to be sound on an empirical analysis.

REFERENCES

[1]   Fenton, N., "Software Measurement: A Necessary Scientific Basis", IEEE Trans. Software Engineering, Vol. SE-20, no. 3, March 1994, pp. 199-206.

[2]   Humphrey, W., A Discipline for Software Engineering, Addison-Wesley,   1995.

[3]   Somerviue, I., Software Engineering, 6th ed. , Addison-Wesley, 2001.

[4]   Gilb, T., Principles of Software Engineering Management, Addison-Wesley,   1988.

[5]   Putnam, L., and W. Myers, Measures of Excellence, Yourdors Press, 1992.

[6]   Felican, L., and G. Zalateu, "Validating Halstead's Theory for Pascal Programs", IEEE Trans. Software Engineering, Vol. SE-15, no. 2, December 1989, pp. 1630-1632.

[7]   Albrecht, A. J., and J. E. Gaffney, "Software Function, Source Lines of Code and Development Effort Prediction: A Software Science Validation", IEEE Trans. Software engineering, November 1983, pp. 639-648.

[8]   A. J. Albrecht, "Measuring application development productivity", Proc.   of the Joint SHARE / GUIDE / IBM Application Development Symposium, Oct.   1979, pp. 83-92.

[9]   A. J. Albrecht, J. E. Gaffney, "Software Function, source lines of code, and development effort prediction: A software science validation ",IEEE Trans. Software Eng. 9, no. 6 (1983) 639-648.

[10]   J. B. Dreger, Function Point Analysis, Prentice-Hall. 1989.

Influence of Velocity Slip on the Peristaltic Pumping of a Jeffrey Fluid in a Non Uniform Annulus

Sudhakar Rao .G[1], S V H N Krishna Kumari. P[2] *, Y. V K. Ravi Kumar[3], V. Naveen[4]

Asst. Professor, Department of Mathematics, Nizam College, Osmania University , Hyderabad, India[1]

Professor, Department of Mathematics, Vidya Jyothi Institute of Technology, Hyderabad, India[2]

Asst. Professor, Practice School Division, Birla Institute of Technology & Science- Pilani, Hyderabad, India[3]

Asst Professor, Methodist College of Engineering & Technology, Hyderabad, India[4]

ABSTRACT: Influence of velocity slip on the peristaltic transport of a Jeffrey fluid in a non uniform annulus is investigated. A Sinusoidal wave with is travelling on the outer tube wall and the inner tube is rigid, uniform and moving with a constant velocity. Expressions for velocity, volume flow rate and pressure rise are obtained. The effect of various parameters on the pumping characteristics is discussed with the help of graphs**.**

KEYWORDS: Peristaltic pumping, Jeffrey fluid, non uniform annulus , permeable wall.

I. INTRODUCTION

Peristaltic pumping is a form of material transport induced by a progressive wave of area contraction or expansion along the length of a distensible tube. Peristaltic motion in a channel/tube is now known as an important type of flow occurring in several engineering and physiological processes. In living systems it is a distinctive pattern of smooth muscle contractions that propel the contents of the tube, as food stuffs through oesophagus and alimentary canal, in transport of urine from kidney to bladder, the movement of chyme in the gastro-intestinal tract, vasomotion of the small blood vessels and in many other glandular ducts. Engineers have used the peristaltic mechanism in developing pumps which have several industrial applications.

The problem of mechanism of peristaltic transport has attracted the attention of many researchers since the experimental investigation of Latham [1]. Subsequently a number of analytical, numerical and experimental studies of peristaltic flow of different fluids have been reported under different conditions with reference to physiological and mechanical situations. Ravi Kumar et.al [2] studied the unsteady peristaltic pumping in a finite length tube with permeable wall.

Most of the researchers assumed that blood and the most of the physiological fluids behave like non-Newtonian fluids. They considered various non-Newtonian fluids   like Viscoelastic fluid (Bohme and Friedrich [3]), power law fluid (Ravi Kumar et al. [4]), Casson fluid (Krishna Kumari et al. [5]) ,micro polar fluid (Srinivasacharya et.al [6]),

Herschel-Bulkley fluid (Ramesh Babu [7] al.) in their theoretical investigations.

The Jeffrey model is relatively simpler linear model using time derivatives instead of converted derivatives for example the Oldroyd – B model does, it represents a rheology different from the Newtonian. Krishna Kumari et al.[8] studied the peristaltic transport of a Jeffrey fluid in a porous tube by considering Beavers – Joseph conditions and Saffman conditions. Peristaltic pumping of a Jeffrey fluid under the effect of a magnetic field in an inclined channel is studied by Krishna Kumari et al. [9].

Gupta and Seshadri [10] discussed the peristaltic flow through non uniform channels and tubes with particular reference to the flow of spermatic fluid in vas deferens considering the inertia terms to be small in comparison to the viscous terms. Chaturani and Ranganatha [11] discussed a mathematical model for solute transfer in ultra filtering glomerular capillaries, where capillaries are taken as permeable tubes. Further it is reported that the blood flow in small vessels occurs due to peristalsis. Slip effect on the flow of a fractional second grade fluid through a cylindrical tube is analyzed   by Rathod.V et al.[12].

With the above discussion in mind, we propose to study the peristaltic transport of Jeffrey fluid through the gap between coaxial tubes, where the outer tube is non-uniform and has a sinusoidal wave traveling down its wall and the inner one is a rigid and uniform tube and moving with a constant velocity V. This investigation may have application in many clinical applications such as the endoscope problem.

Jeffrey model

The constitutive equations for an incompressible Jeffrey fluid are

$$\overline{T} = -\overline{p}\,\overline{I} + \overline{S}$$

$$\overline{S} = \frac{\mu}{1+\lambda_1}\left(\frac{\partial \overline{\gamma}}{\partial t} + \lambda_2 \frac{\partial^2 \overline{\gamma}}{\partial t^2}\right)$$

where $\overline{T}$ and $\overline{S}$ are Cauchy stress tensor and extra stress tensor, $\overline{P}$ is the pressure, $\overline{I}$ is the identity tensor, λ_1 is the ratio of the relaxation to retardation times, λ_2 is the retardation time and γ is the shear rate.

II. MATHEMATICAL FORMULATION OF THE PROBLEM

Let a_1 be the radius of the inner tube and $a_2(\overline{z})$ be the radius of the outer tube at any co-axial distance $\overline{z}$ from the inlet.(Fig.1) ; The geometry of the wall surfaces are $\overline{r_1} = a_1$ (1)

$$\overline{r_2} = a_2(\overline{z}) + bSin\left[\frac{2\pi}{\lambda}(\overline{z} - \overline{ct})\right] \tag{2}$$

International Journal of Innovative Research in Science, Engineering and Technology

(An ISO 3297: 2007 Certified Organization)

Vol. 5, Issue 1, Januray 2016
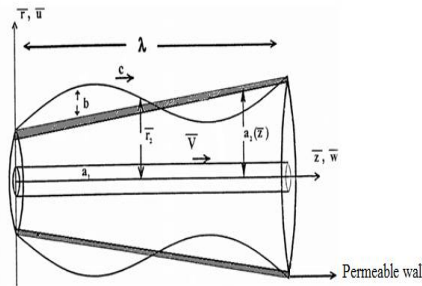
Fig. 1. Physical Model

where $a_2(\bar{z}) = a_3 + kz$ (k = 0 corresponds to uniform tube) (3)

Here a_3 is the radius of the outer tube at the inlet, k (<<1) is a constant whose magnitude depends on the length of the outer tube, b is the wave amplitude, λ is the wave length and $\bar{t}$ is the time. We choose a cylindrical co-ordinate system $(\bar{r}, \bar{z})$ where the $\bar{z}$-axis lies along the centre line of the inner and outer tubes and $\bar{r}$ is the distance measured radially.

The equations of motion of the flow in the annulus between the inner and the outer tubes are

$$\frac{1}{\bar{r}}\frac{\partial}{\partial \bar{r}}(\bar{r}\bar{u}) + \frac{\partial \bar{w}}{\partial \bar{z}} = 0 \tag{4}$$

$$\rho\left(\frac{\partial \bar{u}}{\partial \bar{t}} + \bar{u}\frac{\partial \bar{u}}{\partial \bar{r}} + \bar{w}\frac{\partial \bar{u}}{\partial \bar{z}}\right) = -\frac{\partial \bar{p}}{\partial \bar{r}} + \frac{\mu}{1+\lambda_1}\left\{\frac{\partial}{\partial \bar{r}}\left(\frac{1}{\bar{r}}\frac{\partial}{\partial \bar{r}}(\bar{r}\bar{u})\right) + \frac{\partial^2 \bar{u}}{\partial \bar{z}^2}\right\} \tag{5}$$

$$\rho\left(\frac{\partial \bar{w}}{\partial \bar{t}} + \bar{u}\frac{\partial \bar{w}}{\partial \bar{r}} + \bar{w}\frac{\partial \bar{w}}{\partial \bar{z}}\right) = -\frac{\partial \bar{p}}{\partial \bar{z}} + \frac{\mu}{1+\lambda_1}\left\{\frac{1}{\bar{r}}\frac{\partial}{\partial \bar{r}}\left(\bar{r}\frac{\partial \bar{w}}{\partial \bar{r}}\right) + \frac{\partial^2 \bar{w}}{\partial \bar{z}^2}\right\} \tag{6}$$

where $\bar{u}$, $\bar{w}$ are velocity components in $\bar{r}$ and $\bar{z}$ directions respectively, $\bar{p}$ is the pressure, μ is the viscosity coefficient and λ_1 is the Jeffrey parameter.

The boundary conditions are

$$\bar{u} = 0, \qquad\qquad \bar{w} = V \qquad\qquad at \qquad\qquad \bar{r} = \bar{r}_1 \tag{7}$$

$$\bar{u} = \frac{\partial \bar{r}_2}{\partial \bar{t}}, \qquad\qquad \bar{w} = -\frac{\sqrt{k}}{\alpha}\frac{\partial \bar{w}}{\partial \bar{r}} \qquad\qquad at \qquad\qquad \bar{r} = \bar{r}_2 \tag{8}$$

we introduce the following non-dimensional quantities

$$z = \frac{\bar{z}}{\lambda}, r = \frac{\bar{r}}{a_3}, w = \frac{\bar{w}}{c}, u = \frac{\lambda \bar{u}}{a_3 c}, p = \frac{a_3^2}{\lambda \mu c}\bar{p}, t = \frac{\bar{t}c}{\lambda}, \text{Re} = \frac{\rho c a_3}{\mu}, \delta = \frac{a_3}{\lambda}, Da = \frac{k}{a_3^2}, v = \frac{\bar{v}}{c}, r_1 = \frac{\bar{r}_1}{a_3},$$

$r_2 = \dfrac{\bar{r_2}}{a_3} = 1 + \dfrac{\lambda z k}{a_3} + \phi Sin[2\pi(z-t)]$, where $\phi = \dfrac{b}{a_3} < 1$ (amplitude ratio), Re is the Reynolds number δ is the

wave number ratio and V is the constant velocity of the inner tube.

By using the non-dimensional quantities, the equations (4) to (6) become,

$$\frac{1}{r}\frac{\partial}{\partial r}\left(\frac{ru}{1+\lambda_1}\right) + \frac{\partial w}{\partial z} = 0 \tag{9}$$

$$\frac{\operatorname{Re}\delta^3}{1+\lambda_1}\left(\frac{\partial u}{\partial t} + u\frac{\partial u}{\partial r} + w\frac{\partial u}{\partial z}\right) = \frac{-\partial p}{\partial r} + \delta^2\frac{\partial}{\partial r}\left(\frac{1}{r}\frac{\partial}{\partial r}\left(\frac{ru}{1+\lambda_1}\right)\right) + \delta^4\frac{\partial^2 u}{\partial z^2} \tag{10}$$

$$\frac{\operatorname{Re}\delta}{1+\lambda_1}\left(\frac{\partial w}{\partial t} + u\frac{\partial w}{\partial r} + w\frac{\partial w}{\partial z}\right) = \frac{-\partial p}{\partial z} + \frac{1}{r}\frac{\partial}{\partial r}\left(r\frac{\partial w}{\partial r}\right) + \delta^2\frac{\partial^2 w}{\partial z^2} \tag{11}$$

Using the long wave length, low Reynolds number assumptions and dropping terms of δ and higher order, the Eqn. (10) to (11) become,

$$\frac{\partial p}{\partial r} = 0 \tag{12}$$

$$\frac{\partial p}{\partial z} = \frac{1}{r}\frac{\partial}{\partial r}\left(\frac{r}{1+\lambda_1}\frac{\partial w}{\partial r}\right) \tag{13}$$

The dimensionless boundary conditions are

$$w = V \qquad at \qquad r = r_1 \tag{14}$$

$$w = \frac{-\sqrt{Da}}{\alpha}\frac{\partial w}{\partial r} \quad at \quad r = r_2(z,t) = 1 + \frac{\lambda z k}{a_3} + \phi.Sin[2\pi(z-t)] \tag{15}$$

where α is the slip parameter and Da is the Darcy number.

III. SOLUTION OF THE PROBLEM

Solving the Eqns. (12) and (13) together with boundary conditions (14) and (15), we get the velocity field as

$$w = \frac{\partial p}{\partial z}\left(\frac{r^2 - r_1^2}{4}\right)(1+\lambda_1) + V - \frac{r_2\alpha(1+\lambda_1)}{r_2\alpha\log\left(\frac{r_2}{r_1}\right)+\sqrt{Da}}\left\{\frac{\partial p}{\partial z}\left(\frac{r_2^2 - r_1^2}{4}\right) + \frac{V}{1+\lambda_1} + \frac{\sqrt{Da}}{\alpha}\left(\frac{r_2}{4}\right)\right\}\log\left(\frac{r}{r_1}\right) \tag{16}$$

The instantaneous volume flow rate $Q(z,t)$ is given by

$$Q = \int_{r_1}^{r_2} 2\pi r \left[\frac{\partial p}{\partial z}\left(\frac{r^2 - r_1^2}{4}\right)(1+\lambda_1) + V - \frac{r_2 \alpha (1+\lambda_1)}{r_2 \alpha \log\left(\frac{r_2}{r1}\right) + \sqrt{Da}} \left\{ \frac{\partial p}{\partial z}\left(\frac{r_2^2 - r_1^2}{4}\right) + \frac{V}{1+\lambda_1} + \frac{\sqrt{Da}}{\alpha}\left(\frac{r_2}{4}\right) \right\} \log\left(\frac{r}{r_1}\right) \right] dr$$

(17)

The time mean flow over time period $T = \lambda / c$ is given by

$$\bar{Q}(z,t) = \frac{1}{T}\int_0^T Q(z,t)dt$$

(18)

From equation (17), we get the pressure gradient as

$$\frac{\partial p}{\partial z} = \frac{Q\left(r_2 \alpha \log\left(\frac{r_2}{r_1}\right) + \sqrt{Da}\right) + 2\pi r_2 \alpha V\left(\frac{r_2^2}{2}\log\left(\frac{r_2}{r_1}\right) - \left(\frac{r_2^2 - r_1^2}{4}\right)\right)}{\left(\frac{r_2^2 - r_1^2}{4}\right)(1+\lambda_1)\left\{ \left(\frac{r_2^2 - r_1^2}{4}\right)2\pi c_1 - 2\pi r_2 \alpha\left(\frac{r_2^2}{2}\log\left(\frac{r_2}{r_1}\right) - \left(\frac{r_2^2 - r_1^2}{4}\right)\right)\right\} - (1+\lambda_1)\left(\frac{r_2^2}{2}\right)\frac{\sqrt{Da}}{\alpha}c_1}$$

(19)

The pressure rise Δp is given by, $\Delta p = \int_0^\Lambda \frac{\partial p}{\partial z}dz$ where $\Lambda = L/\lambda$, L is length of the tube, λ is wave length

IV. RESULTS AND DISCUSSIONS

The effect of Jeffrey parameter λ_1 on the pumping characteristics for uniform and non-uniform cases are discussed through Fig 2. It is noticed that for a give time mean flow rate $\bar{Q}$, the pressure rise decreases with increasing λ_1 in all the three regions i.e. pumping region ($\Delta p > 0$), co-pumping region ($\Delta p < 0$) and free pumping region ($\Delta p = 0$). It is observed that the pumping is more in uniform than in non uniform annulus for any given $\bar{Q}$. Also the pumping is more for a Newtonian fluid and the pumping decreases as the non Newtonian nature of the fluid increases.

The effect of slip parameter α on the pumping phenomenon is observed from Figs 3 & 4. It is concluded from these Figs that the pressure rise decreases with increasing α for a fixed $\bar{Q}$. Also for a given Δp, the increase in α decreases the flow rate in the pumping region. The variation of z affects the pumping phenomenon as the pumping is more for uniform case than non uniform case.

From figures (5) and (6) the effect of Darcy number Da is noticed. For a given Darcy number Da the pressure rise decreases for increasing $\bar{Q}$. It is observed that an increase in the flow rate decreases the pressure rise. Also for fixed flow rate, the pressure rise increases with increasing Da. For a given Da, the pressure rise is more for non uniform case than the uniform case. The effect of non Newtonian behavior is also observed from these figures.

From equation (19), we calculated the pressure rise Δp as a function of $\bar{Q}$ for different values of r_1 (radius

of the inner tube) and is shown in Figures (7) and (8) considering uniform and non uniform cases. in the case of uniform annulus. It is observed that for fixed flow rate, the pressure rise Δp increases with increasing r_1 . It is observed that for a given Δp , the increase in r_1 increased the flow rate in all the three pumping regions.

.
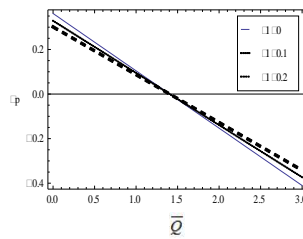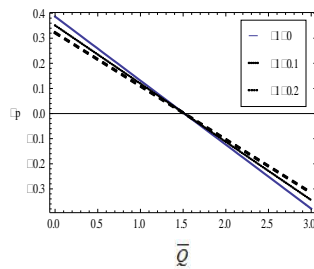
(b)

Fig. 2. Variation of pressure rise Δp with $\overline{Q}$ for different values of Jeffrey parameter λ_1 (a) uniform annulus (b) non uniform annulus.

(a)

International Journal of Innovative Research in Science, Engineering and Technology

(An ISO 3297: 2007 Certified Organization)

Vol. 5, Issue 1, Januray 2016
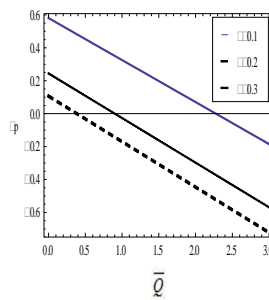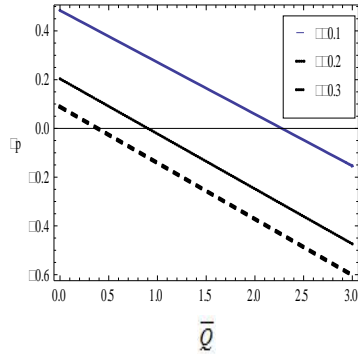
(b)

Fig. 3. Variation of pressure rise Δp with $\overline{Q}$ for a uniform annulus for different values of slip parameter α for (a) Newtonian (b) Non Newtonian fluids
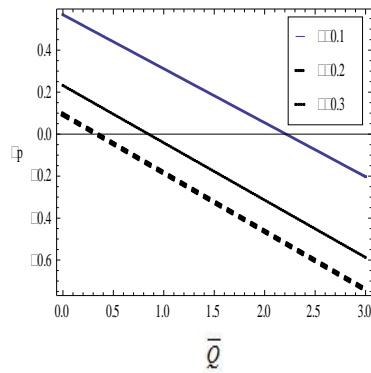
(a)
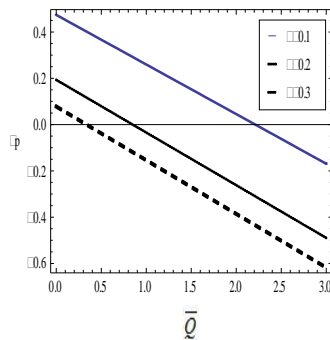
(b)

Fig 4. Variation of pressure rise Δp with $\overline{Q}$ for a non-uniform annulus for different values of α with (a) Newtonian (b) Non Newtonian fluids
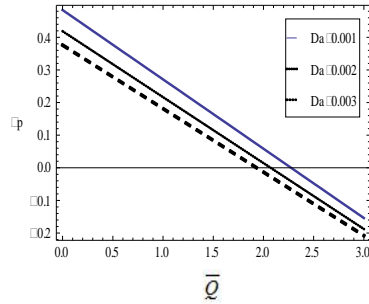
(a)
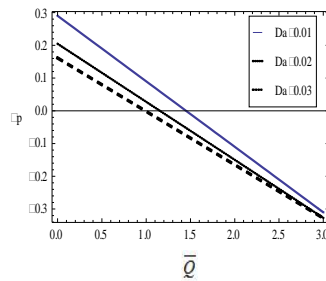
(b)

Fig. 5. Variation of pressure rise Δp with $\overline{Q}$ for a uniform annulus for different values of Da with (a) Newtonian

(b) Non Newtonian fluids
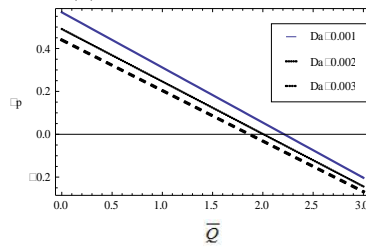
(a)
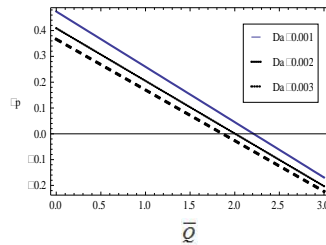
(b)

Fig.6. Variation of pressure rise Δp with $\overline{Q}$ for a non-uniform annulus for different values of Da with with (a)

ewtonian (b) Non Newtonian fluids
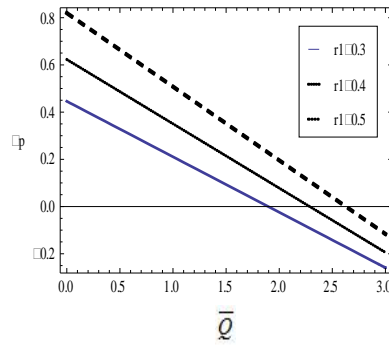
(a)
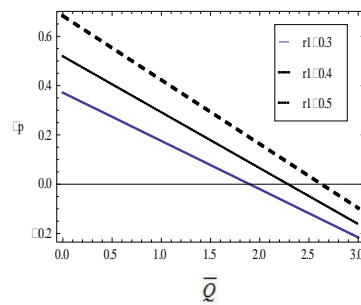
(b)

Fig. 7. Variation of pressure rise Δp with $\overline{Q}$ for a uniform annulus for different values of r1 with (a) Newtonian

(b) Non Newtonian fluids
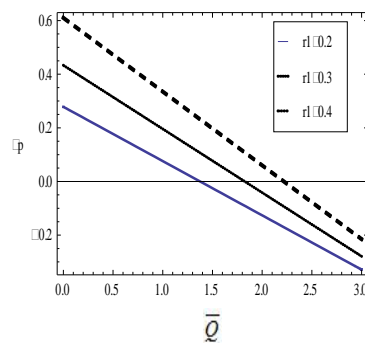
(a)
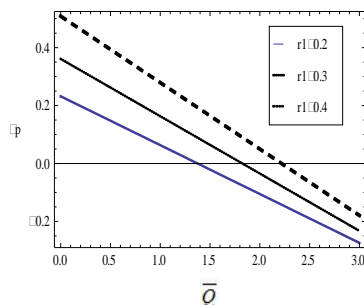
(b)

Fig.8. Variation of pressure rise Δp with $\overline{Q}$ for a non-uniform annulus for different values of r1 with (a) Newtonian

(b) Non Newtonian fluids

REFERENCES

[1] Latham, T.W.,1966, Fluid motion in a peristaltic pump. *M.SC, Thesis. Cambridge,* Mass: MIT-Press.

[2]   Y.V.K.RaviKumar, S.V.H.N.KrishnaKumari, M. V. Ramana Murthy, S.Sreenadh, 2010,"Unsteady peristaltic pumping in a finite length tube with permeable wall", *Trans. ASME, Jr. of Fluids Engg.,* **32**,pp.1012011 – 1012014.

[3] Bohme, G., and Friedrich, R., (1983), "Peristaltic flow of viscoelastic liquids", *J.Fluid   Mech.,* **128**, pp.109-122.

[4] Y.V.K.RaviKumar, S.V.H.N.KrishnaKumari, M. V. Ramana Murthy, S.Sreenadh, 2011, "Peristaltic Transport of a power law fluid in an asymmetric channel bounded by permeable walls" Advances in Applied Science Research,   volume 2 issue 3, pp.396-406.

[5] S.V.H.N.KrishnaKumari, M. V. Ramana Murthy, Y.V.K.RaviKumar, Chenna Krishna Reddy, 2011, " Peristaltic pumping of magneto hydro dynamic Casson fluid in an inclined channel", " Advances in Applied Science Research,   volume 2 issue 2, pp.428-436.

[6] Srinivasacharya , D.,Mishra, M. and   Ramachandra Rao, A.,2003,"Peristaltic pumping of a   micro polar fluid in a tube", *Acta Mechanica,* **161**, pp.165-178.

[7] Vajravelu ,K.,Sreenadh,S and Ramesh Babu,V.,2005,"Peristaltic transport of a Hershel –   Bulkley fluid in an inclined tube",*Int.J.Non Linear Mech.*,**40**, pp.83-90.

[8]   S.V.H.N.Krishna Kumari.P.,Y.V.K.Ravi Kumar,M.V.Ramana   Murthy,   S.Sreenadh,2011,   "Peristaltic transport of a Jeffrey fluid in the porous tube",   *Jr.of Engg.and Appl.Sciences,***6**, No.3,pp..61-66.

[9] S.V.H.N.KrishnaKumari.P.,Y.V.K.RaviKumar, M. V. Ramana Murthy, S.Sreenadh,   2011,"Peristaltic pumping of a Jeffrey fluid under the effect of magnetic field in an inclined   Channel",   *Appl.Math.Sciences,* Vol.5 No.**9** , pp. 447-458.

[10] Gupta, B.B. and Seshadri, V.,1976,"Peristaltic pumping in non-uniform tubes", *J.Biomech.,* **9,**pp**.** 105-109.

[11] Chaturani,P and Ranganatha, T.R,1993," Solute transfer in fluid flow in permeable tubes with application to flow in glomerular capillaries",*Acta Mechanica,* **96**,pp.139-154.

[12] Rathod V, Anita Tuljappa, 2015, "Slip effect on the peristaltic flow of a fractional second grade fluid trough a cylindrical tube" Advances in Applied Science Research, 6(3): 101-111.

Empirical Analysis of Software Projects - Research View

Vuppu Padmakar[1], Dr. B V Ramana Murthy[2], Dr. Vaibhav Bansal[3]

Research Scholar, Department of CSE, OPJS University, Rajasthan, India

Professor, Department of CSE, Mahaveer Institute of Science & Technology, Hyderabad, India

Associate Professor, Department of CSE, OPJS University, Rajasthan, India

ABSTRACT: Empirical Analysis of software projects: Software projects is not a perfect clone of software engineering, but it borrows many of software engineering fundamental concepts and principles. we have addressed the numerical/empirical analysis of software projects, which enables the project manager and software developers to understand software engineering better. We have limited our study to software management in this area. A questionnaire was prepared for the study, based on the four important concepts of software engineering, namely, software attributes, software methods, software framework, software practices. The attributes relevant for each of the above concepts are identified after developers in the industry. The AHP technique is used for designing and evaluating the responses to the questionnaires[6,7]. The AHP techniques given the weights of the attributes considered in the questionnaire, which helps the project manager as a indicator for the further process. Once attributes weights are known group-wise, the task that follows is testing their applicability in practices and relevance of the attributes identified. For the purpose, the questionnaire has been applied for nine real-time projects which are under use and developed by a project manager. The projects were ranked based on the 36 attributes put under 4 graphics, by generating pair-wise comparison matrices using AHP techniques. The Ideal Point Analysis is used which integrates software attributes, weights of respondents and attributes wise weights of projects using AHP given by project manager. The Ideal Point Analysis helps in rating the projects and validation of the research.

KEYWORDS: Software Projects, AHP, FP, Project Manager

I. INTRODUCTION

There are many different types of software System and there is no universal set of software techniques that is applicable to all of these. The software engineering methods and tools used depend on the type of application being developed, the requirements of the customer and the background of the development team.

Application Types

1. **Stand-alone applications:** These are application systems that run on a local computer, such as a PC. They include all necessary functionality and do not need to be connected to a network.

2. **Interactive transaction-based applications:** Applications that execute on a remote computer and are accessed by users from their own PCs or terminals. These include web applications such as e-commerce applications.

3. **Embedded control systems:** These are software control systems that control and manage hardware devices. Numerically, there are probably more embedded systems than any other type of system.

4. **Batch processing systems:** These are business systems that are designed to process data in large batches. They process large numbers of individual inputs to create corresponding outputs.

5. **Entertainment systems:** These are systems that are primarily for personal use and which are intended to entertain the user.

6. **Systems for modelling and simulation:** These are systems that are developed by scientists and engineers to model physical processes or situations, which include many, separate, interacting objects.

7. **Data collection systems:** These are systems that collect data from their environment using a set of sensors and send that data to other systems for processing.

8. **Systems of systems:** These are systems that are composed of a number of other software systems. Some fundamental principles apply to all types of software system, irrespective of the development techniques used: Systems should be developed using a managed and understood development process. Of course, different processes are used for different types of software. Dependability and performance are important for all types of system. understanding and managing the software specification and requirements (what the software should do) are important. Where appropriate, you should reuse software that has already been developed rather than write new software.

II. RELATED WORK

Key Points to develop a software products Software engineering is an engineering discipline that is concerned with all aspects of software production. Essential software product attributes are maintainability, dependability and security, efficiency and acceptability. The high-level activities of specification, development, validation and evolution are part of all software processes. The fundamental notions of software engineering are universally applicable to all types of system development. There are many different types of system and each requires appropriate software engineering tools and techniques for their development. The fundamental ideas of software engineering are applicable to all types of software system.

Empirical Analysis of Software Projects Motivation and Background:-Software projects -based systems and applications deliver a complex array of content and functionality, to a broad population of end-users. Project management is the process that is used to create high-quality software applications. Project management is a perfect clone of a software engineering, but it borrows many of software engineering fundamental concepts and principles. In addition, the project management process emphasizes similar technical and management activities are conducted, but the overriding philosophy dictates a disciplined approach to the development of a computer based system. Software Engineers and non-technical content developers create the software applications[8,9]. As software projects becomes increasingly integrated in business strategies, for small and large companies, the need to build reliable, usable, and adaptable systems grows in importance. That is why a disciplined approach to software application development is necessary[10]. Like any engineering discipline, software engineering applies a generic approach that is tempered with specialized strategies, tactics and methods.

The software engineering process begins with the formulation of a problem to be solved by the software application. The software engineering project is planned and the requirements and design of the application are modelled. The system is constructed, using specialized technologies and tools associated with the software. It is then delivered to end-users and evaluated, using both technical and business criteria. Because software applications evolve continuously, mechanism for configuration control, quality assurance, and on-going support must be established.

Objective: To enable the Project Manager/Software developers to understand Project Management better.

Scope: The research work is helpful for Project Management.

Problem Statement: To provide an indication of the quality of the project management from a technical point of view.

Software projects are not a perfect clone of software engineering, but it borrows many of software engineering fundamental concepts and principles. we have addressed the numerical/empirical analysis of software projects, which

enables the project manager and software developers to understand software engineering better. We have limited our study to software management in this area. A questionnaire was prepared for the study, based on the four important concepts of software engineering, namely, software attributes, software methods, software framework, software practices. The attributes relevant for each of the above concepts are identified after developers in the industry. The AHP technique is used for designing and evaluating the responses to the questionnaires[6,7]. The AHP techniques given the weights of the attributes considered in the questionnaire, which helps the project manager as a indicator for the further process.

Once attributes weights are known group-wise, the task that follows is testing their applicability in practices and relevance of the attributes identified. For the purpose, the questionnaire has been applied for nine real-time projects which are under use and developed by a project manager. The projects were ranked based on the 36 attributes put under 4 graphics, by generating pair-wise comparison matrices using AHP techniques. The Ideal Point Analysis is used which integrates software attributes, weights of respondents and attributes wise weights of projects using AHP given by project manager. The Ideal Point Analysis helps in rating the projects and validation of the research.

The Software Project Management module suggested that management involves the following activities:

1. Planning   –   deciding what is to be done;
2. Organizing   –   making arrangements;
3. Staffing   –   selecting the right people for the job, etc.;
4. Directing   –   giving instructions;
5. Monitoring   –   checking on progress;
6. Controlling   –   taking action to remedy hold-ups;
7. Innovating   –   coming up with new solutions;
8. Representing   –   liaising with users, etc.

The management task is to ask mangers what their most frequent challenges are. A survey of software project mangers produced the following list.

1. Copy with deadlines   -   (85%);
2. Coping with resource constraints   -   (83%);
3. Communicating effectively among task group   (80%);
4. Gaining commitment from team members   (74%)
5. Establishing measurable milestones   -   (70%)
6. Coping with changes   -   (60%)
7. Working out project plan agreement with their team   (57%)
8. Gaining commitment from management   -   (45%)
9. Dealing with conflict   -   (42%)
10. Managing vendors and sub-contractors   -   (38%)

The percentages relate to the numbers of managers identifying each challenge. A manager could identify more than one.

III. SIMULATION RESULTS

As the different software projects like ECS and ES types of projects holds the high cost in development and testing due to complexity of the production follows by DCS, SMSSIM then ECS ITBA and SCA. As the different software projects based on the weightages as suggested by the project manager the following weightages are calculated.

The empirical analysis of types of software projects applications to the development of the product gives project manager an view to gives estimation, the analysis will gives insight of the complexity being obtained by the different types of software projects applications in the form of weightages, more than weightages more to the complexity of development and testing in terms of estimation one more.

Weights of the 10 sample of different types software's projects data

	SLA	ITBA	ECS	BPS	ES	SBSSIS	DCS	S&S	
SLA	1.00	0.17	0.17	0.14	0.33	0.14	0.17	0.33	
ITBA	6.00	1.00	0.25	2.00	5.00	0.50	3.00	3.00	
ECS	6.00	4.00	1.00	4.00	3.00	0.50	0.33	5.00	
BPS	7.00	0.50	0.25	1.00	4.00	5.00	4.00	4.00	
ES	3.00	0.20	0.33	0.25	1.00	0.33	0.25	0.25	
SMSSIS	7.00	2.00	2.00	0.20	3.00	1.00	2.00	4.00	
DCS	6.00	0.33	3.00	0.25	4.00	0.50	1.00	2.00	
S&S	3.00	0.33	0.20	0.25	4.00	0.25	0.50	1.00	
	39.00	8.53	7.20	8.09	24.33	8.23	11.25	19.58	
	SLA	ITBA	ECS	BPS	ES	SBSSIS	DCS	S&S	
SLA	0.03	0.02	0.02	0.02	0.01	0.02	0.01	0.02	0.15
ITBA	0.15	0.12	0.03	0.25	0.21	0.06	0.27	0.15	1.24
ECS	0.15	0.47	0.14	0.49	0.12	0.06	0.03	0.26	1.72
BPS	0.18	0.06	0.03	0.12	0.16	0.61	0.36	0.20	1.73
ES	0.08	0.02	0.05	0.03	0.04	0.04	0.02	0.01	0.29
SMSSIS	0.18	0.23	0.28	0.02	0.12	0.12	0.18	0.20	1.34
DCS	0.15	0.04	0.42	0.03	0.16	0.06	0.09	0.10	1.06
S&S	0.08	0.04	0.03	0.03	0.16	0.03	0.04	0.05	0.46
	1.00	1.00	1.00	1.00	1.00	1.00	1.00	1.00	

Weights of sample 10 for 'C' different projects

Like above the weights of samples of 1 to 10 for different software projects priority of weights range 1 to 7 for calculations and consolidated sample collected and their graph for different software projects weightages as follows.

10 Samples graph for different projects

	Sample1	Sample2	Sample3	Sample4	Sample5	Sample6	Sample7	Sample8	Sample9	Sample10
SLA	0.15	0.20	0.16	0.15	0.13	0.15	0.15	0.15	0.14	0.15
ITBA	1.24	1.19	1.88	1.33	1.25	0.90	1.28	0.72	0.96	0.73
ECS	1.72	2.48	1.39	1.51	1.16	1.22	1.43	1.17	1.14	0.98
BPS	1.73	1.50	1.31	1.77	1.00	1.29	1.09	1.00	1.40	1.67
ES	0.29	0.34	0.59	0.84	0.81	0.98	1.19	1.61	1.30	1.35
SMSSIS	1.34	1.14	1.14	1.11	1.71	1.47	0.50	0.66	1.04	1.13
DCS	1.06	0.64	0.97	0.70	1.07	1.20	1.65	1.37	0.68	0.74
S&S	0.46	0.51	1.51	0.59	0.86	0.79	0.71	1.31	1.33	1.25
	7.99	8.00	8.95	8.00	7.99	8.00	8.00	7.99	7.99	8.00

weights of 'C' different projects of 10 samples

Weights of 'C' different projects of sample 10

Different projects 10 sample graphs

	SLA	ITBA	ECS	BPS	ES	SMSIS	DCS	S&S	
Sample1	39	8.53	7.2	8.09	24.33	8.23	11.25	19.58	126.21
Sample2	40	8.51	2.82	10.12	28.33	10.58	13.95	19.45	133.76
Sample3	39	9.28	8.98	6.81	13.5	9.78	18.89	21.64	127.88
Sample4	38	7.29	9.08	8.98	21.64	10.78	12.33	18.45	126.55
Sample5	40	12.37	7.75	15.07	14	10.87	12.41	14.83	127.3
Sample6	39	16.5	5.9	14.33	12	11.92	7.84	16.17	123.66
Sample7	38	13.74	7.42	12.23	15.59	14.33	12.06	19.58	132.95
Sample8	38	15.92	10.65	15.14	13.01	16.08	12.49	13.87	135.16
Sample9	39	12.23	11	11.45	10.83	11.33	14.48	13.93	124.25
Sample10	37	13.95	13	10.9	10.73	10.89	24.4	15.95	136.82
	387	118.32	83.8	113.12	163.96	114.79	140.1	173.45	

weights of sample 10 for 'C' different projects

weights of sample 10 for 'C' different projects

IV. CONCLUSION AND FUTURE WORK

Software projects are not a perfect clone of software engineering, but it borrows many of software engineering fundamental concepts and principles. We have addressed the numerical/empirical analysis of software projects, which enables the project manager and software developers to understand software engineering better. We have limited our

study to software management in this area. A questionnaire was prepared for the study, based on the four important concepts of software engineering, namely, software attributes, software methods, software framework, software practices. The attributes relevant for each of the above concepts are identified after developers in the industry. The AHP technique is used for designing and evaluating the responses to the questionnaires. The AHP techniques given the weights of the attributes considered in the questionnaire, which helps the project manager as a indicator for the further process.

REFERENCES

[1] Fenton, N., "Software Measurement: A Necessary Scientific Basis", IEEE Trans. Software Engineering, Vol. SE-20, no. 3, March 1994, pp. 199-206.
[2] Humphrey, W., A Discipline for Software Engineering, Addison-Wesley, 1995.
[3] Somerviue, I., Software Engineering, 6th ed. , Addison-Wesley, 2001.
[4] Gilb, T., Principles of Software Engineering Management, Addison-Wesley,   1988.
[5] Putnam, L., and W. Myers, Measures of Excellence, Yourdors Press, 1992.
[6] Felican, L., and G. Zalateu, "Validating Halstead's Theory for Pascal Programs", IEEE Trans. Software Engineering, Vol. SE-15, no. 2, December 1989, pp. 1630-1632.
[7] Albrecht, A. J., and J. E. Gaffney, "Software Function, Source Lines of Code and Development Effort Prediction: A Software Science Validation", IEEE Trans. Software engineering, November 1983, pp. 639-648.
[8] A. J. Albrecht, "Measuring application development productivity", Proc. of the Joint SHARE / GUIDE / IBM Application Development Symposium, Oct.   1979, pp. 83-92.
[9] A. J. Albrecht, J. E. Gaffney, "Software Function, source lines of code, and development effort prediction: A software science validation ",IEEE Trans. Software Eng. 9, no. 6 (1983) 639-648.
[10] J. B. Dreger, Function Point Analysis, Prentice-Hall. 1989.

BIOGRAPHY

Mr. V Padmakar is pursuing PhD in CSE, and has done his M Tech (CSE) from JNTUH, presently working as Professor in Computer Science and Engineering has 17 years of experience in Teaching and Industry. His primary area of interests is Software Engineering, Network Security and Data mining

Dr. B. V.Ramana Murthy has done his PhD from Osmania University, presently he working as Professor in Computer Science and Engineering, has 18 years of experience in Teaching and R&D. His primary area of interest is Software Engineering & Web Engineering.

RESEARCH ARTICLE

FRICTION STIR WELDING OF STAINLESS STEELS – REVIEW.

A. Rajasekhar.

Professor, Methodist College of Engineering & Technology, Abids, Hyderabad, Telangana.-500 001.

Manuscript Info	*Abstract*
	After development of tungsten alloys and polycrystalline cubic boron nitride (PCBN) tools, lot of progress is made in FSW of stainless steel. Although some issues remain to be solved, satisfactory welds are produced and weld properties are found suitable for the intended applications. This paper summarizes the progress of research work on Friction stir welding of different types of stainless steels. It covers the research made in the selection of suitable tool materials, optimizing the process parameters such as tool travel speed, rotational speed, tilt angle etc. The influence of Friction stir welding on microstructure and mechanical properties of welds has also been reviewed.

Introduction:-

Application of high strength, low weight metal alloys are increasing very rapidly in the area of aerospace, aircraft, marine, etc. New technological strategies are required in order to develop welding technology concurrently with the development of new materials. [1]. Both fusion and solid state welding techniques play a major role in welding advanced materials.

Fusion welding involves use of filler materials, shielding gases, and development of high energy density which results wider heat affected zone. The weldments show appreciable modification in the microstructure and properties of weld and heat affected zones, which may result solidification defects like distortion, , lack of penetration, poor fusion, cracks etc. Use of plasma arc and laser beam welding techniques can produce sound welds of thicker materials with narrow heat affected zone [2], however these techniques are not suitable for certain materials such as aluminium, magnesium etc.

The drawbacks in the fusion welding techniques can some extent addressed by solid state welding techniques (e.g. resistance welding, friction welding) in which welding takes place at a temperature lower than the melting point of base metals and also no filler material and / or shielding gases are required. In resistance welding coalescence occurs due to heat generated by contact resistance and applied pressure and hence, it is not suitable for materials having high electrical conductivity (e.g. aluminium, copper). Friction welding employs frictional heat generated when a moving workpiece and a fixed component are forced together in order to obtain the required heat and temperature for weld. However, the application of friction welding is limited by the geometry of the workpieces to be joined.

The above difficulties can successfully overcome by friction stir welding (FSW), a solid state welding process which was developed by the welding institute (TWI) [3] primarily for welding of aluminium and magnesium based alloys. The major advantages of FSW over other welding processes are lower distortion, good dimensional stability, absence of cracking etc.

Corresponding Author:- A. Rajasekhar.
Address:- Professor, Methodist College of Engineering & Technology, Abids, Hyderabad, Telangana.-500 001.

Stainless steels are normally classified on a metallurgical basis depending on the composition and metallurgical structure. Hence, recognition is primarily made of martensitic, ferritic, austenitic and duplex phase alloys. These steels have been welded for many years, and the principal welding characteristics of each microstructural type have been well described elsewhere [4].

Literature survey has indicated that FSW was applied successfully to low softening temperature materials such as aluminum, copper lead, zinc, and magnesium alloys [5]. However, Friction stir welding of Stainless steel has not progressed rapidly due to various reasons; the important one is lack of suitable tool materials. Since, Stainless steel is the most widely used material in the engineering application; research is now focused in studying various aspects of Friction stir welding like tool design, rotational speed, welding speed, tool material etc, and their effect on the weld microstructure and properties of stainless steel.

Friction stir welding – principle:-

In Friction stir welding (FSW) process, coalescence occurs due to thermo-mechanical deformation of workpieces. The temperature developed due to frictional heat exceeds the solidus temperature of workpieces to be joined. The principle of Friction stir welding technique is shown in Figure 1. It consists of a non-consumable rotating tool with a specially designed tool pin and shoulder. Tool pin is plunged into the abutting plates to be joined until the shoulder of the tool touches the upper surface of the material and a downward force is applied to maintain the contact. The tool rotates in the clockwise direction and translates along the joint. Frictional heat generated between tool and workpiece causes the material around the pin to get heated and softened thus forming a solid state joint without melting [6]
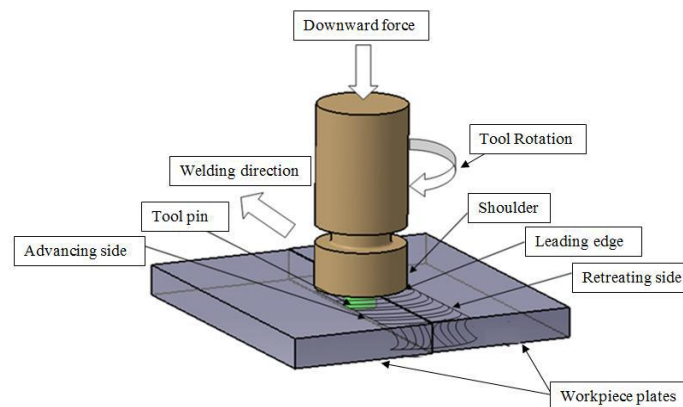
Fig. 1:- Principle of friction stir welding (Backer and Bolmsjo, 2014).

Various micro-structural regions observed in FSW joints are shown in Figure 2. The parent metal region does not undergo any deformation and the microstructure is unaffected by the heat produced in the joint. The heat-affected zone is next to parent metal region and is affected by only heat and there is no plastic deformation takes place in this region; however, the microstructure and mechanical properties are modified by the thermal heat. The next region is thermo-mechanically affected zone which is very close to weld nugget and it experiences lower temperatures and less deformation. Next is nugget zone or stir zone in which severe plastic deformation results due to frictional heat and the material subjected to recrystallization [7].

Microstructure and properties of friction stir welded stainless steels:-

Austenitic Stainless Steels:-

Reynolds et al. (2003) [8] investigated Friction stir welding of 304L stainless steel using a tungsten alloy tool and experiments were carried out at two different rotational speeds with a constant feed rate. It is evident that equiaxed grains are present in the stir zone with smaller grain size as compare to that of base metal. It is also noticed the existence of narrow bands in stir zone for both rotational speeds. The tensile strength of the weld material was found to be higher than the base metal and exhibited excellent ductility, with elongation to fracture of more than 50%. Longitudinal residual stresses were found to be nearly matched to the base material yield stress. Furthermore, it is

concluded that lower energy input due to lower tool rotation would result in lower weld temperature and a fine weld nugget grain size.

When welding 304L stainless steel using PCBN tools under different weld conditions, variations in microstructures were observed by S.H.C. Park et.al. [9]. Under some conditions, rapid formation of sigma phase took place due to the transformation of austenite to delta-ferrite in the stir zone which occurred due to dynamic recrystallization and high strain during the friction stir welding. They also found a banded structure similar to that identified by Reynolds et al. The dark bands were found to be narrow regions of ultrafine grains.
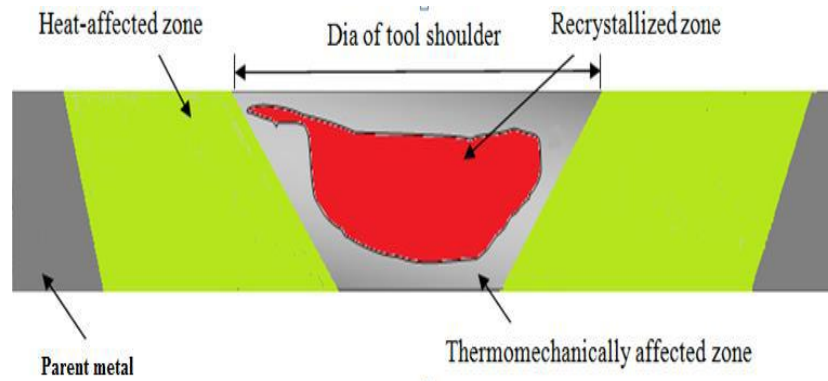
Fig. 2:- Microstructural regions of friction stir welding (Mahoney et al., 1998).

A refined grain structure was also identified in the stir zone of welds produced by friction stir welding of 304 stainless steel welded to low carbon steel. The fine grain structure increased the hardness and tensile strength in the stir zone [10]. Microstructure and mechanical properties of 304 stainless steel welds made by friction stir welding were evaluated by Meran and Kovan [11]. Higher strength of welding was observed when travel speed is 63mm/min and rotational speed is 1000 rpm. Friction Stir Welding (FSW) was applied to AISI 304 austenitic stainless steels and the effect of different tool rotational speeds, traverse speeds, compressive tool forces, and tool angles was investigated by C.Meran et.al [12]. It is found that the maximum tensile strength is observed with 950 rpm rotational speeds and 60 mm/min traverse speed, 9 kN compressive tool force, and 1.5^0 tool tilt angle [Fig.3]. Fine-grained microstructures in the welded area and the dark bands in the weld zone were also detected similar to that identified by Reynolds et al.

An increase in hardness of the SZ and TMAZ as compared to base metal was observed in the welds of 2 mm and 6 mm-thick 304 austenitic stainless steel plates [13]. Maximum hardness was located in TMAZ, which is due to high density of dislocations and sub-grains. The microstructure also revealed the presence of ferrite and sigma phase in austenite matrix in the stir zone. C.D. Sorensen et.al., [14] investigated sigma formation in friction stir welding of various stainless steel alloys and hypothesized that sigma formation was a marker for recrystallization in 304L. They also demonstrated that change in welding parameters affected the amount and location of sigma. Brózda and Madej [15] and Kim and et al [16] found that presence of sigma phase in austenitic steel welded joints is the main reason of cracking with its effect of embrittlement. Formation of sigma phase in 304 L stainless steels was dramatically reduced by modifying the tool design [17]. No sigma has been identified in welds with the new tool.

Sensitization and stress-corrosion cracking (SCC) in 304L stainless steel welds produced by friction stir welding were studied by T.D. Clark [18]. The study reveals that welds analyzed qualified as non-sensitized during an oxalic acid etch test. Increase in corrosion susceptibility away from the surface of the specimen was witnessed in double-loop electrochemical potentiokinetic reactivation testing. The specimen did not show any increase in SCC susceptibility as compared with the base metal when subjected to U-bend test.
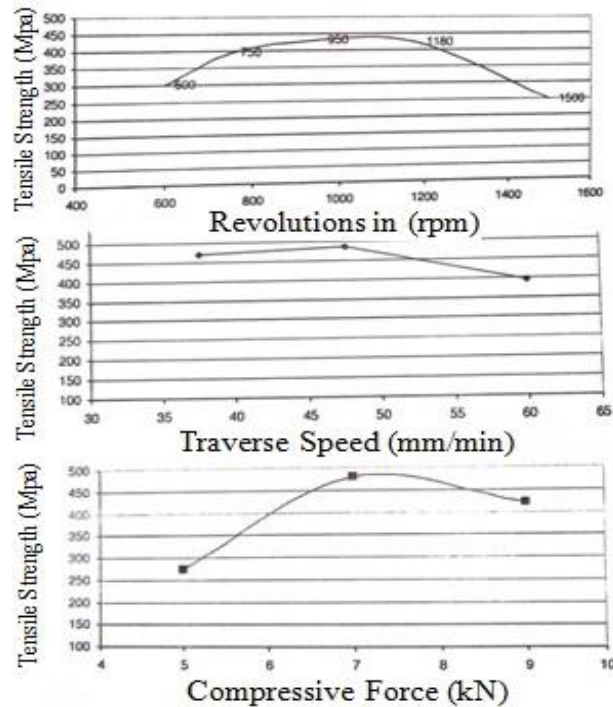
Fig.3:- The influence of the rotational speed, traverse speed and compressive force on the tensile strength of AISI 304 stainless steel produced by FSW. (C.Meran, O.E. Canyurt, 2010)

Welding parameters were optimized in friction stir welding of AISI 316 austenitic stainless steel plates of 4mm thick [19]. Defect free welds were produced with rotational speed of 1100 rpm and traverse speed of 8 mm/min and welds showed similar tensile strength that of the base material with comparable elongation. Zhou et al. [20] tried to address the keyhole gap problem during friction stir welding of 316L stainless steel using consumable tool bar of similar material. Fine grain microstructure is obtained in stir zone, however void defects are observed at the bottom surface of keyhole.

Ferritic Stainless Steel:-
Friction stir welding of 409 ferritic stainless steel welded by Polycrystalline Cubic Boron Nitride (PCBN) tool was studied by Cho et al.[21] and found that fine grain microstructure was resulted by dynamic recrystallization. The microstructure and mechanical properties of friction stir welded 409L stainless steel were investigated by Ahn and et al [22] and found that the mechanical properties in the weld were similar to that of the base material (BM). Microstructure and mechanical properties of friction stir welded 409M ferritic stainless steel joints were evaluated by Lakshminarayanan and Balasubramanian [23] and found that properties such as tensile strength, ductility and impact toughness were observed in acceptable limit at a welding speed of 50 mm/min and rotation speed of 1000 rpm. Investigations on the microstructure of friction stir welded ferritic stainless steel revealed the presence of bainitic structure in nugget zone and hence increase in hardness of the this zone [24]. Fine grains in nugget zone and TMAZ were observed by Han et al. [25] owing to mechanical stirring and heating.

The influence of tool rotational and traverse speed on friction stir weldability of AISI 430 ferritic stainless steels is studied by Bilgin and Meran [1]. They reported that no sigma phase is found in stir zone and HAZ. A study C.Meran et.al [26] has been taken up to compare the microstructures of AISI 430 ferritic stainless steels resulted by friction stir welding and fusion welding (MIG and TIG) methods. It is found the formation of σ-phase has not been reported in friction stir welding processes when compared to traditional fusion welding processes. This may be due to lower heat input in friction stir welding. It is also observed that excessive grain growth problem in fusion welding of stainless steels can also be avoided by friction stir welding.

Duplex Stainless Steel:-
Mechanical properties of friction stir welded 2507 super duplex stainless steel were evaluated by Sato et al. [27] using CBN tool. The microstructure revealed the refinement of grains of ferrite and austenite and hence resulted an increase in strength and hardness. Tensile fracture occurred between HAZ and TMAZ. The influence of welding speed on microstructure and mechanical properties of friction stir welded duplex stainless steel were studied by Saeid et al [28] and found that microstructure of stir zone consists of equiaxed grains of ferrite and austenite. It is further observed that the grain size decreases with increasing welding speed and the hardness and tensile strength increases when feed rate is increased.

Conclusion:-

- Friction stir welding has been found to be technically feasible for a wide range of stainless steel alloys.
- Properties of friction stir welds of stainless steels appear to be excellent. In some cases, they exceed the properties of the base metal. They also exceed the properties of welds made from alternative fusion welding processes (TIG and MIG).
- Initial problems with tool material contamination of the weld appear to have been greatly reduced by the development of tool materials like WC and PCBN.
- The process parameters FSW (tool rotation speed, traverse speed, spindle tilt angle and tool geometry) influence the mechanical and metallurgical behavior of welds and hence, they are crucial in producing the sound and defect-free joints.
- A detailed study is required to explore the effect of preheating and filler metal inclusion on mechanical and metallurgical behavior of FSW joints.
- Though some work is in progress on the weldability of austenitic stainless steel by FSW, yet progress is to be made in FSW of other types like Martensitic and duplex stainless steels.

References:-

1. T.Ueyama // Welding International 24 (2010) 699 and K.Pokhodnya // Welding International 17 (2003) 905
2. Lohwasser and Chen, 2010
3. W.M. Thomas, E.D. Nicholas, J.C. Need-ham, M.G. Murch, P. Templesmith, and C.J. Dawes, International Patent Applica-tion PCT/GB92/02203 and GB Patent Application 9125978.8, 1991
4. Castro, R. & de Cadenet, J.J., "Welding Metallurgy of Stainless and Heat-Resisiting Steels", pub. by Cambridge University Press, 1974
5. R.Mishra and Z.Ma, Mater Sci Eng R Rep, 50 (1-2), 1-78 (2005)
6. Backer, J. D. & Bolmsjö, G. (2014).Temperature control of robotic friction stir welding using the thermoelectric effect. *Int. J. of Adv. Manuf. Technol.,* 70, 375-383.
7. Mahoney, M. W.; Rohdes, C. G.; Flintoff, J. G.; Surling,R. A. & Bingel, W. H. (1998). Properties of friction-stir-welded 7075 T651 aluminum. *Metallurgical and Materials Transactions*, 29,1955-1964
8. A.P. Reynolds, W. Tang, T. Gnaupel-Herold, and H. Prask, Structure, Proper-ties, and Residual Stress of 304L Stainless Steel Friction Stir Welds, *Scr. Mater.,* Vol 48 (No. 9), May 2003, p 1289–1294
9. S.H.C. Park, Y.S. Sato, H. Kokawa, K. Okamoto, S. Hirano, and M. Inagaki, Rapid Formation of the Sigma Phase in 304 Stainless Steel during Friction Stir Welding, *Scr. Mater.,* Vol 49 (No. 12), Dec 2003, p 1175–1180
10. M. Jafarzadegan, A. Abdollah-zadeh, A.H. Feng, T. Saeid, J. Shen and H. Assadi, Microstructure and Mechanical Properties of a Dissimilar Friction Stir Weld between Austenitic Stainless Steel and Low Carbon Steel, *J. Mater. Sci. Technol.,* 2013, 29(4), 367-372.
11. Meran C, Kovan V, Alptekin A (2007) Friction Stir Welding of AISI 304 austenitic stainless steel, Material Science and Engineering Technology, vol.38, issue 10, pp829-835
12. C.Meran*, O.E. Canyurt "Friction Stir Welding of austenitic stainless steels", Journal of Achievements in Materials and Manufacturing Engineering,Volume 43 Issue 1 November 2010, pp.432-439
13. Kokawa H, Hirano S (2005) Microstructures in friction stir welding of 304 austenitic stainless steel. 56:234-236.
14. C.D. Sorensen and T.W. Nelson, Sigma Phase Formation in Friction Stirring of Iron-Nickel-Chromium Alloys, *Trends in Welding Research, Proceedings of the Seventh International Conference,* ASM International, 2005
15. J. Brózda, J. Madej, Cracking of the mixing chamber caused by sigma phase precipitation in austenitic steel welded joints, Engineering Failure Analysis 15 (2008) 368-377.
16. Y.H. Kim, D.J. Lee, J.C. Byun, K.H. Jung, J.I. Kim, H.J. Lee, Y.T. Shin, S.H. Kim, H.W. Lee. The effect of sigma phases formation depending on Cr/Ni equivalent ratio in AISI 316L weldments, Materials and Design 32

(2011) 330-336.

17. C.B. Owen, "Two-Dimensional Friction Stir Welding Model with Experimental Validation," M.S. thesis, Brigham Young University, Provo, UT, 2006

18. T.D. Clark, "An Analysis of Microstruc-ture and Corrosion Resistance in Under-water Friction Stir Welded 304L Stainless Steel," M.S. thesis, Brigham Young Uni-versity, Provo, UT

19. Manish P. Meshram, Basanth Kumar Kodli, Suhash R. Dey "Friction Stir Welding of Austenitic Stainless Steel by PCBN Tool and Its JointAnalyses", Procedia Materials Science 6 (2014) 135 – 139

20. Zhou, L.; Zhou, W. L.; Huang, Y. X. & Feng, J. C. (2015). Interface behavior and mechanical properties of 316L stainless steel filling friction stir welded joints. *Int. J. of Adv. Manuf. Technol*., 81, 577‑583

21. H. Cho, H. N. Han, S. Hong, J. Park, Y. Kwon, S. Kim, and R. J. Steel, "Microstructural analysis of friction stir welded ferritic stainless steel,"*Materials Science and Engineering: A,* vol. 528, no. 6, pp. 2889-2894, 2011.

22. B.W. Ahn, D.H. Choi, D.J. Kim, S.B. Jung, Microstructures and properties of friction stir welded 409L stainless steel using a Si3N4 tool, Materials Science and Engineering A 532 (2012) 476- 479

23. A.K. Lakshminarayanan and V. Balasubramanian, "An assessment of microstructure, hardness, tensile and impact strength of friction stir welded ferritic stainless steel joints", *Materials and Design 31* (2010) 4592–4600

24. Cho, H. H.; Kang, S. H.; Kim, S.H.; Oh, K. H.; Kim, H. J.; Chang, W. S. & Han, H.N. (2012). Microstructural evolution in friction stir welding of high-strength line pipe steel. *Materials & Design*, 34, 258‑267

25. Han; Jian; Li, H.; Zhu, Z.; Barbaro, F.; Jiang, L.; Xu, H. & Ma, L. (2014). Microstructure and mechanical properties of friction stir welded 18cr–2mo ferritic stainless steel thick plate. *Materials & Design*, 63, 238‑246

26. C. Meran, M.B. Bilgin, "Fusion and friction stir welding of X6Cr17 stainless steel", Journal of Achievements in Materials and Manufacturing Engineering Volume 61 Issue 2 December 2013, pp.403-410

27. Sato, Y. S.; Yamanoi, H.; Kokawa, H. & Furuhara, T. (2007). Microstructural evolution of ultrahigh carbon steel during friction stir welding. *Scripta Materialia*, 57, 557‑560

28. Saeid, T; Abdollah-zadeh, A.; Assadi, H. & MalekGhaini, F. (2008). Effect of friction stir welding speed on the microstructure and mechanical properties of a duplex stainless steel. *Materials Science and Engineering*, 496, 262‑268

A Web GIS Based Decision Support System for Agriculture Crop Monitoring System-A Case Study from Part of Medak District

Santosh Kumar K[1]* and Suresh Babu DB[2]

[1]Methodist college of Engineering and Technology, King Koti, Abids, Hyderabad, Telangana, India
[2]Centre for Spatial Information Technology (CSIT), JNTUH, Hyderabad, Telangana, India

Abstract

The success of planning for developmental activities depends on the quality and quantity of information available on both natural and socio-economic resources. It is, therefore, essential to devise the ways and means of organizing computerized information system. These systems must be capable of handling vast amount of data collected by modern techniques and produce up to date information. Remote sensing technology has already demonstrated its capabilities to provide information on natural resources such as crop, land use, soils, forest etc., on regular basis. The role of remote sensing and GIS in agricultural applications can be broadly categorized into two groups-inventorying/mapping and management. While remote sensing data alone are mostly used for, inventorying, crop acreage estimation, crop condition assessment, crop yield forecasting, soil mapping, etc., purposes, the management related activities like irrigation management, cropping system analysis, precision farming, etc., needs various other types of spatial physical! Environmental information. The latter has to be integrated with remote sensing data, where the functionality of GIS will be used. In the present study, techniques of remote sensing and Geographic Information System (GIS) have been used to monitor and map the Sugarcane crop at farm level. The Quick bird data of 60 cm resolution was acquired and was geometrically corrected and georeferenced for subsequent processing and analysis using Digital Image Processing (DIP) and GIS. After the generation of the thematic layers at farm level using GIS, using the various customization tolls available in the GIS a web based monitoring system for the sugarcane has been prepared. This monitoring system helps the decision makers to take appropriate decisions in order to increase the crop production and other activities related to the crop. The Web GIS helps the non-technical users to access the information and take appropriate measures to improve the crop production. These user-friendly systems need to be developed and made simple in order to take the technology from the scientific community to the common man.

Keywords: Customized web GIS based application; Land use planning; Ground water; Agriculture crop monitoring system; Yield information; DSS for agricultural information

Introduction

Agriculture is the backbone of Indian economy, contributing about 40 percent towards Gross National Product (GNP) and providing livelihood to about 70 per cent of the population. So, for a primarily agrarian country like India, accurate and timely information on the types of crops grown and their acreages, crop yield and crop growth conditions are essential for strengthening country's food security and distribution system. Pre-harvest estimates of crop production are needed for guiding the decision makers in formulating optimal strategies for planning, distribution, price fixation, procurement, transportation and storage of essential agricultural products [1]. Advance forecasting about crop condition and crop production has a strong bearing on national economy as well as day-to-day life of the masses. The sugar and onion crises of late 90s showed that a faulty crop forecasting system could create havoc for the government and the public.

The space borne remote sensing and GIS Technology has been providing information for many agricultural applications, such as identification and area estimation of short duration and marginal crops grown in fragmented land holdings, detection of crop stress due to nutrients and diseases, and quantification of its effect on crop yield. There is a strong need to develop methodologies for improving crop yield models, retrieval of agro-met and canopy parameters, quantification of soil loss, damage assessment and generation of information on moisture and nutrient status of soil sub-surface horizons, inorder to achieve the best crop yield [2].

In order to bridge these gaps, the use of WEB GIS and Spatial data base generated through the high resolution satellite imagery will be used for generating the processing and analytical techniques, that would enable integration of ground based parameters with the satellite data.

In order to study the advantage of using the space technology and information technology in crop monitoring and management of various activities involved in achieving a better yield a study is being done using high resolution satellite data and the use of information technology to create a web GIS application for monitoring the crop production with special emphasis on sugar cane crop.

Scope of the Study

For the present study a particular land allotted to the sugar plants by the concerned authorities of the government was taken up for Micro level planning. The Management of the Sugar Plants is responsible for all the measures for improving the Crop Production in the allotted land by proving the Seeds, fertilizers, Pesticides, Loans etc., to the Farmers. The Management is solely responsible for taking all the measures for improving crop production. In order to achieve the above mentioned features the management will do precise Field Wise observation of the

land. To Monitor each and every field and for better Communication from the Field data, management will follow the Hierarchy Like Chief Cane Agriculture Officer, Deputy Cane Agriculture Officer, Area mangers, Field Assistants, Who will be incharge for two to three Villages. In the absence of an online management system it was observed that gaps were arising in the hierarchy which May lead to gaps in the communication and management [3]. Due to the wide extent of the area and the Hierarchy of employees, it is very difficult to monitor the allotted land very closely. Even for Planning the Regular Water, fertilizers and Pesticides Applications to the Fields and for identifying the Optimum way of Transportation of the Crop which is ready for Cutting to the Sugar Plants is being done manually, which is very tidies and it may lead to improper management, this in turn reduces the Crop Production. Most of the Managements are not keeping the records or History of the Fields at one Place and all these are Operated Manually and also not following the Technical Maps, Like Soil, Slope, and Ground Water Maps to Get the More Production. Even to Monitor the Field Assistants performance also management don't have any Specific System.

The proposed System will be used for forecasting of crop production, Identifying the Fields, which are ready for harvesting, need for the use of fertilizer, and application of water, transportation and canal facilities etc., for all the Fields and also to get field wise reports like, Delay in providing water to the crops and use of fertilizers in the field at the appropriate time [4]. This technology is effectively used for monitoring the crop production and yield information of crop pertaining to the total land belongs to the Client.

The end use of such a system will be felt in obtaining higher productivity, lower overheads, data mining for long term planning and efficiency improvement, transparency to the management and cost control, enhanced management satisfaction, faster response and optimum utilization of available resources. The remote sensing coupled with GIS techniques play a vital role to achieve the Objectives [4].

Objectives

- To Develop a WEB GIS Based unified data warehouse Model for Agro based Industries., (A Case Study of Sugar Cane Agriculture i.e., Land which Belongs to a Particular Sugar Plant).
- To provide information access to the Users for improving productivity through web GIS based decision support system for Agriculture Field Monitoring System.
- To develop an open source web GIS based decision support system for Agriculture Field Monitoring System.
- To develop a user-friendly monitoring system with WEB GIS technology and made available to common man apart from the Scientific Community.
- To generate the natural resources thematic layers like LULC, Ground Water, Soil and slope maps for the Study Area and make use for Online Study.

Location and Extent

Zaheerabad Mandal lies in the Medak District which is situated in the Telangana region of Andhra Pradesh, India. Zaheerabad is located about 100 km from Hyderabad on the Mumbai-Hyderabad national highway (NH-9). The mandal is bounded on the north by Nyalkal, Northeast by Jharasangam, Southeast by Kohir mandals of Andhra

Pradesh and Gulbarga and Bidar of Karnataka state in west (Figure 1) [5]. The mandal lies between North Latitudes 17°46' 22" and 17°32' 32" and East Longitudes 77°26' 42" and falls in Survey of India Toposheet Nos. 56G/6, 56G/9 and 56G/10 of scale 1:50000 published by Survey of India in 1973. The total area of the study area is 392.15 sq. km (Table 1).

Methodology

The following methodology is adopted in the present study to meet the above-mentioned objectives. The base map is generated at 1:25,000 scale from the SOI Toposheet. The thematic layers like LULC, Soil, Slope etc., are generated using the IRS P6 LISS IV images. Taking the SOI Toposheets as source, the thematic layers like drainage and contours are prepared at 1: 25,000 scales [6]. The slope map is derived using Survey of India topographical sheets at 1:25000 scale with 5-meter contour interval. The rainfall and temperature data and other collateral data of the study area are collected and are integrated in the GIS Domain. The DEM (Digital Elevation Model) is generated from the contours. The soil map is taken as the base for integration.

A scheme for thematic data integration and recommendation for various combinations of land parameters was evolved by observations in the field. Following the scheme of data integration, action plan maps were generated giving suitable site-specific recommendations for alternate land use and water conservation measures [6]. While formulating the locale-specific action plan, the earlier research carried out by various research centers in the field of agriculture etc., were taken into consideration along with the prevailing socio-economic conditions.

All these data which are generated in the GIS domain are used as inputs in the Application developed using the open source software. The developed open source web based decision support system is an package which works independent of the GIS software's and tools were created in the package in such a that any use user without the Technical Knowledge can also operate the package and can perform some of the functions like displaying the data, querying the data, overlay and union which are there in the GIS software's.

Technologies Used for the Study

For the present study high resolution satellite data of 60 cm resolution is used to prepare the field wise spatial map. The revenue map of the study area is geometrically corrected using the Imagery and also by collecting control points using the GPS from the field. The information related to the each survey number is collected by field survey. This data are linked to the spatial data to generate Information system [7]. The data generated in the GIS are customized using java and a web based spatial decision support system is generated for better planning and management of the Agriculture Crop (Figure 2).

S.No	Type of Software	Purpose of usage	Name of the software with Versions
1	GIS Software	GIS Work	Arc GIS (Ver 9.3)
2	Development software	WEB Portal Development Work	PHP, Openalyers API, PostgreSQL+PostGIS(DBMS) Jquery, Java Script, HTML
3	Animation and Design software	Design, Animation Work (web portal development)	Macromedia Flash (8), Adobe Photoshop CS2, Coreldraw Graphics Suits (12), Adobe Dreamweaver CS3
4	Server Used		Geoserver (Open Source Map Server) Apache (Open Source WEB Server)

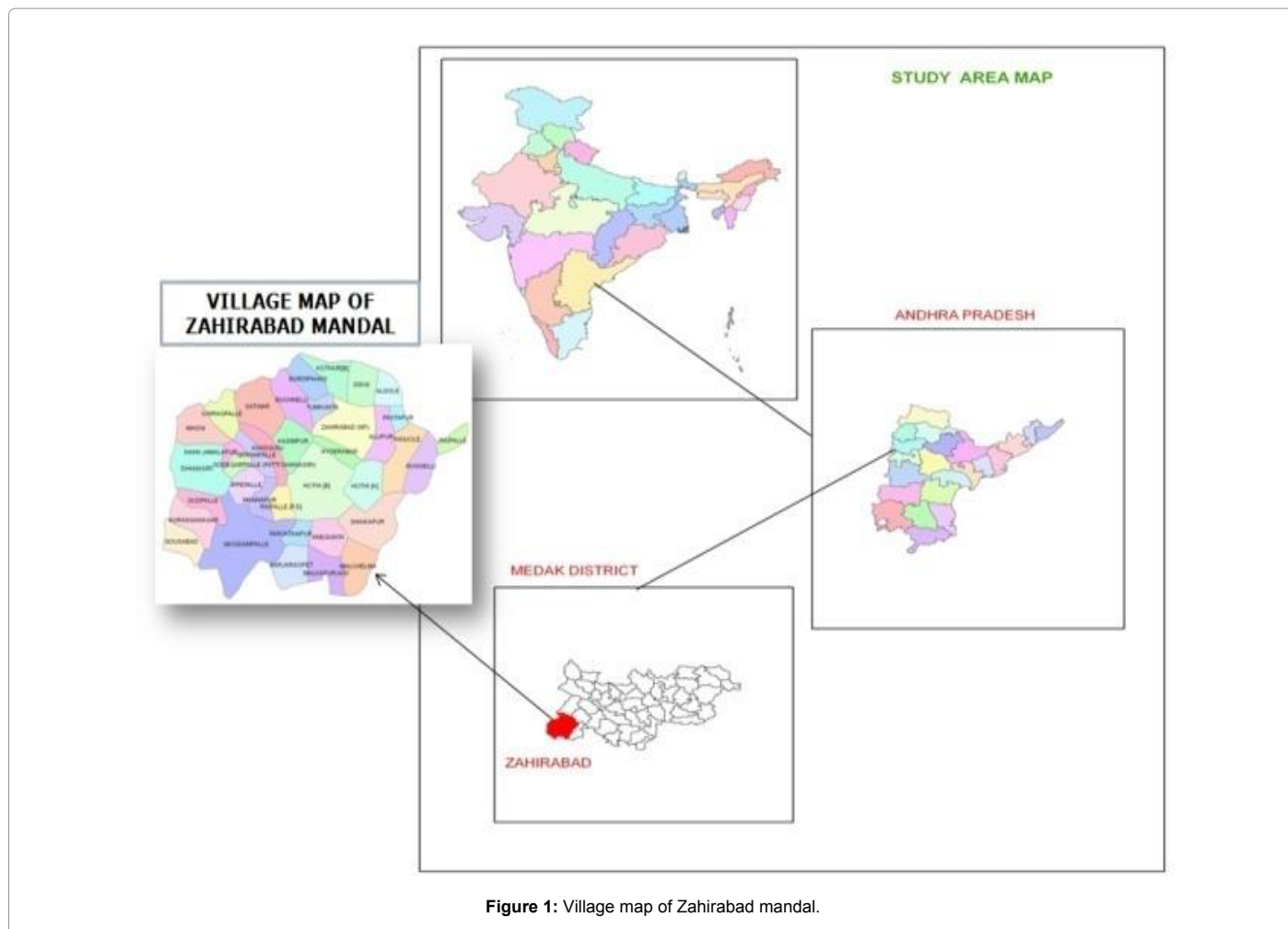**Table 1:** Technologies used for the study.

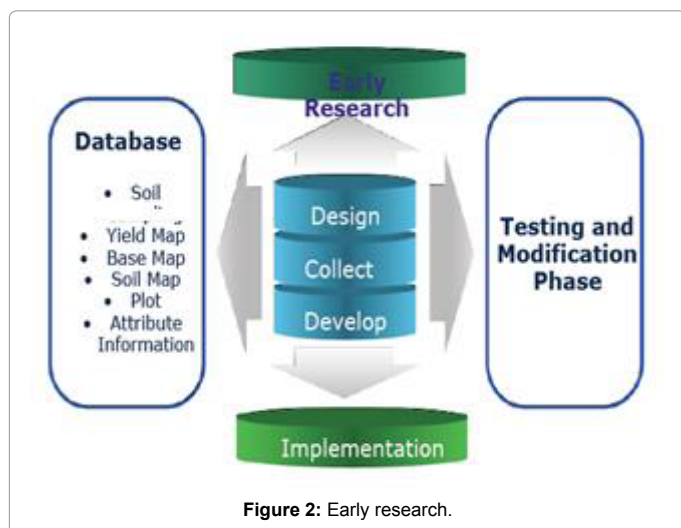**Figure 1:** Village map of Zahirabad mandal.

Figure 2: Early research.

The end use of such a system will be felt in obtaining higher productivity, lower overheads, data mining for long term planning and efficiency improvement, transparency to the management and cost control, enhanced management satisfaction, faster response and optimum utilization of available resources. The remote sensing coupled with GIS techniques play a vital role to achieve the Objectives.

Results and Discussions

Sustainable agricultural land use and cropping pattern plans of the area are generated by GIS based logical integration of crop suitability's, land productivity, land capability, socio-economic and terrain characteristics information. Specific action plans are devised for optimum management of land and water resources through integration of information on natural resources, socio-economic and meteorological data and contemporary technology. An important task of Developed Application is to facilitate the linkage between non-spatial data and the spatial data. The non-spatial data like census, socioeconomics, agricultural inputs, etc., would be available in tabular form and has to be retrieved from the relational database management system (RDBMS). On the other hand, the spatial information is in the form of maps, referenced to the geographic latitudes-longitudes. The non-spatial tabular information is linked to the spatial information through a customized GIS approach. This query-shell facilitates data handling. The strength of GIS is the integration of multi-layered data from different sources and various scales [7]. The integration of different layers of information has been a difficult task manually until the maps were drawn on a transparent film. With the availability of GIS, which takes the data into digital space, the ability to see through maps, which are overlaid one over the other digitally and analyze the maps is achieved. Database management systems integrated with graphic interface have a powerful query capability. This will finally give the analytical ability to pose complex query and extract information spatially.

The conventional monitoring system of management can be enhanced with the integration of latest WEBGIS technology. The existing conventional monitoring system most of the times relay on the oral communication through telephonic conversations as input for the decision making. There is large scope for miscommunication of the information or communication gap due to the higher human interference in the system. This miscommunication may lead to delay in decision making and other works.

Land use/Land cover

The knowledge of spatial distribution of land cover/land use of large area is of great importance to regional planners and administrators. Conventional ground methods are time consuming and no uniform classification system was used in the preparation of maps with the advent of remote sensing technology the above problems have been solved to quite some extent (Figure 3) [8].

Satellite data can provide information on large areas and the temporal data can be utilized for change detection and updating old data. The land use/land cover categories that can be obtained from the remotely sensed data include level I classes of land use classification system such as water bodies, forest, grass land, agricultural land, barren land and scrub land. The Spatial Distribution of the various land use land cover classes found the study are given below in Table 2.

Geo-morphology

The mandal is covered under Godavari basin. Karanja Vagu is a major small river which flows NW-NE direction in this mandal. The drainage pattern is dendritic in granite terrain and parallel in Deccan Traps. The hard rocks viz., Archeans and Deccan Traps occupy 79.35%, soft rocks viz., laterites 20.63% and alluvium 0.2%. The depth to water table in granite varies from 4.5 to 199 mm, in laterites from 5 to 30 m and in alluvium from 0.5 to 7.5 m. In Deccan Traps, Water occurs in fractures, crevices and joints. A number of lineaments form the promising zones for ground water development. Laterites are highly porous and permeable and possess good water bearing capacity. Ground water is moderately hard and is required to be softened before use [8]. The land forms in the district are mostly structural, denudation and fluvial in origin. In the northern parts, crystalline complex represented by meta sediments, gneisses and granite forms a distinct pediplain. This unit resulting out of the denudational process comprises landforms like residual hills, Inselberg and shallow weathered pediplain. In the western part, landforms are of moderately dissected plateau.

Hydro geomorphology

Hydrogeomorphology deals with the study of landform in relation to groundwater occurrence and availability. It is manifested at the surface, mainly by geology, geomorphology, structure and recharge conditions (Figure 4). All the four parameters were studied and integrated to arrive at the groundwater prospects under each geomorphic cum lithologic unit, designated as hydrogeomorphic unit. The following Geomorphic units are mapped in the Zaheerabad Mandal at 1:50,000 scale are listed below in Table 3. The various geomorphic units which are which are present in Zaheerabad Mandal and is given below in Table 3.

Ground water potential map

Ground water potential maps are prepared by integrating information on geomorphology, slope lithology, structural features and the precipitation. Ground water recharge depends on favourable slope, permeability and degree of compactness of the rocks. The movement and occurrence of ground water is controlled mainly by Geology, Geomorphology and Recharge Conditions of the area [9]. The Geology and Geomorphology of the study area have been studied and by combining the individual litholo-landform units the Geomorphology map is prepared. These Geomorphic units have been evaluated for their Ground Water Prospects based on the hydrogeological characteristics of the geological and geomorphological parameters. The areal extent of various Geomorphic units with the ground water potential for the zaheerabad mandal is given in Figure 5.

Soils

The district exhibits a variety of soils. Black cotton soil ranging in thickness from 0.3 to 0.75 m occurs in Zaheerabad, Tumkund, Kotur and Didgi villages. Red soil ranges in thickness from 0.75 to 2 m. It possesses high water retention capacity. Major part of the district is arable unirrigated land around Zaheerabad. Around 17 soil series were mapped for the entire mandal using the satellite imageries and field survey at 1:50,000 (Figure 6).

Derived soil parameters: Soil-site and other land characteristics studied and recorded during field data collection and mapping have been interpreted and the soil map units grouped with respect to the major soil attributes such as soil depth (effective rooting depth), surface soil texture, gravelliness and stoniness, soil drainage, soil available-water capacity, soil slope, soil erosion, calcareousness etc. Such interpretative grouping of soil and land characteristics help in identifying areas that have specific problems like shallow rooting depth, severe erosion, poorly drained areas, sandy areas, steeply sloping lands, salt affected lands etc., and areas that have high potential like very deep soils, non-gravelly soils, non-saline or level areas etc., for sustained agricultural and non-agricultural uses.

Soil depth: Soil depth determines to a great extent the rooting system of plants which is ultimately reflected in crop growth and crop yield (Figure 7). It determines the capacity of the soil column to hold water and supply plant nutrients in relation to soil texture, mineralogy and gravel content. The extent of area under each depth-class association for the study area is given in Table 4.

Soil erosion: Soil erosion refers to the wearing away of the earth's surface by the forces of water, wind and ice. It is both destructive and constructive. It is responsible for causing variations in topography by eroding elevated land surfaces and at the same time depositing the eroded material in the plains, basins and valleys. It is further aggravated by human intervention through indiscriminate felling of trees, overgrazing, mining, and cultivation on steep slopes and degraded lands, thus affecting the natural ecosystem. Based on the intensity of erosion as observed visually during field survey and mapping, and also the amount of soil (loss of A or B horizons) removed in the soil profiles examined, the soils of study area have been classified under three erosion classes 'liz ;- ej-nil or slight erosion, e2-moderate erosion and e3-severe erosion.

Soil calcareousness: Calcareousness (lime content) is the term used to indicate the content of calcium carbonate in the soil. In the field, it is estimated by observation of the effervescence given by the soil when it is moistened with dilute hydrochloric acid. Soil calcareousness classes used were 0-nil effervescence (non-calcareous), 1-slight effervescence (slightly calcareous), 2-strong effervescence (strongly calcareous). Calcareousness influences soil pH and the availability of macronutrients and micronutrients (Figure 8). Physical conditions of soils are also greatly influenced by the quantity and size of lime nodules and concretions. The extent of area under each calcareousness class association for the study area is given in Table 5.
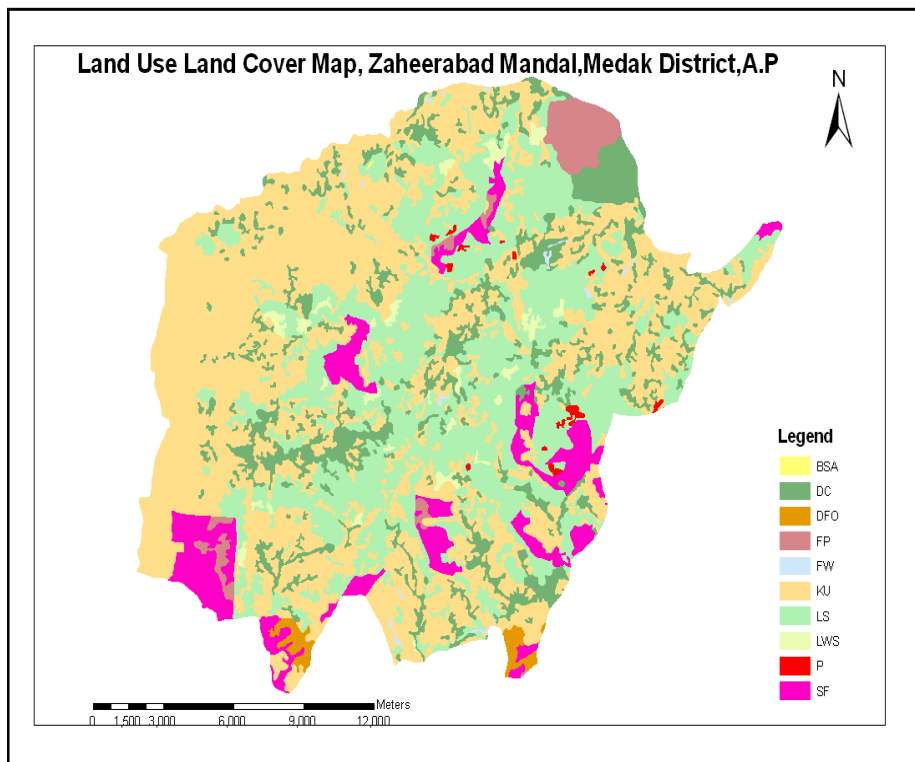
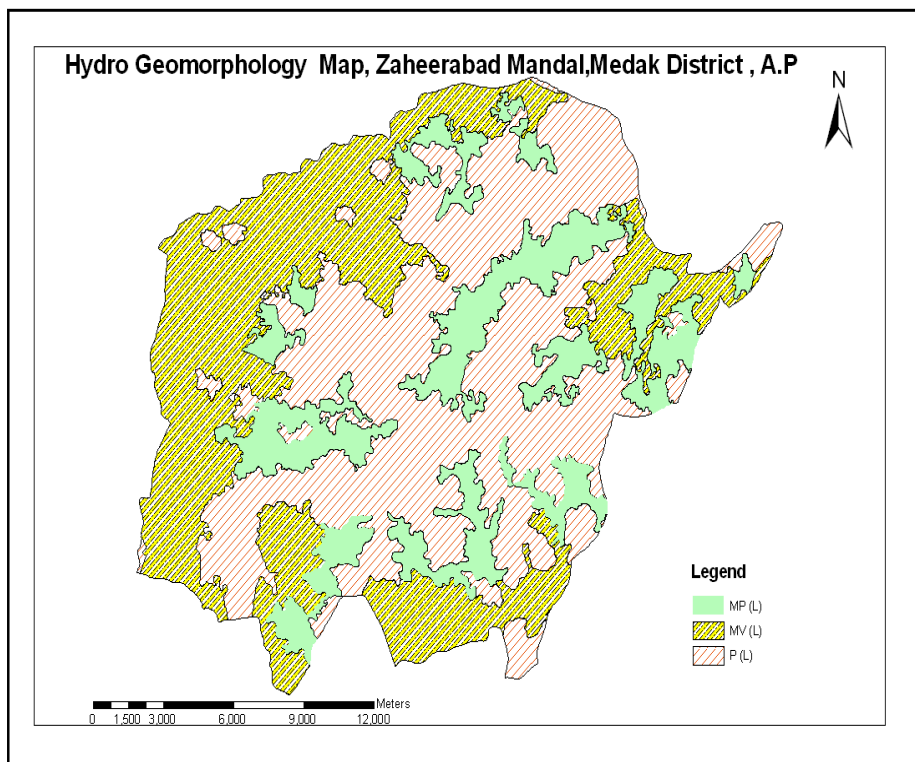**Figure 3:** Land use land cover map, Zaherabad Mandal, Medak District, A.P.

Figure 4: Hydro geomorphology map, Zaheerabad Mandal, Medak District, A.P.
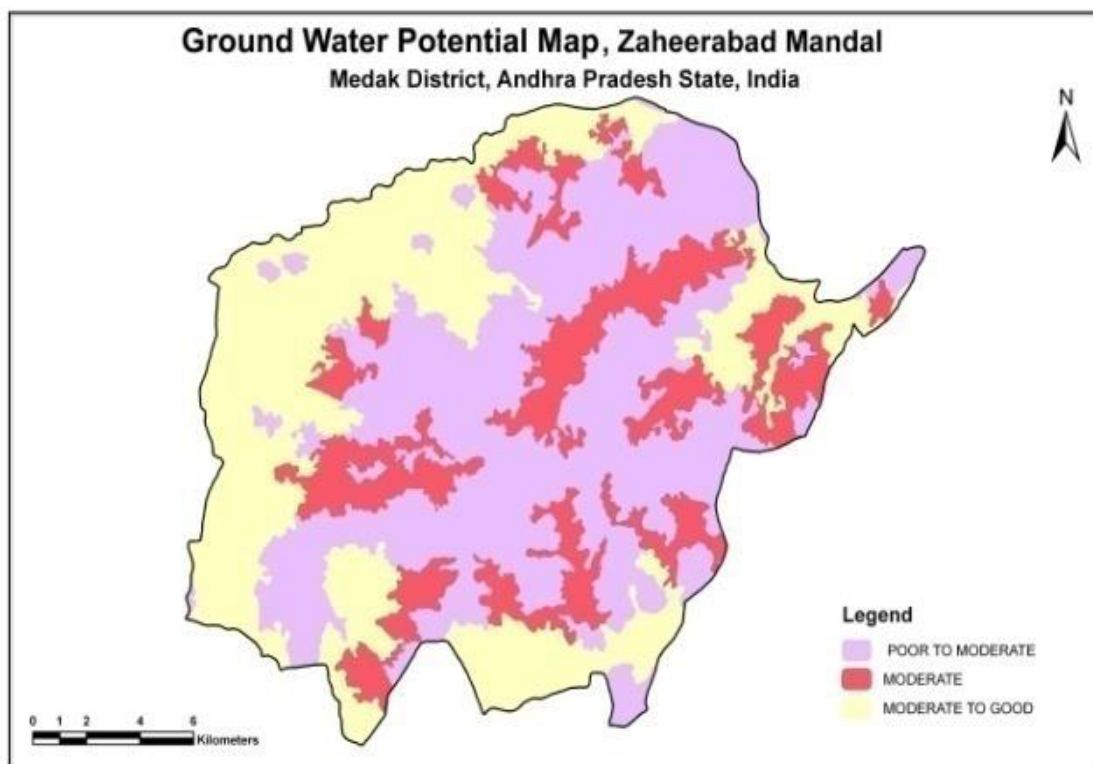
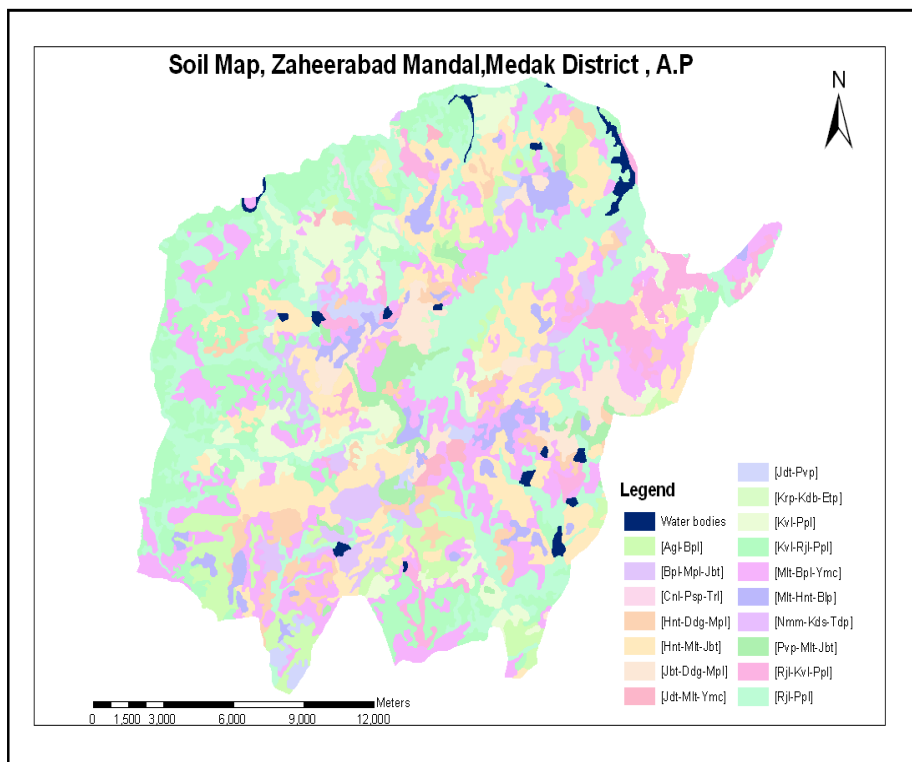**Figure 5:** Ground water potential map, Zaheerabad Mandal, Medak District, A.P.

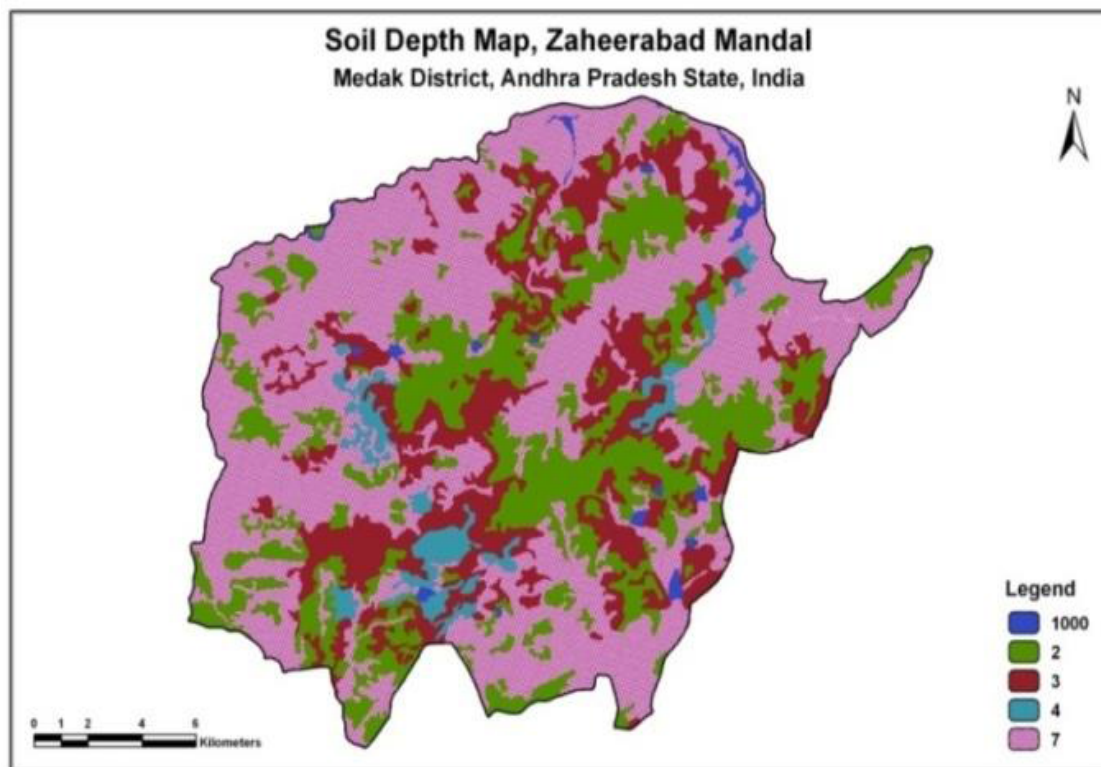**Figure 6:** Soil map, Zaheerabad Mandal, Medak District, AP.

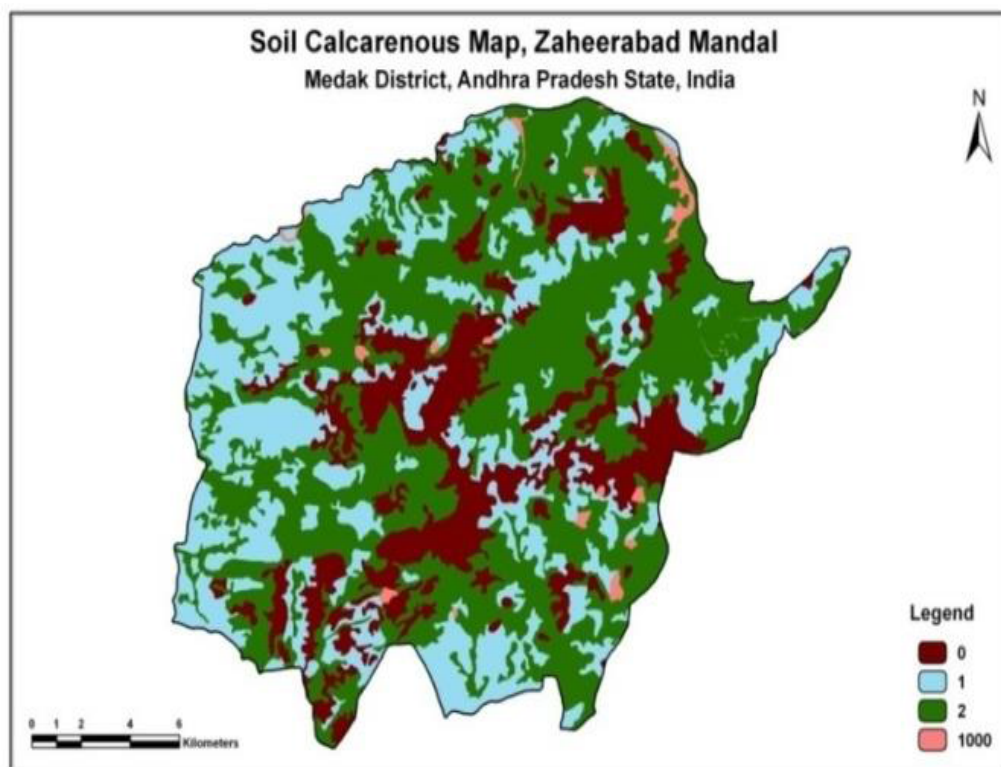**Figure 7:** Soil depth map, Zaheerabad Mandal, Medak District, A.P.

Figure 8: Soil calcarenous map, Zaheerabad Mandal, Medak District, A.P.

Land use/Land cover category (LULC)	Area in Sq. Km	Area in %
Forest Plantation	3.00	0.76
Kharif Unirrigated	188.83	48.13
Scrub Forest	31.20	8
Double Crops	42.46	10.9
Land with Scrub	115.14	29.3
Land Without Scrub	5.71	1.5
Deciduous Forest	3.52	0.9
Fuel Wood species	0.96	0.2
Plantation	1.27	0.3
Barren rocky & Stony waste	0.04	0.01
Total	392.13	100

Table 2: Spatial distribution of the various land use/land cover category.

Geomorphic Units	Ground water Potential	Area in Sq. Km	Area in %
Moderately Thick Lateritic Plateau	Moderate	84.05	21.43
Moderately Thick Lateritic Valley	Moderate to Good	141.80	36.17
Thick Lateritic Plateau	Moderate to Poor	166.28	42.40
Total		392.13	100.00

Table 3: Areal extent of geomorphic units of Zaheerabad Mandal.

Mapping Unit	Description	Area in Sq. Km	Area in %
2	Extremely Shallow	98.99	25.24
3	Shallow	79.52	20.28
4	Moderately Shallow	17.36	4.43
7	Very Deep	192.10	48.99
	Water Bodies	4.16	1.06
	Total	392.13	

Table 4: Areal extent of soil depth units.

Mapping Unit	Description	Area in Sq. Km	Area in %
0	0-15% Non-Gravelly	76.04	19.39
1	15-35 % Slightly Gravelly	117.365	29.93
2	35-60 % Gravelly	194.58	49.62
	Water Bodies	4.16	1.06
	Total	392.13	100.00

Table 5: Areal extent of soil calcareousness units.

Soil available-water capacity: Available-water capacity (AWC) of soils is mainly dependent on the amount, intensity and distribution of rainfall, infiltration, permeability, drainage and texture, type of clay minerals, soil depth and content of coarse fragments. Classes of soil available-water capacity are based on the ability of soil column to retain water between the tensions of 0.33 kPa and 15 kPa in a depth of 100 cm soil or the entire column if the soil is shallower (Figure 9). The AWC of soils of the study area estimated from soil depth, gravel and stone and mineralogy can help in determining the length of crop growing period which helps in land use planning. The AWC classes used for grouping the soils of the district were (1) very low (<50 mm m^{-1}), (2) low (50-100 mm m^{-1}), (3) medium (100-150 mm m^{-1}), (4) high (150-200 mm m^{-1}) and (5) very high (>200 mm m^{-1}). The extent of area under each AWC class association for the study area is given in Table 6.

Graveliness and stoniness: Gravel is the term used for describing coarse fragments between 2 mm and 7.5 cm diameter and stones between 7.5 cm and 25 cm. The presence of gravel and stones in the soil reduces the volume of soil that affects moisture storage, drainage, infiltration and runoff, and hinders plant growth by impeding root

growth and seedling emergence, intercultural operations and farm mechanization (Figure 10).

The gravel and stone content by volume for each of the soil horizon, as well as on the surface recorded during soil survey were used for grouping the soils into different gravelly or stony classes. The gravelly and stony classes used were (1) go-non-gravelly (0-15% gravel), (2) g1-slightly gravelly (15-35% gravel), (3) g2-moderately gravelly (35-60% gravel), (4) g3-strongly gravelly (60-90% gravel), and (5) st 5-strongly stony (>90% stones). The extent of area under each gravelliness / stoniness class association for the study area is given in Table 7.

Slope

Slope refers to the inclination of the surface of the land. It is defined by gradient, shape and length, and is an integral part of any soil as a natural body. The length and gradient of slope influences soil formation and soil depth, which in turn affects land development and land use (Figure 11). Around 97 sq.km of area under mandal is level to nearly level slope, 220 sq.km of area is under very gently sloping lands and 72 sq.km is covered under gently sloping land (Table 8).

Land evaluation methods

Soil map provides the user with information about the soil and landform conditions at any site of interest (Young, 1976). Soil maps are produced to suit the needs of users with widely different problems because they contain considerable detail to show basic soil differences. Land evaluation is a tool for strategic land-use planning. It predicts land performance, both in terms expected benefits from and constraints to productive land use, as well as the expected environmental degradation due to these uses. There are various land evaluation methods used for assessing the potential and productivity of soil for agricultural purposes. Some of them can be listed as below:

(i). Land Capability Classification

(ii). Soil and Land Irrigability Classification

Mapping Unit	Description	Area in Sq. Km	Area in %
1	Very Low	189.17	48.24
2	Low	44.28	11.29
3	Very High	154.52	39.41
	Water Bodies	4.16	1.06
	Total	392.13	100.00

Table 6: Areal extent of soil water capacity units.

Slope Categories	Description	Area in Sq. Km	Area in %
A (0-1%)	Level to Nearly Level	97.07	24.76
B (1- 3%)	Very Gently Sloping	219.20	55.90
C (3 – 8%)	Gently Sloping	71.70	18.28
	Water Bodies	4.16	1.06
	Total	392.13	100.00

Table 7: Areal extent of soil texture units.

Mapping Unit	Description	Area in Sq. Km	Area in %
C	Clay	189.17	48.24
GC	Low	44.28	11.29
GSC	Very High	154.52	39.41
	Water Bodies	4.16	1.06
	Total	392.13	100.00

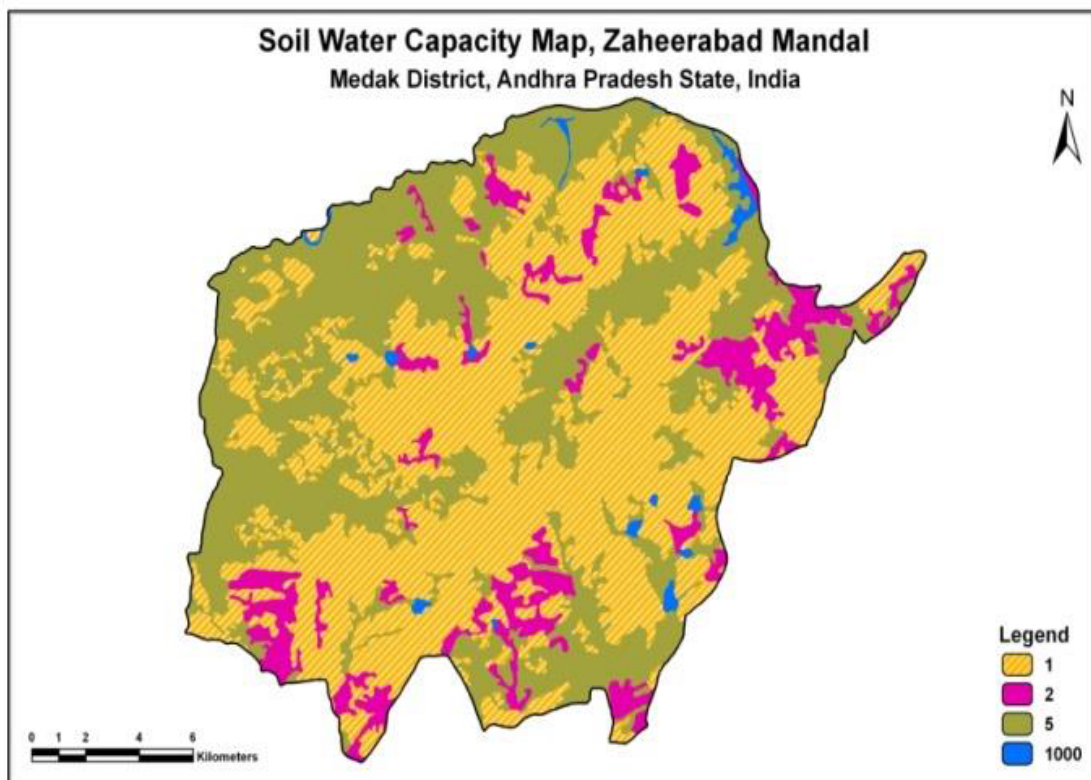**Table 8:** Areal extent of slope units.

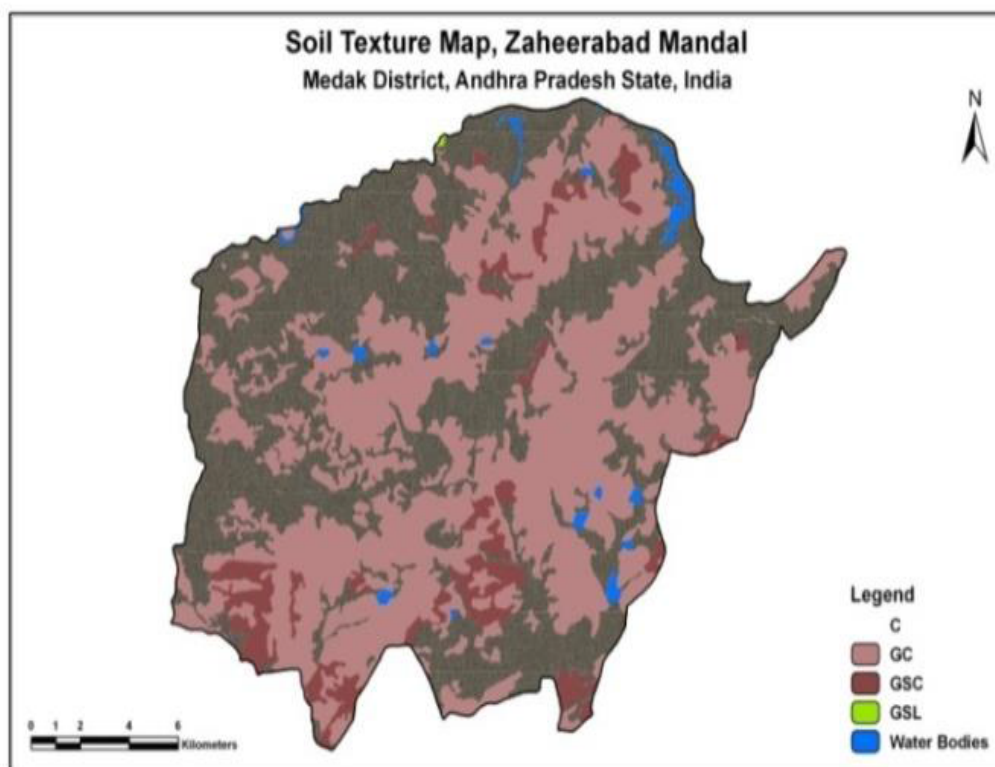**Figure 9:** Soil water capacity map, Zaheerabad Mandal, Medak District, A.P.

Figure 10: Soil texture Map, Zaheerabad Mandal, Medak District., A.P.
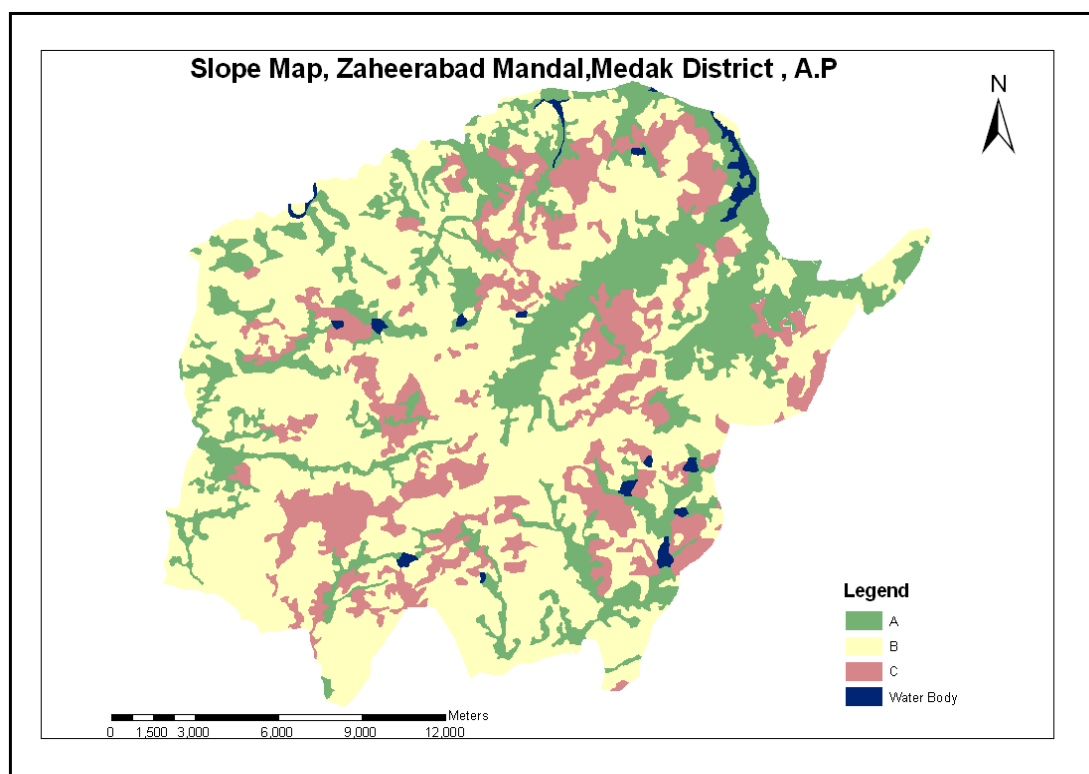
Figure 11: Slope map, Zaheerabad Mandal, Medak District, A.P.

Land capability classification: Land capability classification is an interpretative grouping of soils to show the capability of different soils to produce field crops or to be put to other alternative uses such as pasture, forestry, as habitat for wildlife, recreation etc., on a sustained basis. It is based on inherent soil characteristics, external land features and other environmental factors that limit the use of the land (IARI 1970). Eight land capability classes identified. Soils suitable for agriculture are grouped under classes I to IV according their limitations for sustained agricultural production. Soils not suitable for agriculture are grouped under classes V to VIII for use for pasture, forestry, recreation purposes, quarrying and mining, and as habitat for wildlife (Figure 12). The land capability classes have subclasses to indicate the dominant limitation for agricultural use. Four kinds of limitations are recognized at the subclass level and denoted by "e" for problems caused by water and wind erosion, "w" for problems of drainage, wetness or overflow, "s" for soil limitations affecting plant growth like soil depth, heavy clay or sandy texture, gravelliness and stoniness, salinity or sodicity etc., and "c" for climate limitation. The aerial extents are mentioned in Table 9.

Land irrigability: Land irrigability classification is primarily concerned with predicting the behaviour of soils under the greatly altered water regime brought about by introduction of irrigation. Land irrigability classification is an interpretative grouping of soil map units into soil irrigability classes based on the degree of limitations for sustained use under irrigation and on physical and socio-economic factors (IARI, 1970) Soil irrigability classes are assigned without regard to the availability of irrigation water, water quality, land preparation costs, availability of drainage outfalls and other non-soil related factors. Five soil irrigability classes are recognized. They are class A (none to slight soil limitations), class B (moderate soil limitations), class C

(severe soil limitations), class D (very severe soil limitations) and class E (not suited for irrigation) (Figure 13).

The suitability of land for irrigation depends on the quality and quantity of water, drainage requirements and other economic considerations in addition to the soil irrigability class. Lands suitable for irrigation are grouped under classes 1 to 4 according to their limitations. Lands not suitable for irrigation are grouped under classes 5 (temporarily classed as not suitable pending further investigations) and class 6 (permanently not suitable). Land irrigability classes have subclasses to indicate the dominant limitations for sustained use under irrigation. Three subclasses based on limitations are recognized and denoted by "s" for soil limitations such as heavy clay or sandy texture, soil depth, gravelliness and stoniness, "d" for drainage problems and "t" for limitations of topography. The aerial extents of various land irrgability are mentioned in Table 10.

Finalization of action plan

To analyze and integrate spatial data using GIS, the thematic maps were digitized, coded and stored using GIS software packages. Intersection of various theme maps was done progressively overlaying one layer over the other and by applying suitable decision criteria developed for that area. The final composite units bring out various types of homogeneous units/polygons. These would fit into the decision rules/recommendation arrived at. The draft action plan is discussed with the department officials, district administration, local research centers, NGOs working in the area and some progressive farmers for their feedback. Such feedback is critically evaluated considering the concept of sustainability for suitable modifications/improvements. Subsequently, the draft action plan is validated on the ground before being finalized.
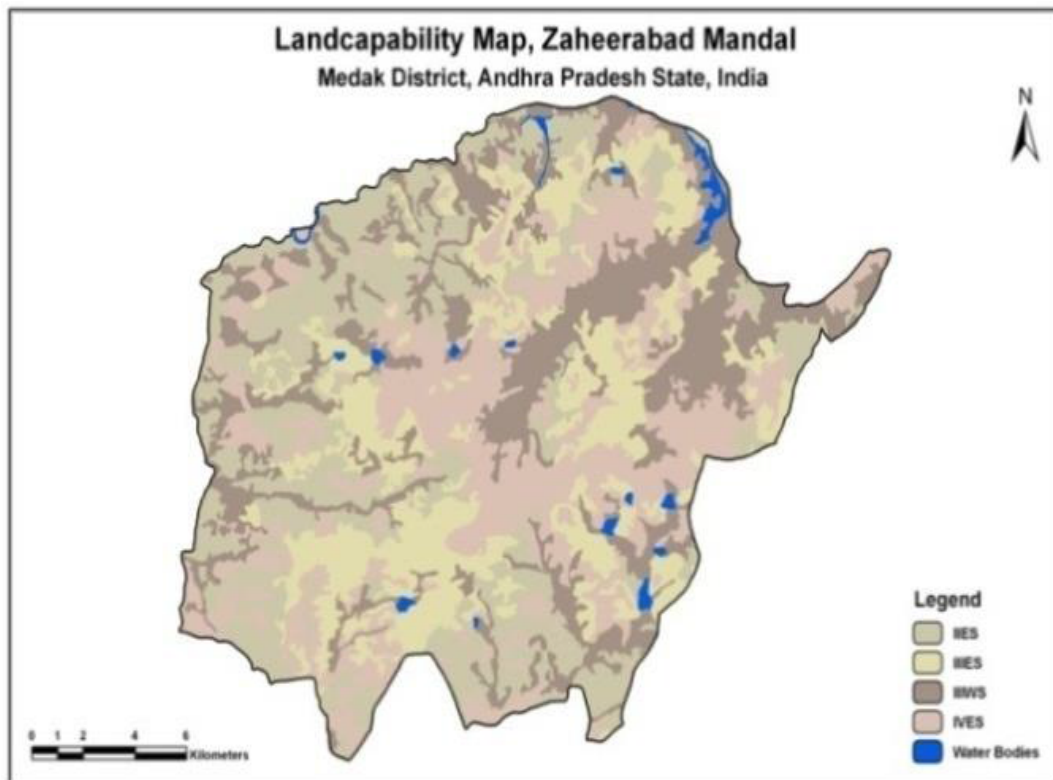
Figure 12: Land capability map, Zaheerabad Mandal, Medak District.A.P.
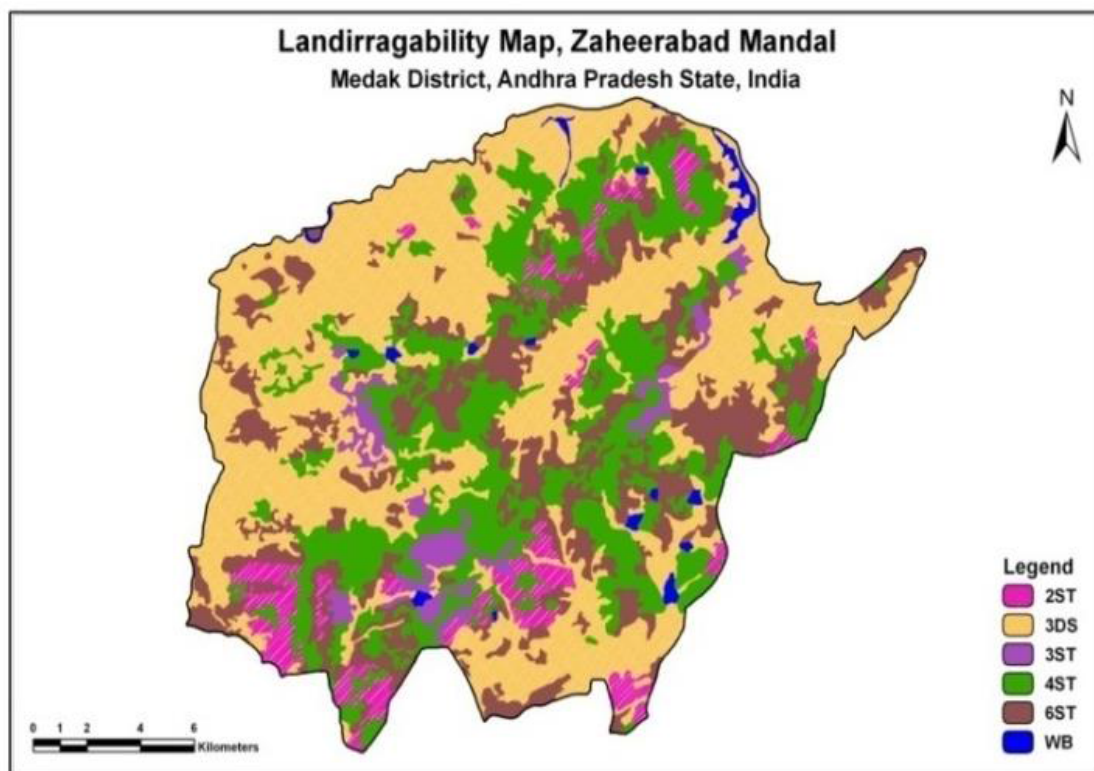
Figure 13: Land irragability map, Zaheerabad Mandal, Medak District.A.P.

Land Capability Units	Area in Sq. Km	Area in %
II ES	98.25	25.05
III ES	90.46	23.07
III WS	94.96	24.31
IV ES	104.3	26.60
Water Bodies	4.16	1.06
Total	392.13	100.00

Table 9: Areal extent of land capability units.

Land Irrigability Units	Area in Sq. Km	Area in %
2ST	31.44	8.02
3DS	165.16	42.12
3ST	20 .36	5.20
4ST	94.06	23.98
6ST	76.95	19.62
Water Bodies	4.16	1.06
Total	392.13	100.00

Table 10: Areal extent of land irrigability units.

Recommendations: The soil and land resource units of Zaheerabad Mandal were assessed and evaluated for their suitability for growing rice, sorghum, maize, sugarcane, cotton, green gram, black gram, bengal gram, red gram, groundnut, sunflower, soybean, safflower, castor, and guava which are the major crops grown in different parts of the mandals. The parametric approach of Sys (1985) which is a modified version of the FAO Framework for Land Evaluation (1976) was used for evaluating the land suitability. The Framework for Land Evaluation has recognized two orders, namely, order S-suitable for agriculture and order N-not suitable for agriculture. These orders are further subdivided into classes, subclasses and units. Order S-suitable for agriculture has three classes, highly suitable-S1, moderately suitable-S2 and marginally suitable-S3. Order N-not suitable for agriculture has two classes, N1-currently not suitable and N2-permanently not suitable for agriculture. The criteria assumed for differentiating into - e classes are that, under a given management level specified to obtain optimum yield from a highly suitable land (Sl), the maximum reduction in yield successively may be in the order of about 25% for S2 and 50% for S3 classes. The suitability subclass reflects the kinds of limitations and indicate the kind of land improvements required within a class. The subclasses are indicated by the symbol using-lower case letters following the arabic numeral (c-climate, e-erosion hazard, f-flood hazard, g-gravelliness, k-workability, I-topography, m-moisture availability, n-nutrient availability, p-crusting, r-rooting condition, t-texture, w-drainage, z-excess of salts/calcareousness). The suitability evaluation shows the areas that are highly suitable (class S1), moderately suitable (subclasses of S2), marginally suitable (subclasses of S3), currently not suitable; (class N1) and permanently not suitable (class N2) for each crop.

Land suitability for rice: The land suitability assessment revealed that there are 4 suitability classes, 5 subclasses and 14 subclass associations with different kinds and degree of limitations. About 13358 has (27.79%) area has been rated as moderately suitable in the mandal, 21614 ha (46.31%) area as marginally and 14186 ha (43.60%) area as unsuitable (N2) for growing Rice crop (Figure 14).

Land suitability for sorghum: The land suitability evaluation showed that there are 4 suitability classes, 5 classes and 17 subclass associations with different kinds and degree of limitations. About 13358 has (27.79% TGA) area has been rated as moderately suitable in the mandal, 21614 ha (46.31%) area as marginally and 14186 ha (43.60%) area as unsuitable (N2) for growing Rice crop (Figure 15).

Land suitability for maize: The suitability evaluation indicated that there are 4 suitability classes, 6 subclasses and 16 associations of subclasses with different kinds and degree of limitations. About 10498 ha (21.01%) area has been rated as highly suitable (S1) in the mandal, 22940 has (46.31%) area as moderately suitable (S2), 2862 (5.79%) area ,as marginally suitable (S3) and 13322 (26.89%) area as unsuitable (N2) for growing maize crop (Figure 16).

Land suitability for sugarcane: The land suitability evaluation showed that there are 4 suitability classes, 5 subclasses and 15 subclass associations with different kinds and degree of limitations. About 10246 ha (20.64% TGA) area has been rated as highly suitable (S1) in the mandal, 15646 ha (31.53%) area as moderately suitable (S2), 16745 ha (33.75%) area as marginally suitable (S3) and 6985 ha (14.07%) area as unsuitable (N2) for growing crop (Figure 17).

The Proposed Approach for System

The real time information of current status of the fields at various locations is possible with the continuous monitoring with the Geographic information Systems with supervisors. The proposed system contains two major components of Geographic Information system. The static data contain detailed mapping of the allotted Field Area as a spatial database in WEBGIS platform. The Dynamic data regarding the Fields of particular Sugar Plants are collected. The Proposed system will takes the input and continuously displays to enable the management for decision making of the realistic situation. The system can be accessed by separate logins for administrator and user. There is a scope for unlimited number of user to login to the system. By logging in the admin we can have an total view of the Area allotted for the particular Sugar Plant. The administrator has the rights to With a Supreme Authority, from this view and Creating new ID for managers, Filed supervisors and other authorized persons etc. (Figure 18).

Development of Open Source Web Based Decision Support System

Web based GIS are evolved from different Web maps and client server architecture to distributed ones. As such, Internet reshapes all functions of information systems including: gathering, storing, retrieving, analyzing, and visualizing data. Moreover, disseminating spatial information on the Internet improves the decision making processes. Development of the Web and expansion of the Internet provide two key capabilities that can greatly help the stakeholders. First, the Web allows visual interaction with data. By setting up a Web Server, clients can produce maps. Since the maps and charts are published on the Internet, other clients can view these updates, helping to speed up the evaluation process. Second, because of the near ubiquitous nature of the Internet, the geospatial data can be widely accessible. Clients can work on it from almost any location. The combination of easy access to data and visual presentation of it addresses some of the primary difficulties in performing geosciences evaluations. Web GIS is not without its challenges. The primary problem is speed; GIS relies on extensive use of graphics. Connection speeds over the Internet can make heavy use of graphics intolerably slow for users. This facility, to view maps with administrative and other necessary overlays. The site have facilitate user in query regarding crops and growing environments (Figure 19). Generally in every Sugar Industry the typical Organization Hierarchy is as follows, Chief Cane manager, Field Manager, field Supervisor and etc.

Admin login

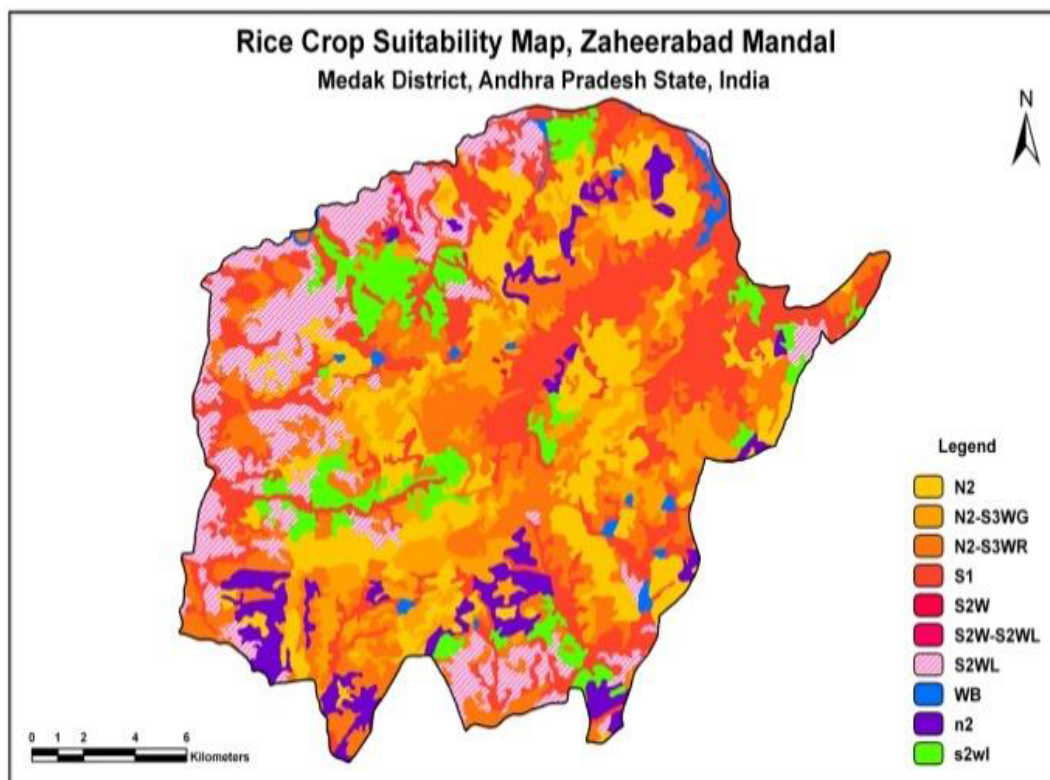From the Given WEB SITE ADMIN can Login like shown in Figure 20.

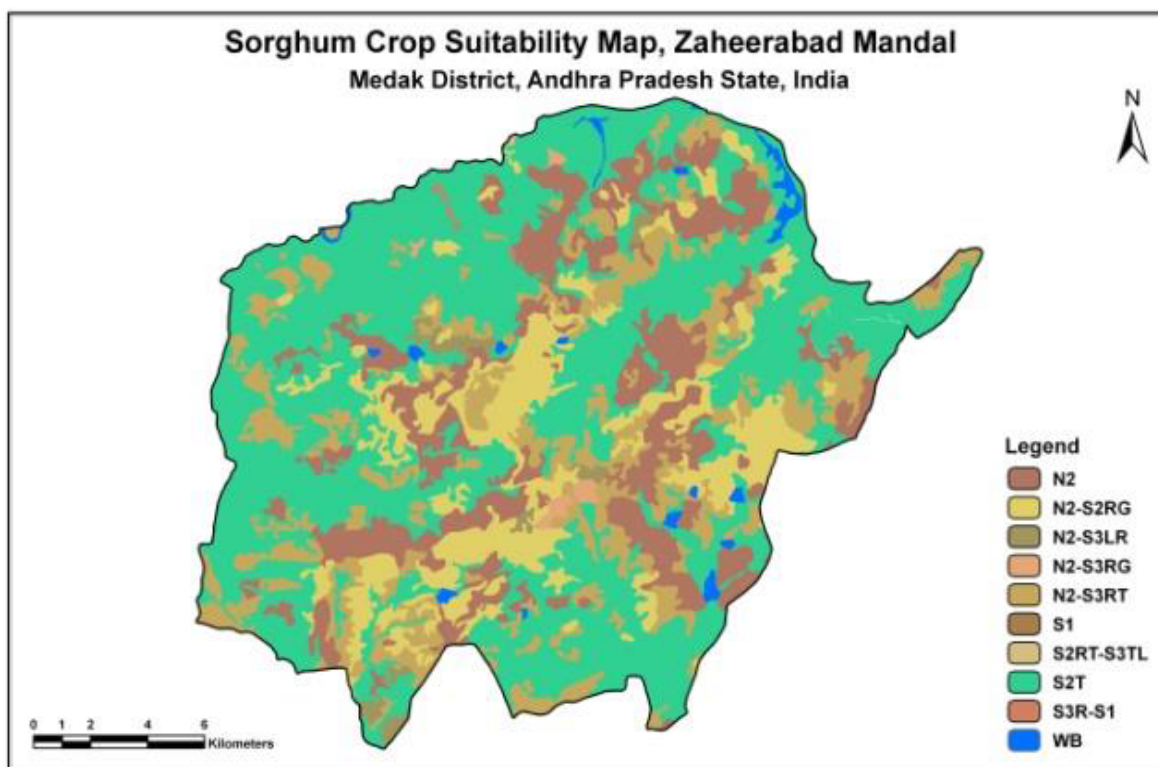**Figure 14:** Rice crop suitability map, Zaheerabad Mandal, Medak District.A.P.

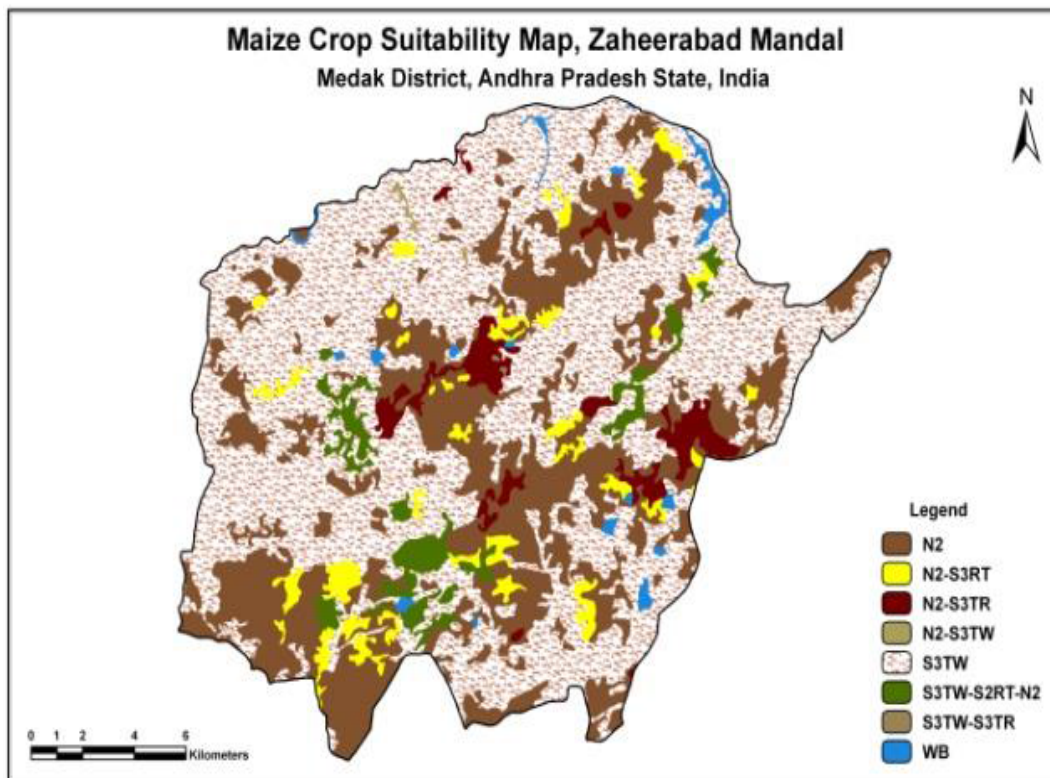**Figure 15:** Sorghum crop suitability map, Zaheerabad Mandal, Medak District.A.P.

Figure 16: Maize crop suitability map, Zaheerabad Mandal, Medak District.A.P.
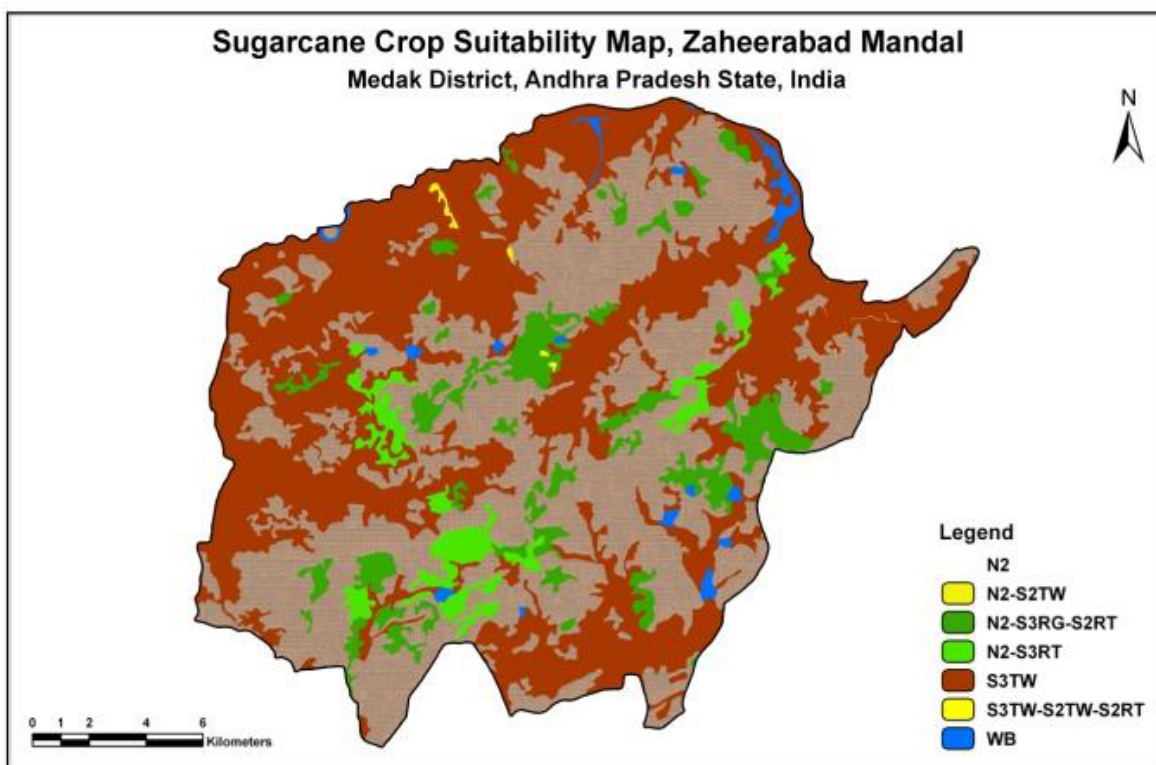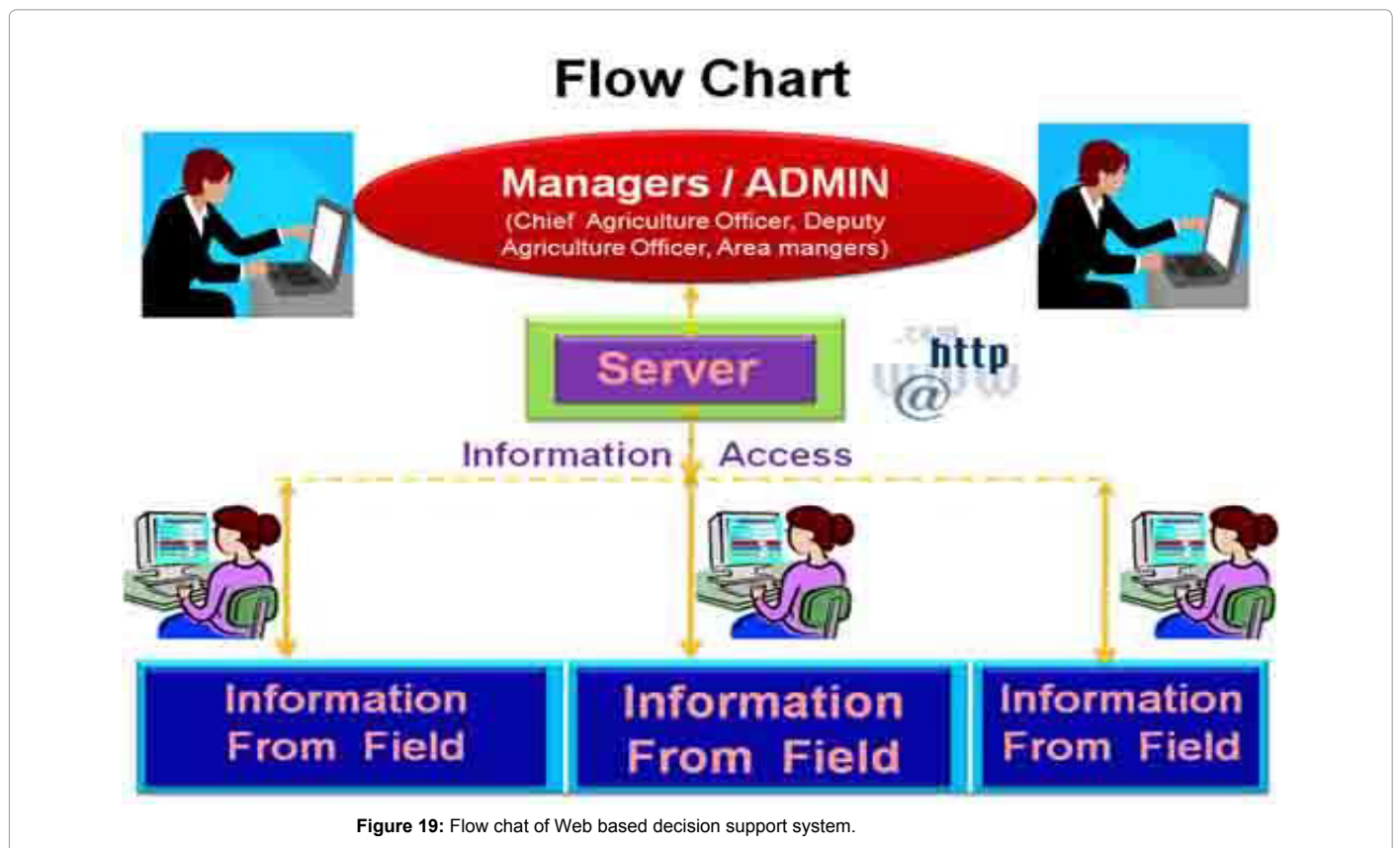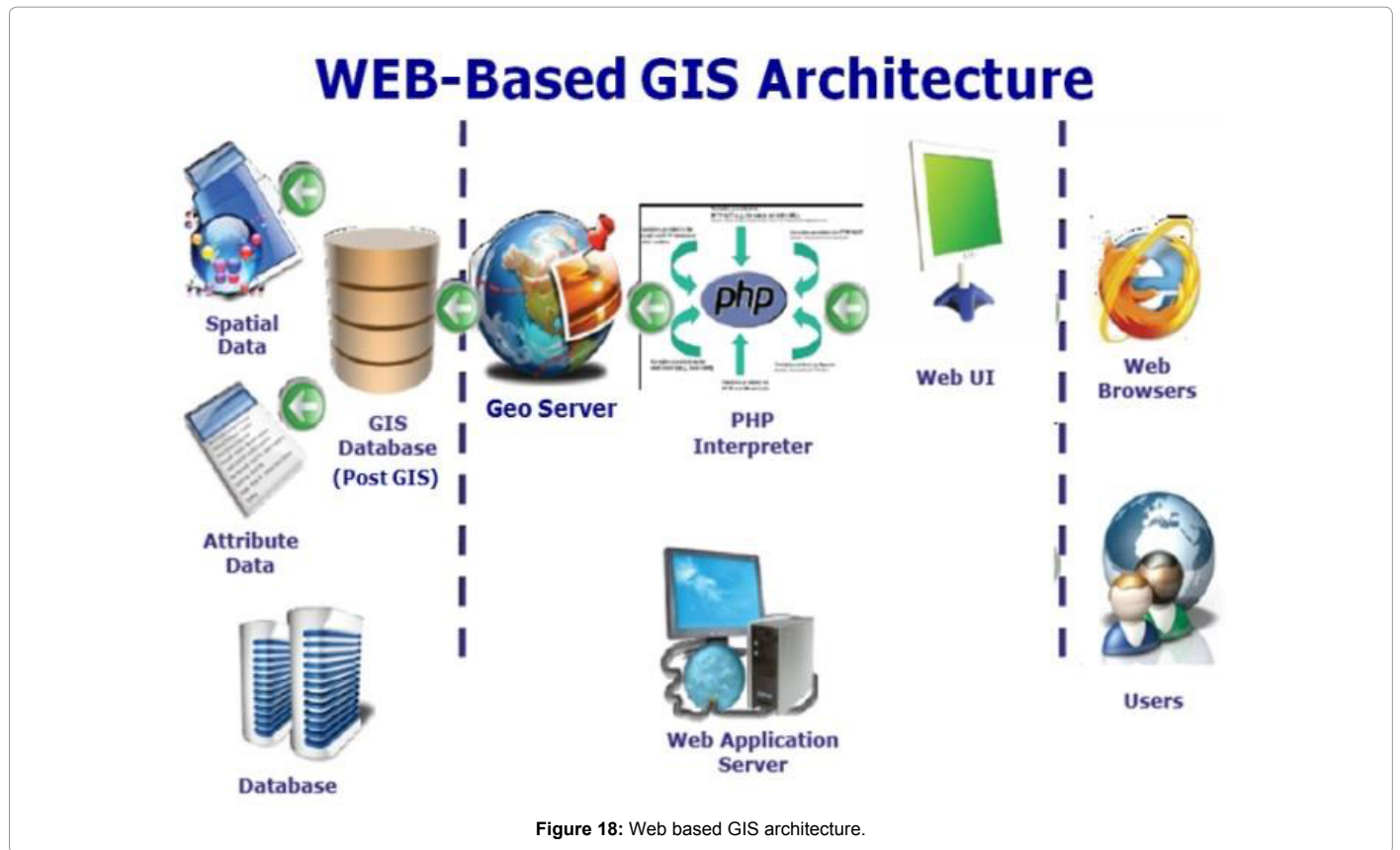

Figure 17: Sugarcane crop suitability map, Zaheerabad Mandal, Medak District.A.P.

Figure 18: Web based GIS architecture.

Figure 19: Flow chat of Web based decision support system.

Field supervisor login

The total spatial view of the area allotted for the Supervisor of the Sugar Plant can be seen after logging in to the system. From the spatial view the information about each individual field like name of the farmer, date of sowing, date of application of fertilizer and water, other crop information etc., which is useful for system to avoid any dependency and dependency on the oral communication. Thus the human error in communication can be minimized with the continuous monitoring of real time data available within the system by any manager prior to taking major decisions (Figure 21).

Field history

From this Package the history related to every field can be analyzed. For example the date on which water and fertilizer can be known for each field. If there is a delay or laxity by the farmer in the applying of water or fertilizer the same can be known from the SDSS package. It also provides information about the date on which the field needs to be watered and also the due date for which the field should be watered. In case of the application of the fertilizers to the field can also be known using this Package (Figure 22).

Manager login

The total view of the Area allotted for the Sugar Plant can be seen after Login in the system. The road network of the study area is captured from the satellite imagery and is overlaid on the map. From this we can do analysis on the nearest route to reach the particular field and the SDSS can also predict alternative root in case of any problem in the main route (Figure 23).

Similarly from the DSS package we can identifying the fields which are ready for cutting and to view the delay reports of water, Fertilizers and etc., from the fields and then see to rectify that delays by avoiding the dependency in the oral communication by seeing the data about each and every field like Farmer name, date of seeding, date of application of fertilizer and water, other crop information and etc., which is useful for continuous monitoring of fields to know the status of the crop and also the performance of the field supervisor and Thus the human error in communication can be minimized with the continuous monitoring of real time data available within the system by any superior prior to implement the decision (Figure 24).
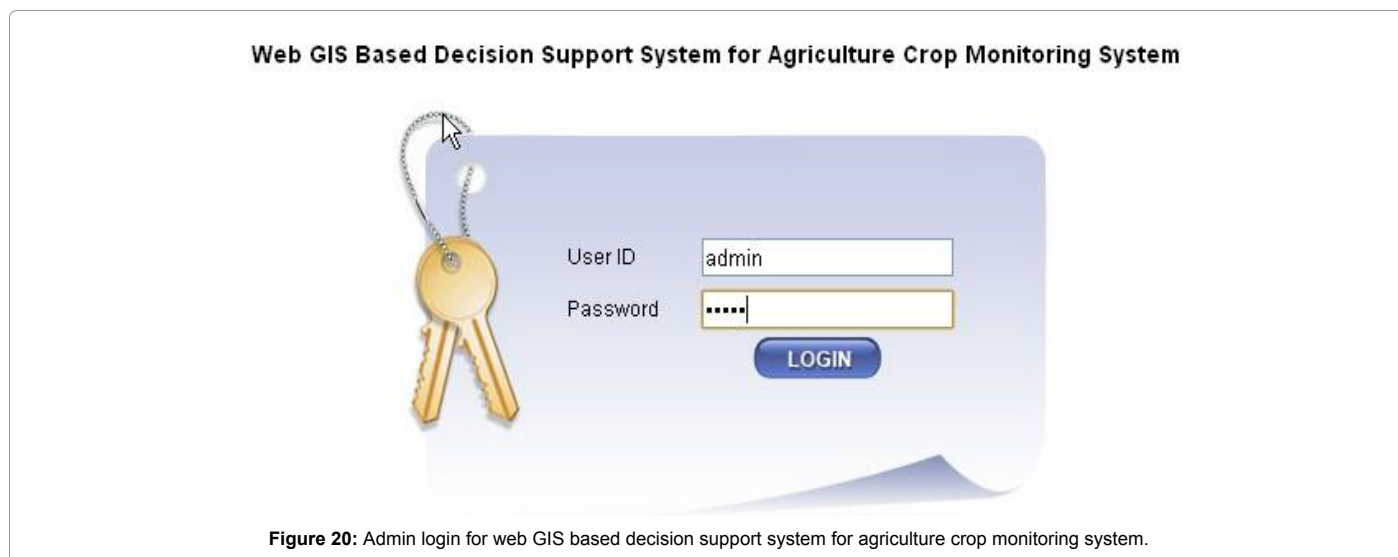
Figure 20: Admin login for web GIS based decision support system for agriculture crop monitoring system.

Figure 21: Field supervisor login for web GIS based decision support system for agriculture crop monitoring system.
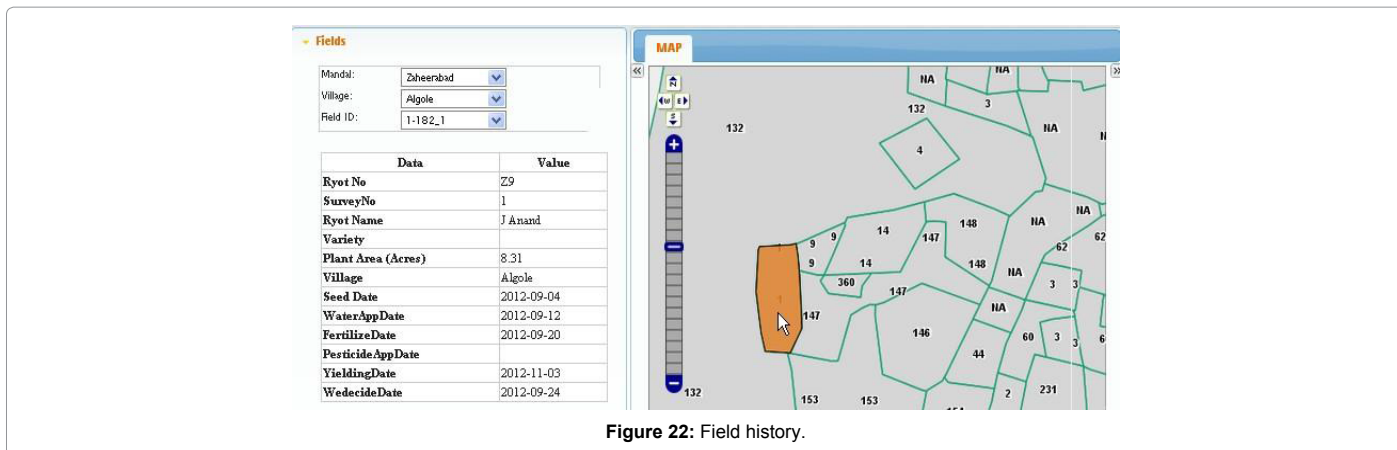
Figure 22: Field history.
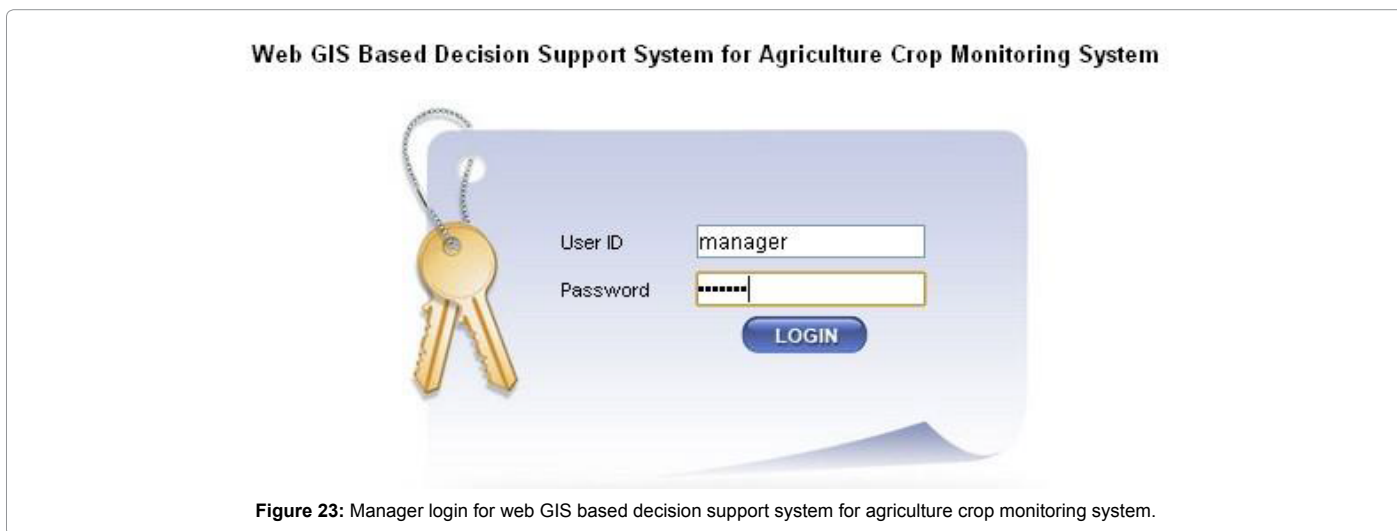
Figure 23: Manager login for web GIS based decision support system for agriculture crop monitoring system.
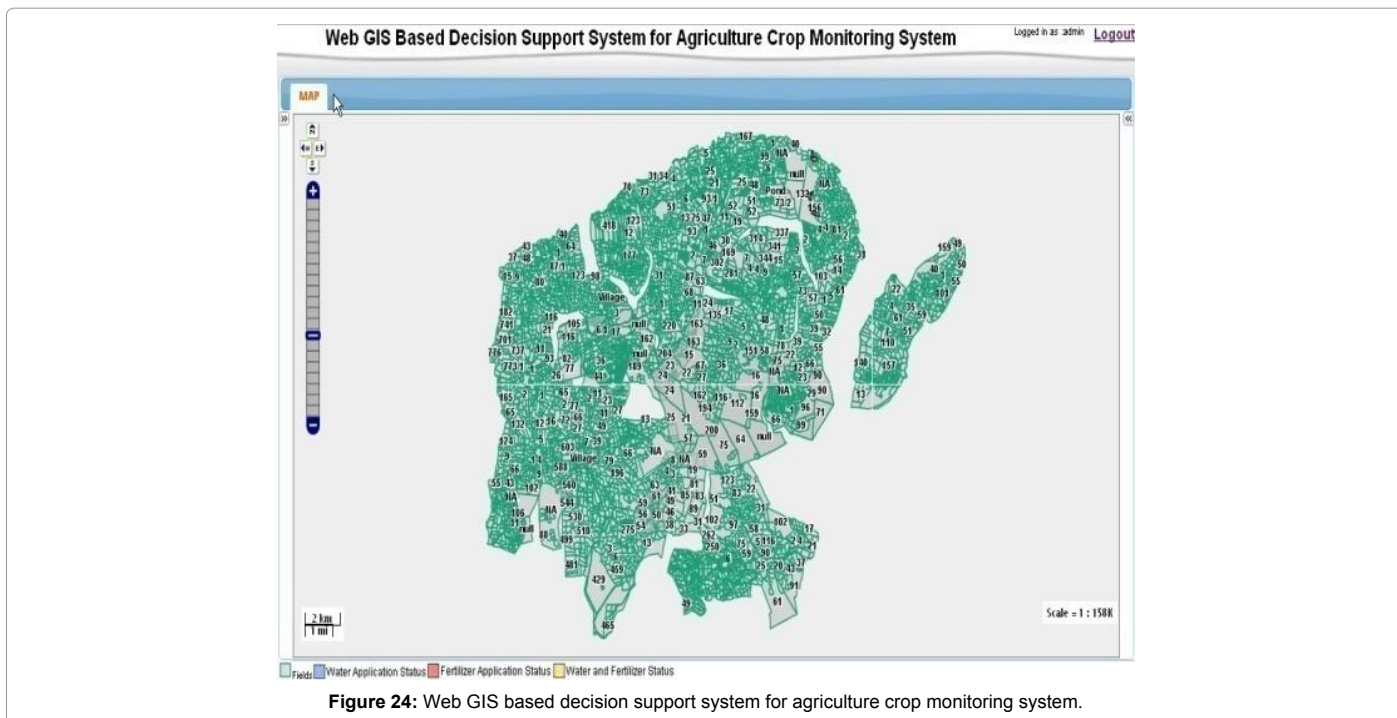
Figure 24: Web GIS based decision support system for agriculture crop monitoring system.

Reports (Figures 25-28)

Facilities provided by decision support system for agriculture crop monitoring

- Easy to use and Access the Data.

- Getting Online information about Fields and Efficiency of the fields yielding & etc.

- Easy to get the performance of Filed Supervisors.

- Easy to get the History of each and every field.

- Giving feel like actual Filed/Site Visit to the Management.

- Reduce the Delay in application of water, Fertilizers and etc.

- Transparency in Crop growth and land activities with Higher productivity and lower overheads

- Transparency to the management and cost control.

- Transparency for Planning of application of water from cannels, Route planning for transportation of crop after yielding to the Sugar plant and etc.

- Easy to Maintain the Fields belongs to particular Sugar Plants.

- Easy to get the status of Each and every Filed, So that Total allotted land status of Each and every Stage of the Crop Route map to reach the location.

- Faster response and optimum utilization of available resources.
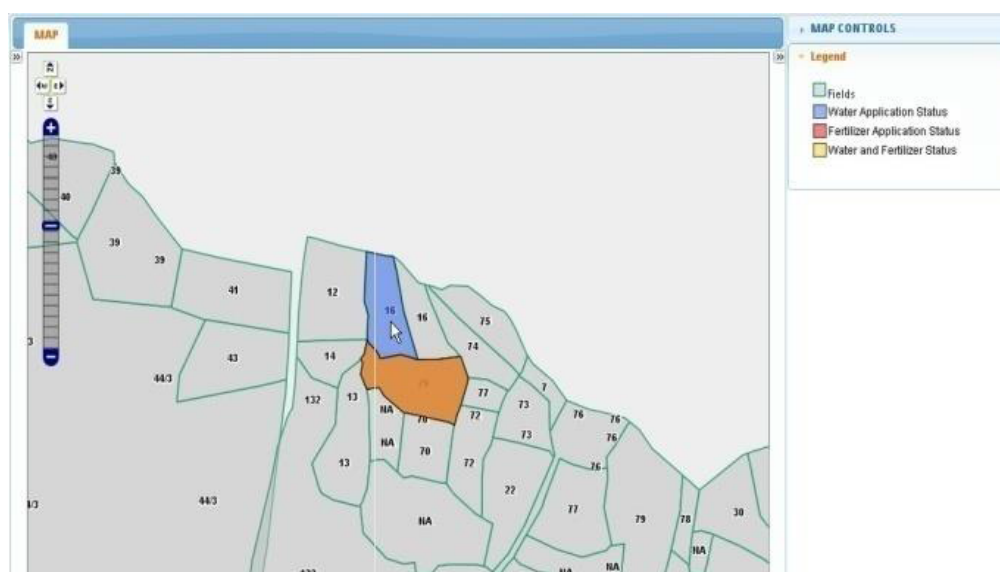
Figure 25: Delay in water application.
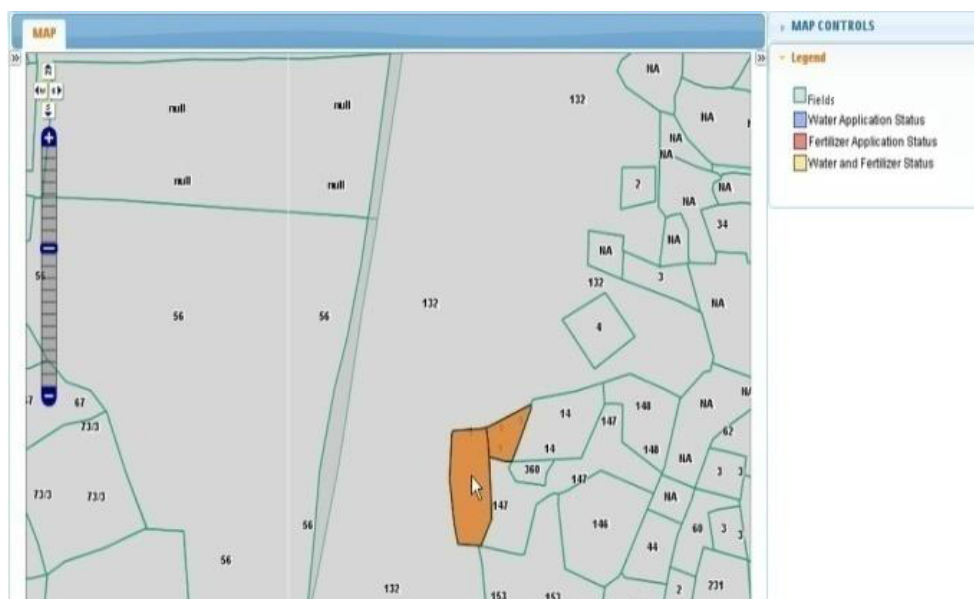
Figure 26: Delay in fertilizer application.

Figure 27: Delay in water and fertilizer application.

Figure 28: Fields ready for cutting.
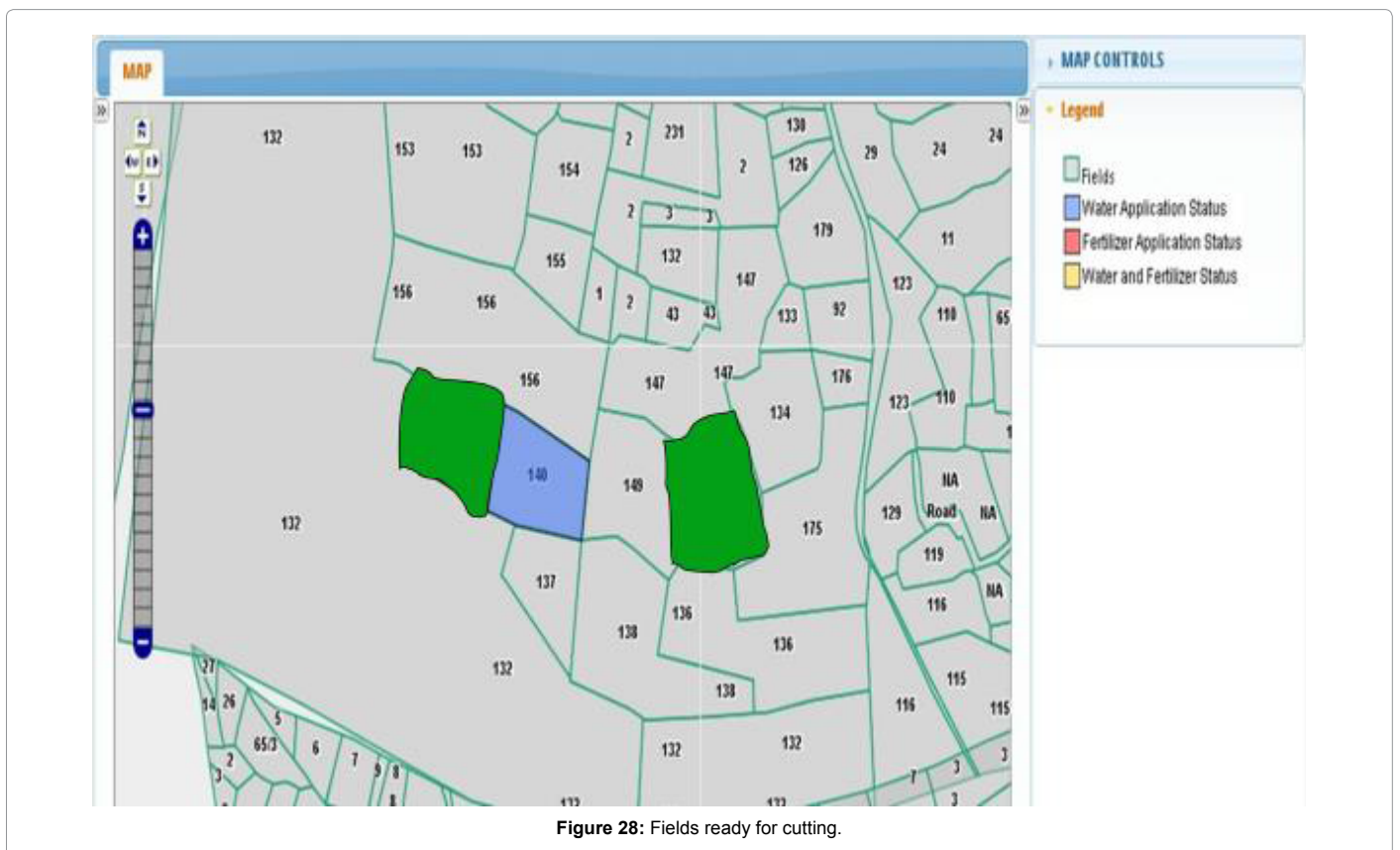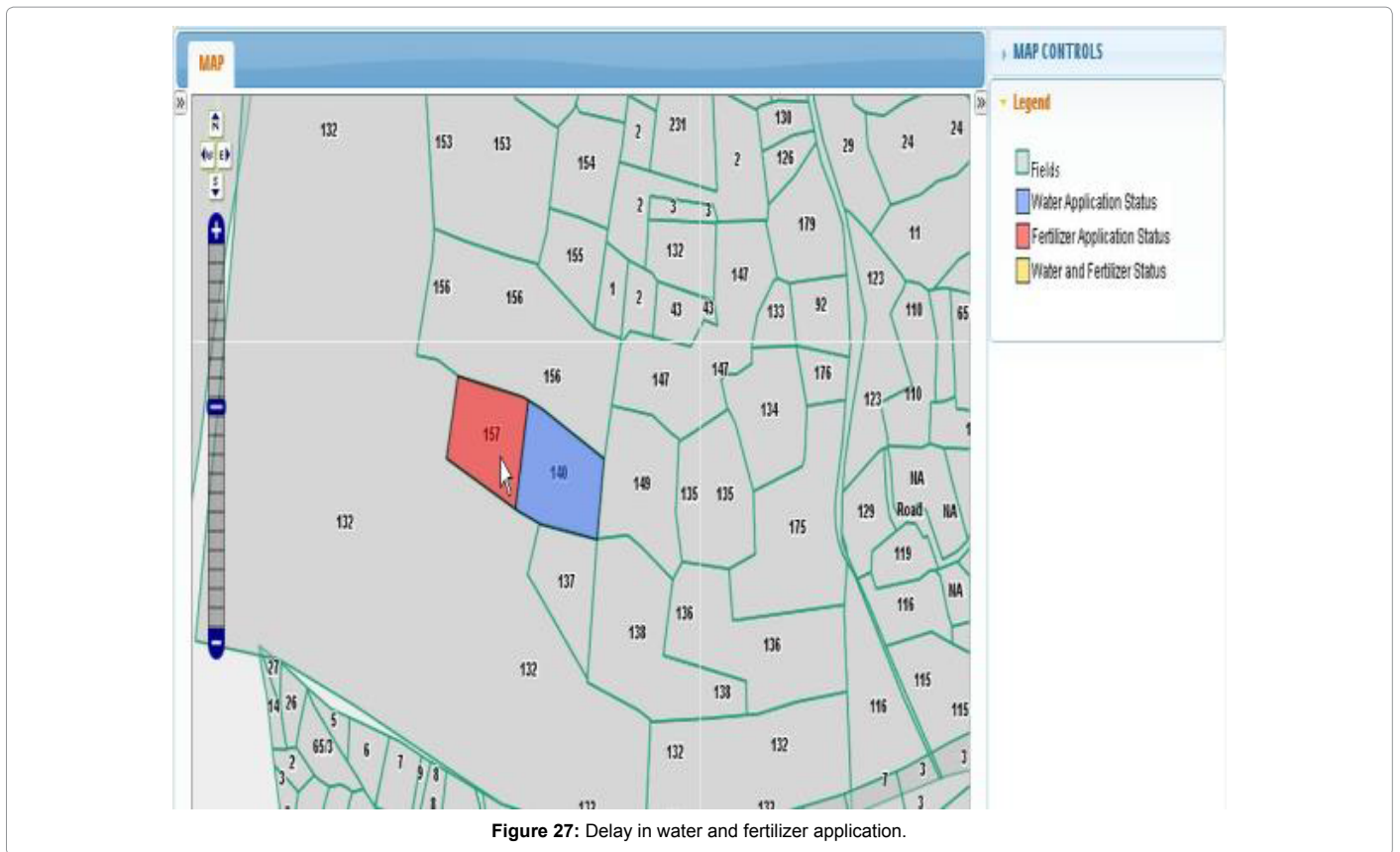
- Getting the Online status of Each and every Stage of the Crop in particular field.

Summary of delay reports to sugarcane plant management: The system provides continuous monitoring on crop activities and facilitates dynamic planning of strategies to meet the changing requirements of the crop or Sugar plant activities with respect to the impedance of the implementation of planned strategies. The scope for the enhancement in the system is much more as the advancement of the web technology. The databases can be made available for all the concerned authorities through Internet and intranet facilities. This connectivity definitely enhances the mutual cooperation of the authorities to accomplish the task with more efficiency.

Conclusion

WEBGIS is essential to effective preparedness, communication, and training tool for the management of Agro based industries, which offers enhancement for the existing manual system to avoid the human error in making the decisions to enhance the crop production and also provides continuous monitoring of the crop and field activities and operations. With the effective utilization of the advantages provided by the WEBGIS spatial database the efficiency in the planning and implementing activities can be improved.

References

1. Bernard A (2003) A DSS is an Integration of Web-Based Programs. Geographic Information Systems (GIS) Capabilities and Databases, USA, pp: 484-495.

2. David H (2006) Web-Based Systems, Client can use any internet-Connected computer or web-enabled Mobile Phone or PDA to gain Real time Access to the data, USA.

3. Mathlyalagana V (2004) Web GIS has the Potential to share data, provide easy access for users with limited GIS Knowledge, USA.

4. Alaguraja P, Durairaju S, Yuvaraj D, Sekar M, Muthuveerran P, et al. (2010) Land Use and Land Cover Mapping-Madurai District, Tamilnadu. India Using Remote Sensing and GIS Techniques. International Journal of Civil and Structural Engineering 1: 91-100.

5. Gupta YK, Gupta RD, Kumar K (2010) Web GIS for Planning Infrastructural Facilities at Village Level. Map india, India.

6. Aydİnoglu AC, Yomralİoglu T, Inan HI, Seslİ FA (2016) Managing land use/cover data harmonized to support land administration and environmental applications in Turkey. Scientific Research and Essays 5: 275-284.

7. Anselin L (1990) What is special about spatial data Alternative perspective on spatial data analysis. In Spatial Statistics: Past, Present and Future, (ed.) Griffith DA, Monograph 12, Institute of Mathematical Geography 21: 265-280.

8. Lillisand (2016) Keefe Fundamentals of Geographic Information Systems.

9. Upton GJ, Fingleton B (1985) GIS Development magazines of August, October 2003. Spatial data analysis by example, volume 1: Point pattern and quantitative data. Wiley, Toronto Singapore, Brisbane 28: 664.

Mango juice clarification with polygalacturonase produced by *Aspergillus awamori* MTCC 9166 - Optimization of conditions

[3]Anuradha, K., [3]Naga Padma, P., [2]Venkateshwar, S. and [1*]Gopal Reddy

[1]*Osmania University, Department of Microbiology, 500 007, Hyderabad, Telangana*
[2]*Osmania University, College of Technology, 500 007, Hyderabad, Telangana*
[3]*BVB Vivekananda College, Department of Microbiology, Secunderabad 500 094, Telangana, India*

Abstract

Pectin rich fruit juices need enzymatic treatment for clarification. As fruits are rich in pectin, pectinolytic treatment can efficiently reduce viscosity resulting in clarified fruit juice. Enzymatic treatment of mango pulp results in 80% recovery of total juice present in the fruit. Use of pectin degrading polygalacturonases increases both fruit juice extraction and clarification. Polygalacturonase (PG) produced by *Aspergillus awamori* MTCC 9166 is studied for mango juice clarification and conditions are optimized by Box-Behnken design. The conditions studied are incubation time (15-45 min), enzyme concentration (0.5-1.5 U/ml), and temperature (25-40^{0}C). Significant regression model describing the change on viscosity with respect to independent variables was established. Based on surface plots and contour plots, the optimum conditions for mango juice clarification were obtained. The recommended enzymatic treatment conditions are enzyme concentration 1.5 U/ml, incubation time 30 min at 40^{0}C. Significant (60%) reduction in viscosity was observed.

Introduction

Mango is one of the important fruits widely grown in tropical countries and   is indigenous to India. The best quality mangoes originate in southern part of India. It is perishable, seasonal fruit which is rich source of pectin and also contains sucrose, glucose and maltose. Pectic substances and pectinolytic enzymes play important role in fruit juice processing (Fogarty and Kelly, 1983). Enzymatic treatment of mango mash results in 80% of total juice present in fruit. Pectinases along with cellulases and xylanases are used to degrade mango pulp (Kashyap *et al.*, 2001).

Pectinases play important role in processing plant materials to food products, such as de-pectinization of fruit juices, maceration of vegetables and fruits, and extraction of vegetable oils (Benen *et al*., 2003). Pectinolytic enzymes are used in fruit processing industry to increase yields, improve liquefaction, clarification and filterability of juices (Harsha *et al*., 2014). Commercial sources of fungal pectinases have been used in fruit juice processing since 1930's for clarifying fruit juices and disintegrating plant pulps to increase juice yields (Macmillan and Sheiman, 1974). Most enzymes are marketed on the basis that they are generally recognized as safe (GRAS) for

their intended use in the juice process (Grassin and Fauquembergue, 1996; Heldt-Hansen *et al*., 1996). *Aspergillus niger* or *Aspergillus aculeatus* are widely used for industrial production of pectinolytic enzymes which are important in food and alcoholic beverage industry (Naidu and Panda, 1998). Both the naturally present (endogenous) enzymes and introduced enzymes (exogenous) catalyze the decomposition of pectin in fruit juice.

The exogenous pectinolytic enzymes improve and influence the efficiency of fruit juice process, which cannot be achieved by the endogenous enzymes alone that occur naturally in the fruit. Upon grinding of the raw fruit, pectinases are added which reduce viscosity of pectin-rich crude juice, also known as pulp enzyming, and therefore improve the processing capacity and yield of fruit juice. The production of fruit juices can also be achieved by liquefaction of fruit tissues. In this process the fruit tissues are solubilized by using a broad spectrum of polysaccharide degrading enzymes, such as pectinases, hemicellulases and cellulases (Benen and Voragen, 2003).

Pectinases assist in pectin hydrolysis, which cause reduction in pulp viscosity and a significant increase in juice yield (Solehah *et al*., 1964; Pilnik and Voragen, 1993;) reported action of commercial

---

*Corresponding author.
Email: gopalred@hotmail.com

pectinolytic enzymes, Pectinex and Ultrazyme, in degradation and hydrolysis of anthocyanin pigments of raspberry juice. Ceci and Jorge Lozano (1998) reported simple method for testing of pectinolytic activities and determined enzymatic activity of commercial pectinases for clarification of apple juice. *Saccharomyces cerevisiae* was cultured in pine apple juice and its pectinolytic enzymes were used for extraction of pine apple juice (Dzogbefia *et al*., 2001). Conversion of fruits in to fruit juices was originally developed for utilizing the surplus fresh fruits, but now processing of fruit juices is firmly established as a major industry. As the demand for fruit juices is increasing, their production has increased considerably in recent years. Therefore there is a need to evolve better approaches for processing of fruits. Here we report the application of polygalacturonase (PG) produced by *Aspergillus awamori* MTCC 9166 for mango juice clarification and establish enzymatic conditions in preparation of clarified mango juice. The parameters like incubation time, enzyme concentration and temperature were studied and optimized by Box-Behnken statistical design to obtain maximum juice yield.

Material and Methods

Enzyme source and enzyme assay

Aspergillus awamori MTCC 9166 was isolated from vegetable dump yard soil and maintained on Potato Dextrose Agar (PDA) slants in refrigerator (Anuradha *et al*., 2010). Submerged fermentation was carried out in 250 ml Erlenmeyer flasks containing 50 ml Czapek's broth with 1% commercial pectin (Citrus peel pectin, SD Fine Chemicals). The flasks were inoculated with 2.5% (v/v) spore suspension containing 1×10^6 spores/ ml and incubated for production of polygalacturonase for 5 days at 27^0C in orbital shaker incubator at 200 rpm. Fermented broth was cold centrifuged at 4^0C, 5000 rpm for 10 minutes and supernatant was taken as crude enzyme source and maintained at 4^0C for further studies. The enzyme was assayed by measuring the D-galacturonic acid released from polygalacturonic acid as substrate. One unit of enzyme activity is defined as the amount of enzyme required to produce 1 µM of galacturonic acid per minute at 50^0C (Nelson, 1944; Collmer *et al*., 1988;).

Fruit juice preparation

Fresh ripe mangoes *(Mangifera indica)* were purchased from local market and used for juice preparation. Mangoes were peeled, deseeded, then ground in a blender to obtain homogenous mango

pulp using distilled water in 1:1 (w/v) ratio. From this homogenate fruit juice about 100 ml was extracted by adding 40% distilled water and maintaining at 60^0C for 1 hour. After this treatment the juice was subjected to both centrifugation and filtration. The filtrate obtained was about 80 ml and it was made up to 100 ml. The pH was found to be 5, which is the pH of fruit juices in general (Jacob *et al*., 2008).

Enzymatic treatment

10 ml of extracted mango juice (as above) was subjected to different enzymatic treatment conditions. The parameters tested were incubation time (15-45 min), enzyme concentration (crude enzyme 0.5-1.5 U/ml) and temperature (25-40^{0}C). After treatment the mango juice was heated to 90^{0}C for 5 minutes to inactivate the enzyme. The treated juice was centrifuged at 10,000 rpm for 15 min, filtered through Whatman no 1 filter paper and filtrate was collected for further analysis.

Viscosity studies

The viscosity of the mango juice was measured using DV-II+ Pro Viscometer Brook field LV-6.3V at 30^{0}C. The viscosity is expressed in milli Poise units (mPa.s).

Experimental design

Box-Behnken design was used for optimization of mango juice clarification. The parameters studied as independent variables were incubation time, enzyme concentration (crude enzyme) and temperature. The parameters selected were analyzed at three different (low, high and medium coded as -1, 0 and 1 levels (Box and Behnken, 1960). A total 17 combinations were used. A second order polynomial equation shown below was used to study the effect of variables in terms of main effects, quadratic effects and interactive effects. Statistical analysis of the data was done using INDOSTAT software.

$$Y = \beta_0 + \sum \beta_i X_i + \sum \beta_{ii} X_i^2 + + \sum \beta_{ij} X_i X_i$$

Where Y is predicted response, Xi coded value of independent variable, β_0 is constant term, β_i coefficient of the linear terms, β_i is the coefficient of the quadratic terms, and β_{ii} is the coefficient interactive terms.

Results and Discussion

Mango (*Mangifera indica* L.) is produced in over 90 countries worldwide with Asia accounting for approximately 77% of global production (Sudheer

Table 1. Box-Behnken experimental design for mango juice clarification using polygalacturonase produced by *Aspergillus awamori* MTCC 9166

Runs	Coded Variables			Uncoded Variables			Viscosity (mPa.s)
	X1	X2	X3	Time (min)	Temp (⁰C)	Enzyme conc. (U/ml)	
1	0	1	1	45	40	1.5	1.998
2	1	0	1	60	37	1.5	1.055
3	1	-1	0	60	25	1	1.039
4	0	0	0	45	37	1	1.045
5	0	0	0	45	37	1	1.045
6	0	-1	-1	45	25	0.5	1.088
7	-1	-1	0	30	25	1	1.082
8	-1	1	0	30	40	1	1.999
9	0	-1	1	45	25	1.5	1.001
10	1	0	-1	60	37	0.5	1.812
11	-1	0	-1	30	37	0.5	1.912
12	1	1	0	60	40	1	1.996
13	0	0	0	45	37	1	1.045
14	0	1	-1	45	40	0.5	1.988
15	0	0	0	45	37	1	1.045
16	0	0	0	45	37	1	1.045
17	-1	0	1	30	37	1.5	1.921

Table 2. Optimization of estimated effects and coefficients for mango juice clarification using polygalacturonase produced by *Aspergillus awamori* MTCC 9166 using Box-Behnken experimental design three variables (A - time, B - case temperature, C - enzyme concentration)

Source	Partial R2	Coef.	Std. Coef.	t value	t prob	Significance
Constant	0.0000	1.0450	0.0681	15.3531	0.0000	
A-Time	0.0382	-0.1265	0.0538	-2.3509	0.0510	*
B-Temperature	0.5303	0.4714	0.0538	8.7601	0.0001	Significant
C-Enzyme concentration	0.0254	-0.1031	0.0538	-1.9165	0.0968	*
A2	0.1401	0.3201	0.0742	4.3160	0.0035	Significant
B2	0.0412	0.1639	0.0742	2.2094	0.0629	*
C2	0.1319	0.3099	0.0742	4.1778	0.0041	Significant
AB	0.0001	0.0100	0.0761	0.1314	0.8991	*
AC	0.0438	-0.1915	0.0761	2.5165	0.0400	Significant
BC	0.0007	0.0243	0.0761	0.3187	0.7593	*

*Insignificant

kumar and Reddy, 2009). Among the Asian countries, India has good production of mango and it is mostly used for commercial production of juice. Mango pulp is rich in pectin, starch and xylan. The isolate under study has not only PG production but also amylase and xylanase activity (Anuradha et al., 2010) and so it could have ample application in mango juice clarification as done by Saisha and Shashidhar (2015). Clarification of mango juice was carried out using polygalacturonase produced by *Aspergillus awamori* MTCC 9166 using Box-Behnken statistical design to optimize conditions like temperature, enzyme concentration and incubation time, which showed significant influence on mango juice clarification. The enzymatic hydrolysis of pectic substances depends on several processing variables such as type of enzyme, hydrolysis time, enzyme concentration, incubation temperature and pH (Robert *et al.*, 1972; Neubeck, 1975; Baumann, 1981). The crude polygalacturonase produced by *Aspergillus awamori* MTCC 9166 had been used for clarification of mango juice using Box-Behnken statistical design (Table 1).The combination 8 showed maximum viscosity and combination 9 showed minimum viscosity. Coefficient of determination, R2, is defined as the ratio explained variation to the total variation and is a measure of the degree of fit. It is also proportion of the variability in the response variables, which is accounted for regression analysis. When R2 reaches unity, the better the empirical model fits the actual data. The analysis of variance (ANOVA) was done using Indostat software which showed that the response surface models developed for all response variables were adequate. The R2 value for viscosity was 0.95163, indicating that regression model explained the reaction well (Table 2). Square

interaction of time and enzyme concentration was found to be significant and adjacent interaction of three variables were found to be insignificant.

The interactive effect of time and incubation temperature on viscosity of mango juice using PG produced by *Aspergillus awamori* MTCC 9166 is indicated in response surface curve and its corresponding contour plot (Figure 1) and it shows that the temperature up to 40⁰C has positive effect and beyond it has negative effect on clarification. Similarly treatment time has positive effect on clarification up to 30 min. The contour plot is semicircular and interaction between these parameters was insignificant. Enzyme concentration up to 1.5 U/ml has positive effect and less than that did not show much effect on clarification and treatment time has positive effect on clarification up to 30 min (Figure 2). The contour plot is circular and indicating significant interactive effect between these parameters. Figure 3 shows that enzyme concentration up to 1.5 U/ml and temperature up to 40⁰C has positive effect on clarification and the semicircular contour plot indicated that interaction between enzyme concentration and temperature was insignificant.

Application of Box-Behnken statistical design in clarification of fruit juices has been reported in literature. Response surface methodology (RSM) was employed to establish optimum conditions for enzymatic clarification of sapodilla juice using polygalacturonase obtained from *Streptomyces lydicus* (Jacob *et al.*, 2008). Diwan and Shukla (2005) developed a process for production of guava juice using purified enzyme at 2% concentration and 20 hours incubation time. Similar studies were done by
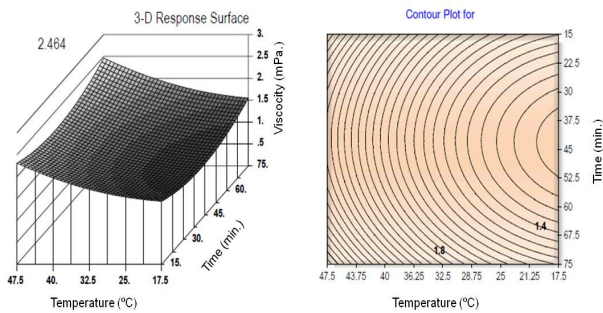
Figure 1. Surface and Contour plots showing interactive effect of time and temperature at various levels on mango juice clarification using polygalacturonase produced *Aspergillus awamori* MTCC 9166
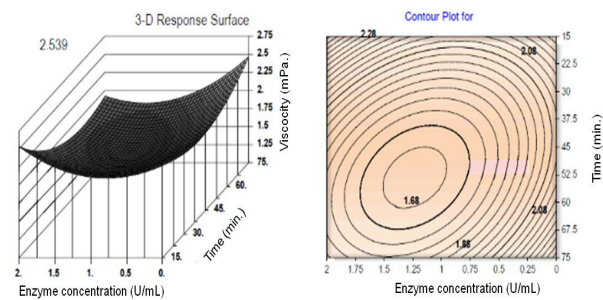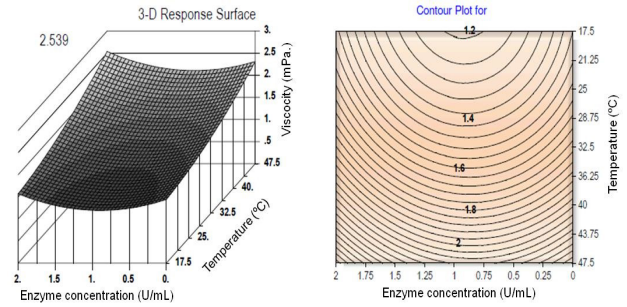

Figure 2. Surface and Contour plots showing interactive effect of time and enzyme concentration at various levels on mango juice clarification using polygalacturonase produced *Aspergillus awamori* MTCC 9166

(Rai *et al*., 2004) to optimize conditions for pectinase for clarification of sweet lime (Mosambi) juice to obtain maximum juice yield.

In view of several advantages offered by Box-Behnken design, it was applied for mango juice clarification studies using polygalacturonase produced from *Aspergillus awamori* MTCC 9166. The statistical analysis results were interpreted as response surface curves and its corresponding contour plots that indicated variation in viscosity of mango juice using PG produced by *Aspergillus awamori* MTCC 9166 (Table 2). In these interactions of treatment time and temperature; enzyme concentration and treatment time; temperature and enzyme concentration were interpreted (Figure 1, 2 and 3). Based on regression coefficient values, response plots and contour plots, the optimum conditions for clarifying mango juice were obtained as enzyme concentration 1.5 U/ml, temperature 40^{0}C and incubation time of 30 min using polygalacturonase produced by Aspergillus awamori MTCC 9166 and 60% viscosity reduction was achieved.

Conclusion

Box-Behnken design was found to be an efficient and valuable statistical tool for analyzing

Figure 3. Surface and Contour plots showing interactive effect of temperature and enzyme concentration at various levels on mango juice clarification using polygalacturonase produced *Aspergillus awamori* MTCC 9166

and optimizing the effects of incubation time, enzyme concentration and temperature on enzymatic clarification of mango juice using polygalacturonase produced by *Aspergillus awamori* MTCC 9166. The recommended enzymatic treatment conditions were enzyme concentration 1.5 U/ml, incubation time 30 min and incubation temperature 40^{0}C. There was 60% viscosity reduction which is significant. The present study would be very useful for fruit juice industry especially mango juice industry as India is potential producer of mangoes and clarified mango juice has good demand for its known nutritive value and taste world wide.

Acknowledgment

References

Anuradha, K., Naga Padma, P., Venkateshwar. and Gopal reddy. 2010. Fungal isolates from natural pectic substrates for polygalaturonase and multienzyme production. Indian Journal of Microbiology 50: 339-344.

Bauman, J.W. 1981. Application of enzymes in fruit juice technology. In G.G Brich, N.Blakebrough and K.J.Parker. (Eds.) Enzymes and fruit processing, p. 129-147. London: Applied science publisher Ltd.

Benen, J.A.E. and Voragen, A.G.J. 2003. Pectic enzymes. In J. R. Whitaker, A.G.J, Voragen and D.W S. Wong. (Eds.) Hand Book of Food Enzymology, p. 845-847. Switzerland: Marcel Dekker Inc. Basal.

Benen, J.A.E., Voragen, A.G.J. and Visser, J. 2003. Pectic enzymes. In J. R. Whitaker A J and Voragen & D. W. S. Wong. (Eds.) Handbook of food enzymology, p. 169-188. New York.

Box, G.E.P. and Behnken, D.W. 1960. Some New Three Level Designs for the Study of Quantitative Variables. Technometrics 2: 455-475.

Ceci, L. and Lozano, J. 1998. Determination of enzymatic activities of commercial pectinases for the clarification of apple juice. Food Chemistry 61: 237-241.

Collmer, A., Reid, J.L. and Mount, M.S. 1988. Assay procedures for pectic enzymes. Methods in Enzymology 161: 329-335.

Diwan, A. and Shukla, S.S. 2005. Process development for the production of clarified guava juice. Journal of Food Science and Technology 42: 245-249.

Dzogbefia, V.P., Ameko, E., Oldham, J.H. and Ellis, W.O. 2001. Production and use of yeast pectolytic enzymes to aid pineapple juice extraction. Food Biotechnology 15: 29-39.

Fogarty, M.V. and Kelly, C.T. 1983. Pectic Enzymes, In Fogarty M.W.(Eds.) Microbial Enzymes and Biotechnology, p.131-182. London:Applied Science Publishers.

Grassin, C. and Fauquembergue, P. 1996. Application of pectinases in beverages. Progress in Biotechnology 14: 453-462.

Harsh, P. S., Hiral, P. and Sugandha, S. 2014. Enzymatic extraction and clarification of juice from various fruits-A review. Trends in Post Harvest Technology 2: 1-14

Heldt-Hansen, H.P., Kofod, L.V., Budolfsen, G., Nielsen, P.M., Huttel, S. and Bladt, T. 1996. Applications of tailor made pectinases. (Pectins and Pectinases) Progress in Biotechnology. 14: 463-474

Jacob, N., Sukumaran, R.K. and Prema, P., 2008. Optimization of enzymatic clarification of Sapodilla juice: A statistical perspective. Journal of Applied Biochemistry & Biotechnology 151: 353-363.

Jiang, J., Paterson, A. and Piggott, J.R. 1990. Effects of pectinolytic enzyme treatments on anthocyanins in raspberry juice. International Journal of Food Science &Technology 25: 596-600.

Kashyap, D.R., Vohra, P.K. and Tewari, R. 2001. Applications of pectinases in the commercial sector. Bioresource Technology, 77: 215-227.

Macmillan, J.D. and Sheiman, M.I. 1974. Pectic Enzymes. In J.R. Whitaker. (Eds.) Food Related Enzymes. Adv. In Chemistry Series), Amer. Chem. Soc, p. 101-130 Washington, D.C.

Naidu, G.S.N. and Panda, T. 1998. Production of pectolytic enzymes-A review. Bioprocess Engineering, 19: 355-361.

Nelson, N.A. 1944. Photometric adaptation of the Somogyi method for the determination of glucose. Journal of Biological Chemistry 153: 375-380.

Neubeck, C.E. 1975. Fruits, fruits products and wines. In:R. Gerald. (Eds.) 6 Enzymes in food processing, p 397–442. New York:Academic Press.

Pilnik, W. and Voragen, A.G.J. 1993. In: Reeds, G. (Eds.) Pectic enzymes in fruit juice and vegetable juice manufacture. Food and Science Technology, Enzymes in Food Processing, p. 363-399. New York: Academic Press.

Rai, P., Majumdar, G.C. and Das gupta, D.E.S. 2004. Optimizing pectinase usage in pretreatment of Mosambi juice for clarification by response surface methodology. Journal of Food Engineering, 64: 397-403.

Robert, A., Baker, H. and Joseph Bruemmer. 1972. Pectinase stabilization of orange juice cloud. Journal of Agricultural Food Chemistry, 20: 1169-1173.

Saisha ,V. and Shashidhar, B. 2015. Optimization Studies on Enzymatic clarification of Mixed Fruit Juices. International Journal of Latest Trends in Engineering and Technology 5: 161-164.

Solehah, A., BalaumanI, V.T. and Amiza, M.A. 1964. Enzyme for improved extraction and stabilization of colour and flavour of orange juice. Journal of Food Science and Technology 31: 508-510.

Sudheer Kumar, Y.S.P. and Reddy, O.V.S. 2009. Optimization of fermentation conditions for Mango (*Mangifera indica* L) wine production by employing response surface methodology. International Journal of Food Science and Technology, 44:2320-2327.

5th International Conference of Materials Processing and Characterization (ICMPC 2016)

Evaluation of Strain and Strain rates at different stages of Superplastic Cone Forming

P Shailesh[a],*, K Vijaya Kumar[b], J Babu[c], K Srinivasa Raghavan[a]

[a]Mechanical Engineering Department, MCET/Osmania University, Hyderabad,500001, India
[b]MED, Research Scholar, NIT, Warangal, 506004, India
[c]MED, St. Joseph's College of Engineering& Technology, Choondacherry, Kerala , 686579, India

Abstract

Superplastic forming (SPF) is a powerful tool to manufacture complex parts for industries like automobile and aerospace where strength to weight ratio of the part is the main criterion. Superplastic forming (SPF) of a sheet metal has been used to produce very complex shapes and integrated structures at much lighter and stronger than the assemblies they replace. Superplastic formed shapes like conical, hemispherical poses a problem of large thickness variation, minimum thickness results at the portion where die contact is made last. Proper understanding of strain and strain rates during forming and using the pressures accordingly can minimize this problem. The present investigation focused on the study of strain and strain rates during the forming, Experiments were carried on a model material Sn-Pb, which can be applicable for any other Superplastic materials. Results revealed that strain rates in the present study are within the range of superplastic regime and no failure of the formed part because of the thinning. Results also revealed that forming time can be reduced by increasing the pressure which in turn increase the strain rate.
©2017 Elsevier Ltd. All rights reserved.
Selection and peer-review under responsibility of Conference Committee Members of 5th International Conference of Materials Processing and Characterization (ICMPC 2016).

*Keywords:*Superplastic forming, Conical shape, Strain, Strain rate

1. Introduction

   Superplastic materials are polycrystalline solids which are having the ability to undergo very large and uniform tensile elongations before the failure occurs. Generally elongations higher than 200% indicate the superplasticity.

* Corresponding author. Tel.: +91-8790595450;
*E-mail address:*vijay.nitw2@gmail.com

Due to this property superplastic forming (SPF) is increasingly used industries like aerospace and automobile to produce complex parts at much lesser efforts and costs when compared with conventional machining [1-3]. Wide varieties of materialsaluminum, magnesium and titanium alloys exhibit the phenomena of superplasticity, when subjected to certain conditions of pressure, temperature and strain-rates [4, 5].The conditions that are necessary for any material to be superplastic material are grain size $\leq 10\mu m$, strain - rates $\leq 10^{-3}$ s^{-1} and temperatures ≥ 0.5 T_m where T_m is the melting point of the material under investigation [6].Most often ultra-fine grained materials are obtained by using severe plastic deformation methods like: high pressure torsion (HPT) [7, 8] equal-channel angular pressing (ECAP) [8,9], multiple forging [3], and multi-axis restrain deformation *(Max Strain)* [10] or cyclic extrusion-compression (CEC) [9].Blow forming of single sheet is essentially based on the application of a gas pressure differential on the super plastic diaphragm, resulting in the deformation of the material into a given die configuration. Pressure, typically in the range 10–30 bars, is applied through the injection, via a series of inlet tubes, of either air or a protective gas (typically argon), depending on the affinity to oxygen of the material to be formed. Die and sheet are maintained at the same temperature within a heating press. The gas pressure is imposed over the sheet causing the sheet to form into the lower part of the die. While it is being formed, the sheet simply vents the gas to atmosphere which was initially located within the lower die chamber. The lower die chamber may be held either under vacuum or under some back pressure to control or even to prevent cavitation in the formed material (e.g. aluminum alloys) [11]. The mechanical characteristics of the finished product are very good, because the hardening of material is practically absent and spring-back is zero, with benefit of obtained dimensional accuracy. The surface finish is excellent, so there is no need to make finish operations [12-15].

Nomenclature

A_f	Surface area of the frustum
ao	Original radius of the circular blank
A_s	Surface area of the dome shape at the required instance ($2\pi\rho h_s$)
a	Radius at the smaller end and the cone
ρ	Radius of curvature
l	Slant length of circular blank at the die opening
h_f	Vertical height of the truncated cone
h_s	vertical height of the dome shape in the total deformed components at any instant
h	Total formed height of the component (measured with depth micrometer) ($h=h_f+h_s$)
ε	Strain
$\acute{\varepsilon}$	Strain rate
σ	Stress

---

2. Methods and materials

Lead –Tin (Pb-40% -Sn-60%) alloy which is used as solders is available in the form of bars was used in the present study. This alloy was cast to slab of dimensions 68mm wide x 720mm long x 30 mm thickness and cold rolled at room temperature to a thickness of 2.45 mm as shown in Fig.1 in a rolling mill at Non-Ferrous Materials Technology Development Centre (NFTDC), Hyderabad, Telangana, India. The lamellar grains broke down to fine globular grains of average size 8 μm as shown in Fig.2. Cone forming tests were carried out in Low cost experimental setup as shown in Fig 3. Sn-Pb blanks of 80mmΦ x 2.45mm thickness were blown by Argon gas in a conical die of 80mm Φ x apex angle 60^0 as shown in Fig 4. under constant gas pressures 3 bar,6 bar and 8 bar. The progress of deformation of the cone with time was monitored at different stages of forming.

- ❖ Free Blowing (deformation without touching die wall)
- ❖ Free Blowing (max. limit of deformation without touching die wall)
- ❖ Cone wall making tangent to the membrane
- ❖ Cone wall formation + free blowing of dome

These four stages go on repeating further till the cone shape is formed.

Fig.1.Experimental Set Up.
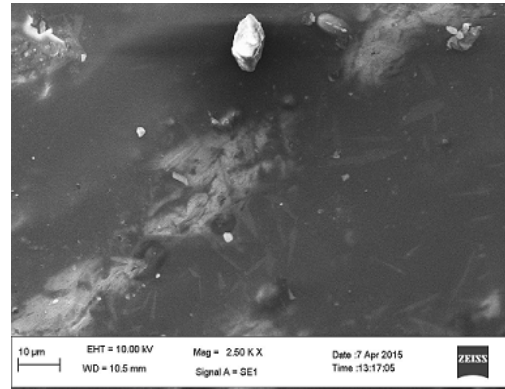
Fig.2. SEM images of Lead –Tin (Pb-40% -Sn-60%) alloy after rolling.

Fig.3. Lead –Tin (Pb-40% -Sn-60%) Alloy sheet thickness of 2.14 mm.
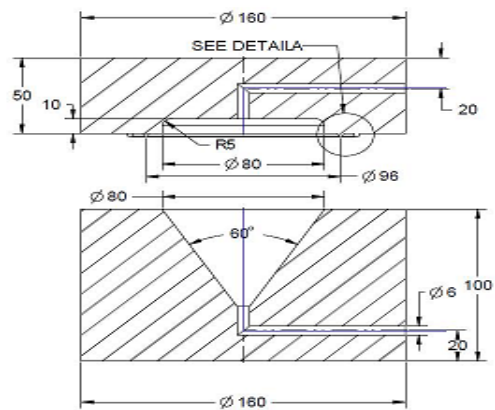
Fig.4. Various stages of superplastic forming in conical die.

As soon as the membrane touches the conical die wall, the thickness freezes and further thinning occurs on the free dome portion.As a result of these dome thickness is less than the cone wall thickness. And finally, in the formed cone the thickness reduces progressively from the base of the cone to the apex.Stress and strains were calculated at different stages of forming for the forming pressures 3 bar, 6 bar and 8 bar.

3. Determination of Stress and Strains at different stages of forming

Stress and strain values of at different stages of forming are calculated. Sample calculations for a forming pressure of 3 bar are shown below

Stage 1. Free Blowing

Original area of the circular blank

$$A_o = \pi(a_o)2 = \pi(40)2 = 5026.5 \text{ mm}2$$

Depth of the formed dome shape $= h$

$$h = \rho - \frac{(\rho2 - a_o2)1}{2} = 1.1547 \, a_o - \frac{((1.1547)2 - a_o2)1}{2} = 0.578 * a_o = 23.12 \text{ mm}$$

$$\rho = a_o2\frac{h2}{2h}(or)\rho = a_o/\sin60=1.1547a_o$$

Stage 2. Free Blowing (max. limit of deformation without touching die wall)

Surface area of truncated cone $= \pi (r + R) l$

$\qquad = \pi (a+a_o) l$

Vertical height of the truncated cone (h_f)

$$= l \cos (\theta/2) \qquad (\theta = 60^0)$$
$$= l \cos 30^0$$

Stage 3. Cone wall making tangent to the membrane

Surface area of the frustum $A_f = \pi (a_o + a) l$

Vertical height of the frustum $= h_f$

h = Total formed height of the component (measured with depth micrometer)

$\quad$ h = $h_f + h_s$ $\qquad\qquad$ $h_f = l \cos 30^0$

$\quad$ $h_s = h - h_f$

Stage 4. Cone wall formation + free blowing of dome

$\qquad$ Surface area of the dome shape at the required instance.

$$A_s = 2\pi\rho h_s$$

$\quad$ Where

$\qquad$ ρ = radius of curvature of the dome shape.

$$\rho = a^2 + h_s^2 / 2h_s$$

$\qquad$ hs = vertical height of the dome shape at that instance.

Total formed area of the deformed components

$$A = A_f + A_s$$

Strain

$$\varepsilon = \ln (A/A_0)$$

Strain rate:

$$\dot{\varepsilon} = \varepsilon / time$$

$$\text{Stress}, \sigma = \left(\frac{\rho}{2t}\right)*P$$

$$\sigma = \left(\left(\frac{A}{2\pi h}\right) / \left(\frac{A_{oto}}{A}\right)\right)*P$$

$$\sigma_{3bar} = ((6599.18)2/(4\pi \times 23.4 \times 5026.5 \times 2.45)) \times 0.03 = 0.360 \text{ N/mm}^2$$

For dome:

Radius of curvature

$\qquad$ $\rho = (a_2 + h_2)/2h = (40_2 + 22.38_2)/(2 \times 22.38) = 46.93$ mm

Area of dome

$\qquad$ $A = 2\pi\rho h = 2\pi \times 46.93 \times 22.38 = 6599.18$ mm2

Strain

$\qquad$ $\varepsilon = A/A_0 = 6599.18/5026.5 = 0.272$

Strain rate

$\qquad$ $\dot{\varepsilon} = 0.272/(50 \times 60) = 9.06 \times 10^{-5}$/sec

For Truncated Cone

$\qquad$ $h_s = h - h_f = 46.38 - 32.04 = 14.34$ mm

Radius of dome

$\qquad$ a = $h_s/0.578 = 24.8$ mm

$\qquad$ $\rho = a/\sin 60^0 = 28.64$ mm

Area of dome

$\qquad$ $A_s = 2\pi\rho h_s = 2\pi \times 28.64 \times 28.64 = 2580.48$ mm2

Area of frustum

$\qquad$ $A_f = \pi l (a_o + a) = \pi \times 37(40 + 24.8) = 7532.28$ mm2

$\qquad$ $A = (A_s + A_f) = 10112.76$ mm2

Strain

$\qquad$ $\varepsilon = A/A_o = 10112.76/5026.5 = 0.699$

Strain rate

$\qquad$ $\dot{\varepsilon} = 0.699/(80 \times 60) = 1.45 \times 10^{-4}$ /sec

4. Results and Discussion

Fig.5 Formation of conical dome at 3 bar pressure at different time intervals in minutes (a) 5 (b) 20 (c) 80 (d) 110

(a)   (b)

(c)   (d)

(a)   (b)

(c)   (d)
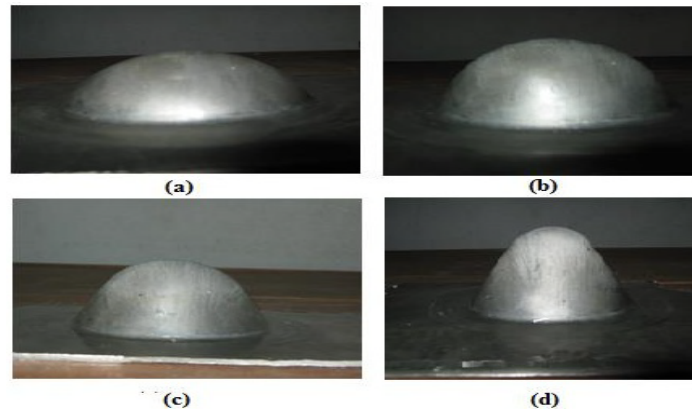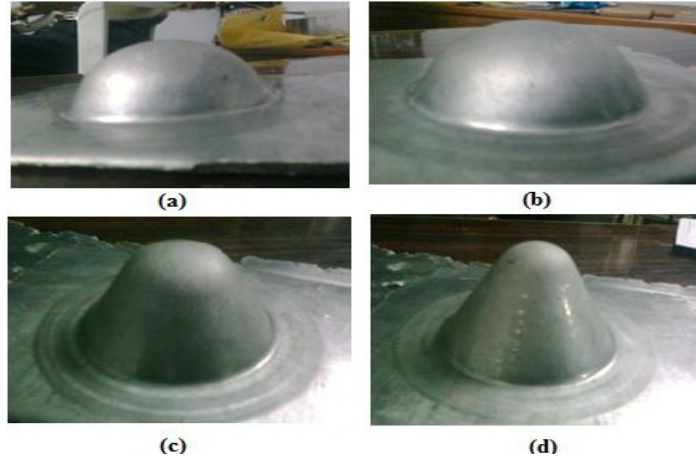
Fig.6 Formation of conical dome at 6 bar pressure at different time intervals in minutes (a) 5 (b) 30 (c) 40 (d) 45

(a)   (b)

(c)   (d)
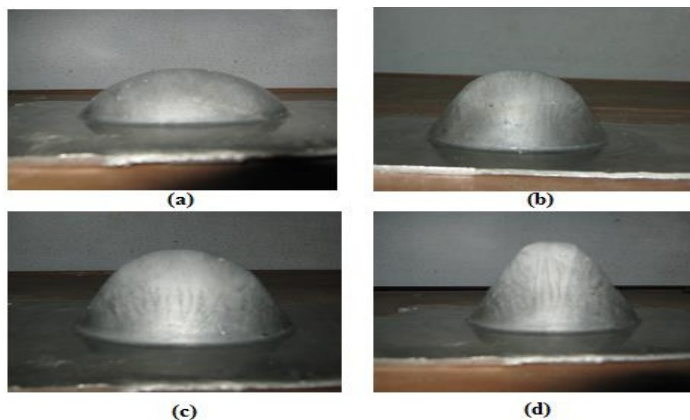
Fig.7 Formation of conical dome at 8 bar pressure at different time intervals in minutes (a) 5 (b) 10 (c) 15 (d) 20

Stress and strain values of at different stages of forming for the forming pressure 3 bar, 6 bar and 8 bar are calculated as per the calculations mentioned in the section.3, and are shown in Tables 1,2 and 3. Conical domes formed at forming pressure 3 bar, 6 bar and 8 bar with different stages are shown Figures 5, 6 and 7.

From the Table 1, one can observe that strain on the material in increasing, but strain rate is decreased in the time interval 5-20 min shows the initial strain hardening of the material, further in the 20-50 min time interval strain rate

is increased as the material is free forming without touching the walls of the conical die. After the touching the wall of the die for 80-140 min time interval the strain rate gradually decreasing and remains a constant value.

Table.1. Strain and Strain rates at different stages of forming at a forming pressure of 3 bar

Time (minutes)	Slant height (mm)	Depth (mm)	Radius of Curvature (mm)	Area (mm^2)	Strain	Strain rate /sec
5	0	5.13	158.51	5109.2	0.016	5.43×10^{-5}
20	0	7.00	117.78	5180.2	0.030	2.50×10^{-5}
50	0	22.38	46.93	6599.18	0.272	9.06×10^{-5}
80	37	46.38	28.64	10112.76	0.699	1.45×10^{-4}
110	51.5	54.38	19.53	10404.52	0.727	1.10×10^{-4}
140	58.3	62.50	24.01	12947.30	0.946	1.10×10^{-4}

Table.2. Strain and Strain rates at different stages of forming at a forming pressure of 6 bar

Time (minutes)	Slant height (mm)	Depth (mm)	Radius of Curvature (mm)	Area (mm^2)	Strain	Strain rate /sec
5	0	18.30	52.86	6078.63	0.190	6.33×10^{-4}
10	0	23.40	42.88	6746.75	0.294	4.90×10^{-4}
15	7.07	27.98	43.67	7722.60	0.429	4.76×10^{-4}
20	16.05	32.00	36.13	7702.60	0.426	3.55×10^{-4}
30	22.54	39.27	39.45	10147.88	0.702	3.90×10^{-4}
40	39.25	48.34	28.66	10579.25	0.744	3.10×10^{-4}
45	47.62	54.50	26.49	11623.02	0.838	3.10×10^{-4}

Table.3. Strain and Strain rates at different stages of forming at a forming pressure of 8 bar

Time (minutes)	Slant height (mm)	Depth (mm)	Radius of Curvature (mm)	Area (mm^2)	Strain	Strain rate /sec
5	0	22.45	46.85	6606.56	0.273	9.10×10^{-4}
10	13.20	31.15	39.39	7950.51	0.458	7.63×10^{-4}
15	22.64	38.10	36.95	9412.27	0.627	6.98×10^{-4}
20	43.05	50.41	33.34	12008.32	0.737	6.14×10^{-4}

At higher forming pressures 6 bar and 8 bar (Table 2 and Table 3) strain rate is gradually decreasing and remains a constant value. However, the initial values strain rates are higher when compared to the forming pressure of 3 bar.It is known facts that blow forming of a cone with apex angle nearer to 60^0, under constant strain rate can be achieved by applying a constant gas pressure [13]. In other wards constant gas pressure induces a constant stress in the membrane which in turn produces constant strain rate. In the present investigation similar behavior is observed.

From the Table 2 and Table 3, it can be observed that at higher forming pressures the forming time can be reduced considerably. This is because of higher strains and strain rates. However higher strain rates lead to the local thinning of the formed part. This can be explained as for superplastic deformation, elastic strains are negligible; therefore, constancy of volume can be assumed. From this consideration, the sum of the plastic strains is zero, and tensile strain in one direction must be balanced by compressive (negative) strain in another. The strains are:

$$\varepsilon_1 + \varepsilon_2 + \varepsilon_3 = 0$$

Where ε is the strain and the subscripts indicate the principal directions. For the present sheet forming operation under plane strain conditions, $\varepsilon_2 = 0$ and $\varepsilon_3 = -\varepsilon_1$, the thinning strain ($\varepsilon_3$) is equal and opposite to the longitudinal tensile strain (ε_1) and the thinning will therefore match the tensile deformation. For large tensile strains, the thinning will be corresponding large. Present investigations do not show any failure of the part during forming because of thinning. This shows pressures considered in the study are suitable forming the conical domes. Calculated strain rate values for the different forming pressures at different stages of forming are within the range of superplastic forming regime, which resulted the forming of conical parts without fracture.

5. Conclusions

Conical forming of lead –tin samples at different pressure were carried out in the present study to know the feasibility of forming without failure of the part. The following conclusions are drawn for this study.

- ❖ Rolling of the cast slab of lead and tin alloy can reduce the grain size approximately 8 μm, which is suitable for superplastic forming.

- ❖ Calculated strain rate values at different stages of forming at forming pressure are almost a constant which is good agreement with published results.
- ❖ Strain rates are higher at higher forming pressures which resulted in lesser the forming time.
- ❖ Calculated strain rate values for the different forming pressures are within the range of superplastic forming regime, which resulted the forming of conical parts without fracture.

References

[1] Barnes J, Superplastic Forming 40 Years and Still Growing, J. Mater. Eng. Perform. 2007; 16: 440-447.

[2] Serra D, 6th EUROSPF Conference EuroSPF08, 3-5 September 2008, Carcassonne, France p 1-10.

[3] Davis.B and Hryn. J. Report, Argonne National Laboratory, U.S. Department of Energy laboratory, 31 January 2008, Assessed online at http://www.osti.gov/bridge/product.biblio.jsp?osti_id=924692, p 9.

[4] Hamilton CH, Paton N, Proceedings of the International conference on the Minerals, Metals and Materials Society, USA, 1988; p706.

[5] ARGARD-LS-154, Advisory Group for Aerospace Research and Development, NATO,1987; p 204.

[6] Hiroyuki Wadena H, Toshiji Makati, Kenji Higashi. Scripta Mater 1999;40(4):477-484.

[7] Sergueeva AV, Stolyarov VV, Valiev RZ, Mukherjee AK, Materials Science Engineering A 2002; 323: 318-325.

[8] Valiev RZ, Islamgaliev RK, Alexandrov IV, Progress in Materials Science 2000; 45 :103-189.

[9] Richert M, Materials Engineering 1997; 2: 59-69.

[10]Chen WC., Ferguson DE., Ferguson HS, Mishra R.S, Jin Z, Materials Science Forum 2001; 357-359: 425-430.

[11] Super plastic forming of Advanced Metallic Materials: Methods and Applications, edited by Gillo Giuliano. 50-51.

[12] Cappetti N, Garofalo L, Naddeo A, Nastasia M, Pellegrino A, Journal of Achievements in Materials and Manufacturing Engineering 2010; 38(2): 187-194.

[13] R.J. Ledrich, S.M.L. Sastry, M. Hayase and T.L. Mackay, Journal of Metals,Aug 1982 pp15-20.

[14] Nitin Kotkunde, Nitin Krishnamurthy, A. K. Gupta, S. K. Singh, Advanced Materials Manufacturing and Characterization 2013; Vol3, Issue 1.

[15] Haoxiang Gao, Nan Li, Hongliang Ho, Yanling Zhang, Ning Zhang, Liliang Wang, Jianguo Lin, Materials Today: Proceedings 2S (2015) S408 – S413.

INDERSCIENCE P U B L I S H E R S
Linking academia, business and industry through research

Home   >   Full-text access for editors

A swarm intelligence approach for the p-median problem
by B. Jayalakshmi; Alok Singh
International Journal of Metaheuristics (IJMHEUR), Vol. 5, No. 2, 2016

Abstract: p-median problem is a well-known facility location problem which aims at locating p number of facilities over n demand points in such a way that the sum of distances from all the demand points to their respective closest facilities is minimised. In this paper, we have proposed an artificial bee colony (ABC) algorithm-based approach for solving this NP-hard problem. The ABC algorithm is a recently proposed metaheuristic technique that has been used successfully for solving numerous NP-hard combinatorial optimisation problems. We have tested the proposed algorithm on the OR-Library and Galvao p-median benchmark test instances, and the results are compared with those obtained with some other approaches available in the literature. The computational results show that the proposed algorithm outperforms other methods.

Online publication date: Sun, 06-Nov-2016

The full text of this article is only available to individual subscribers or to users at subscribing institutions.

Existing subscribers:
Go to **Inderscience Online Journals** to access the **Full Text** of this article.

Pay per view:
If you are not a subscriber and you just want to read the full contents of this article, **buy online access here**.

Complimentary Subscribers, Editors or Members of the Editorial Board of the International Journal of Metaheuristics (IJMHEUR):
Login with your Inderscience username and password:

Username: [_____]   Password: [_____]   [Login]

Forgotten your password?

Want to subscribe?
A subscription gives you complete access to all articles in the current issue, as well as to all articles in the previous three years (where applicable). **See our Orders page to subscribe**.

If you still need assistance, please email subs@inderscience.com

Return to top

Keep up-to-date

- Our Blog
- Follow us on Twitter
- Visit us on Facebook
- Our Newsletter (subscribe for free)
- RSS Feeds
- New issue alerts

Contact us   About Inderscience   OAI Repository   Privacy and Cookies Statement   Terms and Conditions   Help   Sitemap

A Review on Current Trends in PM-EDM using Commercial Kerosene as Di-Electric Fluid

BSV Ramarao[1], Dr. P Sailesh[2] & Dr. M Sreenivasarao[3]

ABSTRACT
Powder Mixed Electrical discharge machining (EDM) process is one of the most commonly used nonconventional material removal processes. It is especially used for the manufacturing complex geometry and hard material parts that are extremely difficult-to-machine by using conventional machining processes. There are various types of products which can be produced using PMEDM. Parts of aerospace, automotive industry and surgical components can be finished by this process. In this paper, authors have reviewed the research work carried out in the development of PMEDM in the current scenario for the improvement of machining characteristics such as Material Removal Rate (MRR), Surface Roughness (SR) and Tool Wear Ratio (TWR) when the commercial kerosene is used as a dielectric fluid with different powder materials.

Introduction
Electrical Discharge Machining
EDM as a process was introduced over fifty years ago; improvements in technology have led to increases in both cutting speeds and component precision. Developing from initially tool making industry sectors of press tool and mould tools, the EDM process is now mainly found within production engineering, aerospace, motor sport, medical and scientific industries. Electrical Discharge Machining (EDM) is non-traditional, no physical cutting forces between the tool and the work piece, high precision metal removal process using thermal energy by generating a spark to erode the work piece. The work piece must be a conductive electricity material which is submerged into the dielectric fluid for better erosion. EDM machine has wide application in production of die cavity with large components, deep small diameter whole and various intricate holes and other precision part.

PM-EDM & Its Technology
In PMEDM process suitable material in the powder form will be mixed into the dielectric fluid in tank. Better circulation of the dielectric fluid can be done by stirring system. Constant reuse of powder in the dielectric fluid can be done by the special circulation system. Generally, various powders of particle that can be added into the dielectric fluid like Aluminum (Al), graphite, copper (Cu), chromium (Cr), Silicon carbide etc. spark gap provided by the additives particles. The powder particles of the material get energized & behave like a zigzag way manner. under the sparking zone, the particles of the material powder comes close to each other & arrange themselves in the form of chain like structure between the work piece surface & tool electrode. The interlocking between the different powder particles occurs in the direction of flow current. The chain formation helps in bridging the discharge gap between the electrodes.

Because of bridging effect, the insulating strength of the dielectric fluid decreases resulting in easy short circuit. This causes early explosion in the gap and series discharge' starts under the electrode area. The faster sparking within a discharge causes faster erosion from the work piece surface and hence the material removal rate increases.

Major Component of Powder mixed Electrical discharge Machining
Power supply: It transforms the alternating current from the main utility supply into the pulse direct current required to produce the spark discharge at the machining gap.
Pulse Generator & Control Unit: This unit is responsible for supplying pulses at a certain voltage and current for specific amount of time. The power supply control the amount of energy consumed. The control unit is control the all function of the machining for example of Ton, Ip, duty cycle, putting the values and maintain the work piece the tool gap.
The servo system: The servo control unit is provided to maintain the pre-determined gap. It senses the gap voltage and compares it with the present value and the different in voltage is then used to control the movement of servo motor to adjust the gap.
Tool holder: The tool holder holds the tool during the process of machining.
Circulating Pump: This unit of the system is responsible for the circulation of powder mixed dielectric.
Electrode: The EDM electrode is the tool that determines the shape of the cavity to be produce
Permanent magnet: Magnetic forces are used to separate the debris from the dielectric fluid. For this purpose, two permanent magnets are placed at the bottom of machining tank
Machining Tank: The system consists of a transparent bath-like container, called the machining tank. It is placed in the work tank of the EDM, and the machining is performed in this container.

Principle of PMEDM
When voltage is applied the powder particles become energized and behave in a zigzag fashion. These charged particles are accelerated due to the electric field and act as conductors promoting breakdown in the gap. This increases the spark gap between tool and the work piece. Under the sparking area, these particles come close to each other and arrange themselves in the form of chain like structures. The interlocking between the powder particles occurs in the direction of flow of current. The chain formation helps in bridging the discharge gap between the electrodes. Because of bridging effect, the insulating strength of the dielectric fluid decreases resulting in easy short circuit. This causes early explosion

in the gap and series discharge' starts under the electrode area. The faster sparking within a discharge causes faster erosion from the work piece surface and hence the material removal rate increases.

Functions of a Dielectric Fluid: The dielectric fluid in an EDM is used to
1. Act as a medium through which controlled electrical discharges occur.
2. Cool the section that was heated by the discharging effect
3. Flush the eroded particles from the machining gap
4. Provide insulation between the electrode and the work piece
5. Act as a medium used to carry away the solidified EDM debris from the discharge gap to the filter system.
6. Act as a heat transfer medium to absorb and carry away the heat generated by the discharges from both the electrode and the work piece

Major types of dielectric fluid
1. Mineral Oils
2. Kerosene
3. Transformer Oil
4. EDM Oils
5. **Synthetic oil**

Properties & Characteristics of Dielectric Fluid
1. Viscosity is the property that describes a fluids resistance to flow.
2. Flash Point-The flash point of a flammable liquid is the lowest temperature at which it can form an ignitable mixture in air.
3. Oxidation Stability is a measure of the dielectric fluids tendency to react with oxygen.
4. Volatility is a measure of the tendency of a dielectric fluid to vaporize
5. Acid Number is used to quantify the amount of acid present in a sample of dielectric oil.
6. Pour Point of oil is the temperature below which the oil no longer pours freely.

Literature
Sanjeev kumara et (1) were performed experiments on three die steel materials- OHNS die steel , D2 high-carbon high-chromium die steel, H13 hot die steel by electrical discharge machining using machining conditions favouring material transfer from tungsten powder suspended in the dielectric medium. They have concluded that surface modification is possible by the EDM method, The presence of tungsten carbide and increase in the percentage of carbon on the machined surface indicate that suspended powder particles can react with carbon (from the breakdown of the hydrocarbon dielectric) at high temperatures of the plasma channel to form carbides and The presence of tungsten carbide and increase in the percentage of carbon on the machined surface indicate that suspended powder particles can react with carbon (from the breakdown of the hydrocarbon dielectric) at high temperatures of the plasma channel to form carbides.

They have also mentioned that Favourable machining conditions for material transfer by EDM is found to be low discharge current (less than 5 A), shorter pulse on-time (less than 10 _s), longer pulse off-time (more than 50 _s) and negative polarity of the tool electrode. Peak current is found to be the most significant factor for the phenomenon of surface modification. They have extended their remarks saying that Surface alloying with tungsten and carbon has a significant effect on its properties as observed from the increase in micro-hardness by more than 100% for all the three work materials. As surface hardness has a direct bearing on abrasion resistance, the life of dies and other press tools can be substantially improved by this method.

F.Q.Hua et (2) conducted experiments on surface properties of SiCp/Al with moderate fraction of Sic particle reinforced Al matrix composites in EDM and PMEDM using Environment scanning electron microscope. They have found that the surface properties are improved greatly in PMEDM than EDM as its surface roughness decreased about 31.5% and is better in corrosion resistance and wear resistance is twice of EDM. Finally they have also mentioned that the PMEDM is having promising applications in metal matrix composites machining field

Gangadharudu Talla et (3) have performed Modeling and multi-objective optimization of powder mixed electric discharge machining process of aluminum/alumina metal matrix composite and an attempt has been made to fabricate and machine aluminum/alumina MMC using EDM by adding aluminum powder in kerosene dielectric. Their results have shown an increase in MRR and decrease in surface roughness (Ra) compared to those for conventional EDM. They have prepared semi empirical models for MRR and Ra based on machining parameters and important thermo physical properties were established using a hybrid approach of dimensional and regression analysis. A multi response optimization was also performed using principal component analysis-based grey technique (Grey-PCA) to determine optimum settings of process parameters for maximum MRR and minimum Ra within the experimental range. They have concluded that the Machining the MMC by suspending conductive powder particle in the dielectric has shown improvement in productivity as well as surface quality. In their work, a combination of dimensional and non-linear regression analysis is used to model material removal rate (MRR) and surface roughness (Ra) by machining Al/Al2O3 MMC in aluminum suspended dielectric. In PMEDM process, using aluminum suspended kerosene dielectric for the machining of resulted in better MRR when compared to conventional EDM process. A significant decrease in Ra is observed. From the model equations, it was understandable that along with machining parameters, thermal conductivity, coefficient of thermal expansion and density of the material also significantly affect both MRR and Ra. PCA technique has been used to determine the weightages for responses while GRA has been used to combine the multiple objectives into single.

2197

Kuldeep Ojha a et (4)have worked on material removal rate (MRR) and tool wear rate (TWR) study on the powder mixed electrical discharge machining (PMEDM) of EN-8 steel and using Response surface methodology (RSM) analysed the experiments. Peak current, pulse on time, diameter of electrode and concentration of chromium powder added into dielectric fluid of EDM were chosen as process parameters to study the PMEDM performance in terms of MRR and TWR. Experiments have been performed on newly designed experimental setup developed in laboratory. Most important parameters affecting selected performance measures have been identified and optimum process conditions have been found. Also recommended optimal conditions have been verified by conducting confirmation experiments. They have concluded that current, powder concentration and electrode diameter are significant factors affecting both MRR and TWR. Both the performance measures were observed an increasing trend with increase in current for any other settings of parameters. MRR shows increasing trend for increase in powder concentration. The trend shows that MRR will increase further with further increase in concentration. TWR increases with lower range of powder concentration and then decreases. The influence of duty cycle is insignificant on MRR for the range of parameters selected for experimentation. Maximum MRR is observed for a tool diameter of 12 mm. MRR shows decreasing trend both below and above 12 mm tool diameter range. Increase in tool diameter results in decreasing tool wear. The confirmation tests showed that the error between experimental and predicted values of MRR and SR are within permissible range. Empirical modelling of the process led to development of quadratic equations for both performance measures. Their research work adds valuable data regarding PMEDM process. They have ended by more work piece/ powder/ electrode materials/ experimental settings combinations are needed to be investigated further for much validation of the process.

M Prabu et (5) have done experimental investigation on effect of graphite powder suspended dielectric in electric in EDM of Al-TiB2 composites. The experiments were conducted on ELEKTRAPULS spark erosion machine. Their objective is to find the effect of parameters viz, current, pulse ON-time, flushing pressure and vibration As a result, the process becomes more stable thereby improving Material Removal Rate (MRR) and reducing Tool Wear Rate (TWR). The EDM set-up is used in their experimental study is M100 model die sinking EDM machine manufactured by Electronica Machine Tools. The Parameters and their settings are in L16 orthogonal array. It uses Kerosene as the dielectric fluid. The primary benefit of using kerosene is that it has very low viscosity and gets flushed away easily. The selected work piece material is Al-TiB2 composites. Each experiment was performed for fixed time period using brass as an electrode. Input process parameters are current, pulse on time and flushing pressure. The material removal rate and tool wear rate are evaluated by using an electronic balance machine. They have concluded that this work evaluates the feasibility of machining Al-TiB2MMC with graphite powder suspended dielectric fluid. MRR was found higher for larger Current. When comparing the

MRR of with powder and without powder the MRR obtained for with powder is found higher. TWR slightly increases with increasing the Current. When comparing the TWR of with powder and without powder the TWR obtained for with powder is found higher. Increase in MRR was found on increasing Pulse ON-time. TWR increases with the increases in pulse ON-time.

Shriram Y. Kaldhone et (6) have studied the influence of operating parameters of tungsten carbide on the machining characteristics such as material removal rate. The effectiveness of PMEDM process with tungsten carbide, WC-Co is evaluated in terms of the material removal rate. They have observed that copper tungsten is most suitable for use as the tool electrode in EDM of WC-Co; better machining performance is obtained generally with the electrode as the negative and the work piece as positive. In their work, a study was carried out on the influence of the parameters such peak current, Duty factor, pulse on time , work piece material, powder type , powder concentration and flushing pressure. Taguchi methodology has been adopted to plan and analyze the experimental results. Experiments have been performed on newly designed experimental setup. In their study seven factors with three levels are investigated using Orthogonal Array (OA) L27.Material removal rate (MRR) in their experiment was calculated by using mathematical method. The result of their experiment then was collected and analyzed using MINITAB 16 software. The recommended best parametric settings have been verified by conducting confirmation experiments for MRR. From their experimental study it is found that addition of Silicon carbide powder enhances machining rate drastically with slightly increase in Tool wear rate. They have concluded that The MRR and TWR are mainly affected by the current and powder. With mixing of silicon carbide powder MRR can be increased by 90%. Current, Pulse on time, work piece material, Powder type and Flushing Pressure significantly affect MRR. The maximum MRR is produced at 8 g/l of SiC powder for Flushing pressure 1.5 Kg/cm2. Duty factor shows least effect on MRR. Finally, it was concluded that SiC powder and Current have impact to great extent on the MRR of Tungsten Carbide

M. A. Razak et (7) have done experiments on improving EDM efficiency with silicon carbide powder mixed dielectric fluid PMEDM works gradually at low pulse energy and distributes evenly the powder in machining area. PMEDM may lead to improve machined part surface finish, improve material removal rate (MRR) and reduce tool wear rate (TWR). Further investigations on powder concentration and powder particles size for silicon carbide (SiC) PMEDM are proposed to conduct. Number of experiments were conducted is based on Taguchi orthogonal array with three level and two factors. The outcomes obtained were capable to increase MRR, improve surface finish, reduce TWR, reduce machining time and reduce machining cost. The objectives of their research work are: To investigate the influence of PMEDM in machining premium stainless mold steel material in terms of MRR, TWR and Ra. They have done the work to analyse the reduction machining time of EDM process with PMEDM and to define the optimal powder

2198

concentration and size of powder particles to achieve the highest efficiency of EDM process. They have concluded that EDM process plays a big role in mold manufacturing industries. Due to longer machining time, it machining cost is high. To increase EDM process efficiency, PMEDM was proposed. Their investigation is on SiC PMEDM powder concentration and powder particles size in cutting Stavax material. Their results have given information on: The influence of PMEDM in machining Stavax material in terms of MRR, TWR and Ra. The optimum powder concentration and size of powder particles to achieve the highest efficiency of EDM

G. Bharath Reddy et (8) presented the outcomes of an experimental analysis carried out to study the effect of micro-sized metal powders, when they are mixed to the dielectric fluid, during Electric Discharge Machining (EDM) of different steels. The work piece material, peak current, pulse on time, duty factor, gap voltage and mixing of fine metal powders(copper and aluminium) in dielectric fluid are taken as process input parameters. Material removal rate and Surface Roughness were taken as output parameters to measure the process efficiency. A newly designed experimental set up was used to perform the task. Taguchi design of experiments was used to conduct experiments. The achieved results of their work indicate that the addition of fine metal powders in dielectric increases the material removal rate and reduces the surface roughness. They have concluded that the Addition of micro-sized metal powders into the dielectric fluid is one of the modern progresses in EDM that confirms better material removal rates at chosen surface quality. From their current investigation, for the selected process parameters the following conclusions were made. Adding aluminium metal powder in dielectric fluid generates superior surface finish than that of the addition of copper metal powder and without the addition of metal powder. The material removal rate is mainly affected by Peak current and pulse on time, and type of metal powder as additive. At the higher value of peak current, greater is the MRR. Powder Mixed EDM makes discharge collapse easier, increases the discharge gaps and expands the discharge channel, and finally forms uniformly distributed large and shallow craters on the work piece. The Surface roughness of the HCH Cr steel is superior compared to EN-31 steel.

R.A.Prajapati et (9) experimented the effect of Silicon Dioxide (SiO2) powder mixing into the dielectric fluid of EDM on machining characteristics of EN-8 with three input parameters Peak current, pulse on time and concentration of powder. Analysis was carried out for surface roughness. The result outcomes identified the important parameters and their effect on SR of En-8 in the presence of SiO2 in a kerosene dielectric of EDM. Analysis was showed that the peak current and pulse on time have higher contribution toward surface roughness. The experimental result analysis showed EDM with zero concentration gives better surface finish rather than PMEDM. Better surface quality obtained at Peak current (9A), Powder concentration = 0 g/lit and 25 µs pulse on time. A series of tests were conducted in order to compare EDM conventional process performance with powder mixed dielectric EDM performance on widely used industrial material EN-8. Based on literature survey three parameters are considered as critical input parameters (1) Peak current (2) Pulse on-time (3) Concentration of powder. Surface roughness measured for each experiment with setting process parameters. 45 work piece of EN 8 of size 50 mm X 30 mm X 6 mm are being produced for experimental work with copper electrode. They have concluded that PMEDM is not preferable. Peak current and pulse on time are the most influential parameters for reducing surface quality. The optimum levels of various process parameters obtained in their experimental work are: Peak current = 9 A, Powder concentration = 0 g/lit and 25 µs pulse on time for better surface quality

Ved Parkash et (10) have conducted the experiments on the effect of powder mixed dielectric on tool wear rate (TWR) in EDM has been observed. Experiments were designed using Taguchi method and appropriate Orthogonal Array and experiments have been performed as per the set of experiments designed in the orthogonal array. Signal to Noise ratios are also calculated to analyze the effect of PMEDM more accurately. They have concluded that the PMEDM (Powder Mixed Electric Discharge Machining) has significant effect on the tool wear rate. The Tool Wear Rate is higher with Copper as an additive and less when Graphite is used in dielectric. As current is directly proportional to discharge energy and pulse on-time. With increase in current and pulse on-time, tool wear rate also increases. The TWR is 3.685gms/µsec. When no additive is mixed in kerosene dielectric medium and this TWR decreases to 3.315gms/µsec. When Copper powder is mixed with dielectric medium and it again decreased to 2.5185gms/µsec. When Graphite powder is mixed with the dielectric medium. As it is known that lesser the TWR means higher the Tool Life, so it is clear that Tool life increases with the addition of Graphite powder in the dielectric medium.

Gurule N. B. et (11) experimented the effect of tool rotation on mrr during powder mixed EDM of die steel They have concluded that Current, on time, tool material, tool rpm and powder concentration significantly affect MRR. The suspension of Al powder into dielectric enhances MRR. The maximum MRR is produced at 4 g/l of Al powder, 900 tool rpm with Cu tool. Flushing shows least effect on MRR. Finally, it was concluded that Al powder and rotary tool have impact to great extent on the MRR of die steel. Their study shows future scope and potential for the improvements in the EDM field.

Abhishek Abrol et (12) studied the effect of chromium powder mixed dielectric fluid on machining characteristics of AISI D2 die steel has been studied. Peak current, pulse on time, pulse off time, concentration of powder are the process parameters. The process performance is measured in terms of material removal rate (MRR), tool wear rate (TWR) and surface roughness (SR). The research outcome will identify the important process parameters that maximize MRR, minimize TWR and SR. The design of experiment was undertaken using Taguchi method. ANOVA analysis was used to investigate the percentage contribution of each process parameter

2199

for optimizing the performance. Their study indicates that all the selected parameters except pulse off time have a significant effect on MRR. Current is found to be the most significant factor for MRR and TWR. With increase in current, TWR increases. Also, surface roughness increases with increase in pulse off time. They have concluded that MRR is mainly affected by current, pulse-on time and powder concentration. With the increase in current and pulse-on time, MRR increases. But it is also observed that with the increased concentration of chromium powder, MRR tends to decrease. TWR is mainly affected by current. With the increase in current, TWR increases. Also, TWR tends to decrease with the increase in chromium powder concentration. Current is the most dominant factor affecting both MRR and TWR. Both the performance data show an increasing pattern with increase in current for any other parameter. Surface roughness is mainly affected by the pulse-off time as per the main effects plot for SR. Surface Roughness is higher with the increase in pulse-off time.

Nimo Singh Khundrakpam et (13) have studied the effect of polarity on Different EDM (EDM, Dry-EDM and Powder Mixed EDM) has been studied in different polarity and dielectric mediums. It was observed experimentally that increase in tool hole diameter increase Material Removal Rate (MRR) and Tool Wear Rate (TWR). Dry-EDM has negligible TWR. In reverse polarity MRR is very low except Dry-EDM. They have concluded that increase in tool hole diameter increase both MRR &TWR. The dry EDM gives negligible tool wear rate. Tool Hole Diameter has more effective on dry EDM in both the polarity. Their Experiment is more suggested to study different powder mixed to dielectric medium for better MRR and TWR.

Mahendra G. Rathi et (14) experimented the Effect of Powder Mixed dielectric in EDM of Inconel 718. The effect of various powder mixed in dielectric is studied input parameters like Duty cycles, current, pulse on time and powder media in that Silicon carbide, Aluminium oxide, Graphite powder used. Machining characteristics measured in terms of Material removal rate, tool wear rate. To obtain the optimal process parameter combination, optimization is carried out by the Signal-to-Noise (S/N) ratio analysis of Taguchi method using L18 Orthogonal Array. An analysis of variance (ANOVA) is used to present the influence of process parameters on material removal rate, tool wear rate. Results obtained by Taguchi method and by ANOVA method, are compared and found that they match closely with each other. As the MRR is depends mostly on current. Current carrying capacity of any material depends on it electric conductivity. Here Graphite is having highest electric conductivity than Aluminium oxide and Silicon carbide and therefore MRR is higher in case of Graphite powder. As well as TWR is less. They have concluded that The Maximum MRR is obtained at a high peak current of 18 A, a moderate Ton of 5μs, duty cycle 85% and Graphite as powder media. Low TWR is achieved at a current of 12 A, a moderate Ton of 20 μs, duty cycle 90% and SiC as powder media.

Marek Rozenek et (15) The EDM characteristics obtained using hydrocarbon dielectric (kerosene) and mixture deionized water with abrasive powder have been compared. The relationship between surface roughness parameters, material removal rate and operating parameters of EDM have been determined for different kind of powder and its concentration in kerosene/water. The investigation results were showed that there are chances for replacing the conventional dielectric with water and that would imply considerable economic and ecology advantages. A copper cylinder of 20 mm in diameter has been used as a tool electrode; the hole has been made in the cylinder in order to pump dielectric into to area of machining. The tool steel NC6, in compliance with Polish Standard, was used as a workpiece. To determine of basic EDM relationships between input parameters such as pulse current, on-time, duty factor, and output parameters namely material removal rate (MRR) and surface roughness (Ra, Rz), factorial design and multiple regression analysis have been used. First series of experiments were carried out using kerosene and kerosene/powder mixture as dielectric and second series with using deionized water and deionized water/powder mixture. During machining negative and positive polarity of tool electrode was used for investigation of polarity effect, it is an especially important when water-based dielectric is used. They have concluded that application of powder in the dielectric lead to reduce surface roughness. The investigation results were showed that there are chances for replacing the conventional dielectric with powder suspended deionized water and that would imply considerable economic and ecology advantages.

B Govindharajan et (16) focused on performance of nickel mixed with kerosene as dielectric medium in electrical discharge machining of Monel 400TM. The optimum range of nickel powder, Graphite powder 6g mixes with the dielectric medium of kerosene servotherm (75:25) were developed experimentally. It was reported slightly more material removal rate, very low tool wear rate, better dimensional accuracy and good surface finsh in Monel 400TM. They have concluded that the experimentally observed performance of kerosene-servotherm of different proportion of nickel powder found that better machining output in EDM of Monel 400TM. The surface smoothness and diameteral accuracy reported by kerosene servotherm of 8g nickel mixed dielectric medium gives better result. After than drawn all graphs which shows the optimum proportion mixture of nickel powder influences the MRR, TWR and OC.8, 6g of nickel and graphite powders are mixed with kerosene-servotherm (75:25) gives better results of MRR, TWR and OC.

Kuldeep Ojha et (17) have presented parametric optimization for material removal rate (MRR) and tool wear rate (TWR) study on the powder mixed electrical discharge machining (PMEDM) of EN-8 steel has been carried out. Response surface methodology (RSM) has been used to plan and analyse the experiments. Average current, duty cycle, angle of electrode and concentration of chromium powder added into dielectric fluid of EDM were chosen as process parameters to study the PMEDM performance in terms of MRR and TWR. Experiments have been performed on newly designed experimental

setup developed in laboratory. Most important parameters affecting selected performance measures have been identified and effects of their variations have been observed. They have concluded that the quantitative analysis of machinability of EN-8 steel in PMEDM process has been carried out. Chromium powder particles are mixed in EDM dielectric fluid. RSM has been applied for analysis. Optimum results have been found as suggested by software.

Nimo Singh KhundrakpamÀ et (18) presented a Central Composite Design (CCD) for combination of variables and Response Surface Method (RSM) have been used to explore the influence of process parameter such as; peak current, powder concentration and tool diameter on the Material Removal Rate (MRR) on EN-8 steel. Analysis Of Variance (ANOVA) at 95% level of significance was performed to obtain the significant coefficients. Significant process parameters have been identified and optimum process conditions have been obtained. A confirmation experiments has been conducted and verified optimal conditions. Percentage errors are predicted and an actual value for developed models was found within 5%. They have concluded that the powder concentration have more significant effect on MRR. The adequacy of the developed models was checked by performing confirmation runs. The variation in prediction errors for MRR was found within ±5.5%. It was concluded that the model is valid to predict the machining responses within the experimental region.

Table:

S.No.	Year	Authors	Inputs	Powder used
1	2012	Sanjeev Kumara et	Peak current, pulse on-time and pulse off-time	tungsten carbide (WC and W2C) powder
2	2013	F.Q. Hua et	Current; pulse duration; pulse interval time; gap voltage	Al powder concentration: 35 g/L Al particle sizes <2 m
3	2015	Gangadharudu Talla et	powder concentration, peak current, pulse on time and duty cycle	Powders of aluminum and alumina of sizes about 15 mm and 90mm
4	2011	Kuldeep Ojha a et	Current, duty cycle, powder concentration and electrode diameter	chromium powder 45-55 µm
5	2015	M Prabu et	current, pulse ON-time, flushing pressure	graphite powder
6	2014	Shriram Y. Kaldhone et	current, Pulse on time ,Duty factor, Work Piece material, Powder type , Powder Concentration, Flushing Pressure	Silicon carbide
7	2015	M. A. Razak et	Powder concentration, Powder particles size	silicon carbide (SiC)
8	2015	G. Bharath Reddy et	The work piece material, peak current, pulse on time, duty factor, gap voltage	copper and aluminium
9	2015	R.A.Prajapati et	Peak current, pulse on time and concentration of powder.	Silicon Dioxide (SiO2) powder
10	2013	Ved Parkash et	peak current, pulse on-time, pulse off-time and polarity	copper and graphite
11	2012	Gurule N. B et	Current, off time, on time, tool material, powder concen, tool rpm & flushing pressure	Aluminium
12	2015	Abhishek Abrol et	Peak current, pulse on time, pulse off time, concentration of powder	chromium
13	2014	Nimo Singh Khundrakpam et	pulse on time, Discharge Current, Duty Factor, Gap Voltage, Gas flow Pressure	Graphite
14	2014	Mahendra G. Rathi et	Powder media (Graphite, Al2O3 ,SiC), Current, Pulse on time, Duty cycle	Graphite powder
15	2014	Marek Rozenek et	Current, grain size, pulse on time, grade,	silicon carbide SiC , Al2O3, Al
16	2014	B.Govindharajan et	Machine voltage, Gap voltage, current, work piece diameter, thickness, tool diameter, tool length	nickel powder, Graphite powder
17	2011	Kuldeep Ojha et	Average current, duty cycle, angle of electrode and concentration of chromium powder	chromium powder
18	2014	Nimo Singh KhundrakpamÀ et	peak current, powder concentration and tool diameter	Silicon Powder

Conclusion: PMEDM is very useful type of EDM which gives better results in terms of MRR, SR & TWR and others even in comparison with conventional EDM. Out of all the di-electric fluids used in PMEDM, commercial

kerosene is the best in view of viscosity because of which it flushes very well. Various powders i.e. silicon powder, chromium powder, nickel powder, graphite powder, Aluminium powder etc were used in PMEDM while kerosene as considered as a dielectric fluid.

REFERENCES:

(1). Sanjeev Kumara, Uma Batrab, "Surface modification of die steel materials by EDM method using tungsten powder-mixed dielectric", Journal of Manufacturing Processes 14 (2012) 35–40

(2). F.Q. Hua, F.Y. Caob, B.Y. Songa, P.J. Houa, Y. Zhanga, K. Chena, J.Q. Weia," Surface properties of SiCp/Al composite by powder-mixed EDM", 2212-8271 © 2013 The Authors. Published by Elsevier B.V.
The Seventeenth CIRP Conference on Electro Physical and Chemical Machining (ISEM, Procedia CIRP 6 (2013) 101 – 106

(3) Gangadharudu Talla a, Deepak Kumar Sahoo a, S. Gangopadhyay a, *, C.K. Biswas," Modeling and multi-objective optimization of powder mixed electric discharge machining process of aluminum/alumina metal matrix composite", Engineering Science and Technology, an International Journal 18 (2015) 369e373

(4) Kuldeep Ojha a, R. K. Garg a, K. K. Singh," Experimental Investigation and Modeling of PMEDM Process with Chromium Powder Suspended Dielectric", International Journal of Applied Science and Engineering 2011. 9, 2: 65-81
Int. J. Appl. Sci. Eng., 2011. 9, 2 65

(5) M Prabu, G Ramadoss, C Senthilkumar, R Boopathi, S Magibalan, "EXPERIMENTAL INVESTIGATION ON EFFECT OF GRAPHITE POWDER SUSPENDED DIELECTRIC IN ELECTRIC DISCHARGE MACHINING OF AL-TIB2 COMPOSITES", National Conference On Recent Trends And Developments In Sustainable Green Technologies Journal of Chemical and Pharmaceutical Sciences www.jchps.com ISSN: 0974-2115 JCHPS Special Issue 7: 2015 NCRTDSGT 2015 Page 52

(6) Shriram Y. Kaldhone , Mukund V. Kavade Umashankar Rawat," Effect of Powder Mixed Dielectric on Performance Measures of EDM for Tungsten Carbide", International Journal of Innovative Research in Advanced Engineering (IJIRAE) ISSN: 2349-2163 Volume 1 Issue 10 (November 2014), IJIRAE, Page - 106

(7) M. A. Razak, A. M. Abdul-Rani, and A. M. Nanimina," Improving EDM Efficiency with Silicon Carbide Powder-Mixed Dielectric Fluid", International Journal of Materials, Mechanics and Manufacturing, Vol. 3, No. 1, February 2015.

(8) G. Bharath Reddy, V.S.P. Vamsi, "PARAMETRIC ANALYSIS ON POWDER MIXED ELECTRIC DISCHARGE MACHINING OF VARIOUS STEELS USING TAGUCHI METHOD", International Journal of Advance Research In Science And Engineering http://www.ijarse.com, IJARSE, Vol. No.4, Special Issue (02), February 2015 ISSN-2319-8354(E)

(9) R.A.Prajapati, Haresh Patel," Experimental Investigation of Powder mix EDM using Silicon Dioxide as a Powder additive for Surface Roughness", International Journal of Advance Engineering and Research Development Volume 2, Issue 1, January -2015

(10) Ved Parkash, Deepak Kumar," Effect of Powder Mixed Dielectric Medium on Tool Wear Rate in EDM", Volume : 2 | Issue : 2 | Feb 2013 • ISSN No 2277 – 8179

(11) Gurule N. B.1, Nandurkar K. N," Effect of Tool Rotation on Material Removal Rate during Powder Mixed Electric Discharge Machining of Die Steel", International Journal of Emerging Technology and Advanced Engineering Website: www.ijetae.com (ISSN 2250-2459, Volume 2, Issue 8, August 2012) 328

(12) Abhishek Abrol, Sunil Sharma," EFFECT OF CHROMIUM POWDER MIXED DIELECTRIC ON PERFORMANCE CHARACTERISTIC OF AISI D2 DIE STEEL USING EDM", IJRET: International Journal of Research in Engineering and Technology eISSN: 2319-1163 | pISSN: 2321-7308 Volume: 04 Issue: 01 | Jan-2015, Available @ http://www.ijret.org 232

(13) Nimo Singh Khundrakpam, Amandeep Singh, 3Jasvir Singh, 4Som Kumar," Experimentally Study the Effect of Polarity and Tool Hole Diameter in EDM Responses", International Journal of Science, Engineering and Technology Research (IJSETR), Volume 3, Issue 4, April 2014

(14) Mahendra G. Rathi, Deepak V. Mane," Study on Effect of Powder Mixed dielectric in EDM of Inconel 718", International Journal of Scientific and Research Publications, Volume 4, Issue 11, November 2014 1 ISSN 2250-3153 www.ijsrp.org

(15) Marek Rozenek, Jerzy Kozak and Lucjan Dabrowski," Electrical Discharge Machiningin Dielectric-Powder Media", Warsaw University of Technology, POLAND

(16) B.Govindharajan, P.Meivel, C.Chelladurai, K.Avinaash," PERFORMANCE AND ANALYSIS OF NICKEL MIXED KEROSENE SERVOTHERM IN EDM OF MONEL 400TM", Journal of Innovative Research and Solution (JIRAS)- A unit of UIIRS Print- ISSN: 2320 1932 / Online ISSN – 2348 3636 Volume1 – Issue No.1 – Jan – Jun 2014 348

(17) Kuldeep Ojha, R. K. Garg1, K. K. Singh," Parametric Optimization of PMEDM Process using Chromium Powder Mixed Dielectric and Triangular Shape Electrodes", Journal of Minerals & Materials Characterization & Engineering, Vol. 10, No.11, pp.1087-1102, 2011 1087.

(18) Nimo Singh KhundrakpamȦ, Harmeet SinghḂ, Som KumarĊ and Gurinder Singh BrarḊ," Investigation and Modeling of Silicon Powder Mixed EDM using Response

Surface Method", International Journal of Current Engineering and Technology
E-ISSN 2277 – 4106, P-ISSN 2347 - 5161

BSV Ramarao[1] is working as Associate Professor of Department of Mechanical Engineering at Aurora's Scientific & Technological Institute Ghatkesar. He is obtained his master degree from Osmania University, Hyderabad. Currently he is pursuing his Ph.D from JNTUH. His research area is advanced manufacturing technology.

Dr. P Sailesh[2] is working as Professor of Department of Mechanical Engineering at Methodist college of Engineering Hyderabad. He is obtained his UG, PG and PhD degrees from Osmania University. He is having more than 20 years of teaching experience and his research area is production engineering.

Dr. M Sreenivasarao[3] is working as Professor & Head of Department of Mechanical Engineering at JNTUH Hyderabad. He is specialized in Industrial Engineering. His Research areas include Stochastic Modelling & Analysis, Machine Reinforced Learning, Multi-task inventory Control Systems, Supply chain Management. His area of interest is Stochastic Modelling of MFY, System Operating Management and RFID

2203

Performance and Emission Studies of a SI Engine using Distilled Plastic Pyrolysis Oil-Petrol Blends

Kareddula Vijaya Kumar[1], Ravi Kumar Puli[1], A. Swarna Kumari[2] and P. Shailesh[3]

[1] *Dept. of Mechanical Engineering, National Institute of Technology, Warangal, TS-506004, INDIA*
[2] *JNTUK/ MED, Kakinada, INDIA*
[3] *MCET, OU/MED, Hyderabad, TS-500001, INDIA*

Abstract. In the present work, an experimental investigation is carried out to evaluate the use of plastic oil derived from waste plastic which used in a Spark Ignition engine. Experiments are conducted, the measured performance and emissions of plastic oil blends at different proportions are compared with the baseline operation of the SI engine running with gasoline fuel. Engine performance and exhaust gas emissions such as carbon monoxide, total unburned hydrocarbons, carbon dioxide and oxides of nitrogen are measured. From the experiments it is observed that 50% Distilled Plastic Pyrolysis Oil (50%DPPO) exhibits the substantial enhancement in brake power, brake thermal efficiency and reduction in brake specific fuel consumption running at full load conditions among different blends and pure petrol. There is also noticed decrement of carbon dioxide and unburned hydrocarbons emissions at the same blend. The experimental result shows that plastic oil shall conveniently be used as a substitute to gasoline in the existing SI engines without any modifications.

1 Introduction

Increasing industrialization, urbanization and changes in the pattern of human life, will accompany the process of economic growth but at parallel causes for increasing quantities of environmental wastes leading to increased threats to it. Developing countries like India depends heavily on oil import. From the last two decades research around the world is concentrating on alternative energy generation techniques, it is the high time to generate the energy by alternative sources. Alternative fuels for both spark ignition and compression ignition engines have become very imperative owing to increased environmental protection concern, need to reduce dependency on petroleum products and even socioeconomic aspects. The past three and half decades are witnessed for an explosive growth of the plastic utilization across world. The production of synthetic polymers represented by polyethylene (PE), polypropylene (PP), polystyrene (PS), and polyvinyl chloride (PVC). These plastics are widely used in many important day to day applications such as clothing, household appliances and in automotive products and aerospace. While we enjoying the conveniences that plastics can provide, the treatment of waste plastic becomes an unavoidable and imminent issue.

In this context, it is urgent need to search a safety and effective ways to recycle waste plastics. Recently new ways of environmental friendly waste plastic recycling have been of interest, and among them, the use of waste plastics as a supplementary fuel has attracted interest of many researchers. Mehdi et al. [1] reviewed the PVC wastes and suggested chemical recycling is the best process for the environmental pollution problems and addressed several recent separation and recycling problems. Mitsuhara et al. [2] attention is also focused on using oil derived from waste plastics in diesel engines. Williams et al. [3] investigated the diesel engines are the most preferred power plants due to their excellent driveability and higher thermal efficiency. Naima et al. [4] had investigated alternative fuels for internal combustion engines by using waste plastics, waste engine oil and waste cooking oil. The properties of the oil derived from these three types of oils were analysed and compared with the diesel fuel. Moinuddin Sarker, et al. [5] used stainless steel reactor to produced hydrocarbon vapors from waste thermoplastics. Plastics are non-biodegradable polymers mostly containing carbon, hydrogen and few other elements which were the root cause for the plastic waste management and environmental issues [6-8]. Many researchers are investigated the usage of waste plastic oil and waste tyre oil as an alternative fuel for diesel engine. Shanmuga Vadivel et al. [9] are investigated the performance and emission characteristics of Nano engine running on plastic oil with gasoline blends. Their results shows an increase in brake thermal efficiency for the blends when compared to that of gasoline fuel. [10-12] were run the diesel engine blended with plastic oil to evaluate the

performance and emission characteristics without any engine modifications, their investigation clears that the plastic oil is alternate fuel for diesel engine. [13-17] are experimentally investigated on a diesel engine using waste plastic oil and tyre oil blends with exhaust gas recirculation. Their results shows that plastic and tyre oil blended engines suffers with high NO_x emission, which can deduced by using exhaust gas recirculation. Vijaya Kumar et al. [18] had investigated the performance and emission characteristics of diesel engine with three hole injector by using tyre oil blends and their results shows that 20% tyre oil blend was given better performance compared with diesel and other blends at all injections pressures. [19-22] are conducted experiments on diesel engine fuelled with tyre pyrolysis oil blended at different proportions to evaluate the performance and emissions with and without ethanol. [23, 24] are investigated the performance, emission and combustion studies using distilled tyre pyrolysis oil blends on diesel engine without any engine modification. However, very little work has been done to test their use in high-speed diesel engines. The main objective of this research is derived from the literature review, analyze the engine performance, combustion and emission characteristics of petrol engine fuelled with distilled waste plastic oil blends with petrol fuel. The crud waste plastic oil prepared from the pyrolysis process was carried out the batch distillation apparatus. This distilled plastic oil blended with gasoline at different volume fractions and the performance and emission characteristics was carried out on 4stroke single cylinder kerlosker petrol engine without any engine modifications.

1.1 Preparation of Plastic Pyrolysis Fuel

The production method for the conversion of plastics to liquid fuel is based on the pyrolysis of the plastics and the condensation of the resulting hydrocarbons are shown in Fig. 1. Pyrolysis refers to the thermos-chemical process for conversion of waste plastic by heating the feed stock at high temperature in absence of air which produces gaseous products which is them condensed to give liquid fuels consisting of pyrolytic oil or liquid oil.
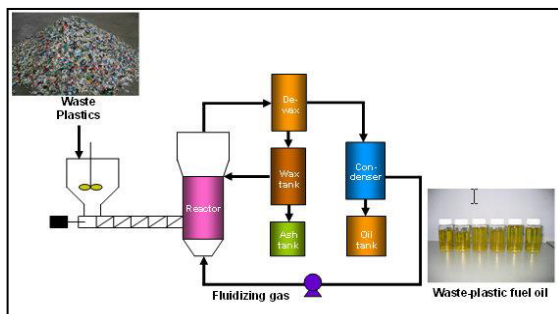
Figure 1. Pyrolysis process of waste plastics

Waste plastic is treated before feed in to the reactor. The feed stock passed to hopper through mills and send in to reactor by the hot screw conveyor. In reactor waste plastic is subjected to high temperature and low pressure by the hot gasses coming from combustion chamber where they will decompose at 450°C to 550°C. Vapors,

gasses and char products are generated and they passed through cyclone filter. The char is collected at the ash tank and gasses are send to condenser. In the condenser heat from this gasses is utilized to generate steam. The steam can used to generate the power as by product. So, that the plastic vapors are gets condensed in the condenser. The condensate oil is separated and used to further transformation, the non-condensable gasses are feed back to the reactor as fluidized gasses. Almost 70-80% of gaseous products are converted in to liquid fuels providing a good quantity of liquid fuel which then can be enhanced.

1.2 Reducing Viscosity of Plastic Pyrolysis Oil

The plastic oil which obtained by the pyrolysis method has some disadvantages such as high viscosity, low volatility, gumming effect and carbon residue. So, that the demerits impose a negative impact on the engine performance, emissions durability. Therefore, before using they as fuels the viscosity of the plastic oil have to be reduced. One interesting method to reduce the viscosity of the plastic oil and also to improve the spray formation so as to use them in the spark ignition engines are distillation. This process applied for petrol and diesel grade fuel production process. Fig. 2, distillation apparatus is used for to remove the impurities from basic fuel and increase the volatility of fuel. After distillation volatility of fuel is increase, it helps to homogenization of air fuel mixture in case of SI engine carburetor itself and also avoid logging of fuel impurities in filter or in nozzle holes.

Figure 2. Batch distillation apparatus

Waste plastic to fuel was use for further distillation process and making petrol grade fuel. Distillation column was use for distillation process. Distillation process set up different columns with different temperature profile like low boiling point fuel to high boiling point fuel. Petrol grade fuel collected from fractional column and temperature range was 90°C to 160°C. This fuel hydrocarbon compound also heavier and this fuel are not igniting. Collected petrol grade fuel percentage was about 42% and rest of all other fractional fuel percentage was 58% including diesel grade fuel and light gas also. Fractional distillation process was also generating some light gases. Plastic pyrolysis fuel to different fuel by using fractional distillation column used for heat applied with different column temperature wise and fuel break down into shorter into longer chain wise and come out

into different fraction column then collected into separate container.

In the present study distillate of the plastic oil is obtained in the same boiling range of petrol (90-160°c). The oil is obtained by pyrolysis come distillation is shown in the below Fig. 3.
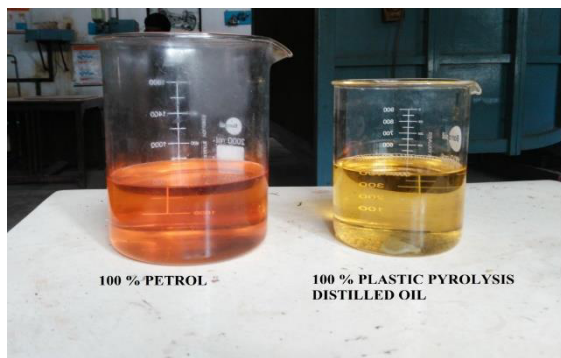
Figure 3. Pure distilled plastic oil and Petrol

Table 1: Basic properties of fuels

S. No.	Characteristics	Petrol	PPO	DPPO
1	Specific Gravity @ 40°C	0.720	0.820	0.780
2	Kinematic Viscosity m^2/sec @ 40°C	0.5×10^{-6}	2.52×10^{-6}	0.7×10^{-6}
3	Calorific Value (kJ/kg)	43953	42808	46817
4	Density @ 40°C (kg/m^3)	720	820	780

As the derived plastic fuel from the waste plastic after pyrolysis and distillation catches fire in room temperature itself, so flash and fire point is not valid for the arrived fuel as same like as petrol. And the extraction from the distillation i.e. plastic fuel slightly having more calorific value compare to that of gasoline, and also having density more than that of the gasoline. Some of the properties of the petrol, plastic pyrolysis oil (PPO) and distilled plastic pyrolysis oil (DPPO) are compared in table 1.
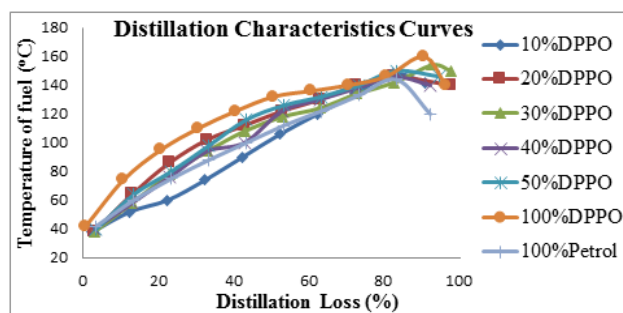
Figure 4. Volatility variation in petrol and DPPO blends

The tendency of a fuel to vaporize is also characterized by determining a series of temperatures at which various percentages of the fuel have evaporated (boiling temperatures), as described in ASTM D86, Test Method for Distillation of Petroleum Products. The temperatures at which 10 percent, 50 percent, and 90 percent evaporation occurs are often used to characterize the volatility of gasoline. The distillation characteristics curves of the petrol and plastic fuel as well as the different blends are shown in Fig. 4. From Fig. 4, it can be observed that the volatility property is more in the plastic pyrolysis distilled oil blends compared to the 100% petrol.

1.3 Preparation of Plastic Oil Blend

The basic properties of DPPO-PF were measured and compared with conventional petroleum fuels. The Carbon content are higher for DPPO than petrol fuel. In the present work 10%DPPO, 20%DPPO, 30%DPPO, 40%DPPO and 50%DPPO of DPPO was blended with petrol fuel on volume basis and observed for 15 days to check for any separation. No such separation was noticed. DPPO blended with PF is indicated as 10%DPPO. For example, 10%DPPO blended with 90% PF is denoted as 10%DPPO.

1.4 Experimental Setup

The Test rig comprises of the following apparatus and the layout is shown in Fig. 5,
- ❖ Petrol engine
- ❖ Electrical Dynamometer
- ❖ Burette setting with fuel consumption pipe and fuel tank
- ❖ Air and fuel supplied to engine
- ❖ Gas analyzer and Display

The test rig consists of single cylinder, 4-stroke, air-cooled petrol engine coupled to a electrical dynamometer, which acts as a loading device. A six channel temperature indicator provided to measure the temperature at various points of the test rig.
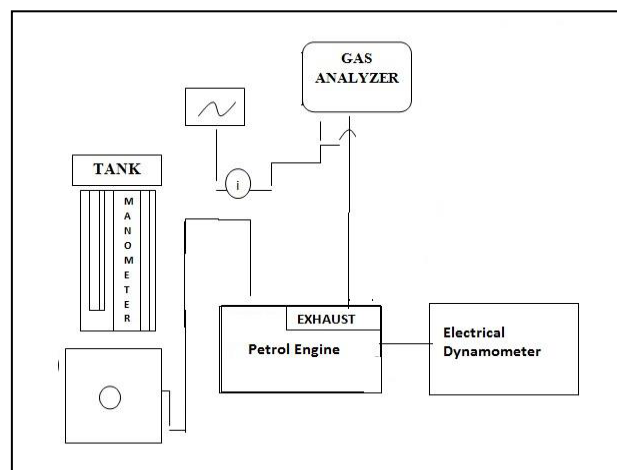
Figure 5. Layout of the Experimental Set up

The engine is complete with carburetor, governor, exhaust silencer, etc... a 2.2 KVA capacity, single phase, DC Generator is coupled on a strong iron base plate with bank (fin type resistor) arrangement a panel board consisting of main switch, voltmeter, ammeter to measure the power output. A fuel tank of about 5 liters capacity, a 100cc x 0.1cc burette and a three way cock arrangement. A silencer is fitted to the exhaust pipe to reduce the noise level to a minimum. A single phase panel board

arrangement consisting of a digital ammeter and voltmeter and single phase main switch. All this above instruments with panel board are mounted on the M.S. Fabricated stand. The speed of the engine is measured by the use of non-contact type digital tachometer.

1.5 AVL Gas Analyzer

The purpose of the AVL gas 444 is to measure the relative volumes of certain gases constituents in the exhaust gas of motor vehicles has shown in Fig. 6. These gases are carbon monoxide, carbon dioxide, hydrocarbons, and oxygen nitric oxide. The air fuel ratio is calculated from the CO, CO_2, HC and O_2, constituents and displayed. The Liquid crystal display shows the constituents of the gas once the gas is allowed to flow in. It is a standard output device for the AVL gas 444. The functional keys serves for various purposes such as to fine filter helps in removal or separation of water which enters into meter with tested gas. This prevents the damage of the machine. Frequently the filter has to be replaced depends on the manufacturer catalogue. The water inlet allows the gas from the engine exhaust into the machine. The exhaust gas probe takes a sample of gas from the exhaust tail pipe of the vehicle and carries it to the gas analyzer via exhaust gas hose. The important elements that are present on the back side are condensate outlet, ventilator and fan, sensors rpm and oil temperature RS 232 connection and power supply.

Figure 6. AVL Gas Analyzer

2 Results and Discussion

2.1 Engine Performance Characteristics

2.1.1 Brake Specific Fuel Consumption

Brake specific fuel consumption of an engine is defined as the rate of fuel consumption per unit power produces. This is an important performance parameter as it determines the mileage of the vehicle. It can be seen from the Fig. 7, that the BSFC of the engine decreased with increase in load and also BSFC decreased with increase in the proportion of plastic oil in the blend. Density and calorific values of the blend increases with increases in

the plastic proportion as the plastic oil is denser than petrol and also have higher calorific value.

2.1.2 Brake Thermal Efficiency

Fig. 8, shows the variation of brake thermal efficiency with load for various blends. Brake thermal efficiency increased with increase in load with the rate of variation decreasing with increase in load acting. For the $1/6^{th}$, $1/3^{rd}$ and 1/2 load conditions the brake thermal efficiency of 50%DPPO is more than the pure Petrol, after half load condition the brake thermal efficiency is fall and again raised at the full load conditions.
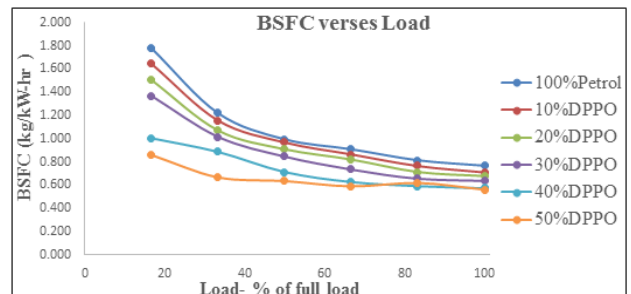
Figure 7. Variation of Brake Specific Fuel Consumption with Load
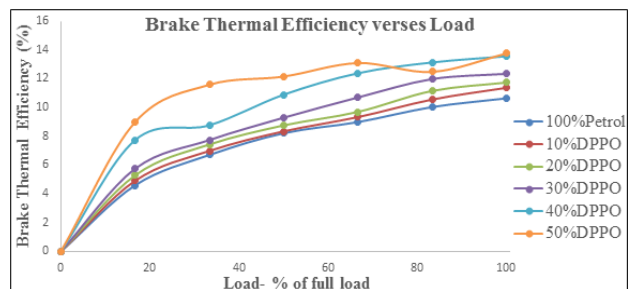
Figure 8. Variation of Brake Thermal Efficiency with Load

2.2 Engine Emission Characteristics

2.2.1 Carbon Monoxide

From Fig. 9, it can be observed that, CO emissions increased with increase in load reached the maximum at 4th or 5th load and there after slightly decreased. CO emissions are due to incomplete complete combustion of fuel either due to inadequate oxygen or flame quenching. In the present study as the engine is equipped with a carburetor to supply fuel to the engine cylinder, fuel air mixture might not be homogenous throughout the cylinder. CO emissions increased marginally with increase in the proportion of the plastic oil in bend.

2.2.2 Oxides of Nitrogen

NO_x emissions increases with increase in the peak cylinder temperature. Peak cylinder temperature increases with increase in load. NO_x emissions also varies with air fuel ratio, but in petrol engine air fuel ratio does not vary much with load. From Fig. 10, it can be observed that

NO_x emissions increased with increase in load as predicted.

2.2.3 Unburnt Hydro Carbons

Fig. 11, shows the variation of unburnt hydro carbon emissions with load for all blends. Unburnt hydro carbon emissions decreased with increase in the proportion of plastic oil in bend. Whereas CO emissions increased with increase in the plastic oil content in blend. In-cylinder temperature is a key factor in determining unburned HC and CO emissions characteristics. Lower temperatures generally cause higher emissions of unburned HCs and CO, however there are certain temperature ranges where HC emissions increase while CO decreases. An important consideration for the HC and CO emissions characteristics is the hot ignition and CO to CO_2 Oxidation threshold temperatures. Prior research has shown that the rapid breakdown of H_2O_2 leading to hot ignition for HC fuels begins at roughly 1000 K. CO-to-CO_2 oxidation requires temperatures of at least 1500 K.
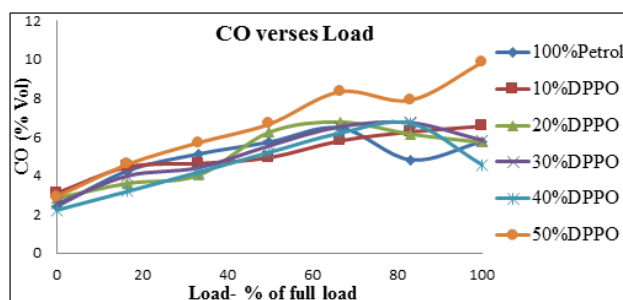
Figure 9. Variation of Carbon Monoxide emission with Load
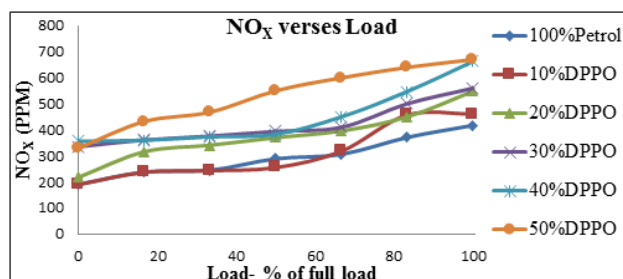
Figure 10. Variation of Oxides of Nitrogen emission with Load
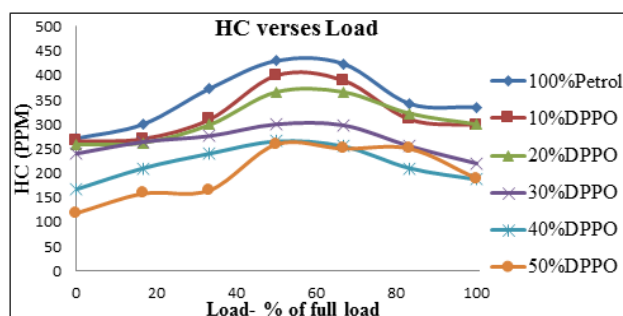
Figure 11. Variation of Unburnt Hydro Carbon emissions with Load

In the present study as the plastic oil has more calorific value than petrol, engine temperatures might be higher when the engine is operated with plastic oil. The HC and CO emissions exhibited an opposite trend with increase in plastic oil content in blend. This might be due

to in-cylinder temperatures being near or below the H_2O_2 breakdown temperature, where radicals released from rapid H_2O_2 breakdown cause HC molecules to break down to form CO . When the temperatures are near or below 1000 K, partial oxidation of HCs into CO does not occur thereby causing higher emissions of HCs and lower emissions of CO.

3 Conclusions

Plastic pyrolysis distilled fuel is tested on the SI engine and the performance and emissions characteristics are compared with the different blends and the following observations are made.

- ❖ Plastic oil obtained from the pyrolysis of a plastic waste can be used as a fuel in petrol engine by obtaining the distillate in the temperature range of petrol.
- ❖ Petrol and plastic pyrolysis distilled fuel can be readily blended without any precautions or the methods as both their viscosity and density are of in the same range.
- ❖ It is observed that the distillation characteristics of both petrol and plastic pyrolysis distilled fuel are more or less similar.
- ❖ The basic specific fuel consumption of the engine fuelled with 50%DPPO is 26.84 % lesser than that of the engine fuelled with sole petrol at full load.
- ❖ The brake thermal efficiency of the engine with 50%DPPO is 19% higher than that of the sole petrol operation.
- ❖ The CO emissions in 50%DPPO are 1.7 times more than that of the engine fuelled with the 100% Petrol.
- ❖ The unburnt hydrocarbons are 43.58% lesser in the 50%DPPO engine operation compared to the sole petrol operation.
- ❖ The NO_x emissions are 1.6 times more in the 50%DPPO compared to that of the engine with 100% petrol as fuel.

In the view of performance, experiments can run beyond 50% distilled plastic pyrolysis oil without any engine modification, but while considering in NO_x emissions, they are proportionately increasing with the percentage of distilled plastic pyrolysis oil compared to 100% petrol. Which should be consider as per EPA regulation.

References

1. Mehdi Sadat-Shojai, Gholam Reza Bakhshandeh, Recycling of PVC wastes, Elsevier, Polymer Degradation and Stability, **96**, 404-415, (2011).
2. Mitsuhara Y, Soloiu VA, Nakaishi Y, Application of new fuel produced from waste plastics and heavy oil to diesel engine, Transaction of the Japan Society of Mechanical Engineers, **67**, 2618-2624, (2001).

3. Williams PT, Williams EA, Interaction of plastics in mixed plastics pyrolysis, J. Energy Fuels, **13**(1), pp 188-196, (1999).

4. Naima K and Liazid A, Waste oils as alternative fuel for diesel engine: A review, Journal of Petroleum technology and Alternative fuels, Vol. **4**(3), pp. 30-43, (2013).

5. Moinuddin Sarker, Mohammad Mamunor Rashid, Mohammad Molla and Ashiquz Zaman, Conversion of Municipal Waste Plastic into Liquid Hydrocarbon Fuel Using a Stainless Steel Reactor, JESE A 1, 721-726, ISSN: 1934-8932, (2012).

6. Mani M, Nagarajan G, Influence of injection timing on performance, emission and combustion characteristics of a DI diesel engine running on waste plastic oil. Energy, **34**, 1617-1623, (2009).

7. Soloiu A, Yoshihara Y, Hiraoka M, Nishiwaki K, Mitsuhara Y, Nakanishi Y, The investigation of a new diesel produced from waste plastics, Eco-Technology Research Center, ISME, (2000).

8. Hai VP, Nishida O, Fujita H, Harano W, Toyoshima N, Iteya M, Reduction of NOx and PM from diesel engines by WPD emulsified fuel, SAE 2001-01-0152, ISSN: 01487191, (2001).

9. T. Shanmuga Vadivel, P. Balashanmugam, T Sivakumar, Performance and emission characteristics of Nano engine running on Plastic oil extract, International Journal of Scientific Research (IJSR), Vol. **3**, Issue 7, ISSN: 2277-8179, (2014).

10. Jane Pratoomyod, Krongkaew Laohalidanond, Performance and Emission Evaluation of Blends of Diesel fuel with Waste Plastic Oil in a Diesel Engine, International Journal of Engineering Science and Innovative Technology (IJESIT), Volume **2**, Issue 2, ISSN: 2319-5967, (2013).

11. M. Mani, C. Subash, G. Nagarajan, Emission and combustion characteristics of a DI diesel engine using waste plastic oil. Applied Thermal Engineering, **29**, 2738-2744, (2009).

12. Senthilkumar Tamilkolundu, Chandrasekar Murugesan, The Evaluation of blend of Waste Plastic Oil- Diesel fuel for use as alternate fuel for transportation. 2nd International Conference on Chemical, Ecology and Environmental Sciences (ICCEES'2012), April 28-29, Singapore (2012).

13. Mani M, Nagarajan G, Sampath S, An experimental investigation on a DI diesel engine using waste plastic oil with exhaust gas recirculation. Fuel **89**, 1826-1832 (2010).

14. M Paul Daniel, Kareddula Vijaya Kumar, B Durga Prasad, Ravi Kumar Puli, Performance and Emission Characteristics of Diesel Engine Operated on Plastic Pyrolysis Oil with exhaust gas recirculation, IJAE, DOI: 10.1080/01430750.2015.1086677.

15. M Paul Daniel, Kareddula Vijaya Kumar, B Durga Prasad, Performance and Emission Characteristics of Diesel Engine Operated on Tyre Pyrolysis Oil with exhaust gas recirculation, IJAE, May 2015, DOI: 10.1080/01430750.2015.1023837.

16. Kareddula Vijaya Kumar, Ravi Kumar Puli, Monika Dixit, D Ravi Chandra, Performance and Emission Evaluation of Tyre Oil blended with Diesel Fuel in Compression Ignition Engine, ICEE-2014, December 2014, JNTUH Kukatpally, Hyderabad, India.

17. Kareddula Vijaya Kumar, Ravi Kumar Puli, A Veeresh Babu, J.A. Ranga Babu, Performance and Emission Evaluation of Plastic Oil blended with Diesel Fuel in Compression Ignition Engine, ICEE-2014, December 2014, JNTUH Kukatpally, Hyderabad, India.

18. K. Vijaya Kumar, Dr. Ravi Kumar Puli, D. Ravichandra, K. Abhishek, Investigation on a CI Engine Fuelled with blends of Waste Tyre oil, Third International Conference on Advances in Mechanical, Aeronautical and Production Techniques (MAPT), April 2015, Malysia.

19. Mr. Hirenkumar M Patel, Prof. Tushar M Patel, performance analysis of single cylinder diesel engine fuelled with pyrolysis oil- diesel and its blend with Ethanol, International Journal of Engineering Research & Technology (IJERT), Vol. **1**, Issue 4, ISSN: 2278-0181, (2012).

20. Jinang M.Patel, Krunal J. Patel, Vatsal V. Patel, Kalpesh V. Vaghela, Investigates that Performance studies of Tire Pyrolysis Oil blends with Diesel Fuel, International Journal of Engineering and Advanced Technology (IJEAT), Volume-**3**, Issue-2, ISSN: 2249–8958, (2013).

21. Murugan. S, M.C. Ramaswamy, G. Nagarajan, Assessment of pyrolysis oil as an energy source for diesel engines, Fuel Processing Technology, **90**, 67-74, (2009).

22. Merchant, A.A., and Petrich, M.A., Pyrolysis of Scrap Tires and Conversion of Chars to Activated Carbon, American Institute Chemical Engineering Journal, Vol. **39**, 1370-1376, (1993).

23. Murugan. S, M.C. Ramaswamy, G. Nagarajan, Performance, emission and combustion studies of a DI diesel engine using distilled tyre pyrolysis oil-diesel blends, Fuel Processing Technology, Elsevier, **89**, 152-159, (2008).

24. Murugan. S, M.C. Ramaswamy, G. Nagarajan, A comparative study on the performance, emission and combustion studies of a DI diesel engine using distilled tyre pyrolysis oil–diesel blends, Fuel **87**, 2111-2121, (2008).

Determination of Best Concentration of Powder to Be Mixed in Di-Electric Fluid of PMEDM

BSV Ramarao[*]
Assoc. Professor, Dept of Mech,
ASTI, Hyderabad, India

Dr. P Shailesh
Professor, Dept of Mech
MCE, Hyderabad, India

Dr. M Sreenivasarao
Professor & Head, Dept of Mech
JNTUH, Hyderabad, India

Abstract:

Titanium alloy is extensively used in many industrial applications because of its corrosive resistance, fracture resistance and high strength to weight ratio and so many other advantages. It is quite necessary to know the best concentration of powder concentration which is to be mixed in the dielectric fluid when working on the aluminium alloy before going to fix the values in the levels of the parameter. In this paper a total of 34 trails were performed on titanium alloy on MRR, SR and TWR to find out the better concentration.

Keywords: PMEDM, MRR, SR, TWR &PC

I. INTRODUCTION-POWDER MIXED EDM

In Powder Mixed EDM suitable material in the powder form will be mixed into the dielectric fluid in tank. For better circulation of the dielectric fluid a stirring system is used. The constant reuse of powder in the dielectric fluid can be done by the special circulation system. Various powders of particle that can be added into the dielectric fluid include Aluminium,graphite, copper, chromium, and Silicon carbide etc. spark gap provided by the additives particles. When the voltage applied between the tool electrode and workpiece are 80-320V with the gap of 25-50μm & electric field range 105- 107 V/m was created. The powder particles of the material get energized & behave like a zigzag way manner. under the sparking zone, the particles of the material powder comes close to each other & arrange themselves in the form of chain like structure between the workpiece surface & tool electrode. The interlocking between the different powder particles occurs in the direction of flow current. The chain formation helps in bridging the discharge gap between the electrodes. Because of bridging effect, the insulating strength of the dielectric fluid decreases resulting in easy short circuit. This causes early explosion in the gap and series discharge' starts under the electrode area. The faster sparking within a discharge causes faster erosion from the work piece surface and hence the material removal rate increases.

II. MAJOR COMPONENTS

Power supply: It transform the alternating current from the main utility supply into the pulse direct currentrequired to produce the spark discharge at the machining gap.

Pulse Generator & Control Unit: This unit is responsible for supplying pulses at a certain voltage and current for specific amount of time. The power supply control the amount of energy consumed. The control unit is control the all function of the machining for example of Ton, Ip, duty cycle, putting the values and maintain the work piece the tool gap.

The servo system: It is provided to maintain the pre-determined gap. It senses the gap voltage and compares it with the present value and the different in voltage is then used to control the movement of servo motor to adjust the gap.

Tool holder: The tool holder holds the tool with the process of machining.

Circulating Pump: Circulation of powder mixed dielectric.

Electrode: The EDM electrode is the tool that determines the shape of the cavity to be produced.

Permanent magnet: Magnetic forces are used to separate the debris from the dielectric fluid.

Machining Tank: The system consists of a transparent bath-like container, called the machining tank.

III. WORKING PRINCIPLE OF PMEDM

When voltage is applied the powder particles become energized and behave in a zigzag fashion. These charged particles are accelerated due to the electric field and act as conductors promoting breakdown in the gap. This increases the spark gap between tool and the work piece. Under the sparking area, these particles come close to each other and arrange themselves in the form of chain like structures. The interlocking between the powder particles occurs in the direction of flow of current. The chain formation helps in bridging the discharge gap between the electrodes. Because of bridging effect, the insulating strength of the dielectric fluid decreases resulting in easy short circuit. This causes early explosion in the gap and series discharge' starts under the electrode area. The faster sparking within a discharge causes faster erosion from the work piece surface and hence the material removal rate increases.

IV. PARAMETERS OF PM-EDM

Parameters of this machine are mainly classified into two categories i.e. Process Parameters&Performance Parameters

Process Parameters: The process parameters in EDM are used to control the performance measures of the machining process. Process parameters are generally controllable machining input factors that determine the conditions in which machining is carried out. These machining conditions will affect the process performance result, which are gauged using various performance measures.

Electrical Parameters

Polarity: Polarity of the electrode can be either positive or negative

Straight polarity: Electrode (-) & workpiece (+)

Reverse polarity: Electrode (+) & workpiece (-)

Supply voltage: The input voltage applied across the tool electrode and workpiece is called the supply or open circuit voltage.

Discharge voltage: This is the electrical energy that is available for material removal. The magnitude of Em is calculated from measured pulse on time, discharge voltage and discharge current values.

Discharge Current: The discharge current is a measure of the amount of electrical charges flowing between the tool and workpiece electrode. As the flow of electrical charges is the heating mechanism in electro-thermal erosion,

Gap Voltage: The pre-set gap-voltage determines the width of the spark gap between the leading edge of the electrode and the workpiece. High voltage settings increase the gap and hence the flushing and machining. However when using graphite electrodes, high open gap voltage drastically increases the electrode wear.

Peak Current: This is the amount of power used in discharge machining, measured in units of amperage, and is the most important machining parameter in EDM.During each on-time pulse, the current increases until it reaches a pre-set level, which is expressed as the peak current. In both die-sinking and wire-EDM applications, the maximum amount of amperage is governed by the surface area of the cut. Higher amperage is used in roughing operations and in cavities or details with large surface areas. Higher currents will improve MRR, but at the cost of surface finish and tool wear. This is all more important in EDM because the machined cavity is a replica of tool electrode and excessive wear will hamper the accuracy of machining.

Average Current: Peak current is the maximum current available for each pulse from the power supply/generator. Average current is the average of the amperage in the spark gap measured over a complete cycle. It is calculated by multiplying peak current by duty factor.

Pulse on Time: The pulse on time represents the duration of discharge and is the time during which the electrode material is heated by the high temperature plasma channel. Material removal is directly proportional to the amount of energy applied during this on-time .A longer pulse on time will increase the discharge energy.

Pulse off time: The pulse off time represents the duration when no discharge exists and the dielectric is allowed to deionise and recover its insulating properties. A longer pulse off time improves machining stabilityas arcing is eliminated.

Pulse Frequency: Pulse frequency is the number of cycles produced across the gap in one second. The higher the frequency, finer is the surface finish that can be obtained.

Pulse waveform: The pulse shape is normally rectangular, but generators with other pulse shapes have also been developed.

Electrode Gap: It is the distance between the electrode and the part during the process of EDM. An electro-mechanical and hydraulic systems are used to respond to average gap voltage. To obtain good performance and gap stability a suitable gap should be maintained. For the reaction speed, it must obtain a high speed so that it can respond to short circuits or even open gap circuits. Gap width is not measured directly, but can be inferred from the average gap voltage.

Duty Factor: Duty factor is a percentage of the pulse duration relative to the total cycle time. Generally, a higher duty factor means increased cutting efficiency

Non-Electrical Parameters

Nozzle flushing: Flushing is defined as the correct circulation of dielectric solution between the electrodes and workpiece. Suitable flushing conditions are essential to obtain the highest machining efficiency. The sinker EDM process has primarily used oil for the dielectric fluid. Flushing system mainly two type i.e., Normal flow & Reverse flow

Powder Based Parameters
Powder type

The powder added into the dielectric fluid could increase the MRR and decrease the tool wear rate (TWR) and improve the surface quality of the work quite clearly. But the different powders would have different impact on the output characteristics of the EDM process. Some kinds of inorganic oxide powders cannot disperse uniformly and persistently in kerosene, concentrate and precipitate quickly, so they do not play a good role in improving the MRR, decreasing the SR and TWR. A powder which can be suspended into dielectric fluid of EDM must have following properties:-

It should be electrical conductive in nature.

It must be non-magnetic in nature.

It must have good suspension capabilities.

It should have good thermal conductivities.

It should be in toxic and odor-less.

Concentration of added powder

Addition of appropriate amount of powder into dielectric fluid plays a very important role on MRR, TWR and SR. The material removal depth reached the maximum value at appropriate concentration. Further increase or decrease in the concentration of the added powder would decrease the MRR.

Mesh size of powders

The size of the powder particles affects the PMEDM performance. A large diameter of the powder particle increases the gap but simultaneously decreases the MRR and then increases the SR.

Electrical properties of powders

The electrical conductivity of the added Powder directly affects EDM performance. This is because the added powder increases the Conductivity of the dielectric fluid and results in the extension of the gap distance.
Powder conductivity
Powder density

Electrode Based Parameters

Electrode material: EDM electrode materials need to have properties that easily allow charge and yet resist the erosion that the EDM process encourages and stimulates in the metals it machines. Alloys have properties which provide different advantages based on the needs of the application.

Brass is an alloy of copper and zinc. Brass materials are used to form EDM wire and small tubular electrodes. Brass does not resist wear as well as copper or tungsten, but is much easier to machine and can be die-cast or extruded for specialized applications. EDM wire does not need to provide wear or arc erosion resistance since new wire is fed continuously during the EDM wiring cutting process.

Copper and copper alloys have better EDM wear resistance than brass, but are more difficult to machine than either brass or graphite. It is also more expensive than graphite. Copper is, however, a common base material because it is highly conductive and strong. It is useful in the EDM machining of tungsten carbide, or in applications requiring a fine finish.

Copper tungsten materials are composites of tungsten and copper. They are produced using powder metallurgy processes. Copper tungsten is very expensive compared to other electrode materials, but is useful for making deep slots under poor flushing conditions and in the EDM machining of tungsten carbide. Copper tungsten materials are also used in resistance welding electrodes and some circuit breaker applications

Graphite provides a cleaning action at low speeds. Carbon graphite was one of the first brush material grades developed and is found in many older motors and generators. It has an amorphous structure.

Molybdenum is used for making EDM wire. It is the wire of choice for small slot work and for applications requiring exceptionally small corner radii. Molybdenum exhibits high tensile strength and good conductivity,making it ideal where small diameter wire is needed for demanding applications.

Silver tungsten material is tungsten carbide particles dispersed in a matrix of silver. Silver offers high electrical conductivity and tungsten provides excellent erosion resistance and good anti-welding characteristics in high-power applications. This composite is thus the perfect choice for EDM electrode applications wheremaximizing conductivity is crucial.

Tellurium copper is useful in EDM machining applications requiring a fine finish. Tellurium copper has a machinability that is similar to brass and better than pure copper.

Electrode Shape& size: The performance of die sinking EDM due to the shape configuration of the electrode. The effect of electrode shape on material removal rate (MRR), electrode wear rate (EWR), wear ratio (WR), and average surface roughness (Ra) has been investigated for mild steel work material and copper electrode. The shapes of the electrodes were round, square, triangular, and diamond of constant cross-sectional area of 64 mm^2.

Electrode Properties:

High electrical conductivity – electrons are cold emitted more easily and there is less bulk electrical heating.

High thermal conductivity – for the same heat load, the local temperature rise would be less due to faster heat conducted to the bulk of the tool and thus less tool wear.

Higher density – for the same heat load and same tool wear by weight there would be less volume removal or tool wear and thus less dimensional loss or inaccuracy.

High melting point – high melting point leads to fewer tools wear due to less tool material melting for the same heat load. Easy to manufacture.Less in cost

Performance Parameters

These parameters measure the various process performances of EDM results. Performance parameters classified into following Categories.

1. Material removal Rate: The Material removal rate is expressed as the weight of material removed from workpiece over a period of machining time in minutes
2. Tool wear Rate: The TWR is calculated by using the weight loss from the tool divided by the time of machining.
3. Relative Wear Ratio: WR is the ratio of TWR/MRR and is used as a performance measure for quantifying tool-workpiece material combination pairs since different material combinations gives rise to different TWR and MRR values. A material combination pair with the lowest WR indicates that the tool-workpiece material combination gives the optimal TWR and MRR condition. The relative wear ratio of the workpiece and tool is expressed.
4. Surface Roughness: It is the classification of surface parameter used to describe an amplitude feature, which translates to roughness of the surface finish. Of the many parameters available to quantify SR, the most

commonly used in EDM are arithmetical mean surface roughness, maximum peak-tovalley surface roughness and root mean square surface roughness. The Surface Roughness of the workpiece can be expressed in different ways like,

a. Arithmetic average
b. Average peak to valley height
c. Peak roughness etc.

Defined as the arithmetic average roughness of the deviations of the roughness profile from the central line along the measurement

5. Surface quality: Surface quality is a broad performance measure used to describe the condition of the machined surface. It comprises components such as surface roughness, extent of heat affected zone, recast layer thickness and micro-crack density.

6. Heat affected Zone: It refers to the region of a work piece that did not melt during electrical discharge but has experienced a phase transformation, similar to that of heat treatment processes, after being subjected to the high temperatures of electrical discharge.

7. Recast layer Thickness: The recast layer refers to the region of re-solidified molten material occurring as the top most layer of the machined surface. The recast layer is usuallylocated above the heat affected zone.

V. LITERATURE SURVEY

F.Q.Huaet (1) conducted experiments on surface properties of SiCp/Al with moderate fraction of Sic particle reinforced Al matrix composites in EDM and PMEDM using Environment scanning electron microscope. They have found that the surface properties are improved greatly in PMEDM than EDM as its surface roughness decreased about 31.5% and is better in corrosion resistance and wear resistance is twice of EDM. Finally they have also mentioned that the PMEDM is having promising applications in metal matrix composites machining field

M Prabuet (2) have done experimental investigation on effect of graphite powder suspended dielectric in electric in EDM of Al-TiB2 composites. The experiments were conducted on ELEKTRAPULS spark erosion machine. Their objective is to find the effect of parameters viz, current, pulse ON-time, flushing pressure and vibration As a result, the process becomes more stable thereby improving Material Removal Rate (MRR) and reducing Tool Wear Rate (TWR). The EDM set-up is used in their experimental study is M100 model die sinking EDM machine manufactured by Electronica Machine Tools. The Parameters and their settings are in L16 orthogonal array. It uses Kerosene as the dielectric fluid. The primary benefit of using kerosene is that it has very low viscosity and gets flushed away easily. The selected work piece material is Al-TiB2 composites. Each experiment was performed for fixed time period using brass as an electrode. Input process parameters are current, pulse on time and flushing pressure. The material removal rate and tool wear rate are evaluated by using an electronic balance machine. They have concluded that this work evaluates the feasibility of machining Al-TiB2MMC with graphite powder suspended dielectric fluid. MRR was found higher for larger Current. When comparing the MRR of with powder and without powder the MRR obtained for with powder is found higher. TWR slightly increases with increasing the Current. When comparing the TWR of with powder and without powder the TWR obtained for with powder is found higher. Increase in MRR was found on increasing Pulse ON-time. TWR increases with the increases in pulse ON-time.

Shriram Y. Kaldhoneet (3) have studied the influence of operating parameters of tungsten carbide on the machining characteristics such as material removal rate. The effectiveness of PMEDM process with tungsten carbide, WC-Co is evaluated in terms of the material removal rate. They have observed that copper tungsten is most suitable for use as the tool electrode in EDM of WC-Co; better machining performance is obtained generally with the electrode as the negative and the work piece as positive. In their work, a study was carried out on the influence of the parameters such peak current, Duty factor, pulse on time , work piece material, powder type , powder concentration and flushing pressure. Taguchi methodology has been adopted to plan and analyze the experimental results. Experiments have been performed on newly designed experimental setup. In their study seven factors with three levels are investigated using Orthogonal Array (OA) L27.Material removal rate (MRR) in their experiment was calculated by using mathematical method. The result of their experiment then was collected and analyzed using MINITAB 16 software. The recommended best parametric settings have been verified by conducting confirmation experiments for MRR. From their experimental study it is found that addition of Silicon carbide powder enhances machining rate drastically with slightly increase in Tool wear rate. They have concluded that The MRR and TWR are mainly affected by the current and powder. With mixing of silicon carbide powder MRR can be increased by 90%. Current, Pulse on time, work piece material, Powder type and Flushing Pressure significantly affect MRR. The maximum MRR is produced at 8 g/l of SiC powder for Flushing pressure 1.5 Kg/cm2. Duty factor shows least effect on MRR. Finally, it was concluded that SiC powder and Current have impact to great extent on the MRR of Tungsten Carbide

R.A.Prajapatiet (4) experimented the effect of Silicon Dioxide (SiO2) powder mixing into the dielectric fluid of EDM on machining characteristics of EN-8 with three input parameters Peak current, pulse on time and concentration of powder. Analysis was carried out for surface roughness. The result outcomes identified the important parameters and their effect on SR of En-8 in the presence of SiO2 in a kerosene dielectric of EDM. Analysis was showed that the peak current and pulse on time have higher contribution toward surface roughness. The experimental result analysis showed EDM with zero concentration gives better surface finish rather than PMEDM. Better surface quality obtained at Peak current (9A), Powder concentration = 0 g/lit and 25 μs pulse on time. A series of tests were conducted in order to compare EDM conventional process performance with powder mixed dielectric EDM performance on widely used

industrial material EN-8. Based on literature survey three parameters are considered as critical input parameters (1) Peak current (2) Pulse on-time (3) Concentration of powder. Surface roughness measured for each experiment with setting process parameters. 45 work piece of EN 8 of size 50 mm X 30 mm X 6 mm are being produced for experimental work with copper electrode. They have concluded that PMEDM is not preferable. Peak current and pulse on time are the most influential parameters for reducing surface quality. The optimum levels of various process parameters obtained in their experimental work are: Peak current = 9 A, Powder concentration = 0 g/lit and 25 μs pulse on time for better surface quality

VedParkashet (5) have conducted the experiments on the effect of powder mixed dielectric on tool wear rate (TWR) in EDM has been observed. Experiments were designed using Taguchi method and appropriate Orthogonal Array and experiments have been performed as per the set of experiments designed in the orthogonal array. Signal to Noise ratios are also calculated to analyze the effect of PMEDM more accurately. They have concluded that the PMEDM (Powder Mixed Electric Discharge Machining) has significant effect on the tool wear rate. The Tool Wear Rate is higher with Copper as an additive and less when Graphite is used in dielectric. As current is directly proportional to discharge energy and pulse on-time. With increase in current and pulse on-time, tool wear rate also increases. The TWR is 3.685gms/μsec. When no additive is mixed in kerosene dielectric medium and this TWR decreases to 3.315gms/μsec. When Copper powder is mixed with dielectric medium and it again decreased to 2.5185gms/μsec. When Graphite powder is mixed with the dielectric medium. As it is known that lesser the TWR means higher the Tool Life, so it is clear that Tool life increases with the addition of Graphite powder in the dielectric medium.

Gurule N. B. et (6) experimented the effect of tool rotation on mrr during powder mixed EDM of die steel They have concluded that Current, on time, tool material, tool rpm and powder concentration significantly affect MRR. The suspension of Al powder into dielectric enhances MRR. The maximum MRR is produced at 4 g/l of Al powder, 900 tool rpm with Cu tool. Flushing shows least effect on MRR. Finally, it was concluded that Al powder and rotary tool have impact to great extent on the MRR of die steel. Their study shows future scope and potential for the improvements in the EDM field.

Nimo Singh Khundrakpamet (7) have studied the effect of polarity on Different EDM (EDM, Dry-EDM and Powder Mixed EDM) has been studied in different polarity and dielectric mediums. It was observed experimentally that increase in tool hole diameter increase Material Removal Rate (MRR) and Tool Wear Rate (TWR). Dry-EDM has negligible TWR. In reverse polarity MRR is very low except Dry-EDM. They have concluded that increase in tool hole diameter increase both MRR &TWR. The dry EDM gives negligible tool wear rate. Tool Hole Diameter has more effective on dry EDM in both the polarity. Their Experiment is more suggested to study different powder mixed to dielectric medium for better MRR and TWR.

Mahendra G. Rathiet (8) experimented the Effect of Powder Mixed dielectric in EDM of Inconel 718. The effect of various powder mixed in dielectric is studied input parameters like Duty cycles, current, pulse on time and powder media in that Silicon carbide, Aluminium oxide, Graphite powder used. Machining characteristics measured in terms of Material removal rate, tool wear rate. To obtain the optimal process parameter combination, optimization is carried out by the Signal-to-Noise (S/N) ratio analysis of Taguchi method using L18 Orthogonal Array. An analysis of variance (ANOVA) is used to present the influence of process parameters on material removal rate, tool wear rate. Results obtained by Taguchi method and by ANOVA method, are compared and found that they match closely with each other. As the MRR is depends mostly on current. Current carrying capacity of any material depends on it electric conductivity. Here Graphite is having highest electric conductivity than Aluminium oxide and Silicon carbide and therefore MRR is higher in case of Graphite powder. As well as TWR is less. They have concluded that The Maximum MRR is obtained at a high peak current of 18 A, a moderate Ton of 5μs, duty cycle 85% and Graphite as powder media. Low TWR is achieved at a current of 12 A, a moderate Ton of 20 μs, duty cycle 90% and SiC as powder media.

MarekRozeneket (9) The EDM characteristics obtained using hydrocarbon dielectric (kerosene) and mixture deionized water with abrasive powder have been compared. The relationship between surface roughness parameters, material removal rate and operating parameters of EDM have been determined for different kind of powder and its concentration in kerosene/water. The investigation results were showed that there are chances for replacing the conventional dielectric with water and that would imply considerable economic and ecology advantages. A copper cylinder of 20 mm in diameter has been used as a tool electrode; the hole has been made in the cylinder in order to pump dielectric into to area of machining. The tool steel NC6, in compliance with Polish Standard, was used as a workpiece. To determine of basic EDM relationships between input parameters such as pulse current, on-time, duty factor, and output parameters namely material removal rate (MRR) and surface roughness (Ra, Rz), factorial design and multiple regression analysis have been used. First series of experiments were carried out using kerosene and kerosene/powder mixture as dielectric and second series with using deionized water and deionized water/powder mixture. During machining negative and positive polarity of tool electrode was used for investigation of polarity effect, it is an especially important when water-based dielectric is used. They have concluded that application of powder in the dielectric lead to reduce surface roughness. The investigation results were showed that there are chances for replacing the conventional dielectric with powder suspended deionized water and that would imply considerable economic and ecology advantages.

B Govindharajanet (10) focused on performance of nickel mixed with kerosene as dielectric medium in electrical discharge machining of Monel 400TM. The optimum range of nickel powder, Graphite powder 6g mixes with the dielectric medium of kerosene servotherm (75:25) were developed experimentally. It was reported slightly more material removal rate, very low tool wear rate, better dimensional accuracy and good surface finsh in Monel 400TM. They have concluded that the experimentally observed performance of kerosene-servotherm of different proportion of nickel

powder found that better machining output in EDM of Monel 400TM. The surface smoothness and diameteral accuracy reported by kerosene servotherm of 8g nickel mixed dielectric medium gives better result. After than drawn all graphs which shows the optimum proportion mixture of nickel powder influences the MRR, TWR and OC.8, 6g of nickel and graphite powders are mixed with kerosene-servotherm (75:25) gives better results of MRR, TWR and OC.

KuldeepOjha et (11) have presented parametric optimization for material removal rate (MRR) and tool wear rate (TWR) study on the powder mixed electrical discharge machining (PMEDM) of EN-8 steel has been carried out. Response surface methodology (RSM) has been used to plan and analyse the experiments. Average current, duty cycle, angle of electrode and concentration of chromium powder added into dielectric fluid of EDM were chosen as process parameters to study the PMEDM performance in terms of MRR and TWR. Experiments have been performed on newly designed experimental setup developed in laboratory. Most important parameters affecting selected performance measures have been identified and effects of their variations have been observed. They have concluded that the quantitative analysis of machinability of EN-8 steel in PMEDM process has been carried out. Chromium powder particles are mixed in EDM dielectric fluid. RSM has been applied for analysis. Optimum results have been found as suggested by software.

Nimo Singh KhundrakpamAet (12) presented a Central Composite Design (CCD) for combination of variables and Response Surface Method (RSM) have been used to explore the influence of process parameter such as; peak current, powder concentration and tool diameter on the Material Removal Rate (MRR) on EN-8 steel. Analysis Of Variance (ANOVA) at 95% level of significance was performed to obtain the significant coefficients. Significant process parameters have been identified and optimum process conditions have been obtained. A confirmation experiments has been conducted and verified optimal conditions. Percentage errors are predicted and an actual value for developed models was found within 5%. They have concluded that the powder concentration have more significant effect on MRR. The adequacy of the developed models was checked by performing confirmation runs. The variation in prediction errors for MRR was found within ±5.5%. It was concluded that the model is valid to predict the machining responses within the experimental region.

VI. EXPERIMENTATION

Experiments have been conducted to find out the quantum of the best concentration which is to be mixed up to get the better results to proceed towards the main experimentation. As a part of it, it is being selected to conduct experiments with 1 gram powder as incremental factor starting with 1 gram till 17 grams. It was tested to find out the Material removal rate, Surface Roughness & Tool Wear Rate in 17 experiments for which two trials were performed for each experiment. Then the values of the MRR, SR & TWR in two trials were shown in the following table along with the average value of the each concentration.

*PC	MRR		Avg MRR	SR		Avg SR	TWR		Avg TWR
	Trial1	Trial2		Trial1	Trial2		Trial1	Trial2	
1	4.143	3.9673	4.05515	4.512	4.457	4.4845	1.0648	0.9646	1.0147
2	5.761	6.564	6.1625	4.634	4.539	4.5865	0.5472	0.6145	0.58085
3	6.85	7.19	7.02	4.768	5.6	5.184	0.6144	0.5819	0.59815
4	5.27	7.88	6.575	4.999	4.244	4.6215	0.7154	0.5638	0.6396
5	9.1089	8.8916	9.00025	5.067	5.003	5.035	0.8462	0.8363	0.84125
6	9.3241	9.1652	9.24465	4.873	4.924	4.8985	0.7245	0.9275	0.826
7	5.5338	9.417	7.4754	4.585	4.321	4.453	0.323	1.0218	0.6724
8	9.1726	9.8272	9.4999	4.865	4.645	4.755	0.734	0.9123	0.82315
9	9.7392	9.7016	9.7204	5.209	4.551	4.88	1.087	1.0667	1.07685
10	9.4563	9.4538	9.45505	4.897	4.568	4.7325	0.532	0.5247	0.52835
11	9.004	9.18	9.092	4.7181	4.582	4.65005	0.524	0.5645	0.54425
12	9.1231	9.0142	9.06865	4.5426	4.623	4.5828	0.567	0.5687	0.56785
13	9.1828	8.21	8.6964	4.362	5.691	5.0265	0.5825	0.5796	0.58105
14	9.3452	8.234	8.7896	4.213	5.321	4.767	0.6438	0.6342	0.639
15	9.6294	8.115	8.8722	3.9591	4.932	4.44555	0.684	0.6985	0.69125
16	9.3412	8.165	8.7531	4.6541	4.967	4.81055	0.623	0.7142	0.6686
17	8.2031	8.224	8.21355	5.1	5.293	5.1965	0.592	0.97	0.781

*PC-Powder Concentration in g/lt

VII. CONCLUSION

In the three machining values it is found that the average of the best and second best together and it is found as 10. Then the possible levels (3) within the prescribed number of experiments (17) are being decided that 5, 10 and 15 g/lt.

REFERENCES

[1]   F.Q. Hua, F.Y. Caob, B.Y. Songa, P.J. Houa, Y. Zhanga, K. Chena, J.Q. Weia," Surface properties of SiCp/Al composite by powder-mixed EDM", 2212-8271 © 2013 The Authors. Published by Elsevier B.V. The Seventeenth CIRP Conference on Electro Physical and Chemical Machining (ISEM, Procedia CIRP 6 (2013) 101 – 106

[2]   M Prabu, G Ramadoss, C Senthilkumar, R Boopathi, S Magibalan, "EXPERIMENTAL INVESTIGATION ON EFFECT OF GRAPHITE POWDER SUSPENDED DIELECTRIC IN ELECTRIC DISCHARGE MACHINING OF AL-TIB2 COMPOSITES", National Conference On Recent Trends And Developments In Sustainable Green Technologies Journal of Chemical and Pharmaceutical Sciences www.jchps.com ISSN: 0974-2115 JCHPS Special Issue 7: 2015 NCRTDSGT 2015 Page 52

[3]   Shriram Y. Kaldhone , Mukund V. KavadeUmashankarRawat," Effect of Powder Mixed Dielectric on Performance Measures of EDM for Tungsten Carbide", International Journal of Innovative Research in Advanced Engineering (IJIRAE) ISSN: 2349-2163 Volume 1 Issue 10 (November 2014), IJIRAE, Page - 106

[4]   R.A.Prajapati, Haresh Patel," Experimental Investigation of Powder mix EDM using Silicon Dioxide as a Powder additive for Surface Roughness", International Journal of Advance Engineering and Research Development Volume 2, Issue 1, January -2015

[5]   VedParkash, Deepak Kumar," Effect of Powder Mixed Dielectric Medium on Tool Wear Rate in EDM",Volume : 2 | Issue : 2 | Feb 2013 • ISSN No 2277 – 8179

[6]   Gurule N. B.1, Nandurkar K. N," Effect of Tool Rotation on Material Removal Rate during Powder Mixed Electric Discharge Machining of Die Steel", International Journal of Emerging Technology and Advanced Engineering Website: www.ijetae.com (ISSN 2250-2459, Volume 2, Issue 8, August 2012) 328

[7]   Nimo Singh Khundrakpam, Amandeep Singh, 3Jasvir Singh, 4Som Kumar," Experimentally Study the Effect of Polarity and Tool Hole Diameter in EDM Responses", International Journal of Science, Engineering and Technology Research (IJSETR), Volume 3, Issue 4, April 2014

[8]   Mahendra G. Rathi, Deepak V. Mane," Study on Effect of Powder Mixed dielectric in EDM of Inconel 718", International Journal of Scientific and Research Publications, Volume 4, Issue 11, November 2014 1 ISSN 2250-3153 www.ijsrp.org

[9]   MarekRozenek, Jerzy Kozak and LucjanDabrowski," Electrical Discharge Machiningin Dielectric-Powder Media", Warsaw University of Technology, POLAND

[10]   B.Govindharajan, P.Meivel, C.Chelladurai, K.Avinaash," PERFORMANCE AND ANALYSIS OF NICKEL MIXED KEROSENE SERVOTHERM IN EDM OF MONEL 400TM", Journal of Innovative Research and Solution (JIRAS)- A unit of UIIRS Print- ISSN: 2320 1932 / Online ISSN – 2348 3636 Volume1 – Issue No.1 – Jan – Jun 2014 348

[11]   KuldeepOjha, R. K. Garg1, K. K. Singh," Parametric Optimization of PMEDM Process using Chromium Powder Mixed Dielectric and Triangular Shape Electrodes", Journal of Minerals & Materials Characterization & Engineering, Vol. 10, No.11, pp.1087-1102, 2011 1087.

[12]   Nimo Singh KhundrakpamȦ, HarmeetSinghḂ, SomKumarĊ and Gurinder Singh BrarḊ," Investigation and Modeling of Silicon Powder Mixed EDM using Response Surface Method", International Journal of Current Engineering and Technology, E-ISSN 2277 – 4106, P-ISSN 2347 - 5161

Obtaining the Output Parameters for Different Powder Concentrationin PMEDM

BSV Ramarao[1],Dr. P Shailesh[2] & Dr. M Sreenivasarao[3]

[1]*Assoc. Professor, DeptOfMech, ASTI, Hyderabad.*
[2]*Professor, Dept of Mech,MCE, Hyderabad.*
[3]*Professor & Head, Dept of Mech, JNTUH, Hyderabad.*

_____

Abstract:*Now-a-days many industries are working to find out the best metal alloys to obtain the optimized outputs for their products all the time. Out of all the available, Titanium alloy is one which is extensively used in many industrial applications because of its positive characteristics like corrosive resistance, fracture resistance and high strength to weight ratio and so on. It is quite necessary to know the better concentration of powder concentration which is to be mixed in the dielectric fluid when working on the aluminium alloy before going to fix the values in the levels of the parameter. In this paper more than 30 trails were performed to determine MRR, SR and TWR.*

_____

Keywords-MRR, SR, TWR, PM-EDM & PC

I. INTRODUCTION

PMEDM is the advanced type of usage of the conventional EDM. In Powder Mixed EDM suitable material in the powder form will be mixed into the dielectric fluid in tank. For better circulation of the dielectric fluid a stirring system is used. The constant reuse of powder in the dielectric fluid can be done by the special circulation system. Various powders of particle can be added into the dielectric fluid. spark gap provided by the additives particles. The powder particles of the material get energized & behave like a zigzag way manner. under the sparking zone, the particles of the material powder comes close to each other & arrange themselves in the form of chain like structure between the workpiece surface & tool electrode. The interlocking between the different powder particles occurs in the direction of flow current. The chain formation helps in bridging the discharge gap between the electrodes. Because of bridging effect, the insulating strength of the dielectric fluid decreases resulting in easy short circuit. This causes early explosion in the gap and series discharge' starts under the electrode area.

II. WORKING PRINCIPAL

When voltage is applied the powder particles become energized and behave in a zigzag fashion. These charged particles are accelerated due to the electric field and act as conductors promoting breakdown in the gap. This increases the spark gap between tool and the work piece. Under the sparking area, these particles come close to each other and arrange themselves in the form of chain like structures. The interlocking between the powder particles occurs in the direction of flow of current. The chain formation helps in bridging the discharge gap between the electrodes. Because of bridging effect, the insulating strength of the dielectric fluid decreases resulting in easy short circuit. This causes early explosion in the gap and series discharge' starts under the electrode area. The faster sparking within a discharge causes faster erosion from the work piece surface and hence the material removal rate increases.

III. PARAMETERS

Parameters of this machine are mainly classified into two categories i.e. Process Parameters &Performance Parameters

Process Parameters: The process parameters in EDM are used to control the performance measures of the machining process. Process parameters are generally controllable machining input factors that determine the conditions in which machining is carried out. These machining conditions will affect the process performance result, which are gauged using various performance measures.

Electrical Parameters
Polarity: Polarity of the electrode can be either positive or negative
Supply voltage: The input voltage applied across the tool electrode and workpiece is called the supply or open circuit voltage.
Discharge voltage: This is the electrical energy that is available for material removal. The magnitude of Em is calculated from measured pulse on time, discharge voltage and discharge current values.

Discharge Current: The discharge current is a measure of the amount of electrical charges flowing between the tool and workpiece electrode. As the flow of electrical charges is the heating mechanism in electro-thermal erosion,

Gap Voltage: The pre-set gap-voltage determines the width of the spark gap between the leading edge of the electrode and the workpiece. High voltage settings increase the gap and hence the flushing and machining. However when using graphite electrodes, high open gap voltage drastically increases the electrode wear.

Peak Current: This is the amount of power used in discharge machining, measured in units of amperage, and is the most important machining parameter in EDM. During each on-time pulse, the current increases until it reaches a pre-set level, which is expressed as the peak current. In both die-sinking and wire-EDM applications, the maximum amount of amperage is governed by the surface area of the cut. Higher amperage is used in roughing operations and in cavities or details with large surface areas. Higher currents will improve MRR, but at the cost of surface finish and tool wear. This is all more important in EDM because the machined cavity is a replica of tool electrode and excessive wear will hamper the accuracy of machining.

Average Current: Peak current is the maximum current available for each pulse from the power supply/generator. Average current is the average of the amperage in the spark gap measured over a complete cycle. It is calculated by multiplying peak current by duty factor.

Pulse on Time: The pulse on time represents the duration of discharge and is the time during which the electrode material is heated by the high temperature plasma channel. Material removal is directly proportional to the amount of energy applied during this on-time .A longer pulse on time will increase the discharge energy.

Pulse off time: The pulse off time represents the duration when no discharge exists and the dielectric is allowed to deionise and recover its insulating properties. A longer pulse off time improves machining stabilityas arcing is eliminated.

Pulse Frequency: Pulse frequency is the number of cycles produced across the gap in one second. The higher the frequency, finer is the surface finish that can be obtained.

Pulse waveform: The pulse shape is normally rectangular, but generators with other pulse shapes have also been developed.

Electrode Gap: It is the distance between the electrode and the part during the process of EDM. An electro-mechanical and hydraulic systems are used to respond to average gap voltage. To obtain good performance and gap stability a suitable gap should be maintained. For the reaction speed, it must obtain a high speed so that it can respond to short circuits or even open gap circuits. Gap width is not measured directly, but can be inferred from the average gap voltage.

Duty Factor: Duty factor is a percentage of the pulse duration relative to the total cycle time. Generally, a higher duty factor means increased cutting efficiency

Performance Parameters

These parameters measure the various process performances of EDM results. Performance parameters classified into following Categories.

1. Material removal Rate: The Material removal rate is expressed as the weight of material removed from work piece over a period of machining time in minutes
2. Tool wear Rate: The TWR is calculated by using the weight loss from the tool divided by the time of machining.
3. Relative Wear Ratio: WR is the ratio of TWR/MRR and is used as a performance measure for quantifying tool-work piece material combination pairs since different material combinations gives rise to different TWR and MRR values. A material combination pair with the lowest WR indicates that the tool-work piece material combination gives the optimal TWR and MRR condition. The relative wear ratio of the work piece and tool is expressed.
4. Surface Roughness: It is the classification of surface parameter used to describe an amplitude feature, which translates to roughness of the surface finish. Of the many parameters available to quantify SR, the most commonly used in EDM are arithmetical mean surface roughness, maximum peak-to valley surface roughness and root mean square surface roughness.
5. Surface quality: Surface quality is a broad performance measure used to describe the condition of the machined surface. It comprises components such as surface roughness, extent of heat affected zone, recast layer thickness and micro-crack density.
6. Heat affected Zone: It refers to the region of a work piece that did not melt during electrical discharge but has experienced a phase transformation, similar to that of heat treatment processes, after being subjected to the high temperatures of electrical discharge.
7. **Recast layer Thickness:** The recast layer refers to the region of re-solidified molten material occurring as the top most layer of the machined surface. The recast layer is usually located above the heat affected zone.

IV. FUNCTIONS OF DI-ELECTRIC FLUID

The dielectric fluid in an EDM serves a number of functions. The dielectric oil acts as a medium through which controlled electrical discharges occur.Cool the section that was heated by the discharging effect. Flush the eroded

particles from the machining gap. Provide insulation between the electrode and the workpiece. The dielectric oil acts as a medium used to carry away the solidified EDM debris from the discharge gap to thefilter system.The dielectric oil acts as a heat transfer medium to absorb and carry away the heat generated by the discharges from both the electrode and the workpiece

Types of dielectric fluid

> Mineral Oils
> Kerosene
> Transformer Oil
> EDM Oils
> Synthetic oil

Properties & Characteristics of Dielectric Fluid

Viscosity is the property that describes a fluids resistance to flow.

The flash point for commonly used EDM dielectric oils ranges from 160º F to 255º F. Obviously for reasons of safety, the higher the flash point the better. The oil temperature at which ignition of the resulting vapor occurs is the Flash Point.

Oxidation Stability is a measure of the dielectric fluids tendency to react with oxygen.

Volatility is a measure of the tendency of a dielectric fluid to vaporize.

Acid Number is used to quantify the amount of acid present in a sample of dielectric oil.

Excessive levels of acid in dielectric oil could lead to corrosion in the dielectric system. The acid number is expressed in units of mg KOH/g, or the amount of Sodium Hydroxide necessary to neutralize the acid present in an oil sample.

V.   LITERATURE SURVEY

KuldeepOjha a et (1)have worked on material removal rate (MRR) and tool wear rate (TWR) study on the powder mixed electrical discharge machining (PMEDM) of EN-8 steel and using Response surface methodology (RSM) analysed the experiments. Peak current, pulse on time, diameter of electrode and concentration of chromium powder added into dielectric fluid of EDM were chosen as process parameters to study the PMEDM performance in terms of MRR and TWR. Experiments have been performed on newly designed experimental setup developed in laboratory. Their research work adds valuable data regarding PMEDM process. They have ended by more work piece/ powder/ electrode materials/ experimental settings combinations are needed to be investigated further for much validation of the process.

M Prabuet (2) have done experimental investigation on effect of graphite powder suspended dielectric in electric in EDM of Al-TiB2 composites. The experiments were conducted on ELEKTRAPULS spark erosion machine. Their objective is to find the effect of parameters viz, current, pulse ON-time, flushing pressure and vibration As a result, the process becomes more stable thereby improving Material Removal Rate (MRR) and reducing Tool Wear Rate (TWR). The EDM set-up is used in their experimental study is M100 model die sinking EDM machine manufactured by Electronica Machine Tools. The Parameters and their settings are in L16 orthogonal array. It uses Kerosene as the dielectric fluid. TWR slightly increases with increasing the Current. When comparing the TWR of with powder and without powder the TWR obtained for with powder is found higher.

Shriram Y. Kaldhoneet (3) have studied the influence of operating parameters of tungsten carbide on the machining characteristics such as material removal rate. The effectiveness of PMEDM process with tungsten carbide, WC-Co is evaluated in terms of the material removal rate. They have observed that copper tungsten is most suitable for use as the tool electrode in EDM of WC-Co; better machining performance is obtained generally with the electrode as the negative and the work piece as positive. They have concluded that The MRR and TWR are mainly affected by the current and powder. With mixing of silicon carbide powder MRR can be increased by 90%. Current, Pulse on time, work piece material, Powder type and Flushing Pressure significantly affect MRR. The maximum MRR is produced at 8 g/l of SiC powder for Flushing pressure 1.5 Kg/cm2.

M. A. Razak et (4) have done experiments on improving EDM efficiency with silicon carbide powder mixed dielectric fluid PMEDM works gradually at low pulse energy and distributes evenly the powder in machining area. PMEDM may lead to improve machined part surface finish, improve material removal rate (MRR) and reduce tool wear rate (TWR). Further investigations on powder concentration and powder particles size for silicon carbide (SiC) PMEDM are proposed to conduct. Number of experiments were conducted is based on Taguchi orthogonal array with three level and two factors. The outcomes obtained were capable to increase MRR, improve surface finish, reduce TWR, reduce machining time and reduce machining cost. The objectives of their research work are: To investigate the influence of PMEDM in machining premium stainless mold steel material in terms of MRR, TWR and Ra. Their results have given information on: The influence of PMEDM in machining Stavax material in terms of MRR, TWR and Ra. The optimum powder concentration and size of powder particles to achieve the highest efficiency of EDM

G. Bharath Reddy et (5) presented the outcomes of an experimental analysis carried out to study the effect of micro-sized metal powders, when they are mixed to the dielectric fluid, during Electric Discharge Machining (EDM) of different

steels. The work piece material, peak current, pulse on time, duty factor, gap voltage and mixing of fine metal powders(copper and aluminium) in dielectric fluid are taken as process input parameters. Material removal rate and Surface Roughness were taken as output parameters to measure the process efficiency. Powder Mixed EDM makes discharge collapse easier, increases the discharge gaps and expands the discharge channel, and finally forms uniformly distributed large and shallow craters on the work piece.

R.A.Prajapatiet (6) experimented the effect of Silicon Dioxide (SiO2) powder mixing into the dielectric fluid of EDM on machining characteristics of EN-8 with three input parameters Peak current, pulse on time and concentration of powder. Analysis was carried out for surface roughness. The result outcomes identified the important parameters and their effect on SR of En-8 in the presence of SiO2 in a kerosene dielectric of EDM. Analysis was showed that the peak current and pulse on time have higher contribution toward surface roughness. They have concluded that PMEDM is not preferable. Peak current and pulse on time are the most influential parameters for reducing surface quality. The optimum levels of various process parameters obtained in their experimental work are: Peak current = 9 A, Powder concentration = 0 g/lit and 25 μs pulse on time for better surface quality

VedParkashet (7) have conducted the experiments on the effect of powder mixed dielectric on tool wear rate (TWR) in EDM has been observed. Experiments were designed using Taguchi method and appropriate Orthogonal Array and experiments have been performed as per the set of experiments designed in the orthogonal array. Signal to Noise ratios are also calculated to analyze the effect of PMEDM more accurately. They have concluded that the PMEDM (Powder Mixed Electric Discharge Machining) has significant effect on the tool wear rate. The Tool Wear Rate is higher with Copper as an additive and less when Graphite is used in dielectric. As current is directly proportional to discharge energy and pulse on-time. With increase in current and pulse on-time, tool wear rate also increases.

Gurule N. B. et (8) experimented the effect of tool rotation on mrr during powder mixed EDM of die steel They have concluded that Current, on time, tool material, tool rpm and powder concentration significantly affect MRR. The suspension of Al powder into dielectric enhances MRR. The maximum MRR is produced at 4 g/l of Al powder, 900 tool rpm with Cu tool. Flushing shows least effect on MRR. Finally, it was concluded that Al powder and rotary tool have impact to great extent on the MRR of die steel. Their study shows future scope and potential for the improvements in the EDM field.

AbhishekAbrol et (9) studied the effect of chromium powder mixed dielectric fluid on machining characteristics of AISI D2 die steel has been studied. Peak current, pulse on time, pulse off time, concentration of powder are the process parameters. The process performance is measured in terms of material removal rate (MRR), tool wear rate (TWR) and surface roughness (SR). The research outcome will identify the important process parameters that maximize MRR, minimize TWR and SR. The design of experiment was undertaken using Taguchi method. Both the performance data show an increasing pattern with increase in current for any other parameter. Surface roughness is mainly affected by the pulse-off time as per the main effects plot for SR. Surface Roughness is higher with the increase in pulse-off time.

Nimo Singh Khundrakpamet (10) have studied the effect of polarity on Different EDM (EDM, Dry-EDM and Powder Mixed EDM) has been studied in different polarity and dielectric mediums. It was observed experimentally that increase in tool hole diameter increase Material Removal Rate (MRR) and Tool Wear Rate (TWR). Dry-EDM has negligible TWR. In reverse polarity MRR is very low except Dry-EDM. They have concluded that increase in tool hole diameter increase both MRR &TWR. The dry EDM gives negligible tool wear rate. Tool Hole Diameter has more effective on dry EDM in both the polarity. Their Experiment is more suggested to study different powder mixed to dielectric medium for better MRR and TWR.

Mahendra G. Rathiet (11) experimented the Effect of Powder Mixed dielectric in EDM of Inconel 718. The effect of various powder mixed in dielectric is studied input parameters like Duty cycles, current, pulse on time and powder media in that Silicon carbide, Aluminium oxide, Graphite powder used. An analysis of variance (ANOVA) is used to present the influence of process parameters on material removal rate, tool wear rate. Results obtained by Taguchi method and by ANOVA method, are compared and found that they match closely with each other. As the MRR is depends mostly on current. Current carrying capacity of any material depends on it electric conductivity. Here Graphite is having highest electric conductivity than Aluminium oxide and Silicon carbide and therefore MRR is higher in case of Graphite powder.

MarekRozeneket (12) The EDM characteristics obtained using hydrocarbon dielectric (kerosene) and mixture deionized water with abrasive powder have been compared. The relationship between surface roughness parameters, material removal rate and operating parameters of EDM have been determined for different kind of powder and its concentration in kerosene/water. The investigation results were showed that there are chances for replacing the conventional dielectric with water and that would imply considerable economic and ecology advantages. The investigation results were showed that there are chances for replacing the conventional dielectric with powder suspended deionized water and that would imply considerable economic and ecology advantages.

B Govindharajanet (13) focused on performance of nickel mixed with kerosene as dielectric medium in electrical discharge machining of Monel 400TM. The optimum range of nickel powder, Graphite powder 6g mixes with the dielectric medium of kerosene servotherm (75:25) were developed experimentally. They have concluded that the experimentally observed performance of kerosene-servotherm of different proportion of nickel powder found that better machining output in EDM of Monel 400TM. The surface smoothness and diameteral accuracy reported by kerosene servotherm of 8g nickel mixed dielectric medium gives better result. After than drawn all graphs which shows the optimum proportion mixture of nickel powder influences the MRR, TWR and OC.8, 6g of nickel and graphite powders are mixed with kerosene-servotherm (75:25) gives better results of MRR, TWR and OC.

KuldeepOjha et (14) have presented parametric optimization for material removal rate (MRR) and tool wear rate (TWR) study on the powder mixed electrical discharge machining (PMEDM) of EN-8 steel has been carried out. Response surface methodology (RSM) has been used to plan and analyse the experiments. Average current, duty cycle, angle of electrode and concentration of chromium powder added into dielectric fluid of EDM were chosen as process parameters to study the PMEDM performance in terms of MRR and TWR. Experiments have been performed on newly designed experimental setup developed in laboratory. They have concluded that the quantitative analysis of machinability of EN-8 steel in PMEDM process was carried out.

VI.   EXPERIMENTATION

Some of the experiments have been conducted to find out the quantum of the best concentration which is to be mixed up to get the better results to proceed towards the main experimentation. As a part of it, it is being selected to conduct experiments with 1 gram powder as incremental factor starting with 1 gram till 17 grams. Firstly it was tested to find out the Material removal rate in more than 30 experiments for which two trials were performed for each experiment. Then the values of the MRR in two trials were shown in the following table along with the average value of the each concentration.

PC (in Grams)	MRR		Avg MRR
	Trial1	Trial2	
1	4.143	3.9673	4.05515
2	5.761	6.564	6.1625
3	6.85	7.19	7.02
4	5.27	7.88	6.575
5	9.1089	8.8916	9.00025
6	9.3241	9.1652	9.24465
7	5.5338	9.417	7.4754
8	9.1726	9.8272	9.4999
9	9.7392	9.7016	9.7204
10	9.4563	9.4538	9.45505
11	9.004	9.18	9.092
12	9.1231	9.0142	9.06865
13	9.1828	8.21	8.6964
14	9.3452	8.234	8.7896
15	9.6294	8.115	8.8722
16	9.3412	8.165	8.7531
17	8.2031	8.224	8.21355

Graphs are being drawn between the powder concentration and material removal rate for the values obtained in two trails and the average of it even. The following figures shows the same

1. PC Vs MRR

2. PC Vs MRR

Avg MRR
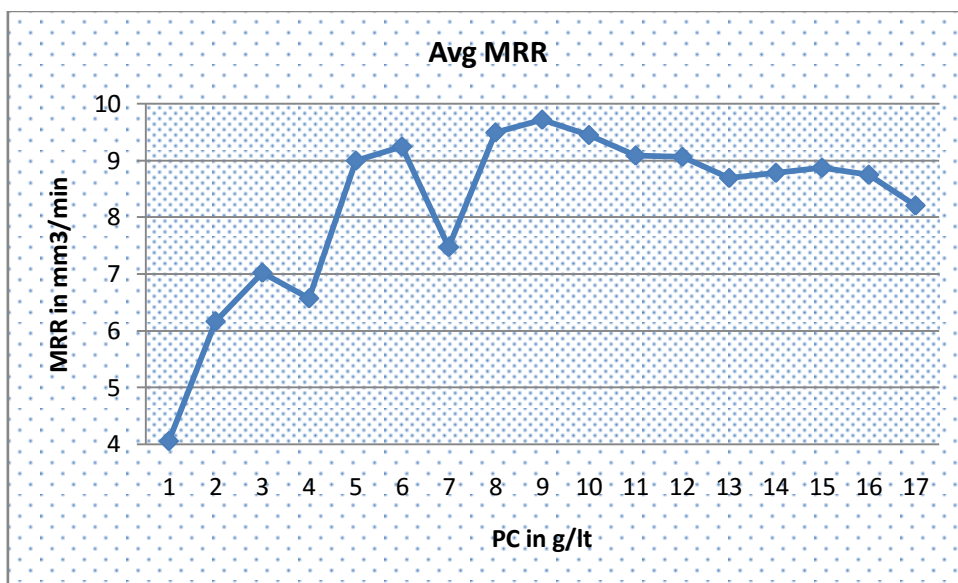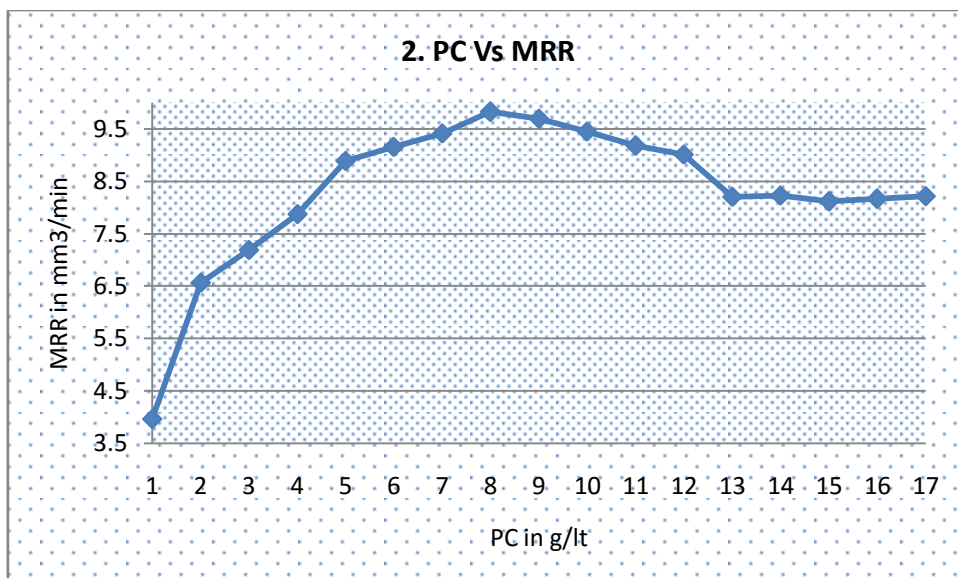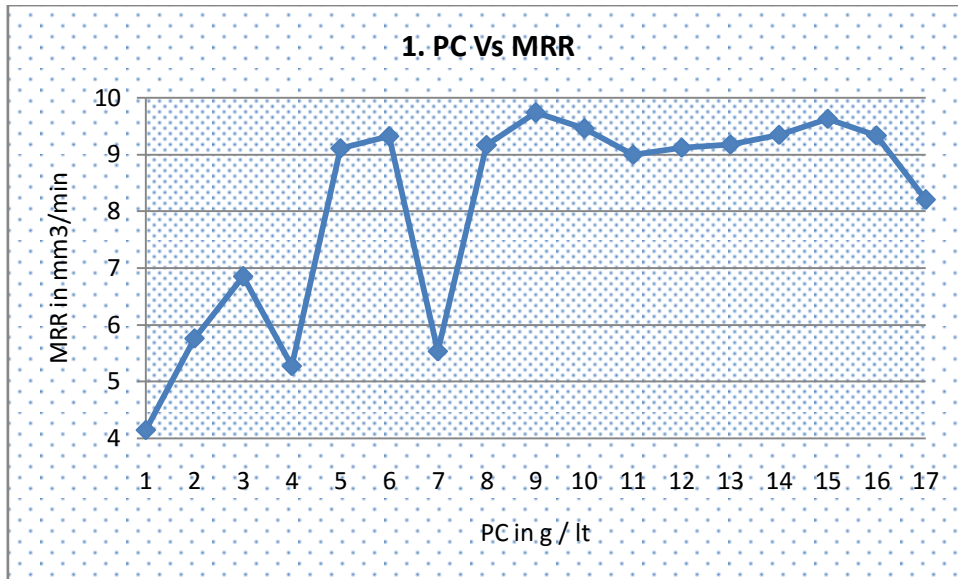
Secondly, the surface roughness was measured in two different trails with the variation of the powder concentration right from 1 gram / litre to 17 grams / litre. The following table exhibits the same along with the average value of surface

roughness followed by the graphs between the quantum of the powder concentration and the surface rough ness in three diagrams indicates the trail 1, trial 2 and average values respectively

PC (In grams)	SR		Avg SR
	Trial1	Trial2	
1	4.512	4.457	4.4845
2	4.634	4.539	4.5865
3	4.768	5.6	5.184
4	4.999	4.244	4.6215
5	5.067	5.003	5.035
6	4.873	4.924	4.8985
7	4.585	4.321	4.453
8	4.865	4.645	4.755
9	5.209	4.551	4.88
10	4.897	4.568	4.7325
11	4.7181	4.582	4.65005
12	4.5426	4.623	4.5828
13	4.362	5.691	5.0265
14	4.213	5.321	4.767
15	3.9591	4.932	4.44555
16	4.6541	4.967	4.81055
17	5.1	5.293	5.1965

Graphs are being drawn between the powder concentration and surface roughness for the values obtained in two trails and the average of it even. The following figures shows the same
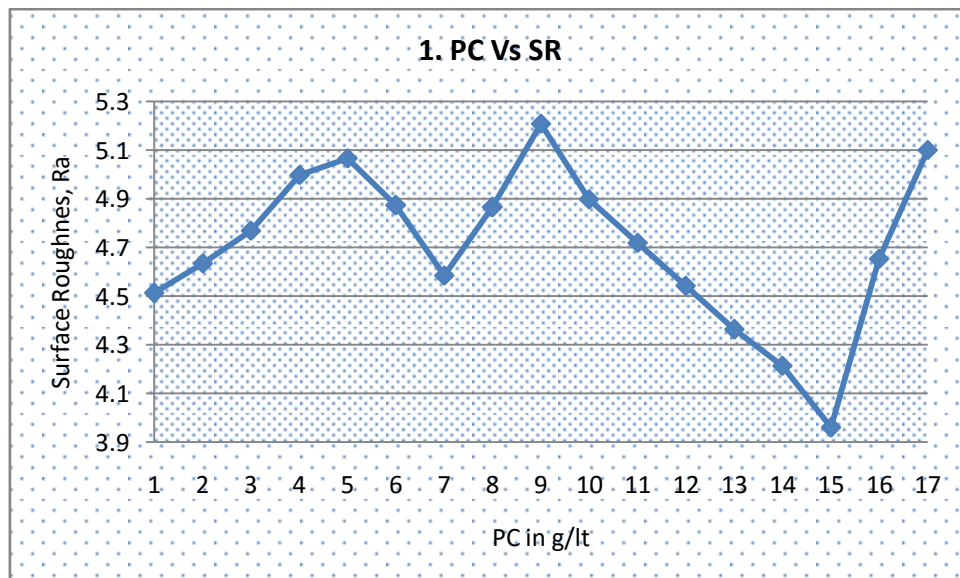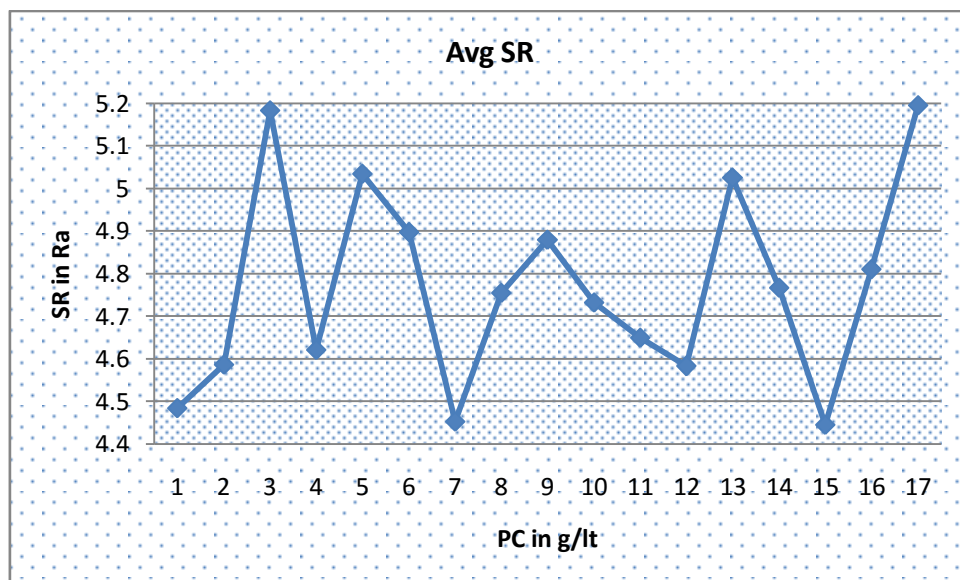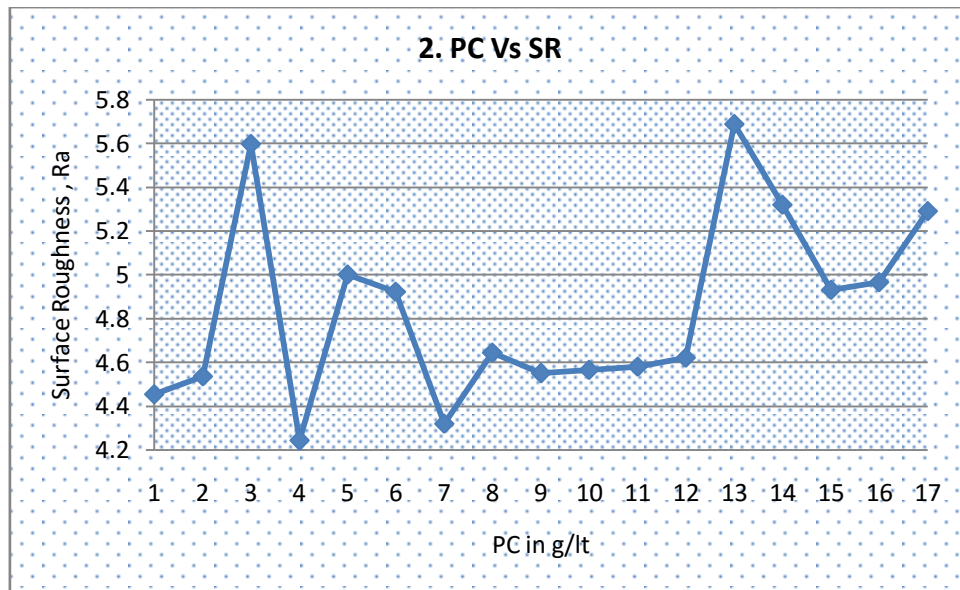
Lastly, the third parameter of the PMEDM is tool wear rate is obtained for the same number of experiments for the same powder concentration variations. The table given below shows the three values i.e. trial1, trial2 and average value of tool wear rate followed by the three graphs between the powder concentration and tool wear rate for the three values respectively

Powder Concentration (In Grams)	TWR		Avg TWR
	Trial1	Trial2	
1	1.0648	0.9646	1.0147
2	0.5472	0.6145	0.58085
3	0.6144	0.5819	0.59815
4	0.7154	0.5638	0.6396
5	0.8462	0.8363	0.84125
6	0.7245	0.9275	0.826
7	0.323	1.0218	0.6724
8	0.734	0.9123	0.82315
9	1.087	1.0667	1.07685
10	0.532	0.5247	0.52835

11	0.524	0.5645	0.54425
12	0.567	0.5687	0.56785
13	0.5825	0.5796	0.58105
14	0.6438	0.6342	0.639
15	0.684	0.6985	0.69125
16	0.623	0.7142	0.6686
17	0.592	0.97	0.781

Graphs are being drawn between the powder concentration and tool wear rate for the values obtained in two trails and the average of it even. The following figures shows the same
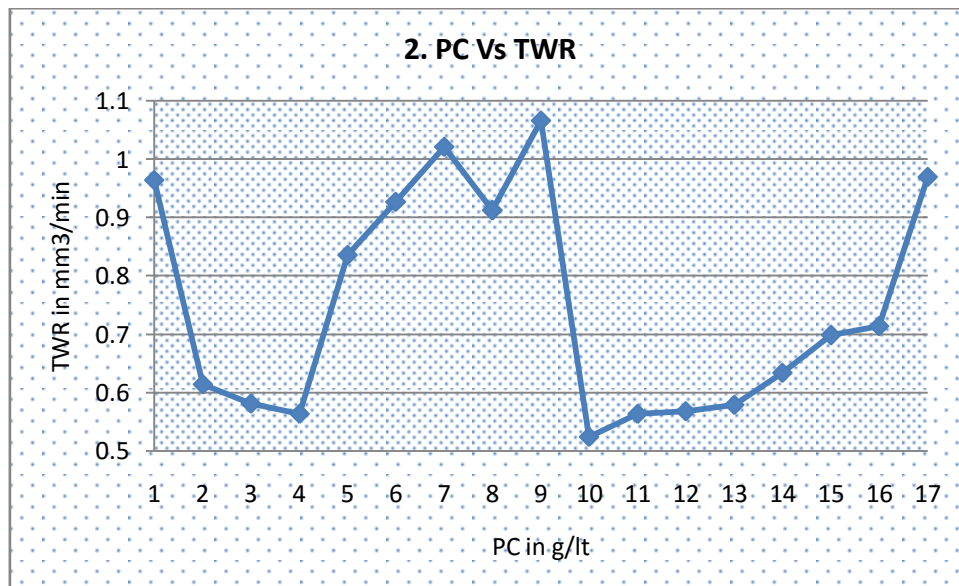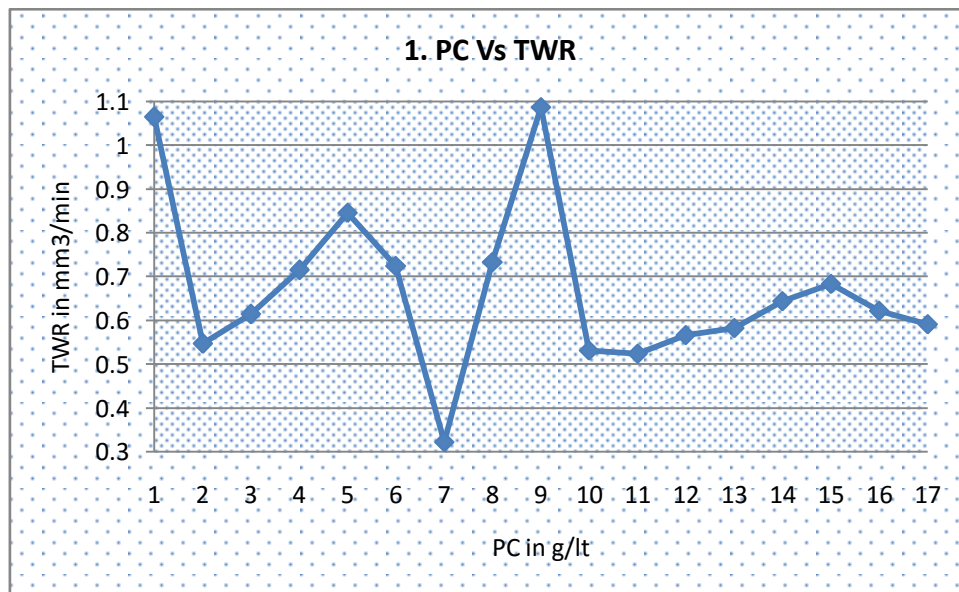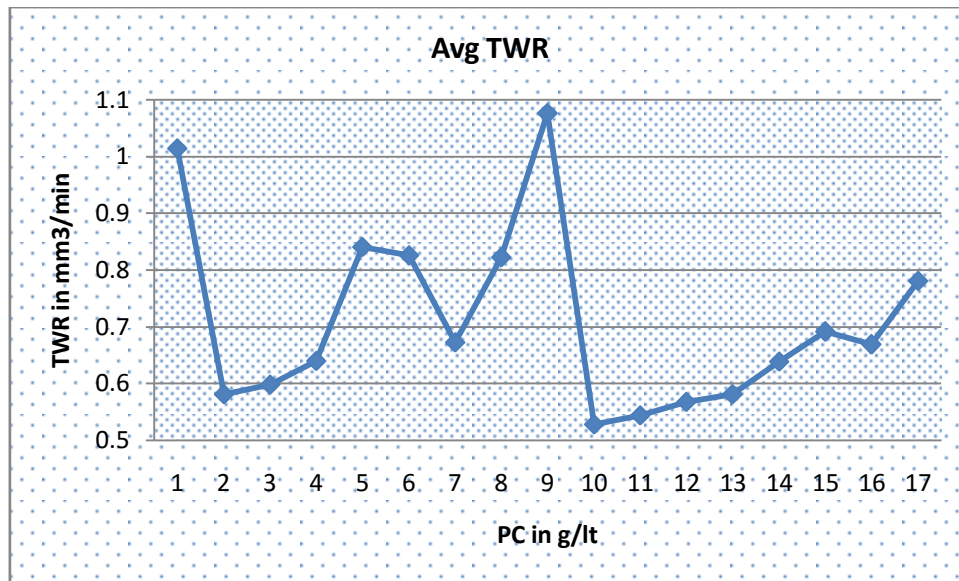
VII.   CONCLUSION

As per the requirement 34 experiments were conducted to find out the each parameter. In the three machining parameter values are obtained when the concentration of the powder is taken as 1-17g/lt at Discharge current – 20 amp, Pulse on time – 65 micro seconds and Pulse off time – 36 micro seconds.Average of each concentration has been calculated and then the relevant graphs were plotted.

VIII.   REFERENCES

(1) KuldeepOjha a, R. K. Garg a, K. K. Singh," Experimental Investigation and Modeling of PMEDM Process with Chromium Powder Suspended Dielectric", International Journal of Applied Science and Engineering 2011. 9, 2: 65-81
Int. J. Appl. Sci. Eng., 2011. 9, 2 65

(2) M Prabu, G Ramadoss, C Senthilkumar, R Boopathi, S Magibalan, "EXPERIMENTAL INVESTIGATION ON EFFECT OF GRAPHITE POWDER SUSPENDED DIELECTRIC IN ELECTRIC DISCHARGE MACHINING OF AL-TIB2 COMPOSITES", National Conference On Recent Trends And Developments In Sustainable Green Technologies Journal of Chemical and Pharmaceutical Sciences www.jchps.com ISSN: 0974-2115 JCHPS Special Issue 7: 2015 NCRTDSGT 2015 Page 52

(3) Shriram Y. Kaldhone , Mukund V. KavadeUmashankarRawat," Effect of Powder Mixed Dielectric on Performance Measures of EDM for Tungsten Carbide", International Journal of Innovative Research in Advanced Engineering (IJIRAE) ISSN: 2349-2163 Volume 1 Issue 10 (November 2014), IJIRAE, Page - 106

(4) M. A. Razak, A. M. Abdul-Rani, and A. M. Nanimina," Improving EDM Efficiency with Silicon Carbide Powder-Mixed Dielectric Fluid", International Journal of Materials, Mechanics and Manufacturing, Vol. 3, No. 1, February 2015.

(5) G. Bharath Reddy, V.S.P. Vamsi, "PARAMETRIC ANALYSIS ON POWDER MIXED ELECTRIC DISCHARGE MACHINING OF VARIOUS STEELS USING TAGUCHI METHOD", International Journal of Advance Research In Science And Engineering http://www.ijarse.com, IJARSE, Vol. No.4, Special Issue (02), February 2015 ISSN-2319-8354(E)

(6) R.A.Prajapati, Haresh Patel," Experimental Investigation of Powder mix EDM using Silicon Dioxide as a Powder additive for Surface Roughness", International Journal of Advance Engineering and Research Development Volume 2, Issue 1, January -2015

(7) VedParkash, Deepak Kumar," Effect of Powder Mixed Dielectric Medium on Tool Wear Rate in EDM",Volume : 2 | Issue : 2 | Feb 2013 • ISSN No 2277 – 8179

(8) Gurule N. B.1, Nandurkar K. N," Effect of Tool Rotation on Material Removal Rate during Powder Mixed Electric Discharge Machining of Die Steel", International Journal of Emerging Technology and Advanced Engineering Website: www.ijetae.com (ISSN 2250-2459, Volume 2, Issue 8, August 2012) 328

(9) AbhishekAbrol, Sunil Sharma," EFFECT OF CHROMIUM POWDER MIXED DIELECTRIC ON PERFORMANCE CHARACTERISTIC OF AISI D2 DIE STEEL USING EDM", IJRET: International Journal of Research in Engineering and Technology eISSN: 2319-1163 | pISSN: 2321-7308 Volume: 04 Issue: 01 | Jan-2015, Available @ http://www.ijret.org 232

(10) Nimo Singh Khundrakpam, Amandeep Singh, 3Jasvir Singh, 4Som Kumar," Experimentally Study the Effect of Polarity and Tool Hole Diameter in EDM Responses", International Journal of Science, Engineering and Technology Research (IJSETR), Volume 3, Issue 4, April 2014

(11) Mahendra G. Rathi, Deepak V. Mane," Study on Effect of Powder Mixed dielectric in EDM of Inconel 718", International Journal of Scientific and Research Publications, Volume 4, Issue 11, November 2014 1 ISSN 2250-3153 www.ijsrp.org

(12) MarekRozenek, Jerzy Kozak and LucjanDabrowski," Electrical Discharge Machiningin Dielectric-Powder Media", Warsaw University of Technology, POLAND

(13) B.Govindharajan, P.Meivel, C.Chelladurai, K.Avinaash," PERFORMANCE AND ANALYSIS OF NICKEL MIXED KEROSENE SERVOTHERM IN EDM OF MONEL 400TM", Journal of Innovative Research and Solution (JIRAS)- A unit of UIIRS Print- ISSN: 2320 1932 / Online ISSN – 2348 3636 Volume1 – Issue No.1 – Jan – Jun 2014 348

(14) KuldeepOjha, R. K. Garg1, K. K. Singh," Parametric Optimization of PMEDM Process using Chromium Powder Mixed Dielectric and Triangular Shape Electrodes", Journal of Minerals & Materials Characterization & Engineering, Vol. 10, No.11, pp.1087-1102, 2011 1087.

Investigations into the Effect of Exhaust Gas Recirculation (EGR) Adopting Different Air Filters on Performance and Emissions of DI Diesel Engines

P. Ravi chander[1], Dr. B. Sudheer Prem Kumar[2], Dr. K. Vijaya Kumar Reddy[3]

[1] Research Scholar, JNTUH, India.
[2] Professor, Mechanical Engineering Department, JNT University, Hyderabad, India.
[3] Professor, Mechanical Engineering Department, JNT University, Hyderabad, India.

Abstract: *The exhaust gas recirculation technique has proven a better solution to reduce NOx emission in diesel engines. EGR method is taken for the study to investigate the engine behavior on its performance and emissions. The paper the performance characteristics such as brake thermal efficiency(BTE),volumetric efficiency(η_{vol}), exhaust gas temperature(EGT), the exhaust gas emissions such as CO, CO_2, NOx, UBHC, O_2, and smoke are presented and discussed. The discussion is presented and supported by experimental results. In the experimentation variation in EGR percentage for different air filters is selected for the study. The engine is run by adopting one type of filter at once at different loads for different percentages of EGR such as 5%, 10% and 15%.*

Key words*: Diesel engine, Air filters, Emissions, EGR.*

I.   Introduction:

Unlike SI engine the CI engine emits smokes and particulate matter along with CO, HC & NOx. Though CO_2 is not an emission for local environment, but as a greenhouse gas, it contributes to global warming. These emissions severely affect human health and the lives of animal and plant. The severity of emission effects depend on their concentration and the time of exposure simultaneously. The actual magnitudes of the emissions from SI and CI engines vary due to the difference in their mixture preparation and combustion mechanisms. Air filters play an important role in minimizing exhaust specially particulate matter.

The air filter separation efficiency was studied for particle size of 50 and 100μm, it was found to be 94.4%. The study was made with both experimental and simulation methods. Pressure drop in the analysis was well matched with experimental results [1]. The air filters (SAE J726 & J1669) used in automotive cabin and engine are investigated for their standards and filtration behaviors. The actual air filter performance and their definitions are related to the real time conditions. In the investigation relation between primary function of the air filter and defined one are analyze and the changes for the recommended [2]. The air filter design is critical because of the factors like limited space availability in the induction system for higher velocity of aerosol passing in the primary air filter but this increased velocity causes re-trapping of dust particles and increased dust penetration through the filter [3]. The frequency of replacing the air filter depends on its optimum usage which can reduce its cost and extended its life. The experiments conducted in optimizing geometrical configuration of intake system to keep reduced pressure drop and improved utilization of filter area. CFD analysis was made to improve air flow characteristics through the filters. An eccentricity was suggested in the filter element The eccentricity place a role of maintaining air velocity at constant in annular portion. This constant value of velocity resulted in lowering pressure drop was found to be higher for an eccentricity placed at 15mm distanced from the inlet [4]. When Exhaust Gas in which the Recirculation (EGR) on the performance and emissions of a single cylinder naturally aspirated constant speed diesel engine is studied. The results showed that EGR would be one option to reduce the nitrous oxide emissions, but with a rise in EGR rate the CO, UHC concentrations in the engine exhaust are increased [5 & 6]. When the effects of hot and cold EGR methods on emissions and efficiency of the engine is provided for obtaining different EGR methods in which the performance parameters were studied with and without exhaust gas recirculation of different methods with 10%, 15% and 20% of EGR[7& 8]. The technology adopted for the reticulated foam multilayer filters calls for no servicing and maintenance throughout the life of the vehicle i.e, 150000 miles. The technology adopted for these type of filters facilitates sum unique advantages compare to traditional air filters [9]. The restriction for air flow will be naturally higher in old filter than that of new [10]. When investigation made on air filters and their traps in different locations with different vegetation zones to study the efficiency of air filters used in motor cars. It was revealed that on efficiency filter traps will capture only the airborne particles. The contamination due to vegetation is also consider along with animal derived debris [11]. In this paper the performance characteristics and the exhaust gas emissions of stationary diesel engine are presented and discussed which is supported by

experimental results. In the experimentation variation in EGR percentage for different air filters is selected for the study. The engine is run by adopting one type of filter at once at different loads for different percentages of EGR such as 5%, 10% and 15%.

II. Experimental Setup:

The experimentation is carried out on a single cylinder, four stroke, water cooled, DI engine. The test set up is developed to carry out set experimentation procedures. The layout of the experimental set up is shown in the Fig. 2.1. and Fig. 2.2 shows Photographic View of Computerized Experimental Diesel Engine Setup.
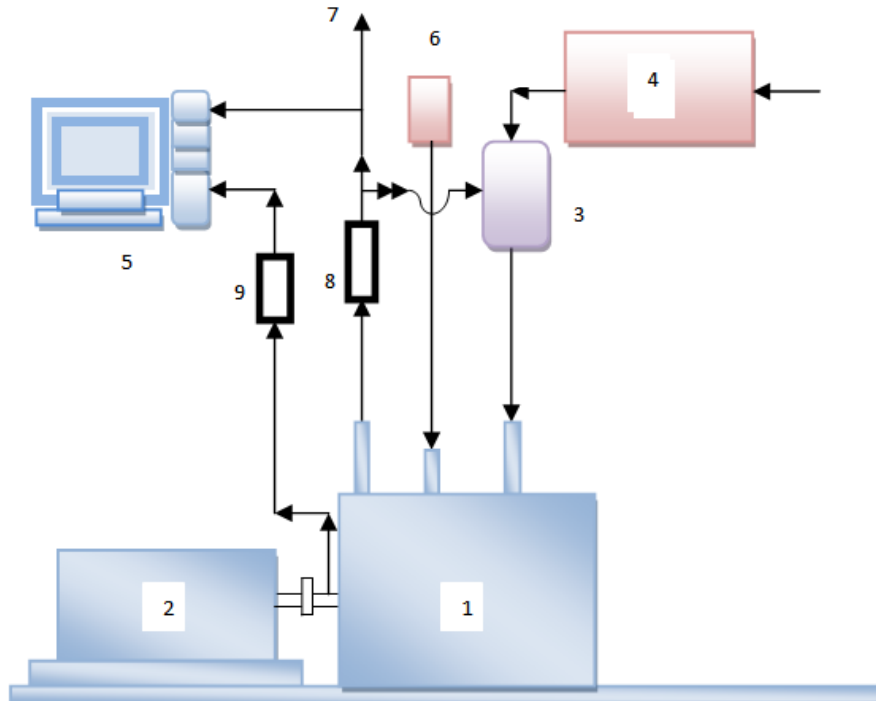
Fig: 2.1 Layout of Experimental Set up

1) Engine, 2) Dynamometer, 3) Air Filter Housing, 4) Air surge tank, 5) Computerized data acquisition, 6) Diesel fuel tank, 7) Exhaust Manifold, 8) Exhaust gas recirculation unit, 9) Crank angle encoder.

Fig: 2.2 Photographic View of Computerized Diesel Engine Setup with Air Filter Housing Arrangements and EGR Facility

Table.1 Engine specification:

Make	Kirloskar AV-1
Engine type	4- stroke single cylinder diesel engine(water cooled)
Rated Power	3.7KW, 1500rpm
Bore & stroke	80mmx110mm
Compression rate	16.5:1 (Variable From 14.3to20)
Cylinder Capacity	553cc
Dynamometer	Electrical-AC alternator

2.2 Experimentation Procedure

The experiments are conducted on test engine in different stages. The engine is experimented without air filter considering as baseline operation to make the comparison study. In second stage the engine is run by adopting the air filter of type 1 (AFM1) - Model No. NF 1004 both with new and clogged filters one after the other. In third stage the engine is run by adopting the air filter of type 2 (AFM2) - Model No. NF615 both with new and clogged filters one after the other. In fourth stage the engine is run by adopting the air filter of type 3 (AFM3) - Model No. NF560 both with new and clogged filters one after the other. . In fifth stage the engine is run by adopting the air filter of type 4 (AFM4) - Model No. 0313AC2261N both with new and clogged filters one after the other.

Fig: 2.4(a) AFM1 (OLD& NEW)

Fig: 2.4 (b) AFM2 (OLD& NEW)

Fig: 2.4 (c) AFM3 (OLD& NEW)

Fig: 2.4 (d) AFM4 (OLD& NEW)

III.   Results And Discussion

3.1 Performance Characteristics

The variation of brake thermal efficiency according to change in brake mean effective pressure of the engine for different filters, AFM1,AFM2, AFM3 and AFM4 with varying percentages of exhaust gas recirculation is presented and discussed below. The exhaust gas percentage is varied like 5, 10 and 15 percentages in the inlet.

3.1.1 Brake Thermal Efficiency (BTE)
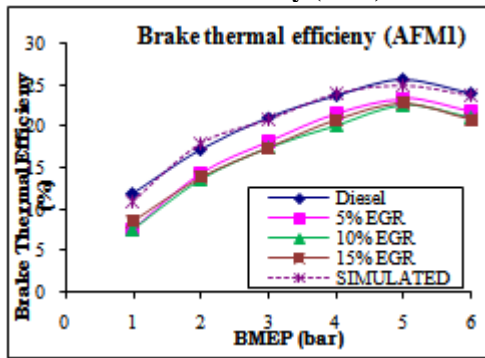
Fig: 3.1.1 (a)
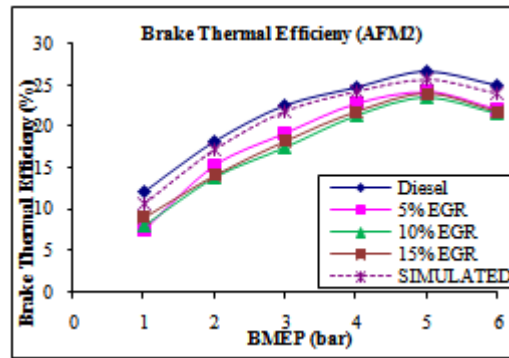
Fig: 3.1.1 (b)
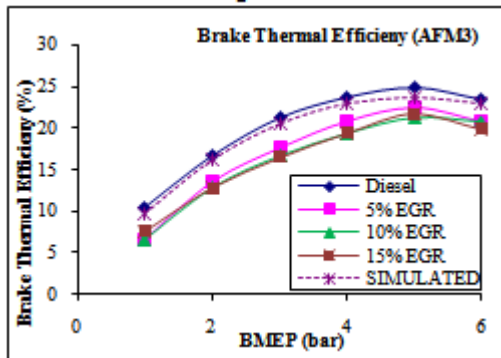
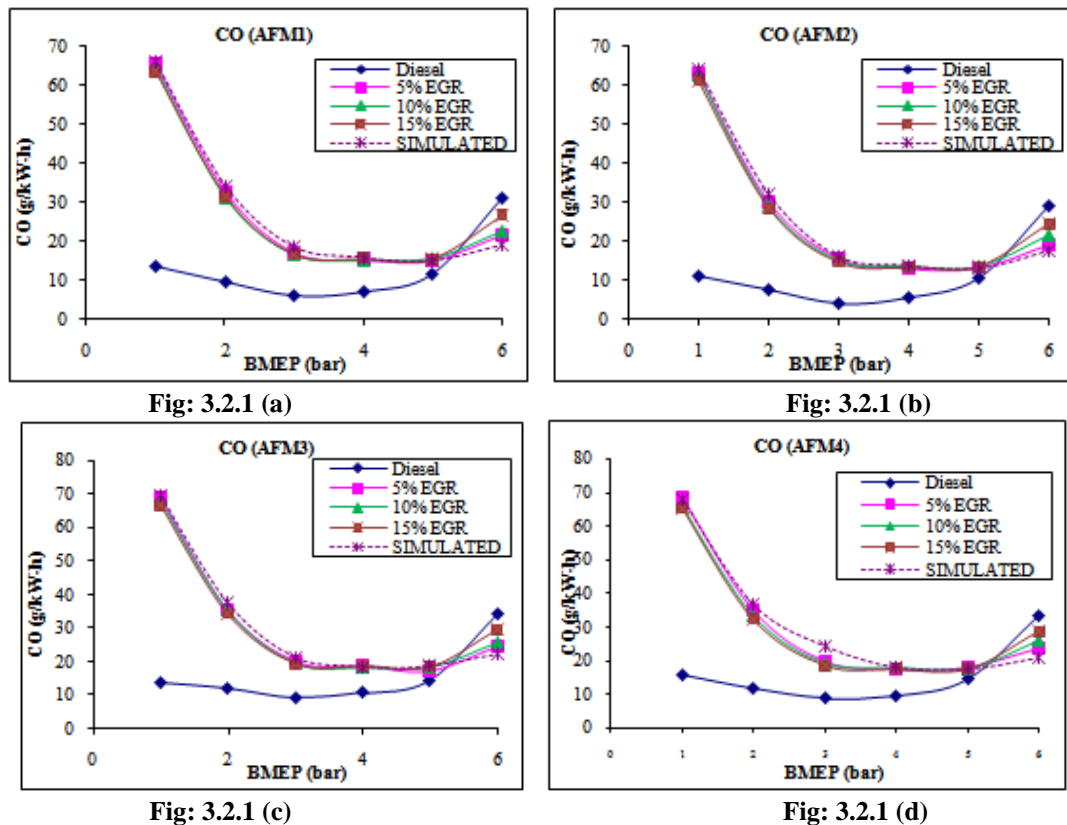Fig: 3.1.1 (c)
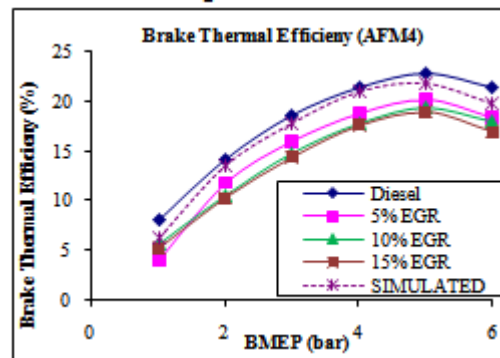
Fig: 3.1.1 (d)

Fig: 3.1.1(a) to **3.1.1(d)**   Effect of EGR percentage on BMEP adopting AFM1, AFM2, AFM3 & AFM4

The figure 3.1.1(a) depicts the effect of percentage of exhaust gas recirculation on brake thermal efficiency for the filter AFM1. For each percentage of EGR the graphs are plotted against BMEP the simulated values are also compared. As the percentage of EGR increases the brake thermal efficiency found to be decreasing when compared to diesel fuel operation without EGR. The variation in brake thermal efficiency is found to be 10, 12 and 15% for 5, 10 and 15% of EGR. The simulated values are found to be validated for diesel operation. Brake thermal efficiency at bmep 5bar was found to be 23.42, 22.56 and 22.91 for 5, 10, and 15% of EGR respectively.

The figure 3.1.1(b) depicts the effect of percentage of exhaust gas recirculation on brake thermal efficiency for the filter AFM2. For each percentage of EGR the graphs are plotted against BMEP the simulated values are also compared. As the percentage of EGR increases the brake thermal efficiency found to be decreasing when compared to diesel fuel operation without EGR. The variation in brake thermal efficiency is found to be 13, 15 and 18% for 5, 10 and 15% of EGR. The simulated values are found to be validated for diesel operation. Brake thermal efficiency at bmep 5bar was found to be 24.23, 23.45 and 23.92 for 5, 10, and 15% of EGR respectively

The figure 3.1.1(c) depicts the effect of percentage of exhaust gas recirculation on brake thermal efficiency for the filter AFM3. For each percentage of EGR the graphs are plotted against BMEP the simulated values are also compared. As the percentage of EGR increases the brake thermal efficiency found to be decreasing when compared to diesel fuel operation without EGR. The variation in brake thermal efficiency is found to be 12, 14 and 16% for 5, 10 and 15% of EGR. The simulated values are found to be validated for diesel operation. Brake thermal efficiency at bmep 5bar was found to be 22.93, 21.24 and 21.67 for 5, 10, and 15% of EGR respectively.

The figure 3.1.1(d) depicts the effect of percentage of exhaust gas recirculation on brake thermal efficiency for the filter AFM4. For each percentage of EGR the graphs are plotted against BMEP the simulated values are also compared. As the percentage of EGR increases the brake thermal efficiency found to be decreasing when compared to diesel fuel operation without EGR. The variation in brake thermal efficiency is found to be 12, 16 and 18% for 5, 10 and 15% of EGR. The simulated values are found to be validated for diesel operation. Brake thermal efficiency at bmep 5bar was found to be 20.14, 19.28 and 18.92 for 5, 10, and 15% of EGR respectively.

3.1.2 Volumetric Efficiency
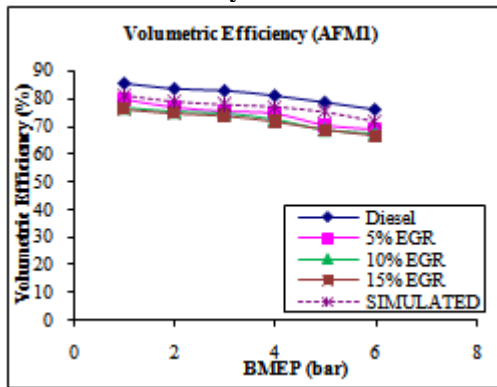
Fig: 3.1.2 (a)
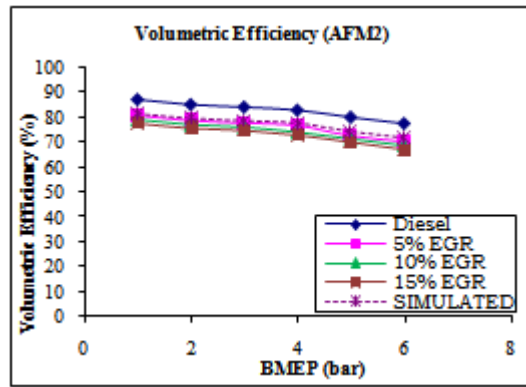
Fig: 3.1.2 (b)
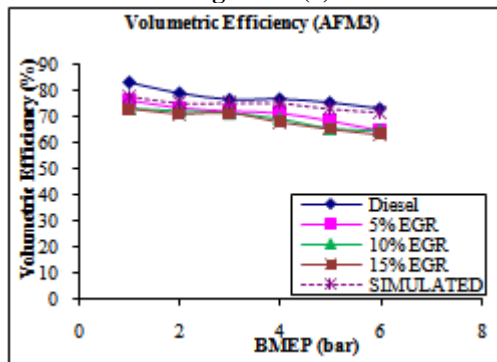
Fig: 3.1.1 (c)
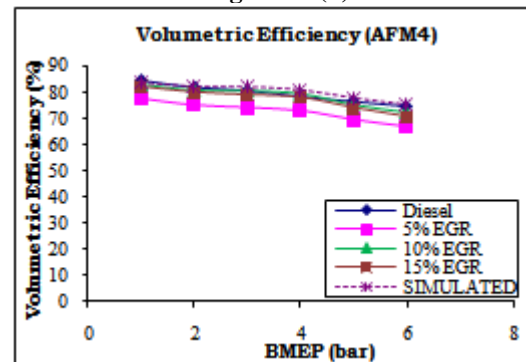
Fig: 3.1.1 (d)

Fig: 3.1.2(a) to 3.1.2(d) Effect of EGR percentage on volumetric efficiency adopting AFM1, AFM2, AFM3& AFM4

The figure 3.1.2(a) shows the effect of percentage of exhaust gas recirculation on volumetric efficiency for the filter AFM1. For each percentage of EGR the graphs are plotted against BMEP the simulated values are also compared. As the percentage of EGR increases the volumetric efficiency found to be decreasing. But when compared to diesel fuel operation without EGR, the volumetric efficiency is found to be lesser for all percentages of EGR. The decrease in volumetric efficiency is found to be 5% among 5, 10 and 15% of EGR variation. Whereas the percentage reduction in volumetric efficiency is found to be a minimum of 10% when compare to diesel fuel operation without EGR. The simulated values are found to be validated for diesel operation. Brake thermal efficiency at bmep 5bar was found to be 70.5, 69 and 68.5 for 5, 10, and 15% of EGR respectively.

The figure 3.1.2(b) shows the effect of percentage of exhaust gas recirculation on volumetric efficiency for the filter AFM2. For each percentage of EGR the graphs are plotted against BMEP the simulated values are also compared. As the percentage of EGR increases the volumetric efficiency found to be decreasing. But when compared to diesel fuel operation without EGR, the volumetric efficiency is found to be lesser for all percentages of EGR. The decrease in volumetric efficiency is found to be 2% among 5, 10 and 15% of EGR variation. Whereas the percentage reduction in volumetric efficiency is found to be a minimum of 8% when compare to diesel fuel operation without EGR. The simulated values are found to be validated for diesel operation. Brake thermal efficiency at bmep 5bar was found to be 72.9, 71.4 and 70 for 5, 10, and 15% of EGR respectively.

The figure 3.1.2(c) shows the effect of percentage of exhaust gas recirculation on volumetric efficiency for the filter AFM3. For each percentage of EGR the graphs are plotted against BMEP the simulated values are also compared. As the percentage of EGR increases the volumetric efficiency found to be decreasing. But when compared to diesel fuel operation without EGR, the volumetric efficiency is found to be lesser for all percentages of EGR. The decrease in volumetric efficiency is found to be 2.5% among 5, 10 and 15% of EGR variation. Whereas the percentage reduction in volumetric efficiency is found to be a minimum of 12% when compare to diesel fuel operation without EGR. The simulated values are found to be validated for diesel operation. Brake thermal efficiency at bmep 5bar was found to be 68.7, 65.6 and 65.6 for 5, 10, and 15% of EGR respectively.

The figure 3.1.2(d) shows the effect of percentage of exhaust gas recirculation on volumetric efficiency for the filter AFM4. For each percentage of EGR the graphs are plotted against BMEP the simulated values are

also compared. As the percentage of EGR increases the volumetric efficiency found to be decreasing. But when compared to diesel fuel operation without EGR, the volumetric efficiency is found to be lesser for all percentages of EGR. The increase in volumetric efficiency is found to be 5% among 5, 10 and 15% of EGR variation. Whereas the percentage reduction in volumetric efficiency is found to be a minimum of 8% when compare to diesel fuel operation without EGR. The simulated values are found to be validated for diesel operation. Brake thermal efficiency at bmep 5bar was found to be 69.7, 75.3 and 74 for 5, 10, and 15% of EGR respectively.

3.1.3 Exhaust gas temperature
the variation in exhaust gas temperature due to change in brake mean effective pressure of the engine for different filters, AFM1,AFM2, AFM3 and AFM4 with varying percentages of exhaust gas recirculation is presented and discussed below. The exhaust gas percentage is varied in 5, 10 and 15 percentages in the inlet.
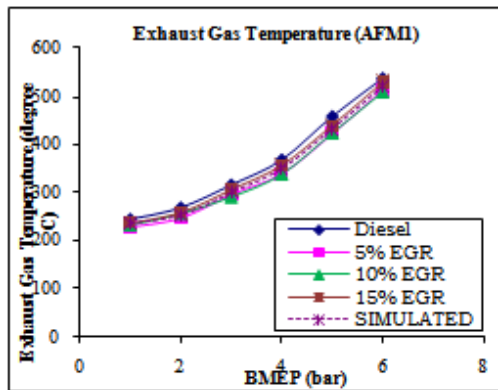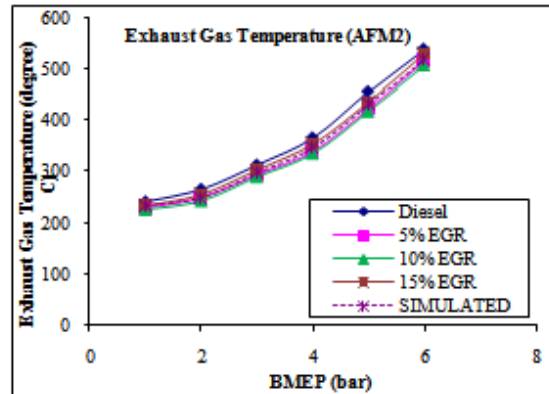
Fig: 3.1.3 (a)   Fig: 3.1.3 (b)
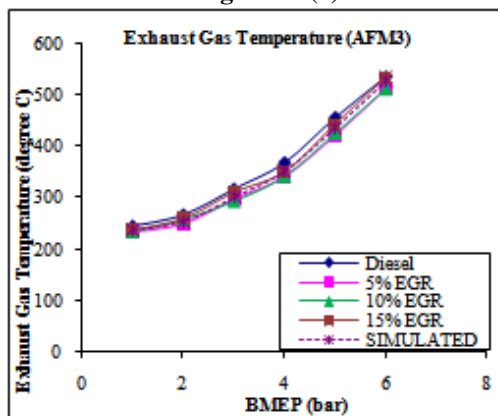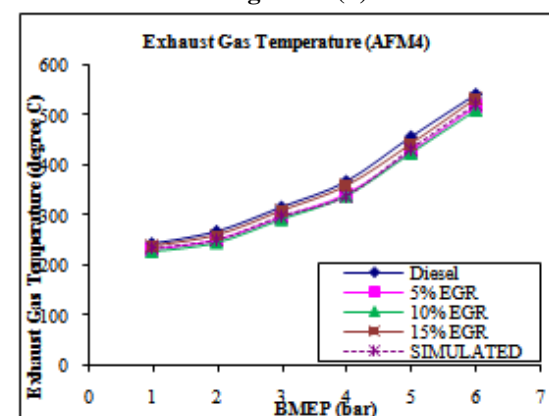
Fig: 3.1.3 (c)   Fig: 3.1.3 (d)

Fig: 3.1.3(a) to Fig: 3.1.3(d) Effect of EGR percentage on Exhaust gas temperature adopting AFM1, AFM2, AFM3 & AFM4.

In the figure 3.1.3(a) the effect of percentage of exhaust gas recirculation on exhaust gas temperature for the filter AFM1is presented. For each percentage of EGR the graphs are plotted against BMEP the simulated values are also compared. As the percentage of EGR increases the exhaust gas temperature found to be decreasing when compared to diesel fuel operation without EGR for 5 & 10 percent of EGR and later it is found to be increasing at 15% of EGR. The decrease in temperature was recorded in the range of 32, 35^{0}C. The values at BMEP 5 bar for 5 & 10 percent of EGR were 422 and 425^{0}C when compared to 458 of diesel operation without EGR. But the temperature was found increasing in the range of 20^{0}C for 15% of EGR when compared to 5 and 10% of EGR.

In the figure 3.1.3(b) the effect of percentage of exhaust gas recirculation on exhaust gas temperature for the filter AFM2 is presented. For each percentage of EGR the graphs are plotted against BMEP the simulated values are also compared. As the percentage of EGR increases the exhaust gas temperature found to be decreasing in a smaller quantity when compared to diesel fuel operation without EGR for 5 & 10 percent of EGR and later it is found to be increasing at 15% of EGR. The decrease in temperature was recorded in the range of 25, 35^{0}C. The values at BMEP 5 bar for 5 & 10 percent of EGR were 425 and 420^{0}C when compared to

456 of diesel operation without EGR. But the temperature was found increasing in the range of 18^0C for 15% of EGR when compared to 5 and 10% of EGR.

In the figure 3.1.3(c) the effect of percentage of exhaust gas recirculation on exhaust gas temperature for the filter AFM3 is presented. For each percentage of EGR the graphs are plotted against BMEP the simulated values are also compared. As the percentage of EGR increases the exhaust gas temperature found to be decreasing in a smaller quantity when compared to diesel fuel operation without EGR for 5, 10 & 15% of EGR. The decrease in temperature was recorded in the range of 30, 25 & 15^0C. The values at BMEP 5 bar were 422, 425 and 445^0C when compared to 458 of diesel operation without EGR.

In the figure 3.1.3(d) the effect of percentage of exhaust gas recirculation on exhaust gas temperature for the filter AFM4 is presented. For each percentage of EGR the graphs are plotted against BMEP the simulated values are also compared. As the percentage of EGR increases the exhaust gas temperature found to be decreasing when compared to diesel fuel operation without EGR for 5 & 10 percent of EGR and later it is found to be increasing at 15% of EGR. The decrease in temperature was recorded in the range of 30, 35^0C. The values at BMEP 5 bar for 5 & 10 percent of EGR were 428 and 425^0C when compared to 459 of diesel operation without EGR. But the temperature was found increasing in the range of 15^0C for 15% of EGR when compared to 5 and 10% of EGR.

3.2 Exhaust Gas Emissions
3.2.1 Carbon Monoxide (CO)

Carbon monoxide is the product of the combustion of a hydrocarbon fuel at intermediate stage. Its presence in the exhaust shows the incomplete or improper combustion. It depends mainly on ratio of air fuel mixture.


| Fig: 3.2.1 (a)	Fig: 3.2.1 (b)
Fig: 3.2.1 (c)	Fig: 3.2.1 (d)

Fig: 3.2.1(a) to Fig: 3.2.1(d) Effect of EGR percentage on CO adopting AFM1, AFM2, AFM3 & AFM4.

The figure 3.2.1(a) depicts the effect of percentage of exhaust gas recirculation on Carbon monoxide for the filter AFM1. For each percentage of EGR the graphs are plotted against bmep the simulated values are also compared. As the percentage of EGR increases the Carbon monoxide found at higher values when compared to diesel fuel operation without EGR. For all the percentages of EGR the carbon monoxide levels were found to be higher at all values of bmep. And the values were recorded very high at smaller values of bmep and were recorded decreasing when bmep values are increased. The values of CO levels are almost similar as the EGR percentage varied. The variation among them is less significant as they recorded in the range of 5 to 10%. But the variation is very large when operated on diesel and are noted 4 to 6 times more than the diesel operation.

The figure 3.2.1(b) depicts the effect of percentage of exhaust gas recirculation on Carbon monoxide for the filter AFM2. For each percentage of EGR the graphs are plotted against bmep the simulated values are also compared. As the percentage of EGR increases the Carbon monoxide found at higher values when compared to diesel fuel operation without EGR. For all the percentages of EGR the carbon monoxide levels were found to be higher at all values of bmep. And the values were recorded very high at smaller values of bmep and were recorded decreasing when bmep values are increased. The values of CO levels are almost similar as the EGR percentage varied. The variation among them is less significant as they recorded in the range of 5 to 10%. But the variation is very large when operated on diesel and are noted4 to 5 times more than the diesel operation.

The figure 3.2.1(c) depicts the effect of percentage of exhaust gas recirculation on Carbon monoxide for the filter AFM3. For each percentage of EGR the graphs are plotted against bmep the simulated values are also compared. As the percentage of EGR increases the Carbon monoxide found at higher values when compared to diesel fuel operation without EGR. For all the percentages of EGR the carbon monoxide levels were found to be higher at all values of bmep. And the values were recorded very high at smaller values of bmep and were recorded decreasing when bmep values are increased. The values of CO levels are almost similar as the EGR percentage varied. The variation among them is less significant as they recorded in the range of 5 to 10%. But the variation is very large when operated on diesel and are noted 5 to 7 times more than the diesel operation.
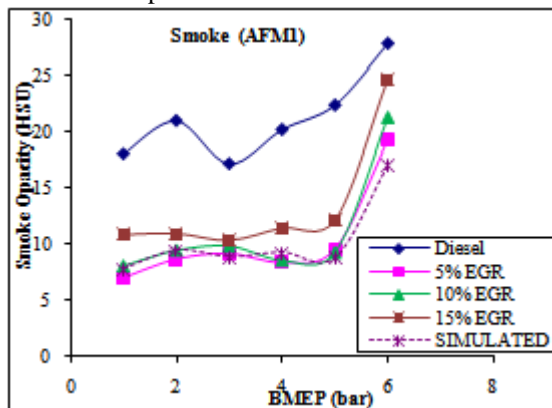
The figure 3.2.1(d) depicts the effect of percentage of exhaust gas recirculation on Carbon monoxide for the filter AFM4. For each percentage of EGR the graphs are plotted against bmep the simulated values are also compared. As the percentage of EGR increases the Carbon monoxide found at higher values when compared to diesel fuel operation without EGR. For all the percentages of EGR the carbon monoxide levels were found to be higher at all values of bmep. And the values were recorded very high at smaller values of bmep and were recorded decreasing when bmep values are increased. The values of CO levels are almost similar as the EGR percentage varied. The variation among them is less significant as they recorded in the range of 5 to 10%. But the variation is very large when operated on diesel and are noted 4 to 6 times more than the diesel operation.

3.2.2 No$_x$

The NO$_x$ percentage in the exhaust is dependent on mean values of cylinder temperature, amount of oxygen availability and residence time of the combustible mixture in the cylinder.
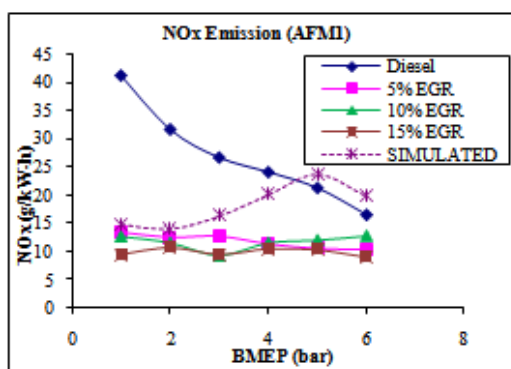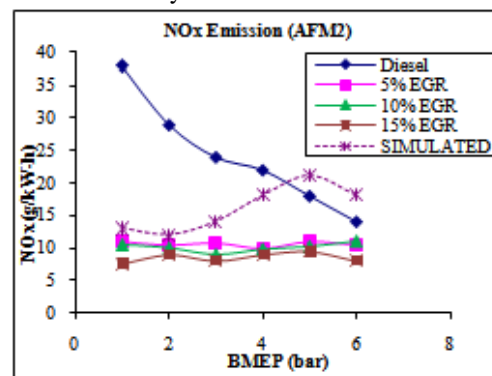

**Fig: 3.2.2 (a)**   **Fig: 3.2.2 (b)**
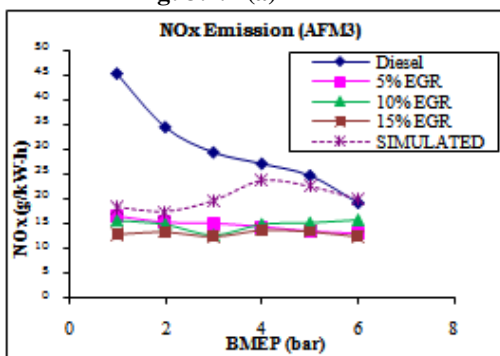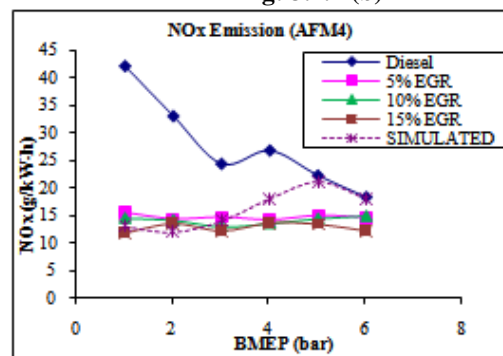
Fig: 3.2.2 (c)   **Fig: 3.2.2 (d)**

Fig: 3.2.2(a) to Fig: 3.2.2(d) Effect of EGR percentage on NO$_X$ adopting AFM1, AFM2, AFM3 & AFM4

The figure 3.2.2(a) depicts the effect of percentage of exhaust gas recirculation on NO_x for the filter AFM1. For each percentage of EGR the graphs are plotted against bmep the simulated values are also compared. As the percentage of EGR increases the NO_x found to be decreasing when compared to diesel fuel operation without EGR. For all the percentages of EGR the NO_x levels were found to be lower at all values of bmep. And the values were recorded lower at smaller values of bmep and were recorded decreasing as bmep values are increased. The values of NO_x levels are almost similar as the EGR percentage varied. The variation among them is less significant as they recorded in the range of 2 to 5%. But the variation is small when operated on diesel and are recorded 2 to 4 times lower than the diesel operation.

The figure 3.2.2(b) depicts the effect of percentage of exhaust gas recirculation on NO_x for the filter AFM2. For each percentage of EGR the graphs are plotted against BMEP the simulated values are also compared. As the percentage of EGR increases the NO_x found to be decreasing when compared to diesel fuel operation without EGR. For all the percentages of EGR the NO_x levels were found to be lower at all values of bmep. And the values were recorded lower at smaller values of bmep and were recorded decreasing as bmep values are increased. The values of NO_x levels are almost similar as the EGR percentage varied. The variation among them is less significant as they recorded in the range of 2 to 4%. But the variation is small when operated on diesel and are recorded 2 to 4 times lower than the diesel operation.

The figure 3.2.2(c) depicts the effect of percentage of exhaust gas recirculation on NO_x for the filter AFM3. For each percentage of EGR the graphs are plotted against BMEP the simulated values are also compared. As the percentage of EGR increases the NO_x found to be decreasing when compared to diesel fuel operation without EGR. For all the percentages of EGR the NO_x levels were found to be lower at all values of bmep. And the values were recorded lower at smaller values of bmep and were recorded decreasing as bmep values are increased. The values of NO_x levels are almost similar as the EGR percentage varied. The variation among them is less significant as they recorded in the range of 2 to 6%. But the variation is small when operated on diesel and are recorded 2 to 4 times lower than the diesel operation

The figure 3.2.2(d) depicts the effect of percentage of exhaust gas recirculation on NO_x for the filter AFM4. For each percentage of EGR the graphs are plotted against BMEP the simulated values are also compared. As the percentage of EGR increases the NO_x found to be decreasing when compared to diesel fuel operation without EGR. For all the percentages of EGR the NO_x levels were found to be lower at all values of bmep. And the values were recorded lower at smaller values of bmep and were recorded decreasing as bmep values are increased. The values of NO_x levels are almost similar as the EGR percentage varied. The variation among them is less significant as they recorded in the range of 2 to 5%. But the variation is small when operated on diesel and are recorded 2 to 4 times lower than the diesel operation.

3.2.3 Unburn Hydrocarbon (UBHC)

The diesel engine produces higher unburned hydrocarbons when it runs at lower loads and it is a serious problem which is to be addressed. The UBHC level indicates incomplete burning of the fuel may be due to poor fuel distribution, smaller exhaust temperatures leaner air fuel mixture pockets and crevices in the cylinder. The influence of EGR on UBHC emission for different filters AFM1, AFM2, AFM3 and AFM4 is presented in the figures from 5.3.3(a) to 3.3.3(d) and the discussion is followed.

The figure 3.2.3(a) depicts the effect of percentage of exhaust gas recirculation on UBHC for the filter AFM1. For each percentage of EGR the graphs are plotted against bmep the simulated values are also compared. As the percentage of EGR increases the UBHC found to be higher when compared to diesel fuel operation without EGR. For all the percentages of EGR the UBHC levels were found to be higher at all values of bmep. And the values were recorded very high at smaller values of bmep and were recorded decreasing when bmep values are increased. The values of UBHC levels are almost similar as the EGR percentage varied. The variation among them is less significant as they recorded below 2%. But the variation is very large when operated on diesel and are noted 4 to 6 times more than the diesel operation.

| **Fig: 3.2.3 (a)** | **Fig: 3.2.3 (b)** |

The figure 3.2.3(b) depicts the effect of percentage of exhaust gas recirculation on UBHC for the filter AFM2. For each percentage of EGR the graphs are plotted against bmep the simulated values are also compared. As the percentage of EGR increases the UBHC found to be higher when compared to diesel fuel operation without EGR. For all the percentages of EGR the UBHC levels were found to be higher at all values of bmep. And the values were recorded very high at smaller values of bmep and were recorded decreasing when bmep values are increased. The values of UBHC levels are almost similar as the EGR percentage varied. The variation among them is less significant as they recorded below 3%. But the variation is very large when operated on diesel and are noted 3 to 6 times more than the diesel operation.
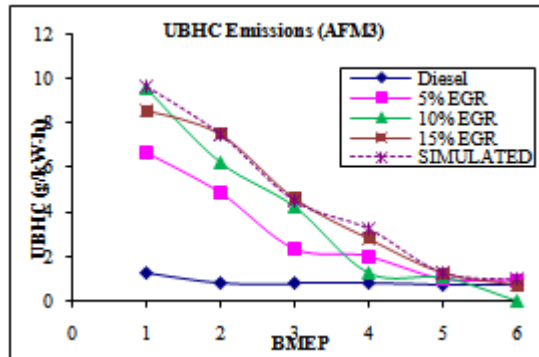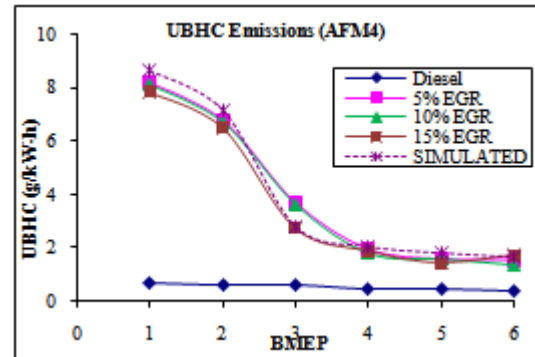
Fig: 3.2.3 (c)   **Fig: 3.2.3 (d)**
Fig: 3.2.3(a) to Fig: 3.2.3 (d) Effect of EGR percentage on UBHC adopting AFM1, AFM2,AFM3 & AFM4

The figure 3.2.3(c) depicts the effect of percentage of exhaust gas recirculation on UBHC for the filter AFM4. For each percentage of EGR the graphs are plotted against bmep the simulated values are also compared. As the percentage of EGR increases the UBHC found to be higher when compared to diesel fuel operation without EGR. For all the percentages of EGR the UBHC levels were found to be higher at all values of bmep. And the values were recorded very high at smaller values of bmep and were recorded decreasing when bmep values are increased. The values of UBHC levels are almost similar as the EGR percentage varied. The variation among them is less significant as they recorded below 3%. But the variation is very large when operated on diesel and are noted 4 to 5 times more than the diesel operation.

The figure 3.2.3(d) depicts the effect of percentage of exhaust gas recirculation on UBHC for the filter AFM4. For each percentage of EGR the graphs are plotted against bmep the simulated values are also compared. As the percentage of EGR increases the UBHC found to be higher when compared to diesel fuel operation without EGR. For all the percentages of EGR the UBHC levels were found to be higher at all values of bmep. And the values were recorded very high at smaller values of bmep and were recorded decreasing when bmep values are increased. The values of UBHC levels are almost similar as the EGR percentage varied. The variation among them is less significant as they recorded below 2%. But the variation is very large when operated on diesel and are noted 3 to 5 times more than the diesel operation.

3.2.4 Smoke
The smoke percentage in the exhaust is the indication of deficiency of oxygen locally in the cylinder of a diesel engine. The variation of smoke as the variation in brake mean effective pressure of the engine for different filters, AFM1,AFM2, AFM3 and AFM4 with varying percentages of exhaust gas recirculation is presented and discussed below. The exhaust gas percentage is varied in 5, 10 and 15 percentages at the inlet.

The figure 3.2.4(a) depicts the effect of percentage of exhaust gas recirculation on smoke for the filter AFM1. For each percentage of EGR the graphs are plotted against BMEP the simulated values are also compared. As the percentage of EGR increases the smoke found to be decreasing when compared to diesel fuel operation without EGR. For all the percentages of EGR the smoke levels were found to be lower at all values of bmep. And the values were recorded lower at smaller values of bmep and were recorded increasing as bmep values are increased. The values of smoke levels are almost similar among themselves as the EGR percentage is varied. The variation among them is less significant as they recorded in the range of 5 to 10%. But the variation is smaller when operated on diesel and are recorded 2 to 6 times lower than the diesel operation.

The figure 3.2.4(b) depicts the effect of percentage of exhaust gas recirculation on smoke for the filter AFM2. For each percentage of EGR the graphs are plotted against BMEP the simulated values are also compared. As the percentage of EGR increases the smoke found to be decreasing when compared to diesel fuel operation without EGR. For all the percentages of EGR the smoke levels were found to be lower at all values of bmep. And the values were recorded lower at smaller values of bmep and were recorded increasing as bmep

values are increased. The values of smoke levels are almost similar among themselves as the EGR percentage is varied. The variation among them is less significant as they recorded in the range of 5 to 18%. But the variation is smaller when operated on diesel and are recorded 2 to 5 times lower than the diesel operation.
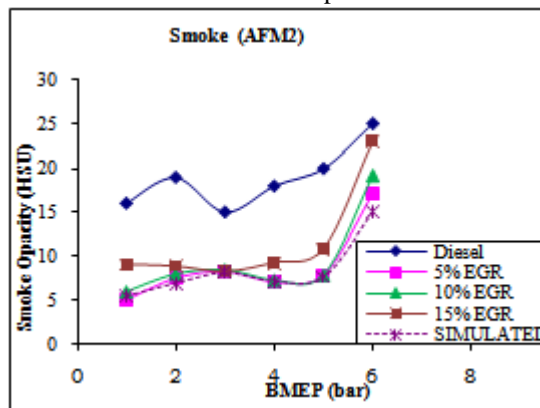
Fig: 3.2.4 (a)	**Fig: 3.2.4 (b)**
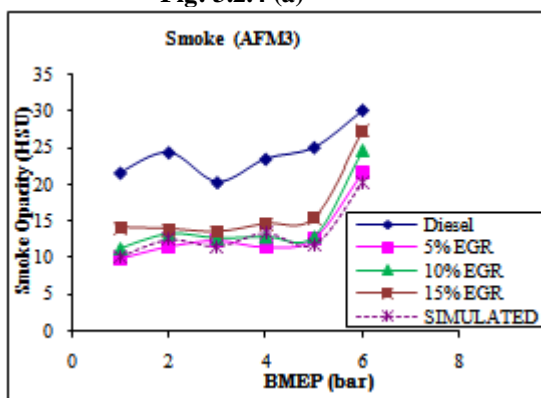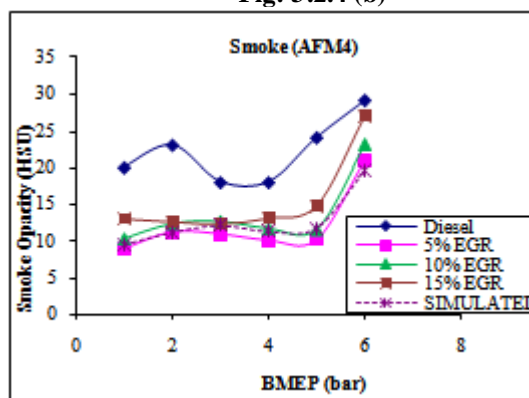
Fig: 3.2.4 (c)	**Fig: 3.2.4 (d)**

Fig: 3.2.4(a) to Fig: 3.2.4 (d) Effect of EGR percentage on smoke adopting AFM1, AFM2, AFM3 & AFM4

The figure 3.2.4(c) depicts the effect of percentage of exhaust gas recirculation on smoke for the filter AFM3. For each percentage of EGR the graphs are plotted against BMEP the simulated values are also compared. As the percentage of EGR increases the smoke found to be decreasing when compared to diesel fuel operation without EGR. For all the percentages of EGR the smoke levels were found to be lower at all values of bmep. And the values were recorded lower at smaller values of bmep and were recorded increasing as bmep values are increased. The values of smoke levels are almost similar among themselves as the EGR percentage is varied. The variation among them is less significant as they recorded in the range of 4 to 9%. But the variation is smaller when operated on diesel and are recorded 2 to 6 times lower than the diesel operation.

The figure 3.2.4(d) depicts the effect of percentage of exhaust gas recirculation on smoke for the filter AFM4. For each percentage of EGR the graphs are plotted against BMEP the simulated values are also compared. As the percentage of EGR increases the smoke found to be decreasing when compared to diesel fuel operation without EGR. For all the percentages of EGR the smoke levels were found to be lower at all values of bmep. And the values were recorded lower at smaller values of bmep and were recorded increasing as bmep values are increased. The values of smoke levels are almost similar among themselves as the EGR percentage is varied. The variation among them is less significant as they recorded in the range of 5 to 9%. But the variation is smaller when operated on diesel and are recorded 2 to 5 times lower than the diesel operation.

IV. Conclusions

➢ The volumetric efficiency is found to better for filter AFM2 due to its design and materials which allows more air flow into the engine cylinder having low pressure differential across the engine cylinder and filter. The exhaust gas recirculation has shown effect when compared to without EGR. With EGR the volumetric efficiency is reduced.

➢ The filter AFM4 has given better results in brake thermal efficiency for a 15% of exhaust gas recirculation due to the design factors of AFM4 filter.

➢ Though exhaust gas recirculation has been widely applied in SI engines for reduction of NOx formation, but nowadays in diesel engines it has become common practice. In the investigations it was observed that the use of EGR, NOx reductions are accompanied with an increase in smoke, particulate, unburned hydrocarbon emissions and fuel consumption.

References:

[1] Nagarajan, G., Kumar, S., and Chowdhury, D., "CFD Analysis of Air Filters for an Off-Highway Vehicle," SAE Technical Paper 2007-26-048, 2007.

[2] Ptak, T. and Walker, M., "Testing Automotive Engine and Interior Air Filters," SAE Technical Paper 970677,1997.

[3] T. Jaroszczyk, J. Wake and M. J. Connor , "Factors Affecting the Performance of Engine Air Filters, Journal of Engineering for Gas Turbines and Power ,Volume 115, Issue 4,Research Paper, *J. Eng. Gas Turbines Power* 115(4), 693-699 (Oct 01, 1993).

[4] M.R.Chopade1, A.P Valavade 2, S. H. Barhatte3, "Performance Enhancement Of Air Filter By Design Optimization", International Journal of Advanced Engineering Technology, IJAET, E-ISSN 0976-3945, Vol.III, Issue I, January-March 2012, pp: 68-70.

[5] Donepudi Jagadish, Dr.Puli Ravi Kumar, Dr.K.Madhu Murthy., "Performance Characteristics of a Diesel engine operated on Biodiesel with Exhaust gas Recirculation," International Journal of Advanced Engineering Technology, E-ISSN 0976-3945, IJAET/Vol.II/ Issue II/April-June, 2011/202-208.

[6] K. Rajan & K. R. Senthilkumar, "Effect of Exhaust Gas Recirculation (EGR) on the Performance and Emission Characteristics of Diesel Engine with Sunflower Oil Methyl Ester," Jordan Journal of Mechanical and Industrial Engineering, *ISSN 1995-6665,* Volume 3, Number 4, December 2009.

[7] R.Senthilkumar , K.Ramadoss & R.Manimaran, "Experimental Investigation of Performance and Emission Characteristics by Different Exhaust Gas Recirculation Methods used in Diesel Engine," Global Journal of Researches in Engineering Mechanical and Mechanics Engineering, ISSN:0975-5861, Volume 13 Issue 1 Version 1.0 Year 2013.

[8] A. Paykani, A. Akbarzadeh and M. T. Shervani Tabar, "Experimental Investigation of the Effect of Exhaust Gas Recirculation on Performance and Emissions Characteristics of a Diesel Engine Fueled with Biodiesel" IACSIT International Journal of Engineering and Technology, *Vol.3, No.3, June 2011*

[9] Neville J. Bugli and Gregory S. Green, "Performance and Benefits of Zero Maintenance Air Induction Systems", SAE Technical Paper Series, April 11-14, 2005-01-1139.

[10] Marius Toma, Gabriel Anghelache, Raluca Moisescu, "Replacement Period Evaluation of Petrol Engines Air Filters Based on Restriction Measurement", Advances in Automatic Control ISBN: 978-960-474-383-4, pp:71-76.

[11] Sandip More1, Kishore Kumar Thapa and Subir Bera1, "Potential of Dust and Soot from Air-Filters of Motor Vehicle Engines as a Forensic Tool", Forensic Research J Forensic Res, Volume 4, Issue 1 1000177.pp:2-7.

Simulation of Critical Crack Length Propagation Using Fracture Mechanics

Mr.DEGALA RAJENDRA[1], Mr. P RAVICHANDER[2] /Prof. R V PRASAD[3]

[1]*Sri Padmavathi Mahila University, Technology Tirupati*
[2,3]*Methodist College Of Engineering & Hyderabad*

ABSTRACT

The focus of this paper is to investigate and analyze the study on the plate of steel, Aluminum and Epoxy with a center crack. Linear elastic fracture mechanics principles have been used for calculating Stress Intensity Factor, Critical crack length, Increment in crack, Mean stress and strain Amplitude at critical fatigue load cycles.

Above calculations will be done on the plate with centre crack of various materials (steel, aluminum and epoxy) to predict crack length to evaluate and to compare the results with theoretical calculations.
.Conclusions/results obtained on the basis of analysis.

Keywords: *FRACTURE MECHANICS,FEM,ANSYS*

I. INTRODUCTION

Basically metal plates cause to fatigue cracks when it crosses its yield strength limit casually ,all the materials withstands up to 10^{+7} (cycles) this is called as **safe zone** limit 10^{+8} to 10^{+10}(cycles) is called **critical zone.** Most failures occur in materials are selection of proper material, processing, manufacturing procedures, incorrect usage. When the material is imposed of stresses, stress fracture of material can be two or more pieces.

Types of failure:
Failures of material are of two types, they are:
Buckling and Fracture.
Buckling:
When the material is subjected to a compressive load, buckling causes a lateral bend in the material. Buckling results failure of material within the catastrophic failure.
Types of fracture: In fracture failures Physical separation, or tearing of the material, through either an internal or external crack. Fracture of material are two types, they are: Ductile and Brittle fracture.

Ductile and brittle fracture

Fracture occurs due to stress concentrations at flaws like Surfaces scratches(stamp marks, inspection marks, surface irregularities), Variation in material properties(blow holes, cavities, weld strikes, and foreign inclusions)Discontinuities in the component(holes, grooves, keyways, screw threads and Abrupt changes in cross section (gears, sprockets, pulleys, ball bearings, splines on shafts)
Ductile fracture:
Ductile fracture materials are calculated by depending on momentum of the material. In Ductile fracture large amount of plastic deformation takes place before the fracture. Slow propagation and absorption of large amount energy is observed before the fracture. In ductile materials, particularly in high purity materials can with stand up to 50-100% large deformation or more strain before fracture under loading condition. Ductile fracture mostly influenced by: Transition temperature, inclusions, and strain hardening.
Brittle fracture:
Brittle fracture materials are calculated by depending on strength of the materials. In Brittle fracture small amount of plastic deformation takes place before the fracture. In brittle materials, particularly in brittle crystalline materials fracture can occur due to the result of tensile stress acting normal to crystallographic. Brittle fracture mostly results in catastrophic failure of a structure. Brittle fracture mostly influenced by: Defects, fatigue, and stress-corrosion.

Fatigue failures:
Fatigue means weakening of materials by applying repeated loading and unloading. When the material is subjected to cyclic loading, progressive and localized structural damage occurs in material. The nominal maximum stress values that cause such damage may be much less than the strength of the material typically quoted as the ultimate tensile stress limit, or the yield stress limit.
If the loads are above a certain threshold, microscopic cracks began to form at the stress concentrators such as surface, persistent slip bands (PSBs), and grain interfaces. Eventually crack will reach a critical size, the crack will propagate suddenly, and structure will fracture. The shape of the structure will significantly affect the fatigue life; square holes or sharp corners will lead to elevated local stresses where fatigue cracks can initiate. Round holes and smooth transitions or fillets will therefore increase the fatigue strength of the structure.

Low Cycle Fatigue:
Low cycle fatigue involves less numbers of cycles (N1000),
Failure of Set screws, short lived devices like missiles.
High cycle fatigue:
High cycle fatigue involves a large number of cycles (N4105 cycles) and an elastically applied stress. High cycle fatigue tests are usually carried out for 10^{+7} cycles sometimes 10^{+8} cycles for nonferrous metals. Although the applied stress is low enough to be elastic, plastic deformation can take place at the crack tip. Failure of Springs, ball bearings, gears subjected to fluctuating stresses. High cycle fatigue data are usually presented as a plot of stress, S, Vs the number of cycles to failure N. along scale is used for the number of cycles. The value of stress, s, can be the maximum stress, S max, the minimum stress, S min, or value of mean stress, S m, or one of the two ratios, R or A. The fatigue life is the number of cycles to failure at a specified stress level, while the fatigue strength (also referred to as the endurance limit) is the stress below which failure does not occur. As the applied stress level is decreased, the number of cycles to failure increases.
Normally, the fatigue strength increases as the elastic tensile strength increases.

II.   EXPERIMENTAL ANALYSIS

Nomenclature

$A_{fracture}$	= cross-section of the specimen at fracture.
A_0	= initial cross-section of the specimen.
C	= fatigue ductility exponent.
E	= young's modulus.
N	= describe the relative position of the crack tip to the grain boundary.
N_f	= number of load cycles to failure.
$\delta^{|}f$	= fatigue strength coefficient.
$\epsilon_{fracture}$	= specific deformation of the specimen at fracture.
$\delta\epsilon$	= specific deformation increment.
$\delta^{|}_f$	= fatigue ductility coefficient.
δuts	= ultimate tensile strength

INPUTS FOR STEEL AISI:

$A_{fracture}$	=	5.89
A	=	6
C	=	3
E	=	180Gpa
N	=	2

N f	=	10^8	
$\delta^l f$	=	2.8	
$\in$ fracture	=	2.03735	
δ'_f	=	10^6	
δ uts	=	400mpa	

Critical crack length calculation:
Fatigue crack initiation:

$$\frac{\Delta\in}{2} = \frac{\delta a}{E} + \frac{\Delta\in p}{2}$$

$$= \frac{\delta^l_f}{E}(2Nf)^b + \in^l f(2.$$

$$\frac{10^6}{180000}(2*10^8)^{.002} + 2.8(2*10^8)^{.003}$$

=55.55*1.04+2.8*1.066

    =56.59+3.866

=60.456

$$\Delta\in = \frac{60.456}{2} = 30.228$$

Strain amplitude:

Marrows (- N) method

$$\in a = \frac{(\delta^l f - \delta m)}{E}$$

$$= (2Nf)^b + \in^l f(2Nf2)^c$$

According to coffin-Manson

$$\in a = 1.75\frac{\delta uts}{E}N_f^{-0.2} + 0.5D^{0.6}N_f^{-0.6}$$

$$D = 1n\frac{A_0}{A_{Fracture}} \cong \in Fracture$$

$$D = \frac{6}{5.8}$$

=2*1.0186   =2.03735

$$\in a = 1.75\frac{400}{180000}10^{8-.02} + 0.5*2.03735^{0.6}*10^{8-.06}$$

1.75*2.2^{-3}*0.083176+0.5*1.53263*3.98^{-6}

=0.01367+2.177^{-4}

Strain =0.0138

Mean stress

Smith Watson Topper Method

$$= \delta^l_f \in^l_f (2Nf)^{b+c}\frac{\delta^{l2}_f}{E}$$

$$= 10^6 * 2.8(2*10^8)^{0.05} + \frac{10^{6^2}}{180000}(2*10^8)^{0.04}$$

8169643.74+235877379.9

=317575023.4 Pascal's

=317.5Mpa

INPUTS FOR ALUMINUM

A fracture	=	5.89	
A_0	=	6	
c	=	3	
E	=	74.5Gpa	
N	=	2	
N f	=	10^8	
$\delta^l f$	=	10^4	
$\in$ fracture	=	2.03735	
δ'_f	=	3.2	
δ uts	=	168mpa	

Critical crack length calculations:
Fatigue crack initiation[1] :

$$\frac{\Delta\epsilon}{2} = \frac{\delta a}{E} + \frac{\Delta\epsilon\, p}{2}$$

$$= \frac{\delta^l f}{E}(2Nf)^{\ b} + \epsilon^l f(2.$$

$$\frac{10^4}{74500}(2*10^8)^{.002} + 3.2(2*10^8)^{.003}$$

=0.1394+3.3888

=3.528

$$\Delta\epsilon = 3.528 * 2 = 7.0565$$

Strain amplitude:
Marrows method

$$\epsilon\, a = \frac{(\delta^l f - \delta m)}{E}$$

$$= (2Nf)^b + \epsilon^l f(2Nf)^c$$

According to coffin-Manson

$$\epsilon\, a = 1.75\frac{\delta uts}{E}N_f^{-0.2} + 0.5D^{0.6}N_f^{-0.6}$$

$$D = 1n\frac{A_0}{A_{Fracture}} \cong \epsilon\, Fracture$$

$$D = \frac{6}{5.8}$$

=2*1.0186   =2.03735

$$\epsilon\, a = 1.75\frac{168}{74500}10^{8^{-.02}} + 0.5 * 2.03735^{0.6} * 10^{8^{-.06}}$$

=4.3270×10⁻⁴+1.2145×10⁻⁵

=0.004448

Strain = 0.004448

Mean stress:
Smith Watson Topper Method

$$= \delta^l_f \epsilon^l_f (2Nf)^{b+c} \frac{\delta^{l2}_f}{E}$$

$$= 10^6 * 2.8(2*10^8)^{0.05} + \frac{10^{4^2}}{74500}(2*10^8)^{0.04}$$

=7281310.163+2883.267

=7284193.43 Pascal's

=72.84Mpa

INPUTS FOR EPOXY

A $_{fracture}$	=	5.89
A $_o$	=	6
c	=	3
E	=	30Gpa
N	=	2
N $_f$	=	10^8
δ ^{1} f	=	10^7
∈ $_{fracture}$	=	2.03735
δ ^1_f	=	2.1
δ uts	=	550mpa

Critical crack length calculations:
Fatigue crack initiation:

$$\frac{\Delta\epsilon}{2} = \frac{\delta a}{E_l} + \frac{\Delta\epsilon\, p}{2}$$

$$= \frac{\delta^l_f}{E}(2Nf)^{\ b} + \epsilon^l f(2.$$

$$\frac{10^7}{30000}(2*10^8)^{.002} + 2.1(2*10^8)^{.003}$$

=346.3225+2.2239   =348.54

$\Delta\epsilon = 348.54 * 2 = 697.09$

Strain amplitude:
Marrows method

$$\epsilon a = \frac{(\delta^l f - \delta m)}{E}$$

$$= (2Nf)^b + \epsilon^l f (2Nf)^c$$

According to coffin-Manson

$$\epsilon a = 1.75 \frac{\delta uts}{E} N_f^{-0.2} + 0.5 D^{0.6} N_f^{-0.6}$$

$$D = 1n \frac{A_0}{A_{Fracture}} \cong \epsilon\, Fracture$$

$$D = \frac{6}{5.8}$$

$= 2*1.0186$
$= 2.03735$

$$\epsilon a = 1.75 \frac{550}{30000} 10^{8-.012} + 0.5 * 2.03735^{0.6} * 10^{8-.06}$$

$= 3.5300 \times 10^{-3}$ Strain = 0.0035

Mean stress:
Smith Watson Topper Method

$$= \qquad \delta_f^l \epsilon_f^l (2Nf)^{b+c} \frac{\delta_f^{l2}}{E}$$

$$= 10^7 * 2.1(2*10^8)^{0.05} + \frac{10^{7^2}}{30000}(2*10^8)^{0.04}$$

$= 7214723960$ Pascal's $= 721.84$Mpa

RESULTS TABLE
Theoretical

	STEEL AIST 1504	ALUMINUM	E-GLASS EPOXY
specific deformation increment	30.228	7.0565	697.09
Strain amplitude	2.03735	2.03735	2.03735
Strain	0.0138	0.004448	0.0035
Mean stress	317.5Mpa	72.84Mpa	721.84Mpa

Analysis results with 10x cycles

	STEEL AIST 1504	ALUMINUM	E-GLASS EPOXY
DISPLACEMENT	0.32605	0.92594	0.87737
STRAIN	0.0086302	0.0240	0.02459
STRESS	1726	1710.2	1781
LIFE	62.39 to $1e^6$	0 to $1e^8$	57.949-$1e^6$
DAMAGE	1000 to $1.602e^7$	10 to $1e^{32}$	1000 to $1.7257e^7$
FACTOR OF SAFTY	2.845	2.832	2.58
BI-INDICATION	0.99891to0.966	0.993 to 0.97666	0.99 to0.867
ALL-STRESS	1726	1710.2	1781
MODE 1	341.51	1631.8	1725.5
MODE 2	632.86	2939.1	3086.6
MODE 3	1540.8	3033.4	3122.7
MODE 4	2853.6	3663.6	3731.6
MODE 5	3132.4	4577	4772.7
MODE 6	3537	5615.1	5779.6

STEEL AIST 1504	
	Analysis
DISPLACEMENT	0.32605
STRAIN	0.0086302
STRESS	1726
LIFE	62.39 to $1e^6$
DAMAGE	1000 to$1.602e^7$
FACTOR OF SAFTY	0.049to2.845
BI-INDICATION	0.99891to0.966
ALL-STRESS	1726
MODE 1	341.51
MODE 2	632.86
MODE 3	1540.8
MODE 4	2853.6
MODE 5	3132.4
MODE 6	3537
Mean stress	

ALUMINUM	
	Analysis 10x
DISPLACEMENT	0.92594
STRAIN	0.0240
STRESS	1710.2
LIFE	0 to$1e^8$
DAMAGE	10 to$1e^{32}$
FACTOR OF SAFTY	0.04838 to2.832
BI-INDICATION	0.993 to 0.97666
ALL-STRESS	1710.2
MODE 1	1631.8
MODE 2	2939.1
MODE 3	3033.4
MODE 4	3663.6
MODE 5	4577
MODE 6	5615.1

E-GLASS EPOXY	
	Analysis 10x
DISPLACEMENT	0.87737
STRAIN	0.02459
STRESS	1781
LIFE	57.949-$1e^6$
DAMAGE	1000 to $1.7257e^7$
FACTOR OF SAFTY	0.048 to2.58
BI-INDICATION	0.99 to0.867
ALL-STRESS	1781
MODE 1	1725.5
MODE 2	3086.6
MODE 3	3122.7
MODE 4	3731.6
MODE 5	4772.7
MODE 6	5779.6
Mean stress	

III.   CONCLUSION

Initially data collection and literature survey was done on critical length on various materials.

By analysis in three materials aluminum has high strength and life cycle and damage will be less compared to E-glass epoxy material.

In aerospace design epoxy's are widely used to make outer body's, these outer bodies caused to damage with small hit or crack initiation so better to use mixture of aluminum and carbon mixture in good qualities.

IV.   FUTURE SCOPE

Epoxy materials are not able to withstand after crossing safe zone (initiation of crack). When we mix the aluminum materials and E-glass epoxy material the material can with stand and life cycle of material can be increased.

REFERENCES

[1]   G. Fajdiga and M. Sraml; Fatigue Crack Initiation and Propagation under Cyclic Contact Loading.

[2]   Mr. Quinton Row son consultant Structural Integrity, Quest Integrity NZL Ltd., New Zealand Mr. Michael Rock engineering Project Manager, Mighty River Power Ltd., New Zealand; Comparison between ductile tearing analysis and linear elastic fracture mechanics analysis.

[3]   Donoso, J.R. and Landes; Materials Science Department, Universidad Tecnica Federico Santa Maria Valparaiso, CHILE juan.Donoso@Usm.Cl [2] MABE Department, The University Of Tennessee Knoxville, TN   Usalandes@Utk.Edu;An instability analysis for a crack growth situation based on the common format.

[4]   fracture and fatigue crack growth analysis of rail steels; Journal Of Mechanics Of Materials And Structures

[5]   M kulkarni1, Ravi prakash2 and A N kumar3; Experimental And Finite Element Analysis Of Fracture Criterion In General Yielding Fracture Mechanics

[6]   H. Sun, S. Rajendran and D. Q. Song: Finite Element Analysis on Delimitation Fracture Toughness Of Composite Specimens

[7]   Tipple and G. Thorwald; Using the Failure Assessment Diagram Method with Fatigue Crack Growth To Determine Leak-Before-Rupture.

Performance Analysis of Grid Connected Hybrid AC/DC Microgrid Using Various Renewable Energy Sources

Balaji Kodanda Ram B.P.U.S. Rompicherla[1], Raghu Chandra Garimella[2*]

[1]Department of Electrical and Electronics Engineering, K L University, Andhra Pradesh, India
[2]Department of Mining Engineering, National Institute of Technology Karnataka, Surathkal, India

ABSTRACT

We in no time appreciate a dominatingly AC electrical distribution system, the engineering reason for which was designed more than 100 years back. While AC distribution system have served us well, we ought to intermittently respite to survey what opportunities we have acknowledged or been precluded by overpowering prevalence from claiming AC electrical power distribution system. What openings could be acquired by designing DC distribution into at any rate parts of our present system? What favorable circumstances of the present AC distribution system ought to be perceived and ensured? This paper proposes a Hybrid AC/DC Microgrid in organization together with Photo Voltaic (PV) energy, Wind Energy and Proton Exchange Membrane (PEM) Fuel cells. The Microgrids are turning out to be progressively appealing to the researchers as a result of the less greenhouse gasses, low running expense, and adaptability to work regarding utility grid. This paper concentrates on distribution within premises and low-voltage distribution system. In particular, this paper tended to the change productivity expenses of receiving different premise AC and DC distribution system topologies. Hybrid AC/DC Microgrid constitutes free AC and DC subgrids, where every comparing source and loads are associated with their particular transports and these transports are interfaced utilizing an interfacing converter. Hybrids AC/DC Microgrid builds system productivity by reducing numerous turn around transformations required in ordinary Renewable Energy Sources (RES) mix to grid. A Small Hybrid AC/DC Microgrid in grid associated model was modelled and simulated in MATLAB/SIMULINK environment. Simulation results are utilized to demonstrate the steady operation considering the vulnerability of generations and loads.

Keywords: hybrid power systems, micro grids, solar energy, wind energy, fuel cells, interfacing converter

***Corresponding Author**
E-mail: raghuchandhra@india.com

INTRODUCTION

Microgrid is a little network developed by saving many different energy resources and loads to upgrade overall reliability and independent advantages. Presently a-days, it is more liked to coordinate renewable energy sources to Microgrid to reduce the CO2 discharge and fossil fuel utilization. Saved Microgrid can be operated either in connection to main grid or operated like isolated "islanded" [1]. Presently a-days, DC loads like LED's, Electric Vehicles and other Electronic Gadgets are being greatly used because of their inherent advantages. Three Phase AC Power systems have existed for over 100 years because of their efficient transformation at different voltage levels and transmission over long distances. Also, inherent features of rotating machines make it possible for larger period.

To connect a conventional AC system to renewable resources, AC Microgrids have been suggested and DC power from various resources like PV panel, Fuel cells etc. are converted into AC to connect to an AC grid, which are implanted by AC/DC Converters and DC/DC Converters [2]. In an AC Grid, many converters are used for various home and office facilities to provide required DC voltages. AC/DC or DC/AC converters are commonly used as drives in order to control the speed of AC motors in industries.

Recently, DC grids are resurging because of development and deployment of renewable DC resources and their inherent gain for DC loads in residential, commercial and industrial applications. Hence, DC Microgrid has been proposed [3]. Anyhow, for conventional AC loads DC/AC inverters are recommended and AC sources are connected using AC/DC Converters.

Many reverse conversions recommended in individual AC or DC grid may include additional loss to the system operation and will make the current home and office appliances more complicated in design and operation [4]. Current research focuses on the concept of smart grid in the electric power industry. One of the most important futures of smart grid is advanced structure which can facilitate connections of different AC and DC generation systems, energy storage options and various AC and DC loads with optimal asset utilization and operational efficiency. Power electronics converter plays the most important role in interfacing AC and DC grids, which makes future grid much smarter.

This research paper concentrates on Hybrid AC/DC Microgrid concept, which is proposed to reduce processes of multiple reverse conversions in an individual AC or DC grid and to facilitate

connections for various energy sources, storage devices and loads [5]. Advanced power electronic devices and control techniques are utilized to harness maximum power from renewable power sources, to reduce power transfer between AC and DC networks. PV system, Proton Exchange Membrane Fuel Cell (PEMFC) constitutes the DC Energy Sources; Wind system constitutes the AC energy source, though Battery and Conventional Grid are used as storage devices whenever required.

SYSTEM CONFIGURATION AND MODELLING

Figure 1 illustrates a compact representation of proposed Hybrid Microgrid Configuration. Hybrid Microgrid was formed by a DC sub grid and an AC sub grid. Every sub-grid has its own sources elements, storage elements and loads of same class grouped together so as to decrease the amount of power conversion required. Both sub-grids are interfaced with the help of interfacing converters. Interfacing converters are bidirectional converters and their major role is to provide bidirectional energy transfer between sub grids depending on the prevailing internal supply – demand conditions.
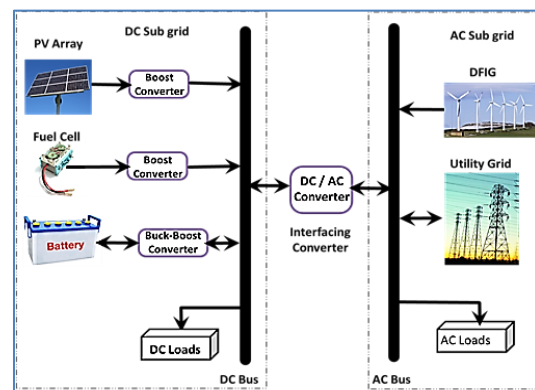
Fig. 1. *A Compact representation of the proposed Hybrid Microgrid [1].*

The established Hybrid grid can be tied to Utility grid using an Intelligent Transfer Switch at point of common combined as

in conventional AC grids. In grid tied mode of operation, surplus energy in the internal sub-grids, if any one, can be injected to the utility grid without violating local utility rules. Similarly, shortfall in both the sub grids, if any, can be absorbed from utility grid.

Proposed Hybrid Microgrid Configuration

PV Array (40kW) and PEM Fuel Cell (50kW) are linked to DC bus via independent DC/DC boost converter to simulate DC sources. Capacitors C_{pv} and C_{fc} are utilise to suppress the high frequency ripples of the PV and FC output voltage.

Also, a wind turbine generator (WTG) with Doubly Fed Induction Generator (50kW) and utility grid are connected to AC bus to simulate AC Sources. In addition, a battery (65Ah) and super capacitor (0.5F) are individually linked as energy storages to DC bus via buck-boost (DC/DC) converter. DC load was taken as pure resistive load and AC loads are considered with RLC which are random in nature. Both the loads are variable between 20kW – 40kW. The rated voltages for both buses are considered as 400V. Parameters of Hybrid Microgrid are tabulated in Table 1 as depicted below.

***Table 1.** Parameters for the hybrid grid.*

Symbol	Description	Value
C_{pv}	Capacitor across the solar panel	110 µF
L_1	Inductor for the boost converter	2.5 mH
C_d	Capacitor across the dc-link	4700 µF
L_2	Filtering inductor for the inverter	0.43 mH
R_2	Equivalent resistance of the inverter	0.3 Ohm
C_2	Filtering capacitor for the inverter	60 µF
L_3	Inductor for the battery converter	3 mH
R_3	Resistance of L3	0.1 Ohm
F	Frequency of AC grid	60 Hz
f_s	Switching frequency of power converters	10 kHz
V_d	Rated DC bus voltage	400 V
V_{ll_rms}	Rated AC bus line voltage (rms value)	400 V
n1/n2	Ratio of the transformer	2:1
C	Capacity of super capacitor	F

Modelling of PV Panel

Figure 2 shows an equivalent circuit of a PV Panel modelled by controlled current source. I_{pv} and V_{pv} are terminal current and voltage of the PV panel, respectively. Current output of the panel is modelled using three equations (1), (2), (3), respectively [6], [7]. The parameters that were taken into consideration for simulation are given in Table 2.

$$I_{pv} = n_p I_{ph} - n_p I_{sat} \times \left[exp\left(\left(\frac{q}{Akt} \right)\left(\frac{V_{pv}}{n_s} + I_{pv}R_s \right) \right) - 1 \right] \qquad (1)$$

$$I_{pv} = \left(I_{sso} + K_i(T - T_r) \right).\frac{S}{100} \qquad (2)$$

$$I_{sat} = I_{rr}\left(\frac{T}{T_r} \right)^3 exp\left(\left(\frac{qE_{gap}}{kA} \right).\left(\frac{1}{T_r} - \frac{1}{T} \right) \right) \qquad (3)$$
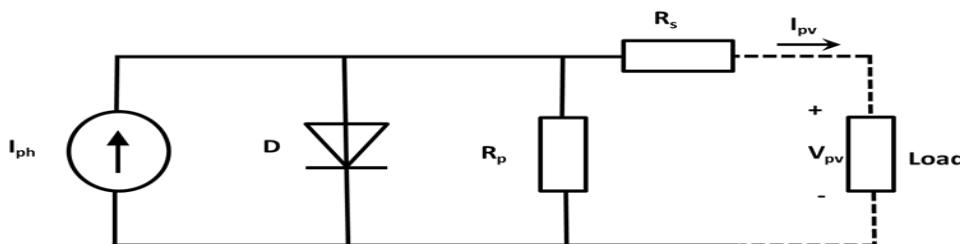
***Fig. 2.** Equivalent circuit of a PV panel.*
***Table 2.** Parameters of photovoltaic panel.*

Symbol	Description	Value
V_{oc}	Rated open circuit voltage	403 V
I_{ph}	Photocurrent	
I_{sat}	Module reverse saturation current	
Q	Electron charge	1.602×10^{-19} C
A	Ideality factor	1.50
K	Boltzmann Constant	1.38×10^{-23} J/K
R_s	Series resistance of a PV cell	
R_p	Parallel resistance of a PV cell	
I_{sso}	Short-circuit current	3.27 A
k_i	SC Current temperature Coefficient	$1.7 e^{-3}$
T_r	Reference Temperature	301.18 K
I_{rr}	Reverse Saturation current at T_r	$2.0793 e^{-6}$ A
E_{gap}	Energy of the band gap for silicon	1.1 eV
n_p	Number of cells in parallel	40
n_s	Number of cells in series	900
S	Solar Irradiation Level	0 ~ 1000 W/m
T	Surface temperature of the PV	

Modelling of Fuel Cell

Figure 3 shows an equivalent circuit of PEM Fuel cell. Ohmic, activation and concentration resistances are represented by R_{Ohmic}, R_{act}, R_{conc}, respectively. C is the membrane capacitance. Membrane voltage equation is given by Equation (4).

$$V_c = \left(1 - \frac{dV_c}{dt}\right)(R_{act} + R_{conc}) \qquad (4)$$

Output voltage of the PEMFC is given by (5)

$$V_{fc} = E - V_c - V_{act} - V_{ohmic} \qquad (5)$$
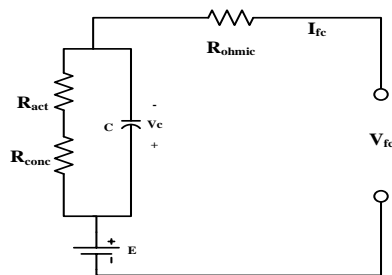
Fig. 3. *Equivalent circuit of PEM Fuel cell.*

Modelling of Battery

Battery is not important in grid-tied mode.

Since, it provides energy storage in to DC subgrid, which can reduce the multiple reverse conversions, whenever required. In emergency i.e. Grid Failed Condition, they plays a vital role in power balance and voltage stability. Battery was modelled using a controlled nonlinear source in series with a constant resistance. State of Charge (SOC) of the battery is given by Equation (6).

$$SOC\% = 100 \left(1 + \frac{\int it\,dt}{Q}\right) \qquad (6)$$

where, it is the extracted capacity and Q is the Maximum capacity if battery.

Modelling of Wind Turbine Generator With DFIG

In this paper, DFIG was examined as a wound rotor induction machine. The power output P_m from a WT is determined by [3]. A 50kW DFIG parameters, used in this paper are shown in Table 3 [8].

$$P_m = 0.5\rho A C_p(\lambda, \beta)V_w^3 \qquad (7)$$

Table 3. *Parameters of DFIG.*

Symbol	Description	Value
P_{nom}	Nominal power	50 kW
V_{nom}	Nominal Voltage	400 V
R_s	Stator resistance	0.00706 pu
L_s	Stator inductance	0.171 pu

R_r	Rotor resistance	0.005 pu
L_r	Rotor inductance	0.156 pu
L_m	Mutual inductance	2.9 pu
J	Rotor inertia constant	3.1 s
n_p	Number of poles	6
V_{dc_nom}	Nominal DC voltage of AC/DC/AC converter	800 V
P_m	Nominal Mechanical power	45 W

CONTROLLERS

Hybrid Microgrid has six types of converters. All converters have to be coordinately controlled with the utility grid to give reliable, high efficiency, high quality power for variable DC and AC loads. The controllers are explained in this section are coordinated successfully in both the grid-tied. A Direct Torque Control Strategy (DTC) with feed forward voltage compensation is selected for DFIG control system [9].

Boost Converter

In grid tied mode, control objective of boost converter is to track MPPT of PV panel and Fuel Cell. PV Panel and Fuel Cell boost converters are designed to support DC bus voltage as shown in Figure 4. To achieve maximum power, P&O Method proposed in their research of Michael and Gonzalez [6].

(a)

(b)
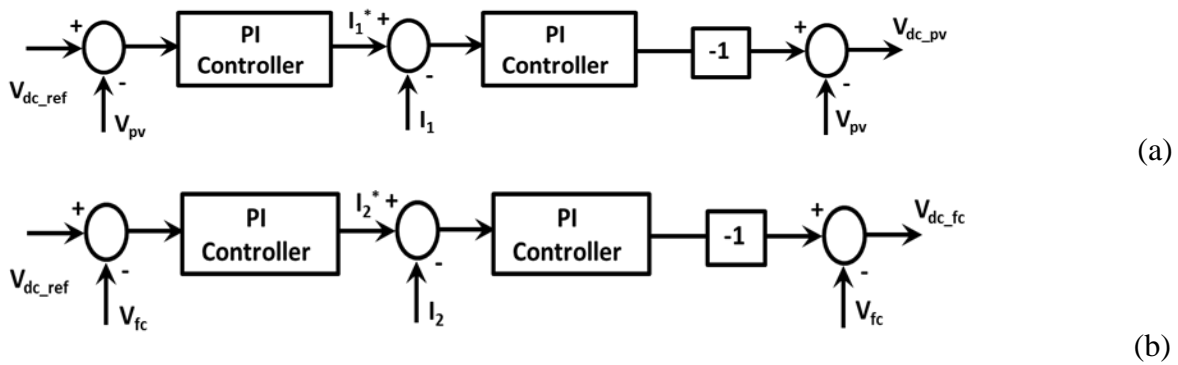
Fig. 4. *Control scheme of PV cell and PEM fuel cell.*

Control of Battery

Battery has high energy density with slow charging and discharging speeds. Control scheme of Battery is shown in Figure 5.
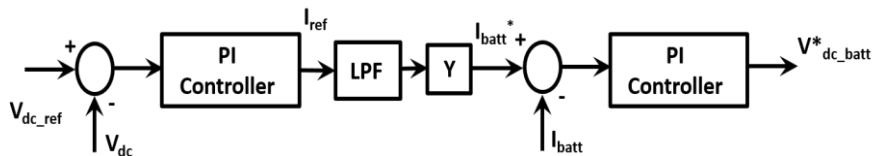
Fig. 5. *Control scheme for battery.*

Interfacing Converter

Major objective of interfacing converter is to interface both sub grids i.e., AC grid and DC grid. Major role of interfacing converter is to exchange power between AC bus and DC bus. When operating in grid tied mode, converter supplies given active and reactive power. Interfacing converter acts DC/AC inverter when supplying power from DC grid to AC grid and acts as AC/DC rectifier when supplying power from AC grid to DC grid whenever required. Interfacing converter works based on droop control [10]. Control scheme of interfacing converter is shown in Figure 6.

Advantages of interfacing converter cannot be realized by just relying on the droop controlled sources. Interlinking

control challenges have to be carefully addressed [11].

(1) Unlike unidirectional sources, interlinking converters have to manage bidirectional active and reactive power flows between sub grids.

(2) At any one instant, interlinking converters have two roles to play. They appear as load to one sub grid where energy is absorbed and appear as source to other grid where energy is injected.
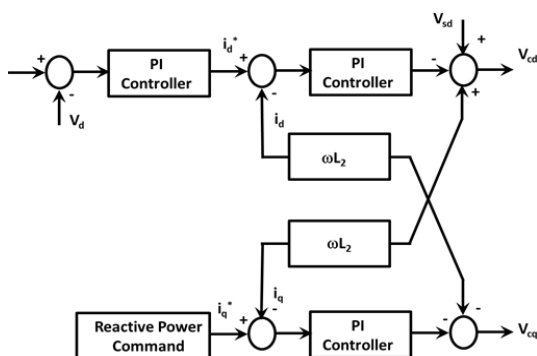
Fig. 6. *Control scheme for interfacing converter.*

SIMULATION RESULTS
Operations of Grid Connected Hybrid AC/DC Microgrid under various source and load conditions are simulated to verify the reliability.

DC RES power is supplied directly to the DC loads and AC RES power is supplied directly to AC loads. Power is balanced directly by the utility grid on AC bus and on DC bus through interfacing converter. Battery is assumed to be fully charged and operated in rest mode. DC bus voltage is controlled and maintained by utility grid through interfacing converter. AC bus voltage is directly maintained by utility grid.

Terminal voltage for change in solar irradiation is shown in Figure 7. Optimal terminal voltage of PV panel is obtained by using the standard P&O algorithm. The solar irradiance was set as $400W/m^2$ from 0.0s to 0.1s, later it was linearly increased to $1000W/m^2$ until 0.2s, kept constant to 0.3s, decreased to $400W/m^2$ by 0.4s and keeps that value until final time 0.5s. Slow tracing speed of the standard P&O algorithm is optimized by using fuel cell in DC subgrid.

Figures 8 and 9 show the curves of PV panel power output and solar irradiation respectively. It was observed that the Power output varies from 4.85 to 13.5 kW, which closely follows solar irradiation curve assuming fixed ambient temperature.

Figure 10 shows the voltage and current responses on AC side of interfacing converter with a fixed DC load of 20 kW. It was noticed that the current direction of interfacing converter was reversed before 0.3s and after 0.4s.

Figure 11 shows the voltage and current responses on AC side of interfacing converter with variable DC load from 20kW to 40kW at 0.25s with fixed solar irradiation at $750W/m^2$. It can be seen that current direction was reversed at 0.25s.

Figure 12 shows the voltage response at DC bus of interfacing converter with Fuel cell shows an improved transient response when compared to [5].
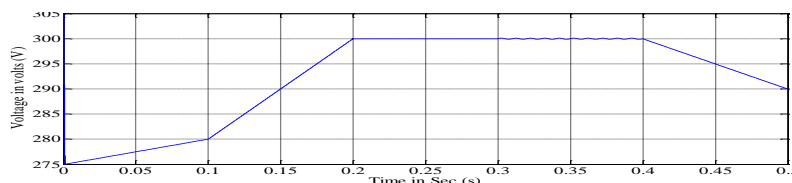
Fig. 7. *Terminal voltage of PV panel.*
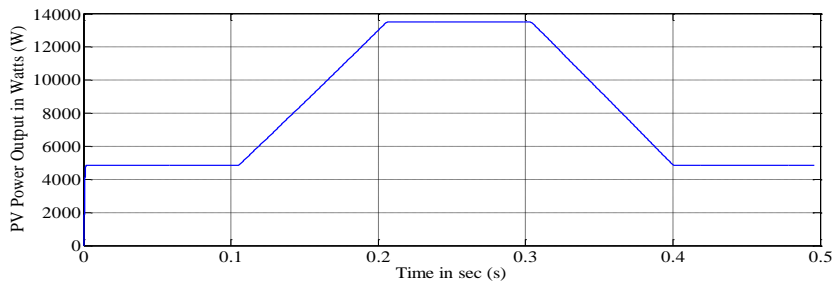
Fig. 8. *Power output of PV panel.*
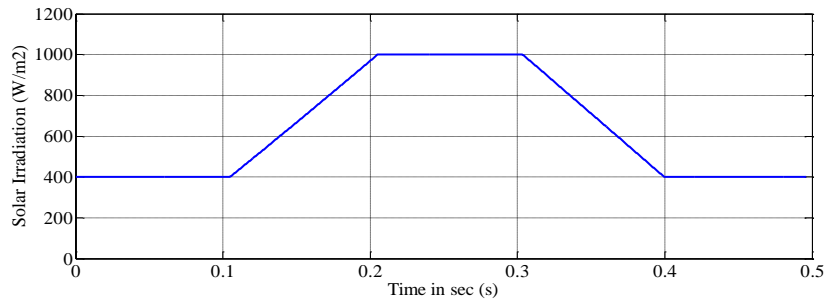
Fig. 9. *Solar irradiation.*
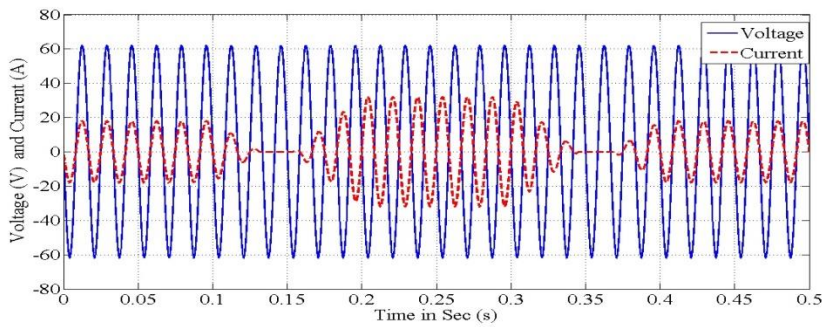
Fig. 10. *AC side voltage and current of the interfacing converter with variable solar irradiation and constant DC load.*
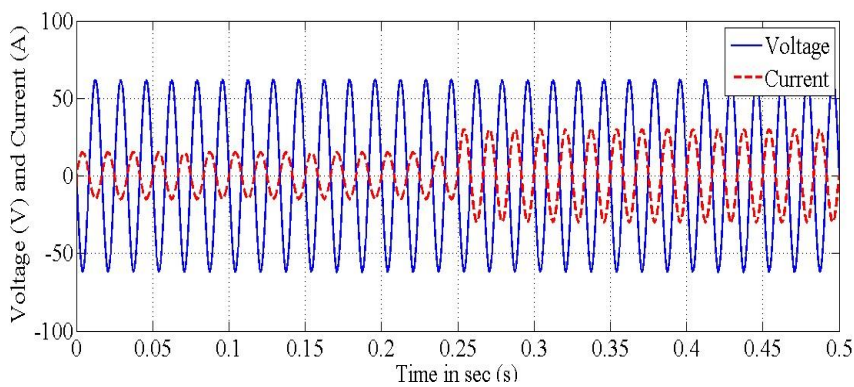
Fig. 11. *AC side voltage and current of the interfacing converter with constant solar irradiation and variable DC load.*
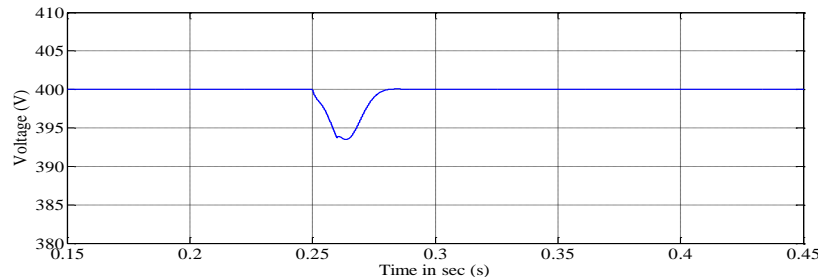
***Fig. 12.** DC bus transient response with fuel cell.*

CONCLUSIONS AND FUTURE SCOPE

A Hybrid AC/DC Microgrid has proposed and comprehensively studied in this paper. Control strategies are concisely stated to maintain stable system operation under various load and resource conditions. Control strategies are verified by using MATLAB/Simulink. Various control methods are incorporated to harness the maximum power from RES during grid connected mode and resembles stable operation.

Interfacing Converter shows stable operation during load variations. However there will be some practical limitations, because of fast and continuous load variations. Even-though, the proposed Hybrid grid reduces the processes of DC/AC and AC/DC conversions in an individual sub grids, the theory is still challenging in the AC dominated infrastructure. Hybrid AC/DC Microgrid has to be tested for various faults on subgrids and their effects on the other grid. Hybrid AC/DC Microgrid is only feasible for new construction either in remote location or industries.

REFERENCES

[1] Loh, P.C., Ding Li, Yi Kang Chai, and Frede Blaabjerg, 2013. "Autonomous Control of Interlinking Converter with Energy Storage in Hybrid AC-DC Microgrid", *IEEE Trans. Industry Applications*, 49(03), 1374-1382.

[2] Lasseter, R.H., 2002. "MicroGrids", *Proc. IEEE Power Eng. Soc.,* Winter meet, 1, 305–308.

[3] Baran, M.E., and Mahajan, N.R., 2003. "DC Distribution for Industrial Systems: Opportunities and Challenges", *IEEE Trans. Industry Applications*, 39(06), 1596-1601.

[4] Peng Wang, Liu, X., Chi Jin, Loh, P.C., and Choo, F.H., 2011. "A Hybrid AC/DC Micro-grid Architecture, Operation and Control", *Proc. IEEE Power and Energy Society General Meeting,* 1-7.

[5] Liu, X., Peng Wang, and Loh, P.C., 2011. "A Hybrid AC/DC Microgrid and Its Coordination Control", *IEEE Trans. Smart Grid*, 2(2), 278-286.

[6] Michael, M., and Gonzalez, S., 2009. "Development of a MATLAB/Simulink Model of a Single-Phase Grid-Connected photovoltaic System", *IEEE Trans. Energy Conversion*, 24(1), 195-202.

[7] Chao, K.H., Li, C.J., and Ho, S.H., 2008. "Modeling and fault simulation of Photovoltaic generation systems using circuit-based model", *Proc. IEEE Int. Conf. Sustainable Energy Technology,* 284-289.

[8] Kodanda Ram, R.B.P.U.S.B., and Venu Gopala Rao, M., 2014. "Performance of A Hybrid AC/DC Microgrid using RES and Super Capacitor in Connected and Islanded Mode", Proc. *IEEE International Conference on Smart Electric Grid – 2014 (IEEE ICSEG -2014),* K L University, India.

[9] Akbari, M., Golkar, M.A., and Tafreshi, S.M.M, 2011. "Voltage Control of a Hybrid AC/DC Microgrid in stand-Alone Operation Mode", *Proc. IEEE PES innovative Smart Grid Technologies,* 363-367.

[10] Akbari, M., Golkar, M.A., and Tafreshi, S.M.M, 2011. "Voltage Control of a Hybrid AC/DC Microgrid in Grid Connected Operation Mode", *Proc. IEEE PES innovative Smart Grid Technologies,* 358-362.

[11] Chi Jin, Loh, P.C., Peng Wang, Yang Mi, and Blaabjerg, F., 2010. "Autonomous Operation of Hybrid AC-DC Microgrids," Proc. IEEE ICSET, 1-7.

BIOGRAPHIES

Kodanda Ram R.B.P.U.S.B. received B.Tech. degree from JNT University Kakinada, India. He received M.Tech. in Power Systems from K L University, Guntur, India. In addition, he is holding MIEEE, MIDES, AMUCEE, MIAENG. He is having vided industrial experience in design, manufacturing, erection and commission of LT Control Panels from Hyderabad. His special fields of interest includes: Smart grids, Microgrids, Hybrid Grids. He is presently working to implement big data analytics and Hadoop in Smartgids.

Raghu Chandra Garimella profile contains B.Tech., PGDM, PGADM, M.Tech., MBA, MIAENG, MIDES, MSIAM, MTheIRED, SMUACEE, (Ph.D. – NIT Karnataka). He received B.Tech. and M.tech. degrees from JNT University Kakinada, India. Later, he completed his PGDM, PGADM and MBA degrees from GITAM University, Visakhapatnam, India. Being an Electrical and Electronics Engineering post-graduate, currently he is working on the Seismic Energy Estimation of ground vibrations caused due to blasting operations based on Signal Processing Approach. He already undergone for a Patent on his research, Piezo based Renewable Energy Generation technique from Blast induced ground vibration waves. His areas of interest includes: Renewable Power Generation, Ground Vibrations, Signal Processing Techniques, Seismic waves, Rock Blasting Mechanisms and Power Electronic Drives.

Ground Vibrations & Water Borne Shock Waves Caused due to Underwater Blasting in Ports – A Case Study

V. Rama Sastry, G. Raghu Chandra, and C. Karthik

Abstract— **Underwater drilling and blasting is adopted in ports as a part of capital dredging. Underwater blasts affect the ambient environment in terms of ground vibrations and water borne shock waves. Knowledge regarding the pressure due to each underwater blast can help us monitor the safety of structures and workers or other aquatic life. Deepening of draught was carried out in the entrance channel / and turning circle of outer harbour in Vishakhapatnam Port, Southern India, involving underwater blasting in about 2,50,000m2 area, for a depth of 8m. Blasts were designed to ensure safety of various structures in the port and its efficacy was established by monitoring of blast vibrations at different structures. The paper describes the methodology adopted, equipment used and various steps taken in the safe execution of the rock dredging project. The paper also discusses the calculation of safe distance from environmental and worker's safety aspect for the safe execution of the rock dredging projects.**

Keywords— **Ground Vibrations, Rock Dredging, Safety, Underwater Blasting, Water Borne Shock Waves.**

I. Introduction

Fragmentation of hard sea bed rock by underwater blasting is a vital operation in rock dredging projects. While desirable results are good fragmentation and throw of fragmented material, the undesirable effects include damage to surrounding structures, accident to workers in vicinity and harmful effect on surrounding marine flora and fauna. The safety aspects of underwater blasts should ensure that these undesirable effects are minimized. To check or ensure that the structures /and vessels surrounding are safe during the blast, the PPVs of generated ground vibrations are monitored. The protection of various marine species both flora and fauna, divers operating in the location is also of utmost importance from the environmental and safety point of view. The pressure of the water waves generated due to shock waves of blast is monitored and the safe distance is established prior to conduct of blast. Based on these data, sufficient precautionary actions and warning can be given to protect the divers and marine life in the vicinity of blast.

II. Literature Review

A. Ground Vibrations

When the intensity of strain waves generated due to detonation in a blasthole, diminishes to the level where no permanent deformation occurs in the rock mass, i.e. beyond the fragmentation zone, strain waves propagate through the strata in the form of elastic waves. These waves in the elastic zone are known as ground vibrations [1]. Ground vibrations may cause structural damage and annoyance to public, while damage to nearby structures/ vessels and marine life may be caused by excessive underwater shock waves. Whenever blast vibration occurs, it vibrates the ground/soil particle with certain velocity and imparts to it certain amount of acceleration. Ground vibrations are, therefore, quantified as displacements that vary with time (in terms of 'mm'), accelerations (in terms of 'g') and/or particle velocities (in terms of mm/s) at particular ground locations [2]. The damage potential also depends upon the predominant frequency besides the PPV. Reference [3] made extensive studies to evaluate the influence of 14 blast variables considered to be having an influence on the amplitude of ground vibrations. They found that charge weight per delay and length of delay to be having the most significant influence on the intensity of ground vibrations. It is very difficult to define the precise level of vibration at which damage begins to occur in a structure. Safe levels for assessing the damage have been defined in terms of Peak Particle Velocity (PPV - mm/s) in different countries. In India, the Directorate General of Mines Safety has given threshold PPVs for different structures based on dominant frequency of the wave form. Standards of DGMS and USBM were used for assigning threshold values of PPV for different structures.

B. Water Borne Shock Waves

In an underwater blast the water is pressurized and displaced due to burning and detonation. A huge amount of energy is released from the blast and this energy moves away from the blast center and spreads in all directions. Reference [4] states that during a blast, in the region beyond the direct effect of thermal and detonation effect, two major impacts are shock waves and the expanding gaseous reaction products. The initial high – intensity shock wave is the most dangerous but it loses its intensity as it moves outward from the source of the explosion. The waves that follow after initial shock waves are less severe. In an underwater explosion initial shock wave is followed by a succession of oscillating bubble pulses. A shock wave is a compression wave that expands radially out from the detonation point of an explosion. At a distance from a

detonation, the propagation of the shock wave may be affected by several components including the direct shock wave, the surface-reflected wave, the bottom-reflected wave, and the bottom-transmitted wave. The direct shock wave results in the peak shock pressure (compression) and the reflected wave at the air-water surface produces negative pressure (expansion). For an explosion with the same energy and at the same distance, an underwater blast is much more dangerous to animals than an air blast. Shock wave in air dissipates more rapidly and tends to be reflected at the body surface; in water the blast wave travels through the body and may cause internal injury to gas-filled organs due to impedance differences at the gas-liquid interface. The pressure generated due to underwater blasting depends on many factors like – type of explosive, size of the charge, characteristics of the seabed, location of the explosive charge, water depth, distance from the explosion and degree of submersion of the diver. If divers are present underwater while a UW blast is being conducted, it can cause severe damage to the divers depending upon the distance between diver and blast location. The human body can survive relatively high blast overpressure without experiencing barotrauma. Reference [5] in their study found that a blast overpressure of 5psi (3.45MPa) will rupture eardrums in about 1% of people exposed to it, and a 45psi (31.26MPa) overpressure will cause eardrum rupture in about 99% of all subjects. Also the threshold for lung damage was suggested to be about 15psi (10.34MPa) blast overpressure and 35-45 psi (24.13MPa to 31.0MPa) overpressure was found to cause 1% fatalities, and 55(37.92MPa) to 65 psi (44.8 MPa) overpressure to cause 99% fatalities.

Underwater blasts cause severe effect on the marine life as well. Damage to swim bladder and other gas containing organs have been found to be the main cause for the death of fish and other marine mammals [6]. Reference [7] suggested that negative phase of the pressure wave causing the swim bladder to burst outward was the main reason for the death of fishes due to underwater blasts. Studies have found that the damage to gas contained organ was the main reason for the death of marine mammals as well [8]. The lungs and intestinal tract was the organ most affected in these species. Studies by US Army Corps, New York Division found that phenomenon of "cavitation hat," observed in blasting of aquatic environment is the major reason for increased mortality in aquatic biota. The negative reflected wave generated by the deflection of the water surface toward the air results in a shallow disc of negative pressure centered over the explosive and there is high potential for overextension of air filled organs in aquatic biota due to the negative pressure associated with the cavitation hat.

III. Investigations

The sea bed of Visakhapatnam Port consists of hard Khondalite rock mass. Method of drilling and blasting for fragmenting and displacing the hard rock mass was proposed to enable the dredging activity. A total area of about 2,50,000m^2 was dredged, from the existing draught of about -8m to -16m, uniformly. As the sea bed consists of hard rock mass, explosive energy was used for breaking the hard sea bed, in order to deploy appropriate dredgers. Fig. 1 shows the plan of the dredging area with structures around.
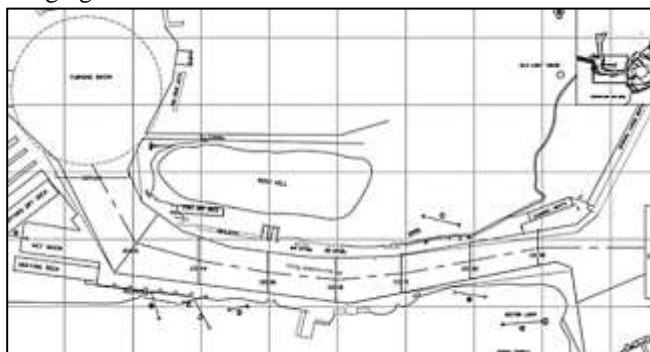
Fig. 1 Entrance channel and turning circle of outer harbor of VPT

A. Methodology for Under Water Blasting

The methodology of underwater blasting for rock dredging consisted of the following stages [9]:
  a. Pre-Blast survey
  • Study bed rock characteristics
  • Study structures around to be protected
  b. In-Blast monitoring
  • Continuous monitoring of ground vibration
  • Reengineering blast design
  • Creation of data-bank
  • Periodic submission of records
  c. Post-Blast survey and analysis
  • Study of vibration records
  • Study of structures around as a part of Post-blast survey

B. Underwater Blasting

Method of confined charges was used as the depth to be dredged varied from about -2m to -8m at different places. Based on the rock mass characteristics, it was fixed to use blastholes of 110mm diameter. All the operations of drilling of required number of blastholes, charging of blastholes with required quantity of explosive, establishing the connections in the blast round and final firing of the blast round were carried out from the floating drill barge. The drill barge had facility for mounting required number of DTH drills, compressors, separate storage for explosives and detonators etc. Three drill barges fitted with 15, 12 and 7 drills were deployed. Each barge was mounted with two units of DGPS systems, for ensuring precise positioning of barge. The cycle of underwater blasting operations consisted of the following activities:
  • Positioning of drill barge
  • Drilling required number of holes
  • Simultaneous charging of blastholes, immediately after completion of drilling
  • Repeating the above operations for required number of rows
  • Establishing the blast layout
  • Marching the drill barge to safe distance
  • Taking all the precautions
  • Firing the blast round

Nitrate based slurry explosive available in couplable plastic tubes was used. Each cartridge was of 1kg and 2kg weights.

Required quantity of explosive to be charged, like 2kg, 3kg, 4kg or 6kg was prepared by coupling the plastic tubes containing explosive. The explosive charge in general varied from 3kg to 8kg per hole as per depth of the blast holes. The maximum permissible charge per delay (determined based on trial blast study initially, for protecting various structures simultaneously) was also considered while determining the charging pattern. Initially, electric short delay detonators, and subsequently shock tube system of initiation was used.

IV. RESULTS AND DISCUSSION

A. Ground Vibrations

During the entire period of rock blasting more than 1,345 blasts were conducted and PPVs were monitored at 65 structures, using Blast Vibrations Monitors, Minimate Plus of Instantel, Canada. Some of the structures of importance are shown in Fig. 2. PPVs recorded using Minimate of Instantel, Canada, at Hindustan Shipyard Ferry Jetty and ORS VPT Dry Dock are shown in Fig. 3.

A. HSL Ferry Jetty

B. VPT Dry Dock

Fig. 2 Some important structures

A

B
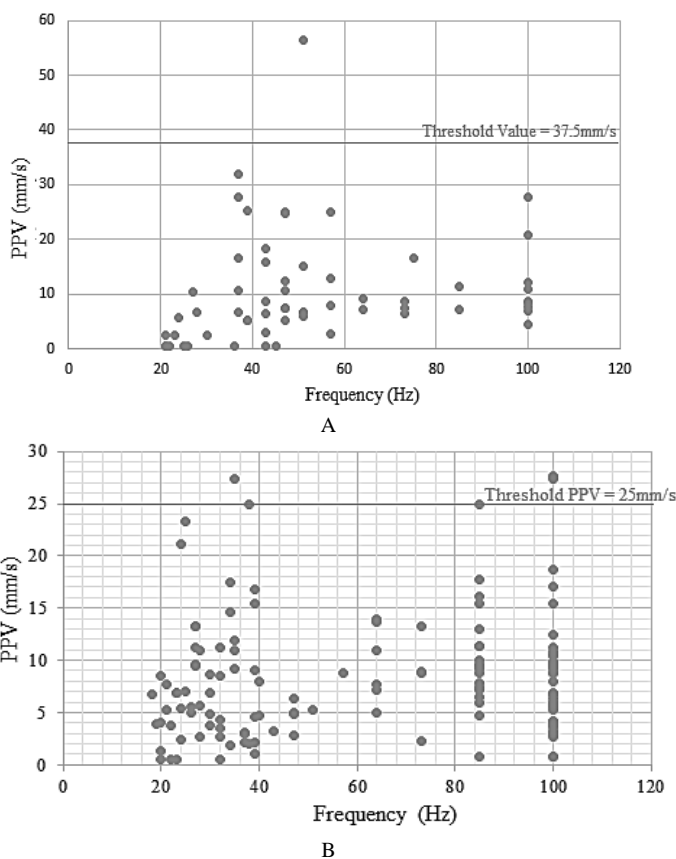
Fig. 3 PPVs recorded at different structures

The PPV values for HSL Ferry Jetty varied from <0.51mm/s to 56.5mm/s. Recorded PPV value exceeded the threshold value of 37.5mm/s only in 1.67% cases and it shows the accuracy and efficiency of blast design. For VPT Dry Dock only in 1.43% cases, the threshold PPV value was exceeded. Similarly, for all other 63 structures in the surroundings, the resulting PPV values were well within limits, indicating very safe underwater blasting operations carried out.

B. Water Borne Pressure Wave and Safe Distances

As per US Navy guidelines the equation given by [10] is used for calculating the overpressure as:

$$P = \frac{13000 \sqrt[3]{W}}{r} \tag{1}$$

where,

    P = Pressure on the diver, psi
    W = Weight of the explosive (TNT), lb
    r = Range of the diver from the explosive, ft

Using the recommended safe exposure values suggested by various standards, reverse calculation was carried out to determine the safe distances using the equation:

$$d_{min} = \frac{13000 \sqrt[3]{w}}{P} \tag{2}$$

where,

    P = Pressure on the diver, psi
    w = Weight of the explosive (TNT), lb
    R = Range of the diver from the blast site, ft

According to US Navy guidelines a safe exposure pressure for underwater blasts is considered to be 50psi (34.5MPa) [11]. Using Greenbaum and Hoff equation, calculations were carried out for the frequently used maximum charge per delays (kg) used for the underwater blasting project at the Vishakhapatnam port [1]. Results obtained are depicted in Fig. 4, as it can be used to interpret safe distance for explosive range up to 60kg.
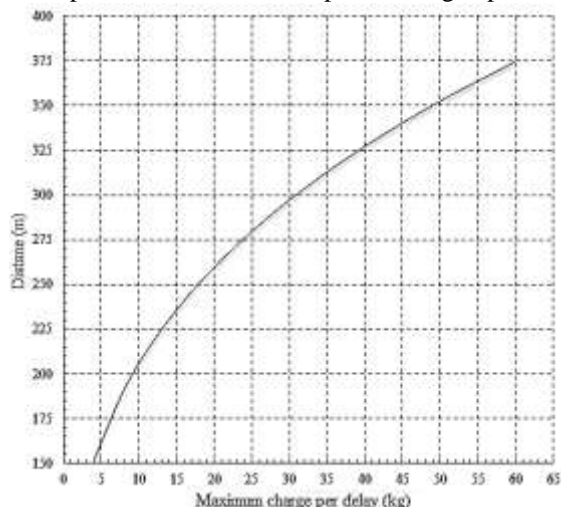
Fig. 4 Safe distance for divers

Reference [12] of the Alaskan Department of Fish and Game's guidelines to protect fish and incubating embryos from the impacts of blasting in and near the water bodies, it is stipulated that blast induced pressures should not exceed 2.7psi (1.9MPa). The Indian Ocean is also home to numerous marine mammals such as dolphins, sharks and porpoise. Studies have shown that blast induced pressures greater than 8psi (5.5MPa) can cause injury to mammals [8]. Accordingly, the safe distances for protecting mammals were determined. The safe distances recommended for fishes, mammals and humans are shown in Fig. 5.
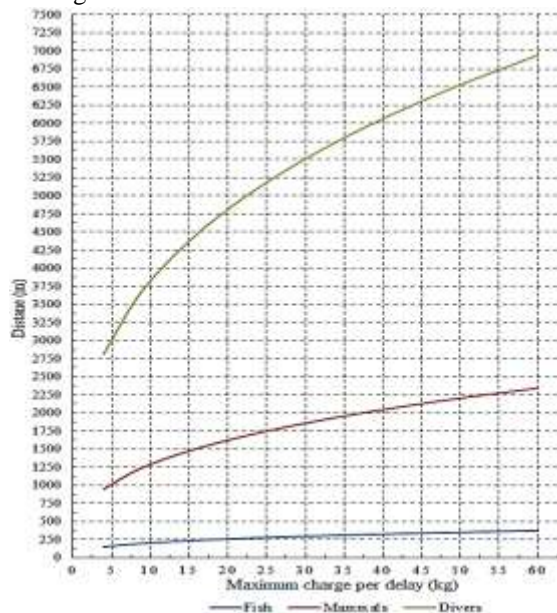
Fig. 5 Combined safety chart for divers, fish and mammals

V. Conclusions

Underwater blasting is a vital component of rock dredging projects in ports. The major environmental impacts associated with underwater blasting are the water borne shock waves and ground vibration. Use of explosives charge confined in blastholes substantially reduces the effects of ground vibrations on submerged structures and objects in water. Safety criteria recommended in terms of PPV for residential, marine and other structures can be used to monitor and protect them from ground vibrations. Underwater blasting operations were carried out in a safe and efficient manner using down-the-hole delay system, for the first time in the country, by dividing the total explosive column in blastholes into 2 or 3 decks, initiating at different timings, in order to maintain the safe maximum charges per delay for protecting close by structures.

Water borne shock waves are detrimental to the safety of not only the divers, but also to aquatic life like fish and marine mammals.

It is not only important to protect structures, but also the aquatic life from the impact of water borne shock waves from underwater blasts. Various safe distances that can be adopted at site for ensuring safety of divers during underwater blasting were arrived at. For a blast having maximum charge per delay of 20kg in the underwater blast, safe distances were found to be 250m for humans, 1650m for mammals and 4875m for fishes, by considering a threshold pressure value of 1.9MPa for fishes as suggested by Alaskan Department of Fish and Games organization United States. The safe distance values calculated for fishes and marine mammals can be made use in field in other projects also, to ensure that project locations having endangered or rarely existing species can be protected at the time of underwater blasting operations as a part of rock dredging projects.

References

[1] V. R. Sastry, "A report on underwater blasting operations for rock dredging in the entrance channel & turning circle of inner harbour of Visakhapatnam Port", An unpublished internal report submitted to Vishakhapatnam Port Trust, India, 2013.

[2] W. I. Duvall, and D. E. Fogelson, *Review of criteria for estimating damage to residences from blasting vibrations*, United States Department of the Interior, pp. 5, 1962.

[3] J. F. Wiss, and P. W. Linehan, *Control of vibration and blast noise from surface coal mining*, USBM OFR, pp. 79–103, 1978.

[4] G. L. Hempen, and T. M. Keevin, *The environmental effects of underwater explosions with methods to mitigate impacts*. US Army Corps of Engineers, St. Louis District, LEGACY Report, pp. 22-25, 1997.

[5] S. Glasstone, and P. J. Dolan, "The effects of nuclear weapons", 3rd ed. *U.S. Department of Defense and the Energy Research and Development Administration*, pp. 552–553, 1997.

[6] D. R. Richmond, J. T. Yelverton, and E. R. Fletcher, *Far-Field Underwater Blast Injuries Produced by Small Charges*, Defence Nuclear Agency, Department of Defence, Washington, D.C. Technical Progress Report, pp. 17–18, 1973.

[7] C. L. Hubbs, and A. B. Rechnitzer, *Report On Experiments Designed to Determine Effects of Underwater Explosions on Fish Life*, California Fish & Game Division. pp. 333–352, 1952.

[8] D. R. Ketten, *Estimates of Blast Injury and Acoustic Trauma Zones for Marine Mammals from Underwater Explosions*, pp. 391 – 407, 1995.

[9] V. R. Sastry, "Underwater blasting for rock dredging for entrance channel and outer harbour circle of VPT", An unpublished report submitted to Visakhapatnam Port Trust, India, 2014.

[10] L. J. Greenbaum, and E. C. Hoff, *A Bibliographic sourcebook of Compressed Air, Diving and Submarine Medicine*, Vol. No.–III, Bureau of Medicine and Surgery, Navy Department, 1966.

[11] Anon, *U.S Navy Diving Manual*, Revision 6, Change A, Published by Direction of Commander, Naval Systems Command, United States Navy, pp. 2.9-2.10, 2011.

[12] K. D. Kristen, and A. M. Catherine, *Blasting Effects on Salmonids*, Alaskan Department of Fish and Game, Division of Habitat, pp. 23, 2013.

Prof. V. Rama Sastry, born on Feb. 16, 1959, obtained his BE degree in Mining Engineering from Osmania University in 1980, and subsequently M.Tech degree in 1983 and Ph.D degree in 1990 in the field of Mining Engineering from Banaras Hindu University, India. His fields of research interests are Rock Mechanics, Rock Fragmentation and Rock Dredging.

Rama Sastry is having teaching and research experience of over 31 years. He is presently working as Professor of Mining Engineering at National Institute of Technology Karnataka, Surathkal, Mangalore (Government of India). He produced 7 Ph.Ds and guiding 6 more scholars in the areas of Rock Mechanics, Tunneling, Underground Large Spaces, Seismic Energy. He guided over 32 PG students projects and over 100 UG projects. He handled 17 R&D Projects and over 165 industry sponsored consultancy projects. He has over 160 research publications to his credit in various conferences and journals.

Prof. Rama Sastry bagged two Gold Medals from The Institution of Engineers (India) and One from Mining, Geological Metallurgical Institute (India) for best paper publication. He served as Director on the Boards of Central Mine Planning & Design Institute Limited (A Govt. of India Public Sector Unit) and KIOCL Limited (A Govt. of India Public Sector Unit).

Under Water Blasting for Rock Dredging and Protection of Structures: A Case Study

V. Rama Sastry*, G. Raghu Chandra, C. Karthik

Department of Mining Engineering, National Institute of Technology Karnataka, Surathkal, Mangalore, India

Abstract

Rock dredging in ports involves under water blasting for the pretreatment of hard sea bed. A rock dredging project covering an area of about 257,058 m^2 involving 400,000 cu.m of hard Khondalite rock mass was taken up in a port in the east coast of Southern India, for deepening of Turning Circle and Inner Harbour Channel. Pre-blast survey was carried out to assess type and condition of various structures standing on different distances from the dredging area and safe Peak Particle Velocities (PPV) were assigned. STADDPro analysis was carried out for determining the natural frequency of some marine structures with pile foundation. Under water blasts were planned with varying blast configurations at different locations from the structures in order to maintain the vibration levels to within prescribed threshold values. In total, 1150 under water blasts were conducted till date, consuming about 425 t of explosives. Down the hole initiation was implemented for protecting nearby structures from blast vibrations. The paper gives details of the methodology of underwater blasting and related studies carried out.

Keywords: blast vibrations, pre-blast survey, protective design, rock dredging, under water blasts

*Corresponding Author
E-mail: vedala_sastry@yahoo.co.in

INTRODUCTION

India is having 12 major sea ports and about 185 minor ports, along a coastline spreading over 7000 km. The Vishakhapatnam Port is one of the major ports operating under government sector on east coast. In order to enhance the cargo handling capacity, in tune with the increasing market demands, a project of deepening the draught has been taken up to dredge Inner Harbour Channel and Turning Circle area for a length of over 1.37 km, from the existing draught of −8 to −16.1 m. Sea bed in this port consists of hard Khondalite rock formation overlain by soil, clay, sand, etc. It is planned to dredge the softer overburden material initially, followed by rock dredging after exposing the rock mass layer. The pre-treatment of hard sea bed was planned by adopting under water blasting methodology, as it is the cheapest method of fragmenting the hard rock mass.

Rock dredging involving under water blasting operation requires meticulous planning, to begin with for designing the floating drilling barge, finalizing the blasthole array like Burden and Spacing in order to fix the Drill machines on the floating barge, for locating the blastholes, achieving good fragmentation, minimizing impact of ground vibrations and water borne shock waves on nearby structures, etc. Economy of any rock dredging project depends on the fragmentation results

achieved from under water blasts. As fragmentation requirement becomes finer, the cost of drilling and blasting operations increases. However, the cost of dredging and transporting operations decreases, and the overall project cost becomes optimum. It is extremely difficult to implement secondary breakage of boulders resulting from primary blasts in an underwater blasting project. Primary blasts should, therefore, be conducted with judicious selection of blast design parameters. As the entrance channel in this port is narrow, which is in between two hills on either side, the area of blasting is close to marine structures (Figure 1).

In addition to various marine structures, there are facilities like Hindustan Shipyard with Dry Dock, Dry Dock belonging to Visakhapatnam Port, old DCI Office, etc. in close proximity to the rock dredging area (Figure 2). In fact under water blasts are to be conducted from 3 m away from

1st row of piles supporting jetties at many places. Necessary care should, therefore, be taken to minimize the impact on the stability of structures. This requires sound knowledge of blast design and the role played by geological and explosive parameters in addition to the blasting process.
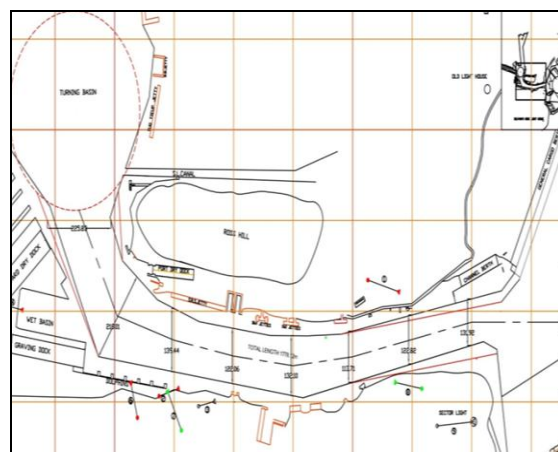
Fig. 1. *Area to be Dredged Surrounded by Many Marine and Other Structures.*
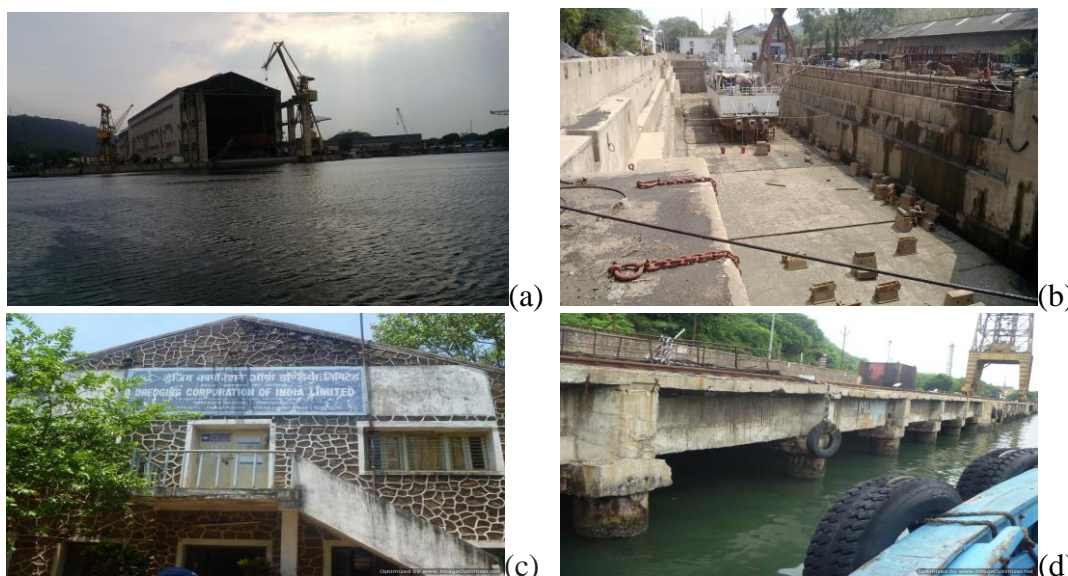
Fig. 2. *Various Structures to be protected. (a) Shipyard With Dry Dock, (b) Dry Dock of VPT, (c) Old DCI Office, and (d) Dolphin Jetty.*

UNDER WATER BLASTING

In order to increase the cargo handling capacity of Visakhapatnam Port, deepening of sea bed (draught) was taken up for a depth of about 6–8 m in the turning circle of outer harbour and inner harbour channel from the existing draught of about −8 to 16.1 m. The total area of rock dredging was about 215,058 m^2.

Initial geotechnical information about the sea bed strata was obtained from boreholes. Bathymetric survey data was used for assessing the sea bed levels. This was followed by Jet probing in a grid of 10 m × 10 m, for establishing the pre dredging rock levels. In order to generate more data about hard sea bed levels, 50 additional open holes were drilled initially at different locations, to establish hard rock bed levels. A pre-blast survey was carried out to understand the characteristics of the sea bed rock mass. In general, the RQD of the rock mass was found to be <75%, indicating that the rock mass is of Poor to Fair condition. As per the characteristics provided in the tender document, the uniaxial compressive strength of the rock mass was found to be between 28 and 50 MPa. However, it was also found that the rock mass is not massive and is having variations, and undulations also, as per the bathymetric survey reports. The preblast survey, thus formed basis for the design of drill barge(s), number of drill holes, explosive charge, etc. Also the bathymetric survey

charts were studied, in order to assess the depth of blastholes in different areas. Total area to be dredged was divided into A–I blocks, for scheduling of operations and to carry out rock dredging with under water blasts in a convenient manner.

In order to protect various structures in the port, a pre-blast survey was taken up involving 65 different structures. Some of these structures are shown in Figure 2. Also there is an old living area outside the port, at a distance of about 150 m from under water blasting site, consisting of domestic houses of various conditions, with an age of more than 60 years (Figure 3). Aim of this exercise was to identify type and condition of structures, and type of cracks present in the structure, so as to assign permissible Peak Particle Velocity (PPV) values. Various ground vibrations standards as per erstwhile USBM standards[1] and Indian DGMS standards[2] were considered for assigning threshold PPV values to various marine and other structures.

(a) (b)

Fig. 3. Houses and Other Structures in Poor Repair Condition in Neighbourhood of Port.

Modelling of Marine Structures

Natural frequency of some piled structures like jetties, was determined as varying from 10 to 26 Hz, by simulation study, creating vibrations in the structure and analysing, using STAADPro software. Figure 4 shows the details of one of the model simulated. Model of the structure was generated using the modules in the software. This software makes use of finite

element analysis. It gives stresses, deflection and the load coming on to the structure for the design purpose. From the software, the natural frequency of structure can be determined. Frequency can be calculated by Rayleigh method and modal calculation method. Modal method gives frequency of the structure in different modes. The structure was subjected to vibrations in different modes. Frequency

with which the structure vibrates in first mode was considered as the natural frequency of the structure. Software also gives a series of frequencies at which the structure vibrates, depending upon the number of modes given in the input.
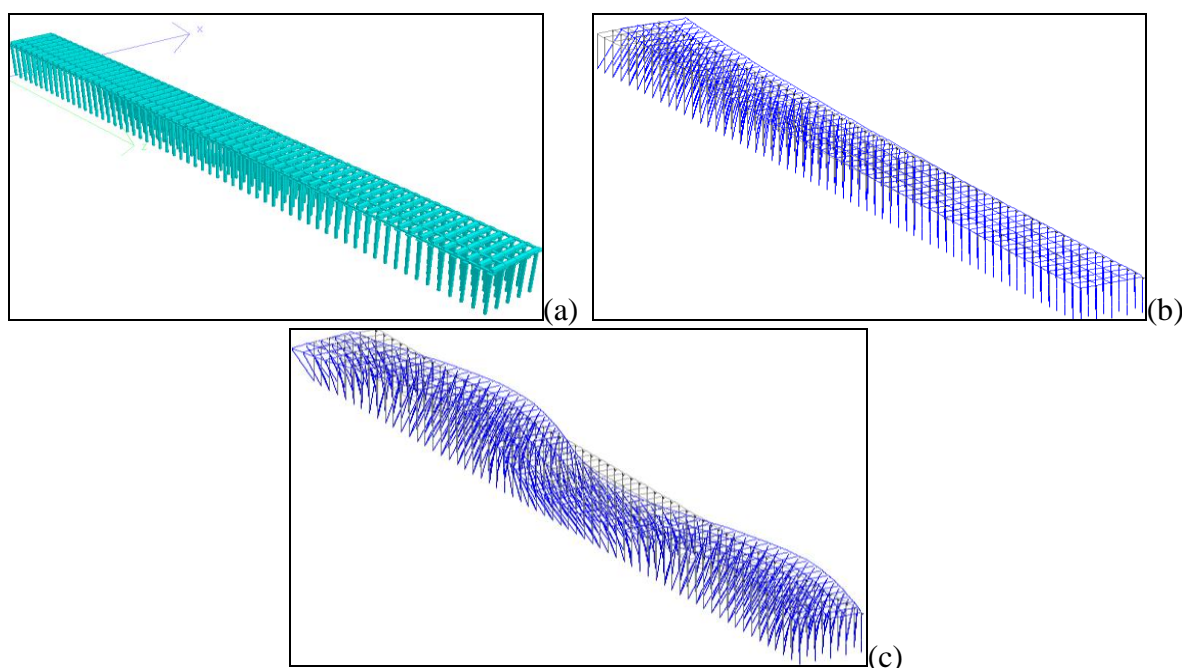
Fig. 4. *Details of the STAADPro Model. (a) 3D View of Marine Structure Simulated in STAADPro, (b) Mode Shape-1 of Structure, and (c) Mode Shape-5 of Structure.*

Under Water Blasting Operations

Two floating drill barges were fabricated mounting 7 and 15 drills on the barge, with 250 mm diameter casing pipes. The third barge was provided with 12 casing pipes of 250 mm diameter, and one drill machine. Diameter of blastholes was 110 mm (Figure 5). Each drill machine was supported by a separate air compressor, located on the floating barge. Each of these barges was provided with 2 DGPS systems, for finer position of barge at designated locations. Blasthole diameter was 110 mm. A burden distance of 2 m was implemented. Spacing between rows of blastholes was varies as 2–2.75 m from location to location, depending upon the distance between the blast site and the nearest structure, and also the desired yield from blast round. Each setting of barge yielded 7, 12, or 15 holes. Each blast round was made with 1–5 rows of blastholes, amounting to 7–60 holes.
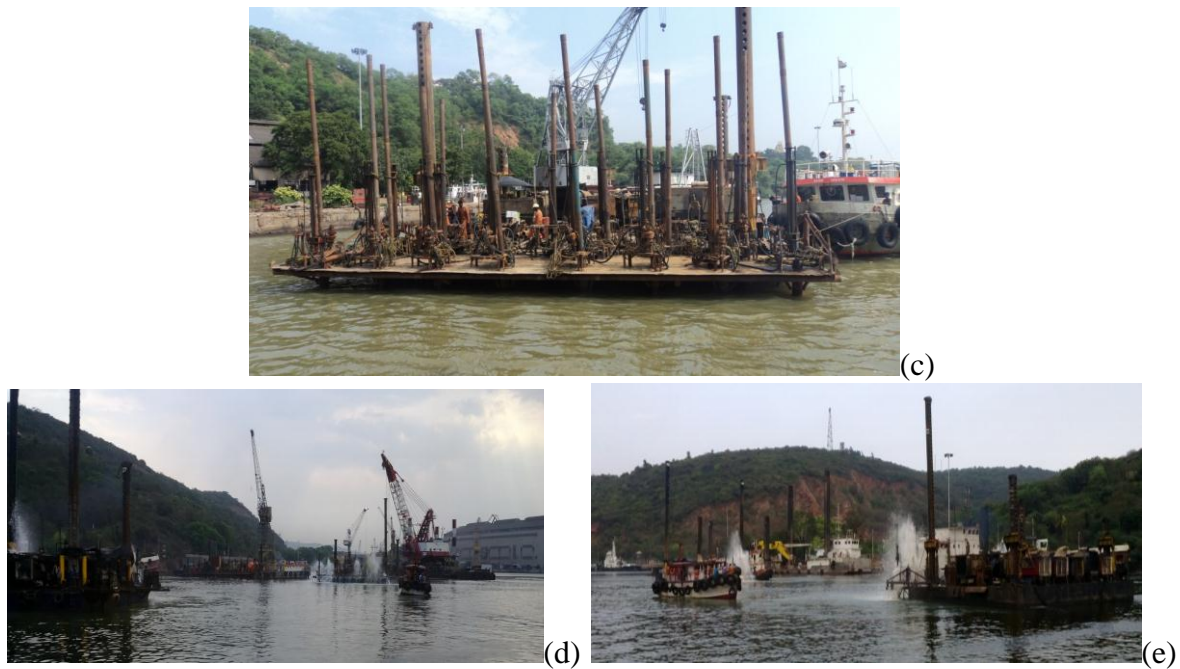
Fig. 5. Floating Drill Barges With Facility to Drill 7, 12, and 15 Blastholes and Drilling Operation in Progress.

Slurry explosives available in couplable tubes were used as explosive charges. Shock tube system of initiation with double sided initiation of Twindet was used for initiating explosive charges in the blastholes (Figure 6). This system provides down the hole initiation (delay) timing of 500 and 50 ms surface delay. Row to row delay of 17 or 25 ms was used. All the blastholes were charged immediately after completion of drilling operation.

Fig. 6. Explosives in Couplable Tubes and Shock Tube Initiators.

Total area of rock dredging, requiring under water blasting was divided into four zones of >50 m, 30—50 m, 30–10 m and <10 m from nearest marine structure. Blast designs were devised accordingly for various areas, taking into account number of blastholes per round, maximum explosive charge per delay, number of explosive decks per hole and the initiation pattern. Depth of blastholes varied from 2 to 7.5 m explosive charge per hole varied from 2 to 26 kg. Maximum charge per delay varied from 2 to 50 kg. Total explosive charge/blast round was varying from 52 to 1236 kg in different blast rounds. Powder factors varied from 0.72 to 3.93 kg/cu.m. Initially, electric short delay detonators were used for initiating blastholes. Subsequently, shock tube system of initiation was adopted, for blasthole initiation and for achieving required delay in blast rounds. In total 1150 under water blasts have been conducted so far. The quantity of explosive used till date is about 425t. Two types of Dredger, one Backhoe dredger of 5 cu.m capacity and a Grab Dredger of 200t capacity were used for dredging the blasted material from sea bed (Figure 7). These dredgers were dumping the material

into bottom discharge hopper barges for transporting and dumping the material at

designated location (Figure 8).

(a)   (b)

***Fig. 7.** Blasted Rock Mass Being Dredged. (a) Backhoe Dredger, (b) Grab Dredger.*

***Fig. 8.** Fragmented Material Loaded into Transport Barge.*

Human beings are far more sensitive to ground vibrations and noise than the structures. People tend to complain about ground vibrations even below the accepted damage levels because of many reasons. In fact, the threshold of a complaint for an individual depends on his health, fear of damage, relationship with project management, frequency of blasting, duration of vibration, etc. Informing neighbours about the blasting operations, time schedule and necessity, often results in an increase in the tolerance levels. As a matter of fact, the human perception of ground vibrations is as low as 1 mm/s. It is reported that if the attitude of local people is hostile towards project management, the tolerance level could be well below 2.5 mm/s, much below the accepted level of damage. Real time monitoring of the ground vibrations caused due to blasting operations assumes significance in that respect.

Initially, 20 trial blasts were conducted to establish the vibrations propagation

equation, to determine the safe explosive charges to be used for protecting structures standing at different distances from the blast site and finalizing blasthole initiation patterns. In fact it is established that progress of delays in a blast round is very important. Intensity of ground vibration (PPV) may be 2–3 times higher if the direction of progress of delays in given blast round.[3,4] When the blast round progresses away from the structures, the PPV values decrease.[5] Thus, the delay system becomes quite significant in controlling the PPV values at given distances. There are other methods like creating a pre-split plane.[6,7] between under water blast site and the structure, and creating a line drilling[8] for screening ground vibrations and protecting structures. Both these techniques are normally used as a last resort, as implemented by the first author in earlier projects.

Effective controlling of ground vibrations could be done using Down the Hole delay system, by creating more than two explosive decks within a blasthole and initiating them at different timings, especially where under water blasting has to be carried out close to the structures (Figure 9). These decks were initiated at different timings, in order to minimize the ground vibrations, and the impact on the structures.[9]

International Journal of Geological and Geotechnical Engineering
Vol. 2: Issue 1
www.journalspub.com
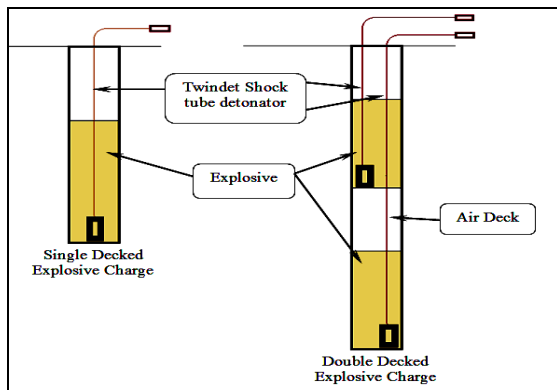
Fig. 9. *Arrangement of Explosive Decks in Blastholes.*

All the underwater blasts were monitored on a continuous basis for the entire duration of project, in order to generate the vibration data and identify the effect of blasting, at different structures inside and outside the port. Blast vibrations monitoring was done using two units of Minimate Plus of Instantel, Canada.[9] These are 4 channelled instruments having facility to monitor ground vibrations in three mutually orthogonal directions of longitudinal, transverse and vertical, and noise in fourth channel.

Vibrations were monitored near foundation of structure and on the marine structures like ORS Dry Dock, Wet Basin, Graving Dock, ORS Jetty-3, HRS Ferry Jetty, Channel Berth, Old and New DC Offices, Dolphin Jetty, Shipyard Dry Dock Structure, and near Temple, foundation of the Mosque and houses in nearby village, etc. In general the dominant frequency of ground vibrations recorded at different structures is greater than 26–30 Hz. Occasionally frequency at the dominant PPV was less than 12 Hz. None of the three orthogonal Longitudinal, Transverse and Vertical components showed frequency of less than 12 Hz at any given peak particle velocity. In 80% of the cases, the frequency component of PPV was greater than 30 Hz. In most of the cases, the intensity of ground vibrations was less than 2 mm/s. In a total of 1150 blats recorded so far, the intensity of vibrations was higher than the prescribed limits at different structures in 1.5% occasions. Under water blasting operations were carried out in a very safe and efficient manner.

CONCLUSIONS

Under water blasting is an essential component of hard rock dredging projects in ports. Sound knowledge of geology, geo-technical parameters of sea bed rock mass and blast design parameters is essential for the design of efficient and safer underwater blasts. Design of underwater blasts should be done judiciously, as the ramifications are quite significant related to project duration and therefore the cost of the entire dredging project. The dredging equipments highly capital intensive, with high economic risk factors. Productivity of these equipments is significantly dependent on the results of underwater blasting operations. Pre-blast and post-blast surveys and effectively designed controlled blasting methodology help in timely achievement of dredging targets. Continuous monitoring of underwater blasts with proper instrumentation will be of immense help in not only minimizing the environmental effects, but in generating data bank about the blast effects on structures, which will act as legal protection for future needs.

Under water blasts were carried out based on pre- and post-blast analysis. Of the 1150 under water blasts conducted so far, the PPV values overshot by the prescribed PPV limits at various structures only on about 1.5% occasions. Each such occasion was analysed immediately and the subsequent blasts were modified accordingly in order to keep the PPV values under threshold limits at various structures.

REFERENCES

1. Siskind D.E., Stagg M.S., Kopp I.W., *et al*. *Structures Response and Damage Produced by Ground Vibrations from Surface Mine Blasting.* USBMRI: 8507, 1981.

2. Anon. *DGMS (Tech)/S&T Circular No. 7.* dated 29-08-1997, 1997.

3. Sastry V.R. *Study into the Effect of Ground Vibrations Generated due to Underwater Blasting in New Mangalore Port on the Surrounding Structures.* Unpublished Internal Report submitted to New Mangalore Port Trust, Mangalore, 1996.

4. Sastry V.R. *Design of Underwater Blasting Operations in Tuticorin Port for the Construction of Multipurpose Berth No. 7.* An Unpublished Internal Report submitted to Tuticorin Port Trust, Tuticorin, 1997.

5. Sastry V.R. *Control of Ground Vibrations and Fly Rock caused due to Blasting Operations in Canal Excavation Work at Shimoga.* Upper Tunga Project, Karnataka Neeravari Nigam Limited, Dept. of Irrigation, Govt. of Karnataka, An Internal Report, 2001.

6. Sastry V.R. *Design of Underwater Blasting operations for Deepening of Dock Basin in front of Jetty No. 6 in Mangalore Port.* An Unpublished Internal Report submitted to the New Mangalore Port Trust, Mangalore, India, 1998.

7. Sastry V.R. *Design of Under Water Blasts or Rock Dredging in front of Berth No. 8.* An Internal Report submitted to Tuticorin Port Trust, Tuticorin, 2003.

8. Sastry V.R. *Protection of Princes Dock and Victoria Dock Structures from the Effects of Under Water Blasts for the Construction of Key Wall for Reclamation.* An Internal Report submitted to Mumbai Port Trust, Mumbai, 2011.

9. Sastry V.R. *Design and Implementation of Under Water Blasts for Deepening of Inner Harbour Channel in Visakhapatnam Port, Dharti Dredging & Infrastructure Limited.* An Internal Report submitted to Visakhapatnam Port Trust, Visakhapatnam, 2014.

Genetic Algorithm Approach For The Position Control Of Permanent Magnetic Synchronous Machine

Garimella Raghu Chandra*[1] and Garimella Atchyut[2]
[1]Department of Mining Engineering, National Institute of Technology Karnataka, Surathkal, India
[2]Gouthami (Medical) Educational Institute, Ravulapalem, Andhra Pradesh, India

Abstract

Permanent Magnetic Synchronous Motors (PMSM or Brushless DC Motor) are widely being used for many industrial applications because of their high efficiency, high torque and low volume. Research has conducted using genetic algorithm to develop a complete model of the BLDC motor and to design an optimal controller for its position control. Generally PID controller is being used for control purposes in many systems because of its simple structure and easy implementation. However, in practice, we often do not get the optimum performance with the conventionally tuned PID controllers. For this purpose, Artificial Intelligence based Genetic Algorithm is proposed as an optimizer to find the optimized PID gains for the position control of PMSM motor. Comparison was made with the traditional method. Simulation results showed that PID control tuned by GA provides more efficient closed loop response for position control of PMSM motor. MATLAB/SIMULINK software package was used for the modelling, control and simulation of the PMSM motor.

Keywords: artificial intelligence, optimized PID controller, permanent magnet synchronous motor, pulse width modulation

*Corresponding Author
E-mail: raghuchandhra@india.com

INTRODUCTION

BLDC engines are exceptionally mainstream in territories which require elite due to their littler volume, high compel, and straightforward framework structure. By and by, the configuration of the BLDCM drive includes a mind boggling process, for example, displaying, control plan choice, reenactment and parameters tuning and so on.

A specialist learning of the framework is required for tuning the controller parameters of servo framework to get the ideal execution. As of late, different present day control arrangements are proposed for the ideal control outline of BLDC motor.[1,2] However, these strategies are mind boggling in nature and require over the top calculation. Interestingly, PID control gives

a straightforward but then powerful answer for some control problems.[3]

In spite of the fact that PID controllers have a straightforward structure however it is very testing to discover the enhanced PID picks up. The proceeding with execution changes of computational frameworks have made Genetic Algorithm (GA) suitable for finding worldwide ideal answer for control framework, for example, the hunt of optimal PID controller parameters.[4,5]

In this paper, extensive modeling of a BLDC motor and GA-based PID scheme is proposed for its position control. The paper is organized in the following manner mathematical modeling, the driving circuitry of BLDC motor, then the design of PID controller using Ziegler-Nichol's (ZN)

method, brief overview of GA, illustration of the design of PID controller using GA method, the comparison between the results obtained by the GA and ZN method and finally, conclusion of the paper.

MATHEMATICAL MODELING

Figure 1 shows the basic building blocks of BLDC motor and its Driving circuitry. The Y -connected, 3-phase motor with 8-pole permanent magnetic rotor is driven by a standard three phase power convertor. The motor specifications are given in Table 1.[6-8]
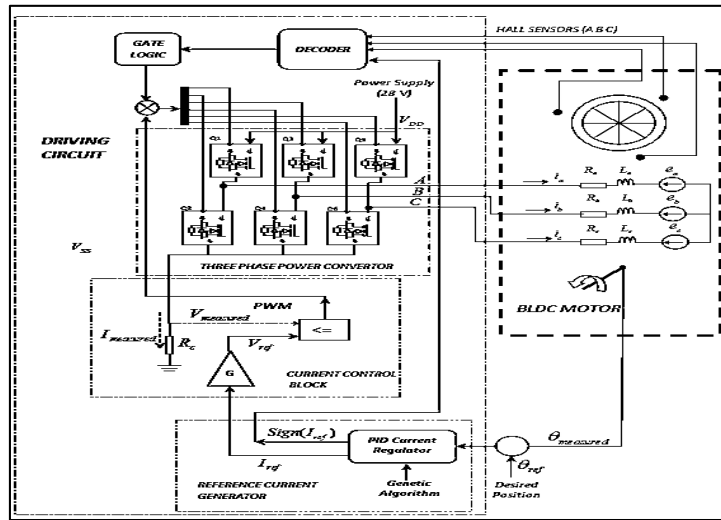
Fig. 1. Block Diagram of BLDC Motor.

Table 1. BLDC Motor Specifications.

Number of Poles	8
Stator resistance	0.0905 ohms
Stator inductance	0.115 mH
Rated Torque	50 Nm
Rated speed	140 deg/sec
Bandwidth	6-8 Hz
Supply voltage	28 V
Nominal current	11 A
Sampling period	10 μs
Friction constant	0.0001 Kg-m s/rad
Motor moment of inertia	0.000018395 Kg-m s^2/rad

Driving circuit consists of Reference Current Generator, PID controller, PWM current controller and MOSFET based three phase Power Converter. Figure 2 shows the complete Simulink model of three phase BLDC motor with its controlling and driving circuitry. The detailed description of the major blocks of BLDC motor is mentioned below.
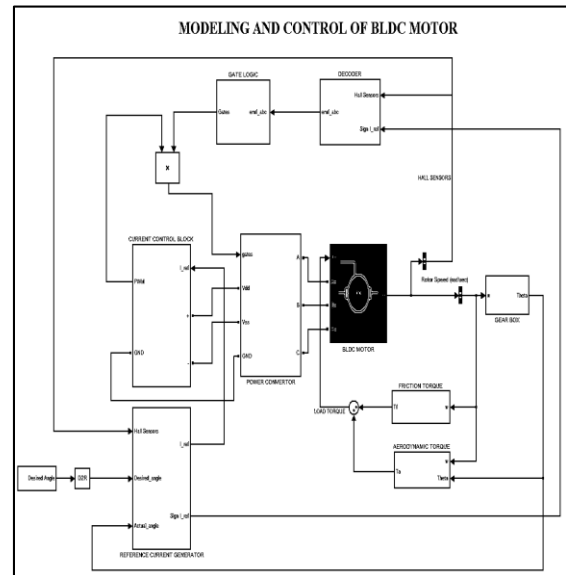
Fig. 2. Simulink Model of BLDC Motor.

The electrical part of DC brushless motor and relationship between currents, voltage, and back electromotive force and rotor velocity is derived using Kirchhoff's voltage law:[6]

Electrical Subsystem

$$v_a = R_a i_a + L_a \frac{di_a}{dt} + M_{ab} \frac{di_b}{dt} + M_{ac} \frac{di_c}{dt} + e_a$$

$$v_b = R_b i_b + L_b \frac{di_b}{dt} + M_{ba} \frac{di_a}{dt} + M_{bc} \frac{di_c}{dt} + e_b$$

$$v_c = R_c i_c + L_c \frac{di_c}{dt} + M_{ca} \frac{di_a}{dt} + M_{cb} \frac{di_b}{dt} + e_c \quad \text{Eq. (1)}$$

Mechanical Subsystem

A mathematical relationship between the shaft angular velocity and voltage input to the DC brushless motor is derived using Newton's law of motion.[6]

$$J \frac{d\omega_r}{dt} = T_e - T_m - F\omega_r \quad \text{Eq. (2)}$$

The angular position is obtained from an integration of the angular velocity.

$$\theta_r = \int \omega_r \, dt \quad \text{Eq. (3)}$$

Generated electromagnetic torque for this 3-phase BLDC motor is dependent on the current, speed and back-EMF waveforms, so the instantaneous electromagnetic torque can be represented as:

$$T_{em} = \frac{1}{\omega_m} (e_a i_a + e_b i_b + e_c i_c) \quad \text{Eq. (4)}$$

Description of Driving Circuitry

Driving circuitry consists of three phase power convertors as shown in Figure 3, which utilize six power transistors to energize two BLDC motor phases concurrently. The rotor position, which determines the switching sequence of the MOSFET transistors, is detected by means of three Hall sensors mounted on the stator.
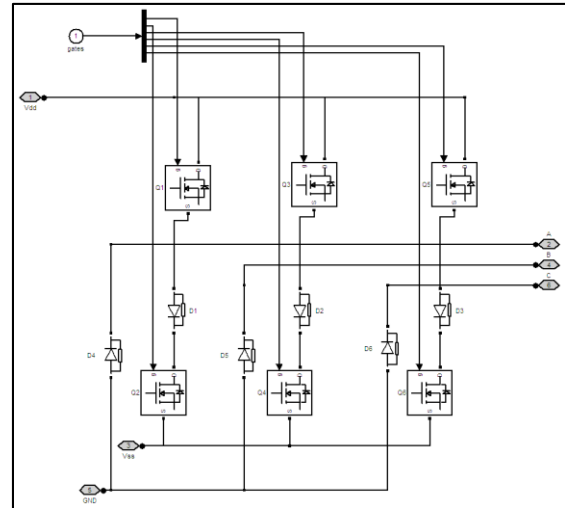
Fig. 3. *Three Phase Power Convertor.*

By utilizing Hall sensor data and the indication of reference current (delivered by Reference current generator), Decoder piece creates signal vector of back EMF. The essential thought of giving so as to run engine in inverse course is inverse current. Based on that, we have Table 2 and Table 3 for calculating back EMF for Clockwise and Anticlockwise direction of motion as shown below:

Table 2 *Clockwise Rotation.*

Hall Sensor A	Hall Sensor B	Hall Sensor C	EMF A	EMF B	EMF C
0	0	1	0	-1	1
0	1	0	-1	1	0
0	1	1	-1	0	1
1	0	0	1	0	-1
1	0	1	1	-1	0
1	1	0	0	1	-1

Table 3 *Anticlockwise Rotation.*

Hall Sensor A	Hall Sensor B	Hall Sensor C	EMF A	EMF B	EMF C
0	0	1	0	1	-1
0	1	0	1	-1	0
0	1	1	1	0	-1
1	0	0	-1	0	1
1	0	1	-1	1	0
1	1	0	0	-1	1

The gate logic to transform electromagnetic forces to the six signal on the gates is given below:

Table 4 Gate Logic.

EMF A	EMF B	EMF C	Q1	Q2	Q3	Q4	Q5	Q6
0	0	0	0	0	0	0	0	0
0	-1	1	0	0	0	1	1	0
-1	1	0	0	1	1	0	0	0
-1	0	1	0	1	0	0	1	0
1	0	-1	1	0	0	0	0	1
1	-1	0	1	0	0	1	0	0

In reference current generator block as shown in Figure 4, PID controller endeavors to minimize the distinction between wanted point and the real measured edge by making a restorative move to produce reference current sign. Direction of rotation is based on the sign of that reference current.

In current control square appeared in Figure 5, the reference current from current generator is changed to reference voltage signal by utilizing Ohm's law *(Vref = Iref R)*. This reference voltage is then contrasted and the deliberate voltage crosswise over control resistance Rc, where *Rc=0.01 Ω.* When the measured voltage is less than the reference voltage, control signal is set to one for t = 2Ts, where T_s is sampling time.

In other case control signal is set to zero. In this way a pulse width modulated (PWM) signal having fixed frequency with variable duty cycle is obtained. This PWM signal is then multiplied with the output from gate logic to drive three phase power convertor.
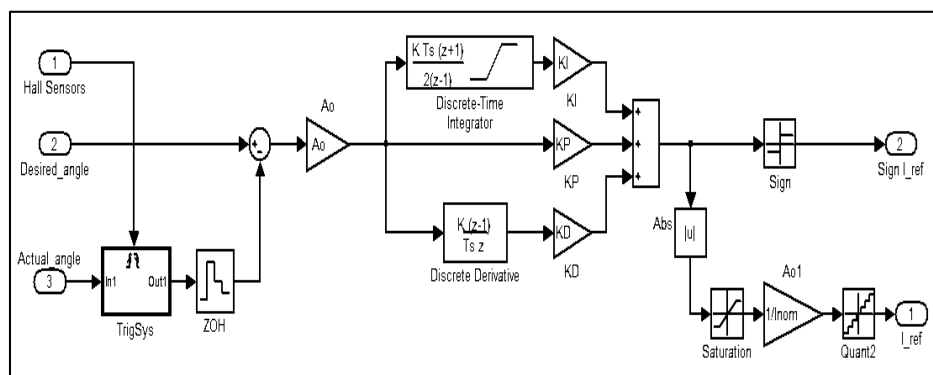
Fig. 4. Reference Current Generator Block.
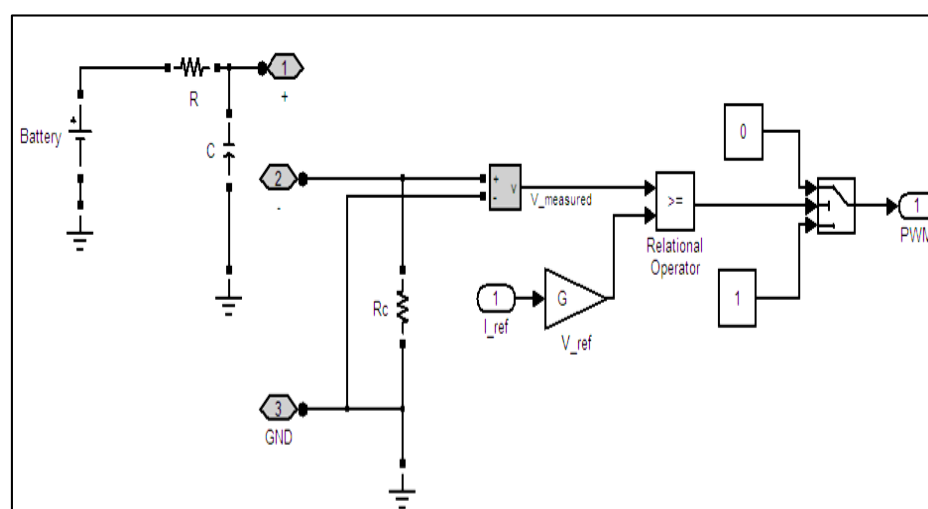
Fig. 5. Current Control Block.

DESIGN OF PID CONTROLLER USING ZIEGLER NICHOLS METHOD

A PID controller is designed using the Ziegler-Nichols frequency response method.[7] The discrete time PID controller is defined as:

$$\delta_c = K_p \left(1 + \frac{T_s z}{T_i(z-1)} + T_d \frac{z-1}{T_s} \right) e$$

Eq. (5)

The addition increasing so as to tune of PID is finished the corresponding addition until the framework wavers, that pick up is K_u.

At this instant, time interim is measured between peaks to get T_u. Table 5 gives estimated values for the controller additions.

Table 5. *The Ziegler-Nichols Rules (Frequency Response Method).*

Controller	K_p	T_i	T_d
PID	0.6 x Ku	$Tu / 2$	$Tu / 2$

From the above algorithm the step response of the system is shown in Figure 6.
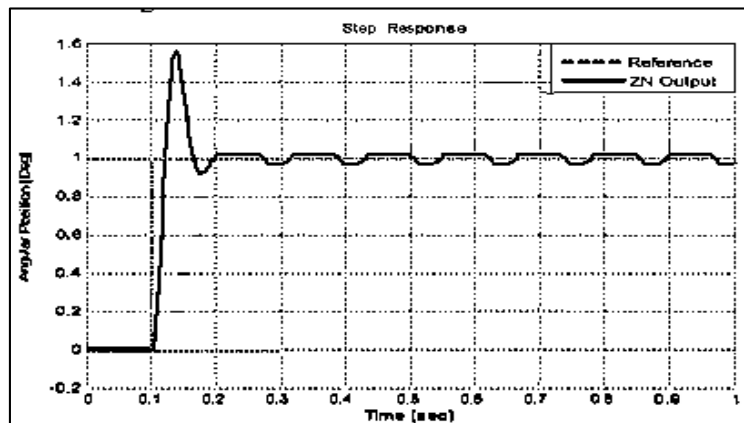
Fig. 6. *Step Response.*

Table 6. *Controller Performance.*

	Ziegler Nichols Method
K_p	2400
T_i	0.02
T_d	0.005
Overshoot	54%
Rise Time	0.03 sec
Settling Time	0.09 sec

Above analysis depicts that the system response is not optimum. In order to achieve better performance, GA approach is used to find the optimal values of PID gains.

OVERVIEW OF GENETIC ALGORITHM

Genetic algorithms try to imitate the properties of natural selection and natural genetics. It begins with initial population that consists of coded strings of binary numbers, called chromosomes that hold possible solutions of the problem. Their performance is evaluated by a fitness function. Strings with higher fitness value are likely to survive to the next generation as parents. It uses three operators namely selection, crossover and mutation to produce next generations. This procedure is repeated until it finds the optimal solution to the problem.

TUNING OF PID CONTROLLER USING GENETIC ALGORITHM APPROACH

The values of the PID controller parameters K_p, T_i and T_d are optimized using GA to ensure optimal control performance. The steps involved in evaluating best possible controller gains are listed below:

Initialization of Parameters

To introduce GA, we need to characterize certain underlying parameters. The execution of the outlined controller depends vigorously on how well we appointed the qualities to these parameters. Parameters with their relegated qualities are recorded beneath:

Table 7. Initialization Parameters.

Generations	100
Population size	30
Bit length of the considered	6
Maximum number of generations	0.8
Selection method	Arithmetic Crossover
Crossover probability	0.8
Mutation type	Uniform mutation
Mutation probability	0.05

Objective Function for the GA

To calculate the fitness of each chromosome, selection of objective function is very critical. The objective functions are mean of the squared error (MSE), integral of time multiplied by absolute error (ITAE), integral of absolute magnitude of the error (IAE), and integral of the squared error (ISE).[4] An integral absolute error (IAE) criterion is used in this paper for calculating performance index of controller as mentioned below.

$$IAE = \int_0^T e(t)dt \qquad \text{Eq. (6)}$$

where T = 1 sec.

The Fitness Values

Target is to minimize the estimation of execution record. The fittest chromosome will be the one which has littlest estimation of that execution index,[5] so we can characterize wellness esteem as

$$Fitness\ value = \frac{1}{PerformanceIndex} \qquad \text{Eq. (7)}$$

Termination Criteria

End of calculation happens when the estimation of the wellness capacity for the best point in the present populace is not exactly or equivalent as far as possible and the adjustment in the estimation of wellness capacity is not as much as capacity resilience. The best individual from the populace was chosen and plotted in the diagram. The variety of the PID parameters K_p, T_j and T_d are appeared, separately, in Figures 7 to 9.
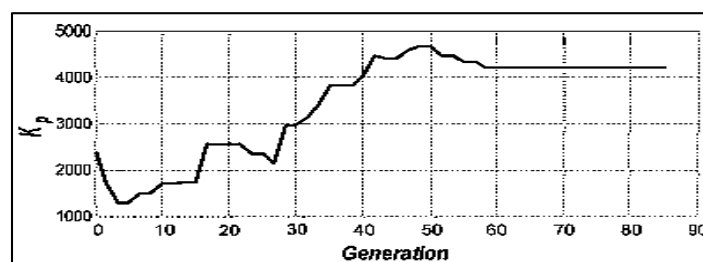
Fig. 7. Kp Convergence.
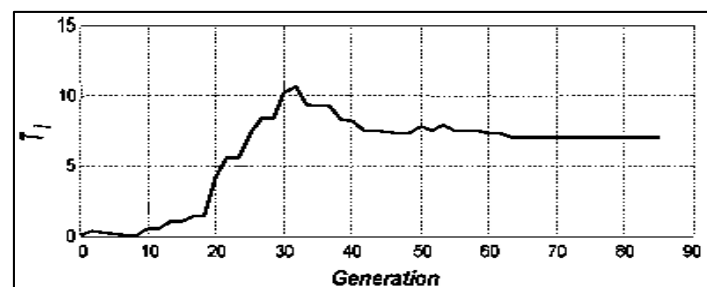
Fig. 8. Ti Convergence.
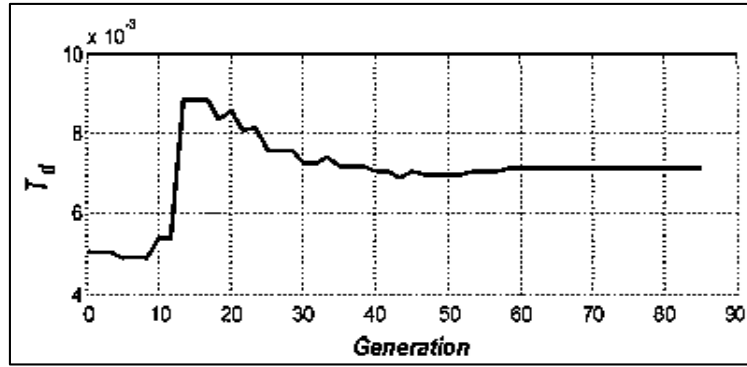
Fig. 9. *Td Convergence.*

It is evident from the results that the best particle has an excellent convergence before reaching generation limit. The plot

of the error, which is based on IAE criterion for all iterations, is shown in Figure 10.
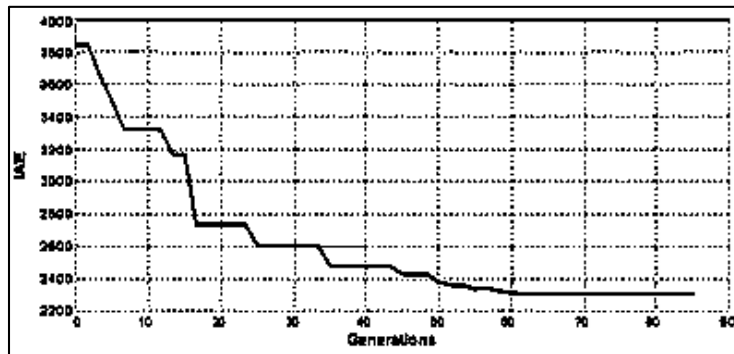
Fig. 10. *JAE Convergence.*

PID parameters acquired after GA optimization are listed below:

Table 8. *Optimized Gain Using Genetic Algorithms.*

K_p	T_i	T_d
4200	7	0.0071429

SIMULATION RESULTS AND COMPARISON

With optimized PID gains using GA, the step response of the controlled system is shown in Figure 11 along with the response obtained from ZN method:
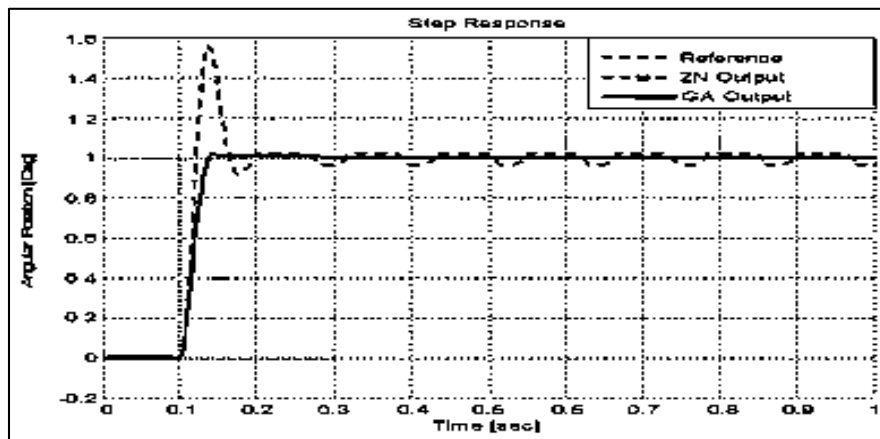
Fig. 11. *Performance Comparison.*

It is apparent from the above step response that the controller performance with GA optimized gains is quite efficient as compared to the response obtained from ZN method. The comparison of results in term of rise time, settling time and overshoot are listed in Table 9 below:

Apart from step response, various simulations are carried out in which sinusoidal and square waves having various amplitude and frequencies are applied. Performance comparison of GA optimized controller with the controller tuned by ZN

method from various simulations are shown in Figures 12 to 15.

Table 9. *Performance Comparison.*

	Ziegler Nichols	**Genetic Algorithm**
K_p	2400	4200
T_i	0.02	7
T_d	0.005	0.007142
Overshoot	54%	Less than 1%
Rise Time	0.03 sec	0.03 sec
Settling Time	0.09 sec	0.051 sec
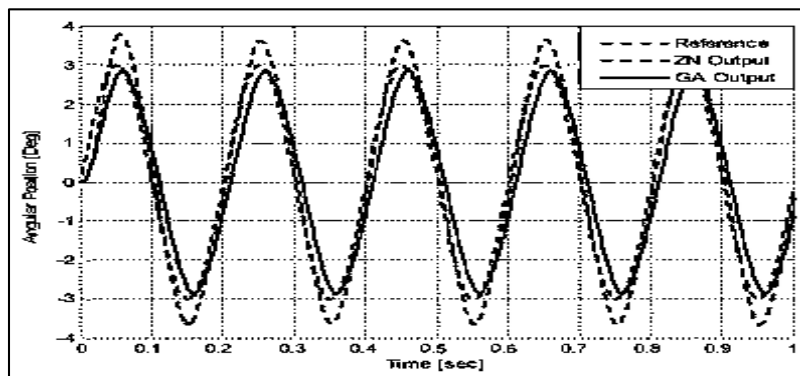
Fig. 12. *Sinusoidal Response 3deg at 5 Hz.*
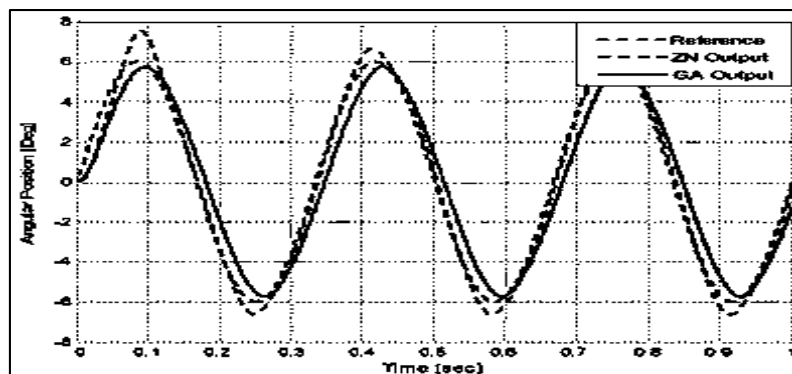
Fig. 13. *Sinusoidal Response 6 deg at 3 Hz.*
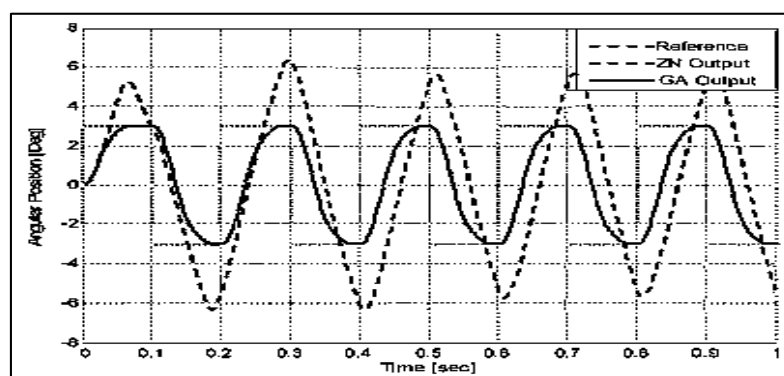
Fig. 14. *Square Wave Response 3 deg at 5 Hz.*
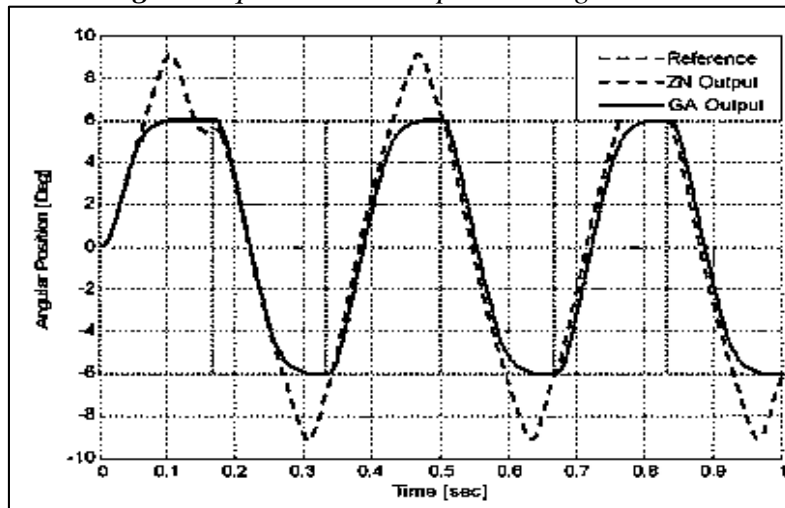
Fig. 15. *Square Wave Response 6 deg at 3 Hz.*

It is clear from Figures 12 to 15 that the controller designed with ZN method has high overshoots as was observed in the step response, while the controller with GA optimized gains precisely follows the input signal. Figure 14 and 15 depict that the response of ZN method appears sinusoidal against square wave input. The reason is that the controller was still in its transient state when the next pulse is arrived.

CONCLUSION

In this paper, modeling of three phase BLDC motor and its optimized PID position control design using GA is presented. Comparative study is carried out in which the response of GA based controller is compared with the controller designed using ZN method. It is obvious from simulation results that the controller performance with GA optimized gains is much more efficient than the ZN method in terms of rise time, settling time, overshoot and set point tracking. However ZN method is good for providing the starting values of PID gains for GA optimization.

Hence it can be concluded that GA provides an efficient controller tuning methodology for obtaining improved and accurate performance of a system.

REFERENCES

1. Hemati N., Thorp J. S., Leu M. C. Robust nonlinear control of Brushless dc motors for direct-drive robotic applications. *IEEE Trans. Ind. Electron.* 1990 Dec ; 37: 460–8p.
2. Pelczewski P. M., Kunz U. H. The optimal control of a constrained drive system with brushless dc motor. *IEEE Trans. Ind. Electron.* 1990 Oct; 37: 342–8p.
3. Ang K., Chong G., Li Y. PID control system analysis, design and technology. *IEEE Trans. Control System Technology*. 2005 July; 13: 559–76p.
4. Mahony T. O., Downing C. J., Fatla K. Genetic algorithm for PID parameter optimization: minimizing error criteria. *Int. Conf. on Process Control and Instrumentation.* 2000 July 26-28. 148–53p.
5. Goldberg D. E. *Genetic Algorithms in Search, Optimization and Machine Learning*. The University of Alabama. Addison-Wesley Publishing Company Inc. 1989.
6. Atef Saleh Othman Al-Mashakbeh. Proportional Integral and Derivative Control of Brushless DC Motor. *European Journal of Scientific Research. 2009* July 26-28; 35: 198–203p.
7. Ziegler J., Nichols N. Optimum settings

for automatic controllers. *Trans of ASME.* 1942; 64: 759–68p.

8. Srikanth S., Raghu Chandra G. Modeling and PID control of the brushless DC Motor with the help of Genetic Algorithm. *IEEE - International Conference On Advances In Engineering, Science And Management.* 2012 March; 639–44p.

Generation and Accuracy Assessment of Digital Elevation Model Using Digital Photogrammetry and Differential Global Positioning System Techniques

V R SASTRY[1], D V REDDY[2], G RAGHU CHANDRA[1], N ADITHYA[1], S A SAIPRASAD[1]

[1]*Department of Mining Engineering, NITK, Surathkal, Mangalore-575025, INDIA*
[2]*Department of Civil Engineering, NITK, Surathkal, Mangalore-575025, INDIA*
Email: vedala_sastry@yahoo.co.in, dvr1952@yahoo.com, raghuchandhra@india.com

Abstract: Blasting can be considered as the most crucial process in an opencast mine. It is therefore important for mining engineers to understand the effect of geological discontinuities and blast design parameters on the results of blasting. Bench height and burden are very important parameters affecting stiffness of bench. Joints alter the results of blasting, by making explosive energy utilization ineffective. Modern tools like high speed videography reveal many aspects of fragmentation process, which otherwise are difficult to visualize and understand. An attempt is made through this paper to present some of the research results of model scale studies, coupled with field study results related to bench height and joints in order to improve blast results.

Keywords: *Rock Fragmentation, Geological Discontinuities, Bench Height, Burden, Joint Orientation, Gas Energy, Shock Energy, High Speed Videography*

1. Introduction:

Detonation of an explosive charge confined in a blasthole releases a vast amount of chemical energy, which is then transformed into gaseous energy. This gaseous energy exerts an enormous amount of pressure on the blasthole wall. This pressure results in the generation of shockwaves carrying shock energy. According to Sadwin and Junk (1965), the explosive can be categorised in this phase by two pressures:

- Detonation Pressure: Dynamic pressure associated with the detonation wave.
- Explosive Pressure: Pressure developed when the explosive reacts to produce gaseous products.

Thus, the detonation of an explosive under confinement creates two types of energies: strain energy (5-20% of total explosive energy) and gaseous energy (80-95% of total explosive energy).

For an efficient blast, it is necessary to utilize the explosive energy for productive work as much as possible. Design of an efficient blast requires sound knowledge about the role of blast design parameters, explosive characteristics and the structural discontinuities in fragmentation process. Joints, the most commonly occurring discontinuities in the rock mass play a significant role in influencing the blast results. This study makes an effort at relating various parameters of a blast, which can be used to design an

efficient blast, with special emphasis on the usage of high speed videography.

2. Literature Review

2.1 Role of strain and gas energies

Before 1959, it was generally perceived that rock breakage is caused mainly by strain waves. However, Fogelson et al. (1959), conducted a series of tests to measure the explosive energy transmitted to rock mass by strain waves, and determined that the strain waves only play a minor role in fragmentation.

Burden rock movement studies by Noren (1956) showed that strain waves cannot be the dominant factor in rock fragmentation, as he showed that it had time to travel the burden distance at least six times before any surface rock movement started. Also, he observed that the burden accelerated continuously during its motion. Had strain waves acted upon it, then the motion would have been discontinuous. Saluja (1963) found out that in case of high explosives, the rock is fractured by a combination of gaseous and strain energy. However, he also showed that in low explosives (gunpowder), the breakage occurs solely due to gaseous energy (Clark and Saluja, 1964).

In 1971, Kutter and Fairhurst proposed a more generalized theory based on their experiments. They argued that:

- Both strain waves and gaseous energy play an important role in fragmentation.

- Strain wave functions to pre-condition the rock mass by initiating radial cracks.
- Gaseous energy then expands and extends the cracks.
- Presence of free surfaces favours extension of gas pressurized radial cracks.
- In-situ stresses significantly influence the direction of radial crack propagation.

According to the gas pressurization configuration given by Kutter and Fairhurst (1971), gases under high pressure penetrate into radial cracks forming a hydrostatically stressed cylinder of material where the hydrostatic stress is equal to the gas pressure (Figure 1). This large hydrostatically stressed cylinder applies pressure at the back of the burden, inducing bulk rock movement (Figure 2).

Fragmentation of rocks can be explained by another mechanism, known as "Flexural Rupture Mechanism", which involves the transverse fracturing of segments formed by radial cracks (Figure 3).
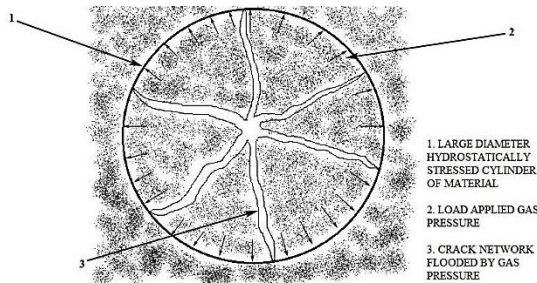
Figure 1. Hydrostatic stress field created around a blasthole (Kutter and Fairhurst, 1971)
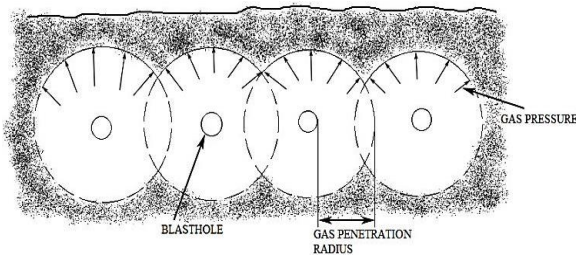
Figure 2. Gas pressure applied load at the periphery of hydrostatically stressed cylinders causing rock movement (John, 1983)

In this theory, 90% of the total energy required to break the rock was assumed to come from gaseous pressure alone. The sustained gaseous pressure drives radial cracks through the burden upto the free face and displaces the rock through bending, in the direction of the least resistance, generally following the naturally occurring weakness planes.
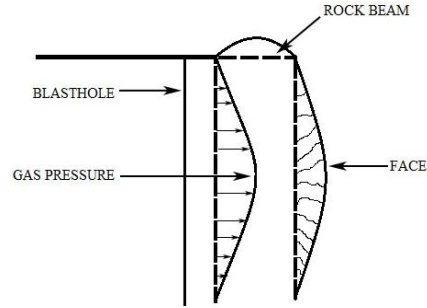
Figure 3. Rock breaking by flexural bending (Ash, 1973)

Ash and Smith introduced the stiffness theory in 1976, according to which, the degree of fragmentation depended upon the stiffness property of the burden rock. In terms of blasting, *Burden, Spacing,* and *Bench Height* are the three main factors affecting the burden rock stiffness. For achieving good fragmentation, the burden to bench height ratio needs to be properly analysed as the stiffness varies to the third power of this ratio. Reducing burden for a given bench height has been shown to have a positive effect. Thus, increase in bench height reduces the stiffness of burden rock mass.

2.2 Effect of joints

Joints are the most common discontinuities present in rock mass. They create impedance mismatch zones in the strain wave transmitting medium and thereby cause unusual reflection and/or refraction of strain energy. Joints interrupt the development of radial crack network, and thus control the shape and size of the crater to a large extent. The crater formed in the jointed rock mass closely conforms to the network of the weakness planes (Bauer et al., 1965).

When a blasthole is intersected by joints, explosive energy escapes through joints, opening them up by wedging action causing a sudden drop in blasthole pressure (Figure 4). In some cases, when weak or open joints extend up to the face, premature venting of gases takes place, giving rise to fly rock and air blast problems (Figure 5).
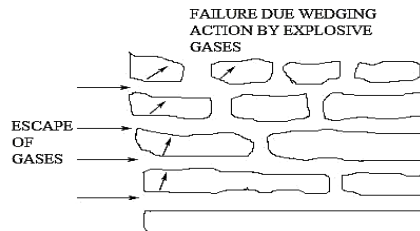
Figure 4. Escape of gases into joints

When there is any open joint opposite to the blasthole, the surfaces of joint cause reflection of the strain wave

which in turn interacts with the incoming strain waves. If this intensity is sufficiently strong, fragmentation occurs due to the internal spalling in that zone. As a result, there may be more boulder formation on the other side of the joint (Singh and Sastry, 1986a; Sastry 1989). Rinehart (1970) analysed the effects of joints on the wave propagation and observed that localization of fragmentation occurs near joint planes.
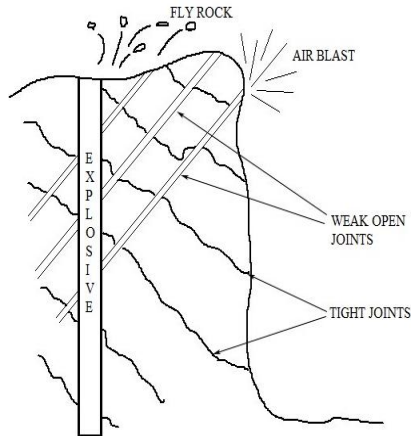
Figure 5. *Air blast and fly rock associated with jointed rock mass*

Similar results were obtained by Sastry (1989) in his laboratory studies on Chunar sandstone models. Pugleise and Atchison (1964) in their comparative studies of explosives in limestone with tight joints found that repeated blasting in the area opened the joints present in the rock mass and thereby affecting the subsequent blasts results.

Emergence of cheaper blasting agents has set a trend towards larger diameter blastholes with increased burdens and spacings. As a result, in blocky strata with large joint spacing, the effects of weakness planes become more pronounced as greater number of joints may be encountered between consecutive blastholes. These results in very poor fragmentation, creating problems to loading, hauling and crushing operations in addition to the unwanted toe formations, as a number of blocks are not penetrated by blastholes (Figure 6). In such cases, small diameter blastholes array with smaller burden and spacings makes the explosive energy distribution more even, giving better results.

Joint planes cause stress concentration zones and create new fractures along the pre-existing flaws. Tests conducted by Barker and Fourney (1979) on Homolite-100 models revealed this phenomenon. This was also supported by the studies of Lande (1983), who suggested that in jointed and highly fractured rock mass, short delays with smaller burdens give better fragmentation.
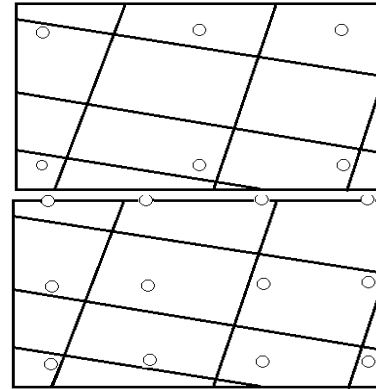
Figure 6. *Effect of joints on blasthole array*

2.3 Type of joints

Joints are of three types – tight, open and filled. The degree of impedance offered to strain waves depends upon the type of joints. Tight joints do not affect the transmission of strain waves as much as open or filled joints. Sometimes the joint plane itself acts as a pseudo-face, especially in the case of open joints, reflecting the strain wave (Sastry, 1989).

Joint filling material, which may be the product of weathering or decomposition of the joint walls, is also a factor exerting considerable influence on the blast results. According to Yang and Rustan (1983), continuity of weakness plane is the major factor affecting fragmentation. Strength of joint, which depends on the filling material, is the next. They observed that open and air filled joints exert a strong control on the fragmentation.

Sastry (1989) observed from the tests on sandstone with four different filling materials (siliceous and calcareous materials, water and air), that the size and shape of bench crater were controlled more by the joint filling material (Figure 7). Larger fragments and larger sockets were observed in models with filled joints.
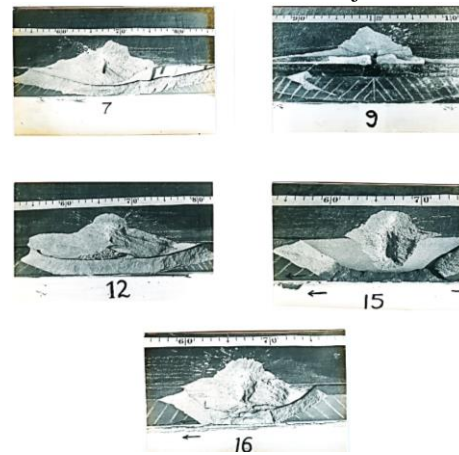
Figure 7. *Model studies performed using filling materials in joints*

2.4 Joint spacing

The spacing or frequency of joints plays a vital role in fragmentation of the rock mass. Resistance to the blasting increases as block size increases or joint frequency diminishes (Da Gama, 1970). For a successful blast design, data on spacing of joints should be obtained from a joint survey. Also, a detailed study of burden (B), joint spacing (S) and maximum allowable size of block (M) helps in overcoming the problems encountered in blocky formations. In general blasting practice, there are six possible cases of above mentioned variables (Table 1).

Table 1. *Relationships between Burden (B), Joint Spacing (S) and Maximum Acceptable Fragment Size (M) (Coates, 1981)*

Cases	Relative values of S and M			Dominant Influence	Boulder Formation (Size > M)
	Greatest	Intermediate	Smallest		
1	B	M	S	Jointing	Low
2	B	S	M	Jointing	High
3	M	B	S	Jointing	Low
4	M	S	B	Explosive	Low
5	S	B	M	Explosive	Medium
6	S	M	B	Explosive	Low

It is clear from Table 1 that Case-1 is the ideal, due to small amount of boulders and reduced explosive consumption, because joints dominate the fragmentation. Case-2 is not desirable due to the formation of large number of boulders as a result of joint spacing being greater than 'M'. Cases-3, 4, and 6 have low probability of occurrence in properly designed blasts, because burden 'B' is smaller than the accepted block size 'M'. Case-5 is also rare, for the burden being less than average joint spacing 'S' causing undesired boulder formation. Hence, blast design must be done in order to find situations, where B<M and M<S, for reducing secondary fragmentation as well as specific explosive consumption.

2.5 Joint orientation

Orientation of weakness planes (joints) has significant influence over size and shape of broken material and excavation (Ash, 1973; Gnirk and Pflieder, 1968). Formation and extension of cracks during blasting are controlled by the pattern of joints (Ash, 1973; Dally and Fourney, 1977). Bauer et al. (1965) and Ash (1973) from their studies concluded that craters formed closely conform to the geometry of weakness planes.

When the face is parallel to and on the dip side of the joints, excessive sliding occurs creating significant overbreak problems. When the joints dip away from the face, there may be problems of overhangs toe, etc., but the walls will be more stable (Larson and Pugleise,

1974). Results from small scale bench blasts showed that when a row of vertical blastholes was oblique to the joint direction, it resulted in poor fragmentation (Sastry, 1989). By orienting the free face parallel to the marked vertical joint planes, better results may be achieved (Belland, 1966).

It is reported that in horizontally bedded deposits, vertical lifter holes produce better fragmentation results (Wild, 1976). Thin and horizontally deposited brittle rocks require only horizontal holes, so that the overlying strata slides down by gravity. Rocks like Basalt, which are deposited in the form of thick vertical columns and the rocks with intersecting slips may require both vertical as well as horizontal holes.

According to Burkle (1980), blasting with dip causes more backbreak, less toe, smooth floor and lower muckpile profile, while blasting against dip creates less backbreak, more toe, rough floor and overhangs. Blasting against strike may result in unequal backbreak conditions, saw toothed floor and unfavourable orientation of face increasing the secondary blasting.

Singh and Sastry (1986a) from their tests on jointed models concluded that the formation of crater, and hence the fragmentation, was highly influenced by joint orientation (Figure 8).
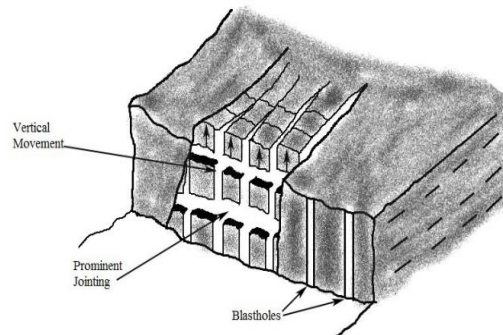
Figure 8. *Vertical movement of rock mass*

Singh et al. (1986) concluded from their study that both the mass and average fragment size of broken fragments were affected by joint orientation. Singh and Sastry (1986a) have done extensive studies on the effect of joints on Chunar sandstone models incorporating joints running parallel, perpendicular and angular to the face (Figure 9). They found that:

- Minimum yield results, when joints are running perpendicular to the face.
- Severe overbreak with uneven face formation results, when orientation of joints is perpendicular to face.
- More overbreaks occur in the condition with joints dipping into the face.
- Mass of fragments, average fragment size, mass surface area, fine and coarse fragmentation indices were significantly affected by orientation and direction of joints (at 5% level).
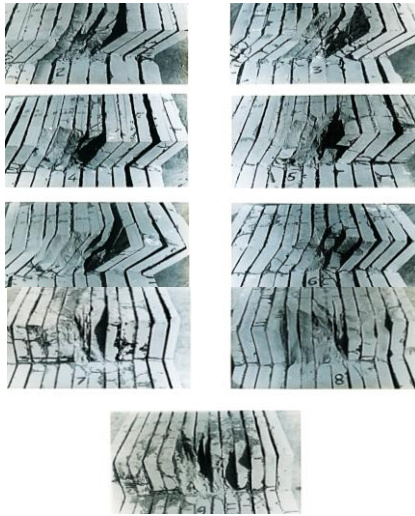
Figure 9. Models with joints running perpendicular to free face

2.6 Role of burden

Burden is one of the most critical geometric parameters of blasting. Burden is considered to have the greatest influence on blast results (Allsman, 1960; Singh and Sastry, 1987; Singh et al., 1986). For any given set of conditions, there exists a burden, which may be termed as "Critical Burden", where the strata gets fractured without displacement. According to Rustan et al. (1983) critical burden is an important factor when describing blastability nature of any rock. They recommended 40 to 90 % of critical burden as the maximum acceptable burden for satisfactory results. When the burden falls below its optimum value, then the effectiveness of strain energy increases and gaseous energy decreases. For very small burdens, strain wave fracturing occurs so rapidly in front of the blasthole that, much of the gaseous energy is lost to the atmosphere resulting in excessive throw of rock (fly rock).

In multi-row blasts, it is essential to keep the front row burden low in order to achieve proper burden relief and displacement, so that subsequent rows are blasted over smoothly, without any problems (Hagan, 1983). Otherwise, there is a possibility of encountering more fly rock and ground vibrations, in addition to undesired toe formation (Figure 10).
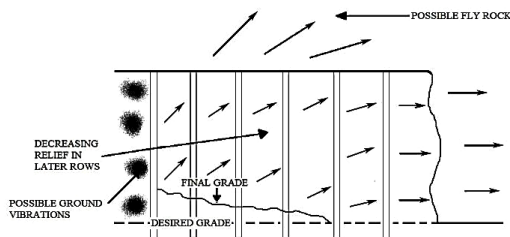
Figure 10. Effect of insufficient burden relief

2.7 Role of bench height

Bench height plays a vital role in influencing the blasting results. For each burden, there exists a maximum bench height to produce a full crater (Mason, 1973). The explosion generated strain in the rock alongside a charge increases as length to diameter ratio of charge increases in the approximate range of 0 to 20, and remains constant for >20. If it decreases to below 20, the optimum burden distances decreases. Therefore, when a charge becomes very short (the case with shallow benches), the burden needs to be reduced considerably. The breakage angle for a given burden increases with increase in bench height up to a certain point, beyond which no further significant change occurs (Atchison, 1968). As bench height increases, burden rock stiffness decreases.

2.8 Rock stiffness

Bending mechanism in rock blasting is not new and was recognised long back, even dating to 1898 (Daw and Daw, 1898). This mechanism was made popular subsequently by Ash (1973), Ash and Konya (1979) and Smith (1976). Stiffness principle and its use in blasting provide a guideline for the selection of an appropriate combination of burden, spacing and bench height.

Ash (1973) constructed an analogy between burden rock and structural beam to analyse the effect of bending on rock fragmentation. Burden on a blasthole was considered as thickness of beam, bench height as its length and average width of crater produced as its width. Cross section of the burden rock beam was defined by burden and spacing (Figure 11).
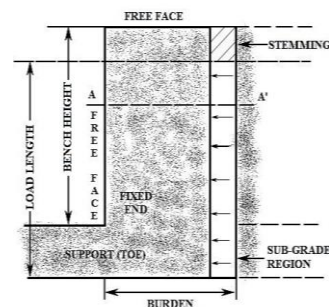
Figure 11. Analogy between burden rock and a structural beam (Ash, 1973)

Smith (1976) correlated the B, S and BH with stiffness of burden rock as:

$$K = CE\, Bx^a\, Sx^b /\, BH$$

where,

K = Stiffness of the burden rock, kg/cm
B = Burden dimension, cm
S = Spacing dimension, cm
BH = Bench height, cm
C = Constant depending on the shape and location of the area

a, b = Exponential constants depending on the shape of the area

E = Young's Modulus, kg/cm^2.

Breakage in shorter benches will be less than that in taller benches for same burdens, as stiffness decreases in the latter case (Figure 12). The cause of fly rock and collar overbreak is that the burden rock has become too stiff due to hole depth being too small or relief of burden being inadequate (Lundborg et al., 1975).
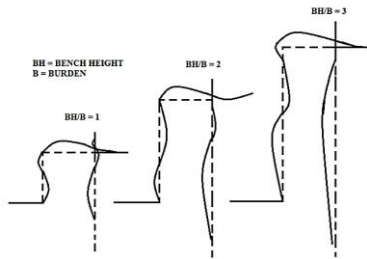
Figure 12. Bending conditions in blasting (Smith, 1976)

3. Investigations

3.1 Role of high speed videography in assessing blast Performance

An average blast is completed within seconds and is not possible to analyse the blasting process with naked eye. Ever since the advent of High Speed Video Cameras (HSC), it has been possible to view an entire blast in a sequence of frames, making analysis of the blasting process much effective. HSC with a capacity of 1000 FPS is capable of recording blasts, with the ability to capture one frame every millisecond in order to track down the delay performance as well. This enables the user to analyse every tiny movement happening in the blast. The HSC can be used to assess blast performance in terms of:

• Tracking of blasted rock mass.
• Tracking of burden rock movement.
• Checking the credibility of delays.
• Assessing the effectiveness of stemming by analysing stemming / gas ejection during blast.
• Determining the displacement of blasted rock mass.

3.2 Methodology

Studies were carried out with a series of bench blasts, in one coal and three limestone mines. All blasts were recorded with a S-Motion type High Speed Video Camera, AOS Technologies AG, Switzerland. High speed videos were analysed using ProAnalyst software to determine the displacement of burden rock and happenings in bench. An attempt was made to assess the influence of Bench Height to Burden ratio (BH/B) to identify important traits of the blasts and the role of jointing in blasting process. Details of blasts studied are given below (Tables 2 to 5).

Table 2. Details of the blasts in Mine-1 (Coal Mine)

Sl. No.	Parameter	Blast. 1	Blast. 2	Blast. 3	Blast. 4
1	Diameter of Blasthole (mm)	250	250	250	250
2	Burden (m)	6	6	7	7
3	Spacing (m)	8	8	9	9
4	Drilling Pattern	Staggered	Staggered	Staggered	Staggered
5	Depth of Blasthole (m)	11.1	11.1	15	14
6	Stemming (m)	5	3.5	7.5	05
7	No. of Rows	6	5	3	4
8	No. of Blastholes	25	30	19	70
9	Expl.Charge / Hole (kg)	276	290	350	410
10	Max.Charge / Delay (kg)	350	290	390	410
11	Total Charge / Blast (kg)	6918	8717	7415	22845
12	Initiation System	Shock tube	Shock tube	Shock tube	Shock tube
13	Rock Mass Movement (m/s)	53.0	111.1	108.3	67.1
14	BH/B Ratio	1.85	1.85	2.143	2

Table 3. Details of the blasts in Mine-2 (Limestone Mine)

Sl. No.	Parameter	Blast. 1	Blast. 2	Blast. 3	Blast. 4
1	Diameter of Blasthole (mm)	115	115	115	115
2	Burden (m)	2.7	2.7	2.5	2.7
3	Spacing (m)	3.7	3.7	3.5	3.7
4	Drilling Pattern	Square	Square	Square	Square
5	Depth of Blasthole (m)	10.0	10.5	8.0	10.0
6	Stemming (m)	2.5	2.75	3.0	3.25
7	No. of Rows	2	2	2	5
8	No. of Blastholes	17	14	16	14
9	Expl. Charge / Hole (kg)	66.17	76.78	48.43	66
10	Max. Charge / Delay (kg)	463.19	307.12	242.15	264
11	Total Charge / Blast (kg)	1125	1075	775	925
12	Initiation System	Shock tube	Shock tube	Shock tube	Shock tube
13	Rock Mass Movement (m/s)	135.7	132.7, 136.9	70.5	108.4
14	BH/B Ratio	3.704	3.889	3.2	3.704

Table 4. *Details of the blasts in Mine-3 (Limestone Mine)*

Sl. No.	Parameter	Blast. 1	Blast. 2	Blast. 3
1	Diameter of Blasthole (mm)	115	115	115
2	Burden (m)	2.7	2.7	2.7
3	Spacing (m)	3.0	3.0	3.2
4	Drilling Pattern	Rectangular	Rectangular	Staggered
5	Depth of Blasthole (m)	7.5	7.0	9.0
6	Stemming (m)	2	2	2
7	No. of Rows	3	2	4
8	No. of Blastholes	13	17	43
9	Expl. Charge / Hole (kg)	54	37.76	55.23
10	Max. Charge / Delay (kg)	215	294.45	994.14
11	Total Charge / Blast (kg)	700	642	2315
12	Initiation System	Shock tube	Shock tube	Shock tube
13	Roc Mass Movement (m/s)	66.2	110.9	77.2, 113.5
14	BH/B Ratio	2.778	2.223	3.148

Sl. No.	Parameter	Blast. 4	Blast. 5	Blast. 6
1	Diameter of Blasthole (mm)	115	115	115
2	Burden (m)	2.7	2.7	2.7
3	Spacing (m)	3.0	3.2	3.2
4	Drilling Pattern	Rectangular	Rectangular	Staggered
5	Depth of Blasthole (m)	9.5	9.5	8.0
6	Stemming (m)	2	2	2
7	No. of Rows	3	2	3
8	No. of Blastholes	10	20	18
9	Expl. Charge / Hole (kg)	62.24	72	44
10	Max. Charge / Delay (kg)	311.2	506	267
11	Total	622.4	1145	3133

Sl. No.	Parameter	Blast. 1	Blast. 2	Blast. 3
12	Charge / Blast (kg) Initiation System	Shock tube	Shock tube	Shock tube
13	Rock Mass Movement (m/s)	122.8, 119.4	125.8	97.0
14	BH/B Ratio	3.334	3.519	2.778

Table 5. *Details of the blasts in Mine-4 (Limestone Mine)*

Sl. No.	Parameter	Blast. 1	Blast. 2	Blast. 3
1	Diameter of Blasthole (mm)	115	115	115
2	Burden (m)	2.5	2.5	2.5
3	Spacing (m)	3.0	3.0	3.0
4	Drilling Pattern	Square	Square	Square
5	Depth of Blasthole (m)	5.0	5.0	5.0
6	Stemming (m)	2.25	2.5	2.0
7	No. of Rows	3	2	4
8	No. of Blastholes	14	16	29
9	Expl. Charge / Hole (kg)	28.57	37.5	31.2
10	Max. Charge / Delay (kg)	114.28	150	156.03
11	Total Charge / Blast (kg)	400	600	905
12	Initiation System	Shock tube	Shock tube	Shock tube
13	Rock Mass Movement (m/s)	49.8, 114.0, 71.9	67.0	104.4
14	BH/B Ratio	2	2	2

4. Results and Analysis

Escape of gas energy was observed through major joints in the bench. Also the escape of gas energy through stemming zone was observed by high speed videos. Figure 13 shows the escape of gaseous energy through weakplanes and stemming zone in the bench, causing depletion of blasthole pressure. Both these reasons caused poor fragmentation.

(a)

(b)

(c)

(d)

(e)

Figure 13. *Escape of gas energy through weakplanes &*
stemming zone

Gas energy is found to escape through horizontal jointing and pushing the beds upwards (Figure 14).
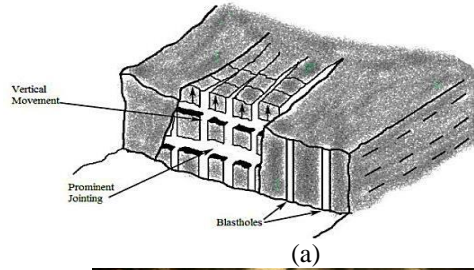
(a)
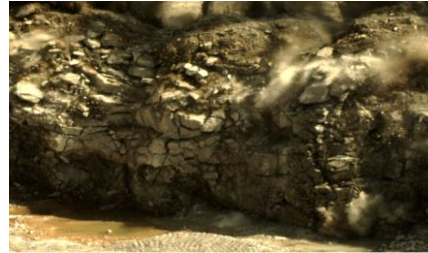
(b)

Figure 14. *Rock fragmentation affected by jointing*
(recorded by HSC)

The HSC could clearly establish the beam bending mechanism as shown in Figure 15. Also the effect of joints on rock fragmentation could be observed as recorded in one of the blasts in a limestone mine.
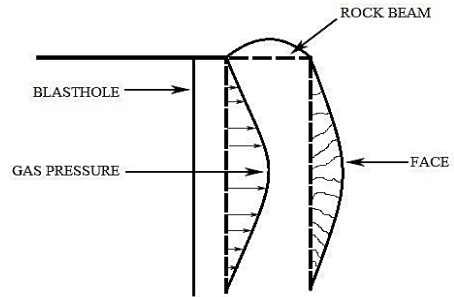
(a)

(b)

(c)

Figure 15. *Flexural bending mechanism*

It could also be seen from Figure 15 that to a large extent, size of one side of the fragments resulting from the blast is controlled by joint spacing.

4.1 Burden rock velocity

Analysis of high speed videography study results revealed that the velocities of blasted rock are higher in case of limestone (7-13m/s) than in argillaceous sandstone overburden formation (6-10m/s) (Table 6). This is due to limestone being more compact and stronger than overburden sandstone, and transmission of strain waves is better in limestone formation.

Table 6. *Relationship between BH/B and average velocity of burden rock mass*

BH/B	BH/B Average	Burden Velocity (m/s)	Avg. Burden Velocity (m/s)
2		53.0	
2		111.1	
2		67.1	
2		49.8	
2	**2**	114.0	79.8
2		71.9	
2		67.0	
2		104.4	
2.14		108.3	
2.22		110.9	
2.77	**2.5**	66.2	95.6
2.77		97.0	
3.14		77.2	
3.14		113.5	
3.20	**3.2**	70.5	100.7
3.33		122.8	
3.33		119.4	
3.51		125.8	
3.70		135.7	
3.70	**3.7**	108.4	127.9
3.88		132.7	
3.88		136.9	

4.2 Effect of BH/B on delay timing

Initiation sequence in a blast is very important, and is a vital factor to be considered in blast design, since several initiation sequences radically alter effective burden and spacing during the blasting process. It also affects rock movement with respect to face and thereby influences the amount of rock shearing and design

boundaries of blast pattern. A systematic release of explosive energy from one hole/row to the other is crucial in maintaining a continuous momentum required for inter-hole/row delay displacements.

It has been suggested by earlier researchers that the burden from first row of blastholes should be displaced by at least one third of the burden distance (1/3 B) before next row of blastholes is fired, for an efficient blast (Figure 16).
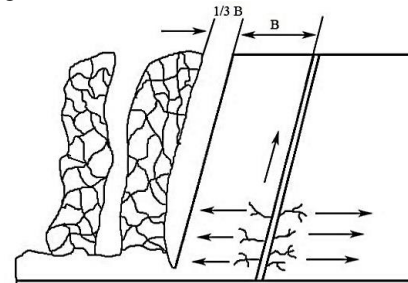
Figure 16. *Required burden movement before blasting of next row*

Burden rock velocity was calculated for different conditions by tracking down the movement of burden rock mass. Figure 17 shows some sample screen shots of high speed videographs of some of the blasts recorded in different mines.

ProAnalyst software was used for tracking down the burden rock movement, for determining the velocity of rock mass. Some sample snap shots of the same are shown in Figure 18.

0ms

100ms

200ms

a. Screenshots of Blast-4 recorded in Mine-1

0ms

100ms

200ms

300ms

b. Screenshots of Blast-5 recorded in Mine-3
Figure 17. *Videographs of some blasts recorded by HSC in different mines*
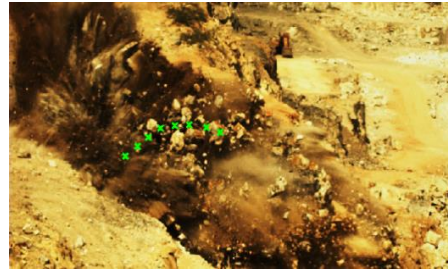
(a)
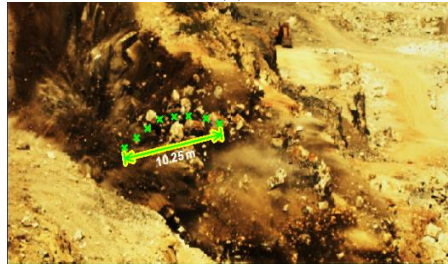
(b)

a. Tracking of rock mass movement (Blast-2 in Mine-3)

(a)

(b)

b. Tracking of rock mass movement (Blast-3 in Mine-4)
Figure 18. *ProAnalyst analysis of some blasts recorded by HSC in different mines*

Based on the burden movement velocity, the minimum delay timing required between rows was analysed (Table 7). Study has shown that as BH/B ratio increasing, the required delay time per metre distance throw of burden rock mass is decreasing. For a BH/B ratio condition of two, the delay time required was determined as 12.5ms per metre, whereas with BH/B value of 3.75 the required delay reduced to 8ms per

metre distance. This is due to the fact that as BH/B is increasing, the bench is becoming less stiff and more flexible resulting in faster movement of burden rock mass.

Table 7. Delay time required between rows based on high speed videography data

BH/B Ratio	Avg. Burden Velocity (m/s)	Delay Time Required (ms/m)
2.0	79.8	12.5
2.5	95.6	10.5
3.2	100.7	10.0
3.75	127.9	8.0

4. Conclusions

Following are the major conclusions drawn from the studies carried out using High Speed Video Camera in four different mines:

- High speed video camera is an excellent tool for analysing the blast results and designing efficient blasts.
- High speed video of the blasts provides clear information about weak zones in the bench being blasted from where escape of gas energy is taking place. Based on this the necessary zones of stemming decks could be finalised.
- For small benches, the velocity of blasted rock mass is slower. This is due to the increased stiffness of short benches.
- Conversely, for the taller benches, the velocities of blasted rock pieces have been recorded to be higher, as benches are becoming more flexible.
- In taller benches, the delay between holes/rows could be 8ms per metre distance. In case of shorter benches the delay time required is about 12ms per metre distance. According to the burden/spacing provided, the necessary delay timing may be adopted.

References

[1] Allsman, P.L., 1960. Analysis of explosive action in breaking rock, Trans. AIME, 217: 471-473.

[2] Ash, R.L., 1973. The Influence of Geological Discontinuition on Rock Blasting, Ph.D Thesis, Univ. of Missouri, Rolla.

[3] Ash, R.L., and Konya, C.J., 1979. Improper spacing – a major problem with surface blasting, Proc. 5th Conf. Expl. Blast. Tech.: 180-183.

[4] Ash, R.L., and Smith. N.S., 1976. Changing borehole length to improve breakage – a case history, Proc. 2nd Conf. Expl. and Blast. Tech.: Louisville, Kentucky: 1-12.

[5] Atchison, T.C., 1968. Fragmentation principles, Surface Mining, (Ed. Pflieder), pp. 355-372 (AMIE: New York).

[6] Bauer, A., 1961. Application of Livingston theory, Quart. Col. Sch. Min. 56 (1): 171-182.

[7] Barker, D.B., and Fourney, W.L., 1978. Photoelectric Investigation of Fragmentation Mechanisms, Part-II - Flaw Initiated Network, Report to NSF: August.

[8] Bauer, A., Harries, G.R., Lang, L., Prezion, P., and Selleca, D.J., 1965. How IOC Puts Crater Resarch to Work, E&MJ, 166 (9): 117 121.

[9] Belland, L., 1966. Structure as a Control in Rock Fragmentation – Coral Lake Iron Ore Deposit, CIM Bull., 59 (645) : 323-328.

[10] Clark, G.B., and Saluja, S.S., 1964. Blasting mechanisms, Trans SME/AMIE, 229: 78-90.

[11] Coates, D.F., 1981, Rock Mechanics Principles (CANNET Energy Mines and Resources: Ottawa).

[12] Dally, J.W., and Fourney, W.L., 1977. The Influence of Flaws on Fragmentation, Proc. 6th Int. Colloq. Gas Dynamics of Explosives and Reactive Systems: Stockholm, Sweden.

[13] Daw, A.W., and Daw, Z.W., 1898. The Blasting of Rock: In Mines, Quarries, Tunnels, Etc., P. 297 (E. and F.N. Spon. Ltd.: London).

[14] DaGama, C.D., 1970. Similitude conditions in models for studies of bench blasting, Proc. 2nd Cong. Rock Mech.: ISRM: Belgrade, III: 105-112.

[15] Fogelson, D.E., Atchison, T.C., and Duvall, W.I., 1959. Strain energy for explosion generated strain pulses in rock, USBM RI: 5514.

[16] Gnirk, P.F., and Pfleider, E.D., 1968. On the correlation between explosive crater formation and rock properties, Proc. 9th Symp. Rock Mech.: Col. Sch. Min.: 321-345.

[17] Hagan, T.N., 1983. The influence of controllable blast parameters on fragmentation and mining costs, Proc. 1st Int. Symp. Rock Frag. by Blast: Lulea, Sweden, 1: 31-51.

[18] Hagan, T.N., and Morphet, R.J., 1986. The Design and Implementation of Bench Blasts in Complex Rock Formations, Proc. Int. Symp. Engg. in Complex Rock Formations: Beijing, China: 628-635.

[19] John, N.E. Jr., 1983. The role of stress waves in explosively induced bulk rock motion, Proc. 1st Int. Symp. Rock Frag. by Blast.: Lulea, Sweden, 1: 53-70.

[20] Kutter, H.K., and Fairhurst, C., 1971. On the fracture process in blasting, Int. J. Rock Mech. Min. Sci. & Geomech. Abstr., 8: 181-202.

[21] Lande, G., 1983. Influence of structural geology on controlled blasting in sedimentary rocks – case history, Proc. 1st Int. Symp. Rock Frag. by Blast.: Lulea, Sweden, 2: 555-563.

[22] Lundborg, N., Persson, P.A., Peterson, A.L., and Homberg, R., 1975, Keeping the lid on fly rock in open pit blasting, E&MJ (May, 1975).

[23] Mason, J.M., 1973. The effect of explosive charge length on cratering, M.S Thesis, Univ. Missouri.

[24] Noren, C.H., 1956. Blasting experiments in granite rock, Quart. Colo. Sch. Min., 51 (3): 211-225.

[25] Pugliese, J.M., and Atchison, T.C., 1964. Comparative studies of explosives in limestone, USBM RI: 6395.

[26] Rinehart, J.S., 1970. Fractures and strain generated in joints and layered rock masses bu explosions, Proc. Symp. Mechanism of Rock Failure by Explosions: Fontineblue.

[27] Rustan, A., Vutukuri, V.S., and Naarttijarvi, T., 1983. The influence from specific charge, geometric scale and physical properties of homogeneous rock on fragmentation, Proc 1st Int. Symp. Rock Frag. by Blast.: Lulea, Sweden, 1: 115-142.

[28] Sadwin, L.D., and Junk, N.M., 1965. Measurement of lateral pressure generated from cylindrical explosive charges, USBM RI: 6701.

[29] Saluja, S.S., 1963. Study of mechanism of rock failure under the action of explosives, Ph.D Thesis, Univ. Wisconsin.

[30] Sastry, V.R., 1989. A Study of the Effect of Some Parameters on Rock Fragmentation due to Blasting, Ph.D. Thesis, BHU, India.

[31] Seinov, N.P., and Chevkin, A.I., 1968. Effect of Fissures on Fragmentation of Medium by Blasting, Sov. Min. Sci., (3) : 254-259.

[32] Singh, D.P., Saluja, S.S., and Rao, Y.V.A, 1986. A Laboratory Study of Effects of Joint on Rock Fragmentation, Proc. 21st US Symp. Rock Mechanics: Univ. Missouri.

[33] Singh, D.P., and Sarma, K.S., 1983. Influence of Joints on Rock Blasting – A Model Scale Study, Proc. 1st Int. Symp. Rock Fragmentation by Blasting: Lulea, Sweden, 2 : 533-554.

[34] Singh, D.P., and Sastry, V.R., 1986a. Influence of Sturctural Discontinuities on Rock fragmentation by Blasting, Proc. Int. Symp. Intense Dynamic Loading and Its Effects: Beijing, China: 980-984.

[35] Singh, D.P., and Sastry, V.R., 1986b. Rock Fragmentation by Blasting - Influence of Joint Filling Material, Int. Jl. Expl. Engg., USA, 3 (5) : 18-27.

[36] Singh, D.P., and Sastry, V.R., 1987. An Investigation into the Effect of Blast geometry on Rock Fragmentation, Jl. Mines, Metals and Fuels, 39 (6) : 226 223.

[37] Smith, N.S., 1976. Burden rock stiffness and its effect on fragmentation in bench blasting, Ph.D Thesis, Univ. Missouri.

[38] Yang, Z.G, and Rustan, A., 1983. The Influence from Primary Structure on Fragmentation, Proc. 1st Int. Symp. Rock fragmentation by Blasting: Lulea, Sweden, 2 : 581-603.

COMPREHENSIVE STUDY OF DESIGN AND FLEXIBLE CONTROL OF A DSTATCOM OPERATING IN VOLTAGE CONTROL MODE

CHANDRA RAKHEE B
Assistant professor
Mail Id: chandrarakhee.b@gmail.com

PULLA REDDY .K
Assistant professor
Mail id: pullareddy.kasireddy@gmail.com

ABSTRACT

In this Project, a new DSTATCOM topology with reduced dc link voltage is proposed. The distribution static compensator (DSTATCOM) is used for load compensation in power distribution network. In the presence of feeder impedance, the inverter switching distorts both the PCC voltage and the source currents. A new DSTATCOM topology with reduced dc link voltage is proposed. The topology consists of two capacitors: one is in series with the interfacing inductor of the active filter and the other is in shunt with the active filter. The series capacitor enables reduction in dc-link voltage while simultaneously compensating the reactive power required by the load, so as to maintain unity power factor without compromising DSTATCOM performance. The shunt capacitor, along with the state feedback control algorithm, maintains the terminal voltage to the desired value in the presence of feeder impedance with the reduction in dc-link voltage, the average switching frequency of the insulated gate bipolar transistor switches of the DSTATCOM is also reduced. Consequently, the switching losses in the inverter are reduced. Detailed design aspects of the series and shunt capacitors are discussed in this paper. A simulation study of the proposed topology has been carried out using MATLAB/SIMULINK. Finally a fuzzy logic controller is applied for further reduction of harmonics on source side.

KEYWORDS: *DSTATCOM, Power quality, Active filter, Voltage control.*

I.INTRODUCTION

An increasing demand for high quality, reliable electrical power and increasing number of distorting loads may leads to an increased awareness of power quality both by customers and utilities. The most common power quality problems today are voltage sags, harmonic distortion and low power factor. Voltage sags is a short time (10 ms to 1 minute) event during which a reduction in r.m.s voltage magnitude occurs. It is often set only by two parameters, depth/magnitude and duration. The voltage sags magnitude is ranged from 10% to 90% of nominal voltage and with duration from half a cycle to 1 minimum.

Voltage sags is caused by a fault in the utility system, a fault within the customer's facility or a large increase of the load current, like starting a motor or transformer energizing. Voltage sags are one of the most occurring power quality problems. For an industry voltage sags occur more often and cause severe problems and economical losses. Utilities often focus on disturbances from end-user equipment as the main power quality problems.

Harmonic currents in distribution system can cause harmonic distortion, low power factor and additional losses as well as heating in the electrical equipment. It also can cause vibration and noise in machines and malfunction of the sensitive equipment.

The development of power electronics devices such as Flexible AC Transmission System (FACTS) and customs power devices have introduced and emerging branch of technology providing the power system with versatile new control capabilities .There are different ways to enhance power quality problems in transmission and distribution systems. Among these, the D- STATCOM is one of the most effective devices.

II.SCHEME OF DSTATCOM

A D-STATCOM (Distribution Static Compensator), which is schematically depicted in Figure, consists of a two-level Voltage Source Converter (VSC), a dc energy storage device, a coupling transformer connected in shunt to the distribution network through a coupling transformer. The VSC converts the dc voltage across the storage device into a set of three-phase ac output voltages. These voltages are in phase and coupled with the ac system through the reactance of the coupling transformer. Suitable adjustment of the phase and magnitude of the D-STATCOM output voltages allows effective control of active and reactive power exchanges between the D-STATCOM and the ac system. Such configuration allows the device to absorb or generate controllable active and reactive power.

The VSC connected in shunt with the ac system provides a multifunctional topology which can be used for up to three quite distinct purposes:

1. Voltage regulation and compensation of reactive power;

2. Correction of power factor; and

3. Elimination of current harmonics.

Here, such device is employed to provide continuous voltage regulation using an indirectly controlled converter.
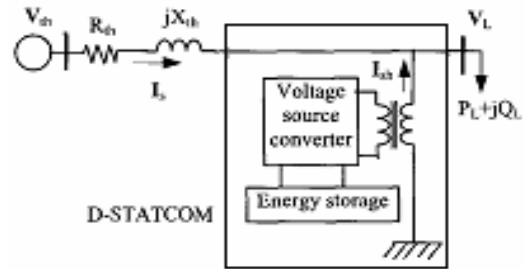
Fig1 Block diagram of D-STATCOM

The shunt injected current I_{sh} corrects the voltage sag by adjusting the voltage drop across the system impedance Z_{th}. The value of I_{sh} can be controlled by adjusting the output voltage of the converter.

III.DSTATCOM IN THE POWER DISTRIBUTION SYSTEM
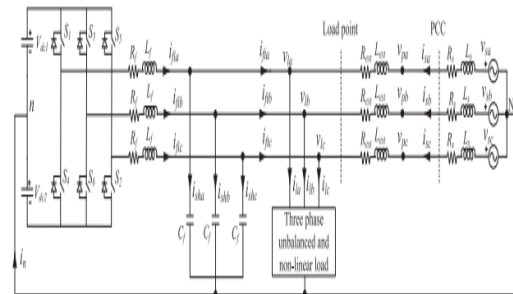
Fig 2. Three-phase equivalent circuit of DSTATCOM topology in the distribution system

Fig.4.1 shows the power circuit diagram of the DSTATCOM topology connected in the distribution system. *Ls* and *Rs* are source inductance and resistance, respectively. An external inductance *L*ext is included in series between load and source points. This inductor helps DSTATCOM to achieve load voltage regulation capability even in worst grid conditions, i.e., resistive or stiff grid.

ANVESHANA'SINTERNATIONALJOURNALOF RESEARCHIN ENGINEERING ANDAPPLIED SCIENCES
EMAILID:anveshanaindia@gmail.com,WEBSITE:www.anveshanaindia.com

81

From IEEE-519 standard, point of common coupling (PCC) should be the point which is accessible to both the utility and the customer for direct measurement. Therefore, the PCC is the point where *L*ext is connected to the source. The DSTATCOM is connected at the point where load and *L*ext are connected. The DSTATCOM uses a three-phase four-wire VSI. A passive *LC* filter is connected in each phase to filter out high-frequency switching components. Voltages across dc capacitors, *V*dc1 and *V*dc2, are maintained at a reference value of *V*dcref.

IV. EFFECT OF FEEDER IMPEDANCE ON VOLTAGE REGULATION

To demonstrate the effect of feeder impedance on voltage regulation performance, an equivalent source-load model without considering external inductor is shown in Fig.4.2. The current in the circuit is given as

$$I_s = \frac{V_s - V_l}{Z_s}$$

where $V_s = V_s\angle\delta$, $V_l = V_l\angle 0$, $I_s = I_s\angle\varphi$, and $Z_s = Z_s\angle\theta_s$, with V_s, V_l, I_s, Z_s, δ, φ, and θ_s are rms source voltage, rms load voltage, rms source current, feeder impedance, load angle, power factor angle, and feeder impedance angle, respectively. The three-phase average load power (*Pl*) is expressed as

$$P_l = \text{Real}\left[3\,V_l\,I_s^*\right].$$

Substituting V_l and I_s into (2), the load active power is

$$P_l = \frac{3\,V_l^2}{Z_s}\left[\frac{V_s}{V_l}\cos(\theta_s - \delta) - \cos\theta_s\right]$$

Rearranging (3), expression for δ is computed as follows:

$$\delta = \theta_s - \cos^{-1}\left[\left[\frac{V_l}{V_s}\left(\cos\theta_s + \frac{P_l Z_s}{3\,V_l^2}\right)\right]\right]$$

For power transfer from source to load with stable operation in an inductive feeder, δ must be positive and less than 90∘. Also, all the terms of the second part of (4), i.e., inside cos-1, are amplitude and will always be positive. Therefore, the value of the second part will be between "0" and "π/2" for the entire operation of the load. Consequently, the load angle will lie between θs and (θs - $\pi/2$) under any load operation, and therefore, maximum possible load angle is θs.
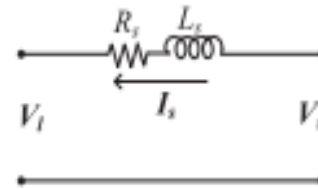
Fig.3. Equivalent source-load model without considering external inductor.

The vector expression for source voltage is given as follows:

$$V_s = V_l + I_s Z_s \angle (\theta_s + \phi).$$

A DSTATCOM regulates the load voltage by injecting fundamental reactive current. To demonstrate the DSTATCOM voltage regulation capability at different supply voltages for different *Rs/Xs*, vector diagrams using (5) are drawn in Fig.4.3. To draw these diagrams, load voltage *Vl* is taken as reference phasor having the nominal value *OA* (1.0 p.u.). With aim of making *Vl* = *Vs* = 1.0 p.u., locus of *Vs* will be a semicircle of radius   *Vl*.

Since the maximum possible load angle is 90° in an inductive feeder, phasor **Vs** can be anywhere inside curve *OACBO*. It can be seen that the value of $\theta s + \varphi$ must be greater than 90° for zero voltage regulation. Additionally, it is possible only when power factor is leading at the load terminal as θs cannot be more than 90°
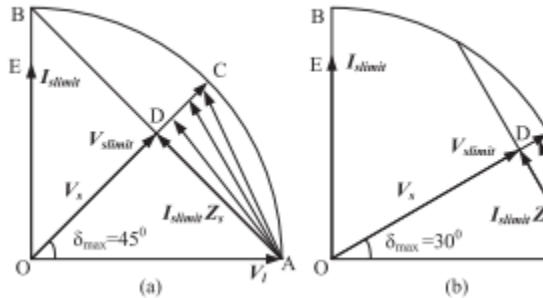
Fig.4. Voltage regulation performance curve of DSTATCOM at different *Rs/Xs* . (a) For *Rs/Xs* = 1. (b) For *Rs/Xs* = √3. (c) For *Rs/Xs* = 3.73

Fig.4(a) shows the limiting case when *Rs/Xs* = 1, i.e., θs= 45°. From (4), the maximum possible load angle is 45°. The maximum value of angle, $\theta s + \varphi$, can be 135° when φ is 90°. Hence, the limiting source current phasor *OE*, which is denoted by *I*slimit, will lead the load voltage by 90°. Lines *OC* and *AB* show the limiting vectors of *Vs* and *IsZs*, respectively, with *D* as the intersection point. Hence, area under *ACDA* shows the operating region of DSTATCOM for voltage regulation. The point *D* has a limiting value of *V*slimit = *IsZs* = 0.706 p.u. Therefore, maximum possible voltage regulation is 29.4%. However, it is impossible to achieve these two limits simultaneously as δ and φ cannot be maximum at the same time. Again if *Zs* is low, the source current, which will be almost inductive, will be enough to be realized by the DSTATCOM

Fig.4(b) considers case when *Rs/Xs* = √3, i.e., θs = 30°. The area under *ACDA* shrinks, which shows that with the increase in *Rs/Xs* from the limiting value, the voltage regulation capability decreases. In this case, the limiting values of *V*slimit and *IsZs* are found to be 0.866 and 0.5 p.u., respectively. Here, maximum possible voltage regulation is 13.4%. However, due to high-current requirement, a practical DSTATCOM can provide very small voltage regulation. Voltage regulation performance curves for more resistive grid, i.e.,θs =15°, as shown in Fig.4(c), can be drawn similarly. Here, area under *ACDA* is negligible. For this case, hardly any voltage regulation is possible.

V. DESIGN EXAMPLE OF EXTERNAL INDUCTOR

Here, it is assumed that the considered DSTATCOM protects load from a voltage sag of 60%. Hence, source voltage *Vs* = 0.6 p.u. is considered as worst case voltage disturbances. During voltage disturbances, the loads should remain operational while improving the DSTATCOM capability to mitigate the sag. Therefore, the load voltage during voltage sag is maintained at 0.9 p.u., which is sufficient for satisfactory operation of the load. In the present case, maximum required value of *Iiml* is 10 A. With the system parameters given in Table I, the effective reactance after solving is found to be 2.2 Ω (*L*sef= 7 mH). Hence, value of external inductance, *L*ext, will be 6.7 mH. This external inductor is selected while satisfying the constraints such as maximum load power demand, rating of DSTATCOM, and amount of sag to be mitigated. In this design example, for base voltage and base power rating of 400 V and 10 kVA, respectively, the value of external inductance is 0.13p.u. Moreover, with a total inductance of 7 mH (external and actual grid

inductance), the total impedance will be 0.137 p. u. The short-circuit capacity of the line will be $1/0.13 = 7.7$ p.u., which is sufficient for the satisfactory operation of the system. Additionally, a designer always has flexibility to find suitable value of Lext if the constraints are modified or circuit conditions are changed. Moreover, the conventional DSTATCOM operated for achieving voltage regulation uses large feeder inductances.
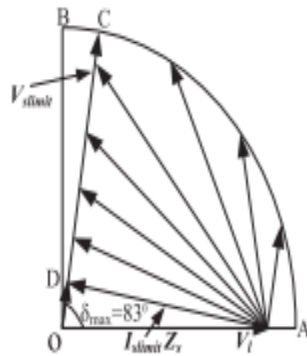
Fig.5. Voltage regulation performance of DSTATCOM with external inductance.

With the external inductance while neglecting its ESR, Rs/Xsef will be 0.13, i.e., θsef = 83∘. Voltage regulation performance curves of the DSTATCOM in this case are shown in Fig.5.

VI. FLEXIBLE CONTROL STRATEGY

This sections presents a flexible control strategy to improve the performance of DSTATCOM in presence of the external inductor Lext. First, a dynamic reference load voltage based on the coordinated control of the load fundamental current, PCC voltage, and voltage across the external inductor is computed. Then, a proportional-integral (PI) controller is used to control the load angle, which helps in regulating the dc bus voltage at a reference value. Finally, three-phase reference load voltages are

generated. The block diagram of the control strategy is shown in Fig.6
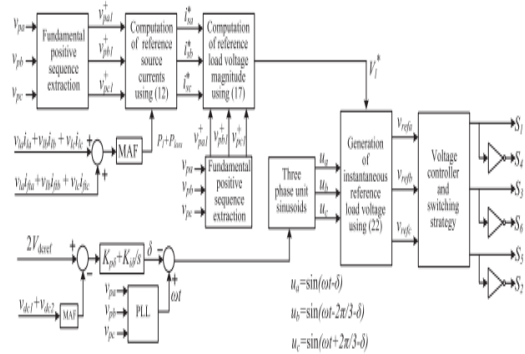
Fig.6. Block diagram of the proposed flexible control strategy.

VII.SIMULATION RESULTS
EXISTING RESULTS
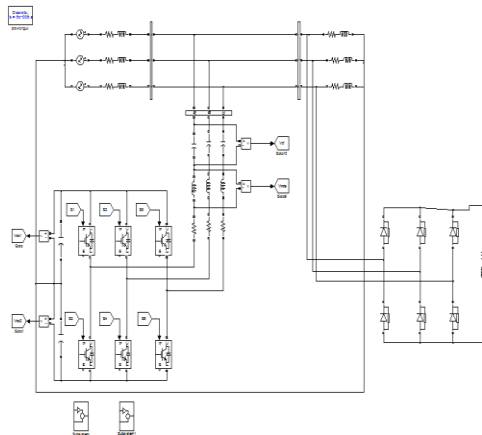
Fig 7. MATLAB/Simulink diagram of EXISTING SYSTEM
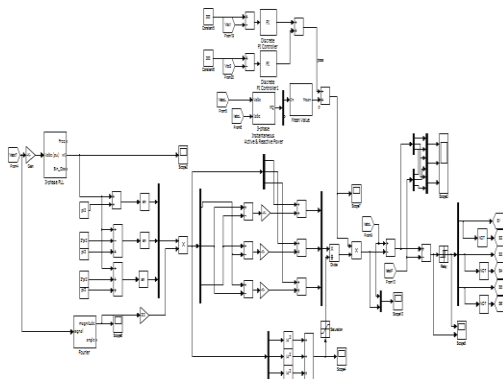
Fig 8. controller subsystem
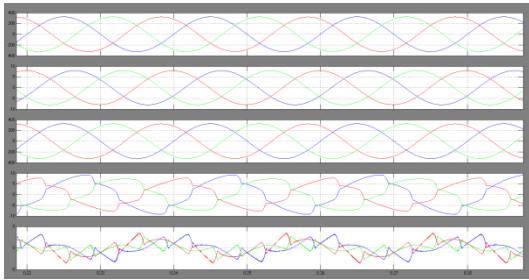
Fig 9. Simluation results of normal operation Source voltage, Source current, Load voltage, Load current, filter current
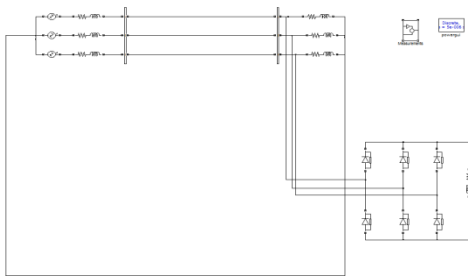
Fig 10. MATLAB/Simulink diagram WITH out DSTATCOM
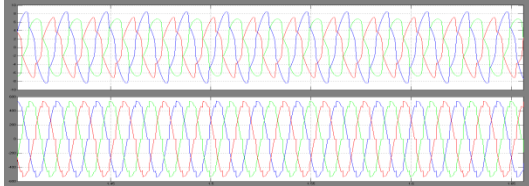
Fig 11. Source Current and Voltage

II. EXTENSION RESULTS
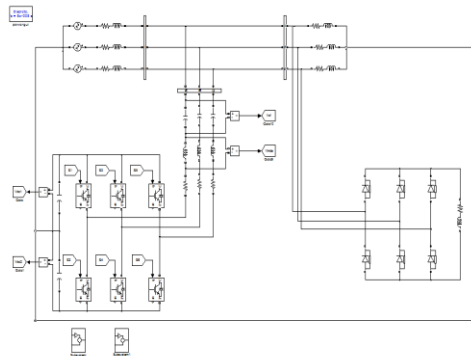
FIG 12. MATLAB/SIMULINK diagram of proposed system
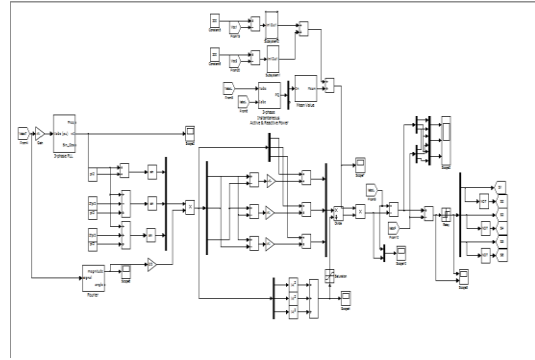
Fig 13. proposed controller
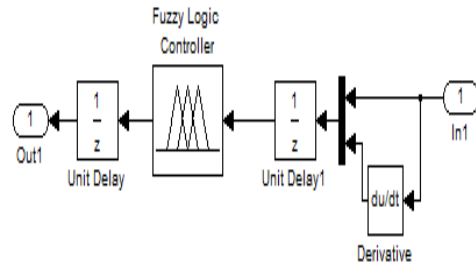
Fig14. fuzzy controller subsystem

CASE1: UNDER SAG CONDITION
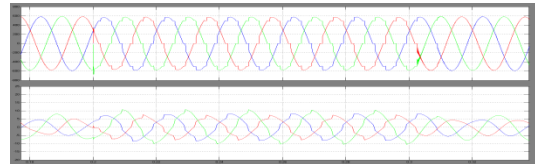
Fig 15 Source voltage and source current
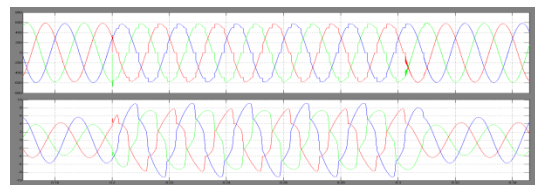
Fig 16. Load voltage and Load current
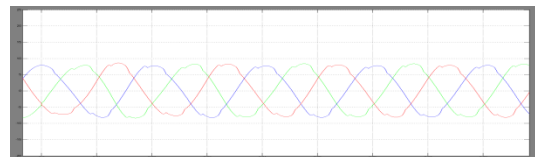
Fig 17. filter current

CASE 2: UNDER SWELL CONDITION
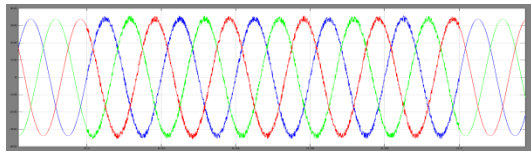
FIG 18. Load voltage
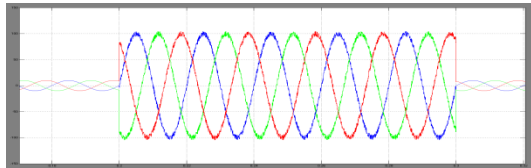
Fig 19. filter output voltage
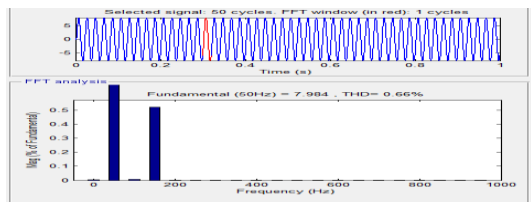
Fig 20. Thd % of Source current without fuzzy controller
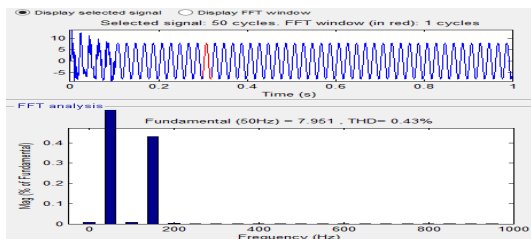
Fig21. Thd % of Source current with proposed fuzzy controller

CONCLUSION

This paper has presented design, operation, and control of a DSTATCOM operating in voltage control mode (VCM). After providing a detailed exploration of voltage regulation capability of DSTATCOM under various feeder scenarios, a benchmark design procedure for selecting suitable value of external inductor is proposed. An algorithm is formulated for dynamic reference load voltage magnitude generation. The DSTATCOM has improved voltage regulation capability with a reduced current rating VSI, reduced losses in the VSI

and feeder. Also, dynamic reference load voltage generation scheme allows DSTATCOM to set different constant reference voltage during voltage disturbances. Simulation results validate the effectiveness of the proposed solution. The external inductor is a very simple and cheap solution for improving the voltage regulation, however it remains connected throughout the operation and continuous voltage drop across it occurs. The future work includes operation of this fixed inductor as a controlled reactor so that its effect can be minimized by varying its inductance.

REFERENCES

[1] R. de Araujo Ribeiro, C. de Azevedo, and R. de Sousa, "A robust adaptive control strategy of active power filters for power-factor correction, harmonic compensation, and balancing of nonlinear loads," IEEE Trans. Power Electron., vol. 27, no. 2, pp. 718–730, Feb. 2012.

[2] J. Pomilio and S. Deckmann, "Characterization and compensation of harmonics and reactive power of residential and commercial loads," IEEE Trans. Power Del., vol. 22, no. 2, pp. 1049–1055, Apr. 2007.

[3] C.-S. Lam, W.-H. Choi, M.-C. Wong, and Y.-D. Han, "Adaptive dclink voltage-controlled hybrid active power filters for reactive power compensation," IEEE Trans. Power Electron., vol. 27, no. 4, pp. 1758– 1772, Apr. 2012.

[4] B. Singh and J. Solanki, "Load compensation for diesel generator-based isolated generation system employing DSTATCOM," IEEE Trans. Ind. Appl., vol. 47, no. 1, pp. 238–244, Jan.-Feb. 2011.

[5] B. Singh, P. Jayaprakash, S. Kumar, and D. Kothari, "Implementation of neural-network-controlled three-leg VSC and a transformer as three phase four-wire dstatcom," IEEE Trans. Ind. Appl., vol. 47, no. 4, pp. 1892–1901, Jul.-Aug. 2011.

[6] J. Liu, P. Zanchetta, M. Degano, and E. Lavopa, "Control design and implementation for high performance shunt active filters in aircraft power grids," IEEE Trans. Ind. Electron., vol. 59, no. 9, pp. 3604–3613, Sep. 2012.

[7] B. Singh and S. Arya, "Adaptive theory-based improved linear sinusoidal tracer control algorithm for DSTATCOM," IEEE Trans. Power Electron., vol. 28, no. 8, pp. 3768–3778, Aug. 2013.

CHANDRA RAKHEE B
Assistant professor
Mail Id: chandrarakhee.b@gmail.com

PULLA REDDY .K
Assistant professor
Mail id: pullareddy.kasireddy@gmail.com

High Gain Zero Voltage Switching Bidirectional Converter with Reduced Number of Switches

K. KRISHNAIAH[1], NIREEKSHAN[2], S. RAJESH[3]

[1]PG Scholar, Dept of EEE, Siddhartha Institute of Engineering and Technology, Ibrahimpatnam, Hyderabad, Telangana, India.
[2]Assistant Professor, Dept of EEE, Siddhartha Institute of Engineering and Technology Hyderabad, Telangana, India.
[2]Assocoaite Professor & HOD, Dept of EEE, Siddhartha Institute of Engineering and Technology Hyderabad, Telangana, India.

Abstract: A non-isolated bidirectional DC-DC Converter has been proposed in this paper for charging and discharging the battery bank through single circuit in applications of Uninterruptible Power Supplies (UPS) and the hybrid electric vehicles. The proposed bidirectional converter operates under zero voltage switching (ZVS) condition and provides large voltage diversity in both the modes of operation. This enables the circuit to step up the low battery bank voltage to high DC link voltage and vice versa. The bidirectional operation of the converter is achieved by employing only three active switches, a coupled inductor and an additional voltage clamped circuit. Complete description of the operation principle of the circuit is explained and design procedure of the converter has been discussed. The experimental results of a 300W prototype of the proposed converter confirmed the validity of the circuit. The maximum efficiency of 96% is obtained at half load for boost operation mode, and 92% for buck mode of operation.
.
Keywords: Bidirectional DC-DC Converter, Zero voltage switching (ZVS), Coupled inductor.

I. INTRODUCTION

Bidirectional DC-DC Converters are widely used in many industrial applications such as hybrid vehicles, auxiliary supplies, and in battery charging/discharging DC converters in UPS system. Usually battery bank are the backup energy source which provides very low voltage at the input of the bidirectional converter. Although, a string of batteries connected in series can provide a high input voltage, but still it has some disadvantages. A larger battery bank increases the size and cost of the system. Also if there is a slight mismatch in the batteries voltage or difference in the batteries temperature within the string, it will cause charge imbalance in the battery bank [1]. This study therefore focuses on the analysis and design of a high efficiency bidirectional converter with high voltage conversion ratio, which helps in reducing the number of batteries in order to elude a larger battery bank. The bidirectional converter may be transformer isolated [2] or non-isolated [3-10]. Isolated bridge-type bidirectional converters are probably the most popular topology in high power applications. However, the major

concerns of this topology are high switching losses, excessive voltage and Current stresses, and significant conduction losses because of the increased in the number of switches [6]. Hence, their practical implementation is quite complex.

With incorporation of coupled inductor and zero voltage switching (ZVS), Non-isolated bidirectional converters has attracted special interest due to high conversion ratio, reduced switching losses, and simplicity in design. These types of topologies are highly cost effective and acceptable due to high efficiency improvement, and considerable reduction in the weight and volume of the system. Several topologies of the non-isolated converters have been proposed so far [3-6]. A ZVS bidirectional converter with single auxiliary switch has been proposed in [3]. Although the main switches operate under ZVS which increase the efficiency of the system, but the auxiliary switch still performs hard switching and the converter offers very limited voltage diversity [7]. Other high voltage gain bidirectional converters have been proposed in [8-11]. These converters provide high voltage gain in both the boost and buck mode of operation but at the cost of high number of active switches and extra auxiliary circuit components used in the circuit. This adds more complexity in the control circuitry, with high size and cost. According to the analysis of the drawbacks related to the aforementioned topologies, this paper proposes a new non-isolated bidirectional DC-DC converter with coupled inductor. The proposed converter has following advantages.

1. High Voltage Gain in both the buck and boost mode
2. Only three active switches are used to perform bidirectional operation.
3. Less number of passive components is used in the circuit
4. Zero voltage switching (ZVS), synchronous rectification, and voltage clamping circuit are used which reduces the Switching and conduction losses.

This paper is organized as follows: the operation of proposed topology is explained in section II. Design considerations are presented in section III, followed by experimental results in section IV and conclusion in Section V.

II. OVERVIEW OF BLDC MOTOR
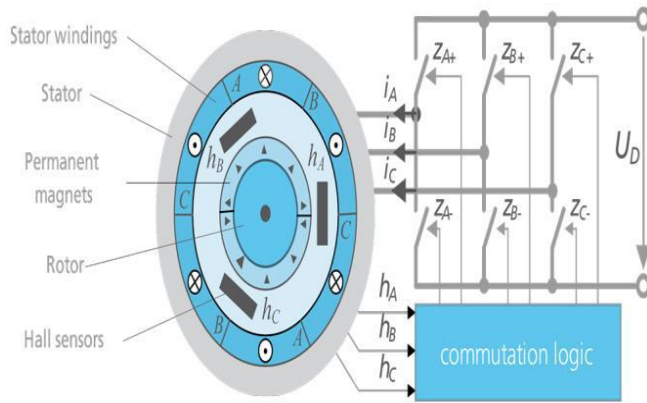
Fig.1. Input inverting stage of BLDC motor.

The control of PMBLDC motors can be accomplished by various control techniques using conventional six pulse inverters which can be classified in two broad categories as voltage source inverter (VSI) and current source inverter (CSI) based topologies. The controllers can further be divided on the basis of solid state switches and control strategies. The BLDCM needs rotor-position sensing only at the commutation points, e.g., every 60°electrical in the three-phases; therefore, a comparatively simple controller is required for commutation and current control. The commutation sequence is generated by the controller according to the rotor position which is sensed using Hall sensors, resolvers or optical encoders. These sensors increase the cost and the size of the motor and a special mechanical arrangement is required for mounting the sensors. The components are DC-AC inverter, DC-DC converter, battery, and electric BLDC motor. DC-AC inverters supply voltage to the electric motor from the battery and also supply utility loads such as air conditioning and AC power outlet.
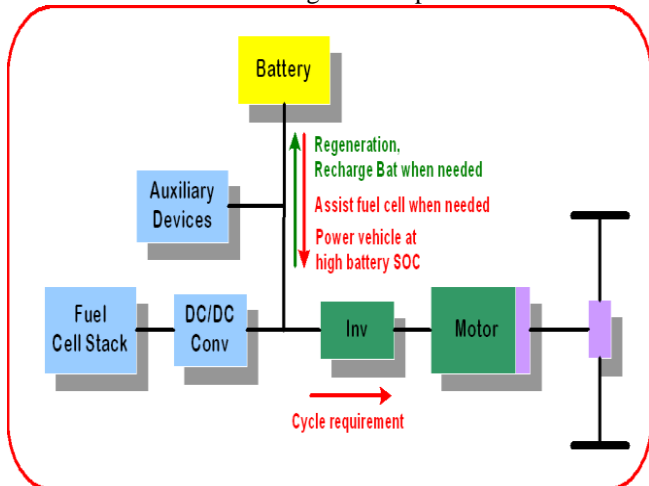
Fig.2. Driving process of high voltage BLDC motor.

DC-DC converters supply voltage to various vehicular loads set to operate at different voltages. In the near future, high power DC-DC converters will be needed for EVs since the vehicular power requirements are continuously increasing due to which the present day 12- V/14-V electrical system will be replaced by 42-V/300-V architecture. DC-DC converters are well developed for low and medium power applications, whereas development of highly efficient and cost effective high power DC-DC converters for vehicular applications is in continuous progress. This is partly due to the stringent Electromagnetic Interference (EMI) standards and also due to temperature related issues. The boost dc voltage is the input of the BLDC motor.

III. HARD SWITCHING VS SOFT SWITCHING

Recently, switch-mode power supplies have become smaller and lighter due to higher switching frequency. However, higher switching frequency causes lots of periodic losses at turn ON and turn OFF, resulting in increasing losses of whole system. Semiconductors utilised in Static Power Converters operate in the switching mode to maximise efficiency. Switching frequencies vary from 50 Hz in a SCR based AC-DC Phase Angle Controller to over 1.0 MHz in a MOSFET based power supply. The switching or dynamic behaviour of Power Semiconductor devices thus attracts attention specially for the faster ones for a number of reasons: optimum drive, power dissipation, EMI/RFI issues and switching-aid- networks. Present day fast converters operate at much higher switching frequencies chiefly to reduce weight and size of the filter components. As a consequence, switching losses now tend to predominate, causing the junction temperatures to rise. Special techniques are employed to obtain clean turn-on and turn-off of the devices. This, along with optimal control strategies and improved evacuation of the heat generated, permit utilisation of the devices with a minimum of deration.
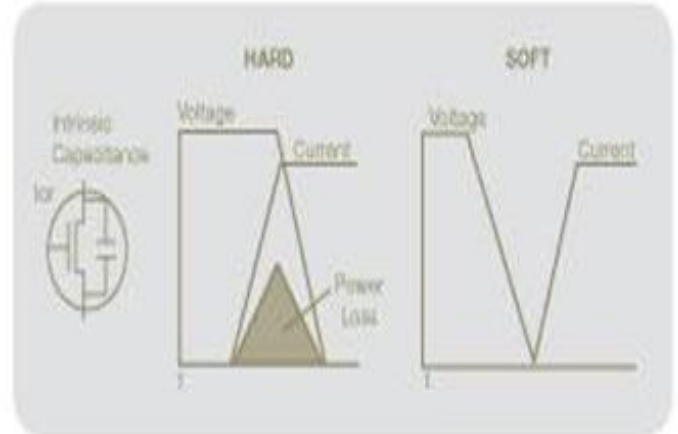
Fig.3. Hard and Soft Switching Waveform.

IV. METHODS OF SOFT SWITCHING.

A. Design a High Frequency PWM Subsystem.

The carrier waveform used is Saw tooth waveform instead of Triangular waveform. When the reference value is more than the carrier waveform the output PWM signal is HIGH. The switching turn ON points is determined by the saw tooth waveform used.
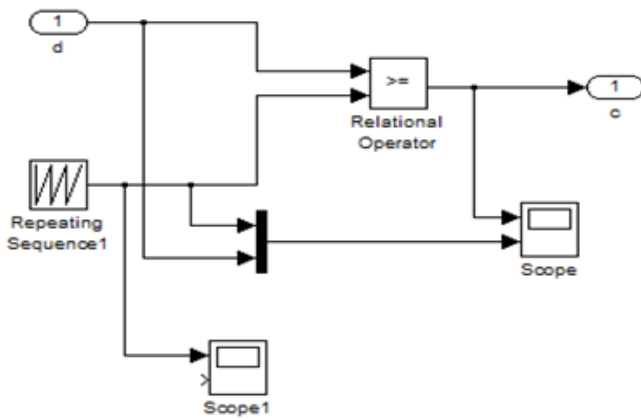
Fig.4. PWM subsystem.
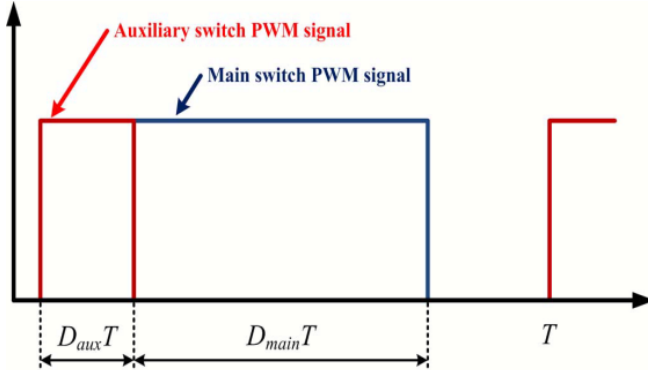
Fig.5. PWM signals of the main and auxiliary switch

The proposed Boost Converter has two switches namely main switch and auxiliary switch. The main switch has a duty ratio of 0.61 while that of auxiliary switch is 0.21. The main switch duty ratio determines the average output voltage. The function of auxiliary switch is to enable the main switch to operate soft switching. First the auxiliary switch is turned ON then the main switch in turned ON after some time delay. The resonant loop of the resonant inductor (Lr) and resonant capacitor (Cr) is completed by the turning ON of the auxiliary switch. By the help of resonance the auxiliary switch is made to operate at ZCS. As the snubber capacitor is discharged the current of the resonant loop flows through the anti-parallel diode of the main switch. By turning ON the main switch the ZVS is assured. As the resonant capacitor is fully discharged the auxiliary switch is turned OFF. The PWM signal of the main switch is given some delay compared to auxiliary switch. The phase difference is obtained by delaying the carrier waveform. The main switch is turned ON while the auxiliary switch is still in the ON state.

B. Configuration of the proposed HI-Bridge Boost converter.

The proposed converter is shown in Fig. 6. The main switch (IGBT) and the auxiliary switch (IGBT1) of the proposed circuit enable soft switching through an auxiliary switching block, consisting of an auxiliary switch, two resonant

capacitors (Cr and Cr2), a resonant inductor (Lr), and two diodes (D1 and D2). The following assumptions are made

1. All switching devices and passive elements are ideal.
2. The input voltage (Vin) is constant.
3. The output voltage(Vo) is constant. (Output capacitor
4. Co is large enough).
5. The recovery time of all diodes is ignored.
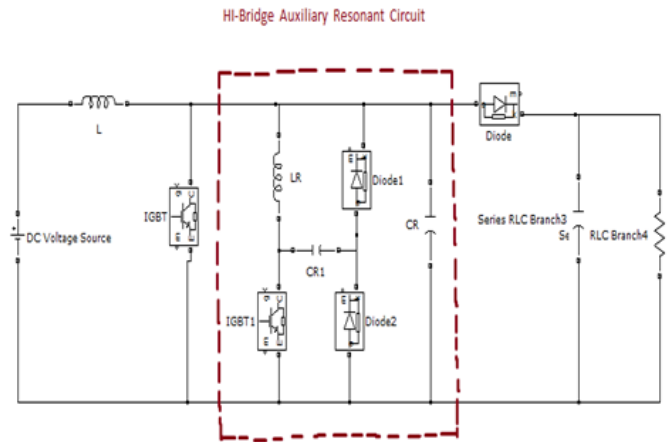
Fig.6. Schematic of the proposed soft-switching boost converter

C. The main switch and auxiliary switch.

There are two switches in this paper. One is the main switch deal with a duty ratio and the other one is the auxiliary switch enables the main switch to operate with a soft switching. The carrier, reference and pulse width modulation(PWM) waveforms of the main switch and auxiliary switch are illustrated in Fig. 4. After the auxiliary switch is turned on, the main switch is turned on. If the auxiliary switch is turned on, the resonant loop of the resonant inductor(Lr) and resonant capacitor(Cr) is made. The auxiliary switch operates with ZCS using the resonance. The current of the resonant loop flows across the anti-parallel diode of the main switch after the snubber capacitor is discharged. Thus, ZVS area is guaranteed by turning on the auxiliary switch. A point the auxiliary switch is turned off is the time the energy of the resonant capacitor(Cr) is fully discharged. The main switch set a voltage gain. A transfer function of the proposed soft switching boost converter is same to the conventional boost converter and that is given by the equation (1) .

$$Gv = (Vout/Vin) = 1/(1-D) \qquad (1)$$

Where Gv is a voltage gain and D is a duty ratio. The PWM has to be made with a delay between the main switch and auxiliary switch. A phase difference can be obtained by delaying the carrier waveform. The main switch always has to be turned on during the auxiliary switch turns on. Points which switches turn on at have to be fixed to realize a soft switching without resonance failure. A Sawtooth waveform is used as a carrier waveform instead of a triangular one. If a reference value is upper than a carrier one, the PWM output

signal becomes high. Thus, switching turn on points can be fixed by using the sawtooth waveform.

V. SIMULATION AND OUTPUT

A. PWM Subsystem output waveform.
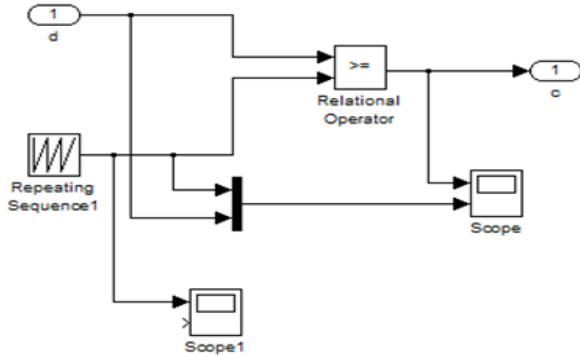
Fig.7. PWM Subsystem.
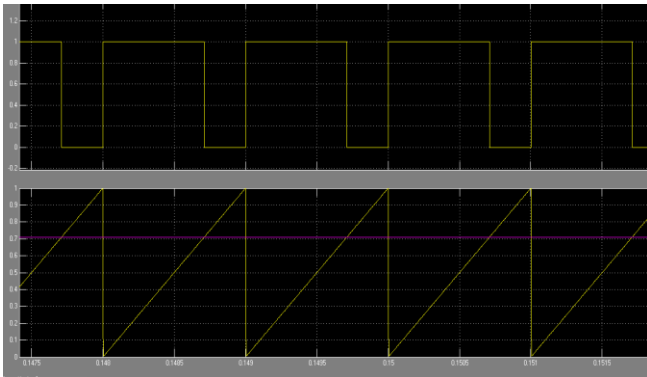
Fig.8.PWM subsystem and output waveform in MATLAB.

B. Simulation of HI-bridge soft-switching boost converter output waveform.
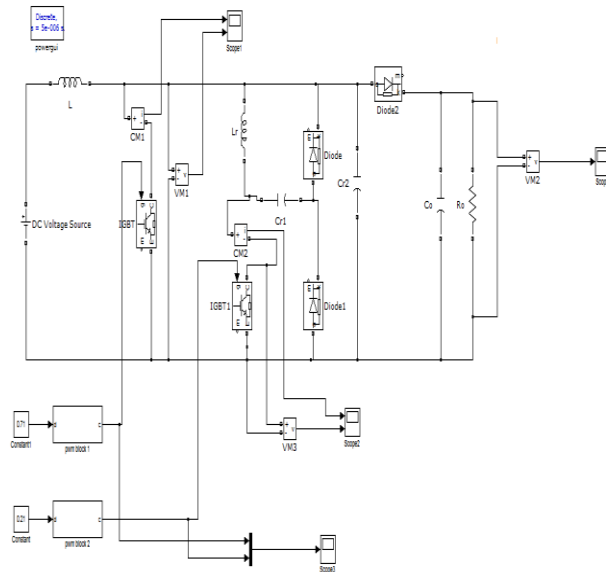
Fig.9. Simulink model of HI-bridge boost converter using auxiliary boost converter.

The above proposed boost converter with auxiliary resonant circuit is simulated in MATLAB-SIMULINK. The values of the circuit parameters are given below:

Table1. Key Data

Parameters	Values
Input voltage (Vin)	130-170[V]
Output voltage (Vo)	400[V]
Switching Freq.(fsw)	30[]KHz
Resonant Cap. (Cr)	3.3[nF]
Resonant Cap. (Cr2)	30[nF]
Resonant Ind. (Lr)	20[µH]
Main Inductor (L1)	560[µH]
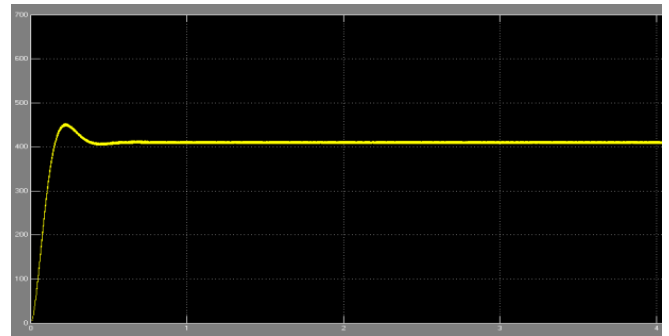
Fig.10. Output Voltage Vs Time Waveform.
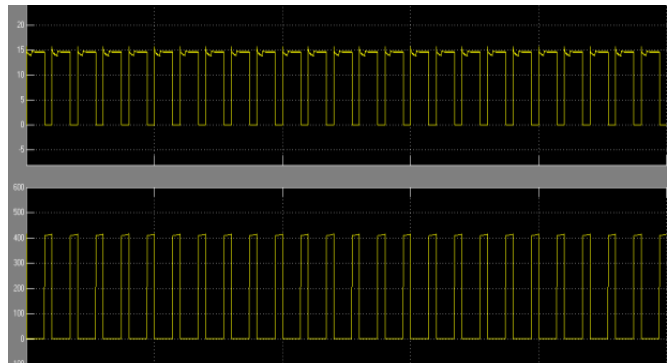
Fig.11. Main switch Current and Voltage.
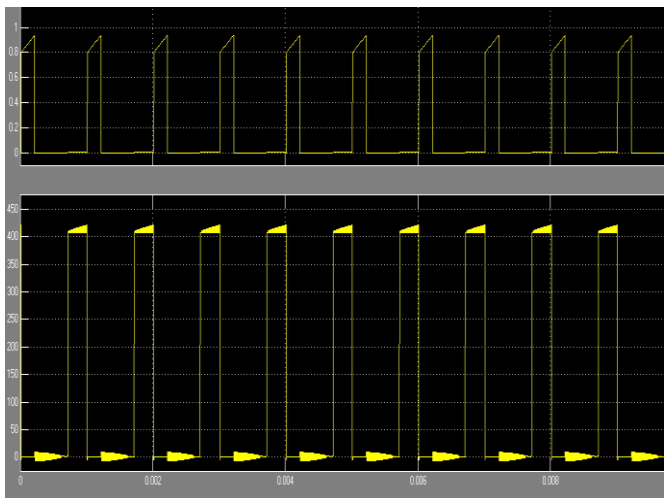
Fig.12. Auxiliary switch Current and Voltage.

VI. DESIGN PROCEDURE

The following design procedure is based on the soft-switching turn-ON and turn-OFF requirements of the main switch, the main diode, and the auxiliary switch.

A. Resonant Capacitor (Cr)

The resonant capacitor (Cr) is selected to allow ZVS of the main switch. The charging time of the resonant capacitor (Cr) must be longer for ZVS of the main switch. Thus, for the resonant capacitor (Cr), it is more than ten times the output capacitance of the main switch. Assume that the maximum current of the resonant inductor is IL max, and the sum of the two inductor currents is the charging current of the resonant capacitor (Cr). In this case, the minimum resonant capacitor (Cr) is equal to 20 times the output capacitance of the main switch.

B. Parameters Design

$D = 1 - (Vin (min) * η)/ Vout$
D= Duty Cycle.
Vin (min) = Minimum input voltage.
Vout = Desired output voltage.
Ƞ = Efficiency of Converter

$$L = (Vin/\Delta IL) * (Vout - Vin) * (1/Vout) * (1/fs)$$

L = Inductance of main Inductor.
fs = Switching frequency.
ΔIL = Estimated Inductor ripple current.
$\Delta IL = (0.2 - 0.4) * Iout (max) * (Vout/Vin).$
Iout (max) = Maximum output current.
$Cout (min) = (Iout (max)/fs) * D/\Delta Vout.$
Cout (min) = Minimum output Capacitance.

VII. EXPERIMENTAL RESULTS

A 300W protype has been built to confirm the feasibility of the proposed circuit. The circuit operated between LVS voltage VL = 24V, and HVS voltage VH =200V. The switching frequency is 20 KHz. The Switches S1-S3 used in the circuit are IPW60R045CP MOSFETs. Coupled inductor is designed using PQ40-40 with magnitising inductance of 24uH, and turns ratio N = 2.5. An inductor L1 has 80uH inductance, so the size is very small. Besides C1 and C2 consist of 4.4uF ceramic capacitors. The diodes D1~D3 used are ultrafast recovery diodes UF5408. Thus all the axilary components are not adding considerable in the size of the circuit. A low cost PWM controller TL494 is employed for controlling the switches of the bidirectional converter. The dead time between the switching PWM is 5us which helps in ZVS of the circuit. An experimental prototype was built to confirm its feasibility. Fig 8 and Fig. 9 shows the experimental waveform during buck and boost mode of the proposed circuit respectively.The voltage stress across both the switches S1 and S2 is about 50V which is quite small as compare to HVS (200V). The voltage across the Switch S2 is quite low, and conduction current in the coupled inductor is

smoothened as shown in the Fig.8. Fig.7 shows the Zero voltage switching in switch S1 during buck mode of operation. Fig. 10 gives the experimental results which shows maximum efficiency of about 96% during boost mode and 92% during buck mode of operation Thus utilizing synchronous rectification and soft switching reduces the switch losses and increases the efficiency of the system. The

V_{DS1}: 50V/div; i_{DS1}:5A/div; Time: 10us/div V_{DS3}: 200V/div; i_{DS3}: 5A/div; Time: 10us/div Vg_1, Vg_3: 20V/div; i_{LP}, i_{LS}: 10A/div; Time:10us/div
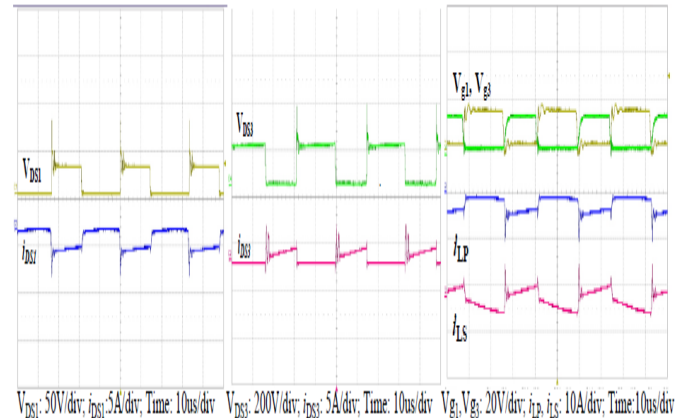
Fig.13. Experimental Waveform of Drain to Source Switch voltages and Inductor current during Buck Mode

V_{DS1}:50V/div; i_{DS1}:10A/div; Time: 10us/div V_{DS3}:200V/div; i_{DS3}: 5A/div; Time: 10us/div, Vg_1, Vg_3: 20V/div; i_{LP}, i_{LS}: 10A/div; Time: 10us/div
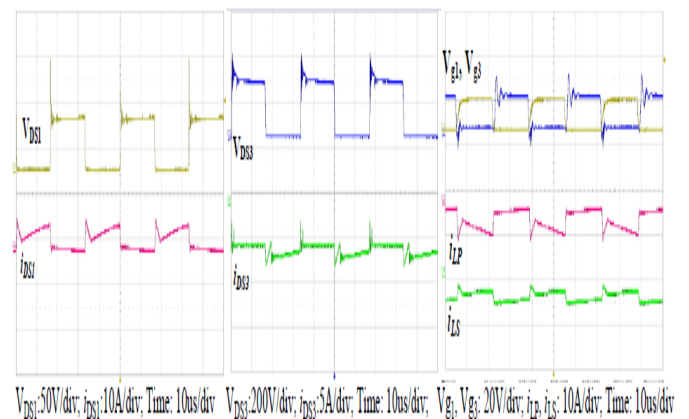
Fig.14. Experimental Waveform of Drain to source voltages and Inductor current during Boost mode
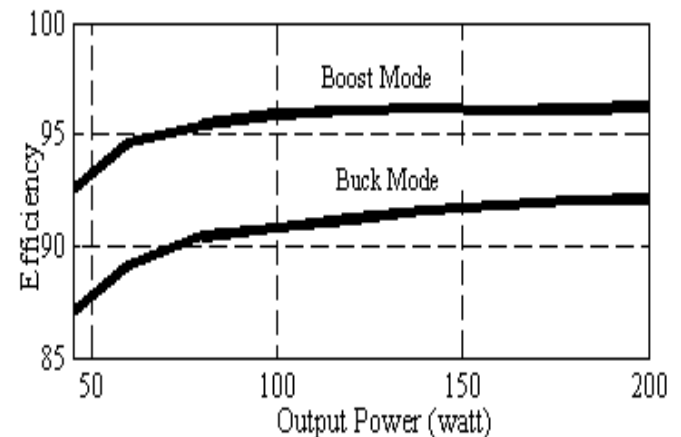
Fig.15. Experimental Efficiency Graphs.

Efficiency during buck mode is less than boost mode due to utilization of an additional switch S2 which is not used in the boost mode. Table. I shows the comparison of different bidirectional converters recently published. The voltage conversion ratio of the proposed converter shows more diversity as compared to [9] and [10], with less no of switches. [11] shows high gain ratio but with five switches which increases the size and cost of the circuit. The size of the proposed circuit is considerable small with small heat sink for the given power rating, and only few passive auxiliary components help in operation under ZVS.

VIII. CONCLUSION

This paper presents a non-isolated ZVS bidirectional DC-DC converter. The most promising features of the converter are high voltage conversion ratio in both modes of operation, with less number of active switches, and low voltage & current stresses on the switches. The operation principle of each mode has been explained and the design steps of the converter are discussed. The experimental results of the proposed converter shows exemplary results with high efficiency of about 96% and 92% in boost and buck modes of operation respectively.

TABLE I. Comparison of Different Topologies

Topology Features	Conv.	[11]	[9]	[10]	Proposed Topology
Switches	2	5	4	4	3
M_{BOOST}	$1/(1-D)$	$\frac{1+N}{(1-D)}+N$	$\frac{2+N}{D}$	$\frac{2}{1-D}$	$\frac{2+ND}{1-D}$
M_{BUCK}	D	$\frac{D}{1+N+DN}$	$\frac{D}{N+2}$	$\frac{D}{2}$	$\frac{D(1-D)}{2N(1-D)^2+1}$
Efficiency (%)	90	96	95	94	96
Size	Small	Large	Medium	Medium	Small
Estimated Cost(US $)	-	~172	~118	~136	~116

VII. REFERENCES

[1] M. Uno and K. Tanaka, "Single-switch cell voltage equalizer using multistacked buck-boost converters operating in discontinuous conduction mode for series-connected energy storage cells," *IEEE Transactions on Vehicular Technology,* vol. 60, pp. 3635-3645, Oct. 2011

[2] L. Zhu, "A novel soft-commutating isolated boost full-bridge ZVS-PWM DC–DC converter for bidirectional high power applications," *IEEE Transactions on Power Electronics,* vol. 21, pp. 422-429, Mar. 2006.

[3] P. Das, B. Laan, S. A. Mousavi, and G. Moschopoulos, "A nonisolated bidirectional ZVS-PWM active clamped DC–DC converter," *IEEE Transactions on Power Electronics,* vol. 24, pp. 553-558, Jan. 2009.

[4] J. Zhang, J.-S. Lai, R.-Y. Kim, and W. Yu, "High-power density design of a soft-switching high-power bidirectional dc–dc converter," *IEEE Transactions on Power Electronics,* vol. 22, pp. 1145-1153, Jul. 2007.

[5] J.-W. Yang, and H.-L. Do, "Soft-Switching Bidirectional DC-DC Converter Using a Lossless Active Snubber," *IEEE Transactions on Circuits and Systems I*, vol. 61, no. 5, pp. 1588-1596, May. 2014.

[6] H. Shiji, K. Harada, Y. Ishihara, T. Todaka, and G. ALZAMORA, "A zero-voltage-switching bidirectional converter for PV systems," *IEICE transactions on communications,* vol. 87, pp. 3554-3560, Oct. 2004.

[7] S.-H. Park, S.-R. Park, J.-S. Yu, Y.-C. Jung, and C.-Y. Won, "Analysis and design of a soft-switching boost converter with an HI-Bridge auxiliary resonant circuit," *IEEE Transactions on Power Electronics,* vol. 25, pp. 2142-2149, Aug. 2010.

[8] M. Kwon, S. Oh, and S. Choi, "High Gain Soft-Switching Bidirectional DC–DC Converter for Eco-Friendly Vehicles," *IEEE Transactions on Power Electronics,* vol. 29, pp. 1659-1666, April. 2014.

[9] R.-Y. Duan and J.-D. Lee, "High-efficiency bidirectional DC-DC converter with coupled inductor," *IET Power Electronics,* vol. 5, pp. 115-123, Jan. 2012.

[10] C.-C. Lin, L.-S. Yang, and G. Wu, "Study of a non-isolated bidirectional DC–DC converter," *IET Power Electronics,* vol. 6, pp. 30- 37, Jan. 2013.

[11] Y.-P. Hsieh, J.-F. Chen, L.-S. Yang, C.-Y. Wu, and W.-S. Liu, "High-conversion-ratio bidirectional dc–dc converter with coupled inductor," *IEEE Transactions on Industrial Electronics,* pp. 210-222, Jan. 2014.

[12] I. Batarseh, *Power electronic circuits*: John Wiley, 2004.

[13] R. W. Erickson and D. Maksimovic, *Fundamentals of power electronics*: Springer, 2001.

Author's Profile:

Mr. K. Krishnaiah has completed his B-Tech in EEE Department from JJ Institute of information Technology, Maheshwaram, RR Dist JNTU University, Hyderabad. Presently he is pursuing his Masters in Power electronics from Siddartha Institute of Engineering Technology, Ibrahimpatnam, Hyderabad, TS India.

Namburi.Nireekshan received the B.Tech degree from JNTU-Hyderabad, India, the M.Tech degree from JNTU-Hyderabad. He is working working as a, Asst. Professor in the Electrical & Electronics Engineering Department, Siddhartha institute of engineering and technology, RR Dist, AP, India . He published nearly four technical papers to his credit in various National & International Journals & conferences.

High Gain Zero Voltage Switching Bidirectional Converter with Reduced Number of Switches

S. Rajesh received M.Tech degree in Power Electronics from Jawaharlal Nehru Technological University Hyderabad, Telangana, India in 2010 respectively. He has presented nearly 5 papers in National level conferences. His research interests are power electronics applications in distributed power generation and analysis of power converters, control and estimation in induction motor drive and wind turbine driven induction generator. Currently he is working on stability studies of Double Fed Induction Generator in Wind power Generation. He is a Student member of IEEE and life Member of ISTE (India). He currently serving as Associate Professor & Head of the Department of Electrical and Electronics engineering in Siddhartha institute of engineering and Technology Hyderabad,Telangana,India.He has 8 years experience in teaching..

A Higher Voltage Multilevel Inverter with Reduced Switches for Industrial Drive

C.S.Pavan Prasad
M-tech Student Scholar
Department of Electrical & Electronics Engineering,
SIDDHARTHA INSTITUTE OF ENGINEERING &
TECHNOLOGY, Vinobha nagar, Ibrahimpatnam,
R.R(Dt); Telangana, India

N.Nireekshan
Assistant Professor
Department of Electrical & Electronics Engineering,
SIDDHARTHA INSTITUTE OF ENGINEERING &
TECHNOLOGY, Vinobha nagar, Ibrahimpatnam,
R.R (Dt); Telangana, India

Abstract - Power electronic inverter become popular for various industrial drives applications. The multi-level inverter system is very promising in ac drives. Large electrical drives and utility application require advanced power electronics converter to meet the high power demands. As a result, multilevel power converter structure has been introduced as an alternative in high power and medium voltage situations. A multilevel converter not only achieves high power rating but also improves the performance of the whole system in terms of harmonics. The inverter output with more numbers of voltage levels with reduced number of switches as compared to cascade H-bridge inverter, which results in reduction of installation cost and have simplicity of control system. In this paper, a new configuration of a three-phase seven-level multilevel voltage source inverter is introduced. The proposed topology constitutes the conventional three-phase five-level bridge with three bidirectional switches.This three phase inverter is fed to induction motor and check the performance chtacteristicsby using matlab/Simulink platform.

IndexTerms—Bidirectional switch, fundamental frequency staircase modulation, multilevel inverter.

I. INTRODUCTION

Multilevel inverters are composed of a number of power electronic switches and DC voltage sources that produce a stepped voltage waveform in its output. Generally, multilevel inverters are divided into three categories as follows: neutral-point clamped inverter (NPC), flying capacitor inverter (FC), and cascaded H-bridge inverter (CHB). These inverters can surrender higher power with lower dv/dt and di/dt in output waveform which is to reduce EMI noise and Size of the output filter. Therefore, using theseinverters is very common nowadays. In recent years, several architectures have been proposed for cascade multilevel inverters. This kind of inverters can produce more voltage levels and also provide higher quality of power in its output. As a result, this kind of inverter is considered more than other kinds of inverters. Cascade inverters are made of series separate single phase inverters with separate dc voltage sources. On the other hand, this inverter consists of a number of basic blocks (sub multilevel inverter) that each of

these blocks has similar control system. One of the major advantages of this type of inverters is the ability of its modulation. So, if an error occurs in one of the blocks, it can replace or fix by using a control system, but there are some disadvantages such as high number of dc voltage sources and power electronic switches. Increasing the number of power electronic switches leads to increase the number of driver circuits too. Both of these issues caused to increase in complexity, size, and cost of the circuit. Thus, reducing the number of power electronic switches is very vital and should be considered.

Some applications for these new converters include industrial drives, flexible ac transmission systems (FACTS), and vehicle propulsion. One area where multilevel converters are particularly suitable is that of renewable photovoltaic energy that efficiency and power quality are of great concerns for the researchers.Some new approaches have been recently suggested such as the topology utilizing lowswitching-frequency high-power devices . Although the topology has some modification to reduce output voltage distortion, the general disadvantage of this method is that it has significant low-order current harmonics.

The purpose of improving the performance of the conventional single- and three-phaseinverters, different topologies employing different types of bidirectional switches. Comparingto the unidirectional one, bidirectional switch is able to conduct the current and withstanding the voltage in both directions.Bidirectional switches with an appropriate control techniquecan improve the performance of multilevel inverters in terms of reducing the number of semiconductor components, minimizing the withstanding voltage and achieving the desired outputvoltage with higher levels. Based on this technical background, this paper suggests a novel topology for a threephase five-level multilevel inverter. The number of switching devices, insulated-gate driver circuits, and installation area and cost are significantly reduced. The magnitudes of the utilized dc voltage supplies have been selected in a way that brings the high number of voltage level with an effective application

of a fundamental frequency staircase modulation technique. Extended structure forN-level is also presented and compared with the conventional well-known multilevel inverters. Simulation results are explained.

II. PROPOSED CONFIGERATION

Fig. 1(a) and (b) shows the typical configuration of the proposed three-phase five-level multilevel inverter. Three bidirectional switches (S1–S6, Da1–Dc2), two switches–two diodes type, are added to the conventional three-phase two-level bridge (Q1–Q6). The function of these bidirectional switches is to block the higher voltage and ease current flow to and from the midpoint (o). A multilevel dc link built by a single dc voltage supply with fixed magnitude of $4V_{dc}$ and CHB having two unequal dc voltage supplies of V_{dc} and 2Vdc are connected to (+,–,o) bridge terminals. Based on the desired number of output voltage levels, a number of CHB cells are used. Since the proposed inverter is designed to achieve five voltage levels, the power circuit of the CHB makes use of two series cells having two unequal dc voltage supplies. In each cell, the two switches are turned ON and OFF under inverted conditions to output two different voltage levels. The first cell dc voltage supply V_{dc} is added if switch T1 is turned ON leading to $V_{mg} = +V_{dc}$ where V_{mg} is the voltage at node (m)with respect to inverter ground (g)or bypassed if switch T2 is turned ON leading to $V_{mg} = 0$. Likewise, the second cell dc voltage supply 2Vdc is added when switch T3 is turned ON resulting in $V_{om} = +2V_{dc}$ where $V_{om}$is the voltage at midpoint(o)with respect to node(m)or bypassed when switch T4 is turned ON resulting in $V_{om}=0$. The peak voltage rating of the switches of the conventional twolevel bridge (Q1–Q6) is 4Vdcwhereas the bidirectional switches (S1–S6) have a peak voltage rating of 3Vdc.InCHBcells,the peak voltage rating of second cell switches (T3 and T4) is $2V_{dc}$ while the peak voltage rating of T1 and T2 in the first cell is V_{dc}.
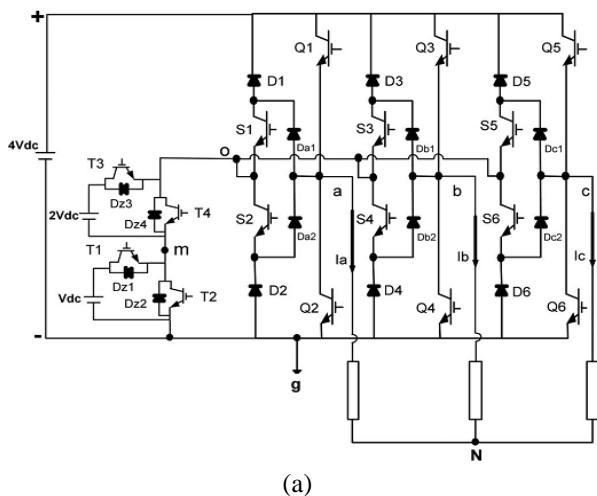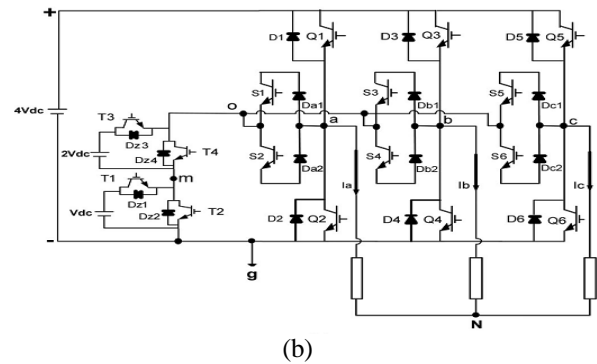
(b)

Fig. 1.Circuit diagram of the proposed three-phase five-level multilevel inverter.

TABLE I
Switching State S_a and Inverter Line-to-Ground Voltage V_{ag}

Sa	Q1	S1	S2	Q2	T1	T2	T3	T4	Vag
4	on	off	off	off	on	off	on	off	+4Vdc
3	off	on	on	off	on	off	on	off	+3Vdc
2	off	on	on	off	off	on	on	off	+2Vdc
1	off	on	on	off	on	off	off	on	+Vdc
0	off	off	off	on	on	off	off	on	0

It is easier to define the inverter line-to-ground voltages V_{ag}, V_{bg}, and V_{cg} in terms of switching states Sa, Sb, and Sc as

$$\begin{bmatrix} V_{ag} \\ V_{bg} \\ V_{cg} \end{bmatrix} = \frac{4V_{dc}}{N-1} * \begin{bmatrix} Sa \\ Sb \\ Sc \end{bmatrix} \tag{1}$$

Where N=5 is the maximum number of voltage levels.

The balanced load voltages can be achieved if the proposed inverter operates on the switching states depicted in Table II. The inverter may have 24 different modes within a cycle of the output waveform. According to Table II, it can be noticed that the bidirectional switches operate in 18 modes. For each mode, there is no more than one bidirectional switch in on state. As a result, the load current commutates over one switch and one diode (for instance: in (410), the load current I_b can flow in S3 and Db1 or S4 and Db2). Since some insulated gate bipolar transistors (IGBTs) share the same switching gate signals, the proposed configuration significantly contributed in reducing the utilized gate driver circuits and system complexity. The inverter line-to-line voltage waveforms V_{ab},V_{bc}, and $V_{ca}$with corresponding switching gate signals are depicted in Fig. 2 where V_{ab}, V_{bc}, and V_{ca} are related to V_{ag}, V_{bg}, and V_{cg} by

$$\begin{bmatrix} V_{ab} \\ V_{bc} \\ V_{ca} \end{bmatrix} = \begin{bmatrix} 1 & -1 & 0 \\ 0 & 1 & -1 \\ -1 & 0 & 1 \end{bmatrix} * \begin{bmatrix} V_{ag} \\ V_{bg} \\ V_{cg} \end{bmatrix} \tag{2}$$

The inverter line-to-neutral voltages V_{aN}, V_{bN}, and V_{cN} may be expressed as

$$\begin{bmatrix} V_{aN} \\ V_{bN} \\ V_{cN} \end{bmatrix} = \frac{1}{3} \begin{bmatrix} 2 & -1 & -1 \\ -1 & 2 & -1 \\ -1 & -1 & 2 \end{bmatrix} * \begin{bmatrix} V_{ag} \\ V_{bg} \\ V_{cg} \end{bmatrix} \tag{3}$$

(a)

213

It is useful to recognize that the inverter voltages at terminals a, b, and c with respect to the midpoint (o) are given by

$$\begin{bmatrix} V_{ao} \\ V_{bo} \\ V_{co} \end{bmatrix} = \begin{bmatrix} V_{ag} \\ V_{bg} \\ V_{cg} \end{bmatrix} - \begin{bmatrix} V_{og} \\ V_{og} \\ V_{og} \end{bmatrix}$$ (4)

Where V_{og} is the voltage at midpoint(o)with respect to ground (g). V_{og} routinely fluctuates among three different voltage valuesVdc,2Vdc, and 3Vdcas follows:

$$V_{og} = \begin{cases} V_{dc}, & \text{if } Sa + Sb + Sc \leq 5 \\ 2V_{dc}, & \text{if } Sa + Sb + Sc = 6 \\ 3V_{dc}, & \text{if } Sa + Sb + Sc \geq 7. \end{cases}$$ (5)

TABLE II
SWITCHINGSTATESSEQUENCE OF THEPROPOSEDINVERTERWITHINONECYCLE

Sa Sb Sc	Period T [s]	ON switches Leg a	ON switches Leg b	ON switches Leg c	ON switches cascaded half-bridge	Vag [V]	Vbg [V]	Vcg [V]
400	t1	Q1	Q4	Q6	T1,T4	4Vdc	0	0
410	t2	Q1	S3, S4	Q6	T1,T4	4Vdc	Vdc	0
420	t3	Q1	S3, S4	Q6	T2,T3	4Vdc	2Vdc	0
430	t4	Q1	S3, S4	Q6	T1,T3	4Vdc	3Vdc	0
440	t5	Q1	Q3	Q6	T1,T3	4Vdc	4Vdc	0
340	t6	S1, S2	Q3	Q6	T1,T3	3Vdc	4Vdc	0
240	t7	S1, S2	Q3	Q6	T2,T3	2Vdc	4Vdc	0
140	t8	S1, S2	Q3	Q6	T1,T4	Vdc	4Vdc	0
040	t9	Q2	Q3	Q6	T1,T4	0	4Vdc	0
041	t10	Q2	Q3	S5, S6	T1,T4	0	4Vdc	Vdc
042	t11	Q2	Q3	S5, S6	T2,T3	0	4Vdc	2Vdc
043	t12	Q2	Q3	S5, S6	T1,T3	0	4Vdc	3Vdc
044	t13	Q2	Q3	Q5	T1,T3	0	4Vdc	4Vdc
034	t14	Q2	S3, S4	Q5	T1,T3	0	3Vdc	4Vdc
024	t15	Q2	S3, S4	Q5	T2,T3	0	2Vdc	4Vdc
014	t16	Q2	S3, S4	Q5	T1,T4	0	Vdc	4Vdc
004	t17	Q2	Q4	Q5	T1,T4	0	0	4Vdc
104	t18	S1, S2	Q4	Q5	T1,T4	Vdc	0	4Vdc
204	t19	S1, S2	Q4	Q5	T2,T3	2Vdc	0	4Vdc
304	t20	S1, S2	Q4	Q5	T1,T3	3Vdc	0	4Vdc
404	t21	Q1	Q4	Q5	T1,T3	4Vdc	0	4Vdc
403	t22	Q1	Q4	S5, S6	T1,T3	4Vdc	0	3Vdc
402	t23	Q1	Q4	S5, S6	T2,T3	4Vdc	0	2Vdc
401	t24	Q1	Q4	S5, S6	T1,T4	4Vdc	0	Vdc

III.SWITCHING ALGORITHM

The staircase modulation can be simply implemented for the proposed inverter. Staircase modulation with selective harmonic is the most common modulation technique used to control the fundamental output voltage as well as to eliminate the undesirable harmonic components from the output waveforms. An iterative method such as the Newton–Raphson method is normally used to find the solutions to(N−1) nonlinear transcendental equations. The difficult calculations and the need of high performance controller for the real application are the main disadvantages of such method. Therefore, an alternative method is proposed to generate the inverter's switching gate signals. It is easier to control the proposed inverter and achieve the required output voltage waveforms in terms of Sa, Sb, and Sc. The operation of the proposed inverter, the switching states Sa, Sb, and Scare determined instantaneously.

The on-time calculations of Sa, Sb, and Sc directly depend on the instantaneous values of the inverter line-to-ground voltages. It is well known that the reference values of Vag, Vbg, and Vcg are normally given by

$$\begin{bmatrix} V_{ag\_ref} \\ V_{bg\_ref} \\ V_{cg\_ref} \end{bmatrix} = \frac{M_a * 4V_{dc}}{2} * \begin{bmatrix} \cos(wt) \\ \cos\left(wt - \frac{2\pi}{3}\right) \\ \cos\left(wt + \frac{2\pi}{3}\right) \end{bmatrix} + \frac{4V_{dc}}{2} * \begin{bmatrix} 1 \\ 1 \\ 1 \end{bmatrix}$$ (6)

Where wt is the electrical angle. Or

$$\begin{bmatrix} V_{ag\_ref} \\ V_{bg\_ref} \\ V_{cg\_ref} \end{bmatrix} = \frac{M_a * 4V_{dc}}{2} * \begin{bmatrix} \cos(wt) \\ \cos\left(wt - \frac{2\pi}{3}\right) \\ \cos\left(wt + \frac{2\pi}{3}\right) \end{bmatrix} + \frac{4V_{dc}}{2} * \left[1 - \frac{M_a}{6}\cos(3wt)\right] * \begin{bmatrix} 1 \\ 1 \\ 1 \end{bmatrix}$$ (7)

From (10), it can be noticed that the third harmonic component is added to the three-line-to-ground voltages. The third harmonic injection may increase the inverter fundamental voltage without causing over modulation. As a result, M_a can reach to 1.15 and Sa, Sb, and Sc can be simply determined by integerzing the reference line-to-ground voltages as

$$\begin{bmatrix} Sa \\ Sb \\ Sc \end{bmatrix} = \text{integer}\left(\frac{N-1}{4V_{dc}} * \begin{bmatrix} V_{ag\_ref} \\ V_{bg\_ref} \\ V_{cg\_ref} \end{bmatrix}\right)$$ (8)

Comparison of the proposed modulation method with the staircase modulation with the selective harmonic method shows that the proposed modulation features less time and needs simple calculations.

Table III
Switching State Sa1 and Inverter Line-To-Ground Voltage Vag at Ma <0.9 (Leg A)

Sa1	Q1	S1	S2	Q2	T1	T2	T3	T4	Vag
2	on	off	off	off	off	on	on	off	+4Vdc
1	off	on	on	off	off	on	on	off	+2Vdc
0	off	off	off	on	off	on	on	off	0

Since the proposed inverter has been designed to achieve five voltage levels, the modulation index must be within range 0.9≤Ma ≤1.15. For modulation index Ma <0.9, only two dc voltage supplies 4Vdcand 2Vdcare utilized and the behavior of the proposed inverter becomes similar to the three-level multilevel inverter. Using (9)–(11) and substituting N=3, the inverter's operating switching states Sa, Sb, and Sc at Ma<0.9 can be defined. The operation principle of the proposed inverter at Ma<0.9 is illustrated in Table III.

V.INDUCTION MOTOR

Induction Motor (1M) An induction motor is an example of asynchronous AC machine, which consists of a stator and a rotor. This motor is widely used because of its strong features and reasonable cost. A sinusoidal voltage is applied to the stator, in the induction motor, which results in an induced electromagnetic field. A current in the rotor is induced due to this field, which creates another field that tries to align with the stator field, causing the rotor to spin. A slip is created between these fields, when a load is applied to the motor.

Compared to the synchronous speed, the rotor speed decreases, at higher slip values. The frequency of the stator voltage controls the synchronous speed [12]. The frequency of the voltage is applied to the stator through power electronic devices, which allows the control of the speed of the motor. The research is using techniques, which implement a constant voltage to frequency ratio. Finally, the torque begins to fall when the motor reaches the synchronous speed. Thus, induction motor synchronous speed is defined by following equation,

$$n_s = \frac{120f}{p}$$

Where f is the frequency of AC supply, n, is the speed of rotor; p is the number of poles per phase of the motor. By varying the frequency of control circuit through AC supply, the rotor speed will change.
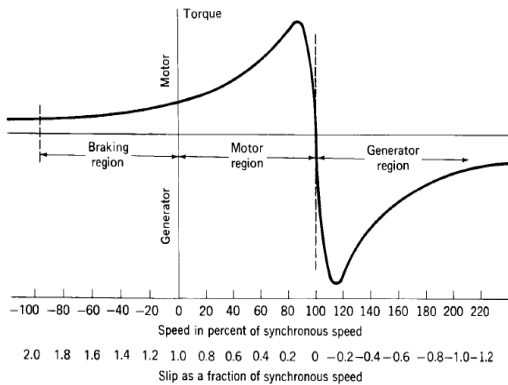
Fig.2.Speed torque characteristics of induction motor

V. MATLAB/SIMULINK RESULTS
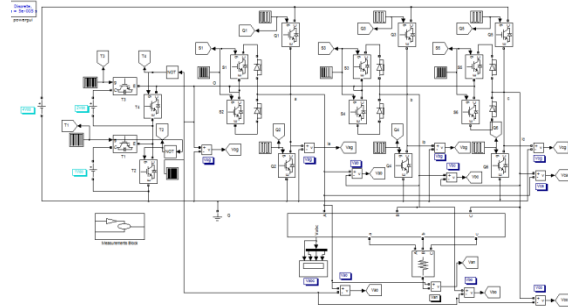
Fig .3.Simulink model of the proposed three-phase five-level multilevelinverter.
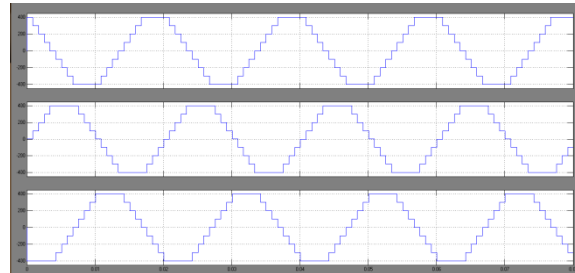
Fig .4. Simulation output Vab,Vbc and Vca of proposed five level inverter.
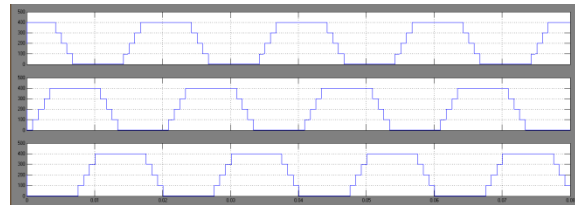
Fig .5. Simulation output Vag,Vbg and Vcg of proposed five level inverter.
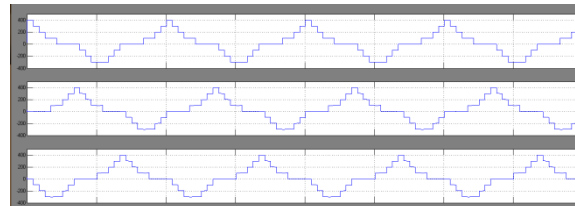
Fig .6. Simulation output Vao,Vbo and Vco of proposed five level inverter.
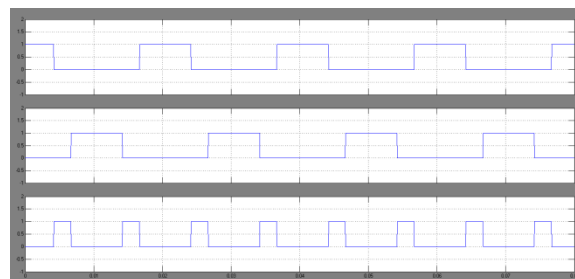
Fig .7. Simulated output wave forms of Q1, Q2 and S1.

215
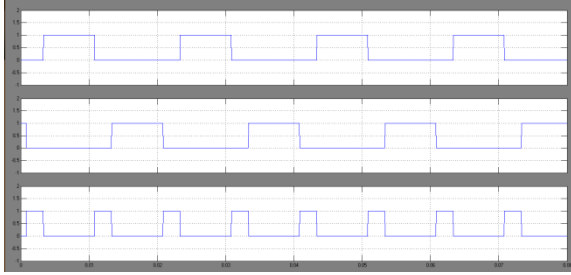
Fig .8. Simulated output wave forms of Q3, Q4 and S3.
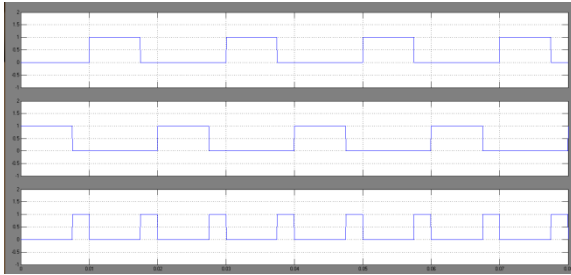
Fig .9.Simulated output wave forms of Q5, Q6 and S5.
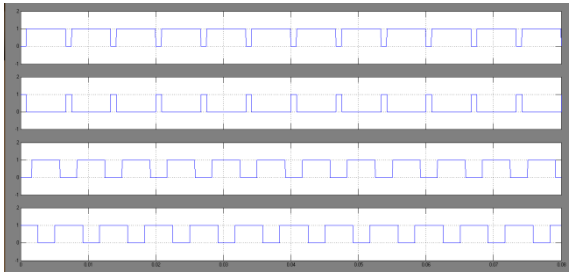
Fig .10. Simulated output wave forms of T1, T2, T3 and T4.
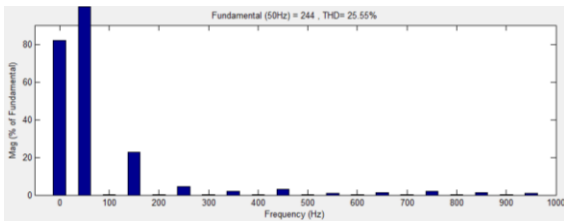
Fig .11. Total Harmonic Distortion of 5 level phase voltage shows 25.55%.
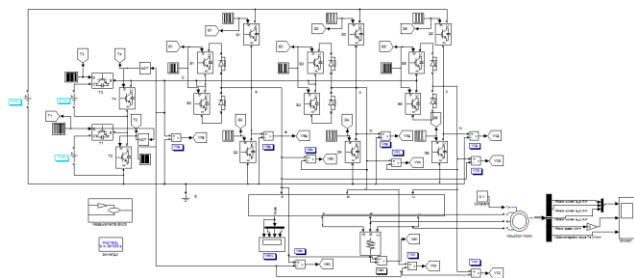
Fig .12. Simulink model of the proposed three-phase five-level multilevel inverter with induction motor
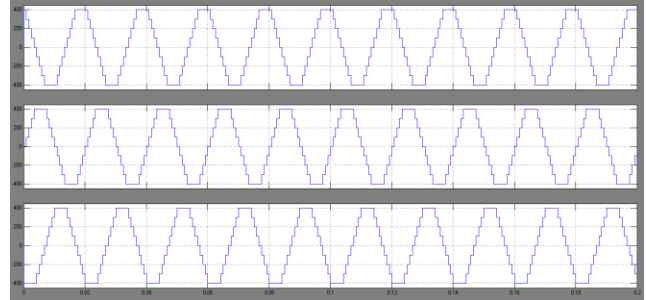
Fig.13.Simulation result for three phase voltages
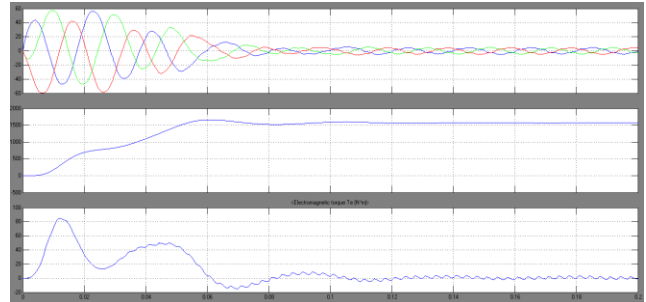
Fig.14.Simulation result for stator currents, speed and electromagnetic torque of induction motor

VI. CONCLUSION

A new topology of the three-phase seven-level multilevel inverter was introduced. The suggested configuration was obtained from reduced number of power electronic components. Therefore, the proposed topology results in reduction of installation area and cost. The fundamental frequency staircase modulation technique was comfortably employed and showed high flexibility and simplicity in control. Moreover, the proposed configuration was extended to N-level with different methods. Furthermore, the method employed to determine the magnitudes of the dc voltage supplies was well executed. In order to verify the performance of the proposed multilevel inverter, the proposed configuration was simulated and its prototype was manufactured. The obtained simulation results met the desired output. Hence, subsequent work in the future may include an extension to higher level with other suggested methods. For purpose of minimizing THD%, a selective harmonic elimination pulse width modulation technique can be also implemented.

REFERENCES

[1] J. A. Ferreira, "The multilevel modular DC converter,"IEEE Trans. Power Electron., vol. 28, no. 10, pp. 4460–4465, Oct. 2013.
[2] K. Ilves et al., "A new modulation method for the modular multilevel converter allowing fundamental switching frequency,"IEEE Trans. Power Electron., vol. 27, no. 8, pp. 3482–3494, Aug. 2012.
[3] W. Yong and W. Fei, "Novel three-phase three-level-stacked neutral point clamped grid-tied solar inverter with a split phase controller,"IEEE Trans. Power Electron., vol. 28, no. 6, pp. 2856–2866, Jun. 2013.

216

[4] Y. Yuanmao and K. W. E. Cheng, "A family of single-stage switchedcapacitor-inductor PWM converters," IEEE Trans. Power Electron., vol. 28, no. 11, pp. 5196–5205, Nov. 2013.

[5] N. A. Rahim et al., "Transistor-clamped H-bridge based cascaded multilevel inverter with new method of capacitor voltage balancing," IEEE Trans. Ind. Electron., vol. 60, no. 8, pp. 2943–2956, Aug. 2013.

[6] I. Abdalla et al., "Multilevel DC-link inverter and control algorithm to overcome the PV partial shading,"IEEE Trans. Power Electron., vol. 28, no. 1, pp. 14–18, Jan. 2013.

[7] Z. Li et al., "A family of neutral point clamped full-bridge topologies for transformerless photovoltaic grid-tied inverters,"IEEE Trans. Power Electron., vol. 28, no. 2, pp. 730–739, Feb. 2013.

[8] L. Zixin et al., "A novel single-phase five-level inverter with coupled inductors," IEEE Trans. Power Electron., vol. 27, no. 6, pp. 2716–2725, Jun. 2012.

[9] S. Mariethoz, "Systematic design of high-performance hybrid cascaded multilevel inverters with active voltage balance and minimum switching losses,"IEEE Trans. Power Electron., vol. 28, no. 7, pp. 3100–3113, Jul. 2013.[10] H. Belkamel, S. Mekhilef, A. Masaoud, and M. Abdel Naiem, "Novel three phase asymmetrical cascaded multilevel voltage source inverter," IET Power Electron., vol. 6, pp. 1696–1706, 2013.

[11] J. Meiet al., "Modular multilevel inverter with new modulation method and its application to photovoltaic grid-connected generator,"IEEE Trans. Power Electron., vol. 28, no. 11, pp. 5063–5073, Nov. 2013.

[12] S. Mekhilefet al., "Digital control of three phase three-stage hybrid multilevel inverter," IEEE Trans. Ind. Electron., vol. 9, no. 2, pp. 719–727, May 2013.

[13] J. Mathewet al., "A hybrid multilevel inverter system based on dodecagonal space vectors for medium voltage IM drives,"IEEE Trans. Power Electron., vol. 28, no. 8, pp. 3723–3732, Aug. 2013.

[14] M. Saeedifardet al., "Operation and control of a hybrid seven-level converter,"IEEE Trans. Power Electron., vol. 27, no. 2, pp. 652–660, Feb. 2012.

[15] S. Mekhilef and A. Masaoud, "Xilinx FPGA based multilevel PWM single phase inverter," inProc. IEEE Int. Conf. Ind. Technol., 2006, pp. 259–264.

[16] E. A. Mahrous and S. Mekhilef, "Design and implementation of a multi level three-phase inverter with less switches and low output voltage distortion,"J. Power Electron., vol. 9, pp. 593–603, 2009.

[17] H. W. Ping, N. A. Rahim, and J. Jamaludin, "New three-phase multilevel inverter with shared power switches,"J. Power Electron., vol. 13, pp. 787– 797, 2013.

[18] S. Suroso and T. Noguchi, "Multilevel current waveform generation using inductor cells and H-bridge current-source inverter," IEEE Trans. Power Electron., vol. 27, no. 3, pp. 1090–1098, Mar. 2012.

[19] M. F. Kangarlu and E. Babaei, "A generalized cascaded multilevel inverter using series connection of submultilevelinverters,"IEEE Trans. Power Electron., vol. 28, no. 2, pp. 625–636, Feb. 2013.

Cluster Analysis of Medical Research Data using R

By Lavanya Pamulaparty, Dr. C.V Guru Rao & Dr. M. Sreenivasa Rao

JNT University, India

Abstract- Cluster analysis divides the data into groups that are meaningful, useful or both. It is also used as a starting point for other purposes of data summarization. This paper discuss some very basic algorithms like K-means, Fuzzy C-means, Hierarchical clustering to come up with clusters, and use R data mining tool. The results are tested on the datasets namely Online News Popularity, Iris Data Set and from UCI data repository and mi RNA dataset for medical data analysis. All datasets was analyzed with different clustering algorithms and the figures we are showing is the working of them in R data mining tool. Every algorithm has its uniqueness and antithetical behavior.

Keywords: *k-means algorithm, fuzzy c-means algorithm, hierarchical clustering algorithm, r tool.*

GJCST-C Classification : *H.3.3 I.5.3*

CLUSTERANALYSISOFMEDICALRESEARCHDATAUSINGR

Strictly as per the compliance and regulations of:

Cluster Analysis of Medical Research Data using R

Lavanya Pamulaparty [α], Dr. C.V Guru Rao [σ] & Dr. M. Sreenivasa Rao [ρ]

Abstract- Cluster analysis divides the data into groups that are meaningful, useful or both. It is also used as a starting point for other purposes of data summarization. This paper discuss some very basic algorithms like K-means, Fuzzy C-means, Hierarchical clustering to come up with clusters, and use R data mining tool. The results are tested on the datasets namely Online News Popularity, Iris Data Set and from UCI data repository and mi RNA dataset for medical data analysis. All datasets was analyzed with different clustering algorithms and the figures we are showing is the working of them in R data mining tool. Every algorithm has its uniqueness and antithetical behavior.

Keywords: k-means algorithm, fuzzy c-means algorithm, hierarchical clustering algorithm, R tool.

I. Introduction

Cluster analysis divides data into meaning full groups (clusters) which share common characteristics i.e. same cluster are similar to each other than those in other clusters. It is the study of automatically finding classes. A web page especially news articles which are flooded in the internet have to be grouped. The clustering of these different groups is a step forward towards the automation process, which requires many fields, including web search engines, web robots and data analysis.

Any new web page goes through numerous phases including data acquisition, preprocessing, Feature extraction, classification and post processing into the database. Cluster analysis can be regarded as a form of the classification which creates a labeling of objects with class labels. However it derives these labels only from the data. Data mining functionalities are the Characterization and discrimination, mining frequent patterns, association, correlation, classification and prediction, cluster analysis, outlier analysis and evolution analysis [1].

Clustering is a vivid method. The solution is not exclusive and it firmly depends upon the analysts' choices. Clustering always provides groups or clusters, even if there is no predefined structure. While applying cluster analysis we are contemplating that the groups exist. But this speculation may be false. The outcome of clustering should never be generalized. [9].

Author α : Department of CSE, Methodist college of Engg. & Tech., OU, Hyderabad. e-mail: lavanya.post@gmail.com
Author σ : Department of CSE, S R Engineering College, JNT University, Warangal.
Author ρ : Department of CSE, School of IT, JNT University, Hyderabad.

II. R Tool

R is a free software environment for statistical computing and graphics. It compiles and runs on a wide variety of UNIX platforms, Windows and Mac OS [12]

R is public domain software primarily used for statistical analysis and graphic techniques [10]. A core set of packages is included with the installation of R, with more than 7,801 additional packages (as of January 2016[update]) available at the Comprehensive R Archive Network (CRAN), Bio conductor, Omegahat, Git Hub, and other repositories.[14] R tool provides a wide class of statistical that includes classical statistical tests, linear and nonlinear modeling, classification, time-series analysis, clustering and various graphical functions.[13]

R uses collections of packages to perform different functions [11]. CRAN project views provide numerous packages to different users according to their taste. R package contain different functions for data mining approaches. This paper compares various clustering algorithms on datasets using R which will be useful for researchers working on medical data and biological data as well. For this IDE, R Studio is used refer the below Figure 1.
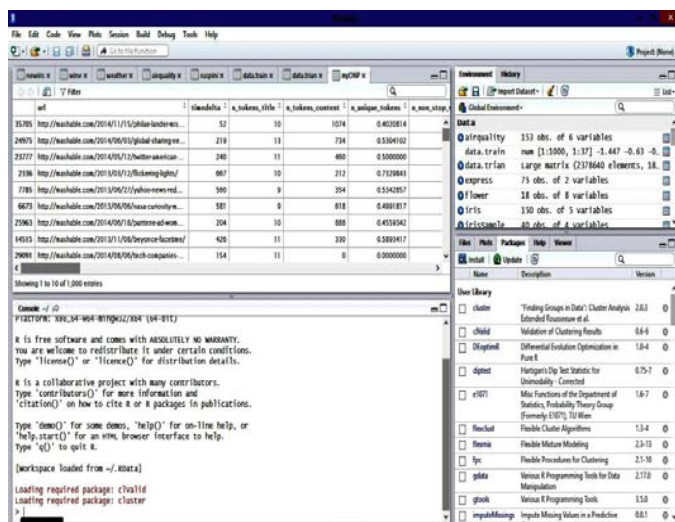
Fig 1: R tool Studio

III. Clustering Algorithms

a) K-Means

The term "k-means" was first used by James Macqueen in 1967 [2], though the idea goes back to

1957 [4]. The K-means algorithm is the most commonly used and simplest method among all partitional clustering algorithms. As Harington and Wong1979 mentioned it is an iterative method which minimizes the sum of the squares for a given number of Clusters.

Here's how the algorithm works [5]:
1. Select k points as initial centroids.
2. Repeat
3. From K clusters by assigning each point to its closest centroid.
4. Recompute the centroid of each cluster.
5. Until centroids do not change.

K-Means reaches a state in which no points are shifting from one cluster to another e.g. repeating until only 1% of the points change clusters.

For measuring the quality of the clustering we measure Sum of the squared error (SSE) or scatter.

$$SSE = \sum_{i=1}^{k} \sum_{x \in c_i} dist(c_i, x)^2$$

Where dist is standard Euclidean distance between two objects in Euclidean space. The centroid (mean) of the ith cluster that minimizes the SSE is defined as

$$\sum_{i=1}^{k} \sum_{x \in c_i} dist(c_i, x)^2$$

The advantage of this method is highly scalable of the huge sum of data sets with $O(n * k * r)$ where r is the number of rounds, where n represent number of data items, k represent numbers of clusters [14]. It has user defined constant K and Runtime is totally dependent on the initial pick of centroids.

b) K-Means Implementation using R

For this analysis we have considered Online News Popularity datasets which consists of articles published by Mash able (www.mashable.com) [4]. Instances are 39797 and Number of Attributes is 61. As the results of the k means are undeterministic, we have followed the practice of running multiple rounds of k means so performed on various k values as k=3, k=5 and k=10. The best iteration is one who minimizes the average distance of each point to its assigned centroid.
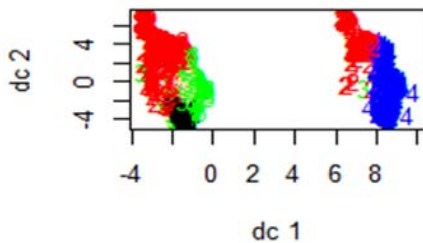
Fig 2 : K means plot with k=5

The Figure 2 shows the results of clustering the Online News Popularity datasets with 39645 number of News articles URL's. The above results show that there is overlapping of clusters. So preprocessing is required

to address this problem and omit the NA values also. Then the following is the code after data cleaning [15].

```
>onpdat<-     kmeans    (myONP  [,    c
("n_tokens_title","n_tokens_content")],    centers=5,
nstart=10)
> Onpdata
```

K-means clustering with 5 clusters of sizes 15, 67, 195, 319, and 404

Cluster means:
```
  n_tokens_title n_tokens_content
1     11.46667      2648.9333
2     10.29851      1469.2985
3     10.41026       897.5897
4     10.50470       492.4044
5     10.28713       211.3886
```

Clustering vector:
```
35705 24975 23777  2336  7785  6673 25963 14515
29091 18807 27116 37480 14360 29375 35316  8015
24621  4744 10096 14587
    3    3    4    5    4    4    3    5    5    5    5    4    5
3    5    4    4    5    4    3
  506 14445 32852 12857 18210 22647 18642  7034
31249 25246 29996  4077 27331 15531 31001 24434
29564 20883 20002 29804
    3    4    4    4    5    3    4    5    5    5    3    5    4
3    5    5    5    5    2    5
  881 18018 27648 26153 18032 32512 16539  9241
2668  3755 11938 19576 24987 15355 34454 11081
17326 12545 24563  9737
    4    2    4    3    5    3    3    5    5    2    5    5    5
4    5    5    4    5    3    1
```

Within cluster sum of squares by cluster:
```
[1] 3437391 3417672 3385646 3069653 3279165
 (between_SS / total_SS =  92.1 %)
```

Available components
```
[1] "cluster"      "centers"      "totss"        "withinss"
"tot.withinss" "betweenss"    "size"
[8] "iter"         "ifault"
> summary(onpdata)
 Length   Class   Mode
cluster     1000   -none- numeric
centers       10   -none- numeric
totss          1    -none- numeric
withinss       5    -none- numeric
tot.withinss   1   -none- numeric
betweenss      1   -none- numeric
size           5    -none- numeric
iter           1    -none- numeric
ifault         1    -none- numeric
library(MASS)
> parcoord(data.train,onpdata$cluster)
>confuseTable.km<-
table(myONP$n_tokens_title,onpdata$cluster)
> confuseTable.km

    1 2 3 4 5
  3  0 0 0 0 1
```

```
5   0  0  0  1  2
6   0  1  1  8 13
7   1  8 10  7 26
8   1  4 29 34 44
9   2 12 25 48 53
10  2 12 39 67 81
11  1 10 35 55 77
12  2  7 22 53 50
13  4  9 24 24 19
14  1  3  7 12 25
15  0  1  2  6  9
16  0  0  0  4  3
17  0  0  0  0  1
18  1  0  1  0  0
> library(flexclust)
> randIndex(confuseTable.km)
    ARI
0.002285344
```

The results are showing the information about cluster means, clustering vector, sum of square by cluster and available components. The fpc package is used to draw the discriminant projection plot using Plotcluster function (Fig3).

The result of plotting the class returned by function application is shown below.
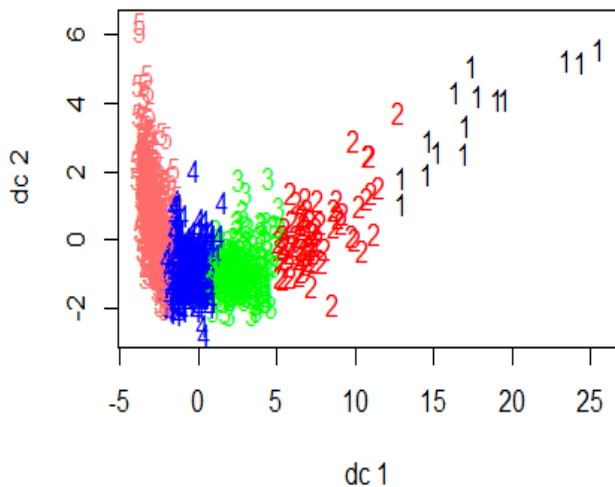
Fig. 3 : Preprocessed K-means plot k=5
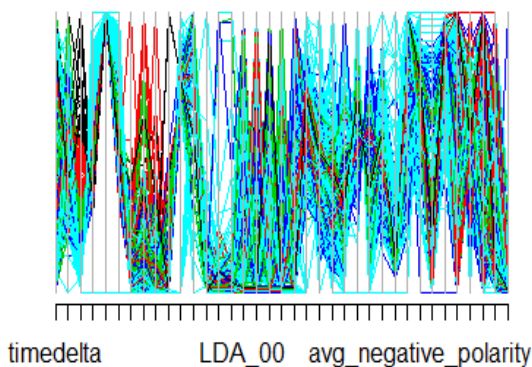
Fig 4 : Parallel coordinators plot

The Figure 4 shows the parallel coordinators plot to see the variables contributed in each cluster.

c) Fuzzy C-Means

Fuzzy c means clustering (FCM), each data point has a fraction of membership to each cluster. This algorithm works iteratively until no further clustering is possible. The membership fraction that minimizes the expected distance to each centroid has to be calculated.

$$J_m = \sum_{i=1}^{N} \sum_{j=1}^{c} u_{ij}^m \left\| x_i - c_j \right\|^2$$

The algorithm is very similar to K-Means, except that a matrix (row is each data point, column is each centroid, and each cell is the degree of membership) is used.

1. Initialize the membership matrix U
2. Repeat step (3), (4) until converge
3. Compute location of each centroid based on the weighted fraction of its member data point's location.

$$c_j = \frac{\sum_{i=1}^{N} u_{ij}^m \cdot x_i}{\sum_{i=1}^{N} u_{ij}^m}$$

4. Update each cell as follows

$$u_{ij} = \frac{1}{\sum_{k=1}^{c} \left(\frac{\left\| x_i - c_j \right\|}{\left\| x_i - c_k \right\|} \right)^{\frac{2}{m-1}}}$$

Notice that the parameter m is the degree of fuzziness. The output is the matrix with each data point assigned a degree of membership to each centroids.

d) Fuzzy C-Means Implementation Using R

The data repositories used in this paper are The Iris Repository [27]. They are obtained from (http://kdd.ics.uci.edu/). The data set is the fragments of iris flower which is clustered based on the degree assigned by a membership.

The following is the code
```
> library(e1071)
> result <- cmeans(iris[,-5], 3, 100, m=2, method="cmeans")
> plot(iris[,1], iris[,2], col=result$cluster)
> points(result$centers[,c(1,2)], col=1:3, pch=8, cex=2)
```

```
> result$membership[1:3,]
        1            2            3
[1,] 0.001072018 0.002304389 0.9966236
[2,] 0.007498458 0.016651044 0.9758505
[3,] 0.006414909 0.013760502 0.9798246
> table(iris$Species, result$cluster)

            1  2  3
setosa      0  0 50
versicolor  3 47  0
virginica  37 13  0
```
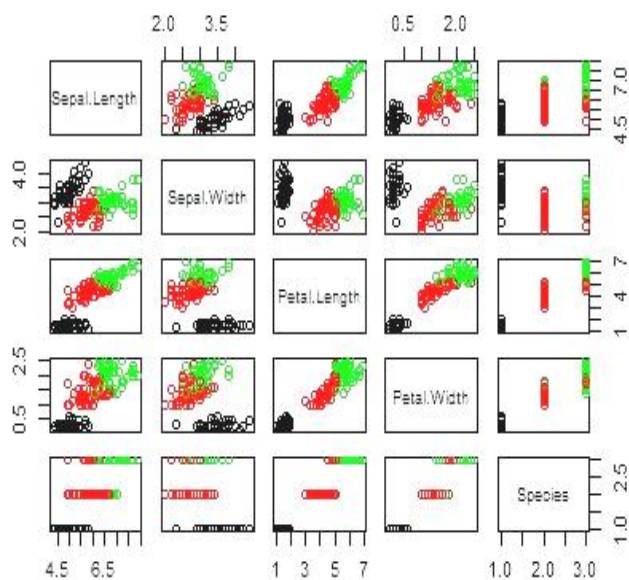

Fig. 5 : Fuzzy C means clustering plot

The observation of the above results and of the Online News Popularity datasets are FCM is mainly dependent on the initial clustering and the computation time is very high for the large data sets. The weight and accuracy are inversely proportional. It is Sensible to noise and membership degree for outliers or noisy points is very low.

e) Hierarchical Clustering

Hierarchical Clustering a series of partitions takes place, which may run from a single cluster containing all objects to n clusters each containing a single object. This clustering builds a cluster hierarchy or, in other words, a tree of clusters, also known as a dendrogram [7]. Hierarchical algorithms can be further categorized into two kinds [3]

i. *Agglomerative clustering*: This clustering starts with *n* clusters and iteratively merges the number of clusters which are most similar objects or clusters, respectively, until only one cluster is remaining (*n* → 1).This requires the defining of closest proximity.

ii. *Divisive clustering:* This clustering starts with one cluster and iteratively splits a cluster until

singleton clusters of individual points remain, so that the heterogeneity is reduced as far as possible (1 → *n*).This requires the decision of splitting at each step.

The Hierarchical Clustering algorithm [6] below takes an n×n distance matrix d input and increasingly gives n different partitions of the data as the tree it outputs result. The largest partition has n single-element clusters, with every element forming its own cluster. The second-largest partition aggregates the two closest clusters from the largest partition, and thus has n−1 clusters. In general, the ith partition combines the two closest clusters from the (i − 1)th partition and has (n − i + 1) clusters. Because of the additional complexity of keeping data in a sorted list or heap, so the time required is $O(m^2 \log m)$ and Space required is $O(m^2)$.
In this approach, it compares all pairs of data points and merges the one with the closest distance.

Algorithm

1: Compute the proximity matrix if necessary
2: repeat
3: Merge the closest two clusters.
4: Update the proximity matrix to reflect the proximity between the new cluster and initial cluster
5: Until only one cluster remains.

The Proximity (C_i,Cj) of clusters C_i and C_j, which are of the size m_i and m_j,respectively is expressed as

$$Proximity\ (c_i, c_j)\ =\ \frac{\sum_{\substack{x \in c_i \\ y \in c_j}} Proximity\ (x,y)}{m_i * m_j}$$

The data set considered is micro RNA expressions. It is actually collected from Fresh paired tumor and control samples from the PAC (Periampullary Carcinoma) patients undergoing Whipple's pan creaticoduodenectomys Data Mining in Health Informatics[15] is an emerging discipline, concerned with developing methods for exploring the unique type of data that come from Health Care database management system. We have also considered the Iris dataset. The code for the implementation is given as follows [16] Figure 6 shows the results of clustering.

Cluster Dendrogram

dist(irisSample)
hclust (*, "average")
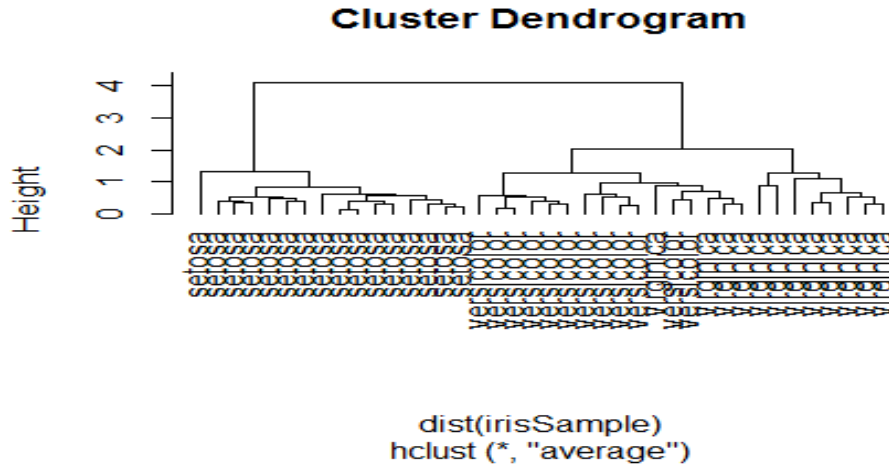
Fig. 6 : Hierarchical Clustering

The Authors [14] have also performed hierarchical clustering on PAC tumors dataset which are distinct from counterpart normal pancreas, normal duodenum, and normal distal CBD and normal ampulla. Unsupervised hierarchical cluster analysis of miRNA Expression profiles were clustered of PAC tumors into pancreatobiliary (n ¼ 23) and intestinal subtypes (n ¼ 17), while normal pancreas (n ¼ 22), normal duodenum (n ¼ 6), normal distal CBD (n ¼ 6) normal ampulla (n ¼ 6) are clustered as different entities (Figure 7).
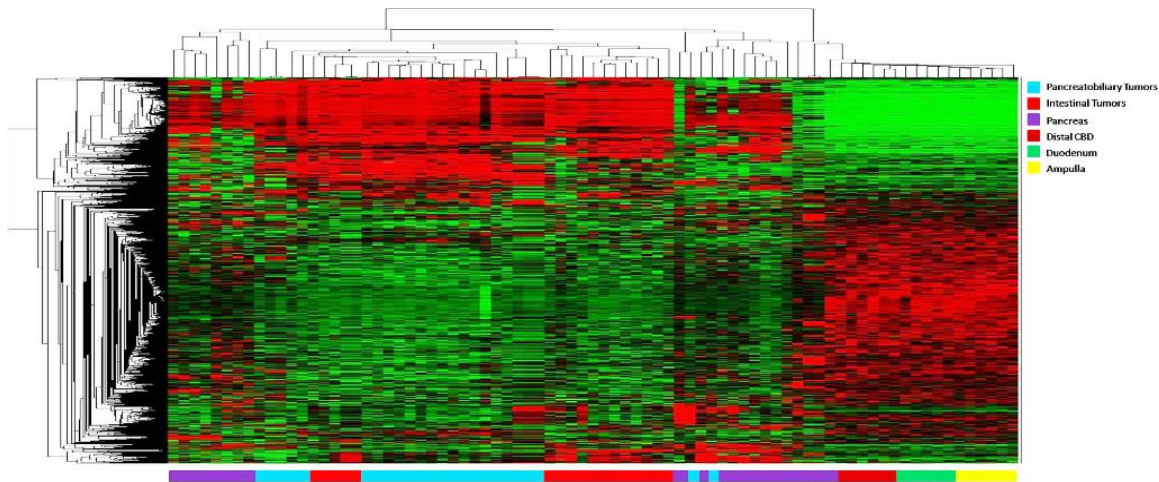
Fig. 7 : The microRNA expression profiles of PAC

IV. CONCLUSION

We have perceived a comprehensive scan of the k-means, Fuzzy C means and Hierarchical clustering methods using medical research datasets and iris dataset. Using R clustering, Statistical Computing and graphics are represented. All the clustering techniques show ambiguity in clustering noisy data and outliers. The Hierarchical clustering shows good results for small data sets and Fuzzy C means for the voluminous amount of data. K means technique has faster performance but finding the appropriate k value is a big challenge especially in medical research data sets. In continuation to this work we would like to improve clustering analysis by considering the time and accuracy for large data sets using R tool statistics.

V. ACKNOWLEDGEMENTS

REFERENCES RÉFÉRENCES REFERENCIAS

1. Han J. and Kamber M.: "Data Mining: Concepts and Techniques," Morgan Kaufmann Publishers, San Francisco, 2000.
2. Pang-Ning Tan, Michael Steinbach and Vipin Kumar. Introduction to Data Mining. Addison Wesley; US edition. May 12, 2005. (HC)
3. Data Mining with R: learning by case studies Luis Torgo(kmeans)

4. K. Fernandes, P. Vinagre and P. Cortez. A Proactive Intelligent Decision Support System for Predicting the Popularity of Online News. Proceedings of the 17th EPIA 2015 - Portuguese Conference on Artificial Intelligence, September, Coimbra, Portugal.

5. Jiawei Han and Micheline Kamber, "Data Mining: Concepts and Techniques", Morgan Kaufmann Publishers, second Edition, (2006).

6. Doug Fisher, Optimization and Simplification of Hierarchical Clustering, KDD(HC)

7. Manish Verma, Mauly Srivastava, Neha Chack, Atul Kumar Diswar and Nidhi Gupta, "A Comparative Study of Various Clustering Algorithms in Data Mining", International Journal of Engineering Research and Applications (IJERA) Vol. 2, Issue 3, May-Jun 2012, pp.1379-1384

8. Frank, A. & Asuncion, A. UCI Machine Learning Repository (http:/ / archive. ics. uci. edu/ ml). Irvine, CA: University of California, School of Information and Computer Science 2010.

9. B¨OHM, C., KAILING, K., KRIEGEL, H.-P., AND KR¨OGER, P. 2004. Density connected clustering with local subspace preferences. In Proceedings of the 4th International Conference on Data Mining (ICDM).

10. Robert Gentleman Rafael A. Irizarry Vincent J. Carey Sandrine Dudoit Wolfgang Huber Editors Bioinformatics and Computational Biology Solutions Using R and Bioconductor, Springer

11. R and Data Mining: Examples and Case Studies 1 Yanchang Zhao

12. https://www.r-project.org/

13. Satish Kumar et al Analysis Clustering Techniques in Biological Data with R, International Journal of Computer Science and Information Technologies (IJCSIT), Vol. 6 (2) , 2015

14. KSS Uma Mahes, Kuruva MM , Mitnala S, Rupjyoti T, Venkat RG, Botlagunta S et al. MicroRNA profiling in periampullary carcinoma. Pancreatology 2014; 14: 36-47

15. Abdul Nazeer, K. A., Sebastian M. P., and. Madhu Kumar S.D., 2011 A Heuristic k-Means Algorithm with Better Accuracy and Efficiency for Clustering Health Informatics Data, Journal of Medical Imaging and Health Informatics(American Scientific Publisher) Vol. 1, 66–71.

The Journal
of CPRI

CENTRAL POWER RESEARCH INSTITUTE

CONTENTS

Investigation of UPQC for Power Quality Distortions in DFIG based Wind Farms

Y. Mastanamma (http://cprijournal.in/index.php/prj/search/authors/view?
firstName=Y.&middleName=&lastName=Mastanamma&affiliation=Associate Professor/HOD EEE
Department&country=) [1*], Bhoj Reddy (http://cprijournal.in/index.php/prj/search/authors/view?
firstName=Bhoj&middleName=&lastName=Reddy&affiliation=Engineering College for Women, Saidabad,
Hyderabad -59, Telangana&country=IN) [2]

Affiliations

1. Associate Professor/HOD EEE Department
2. Engineering College for Women, Saidabad, Hyderabad -59, Telangana, India

Abstract

This paper presents a new Synchronous-Reference Frame (SRF)-based control method to compensate Power-Quality (PQ) problems through a three-phase four-wire Unified PQ Conditioner (UPQC) under unbalanced and distorted load conditions for DFIG based wind farm. The proposed UPQC system can improve the power quality at the point of common coupling on power distribution systems under unbalanced and distorted load conditions. The simulation results based on Matlab/Simulink are discussed in detail to support the SRF-based control method presented in this paper.

Keywords

Active Power Filter (APF), harmonics, Phase Locked Loop (PLL), Power Quality (PQ), Synchronous Reference Frame (SRF), Unified Power-Quality (PQ) Conditioner (UPQC), Doubly Fed Induction Generator (DFIG)

Refbacks

There are currently no refbacks.

Exhaust Gas Emission Analysis for Variable Injection Pressure 1-Cylender Engine for 2 Different Feedstock Biodiesel Blended in Diesel

Md.Fakhruddin H.N.
Department of Mechanical Engineering
Methodist College of Engineering & Technology, Hyderabad, Telangana State, India

Dr.Manzoor Hussain
Professor & Principal
JNTUH College of Engineering Sultanpur, Hyderabad, Telangana State, India

Mohammed Adnan Ahmed
Department of Mechanical Engineering
Methodist College of Engineering & Technology, Hyderabad, Telangana State, India

Abstract– The energy strategy of a country aims at efficiency and security and to provide access which being environment friendly and achievement of an optimum mix of primary resources for energy generation. Fossil fuels will continue to play a dominant role in the energy scenario in our country in the next few decades. However, conventional or fossil fuel resources are limited, non-renewable, polluting and, therefore, need to be used prudently. On the other hand, renewable energy resources are indigenous, non-polluting and virtually inexhaustible. India is endowed with abundant renewable energy resources. Therefore, their use should be encouraged in every possible way. The crude oil price has been fluctuating in the world market and has increased significantly in the recent past, reaching a level of more than $ 140 per barrel. Such unforeseen escalation of crude oil prices is severely straining various economies the world over, particularly those of the developing countries. India's energy security would remain vulnerable until alternative fuels to substitute/supplement petro-based fuels are developed based on indigenously produced renewable feedstocks. In biofuels, the country has a ray of hope in providing energy security. Biofuels are environment friendly fuels and their utilization would address global concerns about containment of carbon emissions. The transportation sector has been identified as a major polluting sector. Use of biofuels have, therefore, becomes compelling in view of the tightening automotive vehicle emission standards to curb air pollution. For the very existence of internal combustion engine in the wide spread as they do now, it is renewable, sustainable and alternative fuel i.e. biodiesel instead of diesel has been increasingly fuelled to study its effects on engine performances and emissions in the recent two decades. In the present work, the performance and emissions of diesel and diesel blended with waste vegetable oil (cooking oil) plus palm staerin is studied, where the fuel, namely, waste vegetable oil biodiesel with palm staerin and diesel were chosen and used as fuel in the form of blends. This work presents the experimental investigation carried on computerized four stroke single cylinder diesel engine with variable compression ratio and variable injection pressure for diesel-(wco + ps)biodiesel blends.

Keywords – Feedstocks, WCOBD, PSBD, emissions, blends, injection pressure etc.

I. INTRODUCTION

Bio-diesel is not your regular vegetable oil and is not safe to swallow. However, biodiesel is considered biodegradable, so it is considered to be much less harmful to the environment if spilled. Biodiesel also has been shown to produce lower tailpipe emissions than regular fuel. The best thing about biodiesel is that it is made from plants and animals, which are renewable resources. The depletion of world petroleum sources and increased environmental concerns has stimulated recent interest in alternative sources for petroleum based fuels. Biodiesel produced from vegetable oil or animal fats by transesterification with alcohol like methanol and ethanol is recommended for use as a substitute for petroleum-based diesel mainly because biodiesel is an oxygenated, renewable, biodegradable and environmentally friendly bio-fuel with similar flow performance and low emission profile. The used cooking oil has been classified as waste, while its potential as a liquid fuel through physical and chemical conversion remains highly interesting. It is increasingly attracting much interest because of its great potential to be used as a diesel substitute known as biodiesel. Direct process via transesterification of cooking oils

will give biodiesel. One of the advantages of these fuels is reduced exhaust gas emissions. Experience has shown that vegetable oil based fuels can significantly reduce exhaust gas emissions, including carbon monoxide (CO), carbon dioxide (CO2), and particulate matter (PM). Because of their less concentration of sulfur, the sulfur dioxide greases cannot only reduce the burden of the government in disposing the waste, maintaining public sewers and treating the oily wastewater, but also helps in lowering the production cost of biodiesel significantly. Furthermore, biodiesel fuel has been shown to be successfully produced from waste cooking oils by an alkali-catalyzed transesterification process and can be considered as alternative fuel in diesel engines and other utilities. There is need to convert waste cooking oil from kitchen waste into biodiesel and transesterification is the most suitable process for this conversion.

The present investigation used the emissions of diesel plus diesel blended with waste vegetable oil diesel also called waste cooking oil biodiesel and palm staerin biobiesel is studied and the best emission of oil blends were identified. The blended form of waste vegetable oil plus palm staerin and diesel does not require any engine modification. Hence, this investigation mainly focused on the emissions of diesel and diesel blended with waste vegetable oil plus palm staerin in the proportionate ratios.

II. WASTE COOKING OIL

Fried food items are very popular in the coastal regions of India. Generally cooking oil used for frying are sunflower oil, palm oil, coconut oil etc. as they are easily available, and especially so of the coconut oil which is abundantly available in south India. It is well known fact that, when oils such as these are heated for an extended time, they undergo oxidation and give rise to oxides. Many of these such as hydro peroxides, peroxides and polymeric substances have shown adverse health/biological effects such as growth retardation, increase in liver and kidney size as well as cellular damage to different organs when fed to laboratory animals [7]. Thus, used cooking oils constitute a waste generated from activities in the food sectors (industries and large catering or community restaurants), which have greatly increased in recent years. Most of the waste (overused /abused) cooking oil are disposed inappropriately, mostly let into the municipal drainage, leading to water pollution. The primary end use of WCO in existence now is to utilize it as a fuel in residential and industrial heating devices. An alternative to prevent inappropriate disposal of WCO is by recycling it. The main use of recycled WCO is in the production of animal feeds and in a much smaller proportion in the manufacture of soaps and biodegradable lubricants. Some health risks can be traced from the use of recycled cooking oils in animal feeding, such as undesirable levels of contaminants, particularly PAHs (Polycyclic aromatic hydrocarbons), PCBs (Polychlorinated biphenyls), dioxins and dioxin related substances [8]. By consumptions of animal origin foodstuffs like milk, meats, poultry and other products, these undesirable contaminants enter the human body and cause serious long term health hazards. As these contaminants are lip soluble, they accumulate in organic lipids and finally in the body, and thereby their concentration increases gradually over the years. In other words, the body is exposed not only to a single acute action, but also to a chronic action of bioaccumulation of these hazardous compounds over the years [8]. Hence utilizing the recycled WCO in any way is not advisable from health standpoint.

III. MATERIALS AND METHODS

Engine Specifications
The test is carried out in an engineering college using a
kirloskar make,
Type 1cylinder,
4 stroke diesel,
Water cooled,
Model tv1,
Stroke 110 mm,
Bore 87.5 mm.
661 cc,
VCR engine CR range 12 to 18
VIP engine IP range 200bar to 250bar
Dynamometer Type eddy current,
Water cooled,
Loading unit Eddy current

Fig.1. Experimental set up

Where,
F1   Fuel consumption
F2   Air consumption
N   Engine speed   rpm
Wt   Loading in   kg
F1   Fuel consumption   kg/hr
F2   Air consumption   kg/hr
F4   Calorimeter water flow   kg/hr
T1   Engine water inlet temperature ^{0}K
T2   Engine water outlet temperature ^{0}K
T3   Calorimeter water inlet temperature ^{0}K
T4   Calorimeter water outlet temperature ^{0}K
T5   Exhaust gas to calorimeter inlet temp. ^{0}K
T6   Exhaust gas from calorimeter outlet temp. ^{0}K

IV. EXPERIMENTATION

A single cylinder, four stroke, air cooled, constant speed direct injection compression ignition with variable injection pressure engine was used in the experimentation. The engine speed was noted using inductive pickup sensor calibrated with digital speed indicator. The mass flow rate of blended fuel is calculated using volumetric basis using a burette and a stop watch. The exhaust gas temperature was measured using a thermocouple attached with digital temperature indicator is employed.

Table1. Composition of fuel mixtures tested

Fuel mixture	Percent diesel (volume)	Percent biodiesel (volume) Feedstock: Waste Cooking Oil	Percent biodiesel (volume) Feedstock: Palm Stearin
1	70	15	15
2	80	10	10
3	90	5	5
4	100	0	0

Note: each fuel mixture is tested for different injection pressure of 200bar, 225bar & 250bar each

Emission analysis was conducted with portable emission analyser DELTA 1600-L. Exhaust gases from the engine was taken directly to the sampling tube. It measures carbon monoxide (CO), carbon dioxide (CO2), hydrocarbons (HC) and nitric oxide (NO). Both heated line and conditioning lines are provide with the instrument. Heated line serves to avoid condensation by ensuring the gas temperature about 200oC and conditioning line maintains the gas temperature bellow 40^0C and the saturation level is correct. The exhaust gas analyzer determines the emissions of CO (carbon monoxides), CO2 (carbon dioxides), HC (hydrocarbons) with means of infrared measurement and O2 (oxygen) and NO (nitrogen oxides) with means of electrochemical sensors. The 5-gas analysis is processed by the integrated microprocessor and described in the display. Table 3 represents specification of emission analyser.

Table2. Specifications of Emission Analyser

Measurement	Measuring Range	Resolution
Oxygen (O2)	0 – 25 % vol	0.01 %
Carbon monoxide (CO)	0 – 15 %	0.01 %
Carbon dioxide (CO2)	0 – 20 %	0.1 %
Carbon hydride (HC)	0 – 20000 ppm n-hexane	1 ppm
Nitrogen monoxide (NO)	0 – 2000 ppm	1 ppm

V. RESULTS AND DISCUSSIONS

A range of fuel mixtures were burned in a systematic study of emission of an IC engine. These mixtures are defined in Table 1 and were tested under three different injection pressures namely 200bar 225bar & 250bar.
 The experimental data were collected and worked upon, leading to the results presented in Figures 2-7. In addition to the fuel mixture, petroleum diesel fuel and biodiesel were burned separately so as to establish engine emission during their combustion processes. For simplicity, only a sample of the results obtained from these experiments have been presented and discussed in this section. This enables the main findings of the study to be identified and explained.
Typical results for the variations of the brake power, carbon monoxide and hydrocarbon emissions during the combustion processes for each of the different mixtures are shown in Figures 2-7.
Carbon Monoxide (CO) Emission
The figure 2 to figure 4 shows the CO emission of blends with various BP. From the plot it is observed that is interesting to note that the engine emits more CO for diesel as compared to biodiesel blends under all loading conditions.
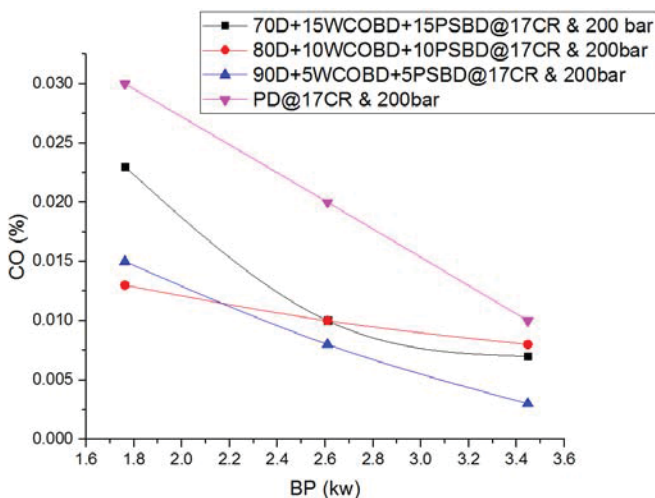
Fig.2. CO % v/s BP(kw) for blends of biodiesel from two different feedstock and diesel @ 200bar injection pressure
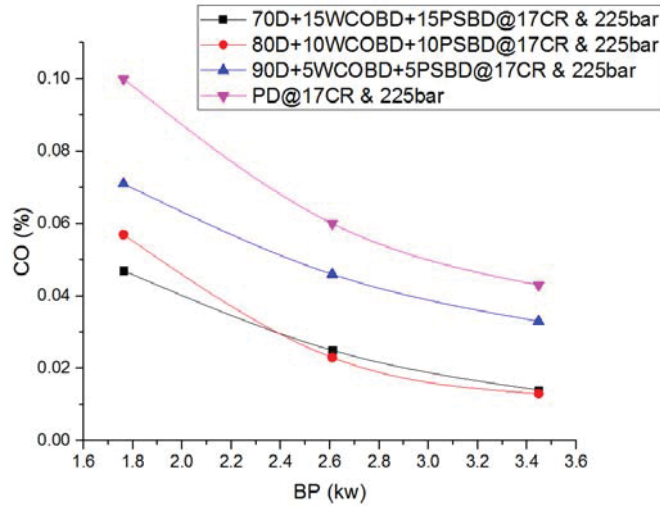
Fig.3. CO% v/s BP(kw) for blends of biodiesel from two different feedstock and diesel @ 225bar injection pressure
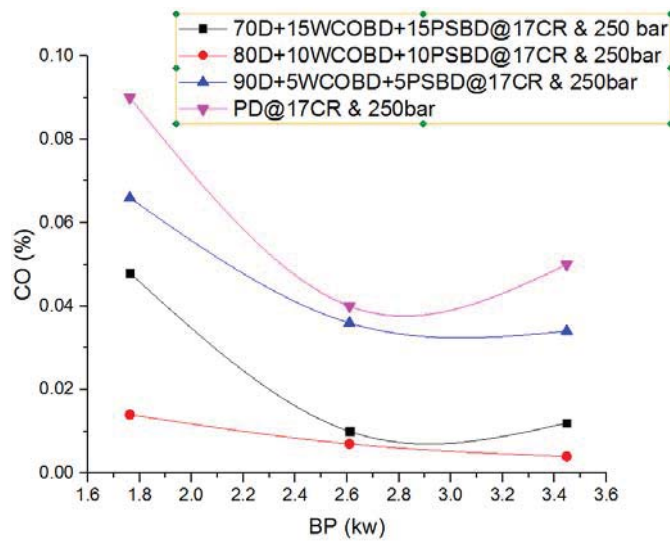
Fig.4. CO % v/s BP(kw) for blends of biodiesel from two different feedstock and diesel @ 250bar injection pressure

As the injection pressure increase the effect on emission is that its component CO decreases further both for the blended and standard diesel.
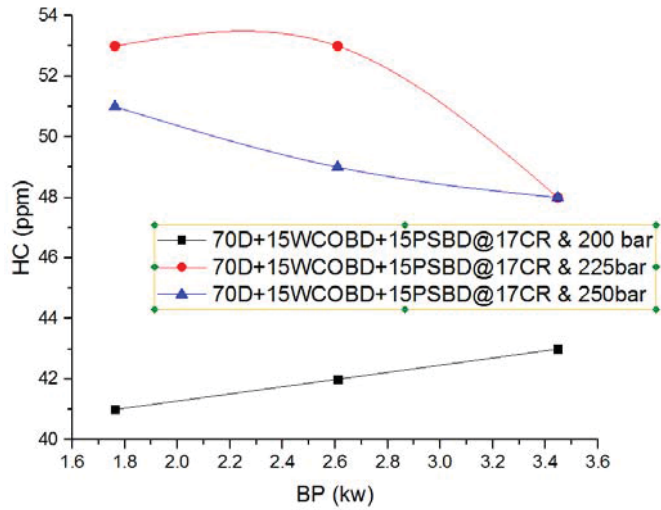
Fig.5. HC (ppm) v/s BP(kw) for a 30%blended diesel from two different feedstock @ different injection pressure
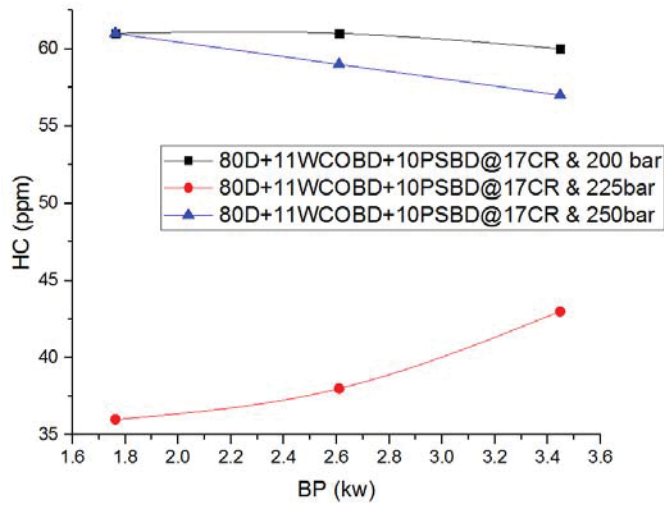
Fig.6. HC(ppm) v/s BP(kw) for a 20%blended diesel from two different feedstock @ different injection pressure
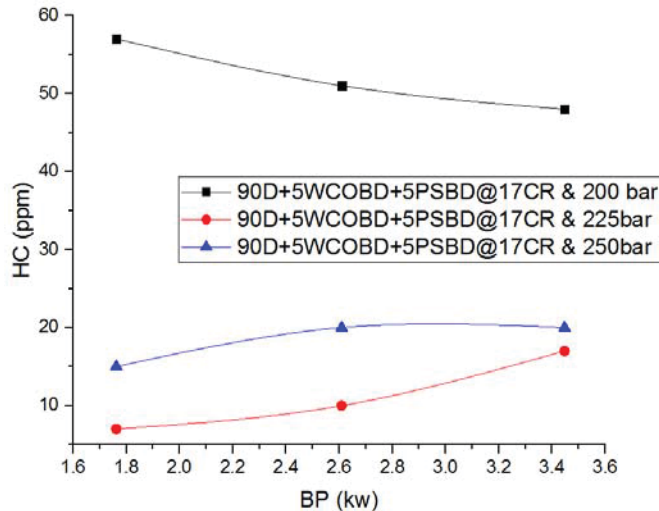
Fig.7. HC(ppm) v/s BP(kw) for a 10%blended diesel from two different feedstock @ different injection pressure

The optimum value for the injection pressure in contest to emission of CO is 225bar where its component

VI. CONCLUSION

The experimental investigation revealed that the emission of the engine when powered by biodiesel and its blends with petroleum diesel is far better and eco friendly compare to its emission when powered by 100% petroleum diesel, exception being in NOx which extend the trend reversely.

Biodiesel are viable alternative to mineral diesel as fuel in Compression Ignition engine. Biodiesel can be prepared from different renewable feedstocks like cooking oil and palm oil, but they contribute directly to human food chain hence their byproducts such as waste cooking oil and palm stearin oil can burnt in engine after tranesterification.

The well known fact that engine performances of biodiesel are comparable to that of mineral diesel and emission characteristics of biodiesel are better than diesel fuel except NOx emission. The carbon monoxide, un-burned hydrocarbonare found to be less in the tail pipe emissions due to the enrichment of oxygen. But and oxides of nitrogen are found to be slightly greater in exhaust in case of biodiesel compared to mineral diesel. The higher viscosity of bioiesel also enhances the lubricating property and excess oxygen content results better combustion for biodiesel.

VII. ACKNOWLEDGEMENTS

REFERENCES

[1]   Government of India Ministry of New & Renewable Energy National Policy on Biofuels Block No. 14, C.G.O. Complex Lodhi Road New Delhi- 110003
[2]   N.Ramakrishna et al.Int. Journal of Engineering Research and Applications www.ijera.com ISSN : 2248-9622, Vol. 3, Issue 6, Nov-Dec 2013, pp.473-478
[3]   Journal of Engineering Science and Technology Vol. 9, No. 5 (2014) 620 – 640 © School of Engineering, Taylor's University
[4]   American Journal of Engineering Research (AJER) e-ISSN : 2320-0847 p-ISSN : 2320-0936 Volume-03, Issue-02, pp-184-190 www.ajer.org
[5]   Smart Grid and Renewable Energy, 2011, 2, 165-168 doi:10.4236/sgre.2011.22019 Published Online May 2011 (http://www.SciRP.org/journal/sgre)
[6]   February. ISSN: 2321-8134 http://www.ijfeat.org(C)InternationalJournalFor Engineering Applications and Technology[49-52]   IJFEAT "Production of Biodiesel, Its Emission And Performance On Diesel Engine".
[7]   Desantes, J. M., Arregle, J., Ruiz, S., & Delage, A. (1999). Characterisation of the injection-combustion process in a DI Diesel engine running with rape oil methyl ester (No. 1999-01-1497). SAE Technical Paper.
[8]   Rakopoulos, D. C., Rakopoulos, C. D., Giakoumis, E. G., Dimaratos, A. M., & Founti, M. A. (2011). Comparative environmental behavior of bus engine operating on blends of diesel fuel with four straight vegetable oils of Greek origin: Sunflower, cottonseed, corn and olive. Fuel, 90(11), 3439-3446.
[9]   IOSR Journal of Mechanical and Civil Engineering (IOSR-JMCE) e-ISSN: 2278-1684,p-ISSN: 2320-334X, Volume 12, Issue 2 Ver. VI (Mar - Apr. 2015), PP 27-33 www.iosrjournals.org

Experimental Investigations on Single Cylinder CI Engine for Variable Compression Ratio & Variable Injection Pressure Using Treble Fuel

Md.Fakhruddin H.N.
Department of Mechanical Engineering
Methodist College of Engineering & Technology, Hyderabad, Telangana State, India

Dr.Manzoor Hussain
Professor& Principal
JNTUH College of Engineering Sultanpur, Hyderabad, Telangana State, India

Md. Samiuddin Siddiqui
Department of Mechanical Engineering
Methodist College of Engineering & Technology, Hyderabad, Telangana State, India

Abstract- **For the very existence of internal combustion engine in the wide spread as they are now, it is renewable, sustainable and alternative fuel that the world looks forward i.e. biodiesel instead of diesel. It has been increasingly fuelled to study its effects on engine performances and emissions in the recent two decades. The researches regarding blend of diesel and single biodiesel have been done already. Very few works have been done with the combination of two different biodiesel blends with diesel and left a lot of scope in this area. The present investigation is to bring performance for two biodiesels from different feedstock i.e. waste cooking oil biodiesel and palm staerin biodiesel. The effects of dual biodiesel in diesel at various proportions were examined in a single cylinder, direct injection, air cooled and high speed diesel engine at various engine loads with constant engine speed of 3000 rpm and with variable compression ratio & variable injection pressure.**

Keywords – variable compression ratio, variable injection pressure, waste cooking oil biodiesel, palm staerin biodiesel

I. INTRODUCTION

India ranks sixth in the world in the term of energy demand accounting for 3.5 % of world commercial energy demand. It is expected to grow at 4.8%. The growth in energy demand in all forms is expected to continue unabated owing to increasing urbanization ,standard of living and expanding population with stabilization not before mid of the current century.[1]
 Bio-diesel consists of mono alkyl esters produced from vegetable oils, animal or old cooking fats. Bio-diesel contains no petroleum diesel, but it can be blended with petroleum diesel**.** Mono-alkyl esters of long chain fatty acids (biodiesel) is a promising substitute of petro diesel fuel that can be produced from natural, renewable resources such as wide variety of vegetable oils and animal fats.[1]
Now-a-days dual fuel technique is most widely adopted with blended fuel and gaseous fuel. In the present experiment, dual biodiesel i.e. waste cooking oil biodiesel plus palm stearin biodiesel and hydrogen are used in compression ignition engine to reduce emission and increase the performance characteristics [2].

II. MATERIALS AND METHODS

A. VCR Engines

The standard available engines (with fixed compression ratio) can be modified by providing additional variable combustion space. There are different arrangements by which this can be achieved. Tilting cylinder block method is one of the arrangements where the compression ratio can be changed without change is combustion geometry. With this method the compression ratio can be changed within designed range without stopping the engineWhere the parameter α is called embedding intensity and their effect of validity of the algorithm directly is apply after this process, after that apply the inverse wavelet transform to the image for find out watermark image.

B. Experimentation
Engine Specifications
The test is carried out in an engineering college using a
kirloskar make,
Type 1cylinder,
4 stroke diesel,
Water cooled,
Model tv1,
Stroke 110 mm,
Bore 87.5 mm.
661 cc,
VCR engine CR range 12 to 18.
Dynamometer Type eddy current,
Water cooled,
Loading unit Eddy current
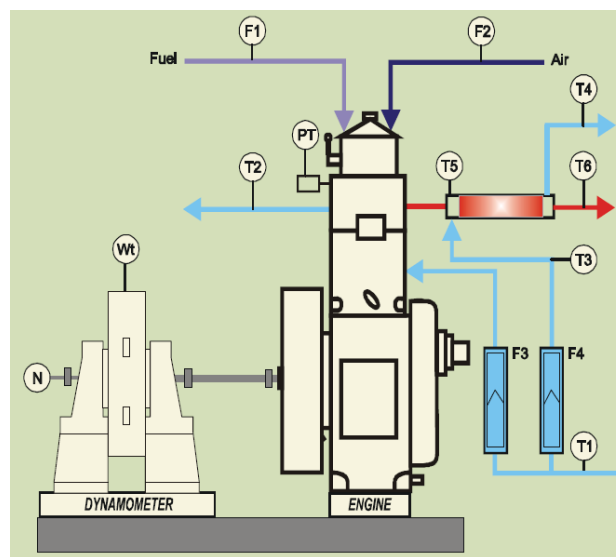
Figure 1.   Block diagram for the test set up

C. Experimental setup
Where,

F1	Fuel consumption	
F2	Air consumption	
N	Engine speed	rpm
Wt	Loading in	kg
F1	Fuel consumption	kg/hr
F2	Air consumption	kg/hr
F4	Calorimeter water flow	kg/hr
T1	Engine water inlet temperature	^{0}K
T2	Engine water outlet temperature	^{0}K
T3	Calorimeter water inlet temperature	^{0}K
T4	Calorimeter water outlet temperature	^{0}K
T5	Exhaust gas to calorimeter inlet temp.	^{0}K
T6	Exhaust gas from calorimeter outlet temp.	^{0}K

Table -1 Properties of diesel, waste vegetable oil [3] & and palm staerin [4]

Properties	Diesel	Waste vegetable oil	Palm Staein oil
Density @ 15°C in gm/cc	0.845	0.8868	0.855@40°C
Viscosity @ 40°C	3.25	6.05 cst	4.5
Flash Point by PMCC method	32	52°C	174°C
Fire Point by PMCC method	78	86°C	--
Calorific Value in Kcal/kg	44938	8919	43938

III. EXPERIMENT AND RESULT
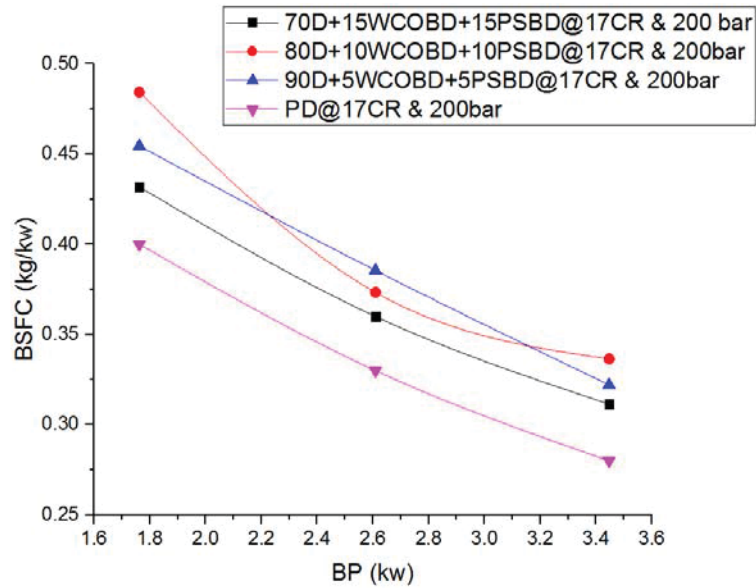
Figure 2.   BP V/S BSFC Plot for WCOBD + PSBD + Diesel @ 17 Compression ratio & 200Bar injection pressure

The above graph reveals that as the biodiesel blends increase in its constituent the bsfc approaches near to diesel fuel, hence 30% biodiesel has been successfully fractioned at 15%wcobd and 15% psbd.
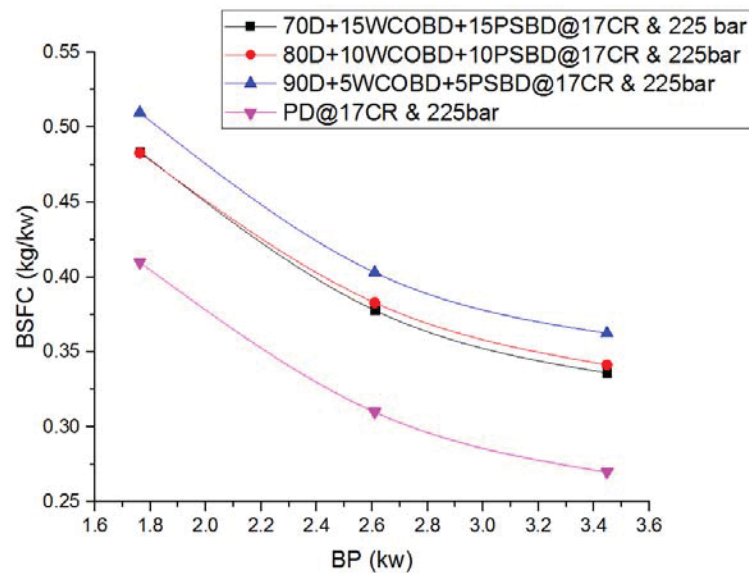
Figure 3.   BP V/S BSFC Plot for WCOBD + PSBD + Diesel @ 17 Compression ratio & 225Bar injection pressure

The above graph reveals that as the biodiesel blends increase in its constituent the bsfc approaches near to diesel fuel, hence 30% biodiesel has been successfully fractioned at 15%wcobd and 15% psbd.
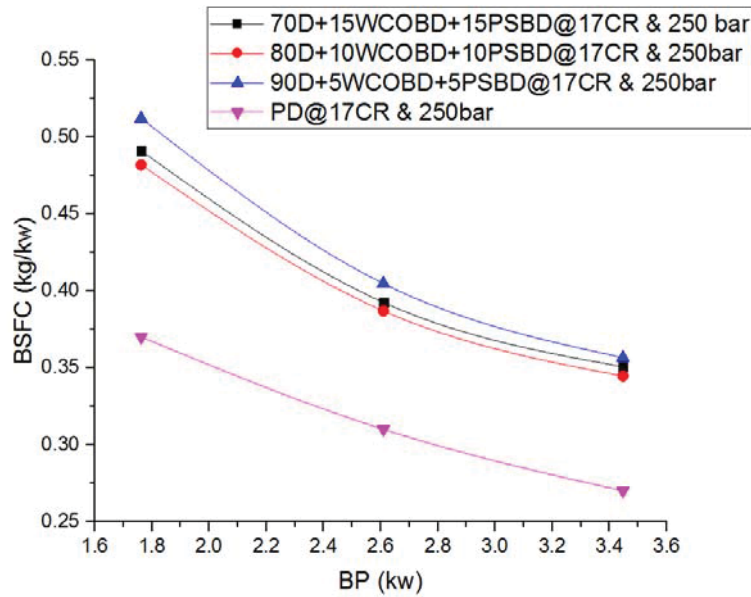
Figure 4.   BP V/S BSFC Plot for WCOBD + PSBD + Diesel @ 17 Compression ratio & 250Bar injection pressure

The above graph reveals that as the biodiesel blends increase in its constituent the bsfc approaches near to diesel fuel, hence 30% biodiesel has been successfully fractioned at 15%wcobd and 15% psbd. The optimum being 20% biodiesel.
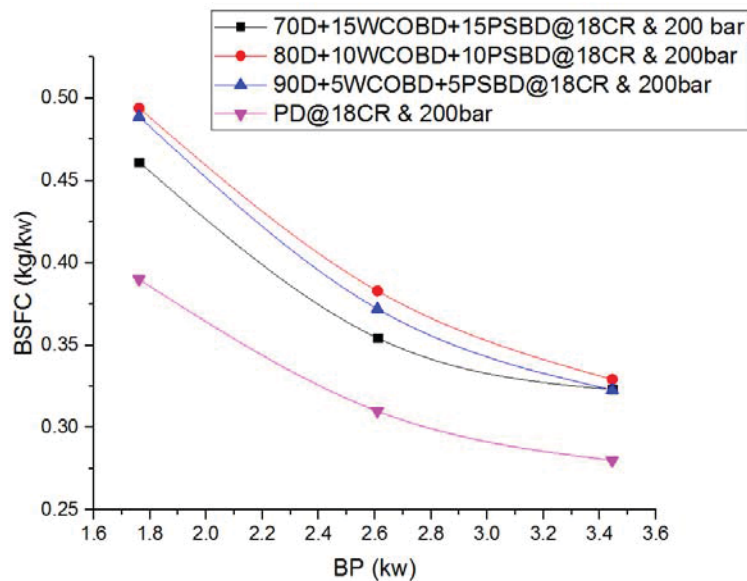
Figure 5.   BP V/S BSFC Plot for WCOBD + PSBD + Diesel @ 18 Compression ratio & 200Bar injection pressure

The above graph reveals that as the biodiesel blends increase in its constituent the bsfc approaches near to diesel fuel, hence 30% biodiesel has been successfully fractioned at 15%wcobd and 15% psbd.
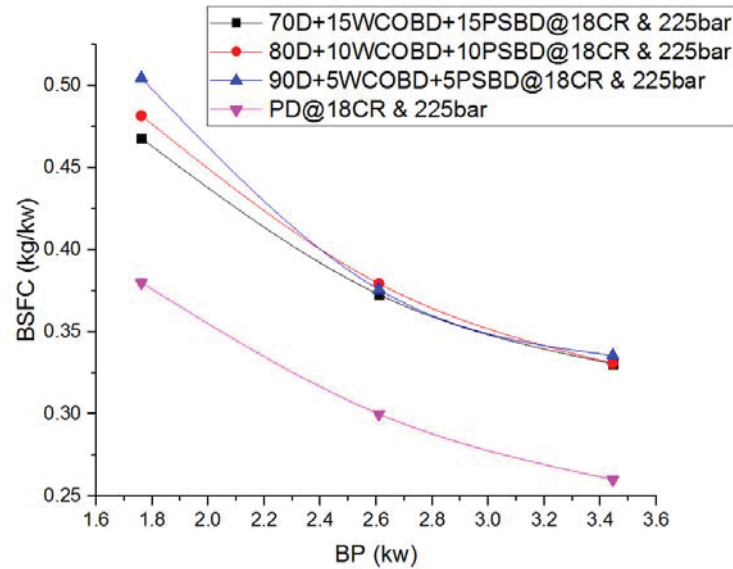
Figure 6.   BP V/S BSFC Plot for WCOBD + PSBD + Diesel @ 18 Compression ratio & 225Bar injection pressure

The above graph reveals that as the biodiesel blends increase in its constituent the BSFC approaches near to diesel fuel, hence 30% biodiesel has been successfully fractioned at 15%wcobd and 15% PSBD. Further at heigher loads i.e. BP the bsfc converge even for low blended mixtures.
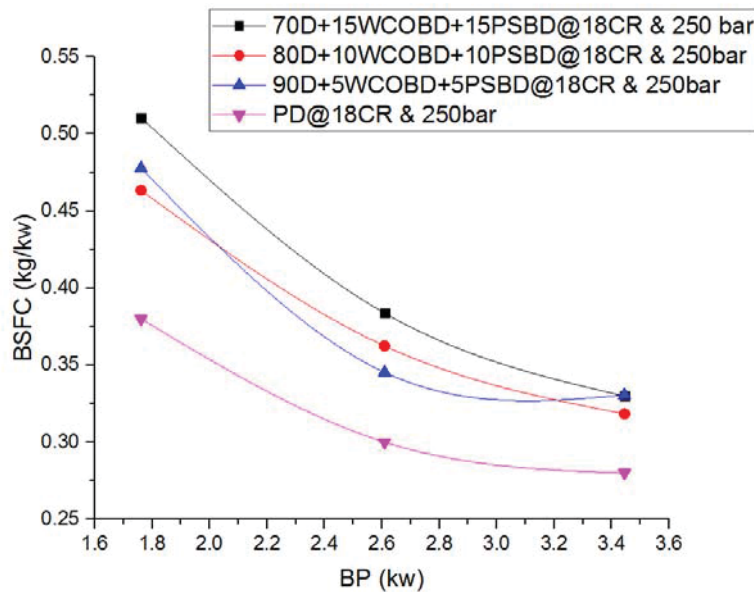
Figure 7.   BP V/S BSFC Plot for WCOBD + PSBD + Diesel @18 Compression ratio & 250Bar injection pressure

The above graph reveals that as the biodiesel blends increase in its constituent the BSFC approaches away from diesel fuel, interpreting to this is that higher cpmoression ratio and injection pressure the treand reverses hence 90% biodiesel has been successfully fractioned at 10%wcobd and 10% psbd, which seems to be optimum . At heigher injection pressure the trend reverse and as more blended mixture BSFC increases

IV.CONCLUSION

Compression ratio and injection pressure play a vital role in the performance of internal combustion engine working on biodiesel. At higher compression ratios and high injection pressure BSFC increase for the blended mixtures when

the proportion is elevated. Hence it is experienced that the optimum operating pressure is 18 @ 225bar injection pressure.

REFERENCES

[1] International Journal of Modern Engineering Research (IJMER) www.ijmer.com Vol.3, Issue.2, March-April. 2013 pp-832-838 ISSN: 2249-6645.

[2] American Journal of Engineering Research (AJER) e-ISSN : 2320-0847 p-ISSN : 2320-0936 Volume-03, Issue-02, pp-184-190 www.ajer.org

[3] N.Ramakrishna et al.Int. Journal of Engineering Research and Applications www.ijera.com ISSN : 2248-9622, Vol. 3, Issue 6, Nov-Dec 2013, pp.473-478

[4] Corresponding Author: Jawad Nagi, Universiti Tenaga Nasional, Malaysia. Email address:jawad@uniten.edu.my. ICCBT 2008 - F - (07) – pp79-94

[5] Bull. Chem. Soc. Ethiop. 2003, 17(1), 19-26. ISSN 1011-3924 Printed in Ethiopia _ 2003 Chemical Society of Ethiopia

[6] Journal of Environmental Protection, 2012, 3, 107-113 http://dx.doi.org/10.4236/jep.2012.31013 Published Online January 2012 (http://www.SciRP.org/journal/jep)

[7] IOSR Journal of Mechanical and Civil Engineering (IOSR-JMCE) e-ISSN: 2278-1684,p-ISSN: 2320-334X, Volume 12, Issue 2 Ver. VI (Mar - Apr. 2015), PP 27-33 www.iosrjournals.org

[8] INTERNATIONAL JOURNAL of RENEWABLE ENERGY RESEARCH Puneet Verma and M.P. Sharma, Vol.5, No.1, 2015

[9] Jordan Journal of Mechanical and Industrial Engineering, Volume 9 Number 1, February.2015 ISSN 1995-6665 Pages 61- 66

International Journal of Computer Science, Information Technology, & Security (IJCSITS)

ISSN: 2249-9555 (Online), 2250-1355 (Print)

🖹 IRACST Home

Click to enable Adobe Flash Player

CONTENTS

International Journal of Computer Science, Information Technology, & Security (IJCSITS)

A.No	Article Title & Authors (Volume 6 Number 4 July-August 2016)	Download	Page
	Round - 1 & 2		
1	A comparative study of content based search and retrieval of video sequences - Azra Nasreen, Dr. Shobha G	PDF	1
2	Hybrid Arabic Speech Recognition System Using FFT, Fuzzy Logic and Neural Network - Salam Hamdan, Adnan Shaout	PDF	4
3	Hiding of Data in Images using Spread Spectrum Technique - T. Sai Sampath, T.S.R. Krishna Prasad	PDF	11
4	Comparative Analysis Of Speaker Dependent, Speaker Independent And Cross Language Emotion Recognition From Speech Using SVM - E. Sarath Kumar Naik, K. Suvarna	PDF	15
5	Proficient And Secure Routing Approach For Wireless Mesh Network - Shilpa, Kamaljeet Kaur Mangat	PDF	20
6	Implementation of Low Power Ultrasonic Phased Array Using ZYNQ-SoC - K. Sai Kumar, Y Sri Chakrapani, Dr. M.Kamaraju	PDF	26
7	Design and Implementation of Energy Efficient Code Converters - T. Durga Prasad, K. Srilakshmi, Y. Syamala	PDF	33
8	Low Power VLSI implementation of error detection and correction codes using OLS codes - G. Rajesh, T. Venkata Lakshmi, M. Kamaraju	PDF	38
9	Implementation of Digital Modulation Techniques using Memristor Based Oscillator - B. Preeti, M. Vijaya Kumar	PDF	42
10	Reversible Data Hiding Based on Generalized Equalization Model - B. Teja Bhaskar, B. Naga Sirisha	PDF	49
11	A Novel Multi-Focus Image Fusion Algorithm Using Stationary Wavelet Transform - Sk.Gouse begum hajma, Ch. Amarnatha sarma	PDF	55
12	Android Based Criminal Location Detector Using Gps And Camera In Handheld Device - MaheshKhanna.R,Hariprakash.B, Ramganesh.T, Anitha.M, Archana.R	PDF	61
13	A Survey paper on RFID Technology, its Applications and Classification of Security/Privacy Attacks and Solutions - Ms.Neha Kamdar, Vinita Sharma, Sudhanshu Nayak	PDF	64
14	A Novel Architecture of 16-Bit Multiplier Using Modified Gate Diffusion Input Logic		69

	- M. Vinay Babu, M. Damodhar Rao, Dr. V. V. K. D. V. Prasad	PDF	
15	Analysis Of Student Behaviour Using R Language - Ashish Soni, Toshi Sharma, Vishal Chhabra	PDF	75
16	Text Steganography: Review - Nitesh Rao M, Lavanya Pamulaparty	PDF	80
17	Developing Assurance Framework of Cloud Computing in the implementation of ERP: A Literature Survey - Vikram Gupta, Dr. Sarvjit Singh Bhatia	PDF	84
18	Enhanced Multiparty Access Control in Online Social Network - Smita Vishnu More, Madhumita Chatterjee	PDF	93

Home | About IJCSITS | Topics | Submission | Editorial Board | Publications | Contact us

.....

Simulation of Critical Crack Length Propagation Using Fracture Mechanics

Mr.DEGALA RAJENDRA[1], Mr. P RAVICHANDER[2] /Prof. R V PRASAD[3]

[1]*Sri Padmavathi Mahila University, Technology Tirupati*
[2,3]*Methodist College Of Engineering & Hyderabad*

ABSTRACT

The focus of this paper is to investigate and analyze the study on the plate of steel, Aluminum and Epoxy with a center crack. Linear elastic fracture mechanics principles have been used for calculating Stress Intensity Factor, Critical crack length, Increment in crack, Mean stress and strain Amplitude at critical fatigue load cycles.

Above calculations will be done on the plate with centre crack of various materials (steel, aluminum and epoxy) to predict crack length to evaluate and to compare the results with theoretical calculations.
.Conclusions/results obtained on the basis of analysis.

Keywords: FRACTURE MECHANICS,FEM,ANSYS

I.   INTRODUCTION

Basically metal plates cause to fatigue cracks when it crosses its yield strength limit casually ,all the materials withstands up to 10^{+7} (cycles) this is called as **safe zone** limit 10^{+8} to 10^{+10}(cycles) is called **critical zone.** Most failures occur in materials are selection of proper material, processing, manufacturing procedures, incorrect usage. When the material is imposed of stresses, stress fracture of material can be two or more pieces.

Types of failure:
Failures of material are of two types, they are:
Buckling and Fracture.

Buckling:
When the material is subjected to a compressive load, buckling causes a lateral bend in the material. Buckling results failure of material within the catastrophic failure.

Types of fracture: In fracture failures Physical separation, or tearing of the material, through either an internal or external crack. Fracture of material are two types, they are: Ductile and Brittle fracture.

Ductile and brittle fracture

Fracture occurs due to stress concentrations at flaws like Surfaces scratches(stamp marks, inspection marks, surface irregularities), Variation in material properties(blow holes, cavities, weld strikes, and foreign inclusions)Discontinuities in the component(holes, grooves, keyways, screw threads and Abrupt changes in cross section (gears, sprockets, pulleys, ball bearings, splines on shafts)

Ductile fracture:
Ductile fracture materials are calculated by depending on momentum of the material. In Ductile fracture large amount of plastic deformation takes place before the fracture. Slow propagation and absorption of large amount energy is observed before the fracture. In ductile materials, particularly in high purity materials can with stand up to 50-100% large deformation or more strain before fracture under loading condition. Ductile fracture mostly influenced by: Transition temperature, inclusions, and strain hardening.

Brittle fracture:
Brittle fracture materials are calculated by depending on strength of the materials. In Brittle fracture small amount of plastic deformation takes place before the fracture. In brittle materials, particularly in brittle crystalline materials fracture can occur due to the result of tensile stress acting normal to crystallographic. Brittle fracture mostly results in catastrophic failure of a structure. Brittle fracture mostly influenced by: Defects, fatigue, and stress-corrosion.

Fatigue failures:

Fatigue means weakening of materials by applying repeated loading and unloading. When the material is subjected to cyclic loading, progressive and localized structural damage occurs in material. The nominal maximum stress values that cause such damage may be much less than the strength of the material typically quoted as the ultimate tensile stress limit, or the yield stress limit.

If the loads are above a certain threshold, microscopic cracks began to form at the stress concentrators such as surface, persistent slip bands (PSBs), and grain interfaces. Eventually crack will reach a critical size, the crack will propagate suddenly, and structure will fracture. The shape of the structure will significantly affect the fatigue life; square holes or sharp corners will lead to elevated local stresses where fatigue cracks can initiate. Round holes and smooth transitions or fillets will therefore increase the fatigue strength of the structure.

Low Cycle Fatigue:

Low cycle fatigue involves less numbers of cycles (N1000),

Failure of Set screws, short lived devices like missiles.

High cycle fatigue:

High cycle fatigue involves a large number of cycles (N4105 cycles) and an elastically applied stress. High cycle fatigue tests are usually carried out for 10^{+7} cycles sometimes 10^{+8} cycles for nonferrous metals. Although the applied stress is low enough to be elastic, plastic deformation can take place at the crack tip. Failure of Springs, ball bearings, gears subjected to fluctuating stresses. High cycle fatigue data are usually presented as a plot of stress, S, Vs the number of cycles to failure N. along scale is used for the number of cycles. The value of stress, s, can be the maximum stress, S max, the minimum stress, S min, or value of mean stress, S m, or one of the two ratios, R or A. The fatigue life is the number of cycles to failure at a specified stress level, while the fatigue strength (also referred to as the endurance limit) is the stress below which failure does not occur. As the applied stress level is decreased, the number of cycles to failure increases.

Normally, the fatigue strength increases as the elastic tensile strength increases.

II.   EXPERIMENTAL ANALYSIS

Nomenclature

$A_{fracture}$	= cross-section of the specimen at fracture.
A_0	= initial cross-section of the specimen.
C	= fatigue ductility exponent.
E	= young's modulus.
N	= describe the relative position of the crack tip to the grain boundary.
N_f	= number of load cycles to failure.
$\delta^{|}f$	= fatigue strength coefficient.
$\varepsilon_{fracture}$	= specific deformation of the specimen at fracture.
$\delta\varepsilon$	= specific deformation increment.
$\delta^{|}_f$	= fatigue ductility coefficient.
δuts	= ultimate tensile strength

INPUTS FOR STEEL AISI:

$A_{fracture}$	=	5.89
A	=	6
C	=	3
E	=	180Gpa
N	=	2

N f   = 10^8

δ^l f   =   2.8

ϵ fracture   =   2.03735

δ'_f = 10^6

δ uts   =   400mpa

Critical crack length calculation:

Fatigue crack initiation:

$$\frac{\Delta\epsilon}{2} = \frac{\delta a}{E} + \frac{\Delta\epsilon\, p}{2}$$

$$= \frac{\delta^l f}{E}(2Nf)^{\ b} + \epsilon^l f(2.$$

$$\frac{10^6}{180000}(2*10^8)^{.002} + 2.8(2*10^8)^{.003}$$

=55.55*1.04+2.8*1.066

   =56.59+3.866

=60.456

$$\Delta\epsilon = \frac{60.456}{2} = 30.228$$

Strain amplitude:

Marrows (- N) method

$$\epsilon\, a = \frac{(\delta^l f - \delta m)}{E}$$

$$= (2Nf)^b + \epsilon^l f(2Nf2)^c$$

According to coffin-Manson

$$\epsilon\, a = 1.75\frac{\delta uts}{E}N_f^{-0.2} + 0.5D^{0.6}N_f^{-0.6}$$

$$D = 1n\frac{A_0}{A_{Fracture}} \cong \epsilon\, Fracture$$

$$D = \frac{6}{5.8}$$

=2*1.0186   =2.03735

$$\epsilon\, a = 1.75\frac{400}{180000}10^{8-.02} + 0.5*2.03735^{0.6}*10^{8-.06}$$

1.75*2.2^{-3}*0.083176+0.5*1.53263*3.98^{-6}

=0.01367+2.177^{-4}

Strain =0.0138

Mean stress

Smith Watson Topper Method

$$= \delta_f^l \epsilon_f^l (2Nf)^{b+c} \frac{\delta_f^{l2}}{E}$$

$$= 10^6 * 2.8(2*10^8)^{0.05} + \frac{10^{6^2}}{180000}(2*10^8)^{0.04}$$

8169643.74+235877379.9

=317575023.4 Pascal's

=317.5Mpa

INPUTS FOR ALUMINUM

A $_{fracture}$ =   5.89

A_0 =   6

c   =   3

E   =   74.5Gpa

N   =   2

N $_f$ = 10^8

δ^l f   = 10^4

ϵ fracture   =   2.03735

δ'_f =   3.2

δ uts   =   168mpa

Critical crack length calculations:
Fatigue crack initiation[1] :

$$\frac{\Delta \in}{2} = \frac{\delta a}{E} + \frac{\Delta \in p}{2}$$

$$= \frac{\delta^l f}{E}(2Nf)^{\ b} + \in^l f (2.$$

$$\frac{10^4}{74500}(2*10^8)^{.002} + 3.2(2*10^8)^{.003}$$

=0.1394+3.3888

=3.528

$$\Delta \in = 3.528 * 2 = 7.0565$$

Strain amplitude:
Marrows method

$$\in a = \frac{(\delta^l f - \delta m)}{E}$$

$$= (2Nf)^b + \in^l f (2Nf)^c$$

According to coffin-Manson

$$\in a = 1.75 \frac{\delta uts}{E} N_f^{-0.2} + 0.5 D^{0.6} N_f^{-0.6}$$

$$D = 1n \frac{A_0}{A_{Fracture}} \cong \in Fracture$$

$$D = \frac{6}{5.8}$$

=2*1.0186 =2.03735

$$\in a = 1.75 \frac{168}{74500} 10^{8 -.02} + 0.5 * 2.03735^{0.6} * 10^{8 -.06}$$

=4.3270×10⁻⁴+1.2145×10⁻⁵

=0.004448

Strain = 0.004448

Mean stress:
Smith Watson Topper Method

$$= \delta^l_f \epsilon^l_f (2Nf)^{b+c} \frac{\delta^{l2}_f}{E}$$

$$= 10^6 * 2.8(2*10^8)^{0.05} + \frac{10^{4^2}}{74500}(2*10^8)^{0.04}$$

=7281310.163+2883.267

=7284193.43 Pascal's

=72.84Mpa

INPUTS FOR EPOXY

A $_{fracture}$	=	5.89
A $_o$	=	6
c	=	3
E	=	30Gpa
N	=	2
N $_f$	=	10^8
δ ^{1} f	=	10^7
Є $_{fracture}$	=	2.03735
δ ^1_f	=	2.1
δ uts	=	550mpa

Critical crack length calculations:
Fatigue crack initiation:

$$\frac{\Delta \in}{2} = \frac{\delta a}{E_l} + \frac{\Delta \in p}{2}$$

$$= \frac{\delta^l_f}{E}(2Nf)^{\ b} + \in^l f (2.$$

$$\frac{10^7}{30000}(2*10^8)^{.002} + 2.1(2*10^8)^{.003}$$

=346.3225+2.2239   =348.54

$\Delta \in = 348.54 * 2 = 697.09$

Strain amplitude:
Marrows method

$$\in a = \frac{(\delta^l f - \delta m)}{E}$$
$$= (2Nf)^b + \in^l f (2Nf)^c$$

According to coffin-Manson

$$\in a = 1.75 \frac{\delta uts}{E} N_f^{-0.2} + 0.5 D^{0.6} N_f^{-0.6}$$

$$D = 1n \frac{A_0}{A_{Fracture}} \cong \in Fracture$$

$$D = \frac{6}{5.8}$$
$=2*1.0186$
$=2.03735$

$$\in a = 1.75 \frac{550}{30000} 10^{8-.012} + 0.5 * 2.03735^{0.6} * 10^{8-.06}$$

$=3.5300 \times 10^{-3}$ Strain $= 0.0035$

Mean stress:
Smith Watson Topper Method

$$= \qquad \delta_f^l \in_f^l (2Nf)^{b+c} \frac{\delta_f^{l2}}{E}$$

$$= 10^7 * 2.1(2*10^8)^{0.05} + \frac{10^{7^2}}{30000}(2*10^8)^{0.04}$$

$=7214723960$ Pascal's$=721.84$Mpa

RESULTS TABLE
Theoretical

	STEEL AIST 1504	ALUMINUM	E-GLASS EPOXY
specific deformation increment	30.228	7.0565	697.09
Strain amplitude	2.03735	2.03735	2.03735
Strain	0.0138	0.004448	0.0035
Mean stress	317.5Mpa	72.84Mpa	721.84Mpa

Analysis results with 10x cycles

	STEEL AIST 1504	ALUMINUM	E-GLASS EPOXY
DISPLACEMENT	0.32605	0.92594	0.87737
STRAIN	0.0086302	0.0240	0.02459
STRESS	1726	1710.2	1781
LIFE	62.39 to 1e^6	0 to1e^8	57.949-1e^6
DAMAGE	1000 to1.602e^7	10 to1e^{32}	1000 to 1.7257e^7
FACTOR OF SAFTY	2.845	2.832	2.58
BI-INDICATION	0.99891to0.966	0.993 to 0.97666	0.99 to0.867
ALL-STRESS	1726	1710.2	1781
MODE 1	341.51	1631.8	1725.5
MODE 2	632.86	2939.1	3086.6
MODE 3	1540.8	3033.4	3122.7
MODE 4	2853.6	3663.6	3731.6
MODE 5	3132.4	4577	4772.7
MODE 6	3537	5615.1	5779.6

STEEL AIST 1504	
	Analysis
DISPLACEMENT	0.32605
STRAIN	0.0086302
STRESS	1726
LIFE	62.39 to $1e^6$
DAMAGE	1000 to$1.602e^7$
FACTOR OF SAFTY	0.049to2.845
BI-INDICATION	0.99891to0.966
ALL-STRESS	1726
MODE 1	341.51
MODE 2	632.86
MODE 3	1540.8
MODE 4	2853.6
MODE 5	3132.4
MODE 6	3537
Mean stress	

ALUMINUM	
	Analysis 10x
DISPLACEMENT	0.92594
STRAIN	0.0240
STRESS	1710.2
LIFE	0 to$1e^8$
DAMAGE	10 to$1e^{32}$
FACTOR OF SAFTY	0.04838 to2.832
BI-INDICATION	0.993 to 0.97666
ALL-STRESS	1710.2
MODE 1	1631.8
MODE 2	2939.1
MODE 3	3033.4
MODE 4	3663.6
MODE 5	4577
MODE 6	5615.1

E-GLASS EPOXY	
	Analysis 10x
DISPLACEMENT	0.87737
STRAIN	0.02459
STRESS	1781
LIFE	57.949-$1e^6$
DAMAGE	1000 to $1.7257e^7$
FACTOR OF SAFTY	0.048 to2.58
BI-INDICATION	0.99 to0.867
ALL-STRESS	1781
MODE 1	1725.5
MODE 2	3086.6
MODE 3	3122.7
MODE 4	3731.6
MODE 5	4772.7
MODE 6	5779.6
Mean stress	

III.   CONCLUSION

Initially data collection and literature survey was done on critical length on various materials.

By analysis in three materials aluminum has high strength and life cycle and damage will be less compared to E-glass epoxy material.

In aerospace design epoxy's are widely used to make outer body's, these outer bodies caused to damage with small hit or crack initiation so better to use mixture of aluminum and carbon mixture in good qualities.

IV.   FUTURE SCOPE

Epoxy materials are not able to withstand after crossing safe zone (initiation of crack). When we mix the aluminum materials and E-glass epoxy material the material can with stand and life cycle of material can be increased.

REFERENCES

[1]   G. Fajdiga and M. Sraml; Fatigue Crack Initiation and Propagation under Cyclic Contact Loading.

[2]   Mr. Quinton Row son consultant Structural Integrity, Quest Integrity NZL Ltd., New Zealand Mr. Michael Rock engineering Project Manager, Mighty River Power Ltd., New Zealand; Comparison between ductile tearing analysis and linear elastic fracture mechanics analysis.

[3]   Donoso, J.R. and Landes; Materials Science Department, Universidad Tecnica Federico Santa Maria Valparaiso, CHILE juan.Donoso@Usm.Cl^2 MABE Department, The University Of Tennessee Knoxville, TN   Usalandes@Utk.Edu;An instability analysis for a crack growth situation based on the common format.

[4]   fracture and fatigue crack growth analysis of rail steels; Journal Of Mechanics Of Materials And Structures

[5]   M kulkarni1, Ravi prakash2 and A N kumar3; Experimental And Finite Element Analysis Of Fracture Criterion In General Yielding Fracture Mechanics

[6]   H. Sun, S. Rajendran and D. Q. Song: Finite Element Analysis on Delimitation Fracture Toughness Of Composite Specimens

[7]   Tipple and G. Thorwald; Using the Failure Assessment Diagram Method with Fatigue Crack Growth To Determine Leak-Before-Rupture.

Economical and Technical Way of Ladle Pre-heating by the Use of Flameless Oxyfuel (HSD/LPG) Gas in the Steel Industry

Article · June 2016

3 authors:

Mohammad S Alsoufi
Umm Al-Qura University
80 PUBLICATIONS   305 CITATIONS

SEE PROFILE

Mohammed Yunus
Umm Al-Qura University,saudi arabia, mecca.
38 PUBLICATIONS   112 CITATIONS

SEE PROFILE

Mohammed Asadulla
Nalla Malla Reddy Engineering college
2 PUBLICATIONS   1 CITATION

SEE PROFILE

Some of the authors of this publication are also working on these related projects:

Project   thermal barrier coating View project

Project   MIM in rectanna View project
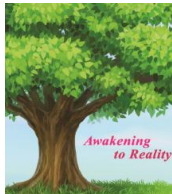
Economical and Technical Way of Ladle Pre-heating by the Use of Flameless Oxyfuel (HSD/LPG) Gas in the Steel Industry

Dr. Mohammad S. Alsoufi[1], Dr. Mohammed Yunus[1] and Mr. Mohammed Asadullah[2]

[1]Mechanical Engineering Department, College of Engineering and Islamic Architecture, Umm Al-Qura University, Makkah, KSA.

[2]Mechanical Engineering Department, NRI Institute of Technology, Hyderabad, India.

ABSTRACT

For efficient heating with lesser fuel consumption and a quick way of heating, oxyfuel has been clearly shown to produce very low emissions of CO_2 and NO_X as compared to air-fuel for fifteen years. Among oxyfuels, flameless oxyfuels can be even more economical and technically superior for higher production rates, excellent uniform heating and very low NO_X emissions. In the present study, our casting centres have accommodated a number of reheating furnaces along with preheating stands working on flameless oxyfuel to one tonne capacity of smallest size ladles. Flameless oxyfuel has improved to a greater uniformity in heat distribution and decreased fuel consumption approximately by 30-65% compared to air-fuel mixture. It also falls to low NO_X emission during high levels of ingress air, which is essential for economical use. In this work it lowered scaling losses, refractory wear during reheating and ladle preheating respectively by improving the steel quality to be produced during casting. It is also seen that for low calorific value (below 7-7.5 MJ/Nm^3) gases such as top gas released from the furnace, use of oxyfuel combustion is an absolute requirement. With the advances in today's technology, combining air-fuel and flameless oxyfuel can create semi-flameless combustion without replacing the air-fuel burners. The paper highlights the working of flameless oxyfuel and its application and also presents the results that have been achieved in controlling pollution and consumption.

1.Introduction

Oxyfuel has taken over the air fuel method of heating in terms of reheating and annealing of furnaces, vessels and so on due to its improved thermal efficiency, the heating rate, uniformity of temperature and increased productivity and also that less amount of fuel is required to heat the product to the desired temperature with minimal CO_2 and NO_X emissions. Now flameless oxyfuel, increase in throughput capacity, fuel saving and reduction of emission of CO_2 are up to 50% along with the reduction of NO_X emissions and scaling losses. In heating, if all the reheating and annealing furnaces would employ oxyfuel combustion, the CO_2 emissions from the world steel industries would be reduced by over 100 million tons per annum. Particularly in vessel preheating using flameless oxyfuel, great benefits are shown. An excellent economic outcome has been obtained from ladle and converter preheating using flameless oxyfuel by converting furnaces and vessel preheating stands into all oxyfuel operating showing energy savings from 25% to 75%, excluding the savings in energy needed to bring natural gas from its sources to the combustion point. During usage of oxyfuel, the systems increased the oxygen content of the combustion air with encouraging results of reduced fuel consumption and increased output (tons per hour) [1].

1.1. Ladle

In a foundry, a ladle is a vessel used to transport and pour out molten metal (as shown in Figure 1). Ladles differ in size ranging from hand carried vessels which resemble a kitchen ladle and have a carrying size of up to 20 kilograms or to large size steel mill ladles that can carry up to 300 tons (330 tons). Most of the non-ferrous foundries also use ceramic crucibles for transporting and pouring molten metal and will also refer to these as ladles. The basic design can therefore include many variations that improve the usability of the ladle for specific tasks, e.g., [2]:

● **Casting Ladle:** This type of ladle is used for pouring molten metal into moulds meant for producing casting/cast products.

● **Transfer Ladle:** Moving a large amount of molten metal from one process to another is carried out by this type of ladle or from a primary stage melting furnace to a holding furnace or auto-pour unit center.

● **Treatment Ladle:** For changing some aspects or treating molten metal to turn it into alloys and to take place within the ladle, e.g., converting cast iron to steel by the addition of various elements into the ladle.

Molten Steel
98% Fe
0.04-1.5% C
1% Mn
Various Alloys
3000°F
Fluidity ~6 cp

Figure 1. ladle containing molten steel, adapted from [2].

Tele:
E-mail address: yunus.mohammed@rediffmail.com

1.2. Pour Designs

Ladles are classified into "*lip pour*" design, "*teapot spout*" design, "*lip-axis*" design or "*bottom pour*" design [3]:

● The "lip pour" design ladle is tilted, and molten metal flows out of the ladle like water from the pitcher.

● The "teapot spout" design ladle resembles a teapot, takes a liquid from the base of a ladle and pours it out through a lip-pour spout. Any of the impurities present in the molten metal will form on the top of the metal so by taking the metal from the base of the ladle, the impurities are not poured into the mould. The same idea is behind the bottom pour process.

● The "lip-axis" design ladle has the pivot point of the vessel as close to the tip of the pouring spout as is practicable and thus when the ladle is rotated the actual pouring point has very little movement. Lip-axis pouring is often used on molten metal pouring systems where there is a need to automate the process as much as possible and the operator controls the pouring operation at a remote distance.

● The "bottom pour" design ladle in which a stopper rod is inserted into a tapping hole in the bottom of the ladle. To pour metal the stopper is raised vertically to allow the metal to flow out the bottom of the ladle. To stop pouring the stopper rod is inserted back into the drain hole. Large ladles in the steelmaking industry may use slide gates below the taphole.

2. Ladle Pre-heating

Due to the importance of drying a new ladle lining to avoid an explosion after adding molten metal observed by operators from past few years in both steel production plants and foundries, the drying or heating operation of ladles has become a necessary process. Ensuring preheating of the ladle lining is both important to the process as well as ensuring the product does not cool excessively and also increases the life of the lining materials. The range of ladle preheating systems operating up to 1300°C. These systems can be manual, or power slew, and all come with local burner control and temperature detector [4]. From few years, in steel and foundry plants, operators started recognizing the importance of drying ladle refractory lining to avoid an explosion at the time of adding molten metal. Thus, the drying or heating operation of ladles is often called ladle preheating. These ladles need preheating, so that thermal shock and damage to the refractory lining and temperature drop in the ladle are minimized. These inventions relate to steelmaking and more particularly to a method of preheating steelmaking ladles. The ladles size may be as large as enough to hold molten steel from 30 to 200 tons or more. To carry out continuous steel production, several ladles need to be rotated through the melt shop and casting shop simultaneously. Thermal state of the ladles plays an important role on the length of the operation in producing steel. The refractories lining of the ladle is continuously be heated to the same temperature (1482 °C to 1593°C) equal to molten steel. The ladles sometimes recycled through the melt and casting shops will cool as the molten steel is discharged into the caster, and cool further before the ladle is returned for recharging in the melt shop. Moreover, if ladles are taken offline in the steel production cycle after cooling down to room temperature, and the replacement ladles have to be heated from ambient temperature to operating temperature. Furthermore, ladles required to be preheated for reducing the length of the operation, facilities and increasing melt shop capacity during steel making [5].

In other words, ladles need to be heated up after pouring molten metal as heat will be absorbed by the refractory lining

from the melt. That means the ladles will be cool down when emptied and the duration of a ladle remaining empty is variable and unpredictable at times. Sometimes due to major delays like repairing hours ladle remains cold. Under this cold condition, the duration of steelmaking operation will be considerably increased as ladles be heated with the molten metal to steel producing temperature.

Usually preheating of ladles has been performed with a gas-fired burner which injected a combustion flame into the interior of the ladle to the desired temperature between 982 °C and 1093°C. The temperature of the ladle during the preheating process may be measured and controlled using a thermocouple or pyrometer. Due to this, damage to the refractories from overheating by a conventional method of ladle preheating. They also have involved consumption of large quantity of fuel, such as natural gas, and have resulted in [6].

Accordingly, there could be many methods to reduce the fuel consumption during preheating of the ladle refractories for use in steelmaking to the desired temperature efficiently while inhibiting damage and wear of the refractories from overheating [7]. Figure 2 is a schematic drawing showing a ladle and a preheater for use in a method of preheating steelmaking ladles [7, 8].
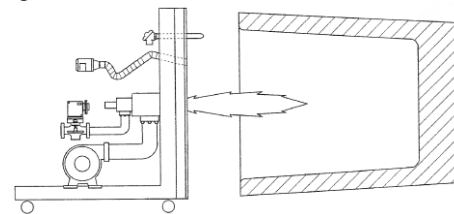

Figure 2: ladle and a pre-heater for method of pre-heating steelmaking ladles, adapted from [7, 8]

2.1. Ladle Pre-heater

A ladle preheater is used for removing the moisture from the ladle to prevent the gas formation or reaction with the liquid metal. It could be designed for both vertical and horizontal type depending on the strength, capacity and size of the ladle. A vertical ladle preheater is one which is designed to have fired from the top to downwards. The preheater will be on an axle so that cowl can rotate up to 360°. The cowl will be lined with refractory to increase the flue travelling time, whereas a horizontal one is designed to fire horizontally. The ladle will be positioned opposite the flame direction with a minimum gap between the burner and the burner firing which will be focused on the side walls of the ladle. In ladle preheaters, the flame will be positioned in such a way as to slide on the ladle side wall to ensure faster heat penetration. A properly designed ladle preheater gives a far more efficient and controlled method of pre-heating a ladle than the traditional methods of using a gas flame. The energy consumption of these systems is notoriously poor and, in some cases, heating a cold ladle using these methods can lead to efficiencies of less than 10%. They can also lead to uneven distribution of heat so that the ladle has both hot and cold spots leading to premature lining failure and variable metal quality. Therefore, a ladle preheater can be economical, more fuel efficient, reduces damages to the refractory lining by proper design. It also minimizes the reduction of the temperature loss of the metal while it is in the refractory lining damage due to a poorly dried lining still having a significant moisture content and ensuring that the ladle is evenly pre-heated [9].

2.2. Necessity to Pre-heat the Ladle

The following procedure are followed [10]:

● Preventing explosions resulting from the sudden conversion of moisture entrapped in the ladle refractory to steam when molten metal is added.

● Removal of metal solidification in the ladle head which requires maintenance time, labor to remove and can affect the metal quality and pouring from the ladle.

● Decreasing pouring temperatures to save metal heating costs.

● Reducing thermal shock to the ladle lining to increase the lining life.

● Enhancing the life of lining from controlled temperatures during drying of new linings.

● Decreasing the losses of heat from molten metal during a continuous casting operation.

● Rapid temperature losses can result in metal freezing in the ladle and tundish nozzles.

2.3. Method of Pre-heating Steelmaking Ladles

A method for preheating a ladle used in steel production to reduce fuel consumption in heating and achieving accurate temperature control. The preheating process temperature can be monitored by a burner unit based on pyrometer measurements of refractories. The heating unit includes an emissive coating to prevent heat loss, and a valve mechanism to vary the flame size of the burner accurately during an idle stage of the preheating process. A preheating method in a steelmaking ladle having an open upper portion and inner refractory surfaces comprises the following steps [11]:

a) Placing a preheater having a radiant reflective surface and at least one burner adjacent to open upper portion of the steel producing ladle comprising an emissive coating.

b) Heating the inner refractory surfaces of the steel producing ladle to the desired temperature by combustion through the preheater burner.

c) Placing a pyrometer to measure current temperature of the inner refractory surfaces of the steel producing ladle at the time of heating.

d) Electrical signals generated should indicate the current temperature of the inner refractory surfaces of the steel producing measured by the pyrometer.

e) Controlling the preheater temperature at the inner refractory surfaces of the steel producing ladle using the generated electrical signals by the pyrometer.

The method of preheating a steelmaking ladle is done where the inner refractory surfaces of the steelmaking ladle are heated to a temperature between 982°C and 1149°C [4].

In this method, open upper portion of the steel producing ladle is positioned substantially opposite the radiant reflective surface with an emissive coating of the pre-heater. A gap of no more than 3 to 8 inches is maintained between the radiant reflective surface of the pre-heater and the open upper portion of the steelmaking ladle where the emissive coating is a silicide coating which is selected from the group consisting of molybdenum silicide, tantalum silicide, niobium silicide and a combination thereof. An emissive coating has an emissivity between 0.85 and 0.95. The radiant reflective surface with the emissive coating is disposed on a refractory surface of the pre-heater. It consists of a burner heating unit, the method comprising of an additional step of regulating a fuel flow rate, air and oxygen to the burner during an idle state of the burner between preheating cycles is set to not higher than 600 SCFH during the idle state and temperature readings obtained from a pyrometer. It comprises of positioning the heating unit adjacent to an open upper portion of the steelmaking ladle, wherein the heating unit comprises a radiant reflective surface having an emissive coating which is disposed on a refractory surface of the heating unit. It also includes heating inner refractory surfaces of the steelmaking ladle to the desired temperature by combustion through the burner of the heating unit where the radiant reflective surface facilitates preheating of the steelmaking ladle [12]. The positioning of a pyrometer of the pre-heater is needed to measure current temperature of an inner refractory surface of the steel producing ladle during preheating and to control the temperature of the preheating by the pre-heater. [1].

3. Ladle Pre-heating Process

The following procedure were followed as mentioned in [13]:

● Keep the new ladle on the ladle preheat stand as near to the burner as possible.

● Start the first heating to remove any moisture in the lining by keeping the flame low (duration 2-3 hrs.).

● Turn off the burner and start the second preheating with a full flame touching up to the ladle bottom.

● Wait until the inside of the ladle becomes dull red in color (approx. temp 1200°C).

● Lift the ladle when required.

3.1. Ladle Pre-heating Cycle

Figure 4 illustrates the ladle pre-heating cycle. The following steps were followed:

● Raising temperature room into 300°C in 3 hours at 100°C/hr.

● Soaking at 300°C for 3 hours.

● Raising temperature from 300°C to 1200°C in 9 hours at 100°C/hr.

● Soaking at 1200°C for 5 hours.

● If preheating is prolonged, lowering temperature from 1200 to 1000°C in 2 hrs.
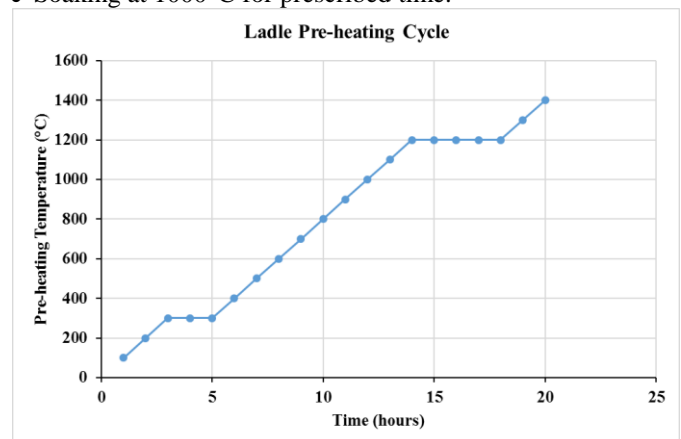
● Soaking at 1000°C for prescribed time.

Figure 4. ladle pre-heating cycle.

3.2. Conceptual System

A ladle preheating station consists of a single firing hood fitted with one burner. The hood is mounted onto a trolley is driven by 0.5HP geared motor for cross movement. Limit switches and mechanical stoppers on both directions restrict this cross movement. The hood with the cross trolley is mounted on the main trolley, which is capable of moving longitudinally on a rail track with an Electro Mechanical through geared motor or the movement. The ladle is positioned in front of the ladle firing hood on a suitable ladle stand.

Once the ladle is placed on the firing hood is to be moved right in front of the ladle (as close as possible) by moving both the main and firing hood trolley. The burner of the firing hood is positioned at the center. The burner is provided with automatically controlled butterfly valves for combustion and atomizing air. The burner is also provided with an oil control sensatory valve. The centrifugal steel plate air blower of capacity 700 CFM at 40 WG driven by 10 HP motor, directly driven is provided. The blower is placed on the main trolley. The airline connecting the burner from the blower is provided with a motorized butterfly valve. The end connection is of flexible type hose to facilitate cross trolley movement. A duplex pumping filtering and pressure control composite unit are provided near the main trolley and a ring main pipe line at a convenient level for flexible connection. The firing hood is provided with a motorized oil control valve near the burner. This oil line also has an oil shut off solenoid valve. The connection between the rings main on these control pipelines is through a quick release braided flexible hose [14].

The firing hood is provided with a thermocouple for sensing the temperature during heating and the signal is fed into an on/off type digital PID controller provided on a separate control panel to set the desired ladle preheating temperature. The controller which actuates the motorized butterfly valve on the combustion air line and oil line which facilitates high/low firing inside the ladle for controlled heating of the ladle [3]. The burner is provided with a pilot burner with an igniter, a UV flame sensor and a flame monitor to ensure the oil throughput to the burner is cut off in case of flame failure [3, 14].

A heating device for preheating a container, such as a ladle transfer, transferring liquid metal, ladle surface is lined with refractory material, wherein the container is heated in a heating stand having a container closure lid, is characterized by the use of porous burners for heating the container and keeping it warm. The vessel is heated in a heating stand that has a vessel cover, for heating and maintaining the vessel temperature. Therefore, the porous burners are constructed and arranged in the form of arrays. [14].

4. Flameless Oxyfuel

In recent times, flameless oxy fuel combustion has been employed with the aim of communicating the visual aspect of the combustion type (either the flame is no longer seen or is easily detected) or that combustion is extended in time and space such as in volume combustion. Such a flame exhibits a uniform and lowers the temperature with the same amount of energy as shown in Figure 5. The uniform reaction of mixture of fuel and oxidant through the flame volume at a rate partial pressures of reactants and their temperature. Flameless oxy fuel burners efficiently disperse the combustion gases throughout the furnace to ensure more efficient and allows uniform heating of the material with a limited number of burners installed. NOx formation reduces as the flame temperature lowered substantially is important from a global warming point of view because global warming will be reduced equivalent to 300 times that of CO_2. Figure 6 shows the increase in the efficiency using flameless oxy fuel. [15].

Oxy-fuel burners have always been powerful, and compact to facilitate an exchange of existing burners and retrofit of new burners. Moreover, flameless oxy-fuel combustion adds advantages of opening up of new applications with a substantially decreased impact of the environment.

This reduces the flame temperature to prevent the formation of thermal NO_X and maintains homogenous heating. The picture (refer figure 5) depicted flameless oxy-fuel combustion with a diluted and changed into transparent flame.
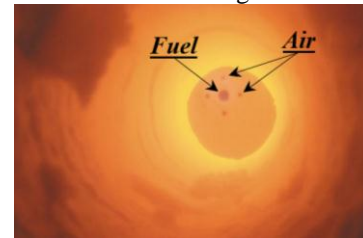
Figure 5. uniform volume combustion and low temperature flame, adapted from [15].
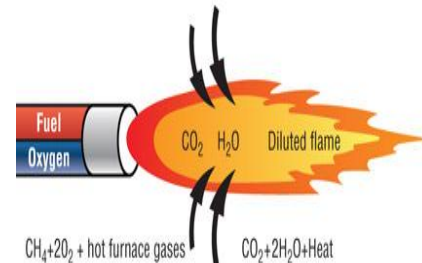
Figure 6. flameless oxyfuel combustion diluted by the hot furnace gases, adapted from [15].

4.1. Advantages of using Flameless Oxyfuel in Ladle Pre-heating

• Surface quality will be improved.

• Temperature uniformity of the slabs is easily achieved.

• Ideal heating curve suggested by the control system can be achieved more easily.

• Improves the plant environment greatly by reducing smoke emitting from the furnace.

• It reduces NO_X emission by 45%.

• Reductions in SO_2 and CO_2 emissions. Therefore, decreases fuel consumption by 25%.

• Increases overall Production process by 15-20%. No negative impact on the surface quality.

4.2. Types of Flameless Oxyfuel

There are two types of flameless oxyfuel used, namely Diesel Fuels (HSD/LDO) and LPG (Liquefied Petroleum Gas). Industries require cost-effective and efficient energy solutions for their various processes. In most applications, LPG is used as a clean and cost-effective fuel in furnaces, kilns, ovens, dryers, boilers, thermic fluid heaters, hot air generators and so on. Besides, providing numerous other benefits. LPG's energy density (calorific value per unit mass) is higher than conventional fuels, and there are no residues and unburnt products of combustion, making it a compact and energy-efficient fuel. LPG is cost-effective compared to electricity, Diesel (HSD/LDO) and Petrol. It gives you savings in fuel bills as well as other associated costs. It provides superior product quality as the temperature can be controlled easily and accurately. It is clean and environmentally-friendly. LPG gives a clean blue flame. Because it does not produce harmful emissions such as soot, smoke, unburnt carbon particles. LPG is easy to operate, much simpler to maintain owing to the availability of fewer accessories. Neither it requires frequent cleaning, nor it gives instant heat. Hence, the desired temperature is reached in quick time increasing productivity. Neither LPG nor its products of combustion contaminate the product ensuring that the product is hygienic and of superior quality [6].

5. Results and Discussions
5.1. Economic Analysis

Graphs 7, 8 and 9 shows the variation of the amount of fuel HSD/LPG consumed by each ladle in pre-heating during a course period of 8 months in pre-heating ladles. As seen in the graph it is found that consumption of HSD to pre-heat ladle is more than that of LPG. Using LPG is economical as consumption of it and pollutants after combustion are lesser than that of HSD [16]. But, it is also evident that HSD is used more frequently than LPG in pre-heating of ladles. It is found that though the consumption of LPG per ladle is less than HSD the cost factor comes on top. It is seen that the cost of HSD is much lower than Industrial LPG and HSD is more freely available in the necessary quantities. Also storage of LPG is very difficult because of its high pressure. It requires high pressure containers to store gas which increases its storage requirements whereas HSD can be stored normally [17].

Taking into account all aspects HSD is superior to LPG. Also, pre-heating of ladles is faster using LPG as the flame is instant and does not require any external aid to increase flame propagation. Ladle pre-heaters using LPG are simple in construction as no aid is required to increase the velocity of the flame as in pre-heaters that use HSD as fuel. Pre-heating of ladles using HSD requires external high pressure for flame propagation. Extra blowers are attached to the system to increase the pressure of inlet HSD for pre-heating of ladles. The flame so produced is not instant and pre-heating of ladles is slower than that of ladle pre-heaters using LPG.
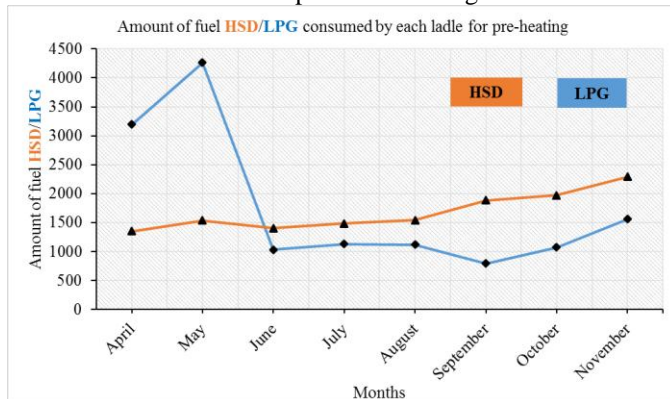
Figure 7. amount of fuel HSD/LPG consumed by each ladle for pre-heating during 8 months.
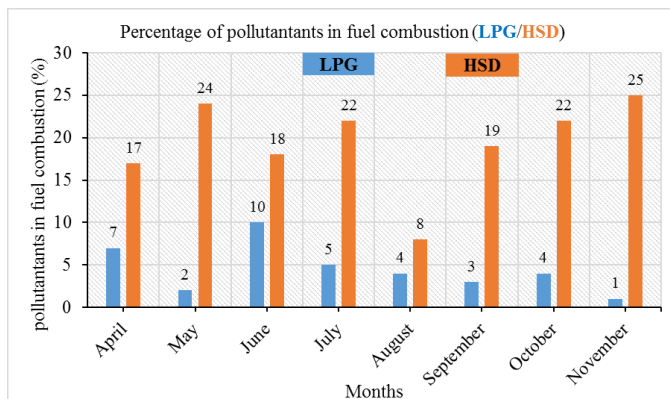
Figure 8. percentage of pollutantants in fuel combustion.
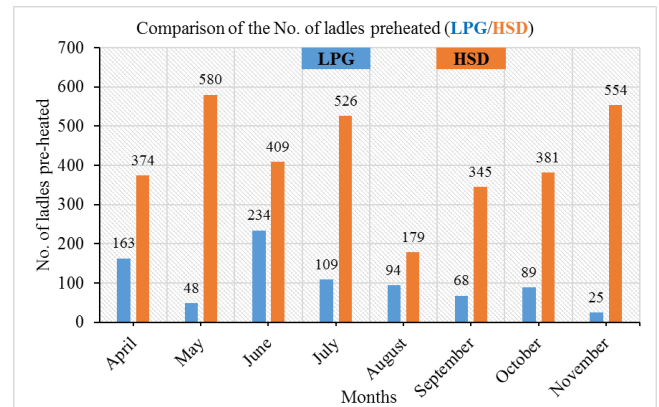
Figure 9. comparison of number of ladles preheated.

5.2. Energy Efficiency

To determine energy efficiency, in an air-fuel burner the burner flame contains nitrogen from the combustion air. A significant amount of the fuel energy is used to heat up this nitrogen. The hot nitrogen leaves through the stack, creating energy losses. When avoiding the nitrogen ballast, by the use of industrial grade oxygen, then not only is the combustion itself more efficient but also the heat transfer. Oxyfuel combustion influences the combustion process in many ways. The first obvious result is the increase in thermal efficiency due to the reduced exhaust gas volume, a result that is fundamental and valid for all types of oxyfuel burners. Additionally, the concentration of the highly radiating products of combustion, CO_2 and H_2O, is increased in the furnace atmosphere. For heating operations these two factors lead to a higher heating rate, fuel savings, lower CO_2 emissions and, if the fuel contains sulphur, lower SO_2 emissions, today's best air-fuel solutions need at least 1.3 GJ to heat a tons of steel to the right temperature for rolling or forging [6].

6. Concluding Remarks

The following conclusions have been drawn from the above studies:

• Air fuel mixture has an overall heating thermal efficiency of 50-60% whereas an oxyfuel (with flame) provides 80%.

• With flameless oxy-fuel, not only does the overall thermal efficiency of heating increase but also fuel consumption or saving of energy in a reheating process is at least 26% at times and frequently it may be even more than 60% compared to air-fuel.

• It is possible to operate a reheat furnace with fuel consumption below 1 GJ per tons with up to 50% reduction in CO_2 emissions and substantial savings in NO_X emissions.

• It has been seen that flameless oxyfuel combustion has many considerable advantages over conventional oxyfuel and many more over any kind of air-fuel combustion such as the fact that improved uniformity of temperature distribution in turn, reduces further fuel consumption.

• In our station, oxy-fuel solutions are used in forge shops, annealing operations and ladle pre-heating. They have improved operational flexibility, heating performance and temperature uniformity while reducing scale formation and also reducing fuel consumption.

• Flameless oxyfuel increased the throughput rate up to 50% and increased production using few furnaces in operation thus providing increased flexibility.

• That means it uses only two furnaces and that these are enough to cover the production work of 3 furnaces thus resulting in decreased fuel consumption.

• Increased capacity can also be used to prolong soaking times. Thanks to the reduced time at elevated temperatures, oxyfuel leads to reduced scale losses, at many installations as high as 50%.

• In the present study, vessel preheating and ladle preheating using flameless oxyfuel, showed considerable benefits with very good economic output.

References

1. Duhamel, S. and D. Verelle, Developments in the Refractory Design of Lids for Ladle Preheating in Dunkirk Steelworks. The Refractories Engineer, Journal of the Institute of Refractories Engineers, 2000: p. 29-33.

2. Wikipedia. Ladle (foundry). 19/03/2016 [cited 2016 17/04/2016]; Available from: https://en.wikipedia.org/wiki/Ladle_(foundry).

3. Kracich, R.E. and K. Goodson, Iron and Steelmaker, 1996. 23(7): p. 41.

4. Bonadia, P., et al., Refractory Selection for Long-Distance Molten Aluminum Delivery. American Ceramic Society Bulletin, 2006. 85(8): p. 9301-9308.

5. Turkdogan, E.T., Ironmaking and Steelmaking. 1988. 15: p. 311.

6. Glaws, P.C. and G.J.W. Kor, The Timken Company, internal reports.

7. Szekely, J., G. Carlsson, and L. Helle, in Ladle Metallurgy, Materials Research and Engineering Series, ed. B. Ilschner and N.J. Grant, 1988, New York: Springer-Verlag.

8. GALEWSKI, G.S., Method of preheating steelmaking ladles, 2008, Google Patents.

9. Hensler, J.M., et al., Operational Testing of an Electrlc Ladle Preheater at Copperweld Steel Company. Iron & Steelmaker, 1988.

10. Committee, A.S., Specification for design of hot metal Ladle Furnace Furnaces, in Association of Iron and Steel Engineers Standard No.91951: Pittsburgh, September 30. p. LS1 - LS16.

11. Cotchen, J.K., Int. Symp. On Ladle Steelmaking and Furnaces (Montreal: The Met. Soc. of CIM), 1988: p. 111.

12. Nandi, D.N., Handbook on Refractories, 1987, New Delhi: Tata McGraw-Hill.

13. Sadual, M.R., S.K. Swain, and M. Kumar, Recent Trend on Tundish Design, 2006, India: McGraw-Hill.

14. Hoeffken, E., H.D. Pflipsen, and W. Florin. Proc. Int. Conf. On Secondary Metallurgy, 1987.

15. Schéele, J.v., V. Zilka, and R. Eichler, Successful Use Of Flameless Oxyfuel In Reheat Furnaces And Ladle Preheating, Brno, Czech Republic, EU, 2011.

16. Engel, R., R. Marr, and E. Pretorius, Keeping Current series, Iron and Steelmaker, 1996: p. 23-24.

17. Ototani, T., in Calcium Clean Steel, Materials Research and Engineering Series (B. Ilschner and N. J. Grant, eds.), 1999, New York: Springer Verlag.

Natural Convective Heat Transfer for Inclined Narrow Plate

VANKAR DURGESH[1], C. SUDHAKAR[2]

[1]PG Scholar, Dept of Mechanical Engineering, Siddhartha Institute of Engineering and Technology, Hyderabad, TS, India,
E-mail: durgesh7563@gmail.com.

[2]Professor, Dept of Mechanical Engineering, Siddhartha Institute of Engineering and Technology, Hyderabad, TS, India,
E-mail: saisudha343@gmail.com.

Abstract: This project mainly deals with the design, analysis and manufacture of inclined plate. The inclined plate is designed and analyzed, the manufacturing process has been studied with the help of solid works software, the component is meshed, analysis is done in ansys software, the thermal behavior is studied, and the results are tabulated. The various stresses acting on the cylinder head under various loading conditions have been studied. In the preset thesis, work has been taken up on the following aspects to cover the research gaps and to present the results based on the systematic studies:

- Temperature distribution and heat flow through the cylinder head of an engine.
- Fea analysis of the cylinder head to measure temperature at the points where it is not possible to find out practically and to observe the heat flow inside the cylinder head.

Keywords: Inclined Narrow Plate ; Solidworks; Ansys; Thermal Analysis.

I. INTRODUCTION

Natural convection is a mechanism, or type of heat transport, in which the fluid motion is not generated by any external source (like a pump, fan, suction device, etc.) but only by density differences in the fluid occurring due to temperature gradients. In natural convection, fluid surrounding a heat source receives heat, becomes less dense and rises. The surrounding, cooler fluid then moves to replace it. This cooler fluid is then heated and the process continues, forming convection current; this process transfers heat energy from the bottom of the convection cell to top. The driving force for natural convection is buoyancy, a result of differences in fluid density. Because of this, the presence of a proper acceleration such as arises from resistance to gravity, or an equivalent force (arising from acceleration, centrifugal force or Coriolis Effect), is essential for natural convection. For example, natural convection essentially does not operate in free-fall (inertial) environments, such as that of the orbiting International Space Station, where other heat transfer mechanisms are required to prevent electronic components from overheating.

A. Convection

Convection is the concerted, collective movement of groups or aggregates of molecules within fluids (e.g., liquids, gases) and rheids, through advection or through diffusion or as a combination of both of them. Convection of mass cannot take place in solids, since neither bulk current flows nor significant diffusion can take place in solids. Diffusion of heat can take place in solids, but that is called heat conduction. Convection can be demonstrated by placing a heat source (e.g. a Bunsen burner) at the side of a glass full of a liquid, and observing the changes in temperature in the glass caused by the warmer fluid moving into cooler areas. Convective heat transfer is one of the major types of heat transfer, and convection is also a major mode of mass transfer in fluids. Convective heat and mass transfer take place both by diffusion – the random Brownian motion of individual particles in the fluid – and by advection, in which matter or heat is transported by the larger-scale motion of currents in the fluid. In the context of heat and mass transfer, the term "convection" is used to refer to the sum of adjective and diffusive transfer. In common use the term "convection" may refer loosely to heat transfer by convection, as opposed to mass transfer by convection, or the convection process in general.

Sometimes "convection" is even used to refer specifically to "free heat convection" (natural heat convection) as opposed to forced heat convection. However, in mechanics the correct use of the word is the general sense, and different types of convection should be qualified for clarity Convection can be qualified in terms of being natural, forced, gravitational, granular, or thermo magnetic. It may also be said to be due to combustion, capillary action, or Marangoni and Weissenberg effects. Heat transfer by natural convection plays a role in the structure of Earth's atmosphere, its oceans, and its mantle. Discrete convective cells in the atmosphere can be seen as clouds, with stronger convection resulting in thunderstorms. Natural convection also plays a role in stellar physics.

Natural Convection: In natural convection, the fluid motion occurs by natural means such as buoyancy. Since the fluid velocity associated with natural convection is relatively low,

the heat transfer coefficient encountered in natural convection is also low.

Mechanisms of Natural Convection: Consider a hot object exposed to cold air. The temperature of the outside of the object will drop (as a result of heat transfer with cold air), and the temperature of adjacent air to the object will rise. Consequently, the object is surrounded with a thin layer of warmer air and heat will be transferred from this layer to the outer layers of air. Natural convection heat transfer from a hot body is the temperature of the air adjacent to the hot object is higher, thus its density is lower. As a result, the heated air rises. This movement is called the natural.

- **Convection Current:** That in the absence of this movement, heat transfer would be by conduction only and its rate would be much lower. In a gravitational field, there is a net force that pushes a light fluid placed in a heavier fluid upwards. This force is called the buoyancy force. Buoyancy force keeps the ship float in water. The magnitude of the buoyancy force is the way to fluid displaced by the body.
- **Effect of Fin Length:** A vertical enclosure the dependence of the Nusselt number (Nu) on fin length (L/H) for different values of Rayleigh number (Ra) ranging from 104 to 3x105 is shown in fig. 2. Nu is plotted against Ra for different values of L/H as a parameter. It can be clearly seen that at any Rayleigh number the effect of increasing/H increases Nu. This increase in Nu with Increasing L/H can be attributed to the increase of heat transfer surface area with increasing L/H. Possibility of formation of separate convection cell between two adjacent fins increases due to increase in L/H for a vertical enclosure and this leads in an enhancement of heat transfer rate.
- **Natural Convection over Surfaces:** Natural convection on a surface depends on the geometry of the surface as well as its orientation. It also depends on the variation of temperature on the surface and the thermo physical properties of the fluid. Note that the velocity at the edge of the boundary layer becomes zero. It is expected since the fluid beyond the boundary layer is stationary.

Natural Convection Correlations: The complexities of the fluid flow make it very difficult to obtain simple analytical relations for natural convection. Thus, most of the relationships in natural convection are based on experimental correlation. The Rayleigh number is defined as the product of the Graphs of and Pr and tl number.

$$Ra = Gr\,\mathrm{Pr} = \frac{g\beta(T_s - T_\infty)\delta^3}{\nu^2}\mathrm{Pr} \qquad (1)$$

Convection is as fallowing

$$Nu = \frac{h\delta}{k} = CRa^n \qquad (2)$$

Natural Convective Heat Transfer from Two Adjacent Narrow Plates: Numerical studies of the interaction of the natural convective flows over two adjacent vertical and inclined narrow isothermal flat plates in the laminar flow region are discussed. Two cases are considered. In one case, the plates are horizontally adjacent to each other, the plates being horizontally separated while in the other case, one plate is symmetrically placed above the other plate the plates being vertically separated. Attention has been given to the effects of the inclination angle of the plates to the vertical, to the effects of the vertical or horizontal dimensionless gap between the heated plates, and to the effects of the dimensionless plate width on the mean heat transfer rates from the two heated plates for a wide range of Rayleigh numbers. It is shown that when there are two adjacent narrow flat plates with a relatively small gap between the plates the flow near the adjacent plates is altered compared to that over a single narrow plate and this can lead to a significant change in the mean heat transfer rate compared to that from a single isolated plate under the same conditions. Empirical equations for both the case of horizontally separated and vertically separated plates are given

B. An Interaction of Natural Convective Heat Transfer from Two Adjacent Isothermal Narrow Vertical And Inclined Flat Plates

Natural convective heat transfer from a two narrow adjacent rectangular isothermal flat plates of the same size embedded in a plane adiabatic surface, the adiabatic surface being in the same plane as the surfaces of the heated plates, has been numerically investigated. The two plates have the same surface temperature and they are aligned with each other but are separated form each other by a relatively small gap. Results for the case where the plates are vertical and where they are inclined at positive or negative angles to the vertical have been obtained. It has been assumed that the fluid properties are constant except for the density change with temperature which gives rise to the buoyancy forces, this having been treated using the Boussinesq approach. It has also been assumed that the flow is symmetrical about the vertical center plane between the two plates. The solution has been obtained by numerically solving the full three-dimensional form of governing equations, these equations being written in dimensionless form. The solution was obtained using the commercial finite volume method based cfd code, FLUENT. The solution has the Rayleigh number, the dimensionless plate width, the angle of inclination, the dimensionless gap between two flat plates, and the Prandtl number as parameters. Results have only been obtained for a Prandtl number of 0.7 Results have been obtained for Rayleigh numbers between 103 and 107 for plate width-to-height ratios of between 0.15 and 0.6, for gap between the adjacent edges to plate height ratios of between 0 and 0.2, for angles of inclination between +45° and −45°.

II. INTRODUCTION TO CAD AND SOLIDWORKS
A. Introduction of Computer-Aided Design And Drafting

It also known as computer-aided design and drafting (CADD), is the use of computer technology for the process of design and design-documentation. Computer Aided Drafting describes the process of drafting with a computer. CADD software, or environments, provides the user with input-tools for the purpose of streamlining design processes;

drafting, documentation, and manufacturing processes. CADD output is often in the form of electronic files for print or machining operations. The development of CADD-based software is in direct correlation with the processes it seeks to economize; industry-based software (construction, manufacturing, etc.) typically uses vector-based (linear) environments whereas graphic-based software utilizes raster-based environments. CAD may be used to design curves and figures in two-dimensional (2D) space; or curves, surfaces, and solids in three-dimensional (3D) objects.

B. Introduction To Solidworks

Solid Works is a 3D solid modeling package which allows users to develop full solid models in a simulated environment for both design and analysis. In Solid Works; you sketch ideas and experiment with different designs to create 3D models. Solid Works is used by students, designers, engineers, and other professionals to produce simple and complex parts, assemblies, and drawings. Designing in a modeling package such as Solid Works is beneficial because it saves time, effort, and money that would otherwise be spent prototyping the design.

Solid Works Components Parts: Before we begin looking at the software, it is important to understand the different components that make up a Solid Works model.

Part:
- The first and most basic element of a Solid Works model is a Part.
- Parts consist of primitive geometry and feature such as extrudes, revolutions, lofts, sweeps, etc.
- Parts will be the building blocks for all of the models that you will create.

Assembly:
- The second component is the assembly. Assemblies are collections of parts which are assembled in a particular fashion using mates (constraints).
- Any complex model will usually consist of one, or many assemblies.
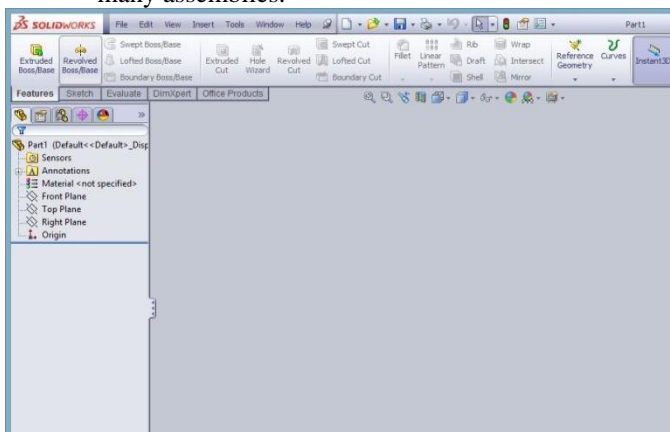
Fig.1.

Drawing: The third and final component in Solid Works is the Drawing.

- A drawing is the typical way to represent a 3D model such that any engineer (or manufacturer) can recreate your part.
- Drawings are important because they provide a standard way of sharing your design.

Let's begin by creating a new part. To do this, click on Part, then OK. Once you do this, you will be brought into the modeling view which should open several toolbars and panes.

C. Terminology

These terms appear throughout the Solid Works software and documentation.

Origin: Appears as two blue arrows and represents the (0, 0, 0) coordinate of the model. When a sketch is active, a sketch origin appears in red and represents the (0, 0, 0) coordinate of the sketch. You can add dimensions and relations to a model origin, but not to a sketch origin.

Plane: Flat construction geometry. You can use planes for adding a 2D sketch, section view of a model, or a neutral plane in a draft feature, for example.

Axis: Straight line used to create model geometry, features, or patterns. You can create an axis in different ways, including intersecting two planes. The Solid Works application creates temporary axes implicitly for every conical or cylindrical face in a model.

Face: Boundaries that help define the shape of a model or a surface. A face is a selectable area (planar or non planar) of a model or surface. For example, a rectangular solid has six faces.

Edge: Location where two or more faces intersect and are joined together. You can select edges for sketching and dimensioning.

Vertex: Point at which two or more lines or edges intersect. You can select vertices for sketching and dimensioning.

User Interface: The Solid Works application includes user interface tools and capabilities to help you create and edit models efficiently, including:

Windows Functions: The Solid Works application includes familiar Windows functions, such as dragging and resizing windows. Many of the same icons, such as print, open, save, cut, and paste are also part of the Solid Works application.

Solid Works Document Windows: Solid Works document windows have two panels. The left panel, or Manager Pane, contains:

Feature Manager /design tree: Displays the structure of the part, assembly, or drawing. Select an item from the Feature Manager Design tree to edit the underlying sketch, edit the feature, and suppress and un suppress the feature or component, for example.
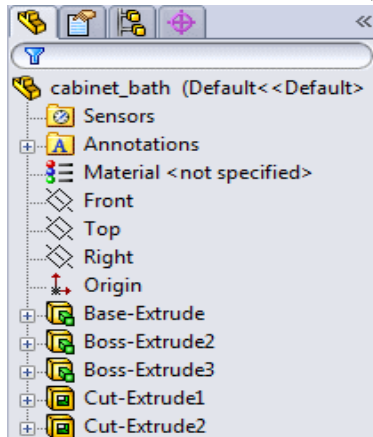
Fig.2.

Property Manager: Provides settings for many functions such as sketches, fillet features, and assembly mates.

Configuration Manager: Lets you create, select, and view multiple configurations of parts and assemblies in a document. Configurations are variations of a part or assembly within a single document. For example, you can use configurations of a bolt to specify different lengths and diameters.

Mouse Buttons: Mouse buttons operate in the following ways:

Left: Selects menu items, entities in the graphics area, and objects in the Feature Manager Design tree.

Right: Displays the context-sensitive shortcut menus.

Middle: Rotates, pans, and zooms a part or an assembly, and pans in a drawing.

Mouse gestures: You can use a mouse gesture as a shortcut to execute a command, similar to a keyboard shortcut. Once you learn command mappings, you can use mouse gestures to invoke mapped commands quickly. To activate a mouse gesture, from the graphics area, right-drag in the gesture direction that corresponds to the command. When you right-drag, a guide appears, showing the command mappings for the gesture directions.

Extrude: The application of this feature is to add or remove the material of a cross section in the normal direction.

Revolve: The application of this feature is to add or remove the material of a cross section in the counter clock direction with reference to an axis.

Mirror: This to create the object with same dimension and to maintain same distance from the reference. The reference which we will take in this operation is Axis, plane and surface.

Datum: This operation is used to create an offset plane with specified dimension.
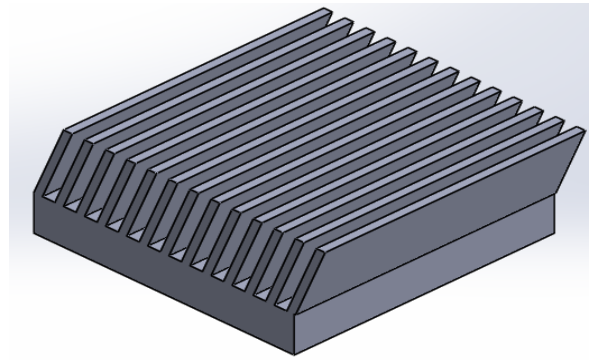
Fig.3.

III. INCLINED FINS

A. Introduction To Fem And Ansys

Introduction To Fem: The finite element method represents an extension of the matrix methods for the analysis of framed structures to the analysis of the continuum structures. The basic philosophy of the method is to replace the structure of the continuum having an unlimited or infinite number of unknowns at certain chosen discrete points. The method is extremely powerful as it helps to accurately analyze structures with complex geometrical properties and loading conditions. In the infinite method, a structure or continuum is discretized and idealized by using a mathematical model which is an assembly of subdivisions or discrete elements, known as finite element, are assumed to be interconnected only at the joints called nodes. The equations, which are obtained using the above conditions, are in the form of force-displacement relationship. Finally, the force-displacement equations are solved to obtain displacements at the nodes, which are the basic unknowns in the finite element method. The basic idea in the finite element method is to find solution of a complicated problem by replacing it by simpler one. Since a simpler one in finding the solution replaced the actual problem, we will be able to find only an approximate solution rather than exact solution. In finite element method, it will often be possible to improve or refine the approximate solution by sending more computational effort. The original body or continuum is then considered as assemblage of these elements connected at a finite number of joints called nodes.

- Equilibrium or steady state or time independent problem,
- Eagan value problem,
- Transient or propagation programs.

General Description of Fem: The step-by-step procedure for static problem can be stated as follows:

- Discretization of continuum
- Selection of proper Interpolation model
- Derivative of element stiffness matrices and load vectors
- Assemblage of element equation to obtain the overall equilibrium equations:
- Solution of systems equations to find nodal values of the displacement:
  - Types of Elements
  - Number of Elements
  - Size of Elements

- Convergence Requirements
- Nodal Degrees of Freedom

Advantages of Fem:

- Its ability to use various size and shape and to modal a structure of arbitrary geometry.
- Its ability to accommodate arbitrary boundary conditions, loading, including thermal loading.
- Its ability to modal composite structures involving different structural components such as stiffening member on a shell and combination of plates, bars and solids, etc.,
- The finite element structure closely resembles the actual structure instead of being quite different obstruction that is hard to visualize.
- The FEM is proven successfully in representing various types of complicated material properties and material behavior (nonlinear, anisotropic, time dependent or temperature dependent material behavior).
- It readily account for non-homogeneity of the material by assigning different properties to different elements or even it is possible to vary the properties within an element according to a pre-determined polynomial pattern.

IV. INTRODUCTION TO ANSYS SOFTWARE

The purpose of a finite element analysis is to model the behavior of a structure under a system of loads. in order to do so, all influencing factors must be considered and determined whether their effects are considerable or negligible on the final result. The ansys program is self-contained general purpose finite element program developed and maintained by swanson analysis systems inc. the program contains many routines, all interrelated and all for main purpose of achieving a solution to an engineering problem by finite element method. Ansys provides a complete solution to design problems. It consists of powerful design capabilities like full parametric solid modeling, design optimization and auto meshing, which gives engineers full control over their analysis. The following are the special features of ANSYS software:

- It includes bilinear elements.
- Heat flow analysis, fluid flow and element flow analysis can be done.
- Graphic package and extensive preprocessing and post processing.
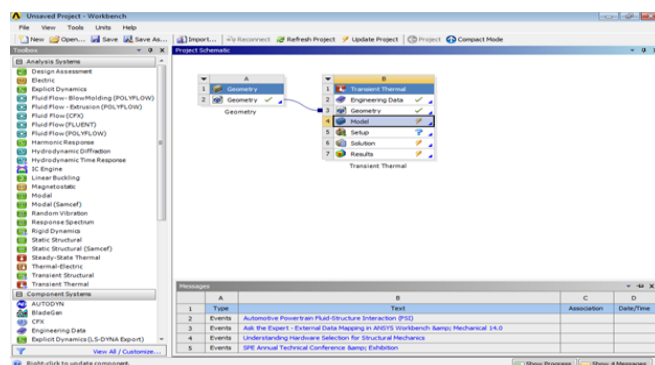
Fig.4.

Meshing: The default meshing controls that the program uses may produce a mesh that is adequate for the model we are analyzing. In this case, we need not specify any meshing controls. However if we do use meshing controls we must set them before meshing the solid model. Meshing controls allow us to establish the element shape, midsize node placement and element size to be used in meshing the solid model, this step is one of the most important of the entire analysis for the decisions we make at this stage in the model development will profoundly affect the accuracy and economy of the analysis. Smart element sizing (Smart sizing) is a meshing feature that creates initial element sizes for free meshing operations. Smart sizing gives the mesher a better chance of creating reasonably shaped elements during automatic mesh generation.

Pre-Processor: The pre-processor stage in ANSYS package involves the following:

- Specify the title, which is the name of the problem.
- Set the type of the analysis to be used, i.e., structural, thermal, fluid, or electro-magnetic, etc.,
- The model may be created in pre-processor or it can be imported from another CAD drafting package through a neutral file format like IGES, STEP
- Apply mesh – Mesh generation is the process of dividing the analysis continuum in to number of discrete parts or finite elements. The finer the mesh, the better the result, but the longer the analysis time. Therefore, the compromise between accuracy and solution speed is usually made.
- Assign the properties – Material properties (Young's Modulus, Poisson's ratio, density, and if applicable coefficient of expansion, friction, thermal conductivity, damping effect, specific heat, etc.,) have to be defined.

Solution:

- Apply the loads. Some type of load is actually applied to the analysis model. The loading may be in the form of a point load, pressure or a displacement in a stress analysis, a temperature or heat flux in a thermal analysis and a fluid pressure or velocity in a fluid analysis.
- Applying the boundary conditions. After applying load to the model in order to stop it accelerating infinitely through the computer virtually either at least one boundary condition must be applied
- FE solver can be logically divided in to three main parts, the pre-solver, the mathematical-engine and the post-solver. The pre-solver reads the model created by the pre-processor and formulates the mathematical representation of the model and calls the mathematical-engine, which calculates the results. The result returned to the solver and the post-solver is used to calculate the strains, stresses, etc., for each node within the component or continuum.

V. PROCESS OF ANALYSIS

Importing of the cylindrical head will be done after opening the workbench. For the supporting purpose of the geometry, the file format of solid works will be changed to step format. This is to match up the graphical properties of the solid works v5 to ansys workbench. The full form of the step is standard for the exchange of product model data which itself states that will exchange the graphical properties of models. The material properties are the important factor which will be considered as the second preference after importing or creating the geometry. The procedure of material application, double click on the engineering data which will appear on the top of the analysis system. The analysis system which we are using in this project is transient thermal analysis. After opening the window of engineering data the material application will be done by selecting the add symbol in the general materials. These materials are available in thermal materials from engineering data source and select the above mentioned material, and reset layout from view menu and update project.
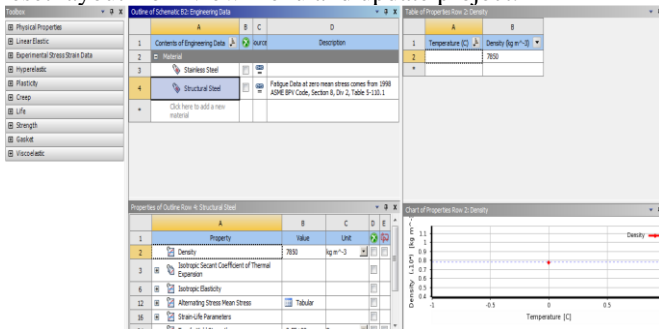
Fig.5.

A. Steady State Thermal Analysis
Work Bench: After importing the model into project schematic window drag and drop the steady state thermal tab on to the screen from the toolbox window and link the geometry to geometry both will be linked together. Double click on the model it opens the mechanical window with object.

Fig.6.

Modal Tree:
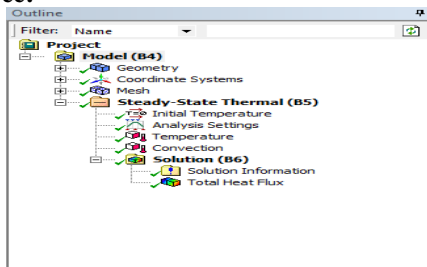
Fig.7.

Geometry And Meshing:
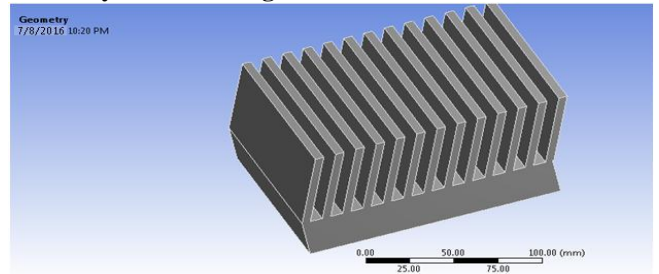
Fig.8.

From the outline tab – select the geometry – Part – from the bottom detailed window- material –Assignment – Select required material.
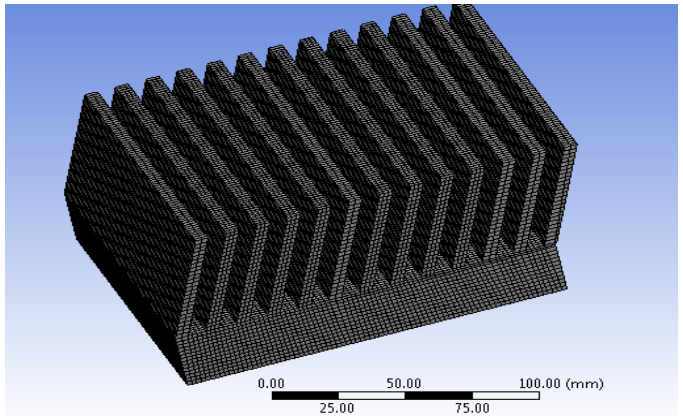
Fig.9.

Mesh: To generate the meshing, there are two methods one is automatic mesh generation and the other is with required size meshing. In this we used auto meshing with medium meshing.

Temperature And Convection:
Set the initial temperature as 30 ^{0}C ,
Right click on Analysis settings – Insert – convection – Enter the film coefficient as 22 ^{0}C & 30 W/mm^2 ^{0}C.

Right click on Analysis settings – Insert – Temperature – enter 300 ^{o}C and select the bottom
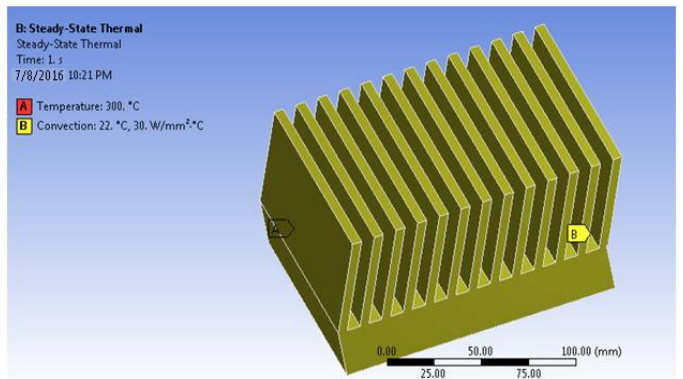
Fig.10.

Solution:
Right Click on solution – Insert Total Heat Flux:
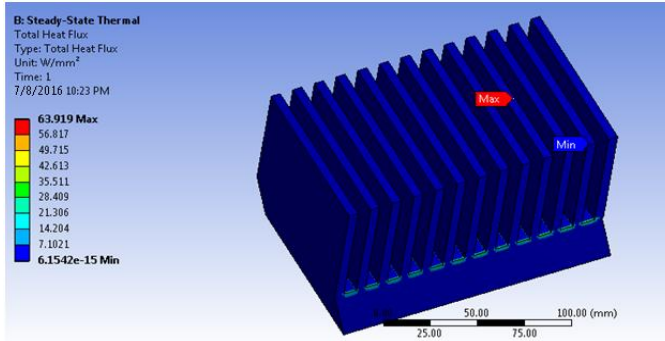
Fig.11.

VI. RESULTS
TABLE I: Aluminum Alloy> Isotropic Resistivity

Resistivity ohm mm	Temperature C
2.43e-005	0
2.67e-005	20
3.63e-005	100

TABLE II: Aluminum Alloy> Isotropic Elasticity

Temperature C	Young's Modulus MPa	Poisson's Ratio	Bulk Modulus MPa	Shear Modulus MPa
	71000	0.33	69608	26692

TABLE III: Aluminum Alloy> Isotropic Permeability

Relative Permeability
1

A. Steady – State Thermal Analysis
The loads are like;
- Convention is maintained at 22°C
- Temperature is varied for different conditions as 300°C, 600°C, 900°C, &1200°C
- And the corresponding

TABLE IV: Thermal Heat Flux Is Tabulated In Below Table

S.NO	TEMP In °C	THF In W/mm2
1	300	63.919
2	600	132.9
3	900	201.81
4	1200	270.85

VII. CONCLUSION
By using solid works the modeling of the parts of the inclined plate's engine were completed successfully. And the component converted into IGES (integrations graphical element system). And analysis was done on master rod of modal analysis and static structural analysis was completed and behavior of the master was examined from these analysis and the natural frequencies, equivalent stress and total deformation were calculated as shown in results page. Thermal analysis was completed and total heat flux and directional heat flux were calculated by using ansys 14.0 work bench.

IX. REFERENCES
[1] Selected Asian Countries. Energy Conversion and Management, 40 (1999), 1141-1162. P. H. Oosthuizen and A. Y. Kalendar, Natural Convective Heat Transfer from Nar-row Plates, SpringerBriefs in Thermal Engineering and Applied Science, DOI: 10.1007/978-1-4614-5158-72.

[2] An Interaction of Natural Convective Heat Transfer From Two Adjacent Isothermal Narrow Vertical and In-clined Flat Plates by Abdulrahim Kalendar, Patrick H Oosthuizen, Bader Kalandar, 10.1115/HT2009-88091 ASME 2009 Heat Transfer Summer Conference .

[3] Journal of theoretical and applied mechanics, 50, 4, pp. 1001-1010, Natural convection boundary layer flow on a horizontal plate with variable wall temperature by Abbasali Abouei Mehrizi, Yousef Vazifeshenas, G. Do-mairry

[4] Natural convection heat transfer above heated hori-zontal surfaces by MASSIMO CORCIONE, 5th WSEAS Int. Conf. on Heat and Mass transfer (HMT'08) , Aca-pulco, Mexico, January 25-27, 2008

[5] Numerical Analysis of Natural Convection in Rectan-gular Enclosure with Heated Finned Base Plate by M. K. Pathak, K. K. S. Mer, Pawan Kumar Pant, IJRMET Vol. 3, Issue 2, May - Oct 2013 ISSN : 2249-5762, ISSN : 2249-5770, International Journal of Research in Mechanical Engineering & Technology

[6] Natural Convective Heat Transfer From an Inclined Narrow Isothermal Flat Plate by Patrick H. Oosthuizen and Abdulrahim Kalendar, HT2008-56190, pp. 549-555; 7 pages, doi:10.1115/HT2008-56190, ASME 2008 Heat Transfer Summer Conference

[7] Laminar natural convection heat transfer from vertical and inclined plates facing upwards and downwards by C. Cianfrinia, M. Corcione, A. D'Oraziob and E. Habib, HE-FAT2008 6th International Conference on Heat Transfer, Fluid Mechanics and Thermodynamics.

[8] Heat transfer correlations for free convection from upward-facing horizontal rectangular surfaces by MAS-SIMO CORCIONE, WSEAS TRANSACTIONS on HEAT and MASS TRANSFER Manuscript received Jun. 23, 2007; revised Dec. 29, 2007

[9] Natural convection from inclined plates to gases and liquids when both sides are uniformly heated at the same temperature by Massimo Corcione, Emanuele Habib , Antonio Campo, International Journal of Thermal Sciences 50 (2011) 1405-1416

[10] Natural convection heat transfer from inclined plate-fin heat sinks by Ilker Tari, Mehdi Mehrtash, Internation-al Journal of Heat and Mass Transfer, Volume 56, Issues 1–2, 1 January 2013, Pages 574–593

Analysis of Thermal Effects on Valve by Conventional and Blended Fuels

Bollapally Suman Goud

M.Tech (Thermal engineering),

P.G. Scholar

Nishitha College of engineering and technology

sumanri123@gmail.com

Rangdal Srikanth

Mtech(AMS), Asst professor

Nishitha College of engineering and technology

ABSTRACT

The valves utilized as a part of the IC motors are of three sorts: Poppet or mushroom valve or Sleeve valve or Rotary valve. Of these three sorts, Poppet valve is most generally utilized. Since both the gulf and fumes valves are subjected to high temperatures of 1930°C to 2200°C amid the force stroke, in this manner, it is important that the materials of the valves ought to withstand these temperatures. The temperature at the channel valve is less contrasted with fumes valve. Accordingly the delta valve is for the most part made of nickel chromium combination steel and fumes valve is made of silchrome steel. Car motors are typically petrol, diesel or fuel motors. Petrol motors are Spark Ignition motors and diesel motors are Compression Ignition motors. Mixed fills are blends of conventional and option powers in differing rates. In this theory, the impact of petrol, diesel and mixed fills on valve is examined by numerical connections applying warm loads created amid burning.

Mixed fills are generally Ethanol energizes mixed in various rates. Rates shift from 10%, 15% and 25%. Interior burning motors produce debilitate gasses at greatly high temperatures and weights. As these hot gasses go through the fumes valve, temperatures of the valve, valve seat, and stem increment. To maintain a strategic distance from any harm to the fumes valve get together, warmth is exchanged from the fumes valve through various parts, particularly the valve seat embed amid the opening and shutting astoundingly into contact with each other. In this theory, a limited component technique is utilized for displaying the warm investigation of a fumes valve. The temperature dissemination and resultant warm hassles are assessed. Itemized investigations are performed to evaluate the limit states of an interior ignition motor. In this proposition, Pro/Engineer is utilized for demonstrating and ANSYS is utilized for examination of the fumes valve.

Keywords: Blended fuels, combustion, exhaust valve, transient thermal

INTRODUCTION

Typically a fossil fuel happens with an oxidizer (generally air) in a chamber that is an indispensable part of the working liquid stream circuit. In an inside ignition motor (ICE) the extension of the high temperature and high-weight gasses delivered by burning apply direct compel to some segment of the motor. The power is connected normally to cylinders, turbine edges, or a spout. This power moves the part over a separation, changing concoction vitality into valuable mechanical vitality. The principal industrially effective inward ignition motor was made by Etienne Lenoir. The term inward ignition motor normally alludes to a motor in which burning is irregular, for example, the more natural four and two-stroke cylinder motors, alongside variations, for example, the six-stroke cylinder motor and the Winkle revolving motor. A worthless of inward burning motors use nonstop ignition: gas turbines, plane motors and most rocket motors, each of which are interior burning motors on the same guideline as beforehand portrayed. The ICE is very unique in relation to outer burning motors, for example, steam or Stirling motors, in which the vitality is conveyed to a working liquid not comprising of, blended with, or sullied by ignition items. Working liquids can be air, high temp water, pressurized or even fluid sodium, warmed in some sort of heater. Frosts are generally controlled by vitality thick fills, for example, gas or diesel, fluids got from fossil energizes. While there are numerous stationary applications, most ICEs are utilized as a part of versatile applications and are the prevailing force supply for autos, flying machine, and pontoons. All interior burning motors rely on upon ignition of a compound fuel, ordinarily with oxygen from the air (however it is conceivable to infuse nitrous oxide to accomplish business as usual thing and increase a force help). The ignition procedure ordinarily brings about the generation of an incredible amount of warmth, and in addition the creation of steam and carbon dioxide and different chemicals at high temperature; the temperature came to is controlled by the concoction cosmetics of the fuel and oxidizers (see stoichiometry), and also by the pressure and different elements.

The most widely recognized cutting edge energizes are comprised of hydrocarbons and are gotten generally from fossil powers (petroleum). Fossil fills incorporate diesel fuel, gas and petroleum gas, and the rarer utilization of propane. Aside from the fuel conveyance segments, most interior burning motors that are intended for gas use can keep running on normal gas or melted petroleum gasses without significant changes. Vast diesels can keep running with air blended with gasses and a pilot diesel fuel ignition infusion. Fluid and vaporous bio energizes,

for example, as soybeanoil), ethanol and biodiesel (a type of diesel fuel that is created from harvests that yield triglycerides such can likewise be utilized. Motors with fitting alterations can likewise keep running on hydrogen gas, wood gas, or charcoal gas, and also from purported maker gas produced using other helpful biomass. As of late, trials have been made

.

with utilizing powdered strong powers, for example, the magnesium infusion cycle.

Inward burning motors require ignition of the blend, either by flash ignition (SI) or pressure ignition (CI). Prior to the creation of solid electrical strategies, hot tube and fire techniques were utilized. Trial motors with laser ignition have been manufactured

THEORETICAL CALCULATIONS

Transmission

Transmission Type	Manual
Gears	5
Gear Box Type	5 Speed
Drive Type	FWD

Fuel Economy

Mileage Highway (km/liter)	20.46
Mileage City (km/liter)	18.0

Dimensions and Weights

Overall Length (mm)	4315
Overall Width (mm)	1822
Overall Height (mm)	1695
Wheel Base (mm)	2673
Ground Clearance (mm)	205
Front Track (mm)	1560
Rear Track (mm)	1567
Gross Vehicle Weight (kg)	1758

No of Doors	5
Minimum Turning Radius (mt)	5.2
Front Brakes	Ventilated Disc
Rear Brakes	Drum

Wheels and Tyres

Wheel Size	R16
Tyre Type	Tubeless Tyres
Tyre Size	215/65 R16

$$P_{bmean} = \frac{n\ W}{vd\ N}$$

P_{bmean} =break mean effective pressure in N/m^2

n= no. of power cycles

N=speed in rev/sec

v_d= Displacement in m^3

PV=MRT

$$V = \text{induced volume} = \frac{capacity\ \times speed}{2}$$

T=temperature in Kelvin

M =mass

R = universal gas constant=8.314 J/k mol

FOR BLENDED FUELS:

Ethanol=10%   Diesel =90%

$$M_d = 1.2 \times \frac{90}{100} = 1.08 \times 0.233 = 0,25164 kg$$

$$M_e = 1.2 \times \frac{10}{100} = 0.12 \times 0.046 = 0.00552 kg$$

$$T = \frac{PV}{MR}$$

$$= \frac{369249.41 \times 0.046}{\frac{1.08}{0.251} + \frac{0.12}{0.00552} \times 8.314}$$

$$= 290.90 k$$

Ethanol=15%   Diesel =85%

$$M_d = 1.2 \times \frac{85}{100} = 1.02 \times 0.233 = 0,237 kg$$

$$M_e = 1.2 \times \frac{15}{100} = 0.18 \times 0.046 = 0.0082 kg$$

$$T = \frac{PV}{MR} = \frac{369249.41 \times 0.046}{\frac{1.02}{0.237} + \frac{0.18}{0.0082} \times 8.314}$$

$$= 288.54 k$$

Ethanol=25%   Diesel =75%

$$M_d = 1.2 \times \frac{75}{100} = 1.9 \times 0.233 = 0,2092 kg$$

$$M_e = 1.2 \times \frac{25}{100} = 0.3 \times 0.046 = 0.0138 kg$$

$$T = \frac{PV}{MR}$$

International Journal of Research

Available at https://edupediapublications.org/journals

p-ISSN: 2348-6848
e-ISSN: 2348-795X
Volume 03 Issue 11
July 2016

$$= \frac{369249.41 \times 0.046}{\frac{0.9}{0.2097} + \frac{0.3}{0.0038} \times 8.314}$$

$$= 291.03k$$

3. DESIGN OF EXHAUST VALVE

a. Size of valve port

$$a_p \, v_p = aV$$

$$a_p = \frac{\pi}{4}(d_p)^2$$

b. Thickness of valve disc

$$t = Kd_p \sqrt{\frac{p}{\sigma_b}}$$

c. Maximum lift of the valve

h = lift of the valve

$$h = \frac{d_p}{4 \cos \alpha}$$

d. Valve steam diameter

$$d_s = \frac{12.768}{8} + 6.35 \quad \text{or}$$

$$d_s = 1.596 + 6.35$$

MODEL OF EXHAUST VALVE
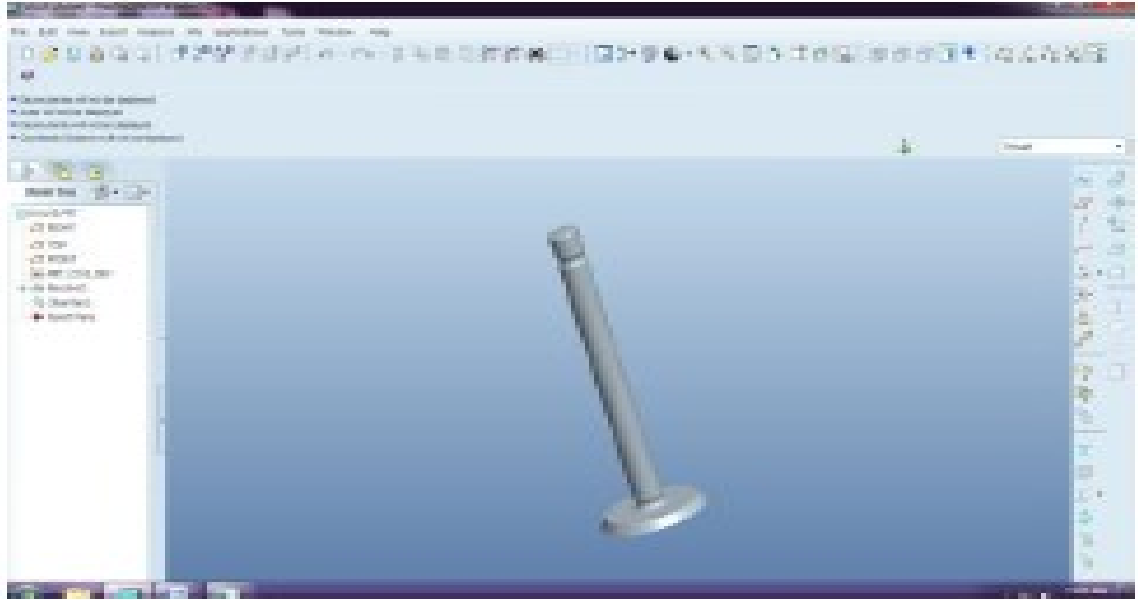
Figure 1: Model of Exhaust Valve
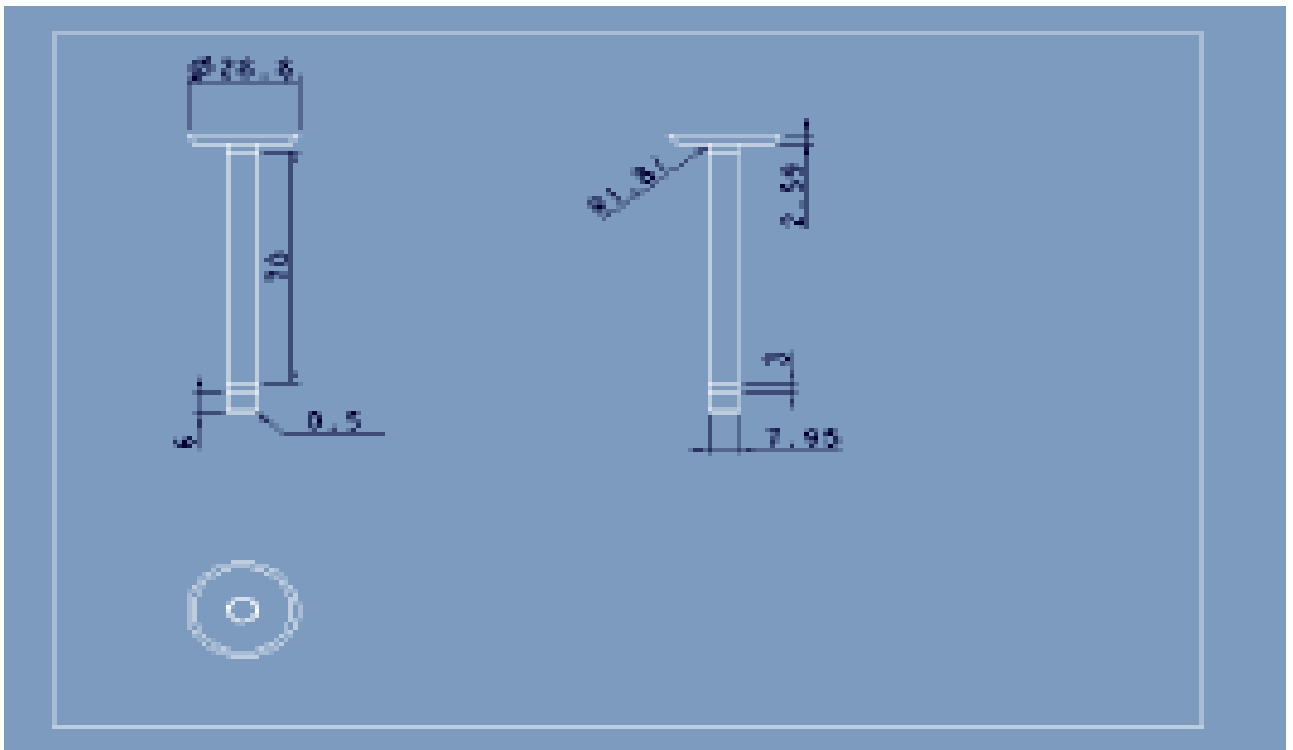
Figure 2: 2D Drafting

Conventional Fuel - Diesel
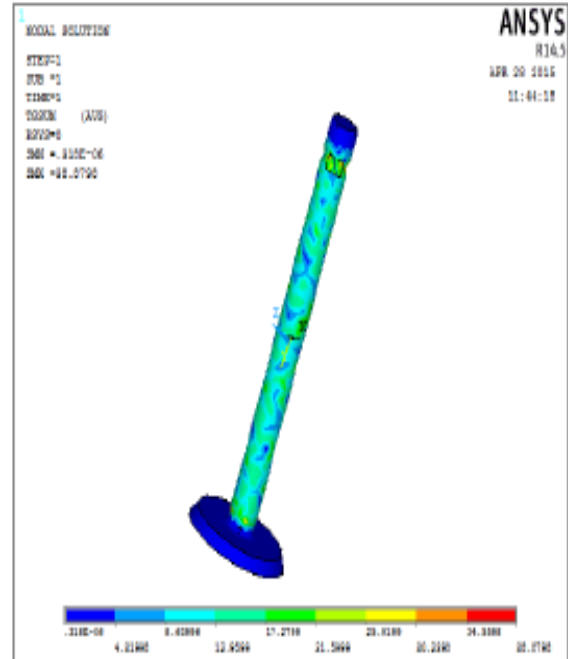
Figure 3: Imported Model
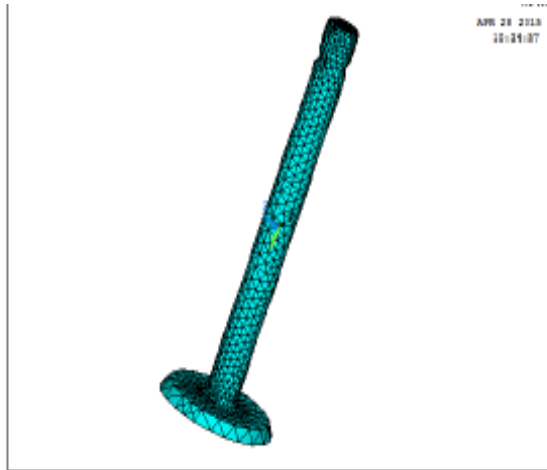
Fig4. Meshed Model

Material Properties: Thermal Conductivity –
0.03W/mmK

Specific Heat – 506 J/Kg K

Density - 0.00000789 Kg/mm³
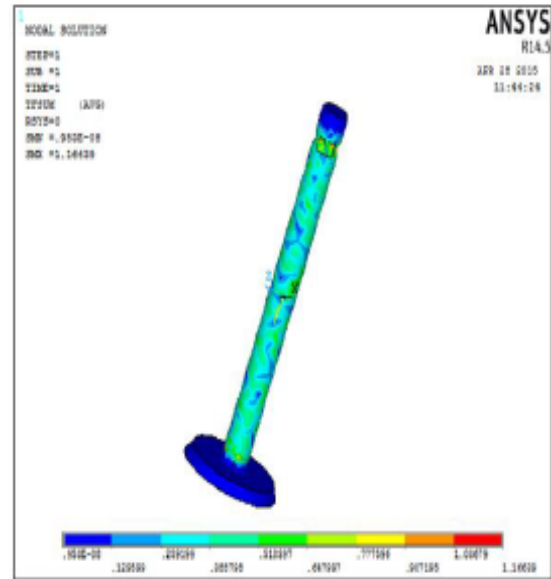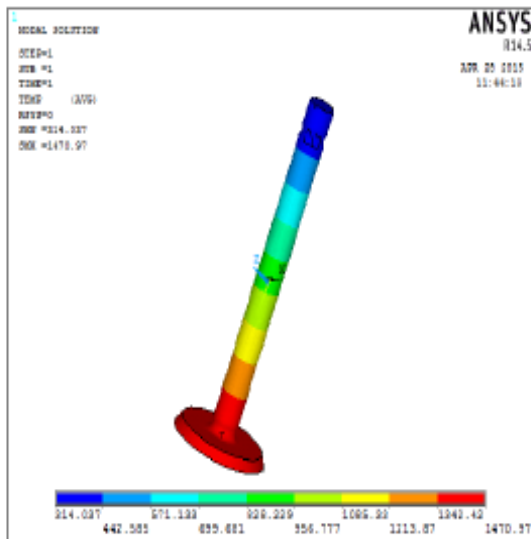
Fig5. Nodal Temperature

Fig7.Thermal Flux

RESULTS TABLE

	NODAL TEMPERATURE (K)	THERMAL GRADIENT (K/mm)	HEAT FLUX (W/mm2)
Conventional Fuel	1470.97	38.8788	1.166639
D – 90%, E – 10%	312.98	0.742026	0.022261
D – 85%, E – 15%	312.978	0.821	0.0246
D – 75%, E – 25%	312.98	0.737661	0.02213

.CONCLUSION

In this proposal, the impact of diesel and mixed fills on fumes valve is examined by scientific connections to figure warm loads created amid burning. Energizes considered are Diesel and Blended fills. Mixed energizes are generally Ethanol fills mixed in various rates. Rates shift from 10%, 15% and 25%. Material utilized for Valve is Steel is Cast Iron. Hypothetical figurings are done to compute the temperature delivered for ignition when fuel is changed. Warm examination is done on the valve applying temperature by changing the fills utilized for ignition.

The cases considered are Diesel, Diesel + 10% Ethanol, Diesel + 15% Ethanol, Diesel + 25% Ethanol. By watching the investigation results, by utilizing just diesel as fuel the warmth exchange rate is more than by taking mixed fills. At the point when the mixed energizes are considered, by expanding the rate of ethanol, the warmth exchange rate is lessening. So it can be presumed that, for mixing powers, less rate of ethanol is better.

FUTURE SCOPE

More analyses must be accomplished for utilizing higher rates of ethanol so that the utilization of routine energizes is diminished with minimizing disservices of utilizing ethanol.

REFERENCES

[1].   Alvydas Pikūnas, Saugirdas Pukalskas, Juozas Grabys - Influence of composition of – ethanol blends on parameters   of internal combustion engines

[2.]   Furey, R.L., Perry, K.L., Composition and reactivity of fuel vapor emissions from Gasoline-oxygenate blend. SAE   Paper   912429.

[3].   Coelho, E.P.D., Moles, C.W., Marco Santos, A.C., Barwick, M., Chiarelli, P.M., Fuel injection components   developed   for Brazilian fuels. SAE Paper 962350.

[4].   Naegeli, D.W., Lacey, P.I., Alger, M.J., Endicott, D.L., 1997. Surface corrosion in ethanol fuel pumps. SAE Paper   971648.

[5] Salih, F.M., Andrews, G.E. The influence of gasoline/ethanol blends on emissions and fuel economy. SAE Paper   922378, SAE Fuel and Lubricants Meeting.

[6]. Abdel-Rahman, A.A., Osman, M.M., Experimental investigation on varying the compression ratio of SI engine   working   under different ethanol–gasoline fuel blends. International Journal of Energy Research 21, 31–40.

[7]. Gorse Jr., R.A., The effects of methanol/gasoline blends on automobile emissions. SAE Paper 920327.

[8]. Bureika G. Research on the feasibility to use the ethanol as transport machine fuel/ doctoral dissertation. Vilnius.

[9]. Palmer, F.H., Vehicle performance of gasoline containing oxygenates. International conference on petroleum based   and   automotive   applications.   Institution   of Mechanical Engineers Conference Publications, MEP, London, UK, pp.   33–46.

[10]. Bata, R.M., Elord, A.C., Rice, R.W., Emissions from IC engines fueled with alcohol–gasoline blends: a literature review. Transactions of the ASME 111, 424–431.

[11]. Alexandrian, M., Schwalm, M. Comparison of ethanol and gasoline as automotive fuels. ASME papers 92-WA/ DE-15.

[12]. Rice, R.W., Sanyal, A.K., Elrod, A.C., Bata, R.M., Exhaust gas emissions of butanol, ethanol and methanol–gasoline blends. Journal of Engineering for Gas Turbine and Power 113, 337–381.

Design and Analysis of Different Material to Increase the Performance of Ac Condenser

Dachepally Raghu Babu
M.Tech (Thermal engineering),
P.G. Scholar
Nishitha College of engineering and
technology

Rangdal Srikanth

Mtech(AMS), Asst professor
Nishitha College of engineering and technology

ABSTRACT

In systems involving heat transfer, a condenser is a device or unit used to condense a substance from its gaseous to its liquid state, typically by cooling it. In so doing, the latent heat is given up by the substance, and will transfer to the condenser coolant. Condensers are typically heat exchangers which have various designs and come in many sizes ranging from rather small to very large industrial-scale units used in plant processes. Air cooled condensers are used in small units like household refrigerators, deep freezers, water coolers, window air-conditioners, split air-conditioners, small packaged air-conditioners etc. These are used in plants where the cooling load is small and the total quantity of the refrigerant in the refrigeration cycle is small. Air cooled condensers are also called coil condensers as they are usually made of copper or aluminum coil. Air cooled condensers occupy a comparatively larger space than water cooled condensers.

In this thesis a design optimization technique that can be useful in assessing the best configuration of a finned-tube condenser. Heat transfer by convection in air cooled condensers is studied and improved in this work. The assessment has been carried out on an air-cooled finned-tube condenser of a vapour compression cycle for air conditioning system. Heat transfer analysis and CFD analysis is done on the condenser to evaluate the better design and material. The materials considered for tube is copper and for fins are Aluminum alloys 1100, 6063 and Magnesium alloy for different refrigerants HCFC and 404R. 3D modeling is done in Pro/Engineer and analysis is done in Ansys. CFD analysis is done at different velocities. Theoretical calculations are done to determine heat transfer rate.

INTRODUCTION

Air Conditioner:

An **air conditioner** (often referred to as **AC**) is a home appliance, system, or mechanism designed to dehumidify and extract heat from an area. The cooling is done using a simple refrigeration cycle. In construction, a complete system of heating, ventilation and air conditioning is referred to as "HVAC". Its purpose, in a building or an automobile, is to provide comfort during either hot or cold weather.
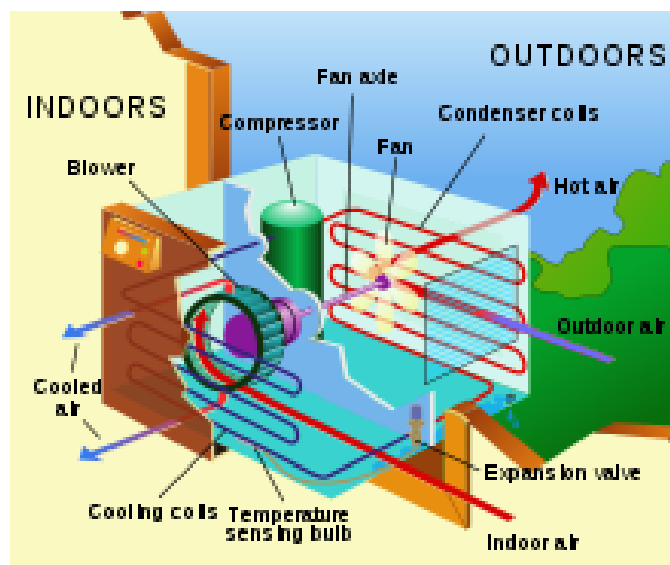
Figure 1: A typical home air conditioning unit

AIR CONDITIONING SYSTEM BASICS AND THEORIES
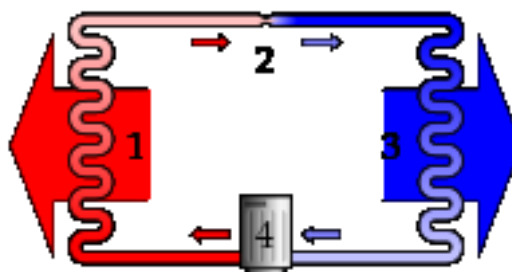
Figure 2: Refrigeration cycle

A simple stylized diagram of the refrigeration cycle: 1) condensing coil, 2) expansion valve, 3) evaporator coil, 4) compressor.

In the refrigeration cycle, a heat pump transfers heat from a lower-temperature heat source into a higher-temperature heat sink. Heat would naturally flow in the opposite direction. This is the most common type of air conditioning. A refrigerator works in much the same way, as it pumps the heat out of the interior and into the room in which it stands. This cycle takes advantage of the way phase changes work, where latent heat is released at a constant temperature during a liquid/gas phase change, and where varying the pressure of a pure substance also varies its condensation/boiling point. The most common refrigeration cycle uses an electric motor to drive a compressor. In an automobile, the compressor is driven by a belt over a pulley, the belt being driven by the engine's crankshaft (similar to the driving of the pulleys for the alternator, power steering, etc.). Whether in a car or building, both use electric fan motors for air circulation. Since evaporation occurs when heat is absorbed, and condensation occurs when heat is released, air conditioners use a compressor to cause pressure changes between two compartments, and actively condense and pump a refrigerant around. A refrigerant is pumped into the evaporator coil, located in the compartment to be cooled, where the low pressure causes the refrigerant to evaporate into a vapor, taking heat with it. At the opposite side of the cycle is the condenser, which is located outside of the cooled compartment, where the refrigerant vapor is compressed and forced through another heat exchange coil, condensing the refrigerant into a liquid, thus rejecting the heat previously absorbed from the cooled space.

By placing the condenser (where the heat is rejected) inside a compartment, and the evaporator (which absorbs heat) in the ambient environment (such as outside), or merely running a normal air conditioner's refrigerant in the opposite direction, the overall effect is the opposite, and the compartment is heated. This is usually called a heat pump, and is capable of heating a home to comfortable temperatures (25 °C; 70 °F), even when the outside air is below the freezing point of water (0 °C; 32 °F). Cylinder unloaders are a method of load control used mainly in commercial air conditioning systems. On a semi-hermetic (or open) compressor, the heads can be fitted with unloaders which remove a portion of the load from the compressor so that it can run better when full cooling is not needed. Unloaders can be electrical or mechanical.

Refrigerants

"Freon" is a trade name for a family of haloalkane refrigerants manufactured by DuPont and other companies. These refrigerants were commonly used due to their superior stability and safety properties. However, these chlorine-bearing refrigerants reach the upper atmosphere when they escape.[6] Once the refrigerant reaches the stratosphere, UV radiation from the Suncleaves the chlorine-carbonbond, yielding a chlorine radical. These chlorine atoms catalyze the breakdown of ozone into diatomicoxygen, depleting the ozone layer that shields the Earth's surface from strong UV radiation. Each chlorine radical remains active as a

catalyst unless it binds with another chlorine radical, forming a stable molecule and breaking the chain reaction. The use of CFC as a refrigerant was once common, being used in the refrigerants R-11 and R-12. In most countries the manufacture and use of CFCs has been banned or severely restricted due to concerns about ozone depletion. In light of these environmental concerns, beginning on November 14, 1994, the Environmental Protection Agency has restricted the sale, possession and use of refrigerant to only licensed technicians, per Rules 608 and 609 of the EPA rules and regulations; failure to comply may result in criminal and civil sanctions. Newer and more environmentally-safe refrigerants such as HCFCs (R-22, used in most homes today) and HFCs (R-134a, used in most cars) have replaced most CFC use. HCFCs in turn are being phased out under the Montreal Protocol and replaced by hydro fluorocarbons (HFCs) such as R-410A, which lack chlorine. Carbon dioxide (R-744) is being rapidly adopted as a refrigerant in Europe and Japan. R-744 is an effective refrigerant with a global warming potential of 1. It must use higher compression to produce an equivalent cooling effect.

Types of air conditioner equipment

The external section of a typical single-room air conditioning unit. For ease of installation, these are frequently placed in a window. This one was installed through a hole cut in the wall. The internal section of the above unit. The front panel swings down to reveal the controls.

Window and through-wall units

Room air conditioners come in two forms: unitary and packaged terminal PTAC systems. Unitary systems, the common one room air conditioners, sit in a window or wall opening, with interior controls. Interior air is cooled as a fan blows it over the evaporator. On the exterior the air is heated as a second fan blows it over the condenser. In this process, heat is drawn from the room and discharged to the environment. A large house or building may have several such units, permitting each room be cooled separately. PTAC systems are also known as wall split air conditioning systems or ductless systems. These PTAC systems which are frequently used in hotels have two separate units (terminal packages), the evaporative unit on the interior and the condensing unit on the exterior, with tubing passing through the wall and connecting them. This minimizes the interior system footprint and allows each room to be adjusted independently. PTAC systems may be adapted to provide heating in cold weather, either directly by using an electric strip, gas or other heater, or by reversing the refrigerant flow to heat the interior and draw heat from the exterior air, converting the air conditioner into a heat pump. While room air conditioning provides maximum flexibility, when cooling many rooms it is generally more expensive than central air conditioning.

Evaporative coolers

In very dry climates, evaporative coolers, sometimes referred to as swamp coolers or desert coolers, are popular for improving

comfort during hot weather. This type of cooler is the dominant cooler used in Iran, which has the largest number of these units of any country in the world, causing some to refer to these units as "Persian coolers." An evaporative cooler is a device that draws outside air through a wet pad, such as a large sponge soaked with water. The sensible heat of the incoming air, as measured by a dry bulb thermometer, is reduced. The total heat (sensible heat plus latent heat) of the entering air is unchanged. Some of the sensible heat of the entering air is converted to latent heat by the evaporation of water in the wet cooler pads. If the entering air is dry enough, the results can be quite comfortable; evaporative coolers tend to feel as if they are not working during times of high humidity, when there is not much dry air with which the coolers can work to make the air as cool as possible for dwelling occupants. Unlike air conditioners, evaporative coolers rely on the outside air to be channeled through cooler pads that cool the air before it reaches the inside of a house through its air duct system; this cooled outside air must be allowed to push the warmer air within the house out through an exhaust opening such as an open door or window.

These coolers cost less and are mechanically simple to understand and maintain.

An early type of cooler, using ice for a further effect, was patented by John Gorrie of Apalachicola, Florida in 1842. He used the device to cool the patients in his malariahospital.

Thermostats

Thermostats control the operation of HVAC systems, turning on the heating or cooling systems to bring the building to the set temperature. Typically the heating and cooling systems have separate control systems (even though they may share a thermostat) so that the temperature is only controlled "one-way." That is, in cold weather, a building that is too hot will not be cooled by the thermostat. Thermostats may also be incorporated into facility energy management systems in which the power utility customer may control the overall energy expenditure. In addition, a growing number of power utilities have made available a device which, when professionally installed, will control or limit the power to an HVAC system during peak use times in order to avoid necessitating the use of rolling blackouts. The customer is given a credit of some sort in exchange, so it is often to the advantage of the consumer to buy the most efficient thermostat possible.

Equipment capacity

Air conditioner equipment power in the U.S. is often described in terms of "tons of refrigeration". A "ton of refrigeration" is approximately equal to the cooling power of one short ton (2000 pounds or 907 kilograms) of ice melting in a 24-hour period. The value is defined as 12,000 BTU per hour, or 3517 watts. Residential central air systems are usually from 1 to 5 tons (3 to 20 kilowatts (kW)) in capacity.

The use of electric/compressive air conditioning puts a major demand on the

electrical power grid in hot weather, when most units are operating under heavy load. In the aftermath of the 2003 North America blackout locals were asked to keep their air conditioning off. During peak demand, additional power plants must often be brought online, usually expensive peaker plants. A 1995 meta-analysis of various utility studies concluded that the average air conditioner wasted 40% of the input energy. This energy is lost in the form of heat, which must be pumped out.

In an automobile, the A/C system will use around 5 horsepower (4 kW) of the engine's power.

unit size, BTU/h × hours per year, h × power cost, $/kW·h ÷ (SEER, BTU/W·h × 1000 W/kW)

(72,000 BTU/h) × (1000 h) × ($0.08/kW·h) ÷ [(10 BTU/W·h) × (1000 W/kW)] = $576.00 annual cost

A common misconception is that the SEER rating system also applies to heating systems. However, SEER ratings only apply to air conditioning.

Air conditioners (for cooling) and heat pumps (for heating) both work similarly in that heat is transferred or "pumped" from a cooler heat source to a warmer "heat sink". Air conditioners and heat pumps usually operate most effectively at temperatures around 10 to 13 degrees Celsius (°C) (50 to 55 degrees Fahrenheit (°F)). A balance point is reached when the heat source temperature falls below about 4 °C (40 °F), and the system is not able to pull any more heat from the heat source

(this point varies from heat pump to heat pump). Similarly, when the heat sink temperature rises to about 49 °C (120 °F), the system will operate less effectively, and will not be able to "push" out any more heat. Geothermal heat pumps do not have this problem of reaching a balance point because they use the ground as a heat source/heat sink and the ground's thermal inertia prevents it from becoming too cold or too warm when moving heat from or to it. The ground's temperature does not vary nearly as much over a year as that of the air above it.

SPECIFICATIONS OF CONDENSOR

The length and size of air conditioner condensers and evaporators have to be sized such that,

- the refrigerant is completely condensed before the condenser's exit, and
- the refrigerant is completely boiled before the evaporator's exit

Those two, depends mainly on the size of the compressor and refrigerant used. Air conditioner manufacturers has to understand how conduction, as well as convection works, to design an **effective**, yet compact air conditioner condenser and evaporator, per unit heat transferred. Normally, the condenser and evaporator will be designed to 110% of the intended heat transfer requirement, to cater for any performance drop during the service life.

It's good that we know the basics now.

Types of Condensers:

1) Evaporative Condenser

2) Air cooled condenser

3) Water cooled condenser

EVAPORATIVE CONDENSER:

Whereas a condenser/cooling tower arrangement requires a system of water distribution piping, this is almost entirely absent in the evaporative condenser. Only enough water need be circulated to ensure that the outside surface of the condenser coils is completely wet. The heat exchange is solely latent, and less water is required in circulation than is necessary with a condenser/cooling tower, where a sensible heat exchange occurs in the shell-and tube condenser. The evaporative condenser is thus more compact and is cheaper. It suffers from lack of flexibility, and oil return and other problems demand that the condenser should not be too far from the compressor. A cooling tower, on the other hand, may be a considerable distance away, the condenser then being adjacent to the compressor. Scaling on the tubes of an evaporative condenser may be something of a problem, particularly if a high condensing temperature is used. Cleaning difficulties, caused by the presence of scale, dirt and corrosion, and by the close nesting necessary for the tubes (the use of finning being impossible), have considerably reduced the popularity of the evaporative condenser in recent years.

AIR COOLED CONDENSER:

Unlike evaporative condensers, air-cooled condensers have a capacity which is related to the dry-bulb temperature of the ambient air, rather than to its wet-bulb temperature. If working condenser pressures are not to become excessively high, making the plant expensive to run, large condenser surface areas must be used. This has set a limit on the practical upper size of air-cooled condensers. Their use in air conditioning has been commonly confined to plants having a capacity of less than 70 kW of refrigeration, although they have been used for duties as high as 2000 kW, in temperate climates. The hot gas discharged from the compressor is de superheated over approximately the first 5 per cent of the heat transfer surface, followed by condensation over the succeeding 85 per cent, with a small drop in the condensing temperature, related to the frictional pressure loss. A certain amount of sub-cooling of the liquid can then occur. Additional heat transfer surface may be provided to assist the sub-cooling, achieving an increase of about 0.9 per cent in the cooling capacity for each degree of liquid temperature drop, according to ASHRAE (1996).Propeller fans, direct-coupled to split-capacitor driving motors, are most commonly used to promote airflow, although axial flow or centrifugal fans are also sometimes adopted. Fan powers are about 20 to 40 W for each kW of refrigeration capacity. Noise is often a problem and this is made worse if there are obstructions in the inlet or outlet airflow paths. Although vertical fan arrangements are possible, with horizontal cooling airflow paths, these are susceptible to wind pressures and it is recommended that the

condenser coils should be horizontal with vertical cooling airflow paths.

Propeller fans will not deliver airflow against any significant external resistance. It follows that ducting connections are then not possible if these fans are used. A 20-degree difference between the entering dry-bulb temperature and the condensing temperature is often consistent with the avoidance of excessively large condenser surface areas. Air-cooled condensers are increasing in popularity because of the absence of water piping, the consequent simplicity of operation and the freedom from any health risk associated with the use of spray water.

One objection to their use is that the capacity of the refrigeration plant does not gradually reduce as the ambient dry-bulb rises but ceases suddenly when the high pressure cut-out operates. A partial solution is to arrange for some of the compressor to be unloaded when the condensing pressure rises, before it reaches the cut-out point. Continued operation at a reduced capacity is then possible beyond the design ambient dry-bulb. It is a good plan to select air-cooled condensers to operate in an ambient temperature two or three degree higher than the design value chosen for the rest of the air conditioning system.
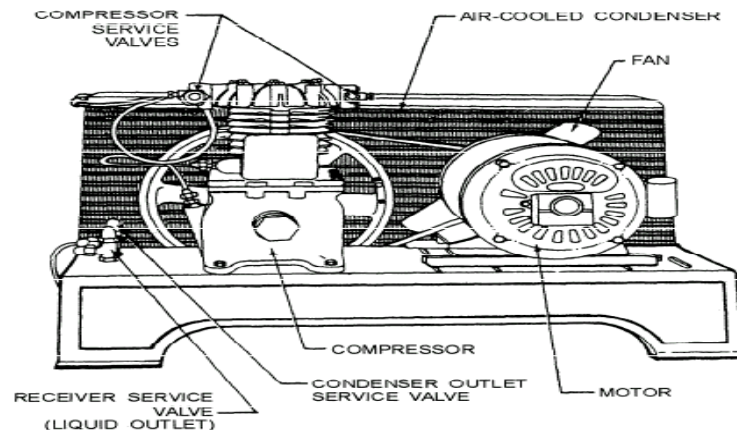
WATER COOLED CONDENSER:

Water is used to cool condensers. One method is to cool condensers with water from the city water supply and then exhaust the water into the sewer after it has been used to cool the refrigerant. This method can be expensive and, in some instances, is not allowed by law. When there is a sewer problem, a limited sewer treatment plant capacity, or drought, it is impractical to use this cooling method. The use of recirculation to cool the water for reuse is more practical. However, in recirculation, the power required to pump the water to the cooling location is part of the expense of operating the unit. There are three types of water-cooled condensers.

They are:
• The double tube
• The shell and coil
• The shell and tube types

The double-tube type consists of two tubes, one inside the other. Water is piped through the inner tube. Refrigerant is piped through the tube that encloses the inner tube. The refrigerant flows in the opposite direction than the water.

METHODOLOGY

In this thesis a design optimization technique that can be useful in assessing the best configuration of a finned-tube condenser. Heat transfer by convection in air cooled condensers is studied and improved in this work. The assessment has been carried out on an air-cooled finned-tube condenser of a vapour compression cycle for air conditioning system.

- The materials used for tube is copper and for fins are Aluminum Alloy 1100, Aluminum alloy 6063 and Magnesium. The refrigerants are HCFC, 404R.
- Cooling load calculations are done to determine the capacity of air conditioner required to cool the required room.
- Thermal flux calculations are done theoretically to compare the results with analytical results.
- 3D modeling is done in Pro/Engineer. The dimensions of the condenser are taken from the component itself using reverse engineering process.
- Heat transfer analysis is done on the condenser to evaluate the better design and material. Analysis is done in Ansys. The analysis is done to verify the heat transfer rate, temperature distribution.
- The better material for fin and better refrigerant are analyzed using heat transfer analysis.

THERMAL FLUX CALCULATIONS

Inside temperature = 50^0C+273 = 323K

Atmospheric temperature =40^0C+273 = 313K

Total area = 39807.7

Contact area = 47.12

Discharge of heat flow = x = 21mm

Tube thickness = 1

Calculating heat flux for 3 different materials:

1. Copper : Thermal conductivity = K =390W/mk
2. Aluminum(1100): K = 220 W/mk
3. Aluminum(6063): K = 193W/mk
4. Mg : K = 160 W/mk
   For HCFC Heat Transfer Coefficient = 243

Heat flux for Aluminum 1100 and R404 as refrigerant

Heat flow is given by = q = U

Where U = overall heat transfer coefficient

A = contact area = $0.002073 m^2$

MODEL OF CONDENSER

TUBE
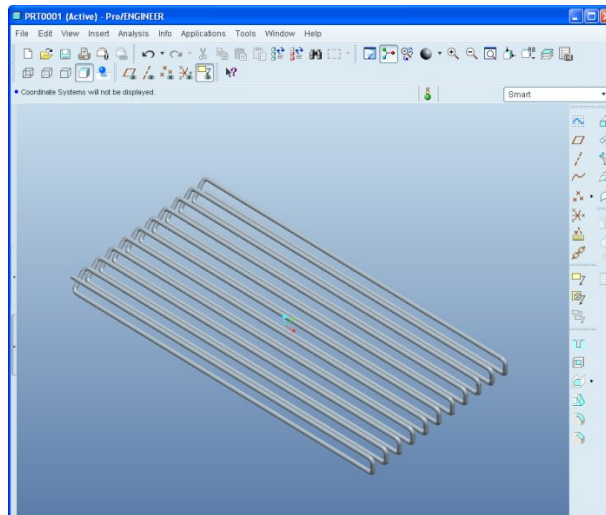
PLATE
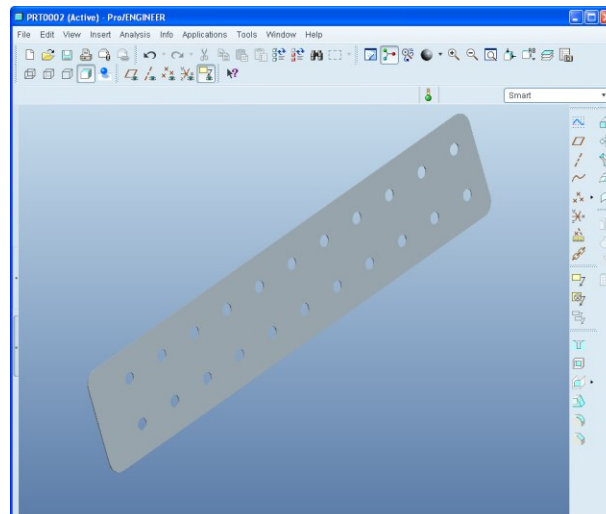
ASSEMBLY
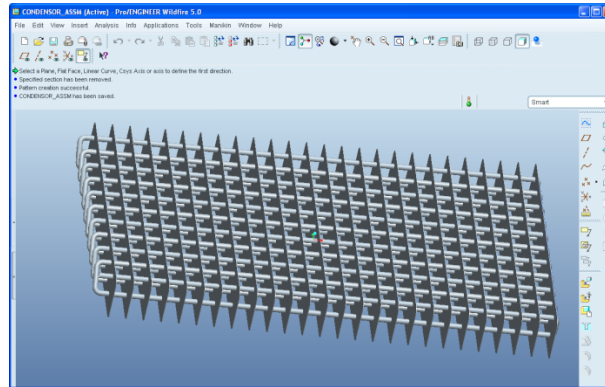
ASSEMBLY
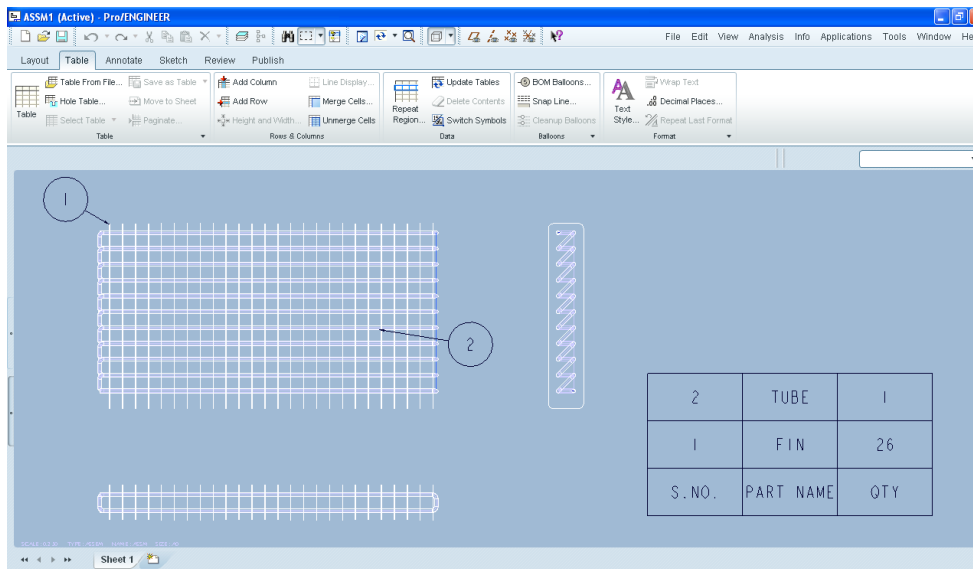
THERMAL ANALYSIS OF CONDENSER

Aluminum1100, Aluminum6063, Magnesium, Copper

Thermal analysis of condenser for HCFC refrigerant: Al 1100 for tubes

Thermal conductivity=230w/mk, Specific heat=900J/Kg.k, Density=2705Kg/m^3

Copper for fins, Thermal conductivity=390w/mk, Specific heat=390J/Kg.k, Density=8900Kg/m^3

Imported model
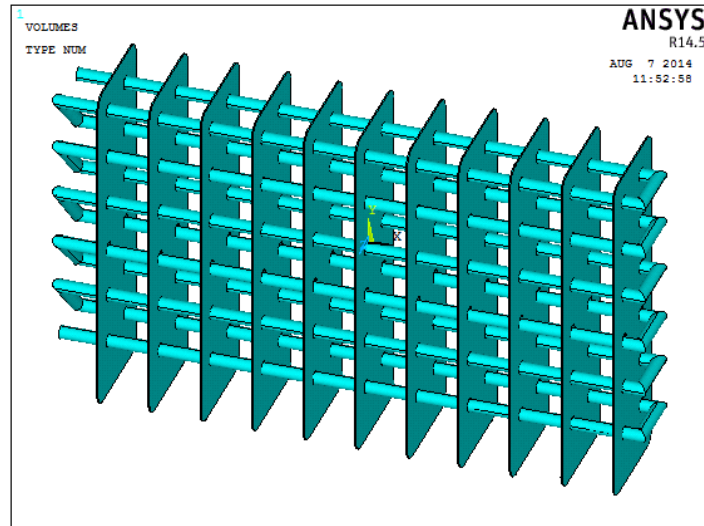
Meshing>mesh tool>smart sizes on> mesh>ok

Meshed model
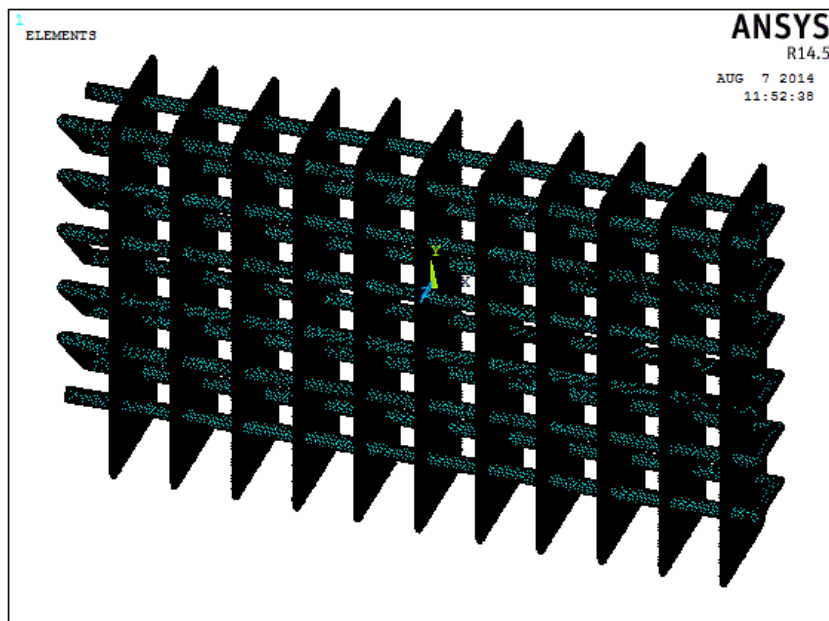
Boundary conditions

The temperature is applied inside the tube of the condensor

The convection is applied on the fins

Solution>solve>current Ls>ok

General post processor>plot results>counter plot>nodal solution>dof solution>nodal temperature>ok

Nodal temperature
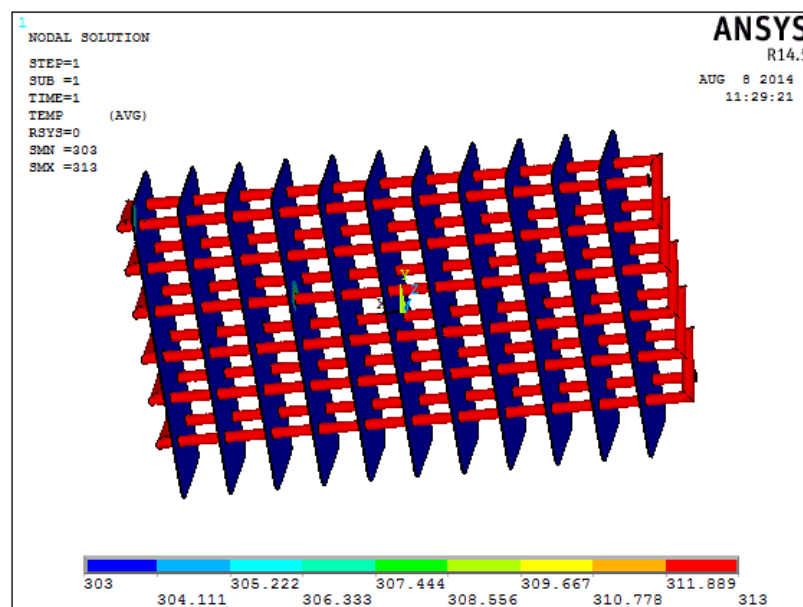
The above figure indicates that the maximum temperature (311.889K to 313K) is in the tubes and is reducing on the fins (303K to 304.111K).

Thermal gradient>vector sum thermal gradient>ok

Thermal gradient
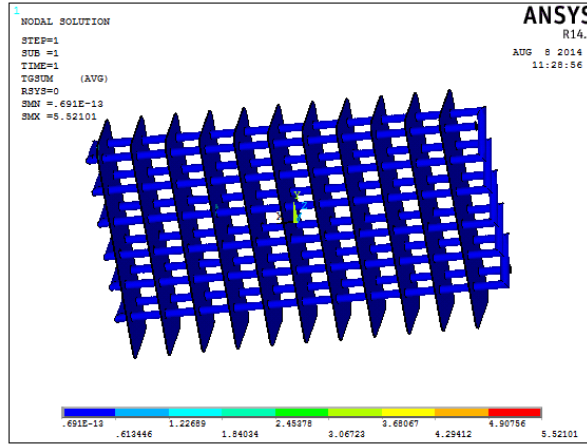
The maximum change in temperature is 5.52101K/mm and minium is $0.691e^{-13}$

Heat flux>vector sum heat flux>ok Heat flux
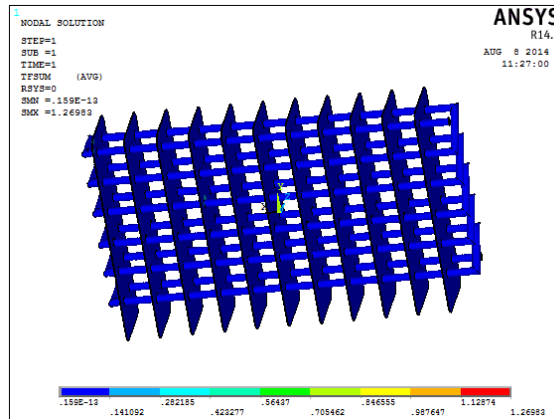
The maximum heat transfer rate is $1.26983W/mm^2$ and the minimum value is $0.159e^{-13}$

Thermal analysis of condenser for HCFC refrigerant

Al6063 for tubes

Thermal conductivity=193w/mk, Specific heat=900J/Kg.k, Density=27000Kg/m^3

Copper for fins

Thermal conductivity=390w/mk, Specific heat=390J/Kg.k, Density=8900Kg/m^3

RESULTS AND DISCUSSION

REFRIGERANTS	MATERIALS	RESULTS		
		Nodal Temperature (K)	Thermal Gradient (K/mm)	Heat flux (W/mm²)
HCFC	Aluminum 1100	313	5.52101	1.26983
	Aluminum 6063	313	5.82506	1.12424
	Magnesium	313	6.16722	0.986754
404R	Aluminum 1100	313	6.43696	1.4805
	Aluminum 6063	313	6.07077	1.28162
	Magnesium	313	6.94673	1.11148

In the above table, the nodal temperature, thermal gradient and thermal flux values are presented from thermal analysis results. From the results, thermal flux is more when Aluminum alloy 1100 is used for fin and refrigerant used is 404. That is the heat transfer rate is more. Thermal gradient is also more that is the change in temperature over a distance is more.

THEORETICAL THERMAL FLUX RESULTS

	Al ALLOY 1100	Al ALLOY 6063	MAGNESIUM
HCFC	2.64	2.44	2.21
R404	2.69	2.488	2.24

In the above table, thermal flux values are presented from theoretical calculations. From the results, thermal flux is more when Aluminum alloy 1100 is used for fin and refrigerant used is 404. That is the heat transfer rate is more.

COMPARISON GRAPHS

THERMAL GRADIENT COMPARISON GRAPH
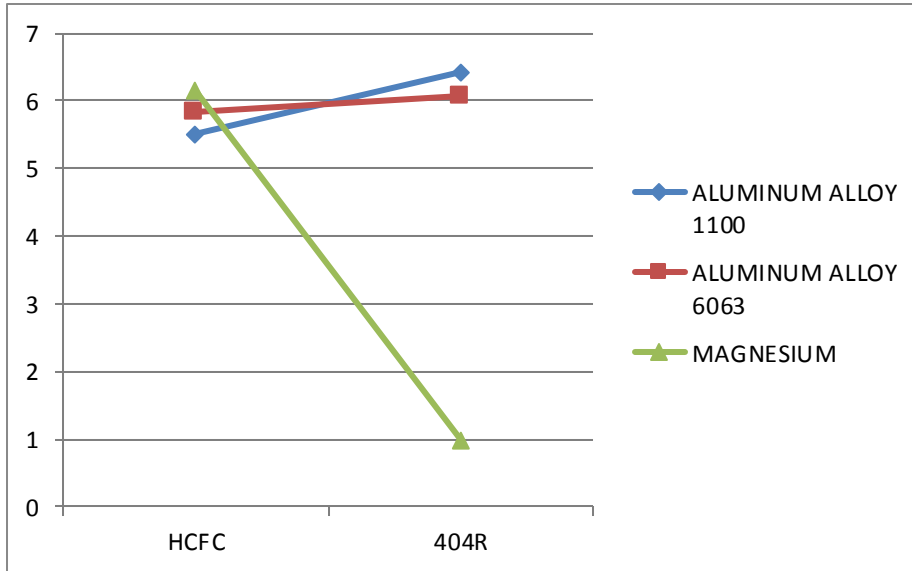
The above graph represents the comparison of thermal gradient values for all the 3 materials and two refrigerants. It shows that refrigerant 404R and aluminum alloy 1100 has more thermal gradient value.

THERMAL FLUX COMPARISON GRAPH
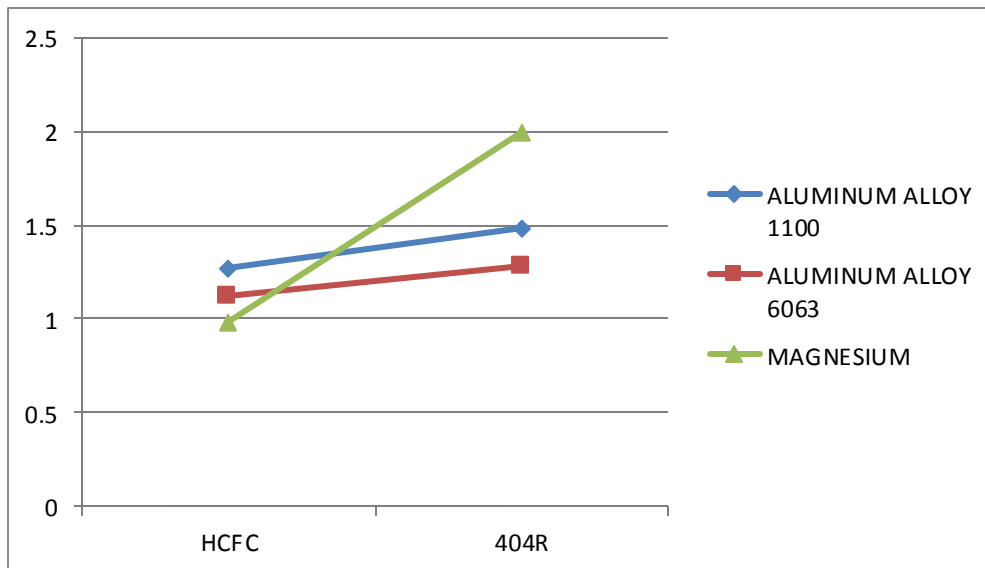
The above graph represents the comparison of thermal flux values for all the 3 materials and two refrigerants. It shows that refrigerant 404R and aluminum alloy 1100 has more thermal flux value.

CFD ANALYSIS OF FIN USING REFRIGERANTS HCFC AND 404R

REFRIGERANT - HCFC

INLET VELOCITY – 2.5m/s

Imported model from Pro/Engineer
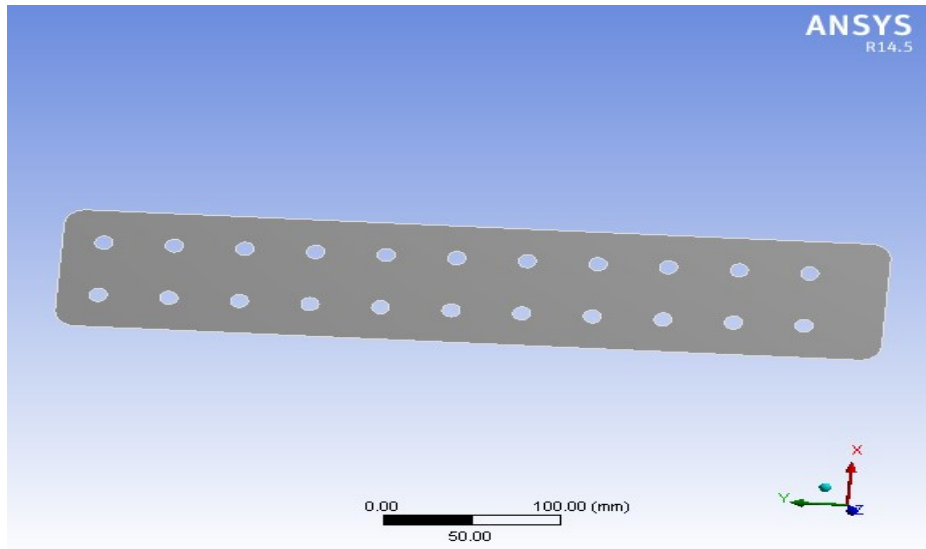
Meshed model
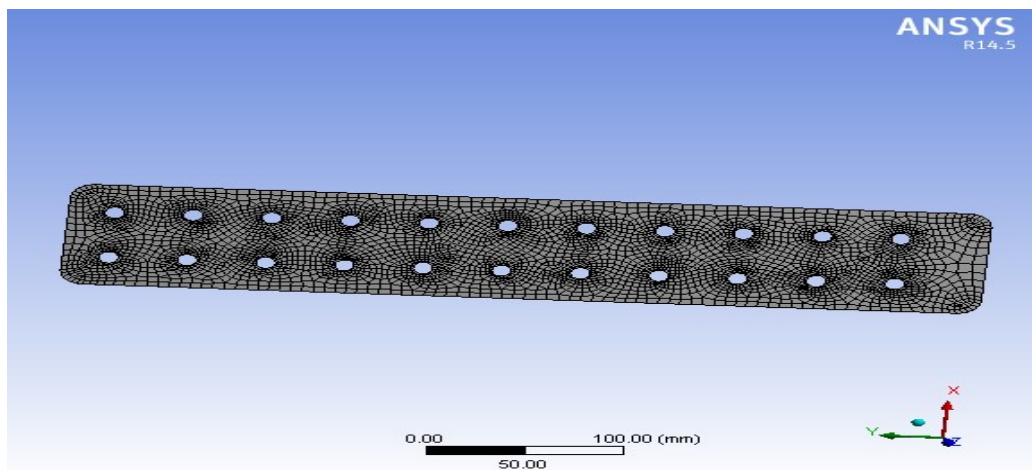
Inlet
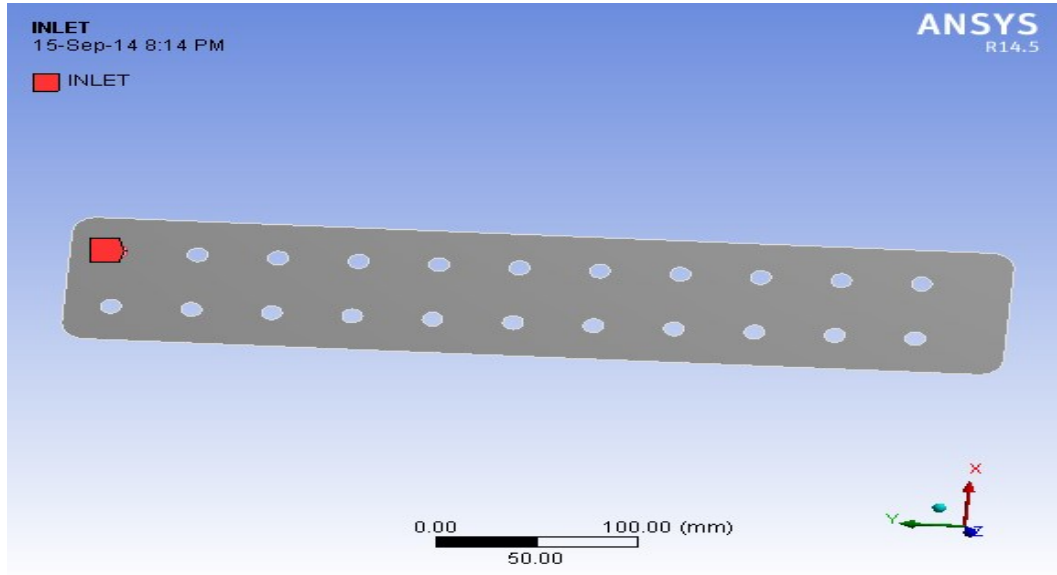
Outlet
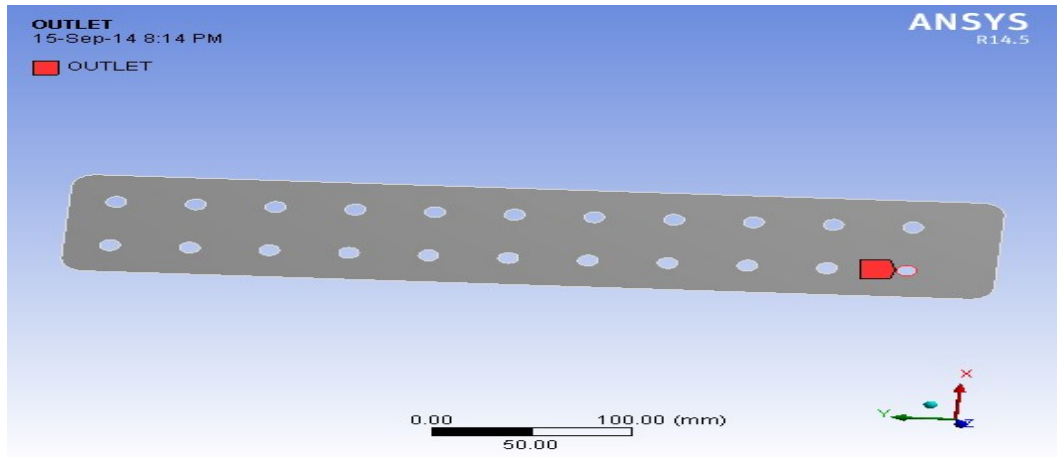
SPECIFYING BOUNDARIES FOR INLET AND OUTLET

Velocity magnitude

Contours of Velocity Magnitude (m/s)

Sep 15, 2014
ANSYS Fluent 14.5 (2d, dp, pbns, ske)
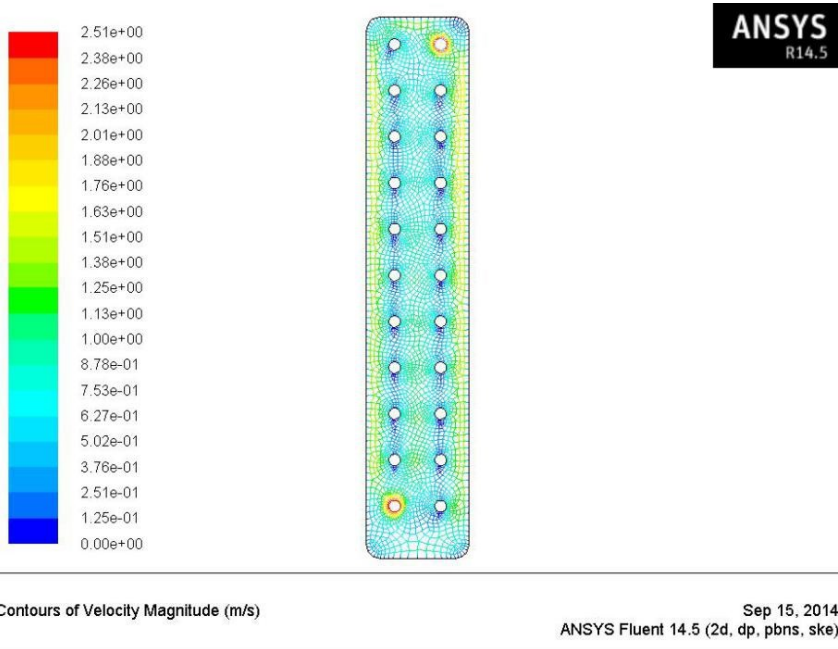
According to the contour plot, the maximum velocity at inlet and outlet holes is 2.51e+00 m/s and the minimum at in between inlet and outlet holes is 1.25e-01 m/s

Static Pressure
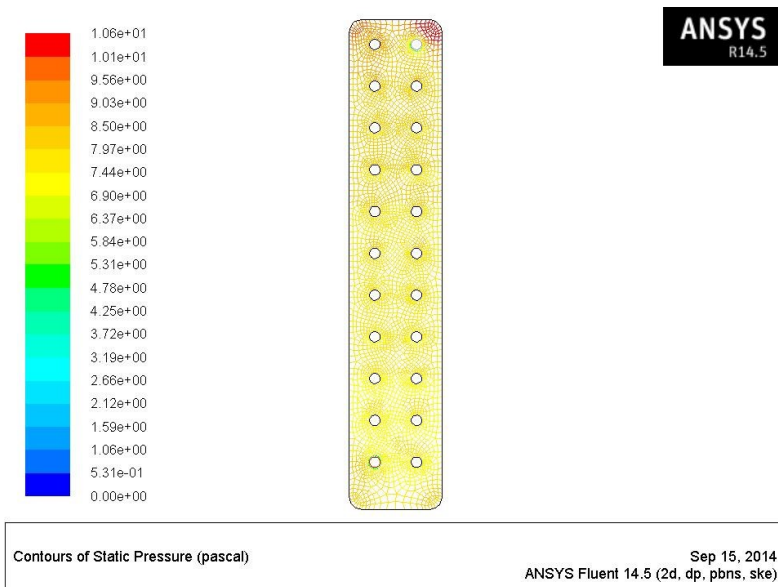
Contours of Static Pressure (pascal)

Sep 15, 2014
ANSYS Fluent 14.5 (2d, dp, pbns, ske)

According to the contour plot, the maximum static pressure at outlet hole beside corners is

1.06e+01pa and the minimum at inlet hole 5.31e-01pa

Temperature
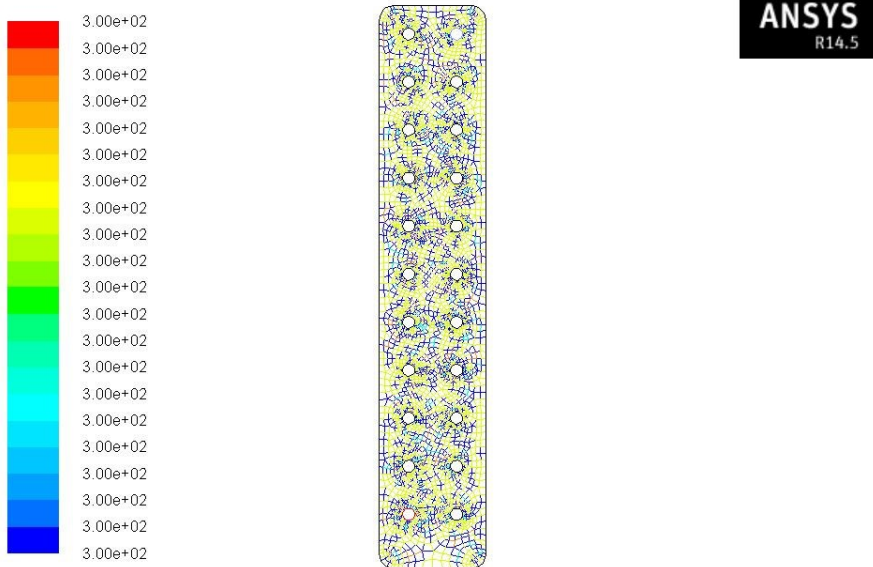
Contours of Static Temperature (k)   Sep 15, 2014
ANSYS Fluent 14.5 (2d, dp, pbns, ske)

According to the contour plot, the maximum temperature at fin body is 3.00e+02 k

Mass flow report

"Flux Report"

	Mass Flow Rate (kg/s)
inlet	0.09587553
interior-_trm_srf	-1.0707636
outlet	-0.095938734
wall-_trm_srf	0
Net	-6.3204351e-05 kg/sec.

The net mass flow rate of fin body is -6.3204351e-05 kg/sec

"Flux Report"

Total Heat Transfer Rate	(w)
inlet	178.51022
outlet	-178.6279
wall-_trm_srf	3.5367242e-13

Net   -0.1176799 w

The net Total heat transfer rate of fin body is -0.1176799 w.

HCFC velocity 5(m/s)
Velocity Magnitude
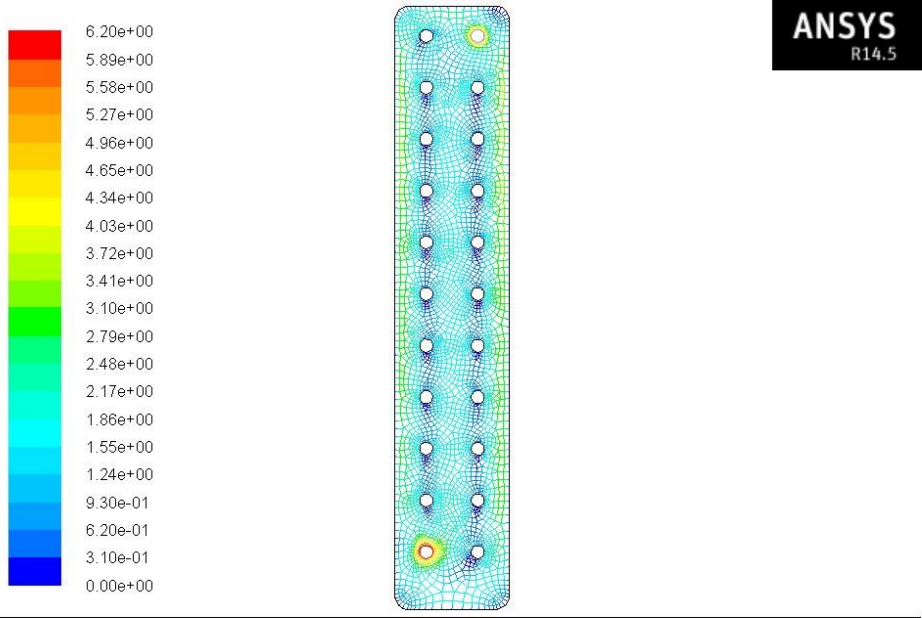
Contours of Velocity Magnitude (m/s)

Sep 16, 2014
ANSYS Fluent 14.5 (2d, pbns, ske)

According to the contour plot, the maximum velocity at inlet and outlet holes is 6.20e+00 m/s and the minimum at in between inlet and outlet holes is 3.10e-01m/s

Static pressure
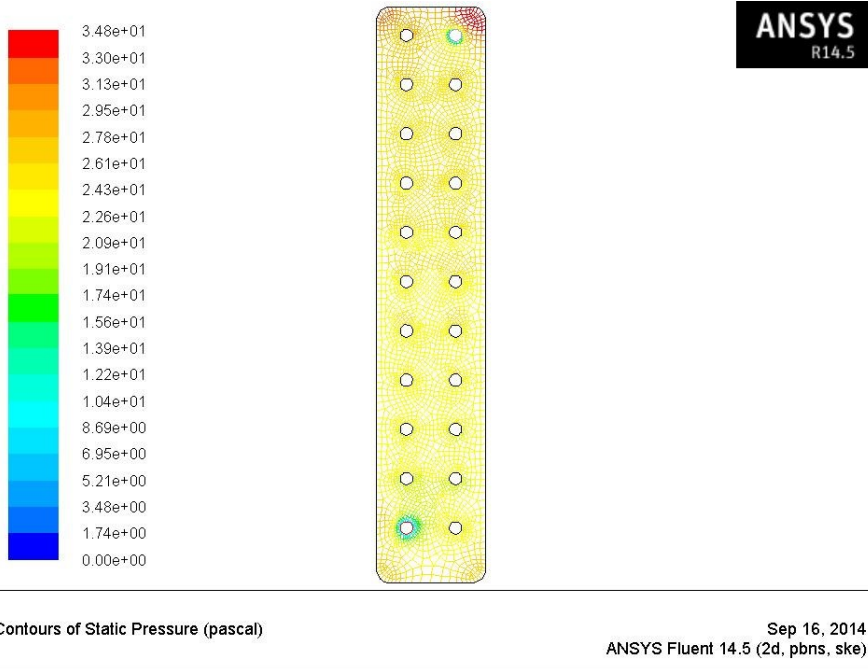
Contours of Static Pressure (pascal)   Sep 16, 2014
                                     ANSYS Fluent 14.5 (2d, pbns, ske)

According to the contour plot, the maximum static pressure at outlet hole beside corners is

3.48e+01pa and the minimum at inlet hole 1.74e+00pa

Temperature

Contours of Static Temperature (k)   Sep 16, 2014
ANSYS Fluent 14.5 (2d, pbns, ske)
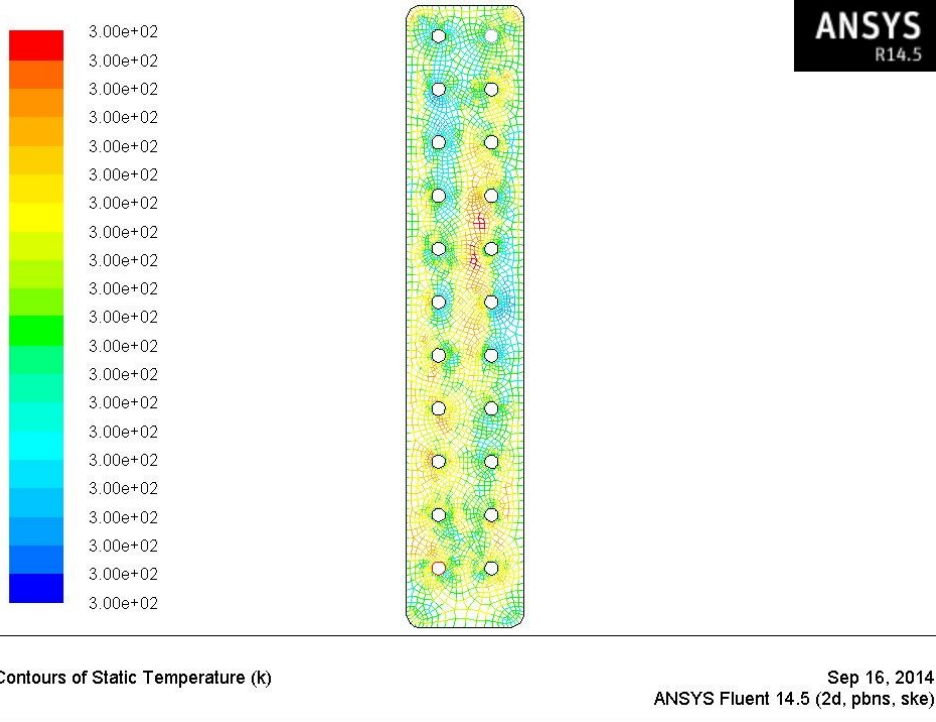
According to the contour plot, the maximum temperature at fin body is 3.00e+02 k

Mass flow rate
"Flux Report"

```
        Mass Flow Rate          (kg/s)
-------------------------------- ---------------------
            inlet        0.191751
   interior-_trm_srf        -1.537853
           outlet        -0.1914832
      wall-_trm_srf            0
   ---------------- -------------------
            Net      0.00026780367  kg/sec
```

The net mass flow rate of fin body is 0.00026780367kg/sec

"Flux Report"
Total Heat Transfer Rate   (w)

```
-------------------------------- ---------------------
            inlet        357.02032
           outlet       -356.51999
      wall-_trm_srf      -0.0013494033
   ----------------- -------------------
            Net         0.49898629  w
```
The net Total heat transfer rate of fin body is 0.49898629w

404R Velocity 2.5(m/s)

Import model
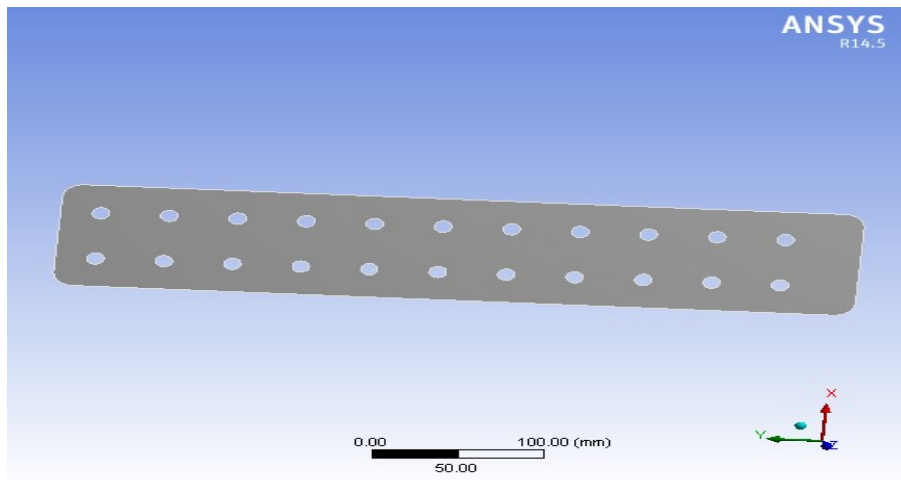
Meshed model
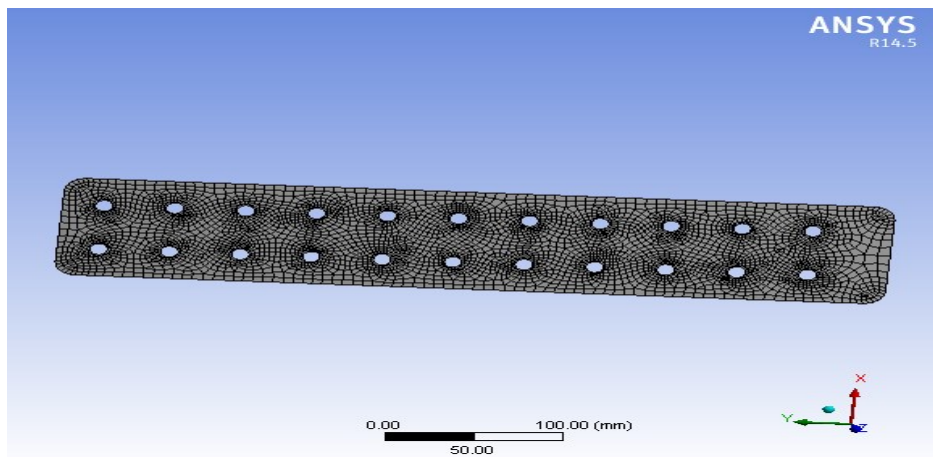
Inlet view
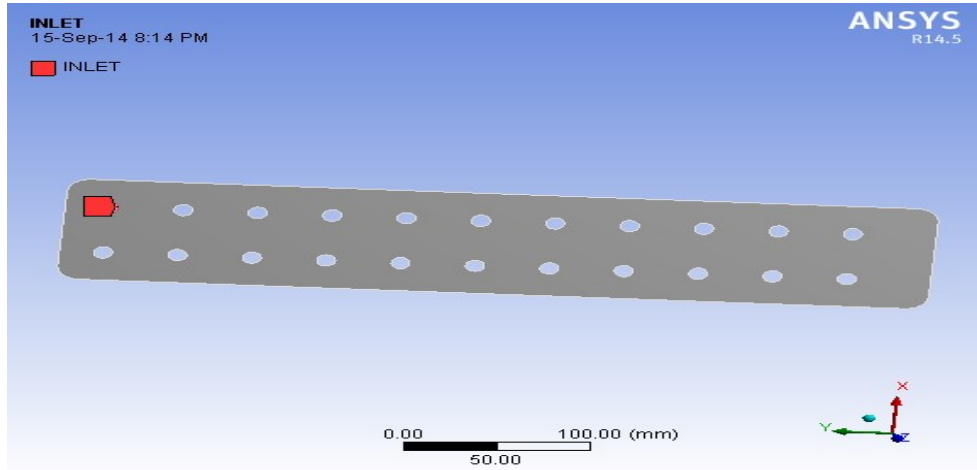
Outlet view
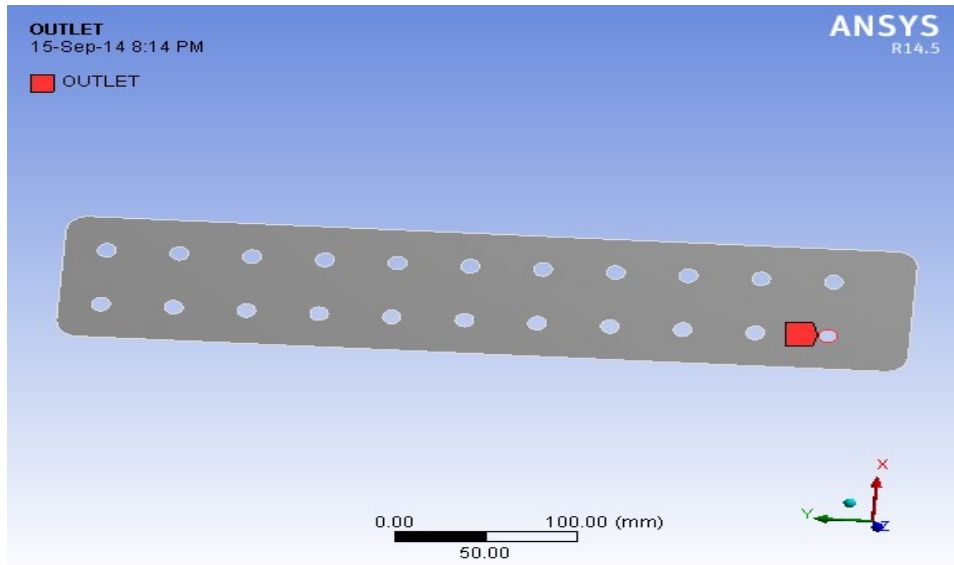
RESULTS TABLE

		Velocity Magnitude (m/s)	Static pressure (Pascal)	Temperature (k)	Mass Flow Rate (kg/s)	Heat Transfer Rate (w)
	2.5m/s	2.51e+00	1.06e+01	3.00e+02	6.3204351e-05	0.1176799
Hcfc	5 m/s	6.20e+00	3.48e+01	3.00e+02	0.00026780367	0.049898629

		Velocity Magnitude (m/s)	Static pressure (Pascal)	Temperature (k)	Mass Flow Rate (kg/s)	Heat Transfer Rate (w)
	7.5 m/s	9.02e+00	7.21e+01	3.00e+02	0.00015335049	0.28552244
404R	2.5 m/s	3.58e+00	5.23e+01	3.00e+02	0.0052805282	9.8317916
	5 m/s	5.40e+00	2.96e+01	3.00e+02	7.5668995e-05	0.14088776
	7.5 m/s	7.51e+00	1.70e+02	3.00e+02	0.000562426693	1.0506061

GRAPHS

VELOCITY MAGNITUDE
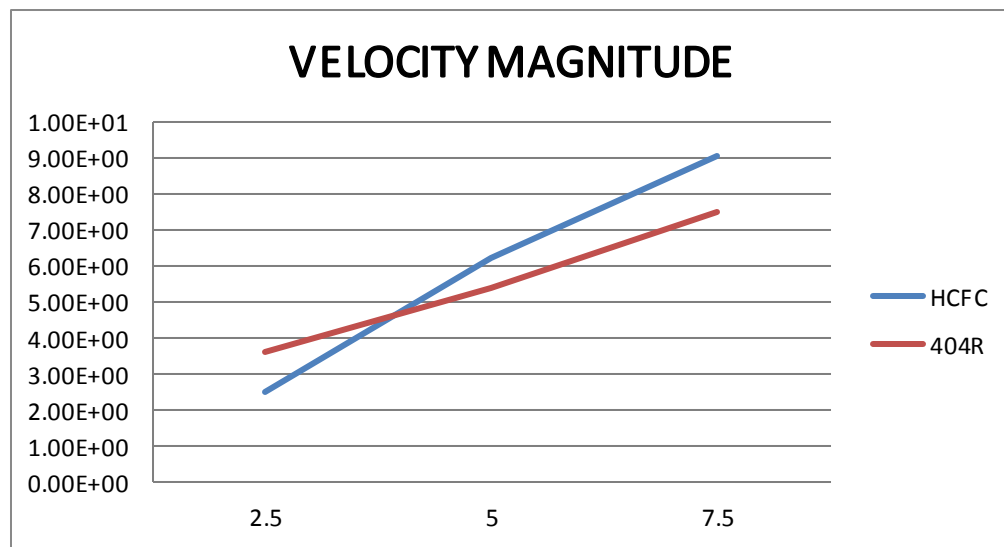
The above graph represents the comparison Between refrigerant and velocities for the 2 materials of HCFC and 404R refrigerant. It shows that the HCFC has more velocity magnitude than 404R.

STATIC PRESSURE
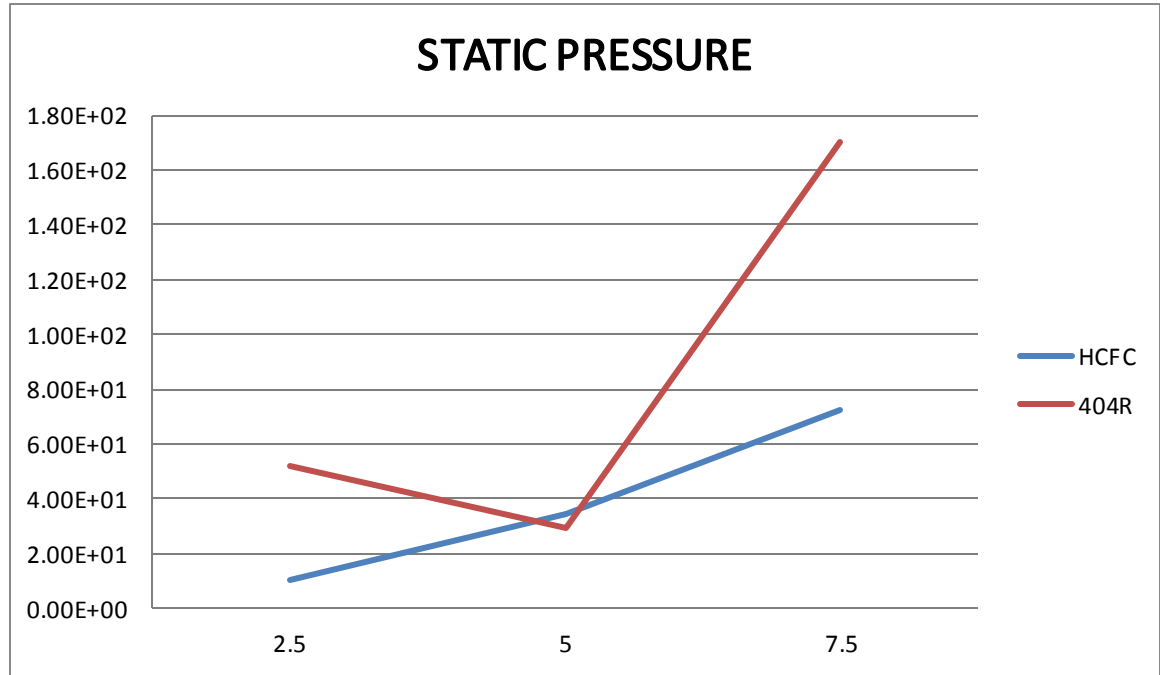
The above graph represents the comparison Between refrigerant and velocities for the 2 materials of HCFC and 404R refrigerant. It shows that the 404R has more static pressure than HCFC

TEMPERATURE
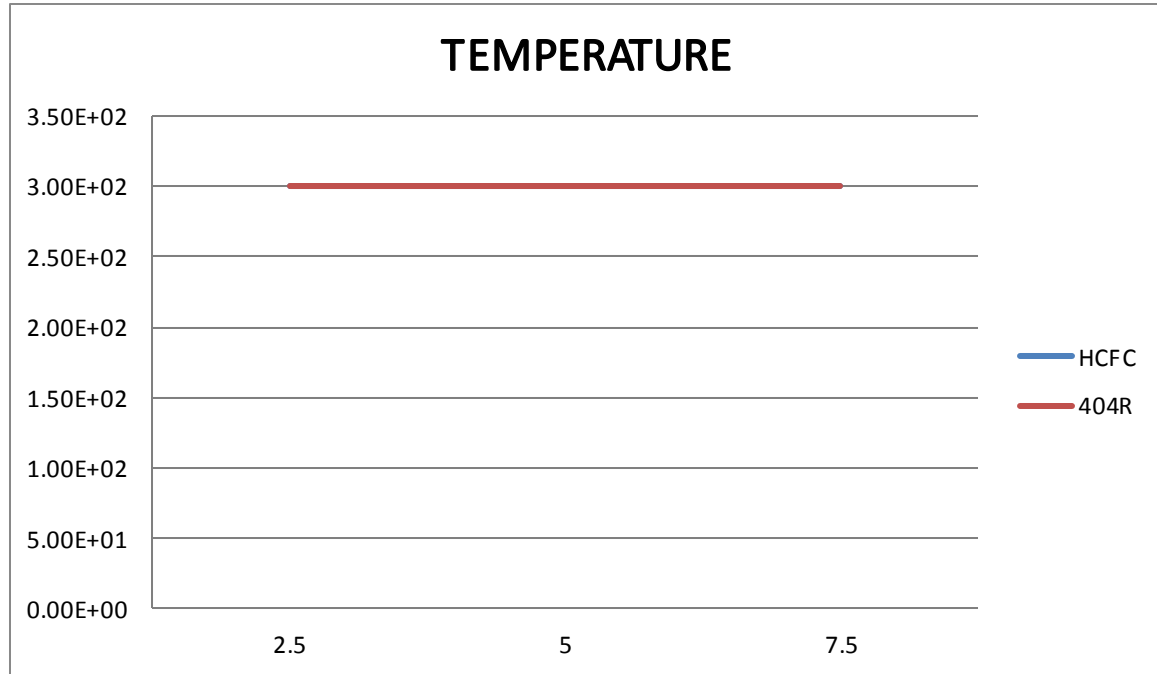
TEMPERATURE

The above graph represents the comparison Between refrigerant and velocities for the 2 materials of HCFC and 404R refrigerant. It shows that the HCFC and 404R are equal.

TOTAL MASS FLOW RATE
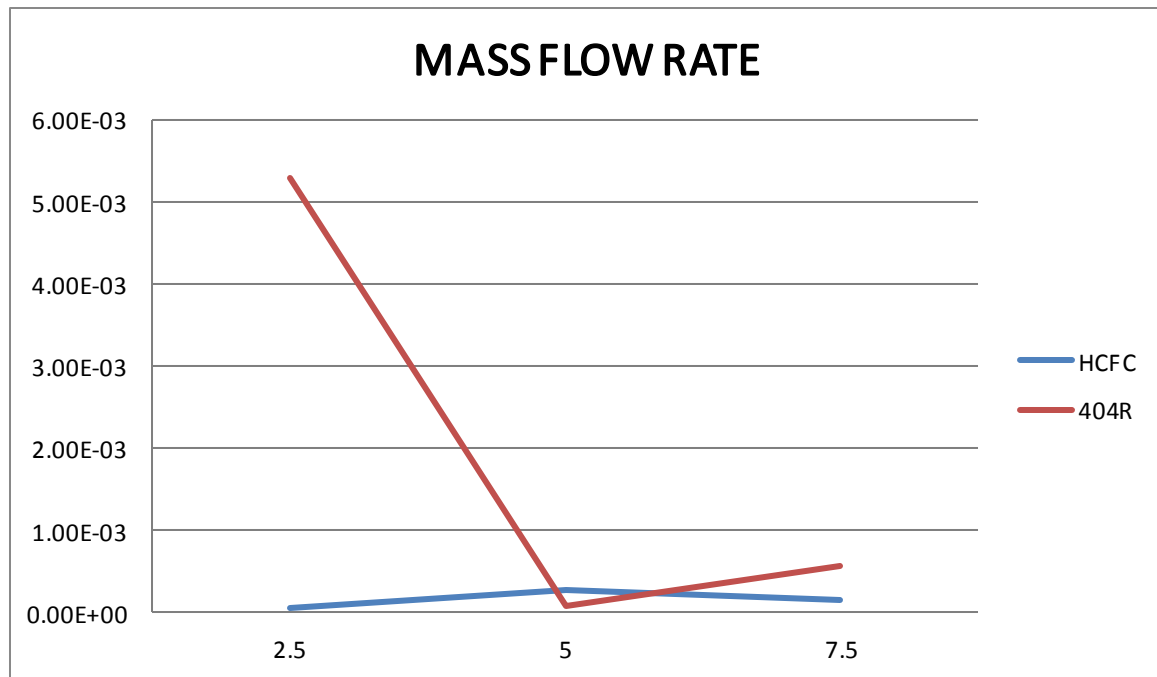
MASS FLOW RATE

The above graph represents the comparison Between refrigerant and velocities for the 2 materials of HCFC and 404R refrigerant. It shows that the HCFC has more mass flow rate than 404R.

TOTAL HEAT TRANSFER RATE
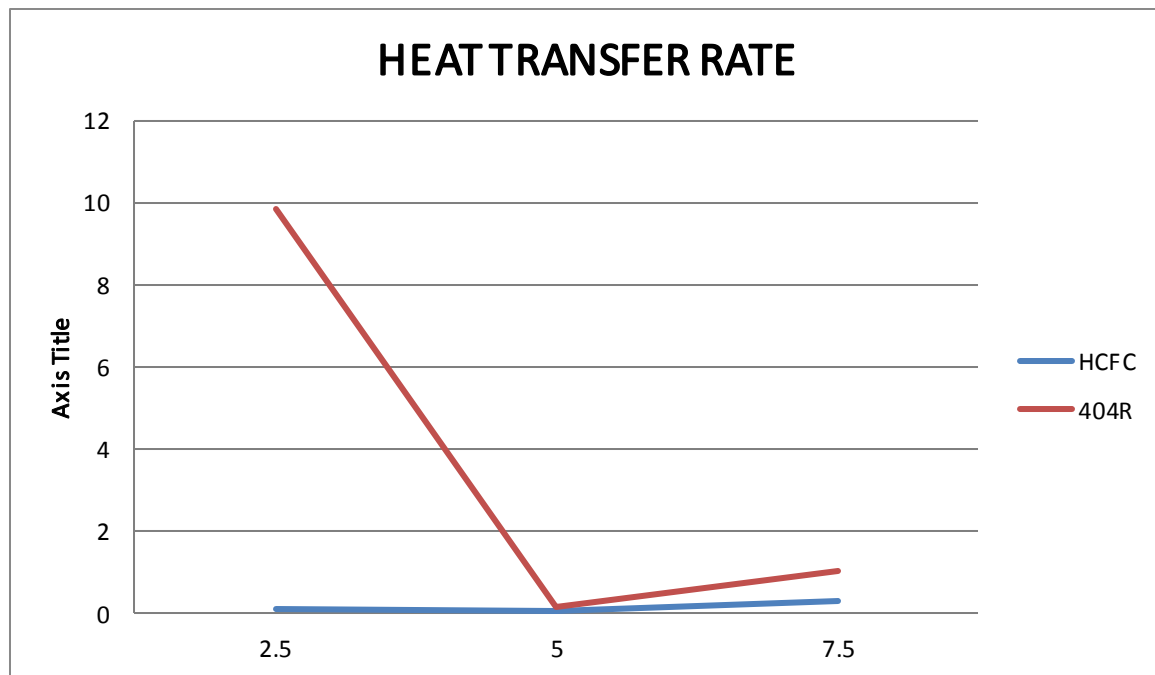
The above graph represents the comparison Between refrigerant and velocities for the 2 materials of HCFC and 404R refrigerant. It shows that the HCFC has more heat transfer rate than 404R.

CONCLUSION

In this thesis, an ac condenser is designed and optimized for better material, refrigerant and thickness to improve the heat transfer rate. Present used material for fin is Aluminum alloy 204 and cooling fluid is HCFC. Modeling is done in Pro/Engineer. To optimize the condenser for best result, thermal analysis is done on the condenser. Analysis is done using fin materials Aluminum Alloy 1100, Aluminum Alloy 6063 and Magnesium alloy. And also by changing the cooling fluid HCFC and R404.

By observing the thermal analysis results, by using fin material Aluminum alloy 1100, thermal flux is more than by using other two materials. So by using Aluminum alloy 1100, the heat transfer rate increases. And also by taking refrigerant R404 is better. Thermal flux is also calculated theoretically, by observing the results, using fin material Aluminum alloy 1100 and refrigerant R404 has more heat transfer rate.

FUTURE SCOPE

The use of material Aluminum alloy 1100 is better analytically. More experiments have to be done to check the feasibility of using the material depending on other factor like environment conditions and cost analysis. Refrigerant 404R is better. Experiments are to be done also for that.

REFERENCES

[1]. Experimental Investigation of Split air Conditioning System by liquid Based Cooling System by Balaji N, Suresh Mohan kumar P

[2]. EFFICIENT USAGE OF WASTE HEAT FROM AIR CONDITIONER by M. Joseph Stalin, S. Mathana Krishnan, G. Vinoth Kumar

[3]. Comparitive analysis of an automotive air conditioning systems operating with CO2 and R134a by J. Steven Brown a, Samuel F. Yana-Motta b,Piotr A. Domanski c

[4]. Performance Enhancement of Air-cooled Condensers by M. M. Awad , H. M. Mostafa , G. I. Sultan , A. Elbooz

[5]. S.H. Noie-Baghban, G.R. Majideian, "Waste heat recovery using heat pipe heat Exchanger (HPHE) for surgery rooms in hospitals", Applied Thermal Engineering, Vol. 20, (2000) 1271-1282.

[6]. P.Sathiamurthi, R.Sudhakaran "Effective utilization of waste heat in air conditioning. Proc. (2003) 13-14.

[7]. P. Sathiamurthi, PSS.Srinivasan, design and development of waste heat recovery system for air conditioner, European Journal of Scientific Research ISSN 1450-216X Vol.54 No.1 (2011), Pp.102-110.

[8]. N.Balaji, P.Suresh Mohan Kumar, Eco friendly Energy Conservative Single window Air Conditioning System by Liquid Cooling with helical inter cooler ISSN 1450-216X Vol.76 No.3 (2012), pp.455-462

[9] S.C.Kaushik, M.Singh. "Feasibility and Refrigeration system with a Canopus heat exchanger", Heat Recovery Systems & CHP, Vol.15 (1995)665 - 673.

[10] R.Tugrul Ogulata, "Utilization of waste-heat recovery in textile drying", Applied Energy.

Design and Thermal Analysis by Finite Element Methods of Cylinder Head of SI Engine

Aerukonda sandeep kumar

M.Tech (Thermal engineering),

P.G. Scholar

Nishitha College of engineering and technology

Sandeepmystar@gmail.com

Rangdal Srikanth

Mtech(AMS), Asst professor

Nishitha College of engineering and technology

ABSTRACT

The paper which was presented bargains warm investigation of the chamber head get together of the four stroke motor. A nitty gritty FE model was made for this reason. The FE model comprises of principle parts of the barrel head gathering and it incorporates a depiction of warm and mechanical loads and contact cooperation between its parts. The model considers a temperature reliance of a warmth exchange coefficient on divider temperature in cooling Passages as balances. The paper displays an examination of figured and measured temperature. The investigation was completed utilizing the FEM program. The limited component technique is connected to discover the temperature dissemination field from the parts of barrel head of SI motor. This paper means to concentrate on the temperature on a motor barrel head sparkle ignition, which is known helpful qualities and the warm parameters. The paper manages warm investigation and change of the barrel head get together of SI (Spark Ignition) motor. The outline was done utilizing the SolidWorks v12 and investigation was done utilizing the FE program ANSYS v14.

Keywords: *Actual process, Cylinder Head, Deformation Spark Ignition Engine, Temperature, Finite element, Stresses, mesh.*

INTRODUCTION

Plan work of current warmth motors requires precise determination of temperature, keeping in mind the end goal to streamline the relationships between's size, shape and properties of materials utilized for parts from one viewpoint, and the thermo-mechanical applications, on the other. This paper intends to think about the temperature dispersion in single barrel head sparkle ignition motor. Barrel head temperature has extensive impact on effectiveness, outflow, and execution of the SI (Spark Ignition) motor. Motivation behind this examination is estimation of chamber head transient temperature at a few focuses. On the chamber head temperature changes with time and motor velocity, from cool begin to consistent condition and examination with aftereffects of limited component investigation. From explanatory examination of chamber head, it is proposed to lead stress investigation of a thick walled barrel head close to the spiral opening at first glance. The writing demonstrated that there will be a malleable crack happening in such cases. The spiral gaps can't be maintained a

strategic distance from because of different connections. Thus the anxiety investigation of barrel head and its definitive disappointment under inner weight past versatile breaking point is a fitting situation. It is watched that there are a few elements which impact stress power elements. The Finite component investigation is led utilizing business solvers ANSYS and SolidWorks. Hypothetical formulae based results are gotten from ANSYS programs. The single-chamber petrol motor has the properties of little volume, high power, high torque at low speed, great start-up and increasing speed execution, low oil wear and shabby, and it has been broadly utilized. Embracing the aluminum compound motor barrel head can viably lessen the aggregate weight of the motor. In any case, the flexible modulus of aluminum compound is far not as much as that of cast iron, the twisting measure of the motor barrel head and related parts strongly increment with the fuel gas most extreme burning weight.

Twisting of the barrel head will bring about gas spillage, sleek smoke, shut down, fuel utilization expand, build the likelihood of cylinder scratching; Deformation of chamber top surface will build the likelihood of the barrel gasket

and reduction mechanical effectiveness, moving parts can't work ordinarily. Something else, as a result of the high warm conductivity of aluminum composite, the warmth of burning chamber can exchange to crankcase effortlessly and make the oil temperature rise so that grease execution of motor deteriorate, motor force diminish and can't work regularly in genuine case. The metals are ordinarily amalgams of aluminum, magnesium, or titanium The specialbenefits showed by metal lattice composites, for example, lower thickness, higher particular quality and firmness, high temperature execution confines, and enhanced wear-scraped area resistance on the properties of the framework compound subject to the properties of the network combination. In the burning chamber, there are high tops of ignition weight and temperature in the request of 15 MPa and 2500K. The most extreme temperature of the head material is much lower and the districts around the burning load should be securely cooled to anticipate overheating these truths are key components to numerous bargains in configuration, which can be wellsprings of disappointments in operation. To invalidate the danger of operational

disappointment is one of the objectives of motor creators.

The configuration of the motor head must be tried under these operational conditions. This methodology is important however costly. FE demonstrating of the chamber head get together operation conditions is a fitting supplement to the operational testing. A itemized FE quality examination gives significant data about temperature dispersion and mechanical hassles in the general gathering of the chamber head. Temperature and mechanical anxieties is broke down utilizing temperature field, ignition weight in the burning chamber and mechanical burdens, for example, jolt pre-stress, formed seats and valve guides, and so on. The subsequent relocation/stress fields i.e. contact weight amongst valves and valve parts consistency and in addition quality and disappointment resistance of the get together. Such data adds to a definite assessment of the warm and mechanical procedures in barrel head get together under motor operation, which is an essential for further advancement of motor configuration. Chamber head Distortion implies deviation from perfect roundabout shape (roundness), or barrel head out of roundness. At first it is

comprehended that assembling resistances can bring about the barrel head to go astray from perfect condition.

1. Some Concept about Finite Element Method

The limited component strategy is a standout amongst the most utilized techniques that are accessible as a part of our days for various counts in the field of building. This technique and the projects taking into account it get to be essential parts in the PC supported outline frameworks. They are fundamental in all designing exercises where elite is required. One of the real points of interest in the limited component technique is the effortlessness of its essential ideas. It is imperative that the limited component technique client learn and accurately comprehend these ideas, since they incorporate certain speculations, rearrangements and speculations. To play out a limited component examination, the client must build up a math model of the broke down pieces. These models are just estimated numerical models of the pieces. There are no calculations and general techniques for building up a special model that estimated, with a known mistake, the genuine structure of the broke down piece.

The model ought to effectively blend all the accessible data about the broke down piece, a model comprises of lines, planes or bended surface and volumes, created in a 3D CAD environment. In this phase of advancement, the model is constant, with a limitless number of focuses, as the genuine pieces that is examined. The principle objective of the limited component technique is to get the limited component network, changing the consistent structure into a watchful model, with a limited number of focuses. This operation is done utilizing a cross section for the model, which is right from a designing perspective, the information of hassles and relocations in a specific number of focuses inside the piece is typically enough to portray the mechanical and thermic conduct of the piece. The limited component strategy characterizes these questions just in the hubs of the model and figures their qualities in these focuses. That is the reason the cross section process must be performed so as to have various hubs sufficiently extensive in the zones of extraordinary enthusiasm for request to accomplish an attractive estimation for the geometry of the piece and for the limit and stacking conditions. In this way, the cross section of the piece has a

noteworthy significance in the limited component strategy investigation. The focuses characterized in the cross section are called hubs. The essential questions of limited component strategy are characterized in hubs, and their qualities are the investigation results.

These questions recognized can be relocations, dislodging model or anxieties, stress model. For the uprooting model, it can be conceded that the disfigured state of the piece under a specific stacking case, is characterized by the relocations of the considerable number of hubs regarding the underlying hub net. Every hub may have a greatest of six parts of the uprooting, called nodal removals in a direction framework: three straight relocations and three revolutions. The cross section process separates the model into a specific number of limited components. These components are amassed together in like manner hubs.

Finite Element Model

The SI engine cylinder head shown as Fig.1

Along these lines, the investigation of the genuine piece is supplanted with the investigation of the gathering of limited components got by cross section, in a glorification of the genuine piece which is broke down. For better results, the procedure ought to be satisfactory to the motivation behind the examination, inferring the appreciation for some imperative principles in regards to the lattice procedure and the elaboration of the model, furthermore to utilize sufficient limited components. The cross section of an examined piece can incorporate components characterized for various sorts of examination, as: straight versatile, nonlinear, heat exchange, liquid mechanics, electromagnetism, and so on. In the limited component technique hone, the part of the material's attributes is essential and for this situation the material appended to the limited component can be homogeneous, isotropic or with a specific anisotropy.
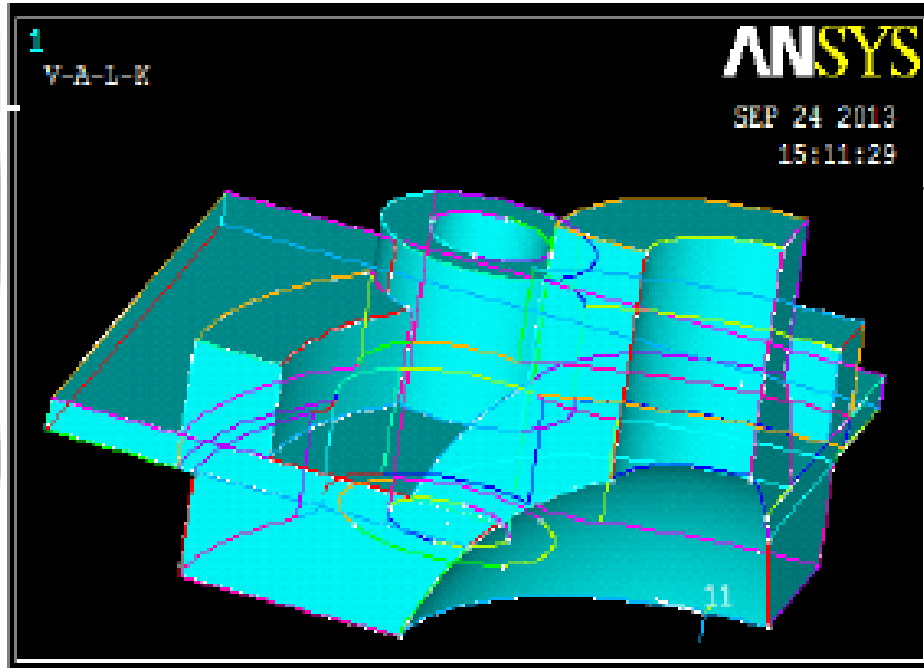
Figure 1: SI engine cylinder head
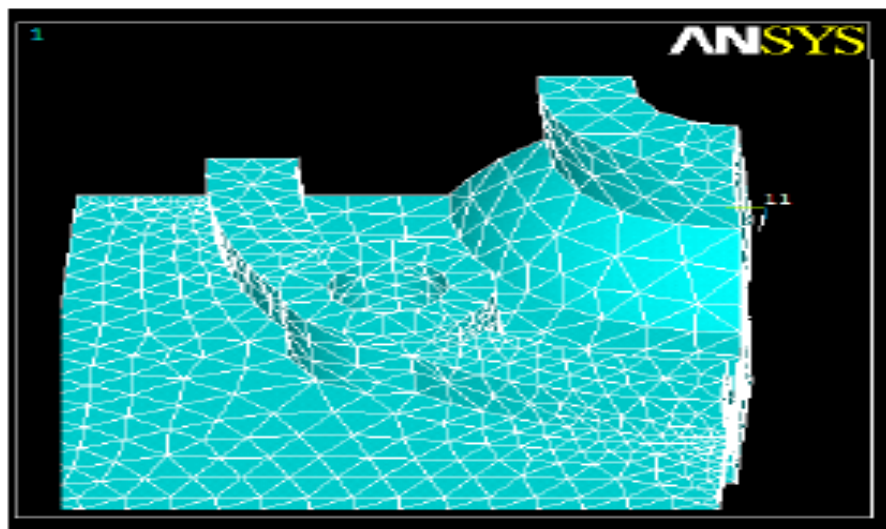
Figure 2: Mesh Model of cylinder head
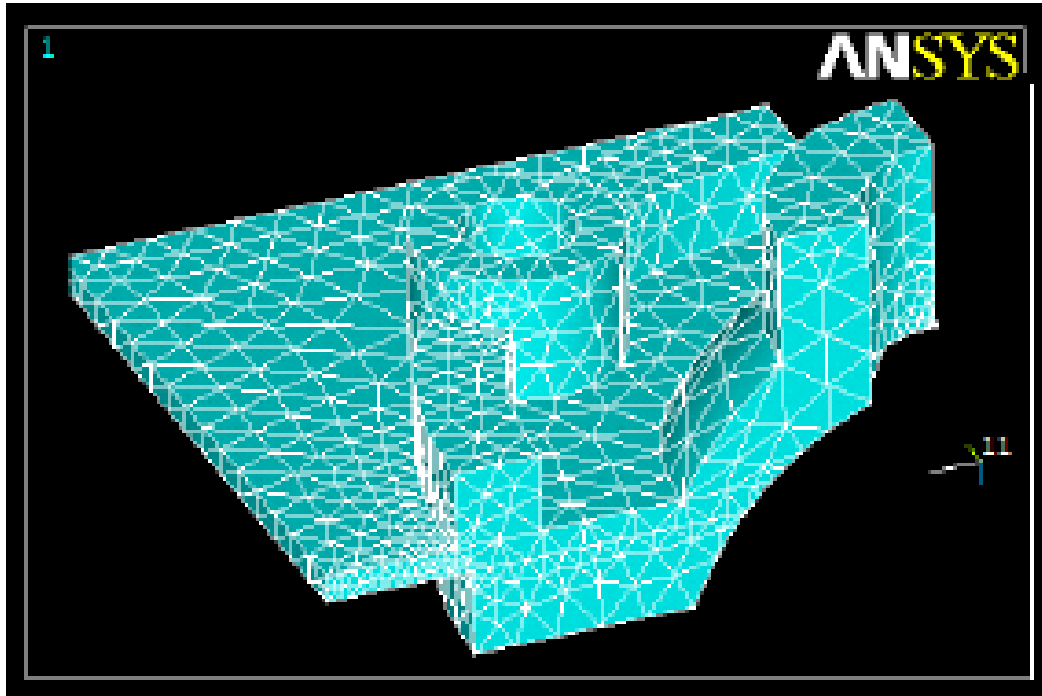
Figure 3: Meshing model

Thermal Properties

• Thermal conductivity, $K = 0.02598$ W/mm° C

• Specific heat, $C = 0.251$ KJ/Kg° C

• Density, $P = 0.01022$ Kg/

Convection Properties

• Heat transfer film coefficient (inner surface) $= 6.015E-4$

• Bulk temperature (inner surface) $=$

• Heat transfer film coefficient (outer surface) $= 30E-6$

• Bulk temperature (Outer surface) $=$

Dislodging imperatives of the X, Y, Z three headings are forced on the area of the four jolt gaps of the lower body. So as to explore the impact of side weight of barrel head, constrained with the greatest side weight of chamber head.

CALCULATION SCHEMES

Schemes1: The lists of the anxiety, the evenness of the chamber head end surface and the rate of light spillage of every cross segment of the petrol motor barrel head joined parts can be got by breaking down the cast-iron motor chamber head as per limited component strategy. Those files are as assessing pointer of the enhanced plans.

Scheme2: Changing the cast-iron motor body into aluminum composites chamber head, and afterward breaking down the assessments lists of scheme1 and scheme2 by limited component technique contrastively.

Scheme3: Expanding the profundity of the counter bore of chamber head jolt from 5mm to 12mm and thickness of the four stiffeners behind the barrel head jolt from 6mm to 10mm, digging the Partial metal close to the two jolts on the abdominal area, expanding the zone of the stiffener over the Body's head. At that point dissect the assessing marker of

scheme3 and scheme1 by limited component technique contrastive.

Scheme4: Expanding the profundity of the counter bore of barrel head jolt from 5mm to 15.2mm; other change measures are same as scheme3. At that point break down the assessing marker of scheme3 and scheme1 by limited component technique contrastively.

THERMAL ANALYSIS

Thermal Investigation the temperature circulation and related warm amounts in a framework or segment. Run of the mill warm amounts of interest are:

• The temperature distributions.

• The amount of heat lost or gained.

• Thermal gradients.

• Thermal fluxes.

Types of Thermal Analysis

ANSYS supports two types of thermal analysis:

•An enduring state warm examination decides the temperature dissemination and other warm amounts understeady-state stacking conditions. An unfaltering state stacking condition is a circumstance where heat stockpiling impacts shifting over a timeframe can be overlooked.

• A transient warm investigation decides the temperature circulation and other warm amounts under conditions that shift over a timeframe.

Transient Thermal Analysis

Transient warm examination is the warm investigation where in limit conditions and properties Change with time. This is to say that the requirements, for example, encompassing temperature, warm coefficient and material properties and so on are time subordinate. Transient warm examination is imperative in dissecting models that are subjected to limit conditions and material properties that with time and temperature. Barrel head utilized as a part of SI motors are subjected to high temperature rise. Since the chamber head is subjected to substantial temperature variety, the material properties, for example, particular warmth, enthalpy and youthful's modulus experience varieties

with time. In such conditions there is the likelihood of disappointment of the barrel head if the chamber head is not outlined mulling over the transient impacts. Toward the start of the chilly begin, the segment is at uniform encompassing temperature. At the point when an icy metal segment is presented to a hot liquid medium, warm angles set in over the thickness and along the length. In the midst of the warm transient, this temperature slope changes with time till the metal achieves its relentless state temperature circulation. Because of warm vitality of the metal, it takes more opportunity to achieve its consistent state esteem by conduction than the genuine term of liquid temperature change amid the transient.

Coupled Thermal Structural Analysis

A consecutively coupled material science examination is the blend of investigations from various designing orders which communicate to take care of a worldwide building issue. At the point when the contribution of one material science examination relies on upon the outcomes from another investigation, the investigations are coupled. In this way, each diverse material science environment must be developed

independently so they can be utilized to decide the coupled material science arrangement. Notwithstanding, take note of that a solitary arrangement of hubs will exist for the whole model. By making the geometry in the principal physical environment, and utilizing it with any after coupled situations, the geometry is kept steady. For our case, we will make the geometry in the Thermal Environment, where the warm impacts will be connected. Despite the fact that the geometry must stay consistent, the component sorts can change. Case in point, warm components are required for a warm investigation while basic components are required to decide the anxiety in the rotor and packaging. It is essential to note, however that exclusive certain blends of components can be utilized for a coupled material science investigation.
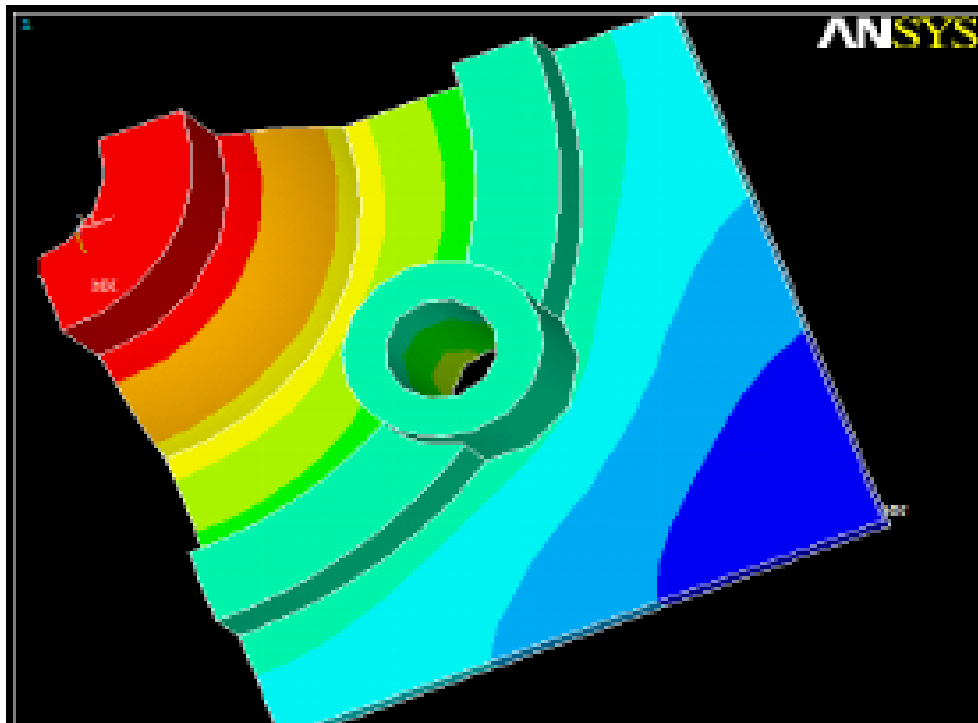
Figure 4: Temperature Distribution
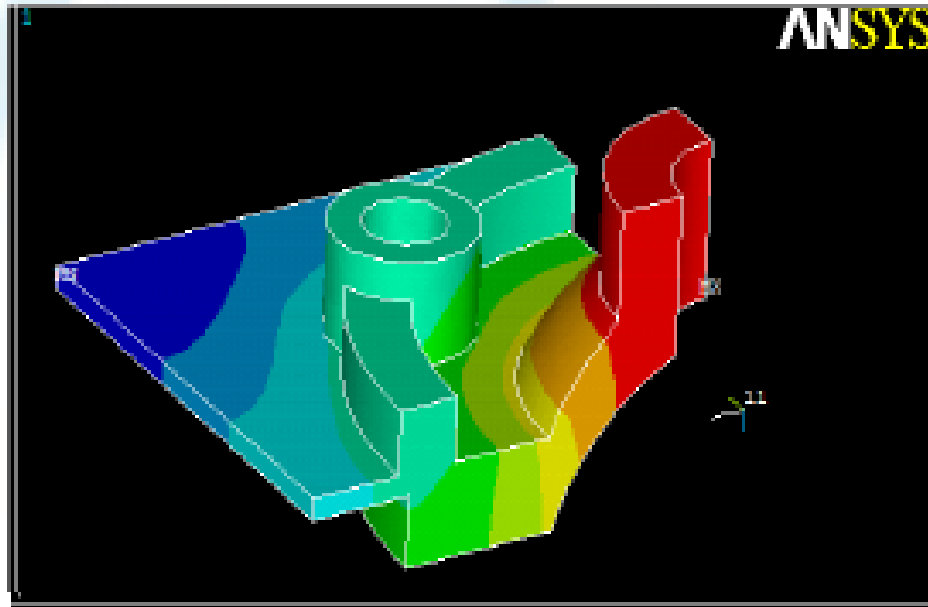
Figure 5: Model Analysis

RESULTS AND DISCUSSIONS

Transient Temperature Distribution and Thermal stress

Toward the start of the cool begin, the part is at uniform surrounding temperature. At the point when a cool metal part is presented to a hot liquid medium, warm inclinations set in over the thickness and along the length. Amid the warm transient, this temperature angle changes with time till the metal achieves its relentless state temperature circulation. Because of warm latency of the metal, it takes more opportunity to achieve its relentless state esteem by conduction than the genuine length of liquid temperature change amid the transient.

Thermal Stress Analysis

The warm inclinations produce warm burdens, in transient and consistent state conditions, in the segment. Stress examination is completed on Finite component model of the part at the basic time of transient, when warm slope is high.

Static Analysis

The liquid weight produces static hassles, in consistent state conditions, in the part.

Stress examination is done on Finite component model of the segment at various weight loads.

Static Transient Thermal Analysis

Stresses because of liquid weight are added to the warm burdens. These aggregate anxieties differ as elements of space and time. Weight burdens and Thermal inclinations are connected at once to discover the anxieties.

Displaying was performed for the gas pressure $pg = 3$ N/ and temperature $Tg = 1900$ K

were determined by diagrams of the engine indicated in the nominal regime. The material properties are: Young modulus (7· 1010 N/), Poisson proportion (0.346), thickness (2710 kg/),

warm development (2.36105 K) and the yield quality (9.5 107 N/).

The strong model of the chamber head is introduced in fig. The condition of burdens investigation of chamber head will be considered both mechanical and warm loads. They are esteemed as takes after: circulated mechanical burden (inner or outside weight, own weight); mechanical burdens concentrated on little zones (load from the mass of a component over another) and loads because of differential warm development brought on by temperature variety starting with one point then onto the next on the same piece (the thickness, length or the width). Mechanical burdens are utilized as a part of demonstrating are the powers and minutes whose qualities are displayed in table 1.

Table 1: The value of forces and moment used in modeling

Mechanical Components		Values	Reactions(N)
Load[N]	Fx	-4150	4150
	Fy	968-9	-968.91
	Fz	2662.1	-2662.1
Moment[N-mm]	Mx	5.349	-53496
	My	-853.12	853.12
	Mz	310.51	-310.51

Note that in displaying or considered most extreme estimations of mechanical burdens and warm loads in view

themselves as center qualities. For this situation the greatest weight is $pg = 7.8$ N/and temperature is $Tg = 2200$ K In the

phase of the lattice of the chamber head have been utilized various 55539 limited components with various 13208 hubs. In fig. is displayed chamber head on the top, inspected from the limited component network Complete anxiety and misshapening tensors, relocations and contact weight are accessible as consequences of basic investigation. Every one of these outcomes give us new learning about burdens on parts consequences of basic investigation.

Their translation is general and extremely mind boggling, basically because of the dubious impact of model rearrangements and approximations. Table 2 demonstrates the most extreme and least foremost hassles acquired from displaying barrel head, the hubs are recorded these qualities and the position of those hubs to the picked reference framework demonstrating.

Table 2: The maximum and minimum principal stresses

Principal stresses		Values [N/mm²]	Nodes	Nodes coordinates to the reference system chosen		
				X[mm]	Y[mm]	z[mm]
σ x	Min	3.2463× 10⁷	5619	324.63	-52.706	-21.287
	Max	3.7036× 10⁷	11169	374.75	-12.787	-27.840
σ y	Min	3.2904× 10⁷	5619	324.63	-52.706	-21.287
	Max	3.427× 10⁷	5671	298.76	-27.575	-9.4410
σ z	Min	4.1075× 10⁷	5618	325.98	-45.991	-21.329
	Max	4.3755× 10⁷	959	281.07	-20.228	-21.783

Table 2 demonstrates that the same least esteem is in hub 5619 and the hub 5618 has a base worth, situated beside the past hub. As to the greatest, they are acquired in the relating range of the extension hubs related valves. The majority of the three parts have the most noteworthy quality. The investigation of anxieties is more compelling on the off chance that we

utilize the hypothesis of the particular structure altering vitality (expressed by von Mises) as a deciding component for achieving the farthest point stages. By dissecting the burdens fields, we can see the principle basic territory of the chamber head. Von Misses stress state speaks to the estimations of a scalar field vitality thickness got from the volume

used to gauge strain and anxieties made in the model. In fig. presents the outcomes encapsulated in the von Mises stress as a result of warm and mechanical burdens on the highest point of the barrel head analyzed.

CONCLUSION

Model figuring from the barrel head plan arrangement tailed, this circumstance of misuse to fulfill similarity and balance conditions inside the limited components and the whole barrel head framing, so rearrangements acknowledged displaying examination does not change the outcomes. In building up the model figuring to consider the state of symmetry of the chamber head this marvel communicates reliably contemplated the barrel leader of their work cycle motor, on the grounds that the conditions forced meet the real states of the blueprint application furthermore make note of limited component properties. is noticed that the most extreme utilization of anxiety concentrators emerge in territories of hassles in the deck of the admission valve and fumes valve which affirms the legitimacy of the demonstrating in light of the fact that

they are zones characterized by the hypothetical writing. This zone is the most asked for where variable temperature fields make fervor that overlaid the mechanical create huge interest.

Conclusions are drawn from this examination are;

1. Weight of the Cylinder Head can be minimized by making Cylinder head with metal

network composites rather than Cast iron.

2. Temperature conveyance is brought out through FE model.

3. Assention somewhere around 2D and 3D is arrived.

4. Computational time is diminished.

5. This Analysis is convenient in car applications.

REFERENCES

1. Saniel, M. - Macek, J. - Diviš, M. - Tichánek, R. SteadyState Heat Analysis of Engine Head, Abstracts of 20[th]Danubia- Adria Symposium on Experimental Methods inSolid Mechanics. Gyor: Széchenyi István

University ofApplied Sciences, 2003, s. 74-75.ISBN 963-9058-20-3.

2. Macek, J. – Vítek, O. – Vávra, J.: Kogeneraèní jednotka splynovým motorem o výkonu vìtším než 3 MW –II.ÈVUT v Praze, Fakulta strojní, 2000. (in Czech)

3. Horák, F. – Macek, J.: Use of Predicted Fields in MainParts of Supercharged Diesel Engine. Proceedings ofXIX.Conferenceof International Centre of Mass and Heat Transfer.Pergamon, Press, New York, 1987.

4. Kreith, F. – Black, W.: *Basic Heat Transfer.* Harper andRow, New York, 1980.

5. Baehr, H.D. – Stephan, K.: *Heat and Mass Transfer.*Springer-Verlag, Berlin, 1998.

Design and Thermal Analysis of Combustion Outer Case for Turbo Engine

Dhondi Sindhuja

M.Tech (Thermal engineering),
P.G. Scholar

Nishitha College of engineering and technology

chinnu.sinduja@gmail.com

Rangdal Srikanth

Mtech(AMS), Asst professor

Nishitha College of engineering and technology

ABSTRACT

A turbocharger or turbo is a gas compressor that uses the turbine driven forced induction device that increases an engine's efficiency and power by forcing extra air into the combustion chamber. A turbocharger has the compressor powered by a turbine. The turbine is driven by the exhaust gas from the engine. It does not use a direct mechanical drive. This helps improve the performance of the turbocharger. The main problems with the turbo charger are oil leakage, damage of blades, whistling, sluggish, and outer case compression problem to overcome this problem many of the peoples work on the problem and they came out with new solutions to it. The objective of this project is to be design the outer case of a turbocharger for a diesel engine to increase its power and efficiency, and showing the advantage of designing of a turbocharger. The project tends to usage of new materials is required. In the present work impeller was designed with three different materials. The investigation can be done by using Creo-2 and ANSYS software. The Creo-2 is used for modeling the impeller and analysis is done in ANSYS .ANSYS is dedicated finite element package used for determining the variation of stresses, strains and deformation across profile of the impeller.

INTRODUCTION

Internal Combustion Engine

The internal combustion engine is the powerhouse of a variety of machines and equipment ranging from small lawn equipment to large aircraft or boats. Given the focus of this paper, the most important machine powered by an internal combustion engine is the automobile. The engine literally provides the driving force of the car while also directly or indirectly powering just about every other mechanical and electrical system in the modern automobile. While there are several types of internal

combustion engines that cover the aforementioned large range of applications, they all basically do the same thing.

They all convert the chemical energy stored in a fuel of some kind into mechanical energy, which can then be converted into electrical energy. The three most common types of internal combustion are the 4-stroke gasoline engine, the 2-stroke gasoline engine, and the diesel engine. A brief description of each the common types of internal combustion engine are provided below.

The 4-stroke gasoline engine is the most frequently used engine in cars and light trucks as well as in large boats and small aircraft. The major components of the cylinder of a 4-stroke gasoline engine. While the arrangement and number of the cylinders in an engine tends to vary, the parts that make up an individual cylinder remain pretty constant. The most significant component is the piston which is connected to the crankshaft via a connecting rod. The motions of the piston and crankshaft are always related, with one always forcing the other to move. The two valves, intake and exhaust, at the top of the cylinder are opened and closed by separate camshafts that precisely control the timing of each valve's movement. The spark plug at the top of the cylinder is powered by the engine battery and activated by the engine computer at the appropriate time. Finally, the entire cylinder is surrounded by coolant channels that run through the engine block to remove the massive amount of heat generated by the running engine.
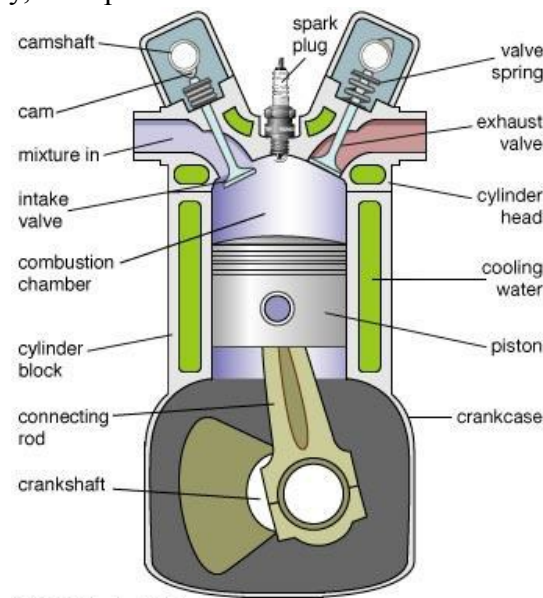
Figure 1 Components of a 4-stroke gasoline engine cylinder.

The four strokes of a 4-stroke gasoline engine, illustrated in Fig. 1.2, are intake, compression, power and exhaust. During the intake stroke, the camshaft opens the intake valve as the crankshaft lowers the piston, which allows the cylinder to be filled with a precise mixture of air and gasoline. Once the piston reaches the bottom of the cylinder, the

camshaft closes the intake valve. The piston is now at what is known as bottom dead

center, and the cylinder is completely filled with the air/fuel mixture.
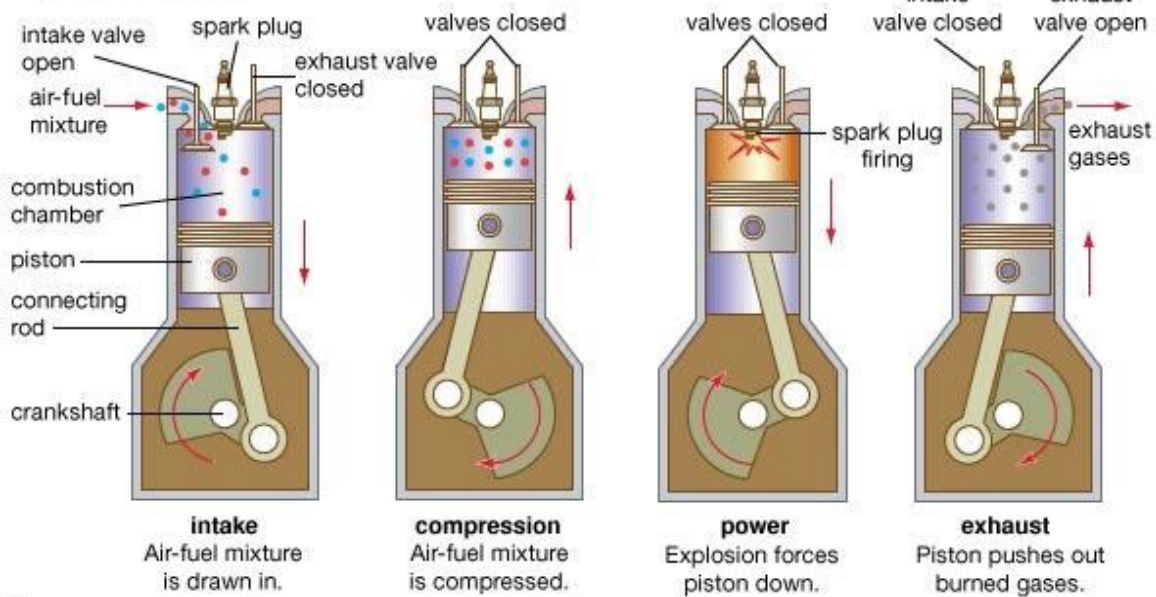
Figure 2 Engine cycle of a 4-stroke gasoline engine.

The compression stroke comes next. With both intake and exhaust valves closed, the crankshaft raises the piston, compressing the air/fuel mixture. When the piston has been raised to the top of the cylinder, it is said to be at top dead center. Once the cylinder has reached top dead center, the air/fuel mixture has been compressed as much as possible.The power stroke is next up. With the piston still at top dead center and both valves closed, the spark plug fires, igniting the compressed air/fuel mixture. Once ignited, a flame begins to move through the mixture, causing it to expand downward smoothly. This expansion downward forces the piston to move down. This means that the piston is rotating to the crankshaft, whereas the rotation of the crankshaft moves the piston in the other three strokes. The fact that the piston is driving the crankshaft means that energy is being transferred to the crankshaft. This is how an internal

combustion engine transforms chemical energy in the fuel into mechanical energy. The power stroke is completed once the expanding gases have forced the piston to bottom dead center. The final stroke is the exhaust stroke. The camshaft opens the exhaust valve as the crankshaft raises the piston, which pushes the exhaust gases out of the cylinder. Once the piston has reached top dead center, all of the exhaust gases have been removed from the cylinder. The cylinder is now ready to start the cycle over again with another intake stroke.The 2-stroke gasoline engine accomplishes the same thing as the 4-stroke gasoline engine but with half as many strokes. Since they can produce a good amount of power for their relatively small size, 2-stroke gasoline engines are found on a variety of lawn care and recreational equipment like lawnmowers, chainsaws, snowmobiles and small boat engines. They are generally not used for

larger application because they are less efficient and dirtier than their 4-stroke counterparts. Aside from having fewer strokes, 2-stroke engines differ from 4-stroke engines in their fuel mixtures and cylinder components. The two strokes, upstroke and downstroke, of a 2-stroke engine along with the cylinder setup.
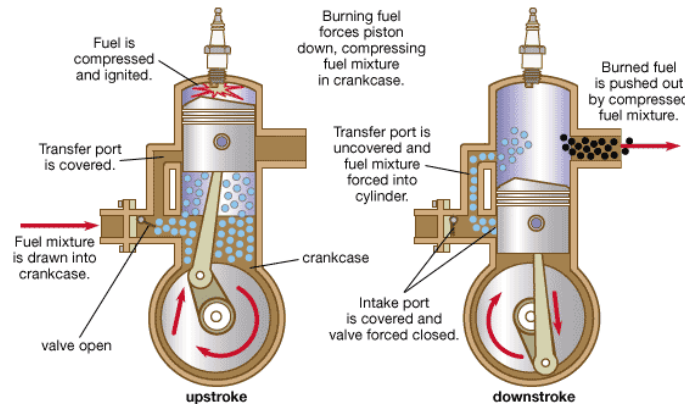
Figure 3 Engine cycle of a 2-stroke gasoline engine.

There are no camshafts or complicated valve trains involved here, meaning the piston basically has to perform more diverse functions that in 4-stroke engines. Furthermore, special two cycle oil is mixed in with the gasoline to help lubricate the piston, so the air/fuel mixture in a 2-stroke engine includes oil. When the piston is at the bottom of the cylinder, the already compressed air/fuel mixture has moved via the transfer port into the top of the cylinder. On the upstroke, the piston further compresses the air/fuel mixture, creates a vacuum in the crankcase and uncovers the intake port. The vacuum opens the intake valve and draws more air/fuel mixture into the crankcase. The spark plug fires and ignites the mixture, which forces the piston down just like in the 4-stroke cycle. On the down stroke, the piston transfers energy to the crankshaft while compressing the air/fuel mixture in the crankcase and uncovering the exhaust port. As the piston reaches the bottom of the cylinder, the compressed air/fuel mixture is again forced into the top of the cylinder via the transfer port, which forces the remaining exhaust out of the cylinder. The cycle can now begin again.Diesel engines can have a 2-stroke cycle, but most have a 4-stroke cycle, particularly those used by large trucks. The 4-stroke diesel engine will thus be focused on. The 4-stroke diesel cycle is very similar to the 4-stroke gasoline cycle with the big differences, aside from fuel type, being the fuel injection timing and ignition method. During the intake stroke, the intake valve opens as the crankshaft lowers the piston, drawing in pure air. Once the piston reaches bottom dead center, the intake valve closes. The crankshaft then raises the piston, compressing the air. Diesel engines compress the air to much higher compression ratios than their gasoline counterparts do the air/fuel mixture, which means the compressed air reaches scorching temperatures. The compression stroke is complete when the piston reaches top dead center and the air is completely compressed. It is at this moment that the fuel is injected into the compressed air. The extreme temperature of the compressed air immediately ignites the fuel. The expanding gases then force the piston down,

transferring energy to the crankshaft. The power stroke is complete when the piston reaches bottom dead center. During the exhaust stroke, the crankshaft raises the piston, forcing the exhaust gases out of the now open exhaust valve. Once the piston reaches top dead center, the cycle is ready to begin again.

Turbochargers

As stated in the previous section, a turbocharger is a device that uses engine exhaust gases to power a compressor that increases the pressure of the air entering the engine, which results in more power from the engine. Air enters the compressor from the left, is compressed and then directed to the intake valve of the cylinder. Exhaust exits the exhaust valve of the cylinder, spins the turbine and is expelled. The three major pieces of a turbocharger introduced in the previous section and shown in Fig. 1.6 are the compressor, bearings section and turbine. Each of these sections has an important function and deserves further attention. It is also important to recognize in any discussion of turbo charging that turbo charging an engine involves more than just slapping a turbocharger on to the engine. An entire system must be developed for the turbocharger, including a means of temperature and pressure control.
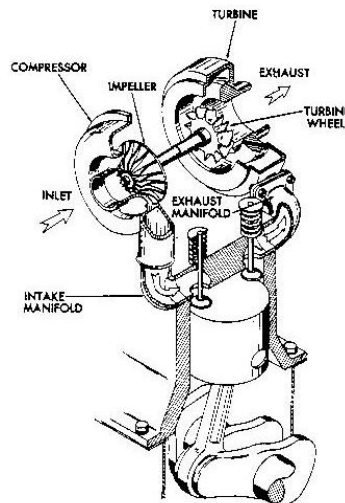
Figure 4: Simplified drawing of turbocharger and engine cylinder.

Turbocharger as a Device

Before getting into the details of a turbocharged system, the turbocharger as a device will be described in more detail. It effectively illustrates the relationship between the three sections as well as the input and output of each section. The heart of the turbocharger is the assembly of compressor blades, shaft and turbine blades. It is this assembly that rotates at over a 100000 RPM when the turbocharger is operational. This assembly also serves as the common connection between the three major components of the turbocharger, which otherwise are independent of each other.

The compressor blades, shaft and turbine blades that make up the rotating assembly are distinctly inside of the compressor housing, bearings housing and turbine

housing, respectively. The role of the compressor housing is to direct ambient air axially into the spinning compressor blades. The blades and housing are designed together such that the ambient air is compressed and forced into the air channel wrapped around the center of the compressor housing, which expels the compressed air tangentially. The compressed air leaves the compressor with higher pressure and temperature. The pressure increase across the compressor is known as boost. For example, if ambient air enters the compressor at atmospheric pressure (14.7psi) and leaves at a pressure of 19.7psi, the turbocharger is said to be creating 5psi of boost. Generally speaking, the higher the boost pressure, the higher the power gains but more difficulty and cost are involved in developing the system. The compressor works best at a particular combination of airflow and boost pressure. The compressor should be chosen wisely to ensure most efficient operation. The primary function of the bearings housing is to guide the rotating shaft connecting the compressor and turbine blades. This shaft is guided using either journal or ball bearings. The bearings housing has a secondary function of lubricating the shaft and bearings. This is accomplished by routing engine oil into the bearings housing, which distributes the oil around the shaft and bearings. The oil is then drained out of the bearings section at which point it can be returned to the engine. Heat from the exhaust gases can lead to oil coking, the charring of the oil on to the oil channels. This restricts oil flow and eventually destroys the bearings. Some bearings sections have water jackets that allow engine coolant to reduce the temperature of the oil.

The main function of the turbine housing is to direct exhaust gases to the turbine blades to accelerate them as quickly as possible.

Exhaust gas enters the turbine housing tangentially and travels through the channels surrounding the center of the turbine. These channels lead the air into the turbine blades, forcing them to rotate. The exhaust is then expelled from the turbine housing axially. The size of the turbine housing has a significant impact on the behavior of the turbine. In particular, changing the size of the turbine effects turbocharger response, power gains and the engine speed at which the turbocharger is most effective.

Turbocharger as a System

Now that the basics of a turbocharger have been covered, the major components of a turbocharged system can be discussed. Unfortunately, a turbocharged system is a lot more complicated than the illustration. Plumbing, engine modifications, intake air temperature and boost control are all major concerns that need to be addressed. It includes all the plumbing for the intake and exhaust, oil feed and drain lines, an intercooler for temperature control and a wastegate for boost control. These components will be discussed briefly here and then at length in subsequent sections of the paper. The intake system consists of everything from the air filter to the intake ports on the engine. This includes the compressor, intercooler (see next paragraph), manifold and throttle bodies. The job of the intake system is to connect all of these components with hoses or pipes. The design of the manifold, which consists of the plenum and runners, and the throttle bodies are also considered part of the intake system. The intake system in general and specifically for this project will be discussed at length in section 6 – Intake System. The intercooler is a heat exchanger that is included to remove the unwanted heat added to the intake air by the compressor. It is impossible to prevent

the compressor from adding heat to the air as it compresses it, though the amount of heat added can be limited by choosing a properly sized compressor. It is undesirable to just allow the hot intake air to go straight to the engine as it can reduce power gains and lead to engine knocking. An intercooler is thus included in the system to remove the heat added by the compressor. The heat is removed via cross flow of a cooling fluid, either air or water. The air is then free to flow to the engine with a lower temperature but still higher than atmospheric pressure.

The concept of boost was introduced in the previous section as was the relationship between boost and the system. That is to say that while higher boost generally leads to higher power it also leads to increasingly complicated and expensive system requirements. Since a turbocharged system is rarely designed with unlimited budget and design freedom, there will always be a maximum boost that the system is designed to accommodate. This maximum boost is usually chosen based on performance goals, and the system is then designed specifically for that boost pressure. If this maximum boost pressure is exceeded, the system could very likely fail, resulting in damage to the turbocharger or engine. If left unchecked though, the turbocharger will continue to create boost well past the maximum boost pressure. A boost control system is thus added to limit the boost created by the turbocharger. A waste gate works by bleeding exhaust gas away from the turbine once the maximum boost pressure is
.

reached. As less exhaust reaches the turbine, the turbocharger slows down and creates less boost pressure.

The exhaust system consists of everything from the engine exhaust ports to the tailpipe. This includes the manifold, turbine, waste gate and the muffler. The job of the exhaust system is to connect and support all of these components with pipes. The design of the exhaust manifold, including the primaries and merge collectors, is considered part of the exhaust system. The final major system component is the lubrication system for the turbocharger bearings. In the drawing, this system consists of an oil feed line and an oil drain line between the turbocharger bearings and the engine. The oil feed line is connected to the engine at a location with positive oil pressure, and the oil drain line is connected to the engine's oil pan. More complicated systems including dedicated pumps and oil reserves are not uncommon. The coolant lines between the turbocharger bearings and the engine's radiator circuit are not included in the figure as water jackets are not available on all turbochargers and thus are not considered to be standard. In addition to these components, any high boost turbocharged system is going to require modifications to various engine parts. Electrical and ignition systems may need to be upgraded to ensure proper ignition. The fuel injection systems may need to be upgraded to maintain the correct AFR. The throttle bodies and valve train may need to be changed to provide for proper flow conditions

Input Data of Turbo Casing:

Engine capacity (L) Up to 7

Output range (hp) 100 to 310

Airflow (max) 0.46 kg/s
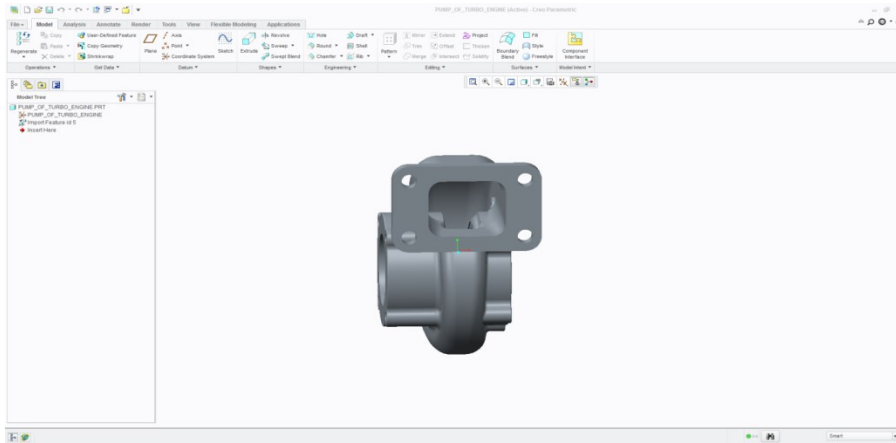
Length (mm) 250

Width (mm) 240

Height (mm) 220

Mass (kg) 16 to 17

Turbo outer Casing stress analysis

Stain less steel	CF8C plus cast stain less steel	HK30Nb stainless alloy
Density	7.96	7.81
Ductility	0.32	0.34
Elastic limit	209MPA	207MPA
Thermal conductivity	14.54w/mk	15.23w/mk
Heat input	350ºc	350ºc

3-D MODELING OF TURBO CASING
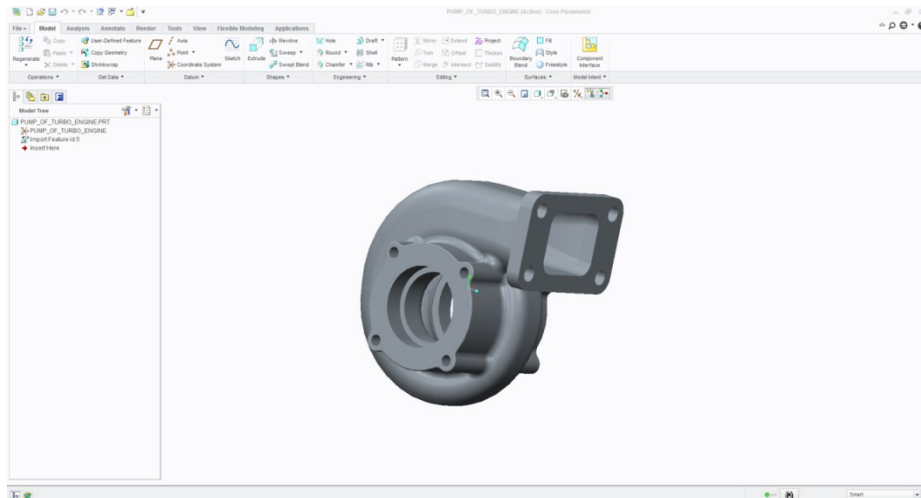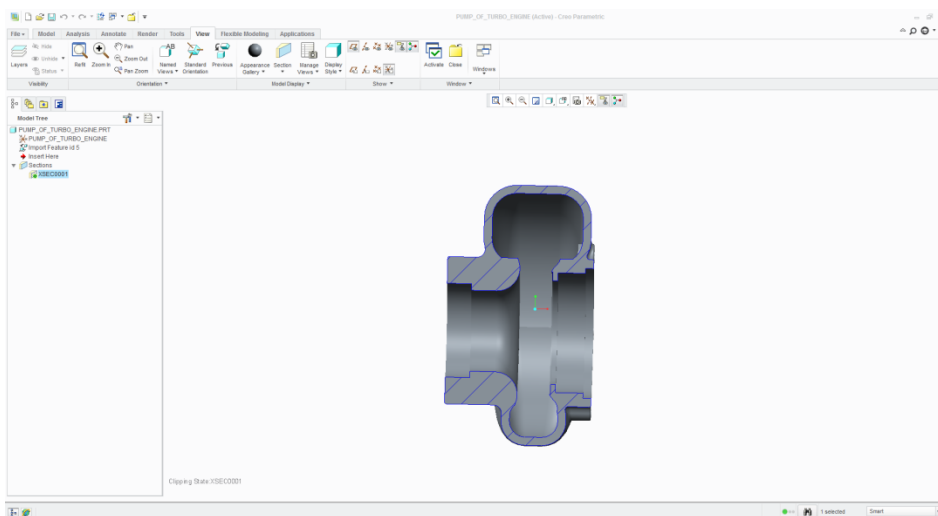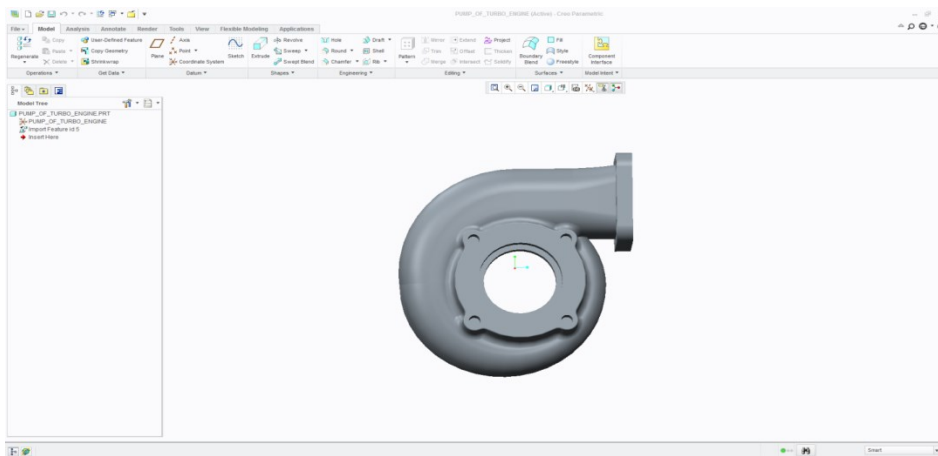
MODAL ANALYSIS

A modal analysis is typically used to determine the vibration characteristics (natural frequencies and mode shapes) of a structure or a machine component while it is being designed. It can also serve as a starting point for another, more detailed, dynamic analysis, such as a harmonic response or full transient dynamic analysis.Modal analyses, while being one of the most basic dynamic analysis types available in ANSYS, can also be more computationally time consuming than a typical static analysis. A reduced solver, utilizing automatically or manually selected master degrees of freedom is used to

.

drastically reduce the problem size and solution time.

HARMONIC ANALYSIS

Used extensively by companies who produce rotating machinery, ANSYS Harmonic analysis is used to predict the sustained dynamic behavior of structures to consistent cyclic loading. A harmonic analysis can be used to verify whether or not a machine design will successfully overcome resonance, fatigue, and other harmful effects of forced vibrations

THERMAL ANALYSIS OF TUBO CASING
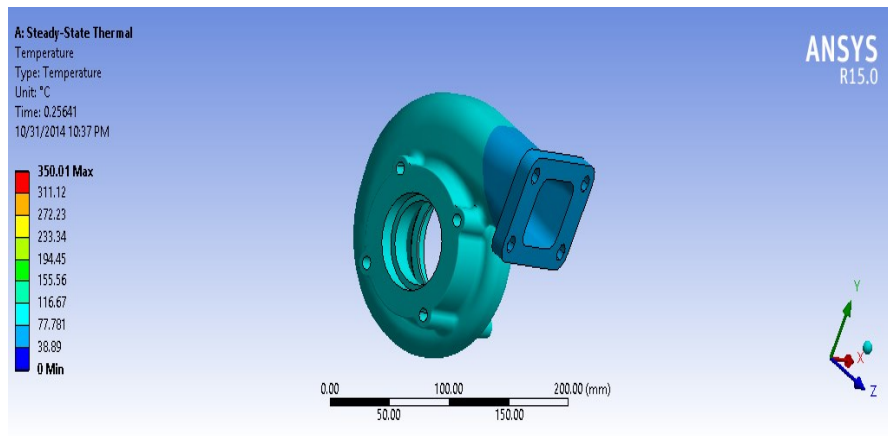
Material Properties:

Stain less steel	HK30Nb stainless alloy
Density	7.81
Ductility	0.34

Elastic limit	207MPA
Thermal conductivity	15.23w/mk
Heat input	350ºc

Units:

TABLE 1

Unit System	Metric (mm, kg, N, s, mV, mA) Degrees rad/s Celsius
Angle	Degrees
Rotational Velocity	rad/s
Temperature	Celsius

TABLE 2
Model (A4) > Geometry

Object Name	*Geometry*
State	Fully Defined
Definition	
Source	E:\sanya\turbocasingthermalanalysisinputdatasanyatechnologie\turbo housing\turbo housing\pump_of_turbo_engine3.stp
Type	Step
Length Unit	Meters
Element Control	Program Controlled
Display Style	Body Color
Bounding Box	
Length X	109. mm
Length Y	170.87 mm
Length Z	160.7 mm
Properties	
Volume	5.1095e+005 mm³
Mass	0. kg
Scale Factor Value	1.
Statistics	
Bodies	1
Active Bodies	1
Nodes	25639
Elements	14257

International Journal of Research

Available at https://edupediapublications.org/journals

p-ISSN: 2348-6848
e-ISSN: 2348-795X
Volume 03 Issue 11
July 2016

Mesh Metric	None
Basic Geometry Options	
Solid Bodies	Yes
Surface Bodies	Yes
Line Bodies	No
Parameters	Yes
Parameter Key	DS
Attributes	No
Named Selections	No
Material Properties	No
Advanced Geometry Options	
Use Associativity	Yes
Coordinate Systems	No
Reader Mode Saves Updated File	No
Use Instances	Yes
Smart CAD Update	No
Compare Parts On Update	No
Attach File Via Temp File	Yes
Temporary Directory	C:\Users\kishore\AppData\Local\Temp
Analysis Type	3-D
Mixed Import Resolution	None
Decompose Disjoint Geometry	Yes
Enclosure and Symmetry Processing	Yes

TABLE 3: Model (A4) > Geometry > Parts

Object Name	PUMP_OF_TURBO_ENGINE
State	Meshed
Graphics Properties	

Visible	Yes
Transparency	1
Definition	
Suppressed	No
Stiffness Behavior	Flexible
Coordinate System	Default Coordinate System
Reference Temperature	By Environment
Material	
Assignment	material 2
Nonlinear Effects	Yes
Thermal Strain Effects	Yes
Bounding Box	
Length X	109. mm
Length Y	170.87 mm
Length Z	160.7 mm
Properties	
Volume	5.1095e+005 mm³
Mass	0. kg
Centroid X	-10.023 mm
Centroid Y	15.766 mm
Centroid Z	3.0438 mm
Moment of Inertia Ip1	0. kg·mm²
Moment of Inertia Ip2	0. kg·mm²
Moment of Inertia Ip3	0. kg·mm²
Statistics	
Nodes	25639
Elements	14257
Mesh Metric	None

Coordinate System:

TABLE 4: Model (A4) > Coordinate Systems > Coordinate System

Object Name	Global Coordinate System
State	Fully Defined
Definition	

Type	Cartesian
Coordinate System ID	0.
Origin	
Origin X	0. mm
Origin Y	0. mm
Origin Z	0. mm
Directional Vectors	
X Axis Data	[1. 0. 0.]
Y Axis Data	[0. 1. 0.]
Z Axis Data	[0. 0. 1.]

TABLE 5: Model (A4) > Mesh

Object Name	*Mesh*
State	Solved
Defaults	
Physics Preference	Mechanical
Relevance	0
Sizing	
Use Advanced Size Function	Off
Relevance Center	Coarse
Element Size	Default
Initial Size Seed	Active Assembly
Smoothing	Medium
Transition	Fast
Span Angle Center	Coarse
Minimum Edge Length	2.9763e-002 mm
Inflation	
Use Automatic Inflation	None
Inflation Option	Smooth Transition
Transition Ratio	0.272
Maximum Layers	5
Growth Rate	1.2
Inflation Algorithm	Pre
View Advanced Options	No
Patch Conforming Options	
Triangle Surface Meshed	Program Controlled
Patch Independent Options	

Topology Checking	Yes
Advanced	
Number of CPUs for Parallel Part Meshing	Program Controlled
Shape Checking	Standard Mechanical
Element Midsize Nodes	Program Controlled
Straight Sided Elements	No
Number of Retries	0
Extra Retries For Assembly	Yes
Rigid Body Behavior	Dimensionally Reduced
Mesh Morphing	Disabled
Defeaturing	
Pinch Tolerance	Please Define
Generate Pinch on Refresh	No
Automatic Mesh Based Defeaturing	On
Defeaturing Tolerance	Default
Statistics	
Nodes	25639
Elements	14257
Mesh Metric	None

Steady State Thermal (A5)

TABLE 6: Model (A4) > Analysis

Object Name	Steady-State Thermal (A5)
State	Solved
Definition	
Physics Type	Thermal
Analysis Type	Steady-State
Solver Target	Mechanical APDL
Options	
Generate Input Only	No

TABLE 7: Model (A4) > Steady-State Thermal (A5) > Initial Condition

Object Name	Initial Temperature
State	Fully Defined
Definition	
Initial Temperature	Uniform Temperature
Initial Temperature Value	22. °C

TABLE 8: Model (A4) > Steady-State Thermal (A5) > Analysis Settings

Object Name	Analysis Settings
State	Fully Defined
Step Controls	
Number Of Steps	1.
Current Step Number	1.
Step End Time	1. s
Auto Time Stepping	Program Controlled
Solver Controls	
Solver Type	Program Controlled
Radiosity Controls	
Radiosity Solver	Program Controlled
Flux Convergence	1.e-004
Maximum Iteration	1000.
Solver Tolerance	1.e-007 W/mm²
Over Relaxation	0.1
Hemicube Resolution	10.
Nonlinear Controls	
Heat Convergence	Program Controlled
Temperature	Program Controlled

Convergence	
Line Search	Program Controlled
Output Controls	
Calculate Thermal Flux	Yes
General Miscellaneous	No
Store Results At	All Time Points
Analysis Data Management	
Solver Files Directory	C:\Users\kishore\AppData\Local\Temp\WB_CHANDU_kishore_35752_2\unsaved_project_files\dp0\SYS\MECH\
Future Analysis	None
Scratch Solver Files Directory	
Save MAPDL db	No
Delete Unneeded Files	Yes
Nonlinear Solution	Yes
Solver Units	Active System
Solver Unit System	nmm

TABLE 9: Model (A4) > Steady-State Thermal (A5) > Loads

Object Name	*Temperature*	*Convection*
State	Fully Defined	
Scope		
Scoping Method	Geometry Selection	
Geometry	41 Faces	1 Body
Definition		
Type	Temperature	Convection
Magnitude	350. °C (ramped)	
Suppressed	No	
Film Coefficient		Tabular Data
Coefficient Type		Average Film Temperature
Ambient Temperature		22. °C (ramped)
Convection Matrix		Program Controlled
Edit Data For		Film Coefficient
Tabular Data		

Independent Variable		Temperature
Graph Controls		
X-Axis		Temperature
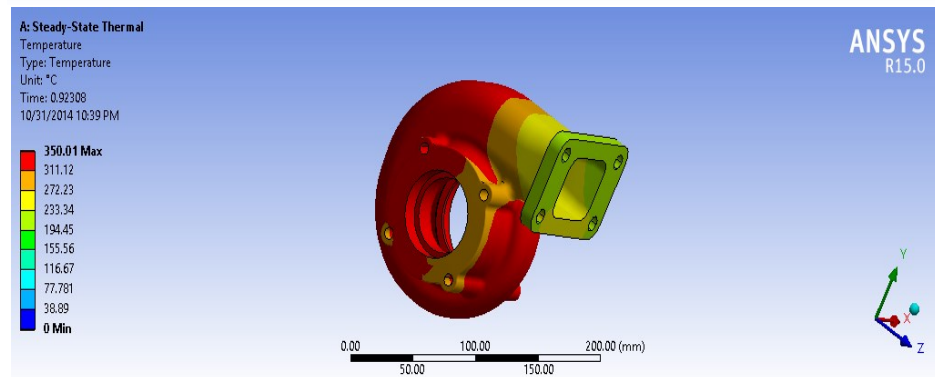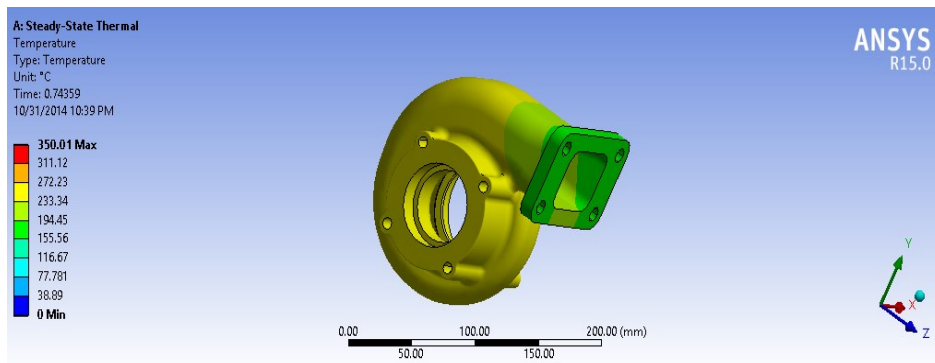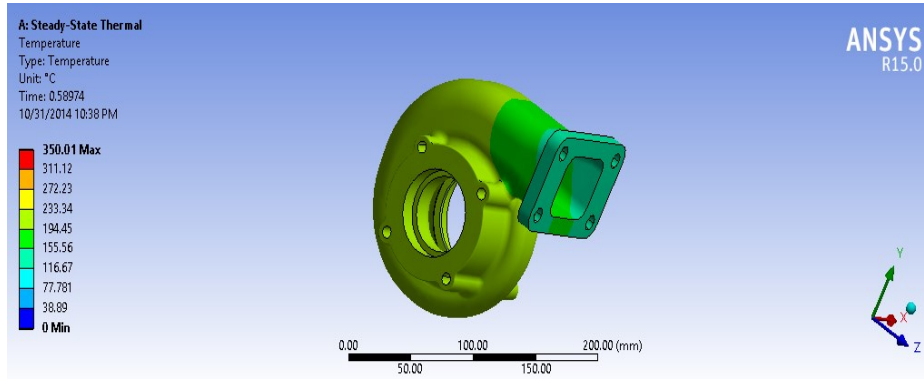
TABLE 10: Model (A4) > Steady-State Thermal (A5) > Convection

Temperature [°C]	Convection Coefficient [W/mm²·°C]
1.	9.5e-007

![IJR logo] International Journal of Research

International Journal of Research

Available at https://edupediapublications.org/journals

p-ISSN: 2348-6848
e-ISSN: 2348-795X
Volume 03 Issue 11
July 2016

10.	2.05e-006
100.	4.41e-006
200.	5.56e-006
300.	6.36e-006
500.	7.54e-006
700.	8.43e-006
1000.	9.5e-006
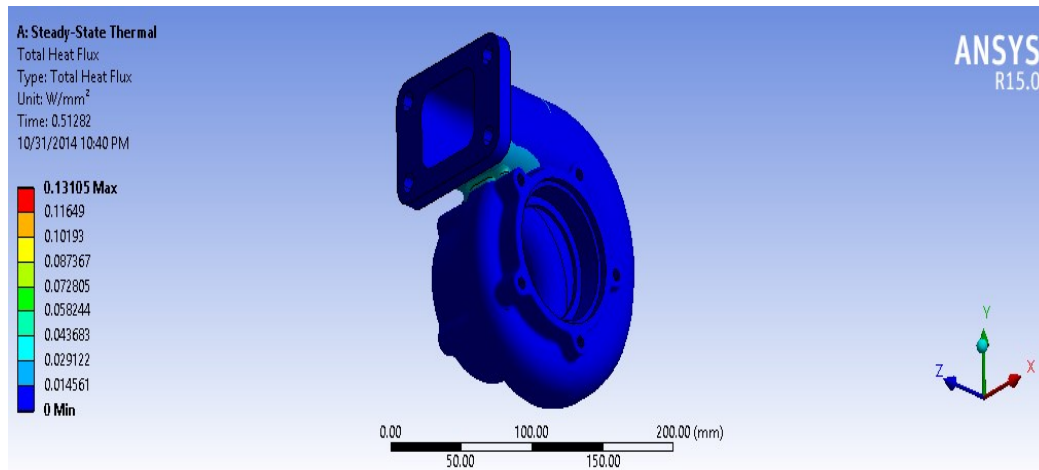
TABLE 11: Model (A4) > Steady-State Thermal (A5) > Solution

Object Name	Solution (A6)
State	Solved
Adaptive Mesh Refinement	
Max Refinement Loops	1.
Refinement Depth	2.
Information	
Status	Done

TABLE 12: Model (A4) > Steady-State Thermal (A5) > Solution (A6) > Solution Information

Object Name	Solution Information
State	Solved
Solution Information	
Solution Output	Solver Output

Update Interval	2.5 s
Display Points	All
FE Connection Visibility	
Activate Visibility	Yes
Display	All FE Connectors
Draw Connections Attached To	All Nodes
Line Color	Connection Type
Visible on Results	No
Line Thickness	Single
Display Type	Lines

TABLE 13: Model (A4) > Steady-State Thermal (A5) > Solution (A6) > Results

Object Name	*Temperature*	*Total Heat Flux*
State	Solved	
Scope		
Scoping Method	Geometry Selection	
Geometry	All Bodies	
Definition		
Type	Temperature	Total Heat Flux
By	Time	
Display Time	Last	
Calculate Time History	Yes	
Identifier		
Suppressed	No	
Results		
Minimum	235.63 °C	2.2085e-005 W/mm²
Maximum	350.01 °C	0.13105 W/mm²
Minimum Value Over Time		
Minimum	235.63 °C	2.2085e-005 W/mm²
Maximum	235.63 °C	2.2085e-005 W/mm²
Maximum Value Over Time		
Minimum	350.01 °C	0.13105 W/mm²
Maximum	350.01 °C	0.13105 W/mm²
Information		
Time	1. s	
Load Step	1	

International Journal of Research

Available at https://edupediapublications.org/journals

p-ISSN: 2348-6848
e-ISSN: 2348-795X
Volume 03 Issue 11
July 2016

Substep	1
Iteration Number	3
Integration Point Results	
Display Option	Averaged
Average Across Bodies	No
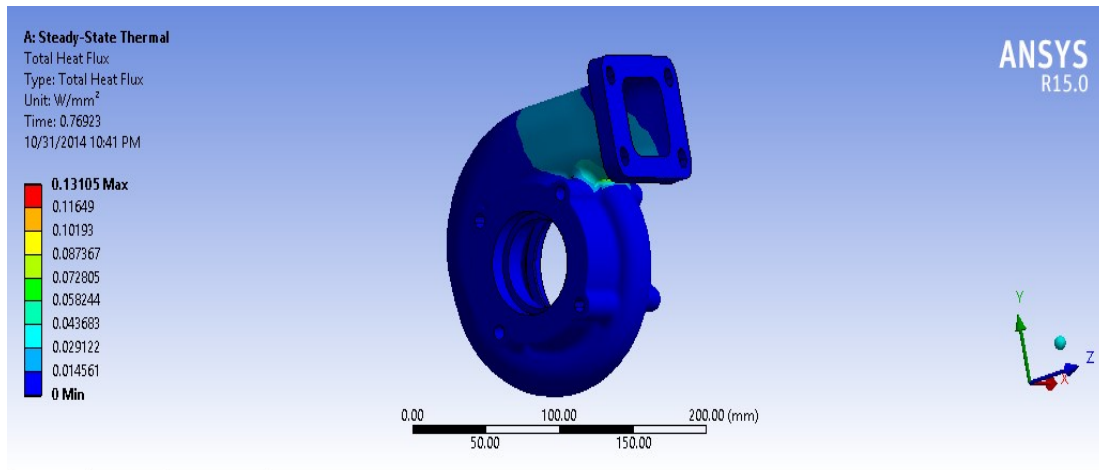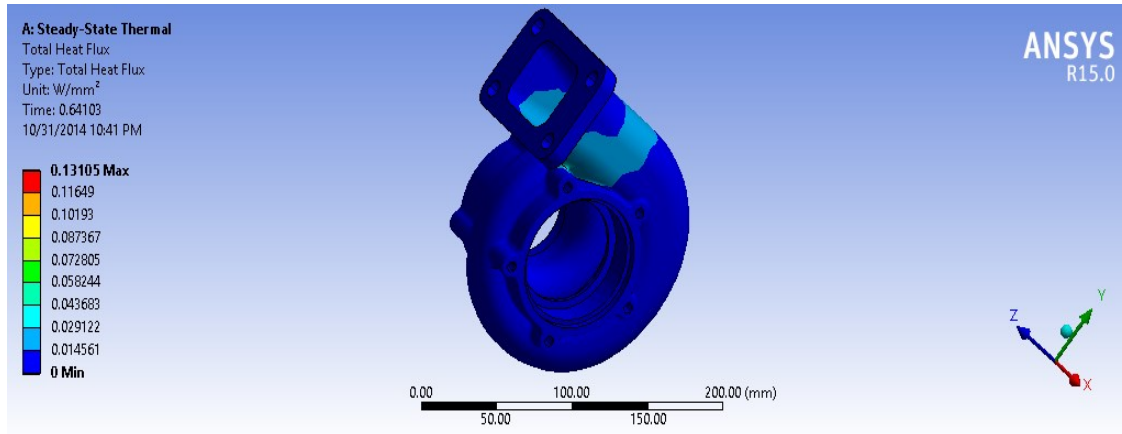
Material Data

TABLE 14: Material 1 > Constants

Thermal Conductivity	1.523e-002 W mm^-1 C^-1

THERMAL ANALYSIS OF TUBO CASING
Material -2
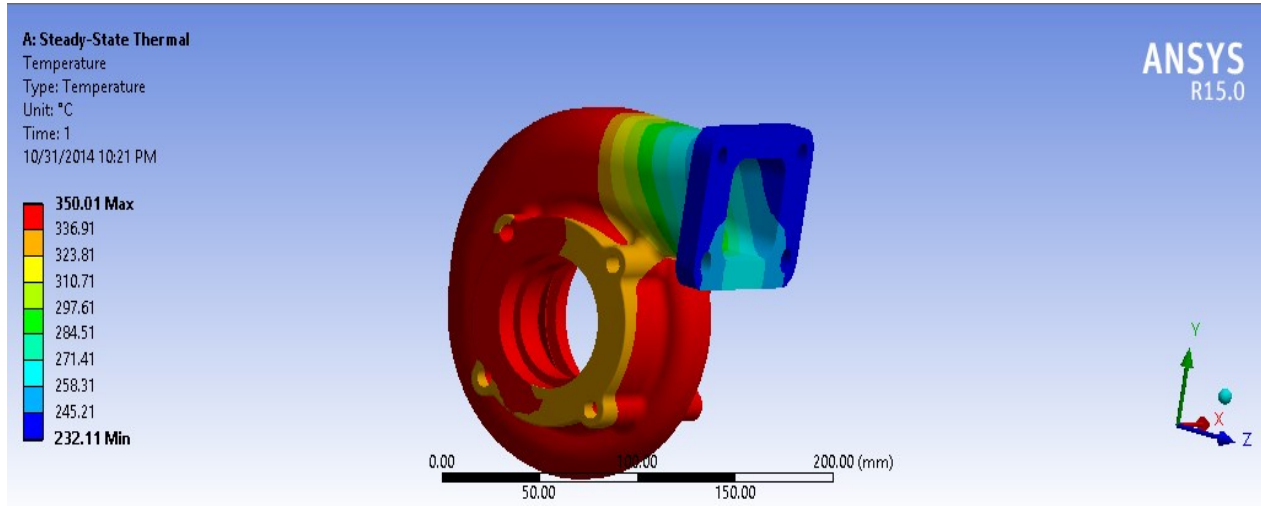
Material Properties

Stain less steel	CF8C plus cast stain less steel
Density	7.96
Ductility	0.32
Elastic limit	209MPA
Thermal conductivity	14.54w/mk
Heat input	350ºc

Units:

TABLE 15

Unit System	Metric (mm, kg, N, s, mV, mA) Degrees rad/s Celsius
Angle	Degrees
Rotational Velocity	rad/s
Temperature	Celsius

TABLE 16: Model (A4) > Geometry

Object Name	*Geometry*
State	Fully Defined
Definition	
Source	E:\sanya\turbocasingthermalanalysisinputdatasanyatechnologie\turbo housing\turbo housing\pump_of_turbo_engine3.stp
Type	Step

Length Unit	Meters
Element Control	Program Controlled
Display Style	Body Color
Bounding Box	
Length X	109. mm
Length Y	170.87 mm
Length Z	160.7 mm
Properties	
Volume	5.1095e+005 mm³
Mass	0. kg
Scale Factor Value	1.
Statistics	
Bodies	1
Active Bodies	1
Nodes	25639
Elements	14257
Mesh Metric	None
Basic Geometry Options	
Solid Bodies	Yes
Surface Bodies	Yes
Line Bodies	No
Parameters	Yes
Parameter Key	DS
Attributes	No
Named Selections	No
Material Properties	No
Advanced Geometry Options	
Use Associativity	Yes
Coordinate Systems	No
Reader Mode Saves Updated File	No
Use Instances	Yes
Smart CAD Update	No
Compare Parts On Update	No
Attach File Via Temp File	Yes
Temporary Directory	C:\Users\kishore\AppData\Local\Temp
Analysis Type	3-D

Mixed Import Resolution	None
Decompose Disjoint Geometry	Yes
Enclosure and Symmetry Processing	Yes

Coordinate Systems:
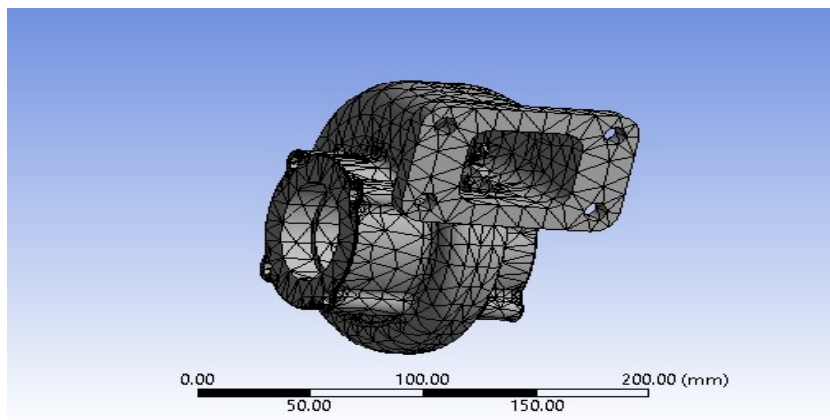
Steady – State Thermal (A5):

TABLE 17: Model (A4) > Analysis

Object Name	*Steady-State Thermal (A5)*
State	Solved
Definition	
Physics Type	Thermal
Analysis Type	Steady-State
Solver Target	Mechanical APDL
Options	
Generate Input Only	No

TABLE 18: Model (A4) > Steady-State Thermal (A5) > Analysis Settings

Object Name	*Analysis Settings*

State	Fully Defined
Step Controls	
Number Of Steps	1.
Current Step Number	1.
Step End Time	1. s
Auto Time Stepping	Program Controlled
Solver Controls	
Solver Type	Program Controlled
Radiosity Controls	
Radiosity Solver	Program Controlled
Flux Convergence	1.e-004
Maximum Iteration	1000.
Solver Tolerance	1.e-007 W/mm²
Over Relaxation	0.1
Hemi cube Resolution	10.
Nonlinear Controls	
Heat Convergence	Program Controlled
Temperature Convergence	Program Controlled
Line Search	Program Controlled
Output Controls	
Calculate Thermal Flux	Yes
General Miscellaneous	No
Store Results At	All Time Points
Analysis Data Management	
Future Analysis	None
Scratch Solver Files Directory	
Save MAPDL db	No
Delete Unneeded Files	Yes
Nonlinear Solution	Yes
Solver Units	Active System
Solver Unit System	nmm
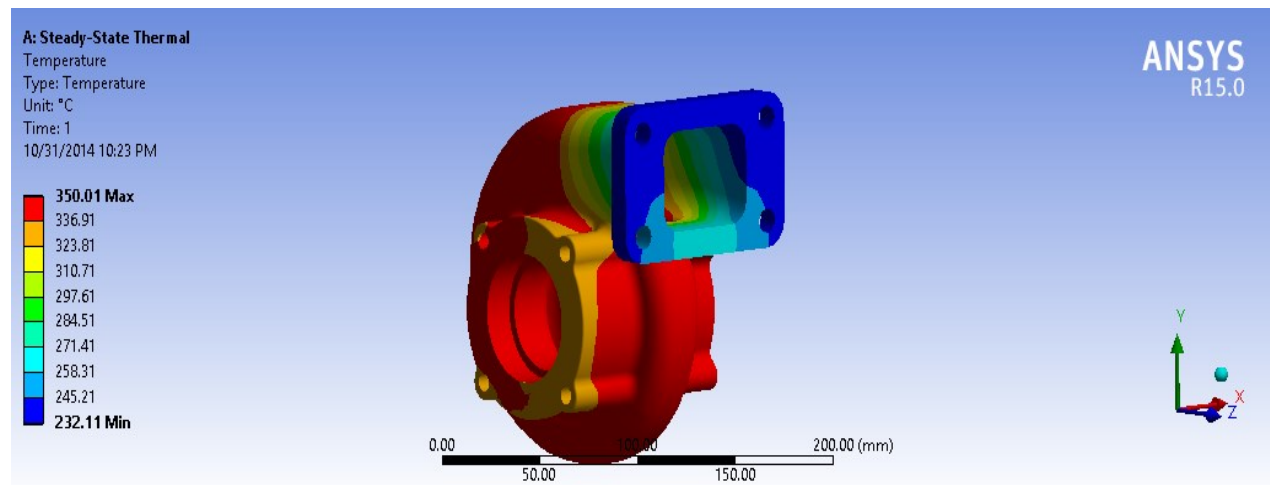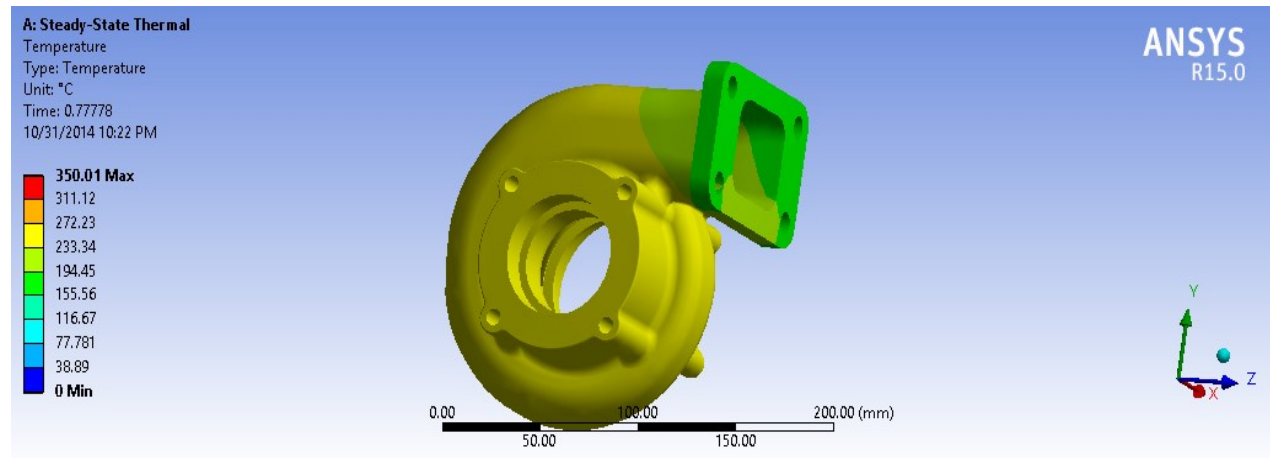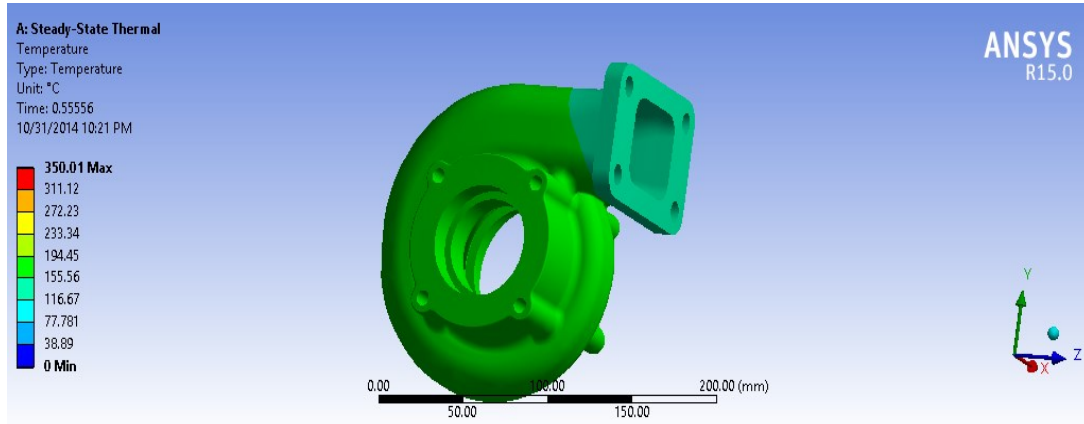
TABLE 19: Model (A4) > Steady-State Thermal (A5) > Convection

Temperature [°C]	Convection Coefficient [W/mm²·°C]
1.	9.5e-007
10.	2.05e-006
100.	4.41e-006
200.	5.56e-006
300.	6.36e-006
500.	7.54e-006
700.	8.43e-006
1000.	9.5e-006
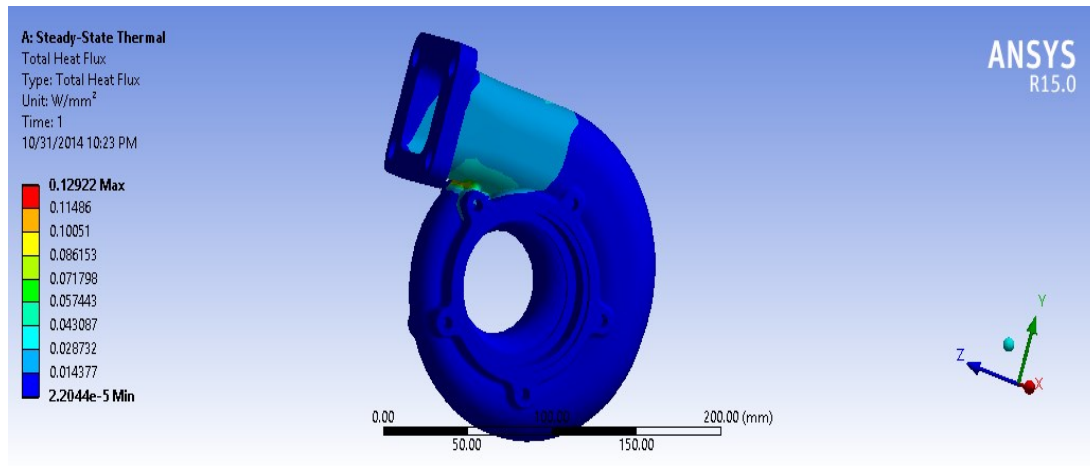
TABLE 20: Model (A4) > Steady-State Thermal (A5) > Solution (A6) > Results

Object Name	Temperature	Total Heat Flux
State	Solved	
Scope		
Scoping Method	Geometry Selection	

Geometry	All Bodies	
Definition		
Type	Temperature	Total Heat Flux
By	Time	
Display Time	Last	
Calculate Time History	Yes	
Identifier		
Suppressed	No	
Results		
Minimum	232.11 °C	2.2044e-005 W/mm²
Maximum	350.01 °C	0.12922 W/mm²
Minimum Value Over Time		
Minimum	232.11 °C	2.2044e-005 W/mm²
Maximum	232.11 °C	2.2044e-005 W/mm²
Maximum Value Over Time		
Minimum	350.01 °C	0.12922 W/mm²
Maximum	350.01 °C	0.12922 W/mm²
Information		
Time	1. s	
Load Step	1	
Substep	1	
Iteration Number	3	
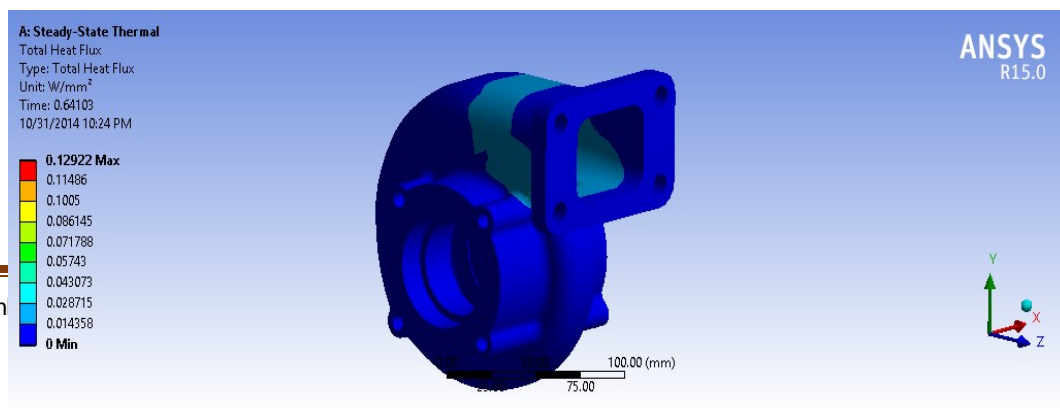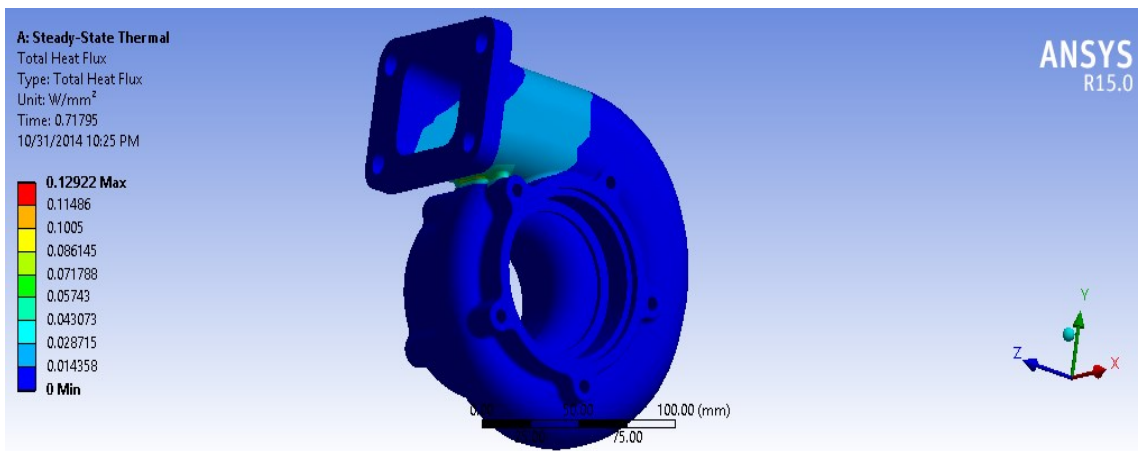
Material Data

Material 2

TABLE 21: material 1 > Constants

Thermal Conductivity	1.454e-002 W mm^-1 C^-1

CONCLUSION

In this project we designed the outer case of a turbocharger for a diesel engine to increase its power and efficiency, and showing the advantage of designing of a turbocharger. In this project tends to usage of new materials is required. In the present work impeller was designed with three different materials. The investigation can be done by using Creo-2 and ANSYS software. The Creo-2 is used for modeling the impeller and analysis is done in ANSYS .ANSYS is dedicated finite element package used for determining the variation of stresses, strains and deformation across profile of the impeller.

Material 1: HK30Nb stainless alloy

Results		
Minimum	235.63 °C	2.2085e-005 W/mm²
Maximum	350.01 °C	0.13105 W/mm²
Minimum Value Over Time		
Minimum	235.63 °C	2.2085e-005 W/mm²
Maximum	235.63 °C	2.2085e-005 W/mm²
Maximum Value Over Time		
Minimum	350.01 °C	0.13105 W/mm²
Maximum	350.01 °C	0.13105 W/mm²

Material 2: CF8C plus cast stain less steel

International Journal of Research

Available at https://edupediapublications.org/journals

p-ISSN: 2348-6848
e-ISSN: 2348-795X
Volume 03 Issue 11
July 2016

Results		
Minimum	232.11 °C	2.2044e-005 W/mm²
Maximum	350.01 °C	0.12922 W/mm²
Minimum Value Over Time		
Minimum	232.11 °C	2.2044e-005 W/mm²
Maximum	232.11 °C	2.2044e-005 W/mm²
Maximum Value Over Time		
Minimum	350.01 °C	0.12922 W/mm²
Maximum	350.01 °C	0.12922 W/mm²

So, by this **HK30Nb stainless alloy** is best material for the turbo casing design It have the bypass to control the air flow in the system which it will through the intercooler or release direct to the ambient.

REFERENCES

[1] C. Berrou, A. Glavieux, and P. Thitimajshima, "Near Shannon limit error-correcting coding and decoding: Turbo-codes," in ICC Proc., May 1993, pp. 1064–1070.

[2] S. Benedetto and G. Montorsi, "Unveiling turbo codes: Some results on parallel concatenated coding schemes," IEEE Trans. Inform. Theory, vol. 42, pp. 409–429, Mar. 1996.

[3] S. Benedetto, D. Divsalar, G. Montorsi, and F. Pollara, "Serial concatenation of interleaved codes: Performance analysis, design, and iterative decoding," IEEE Trans. Inform. Theory, vol. 44, pp. 909–926, May 1998.

[4] L. C. Perez, J. Seghers, and D. J. Costello, Jr., "A distance spectrum interpretation of turbo codes," IEEE Trans. Inform. Theory, vol. 42, pp. 1698–1709, Nov. 1996.

[5] O. Y. Takeshita and D. J. Costello, Jr., "New classes of algebraic interleavers for turbo-codes," in Proc. 1998 IEEE Int. Symp. on InformationTheory, Cambridge, MA, Aug. 16–21, p. 419.

[6] D. Divsalar and R. J. McEliece, "Effective free distance of turbo codes," Electron. Lett., vol. 32, no. 5, pp. 445–446, Feb. 1996.

[7] O. Y. Takeshita, O. M. Collins, P. C. Massey, and D. J. Costello, Jr., "On the frame error rate of turbo-codes," in Proc. ITW 1998, Killarney, Ireland, June 22–26, 1998, pp. 118–119.

[8] S. Benedetto, D. Divsalar, G. Montorsi, and F. Pollara, "Analysis, design, and iterative decoding of double serially concatenated codes with interleaves," IEEE J. Select. Areas Common., vol. 16, pp. 231–244, Feb. 1998.

Design and Thermal Analysis of Cylinder Head in Diesel Engine

Md Shabuddin
M.Tech (Thermal engineering),
P.G. Scholar
Nishitha College of engineering and technology
shabu335@gmail.com

Rangdal Srikanth
Mtech(AMS), Asst professor
Nishitha College of engineering and technology

ABSTRACT

The aim of this study is to discover the characteristics of the cooling water in the cylinder head of a high-power diesel engine by using the Computational Fluid Dynamics (CFD). A 3-D geometric model of a cylinder head water jacket was previously constructed using Unigraphics software. A mesh was then imposed on the model using the preprocessor of Fluent software, GAMBIT. Three types of thermal boundaries are defined and the standard model is utilized to carry out numerical simulations with the CFD software Fluent. The pressure distribution, velocity field distribution, heat transfer coefficient distribution, and temperature distribution of the cylinder head water jacket are presented and analyzed. In addition, the impact flow rates have on the cooling system of a cylinder head is studied. The relevant figures show that enhancement in flow rate will increase the velocity and heat transfer coefficient of the coolant flow but in the meanwhile bring in higher pressure loss. The design of the cylinder head water jacket is evaluated to be satisfactory in terms of cooling effects. Simulation results are compared with the work done by others and limited experimental data, and it is pointed out that the disparity of heat transfer coefficients is mainly due to over simplification of the model and inappropriate use of the turbulence model or wall function heat transfer coefficient. Some suggestions on the types of boundary conditions and appropriate turbulence models are proposed, which include the definition of boundary conditions on different locations and the use of coupled simulation.

Key words: cylinder head water jacket; coolant flow; numerical simulation; CFD

INTRODUCTION
Motivation and Significance of Study

Internal Combustion (IC) Engines play an important role in the modern industry. Great efforts are put to improve the power performance and fuel economy of IC

Engines. As the speed and loading capability of IC engines increase, the thermal and mechanical load increase greatly. Under normal working condition, the peak temperatures of burning gases inside the cylinder of IC Engines are of the order of 2500 K, consequently the temperatures of parts, including valves, cylinder head, and piston in contact with gases, rise rapidly due to a large amount of heat absorbed. The substantial heat fluxes and temperatures lead to thermal expansion and stresses, which further destroy the clearance fits between parts and escalate the distortions and fatigue cracking of parts. To prevent overheating, cooling must be provided for the heated surfaces. However, it should be noted that overcooling will also cause some serious problems, such as combustion roughness, lower overall efficiency and high emission pollution. To some extent, further improvements on the performance of an IC Engine depend on the effective resolution of heat transfer problems. Therefore, an optimal design of the cooling system is required to maintain trouble-free operation of engines, which must take into account all the considerations described above.

As one of the most complicated parts of an IC Engine, the cylinder head is directly exposed to high combustion pressures and temperatures. In addition, it needs to house intake and exhaust valve ports, the fuel injector and complex cooling passages [1]. Many compromises must be made in design to satisfy all these requirements. The complicated structure of a cylinder head leads to the difficulty in acquiring necessarily detailed information for design for conducting flow and heat transfer experiments. With improved computer performance and rapid development of Computational Fluid Dynamics (CFD), numerical simulation provides a tool for engineers to use in evaluating their design. With the assistance of numerical simulation techniques, some basic features, such as pressure and velocity distributions of the flow field, can be easily predicted. Coupled with Computer-Aided Design (CAD), the structure of a cooling system for an engine can be modified and optimized, in order to control the temperature at key zones, decrease the power loss, and improve the reliability of parts working at high temperatures.

GEOMETRIC AND MESH MODELS
Geometric model
Characteristics of the Solid Model

The geometric model of the cylinder head was created using the software Unigraphics (UG) modeling software, which is useful in component and surface modeling, virtual assembly, and in generating engineering drawings. The component studied in this project is one cylinder head of an eight-cylinder 1015 high-power diesel engine. Some of the characteristic parameters of the investigated engine are presented in the table below.

Table 2 Engine Characteristics

Engine Type	Diesel TC
Cylinders	8V
Bore	132mm
Stroke	145mm
Displacement	16L
Compression Ratio	17
Rated Power	440kW
Rated Engine Speed	2100r/min

The 1015 engine has a split structure, namely one cylinder head for one cylinder. The cooling system of this engine is distinguished by the manner in which coolant is distributed. The cylinder block water jackets are connected in series, while the cylinder head water jackets are connected in parallel. This design enables the coolant collected in

cylinder blocks to enter each cylinder head separately through transfer channels separately, which is also the reason why only one cylinder head has been investigated.

Principles of Modeling

Based on experience gained from the repeated modeling and numerical simulation process, the following principles of modeling are recommended.

1. Embodiment of features of the structure and flow

A cylinder head consists of the firedeck, side plate, fuel injector protection sleeve and valve guide. It can be described as a box that has been trimmed by intake and exhaust ports and padded by intake and exhaust valves, and fuel injector. All these features create a rather irregular cylinder head structure with special cavities and bores, which complicate the process of building a water jacket model, since the shape and position of parts in cylinder head determine the shape of the water jacket. Moreover, the most complicated areas in the cylinder head usually happen to be key places where investigators put most emphases. In those locations, either the velocity and heat fields have large gradients, or advection is significant. Therefore, the geometric

features of these parts should be modeled as accurately as possible.

2. Impact on mesh generation

Complexity of the solid models may result in potential difficulty in mesh generation, poor quality of the mesh model and unnecessary work. To simulate viscous effects near walls, it is usually needed to create a boundary layer, which requires some simplification in order to avoid unacceptable meshes due to severe curvature change of surfaces.

It can be concluded that building the solid model is a trade-off process between the above two principles. Appropriate simplification is needed on the premise that most geometric details have been retained.

The completed cylinder head solid model is displayed below.
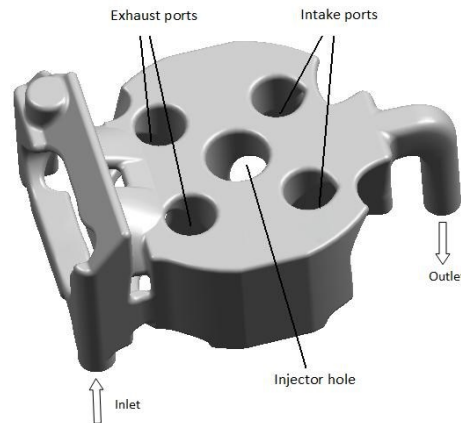
Figure 2 Geometric Model of Cylinder Head Water Jacket

Mesh Model

A high quality mesh model is one of the most important factors that determine the successful prediction of the behavior of an objective. The geometric model of cylinder head water jacket was imported to GAMBIT, a preprocessor of the CFD software Fluent. Tetrahedral volume meshing elements were chosen to generate the mesh model. The mesh model is shown below, which contains 130365 cells and 29150 nodes.
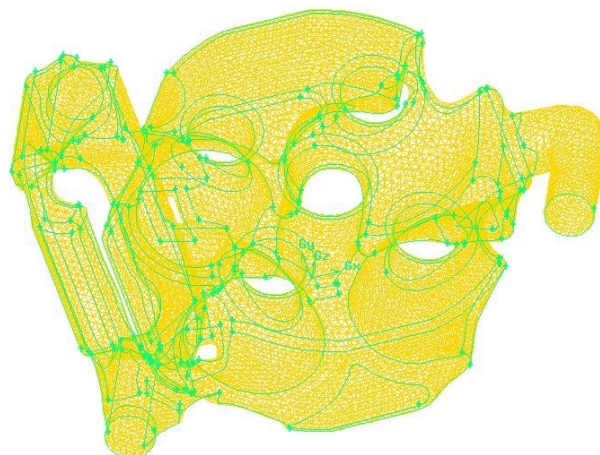
Figure 3 Mesh Model

Using a 0-1 scale for mesh quality with 0 representing the best and 1 the poorest, more than 90 percent of the cells are of the scale less than 0.5, which implies a high quality of the mesh model.

RESULTS AND ANALYSIS

With the high quality mesh model, the solutions converge within half an hour after 400-600 iterations, depending on the cases studied. In this paper, the results of pressure field, velocity field and temperature field are presented and analyzed. More attention is paid to the heat transfer process. The influence of flow rates on those parameters mentioned above is discussed. Refer to Figure 2 for the definition of coordinates. The bottom of the cylinder head water jacket, where inlet and outlet are located, is referred to as the datum plane, and the center of the fuel injector bore on this plane is the origin. The positive z-axis is directed toward the top of cylinder head water jacket, the positive y-axis is directed toward the paper, and the positive x-axis is directed toward the outlet. Because the computation of the pressure and velocity fields is independent of the temperature, the simulation results of these two fields will only be presented once, for all three thermal boundary conditions. The results shown were calculated at the inlet flow rate of 1.0508 kg / s if they were not specified.

Simulation Results with Convection Thermal Boundary
1. Pressure Field Distribution
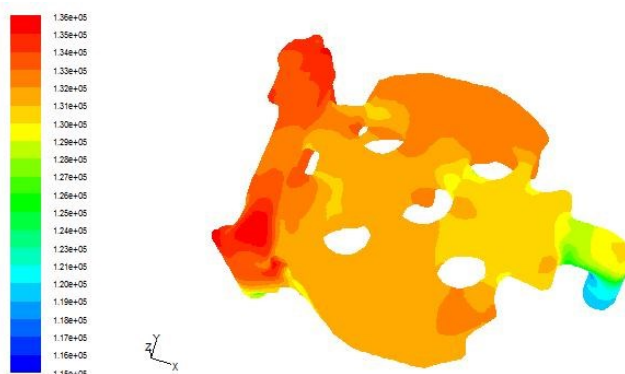
Figure 4 Contour of Pressure Field Distribution (Pa)

It can be seen from the contour of pressure that the outlet displayed the lowest pressure, while the side plate presented the highest pressure, which indicated that the largest pressure drop occurs between the inlet and outlet. The interior of the water jacket does not have obvious pressure drop. The pressure loss between the inlet and outlet is calculated to be 8.4177 kPa, which is a good indicator of low resistance in flow and potential to enhance mechanical efficiency.
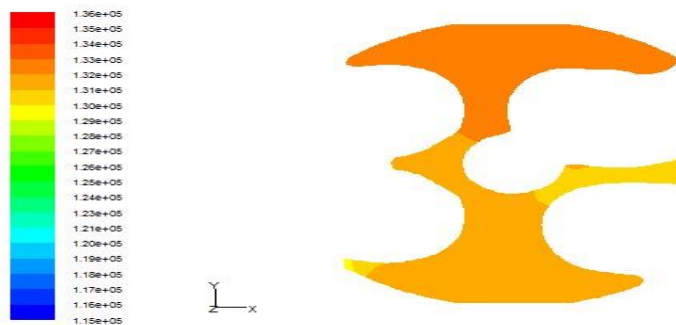
Figure 5 Pressures (Pa) on Nose Zones at z = 35 mm

Focusing on the nose zones, the narrow bridges between intake ports, exhaust ports, intake and exhaust ports, and two ports and the fuel injector, it is noticed from Figure 5 that the pressure varies between 129 kPa and 132 kPa, which is a small difference that reduces the possibility of bubble producing, and therefore the destruction of the cylinder head.

2. Velocity Field Distribution
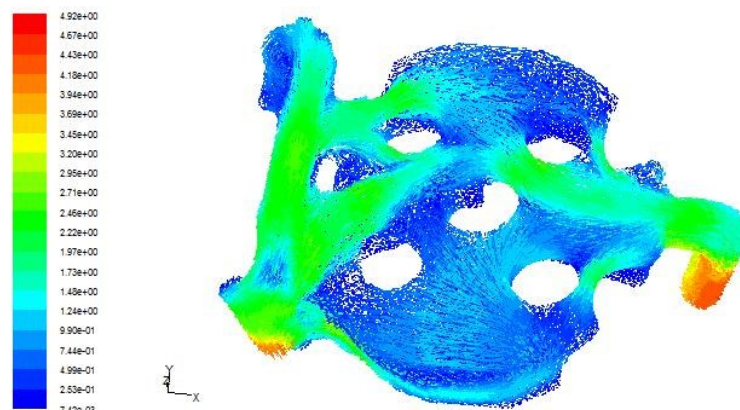
Figure 6 Contour of Velocity Field Distribution (m/s)

The average velocity magnitude over the whole flow field is 0.892 m/s, which meets the need of flow rate 0.5 m/s for cooling the engine. Some key zones were investigated particularly.

1) Exhaust port

The design for this cylinder head forced the flow to go around the exhaust port first, where most of the heat was output, then cooled down the fuel injector and finally the intake port. It is seen that the velocity of the flow around the exhaust port was higher than other locations, which ensures that the cylinder head is relatively evenly cooled. Because of the small inlet and outlet diameters, the velocity at these locations was largest.

2) Fuel injector
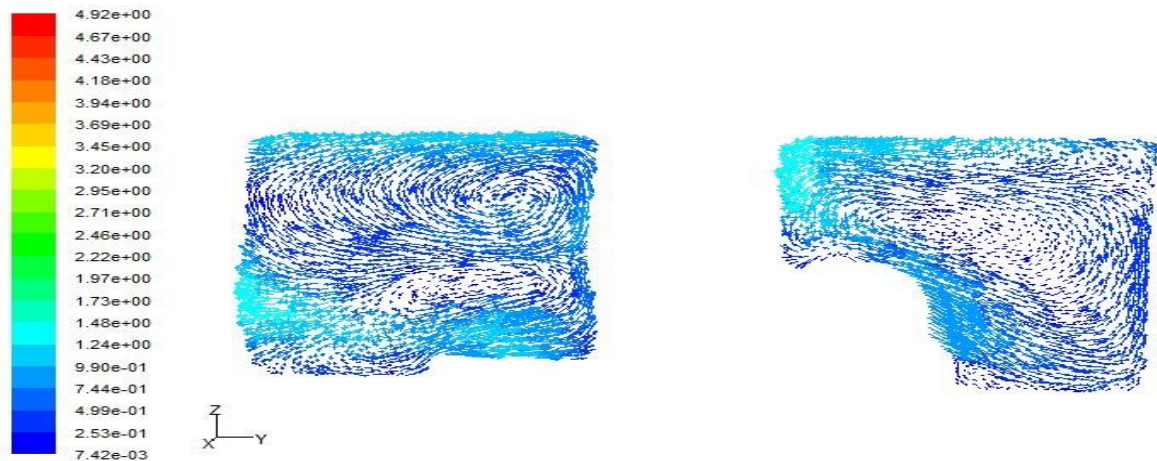
Figure 7 Velocity Field around the Fuel Injector (m/s)

The upper part of the fuel injector hole is narrower than the lower part. Such a design coordinates with the flow regularity that the flow comes from the under part of the hole and up to the top of the cylinder head, which ensures a relatively high velocity of the flow on the top. In this case, the velocity changed from 0.7m/s to 1.25m/s.

1) Nose zones

International Journal of Research

Available at https://edupediapublications.org/journals

p-ISSN: 2348-6848
e-ISSN: 2348-795X
Volume 03 Issue 11
July 2016
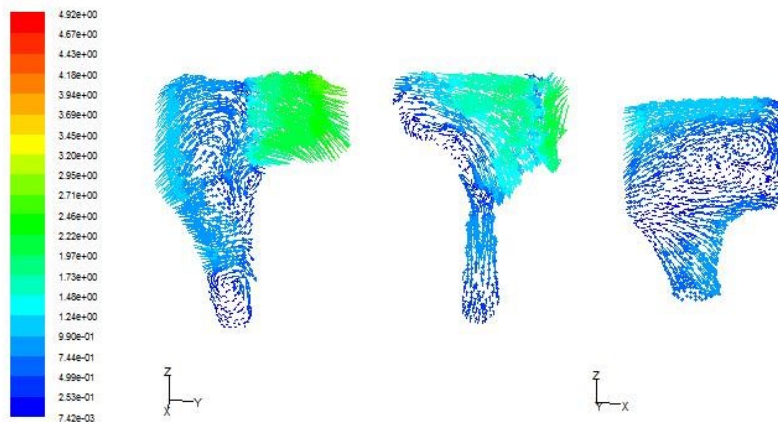
The higher flow rate in the narrow bridges between intake and exhaust valves ensured the cooling effects in the most problematic regions.

3. Heat Transfer Coefficient Distribution

The cooling effects can be reflected directly by the heat transfer coefficient (HTC). The HTC shown below is the surface HTC provided by Fluent.

The simulation results of the surface heat transfer coefficients are as follows:

1) Wall
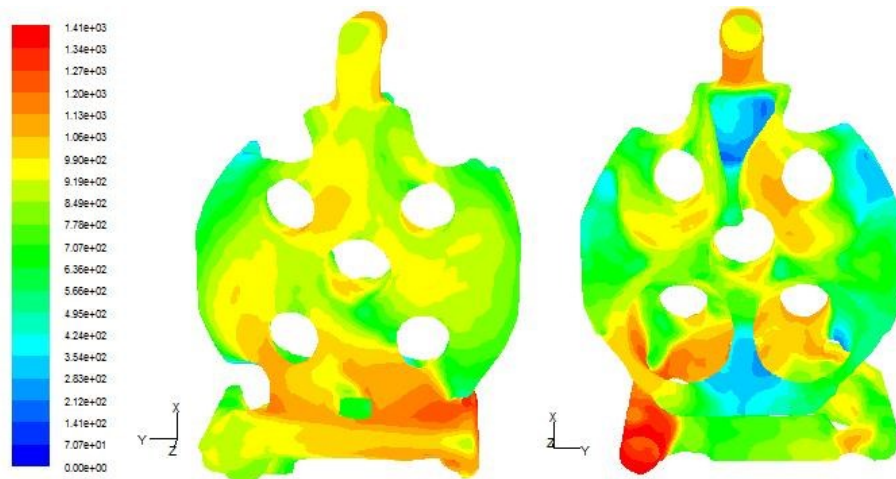
Figure 9   Contour of Surface HTC Distribution ($W/(m^2 \cdot K)$)

The area-averaged surface HTC is calculated to be 836.52 $W/(m^2 \cdot K)$.

2) Specific regions
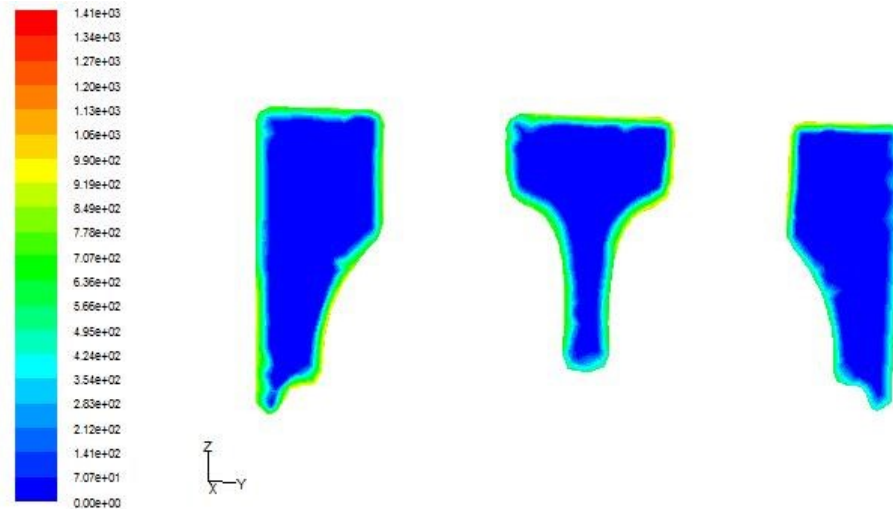
Figure 10 Surface HTC ($W/(m^2 \cdot K)$) on Nose Zones at x = -30 mm

Figure 10 displayed the surface heat transfer coefficient distribution of the narrow bridge regions at x =-30 mm . Data at different locations and on different height planes was collected and summarized in the table below.

Table 4 Surface HTC at Different Locations

HTC Section	Exhaust valves	Intake and exhaust valves	Intake valves	Fuel injector
z=18mm	600-750	——	——	——
z=20mm	700-900	600-800	——	600-700
z=25mm	900-1000	800-900	700-800	700-800
z=30mm	900-1200	800-900	750-900	900-1100

The fire deck is located at the plane where $z = 0$.

4. Temperature Distribution
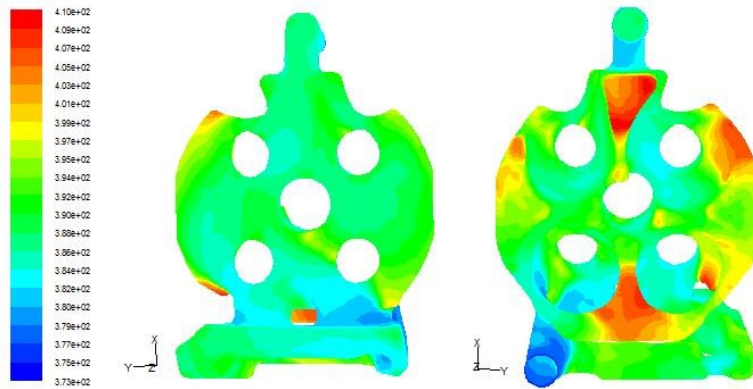
Figure 11 Contour of Temperature Distribution (K)

With the limitation of the boundary conditions, the temperature distribution was displayed in the range of 373K and 418K. The bottom contacted with the fire deck, was of extremely high temperature, which is reasonable in the sense of the structure characteristics and work principle of the cylinder head. The temperatures around the wall of the annular cavities, where the fresh air and exhaust passed, were ranging from 384K to 397K, which showed acceptable cooling effects of the cylinder head. By comparison of HTC and temperature distributions, it is evident that the regions with high heat transfer coefficient correspond to ones with low temperature, and vice versa. This also implies the inherent relations between the velocity and heat transfer coefficient, which will be discussed.

Simulation Results with Fixed Heat Flux Thermal Boundary

1. Heat Transfer Coefficient Distribution
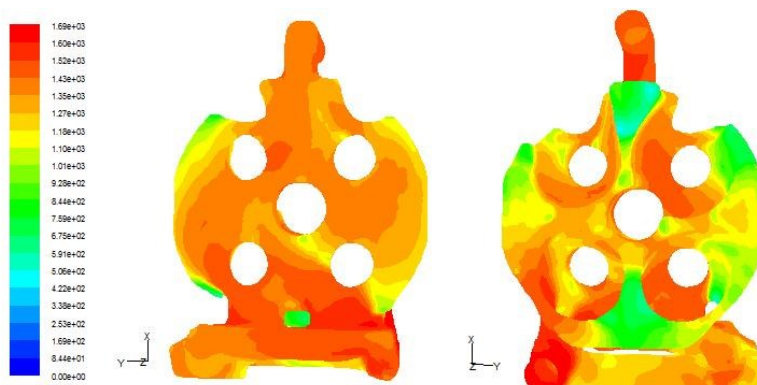
Figure 12 Contour of Surface HTC Distribution ($W/(m^2 \cdot K)$)

The area-averaged surface HTC at the wall is 1287.0704 $W/(m^2 \cdot K)$, indicating a relatively good cooling effect.

2. Temperature distribution
1) At the wall surface
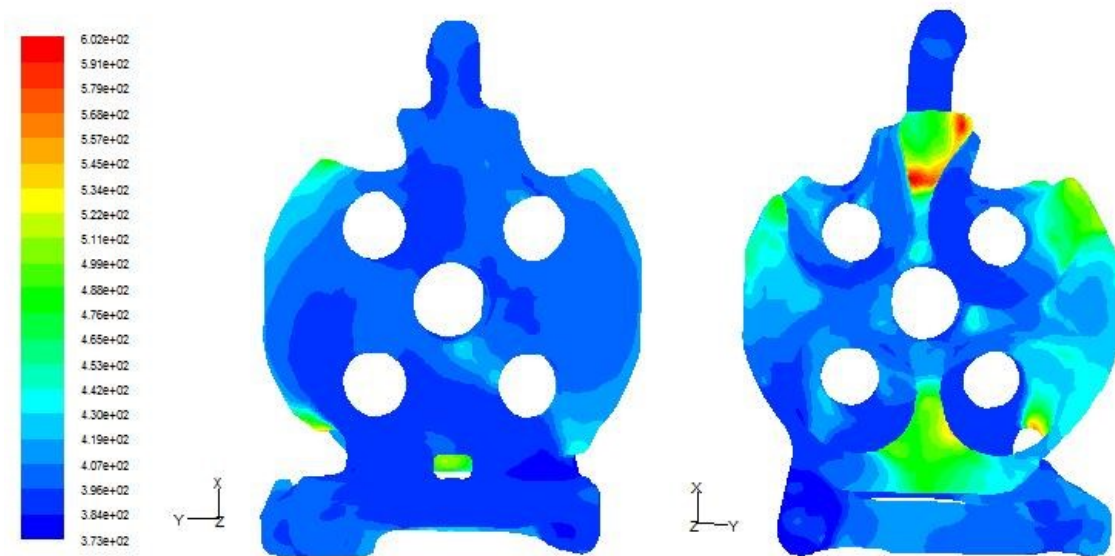
Figure 13 Contour of Temperature Distribution at Wall (K)

2) Sections orthogonal to z-axis
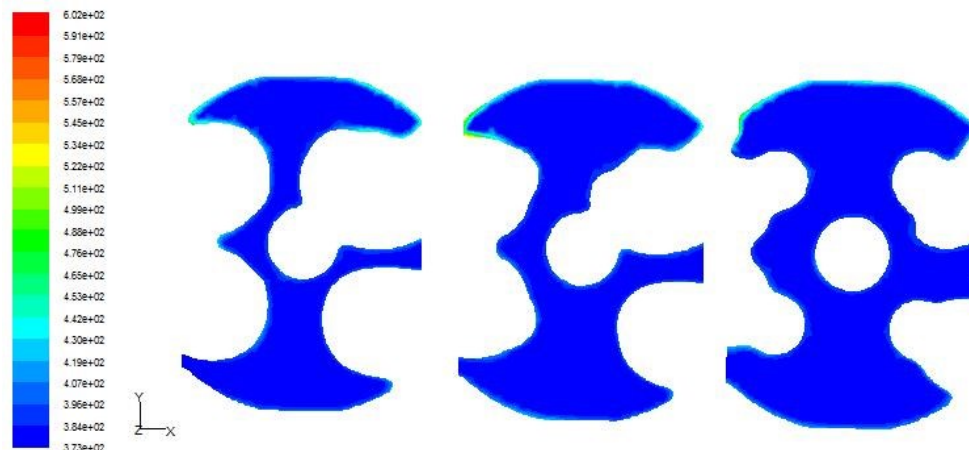
Figure 14 Contour of Temperature Distribution at z = 35mm , 45mm and 55mm (K)

The contour of the wall surface shows that the hottest part is located at the narrow bridge on the heating surface, but the magnitude exceeds the boiling point of glycol, which means either it is not realistic, or the design of the cylinder head will cause destruction due to film boiling.

Simulation Results with Fixed Temperature Thermal Boundary
Heat Transfer Coefficient Distribution
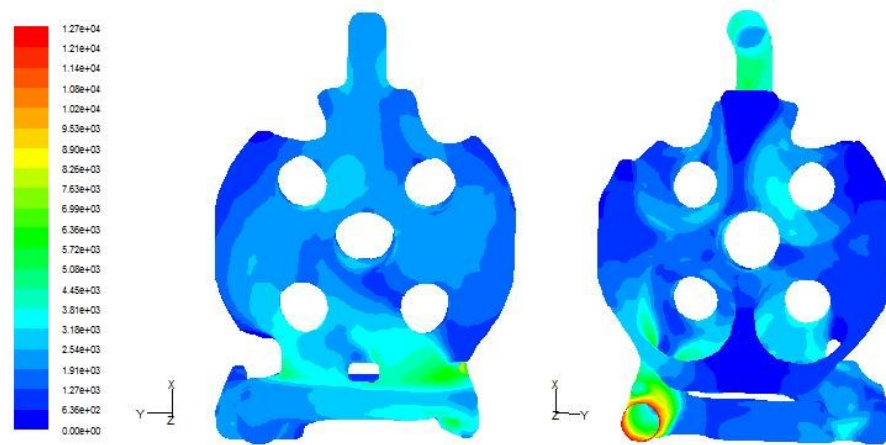
Figure 15 Contour of Surface HTC Distribution ($W/(m^2 \cdot K)$)

The area-averaged surface HTC at the wall is 2142.2268 $W / (m^2 \cdot K)$), which is greater than the results of convection and fixed heat flux thermal boundaries. Moreover, the area-averaged total surface heat flux reaches 277706.5 W/m^2 , which is almost twice the referenced [22] heat flux of 150 kW/m^2 . In a cylinder head of an engine, the temperature varies from point to point, which depends on the location of the heat source and the detailed structures of different regions. It is not practical to assume the temperature is constant over the wall surface, but the simulation conducted under the fixed temperature thermal boundary provided a profile of the heat transfer coefficient, which depicted the general distribution, but not the exact value of the heat transfer coefficient.

HTC Distribution Using Wall Function Formula

The wall function HTC is based on the semi-empirical formula for HTC (refer to Equation 2.31), in spite of the different thermal boundaries chosen. Therefore, the wall function HTCs in the previously described three types of wall boundary conditions give the same result, the contour of which is shown in Figure 16.
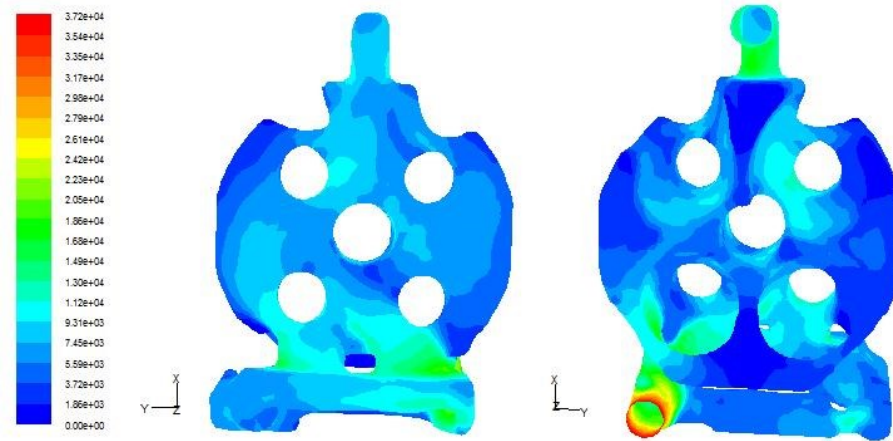
Figure 16 Contour of Wall Function HTC Distribution ($W/(m^2 \cdot K)$)

In addition, the surface HTC and wall function HTC distributions present similar profiles. It means that locations of high HTC and low HTC are almost the same in different contours, but the magnitudes of HTC at these locations are different. It can be expected that the wall function HTC will be more reliable when heat flux or temperature gradient is sufficiently large.

Effects of Flow Rates

As the engine has been strengthened, it's necessary to check the consequent effects on the cooling system. Four typical working conditions (refer to Table 3) were taken into

1. Pressure Loss

account, as listed in figures below. The convection thermal boundary condition is the most reasonable one for numerical simulation, which gives not only the variations of the pressure field, velocity field, temperature field and heat transfer coefficient field at different zones, but also the magnitudes of these parameters at particular points, which are close to the experimental data. Therefore, the simulation results used below are obtained from this condition.

Pressure loss is computed by taking the difference of area-averaged pressures at the inlet and outlet.
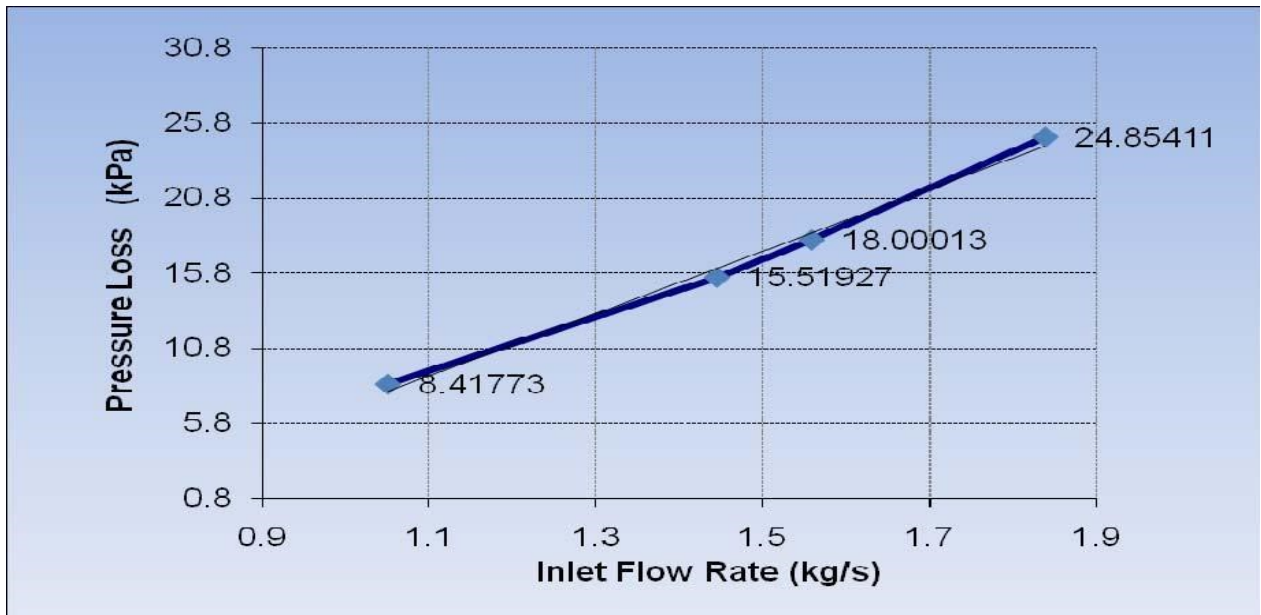
Figure 17 Pressure Losses at Different Flow Rates

2. Velocity

The velocity presented below is the volume-averged velocity calculted over the interier of the water jacket.
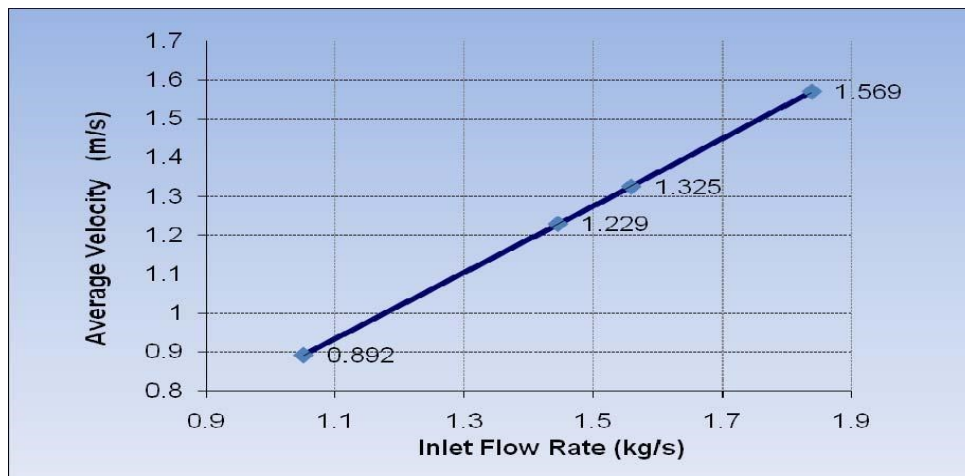
Figure 18 Average Velocity at Different Flow Rates

3. Surface HTC with Convection Boundary Condition

The surface heat transfer coefficient is the area-averaged HTC at the surface of the water jacket.
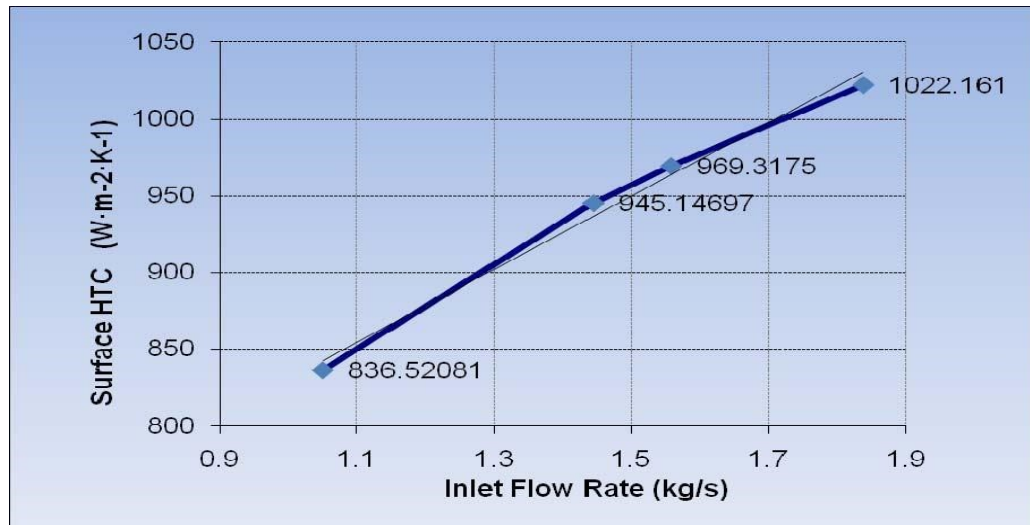
Figure 19 Surface HTC at Different Flow Rates

With the increase of rated power, the inlet flow rate increases, the velocity and heat transfer coefficient increase consequently. However, the pressure loss will increase too, which indicates the decrease of the torque efficiency. It is known that if the pressure loss exceeds 50 *kPa* , the resistance of the cooling system will be large, and loss of the power will be considered to be high.

CONCLUSIONS AND FUTURE WORK
Evaluation of Cooling Effects of the Cylinder Head
In general, the work of this cylinder head water jacket satisfied the demand of cooling effects, which can be analyzed in the following ways.

1. The coolant in cylinder head performed a good flow rate distribution, and relatively even

pressure distribution.

2. The arrangement of the parts in cylinder head provided necessary forces to enhance the cooling in problematic zones, so that the intake and exhaust valves and the fuel injector will not be too hot to break down.

Evaluation of the Simulation
The flow field and heat field of the cylinder head water jacket were computed based on the boundary condition values, which were obtained from the experiments and experience. However, they should also be tested and verified by available information. The following table provides some information of the coolant-side heat transfer process, which was reported in the literature.

Table 5 Boundary Conditions Considered in the Mode

Boundary condition description	Link	Heat transfer coefficient [$\text{W m}^{-2}\text{K}^{-1}$]	Bulk temperature [K]
Insulated surfaces (negligible heat-transfer rate)	20	0 (adiabatic)	–
Free surfaces (contact with ambient air)	29	5	320
Cooling passages	30	3 000*	350
In-cylinder surfaces	21	450	1120
Intake-port surfaces	22	800	330
Exhaust-port surfaces	23	800	700

In spite of the different types of engines studied, the results should not be of way too big differences.

By the careful comparison with all available, but limited papers on the heat transfer analysis of a cylinder head, it can be seen that the simulation results of the pressure and flow rate distributions are relatively consistent with each other, while the results on heat transfer vary a lot.

According to the information given in the above table, this present study showed more accurate simulation results. Moreover, it should be noticed that many of the

investigators obtained rather high heat transfer coefficients, even higher than $10^4\,W$ / ($m^2{\cdot}K$), which deviated from the experimental data. The main causes of the disparity may lie on two aspects:

1. The geometric model and mesh model are over simplified or some of the important characteristics of the structure are ignored.
2. The chosen turbulence model is not appropriate for the studied model, and the wall function HTC is not an acceptable prediction for the HTC profile of the coolant flow given the boundary conditions described previously.

Future Work

It has been years that researchers put efforts on a realistic and reliable simulation of the cooling system of the cylinder head. Until now, there are a variety of results especially in heat transfer coefficient, some of which

are not consistent with the experimental data. This study is another attempt to better describe the heat transfer process in a cylinder head. The results are closer to the limitedly available information obtained directly from the experiments, but they still need to be improved on the following

potential aspects.

1. Boundary conditions

This study already showed that the convection thermal boundary for the wall is the best way of simulating the heat transfer process, and the same value was considered for the whole wall surface. However, it is evident that different zones of the wall are exposed to different environment, resulting in different boundary conditions which should be set separately according to the locations of the zones.

To achieve this purpose, boundary layers should be employed to divide the model into different areas in Gambit, which will take effect when adding wall boundaries in Fluent.

2. Turbulence model and semi-empirical HTC formula

The classical two-equation $k-\varepsilon$ model has been widely used with its accuracy and universality. The simplicity is also an advantage of this model, which is based on and developed from the Reynolds' analogy. All the assumptions of the Reynolds' analogy made the problems simpler and easier to solve. Nevertheless, the $k-\varepsilon$ model can not reflect the Reynolds' relaxation effect along the stream line, so it's not the best simulation tool for more complex flow in engineering.

It is shown that the standard wall function described the distribution of heat field with relatively high heat transfer coefficients, which were inconsistent with the available experimental results. The semi-empirical heat transfer coefficient formula could be improved further, which needs to be investigated.

3. Coupled simulation

In this study, the entity is the water jacket of a cylinder head. If we can set up the solid cylinder head model as well, both structural and fluid simulations can be carried on to obtain a more satisfactory result. Finite Element Method will be applied in this kind of simulation.

4. Improvement of design

Once the cooling effects of the current model were figured out, it is significant to make some change in design to achieve a better cooling model, to carry on simulations and evaluate the new model, and to modify it again, which is a repeating process. For this cylinder head model, it is worth trying to add a water hole in order to strengthen the cooling effect around the fuel injector.

REFERENCES

[1]. M. Diviš, R. Tichánek, M. Španiel, Heat Transfer Analysis of a Diesel Engine Head. *Acta Polytechnica*, 2003 Vol. 43, No. 5 : 34-39.

[2]. Malcolm H.Sandford,Lan Postlemthwaite. Engine Coolant Flow Simulation-A Correlation Study.*SAE TECHNICAL PAPER SERIES*, 930068.

[3]. Mark D.Moechel. Computational Fluid Dynamic (CFD) Analysis of

a Six Cylinder Diesel Engine Cooling System with Experimental Correlations. *SAE TECHNICAL PAPER SERIES*, 941081.1994.

[4]. Franz J.Laimbock, Gerhard Meister et al. Application in Compact Engine Development. *SAE TECHNICAL PAPER SERIES*, 982016.

[5]. Toyoshige SHIBATA, Hideo MATSUI, Masao TSUBOUCHI et al. KATSURADA. Evaluation of CFD Tools Applied to Engine Coolant Flow Analysis, MITSUBISHI MOTORS TECHNICAL REVIEW 2004, (16):56-60.

[6]. Curtis M.Hill, Glenn D.Miller, Robert C. Gardner. 2005 Ford GT Powertrain-Supercharged Supercar. *SAE TECHNICAL PAPER SERIES*, 2004-0101252.

[7]. Xunjun Liu, Qun Chen, Ju Li, Kang Li, Haie Chen, Automotive Diesel Engine Water Jacket CFD Analysis[J]. *Transaction of CSICE*, 2003, Vol.21, No.2: 125-129.

[8]. Haie Chen, Fanchen Meng, Jianlong Song, Jun Li, CFD Analysis on Engine Cooling Jackets[J]. *Design Computation Research*, 1000-3703(2003).

[9]. Qun Chen, Xunjun Chen, CFD Analysis of Cooling Water Jacket of Vehicle Diesel Engine CA498 [J]. *Design Computation Research*, 1000-3703(2003)11-0008-04:8-11.

[10]. Numerical Simulation on Flow and Heat Transfer of Cooling System in a Six-Cylinder Diesel Engine [J]. *Transaction of CSICE*, 2004, Vol.22, No.6: 525-531.

[11]. Shengguan Qu, Wei Xia, Numerical Simulation and Experimental Research on Cooling Water Flow around Cylinder liner for Heavy Duty Diesel Engine [J].*Chinese Internal Combustion Engine Engineering*, 2004, Vol.25 No.4: 32-35.

Investigation of Thermal Field in Friction Surfacing Different Tool Pin Profiles Square and Circular

Syed Basith Ahmed
M.Tech (Thermal engineering),
P.G. Scholar
Nishitha College of engineering and technology
Abdulbasith9533@gmail.com

Rangdal Srikanth
Mtech(AMS), Asst professor
Nishitha College of engineering and technology

ABSTRACT:

Friction-stir welding (FSW) is a solid-state joining process (the metal is not melted) and is used when the original metal characteristics must remain unchanged as much as possible. It mechanically intermixes the two pieces of metal at the place of the join, then softens them so the metal can be fused using mechanical pressure, much like joining clay, dough, or plasticine. It is primarily used on aluminum, and most often on large pieces that cannot be easily heat-treated after welding to recover temper characteristics. In this project, FEA analysis is performed for friction stir welding of aluminum and copper. The welds are produced by varying the process parameters; the rotational speed was varied between 600 to 1200 rpm and the welding speed varied between 50 and 300 mm/min. Structural and thermal analysis are done. A parametric model with the weld plates and cutting tool is done in Creo-2. The effects of different tool pin profiles on the friction stir welding are also considered for analysis. Different tool pin profiles are square and circular. So in this project we want to create simple model of FSW tool and two work pieces to be joined by butt by using Creo workbench and also analysis the working pieces that is effected by the thermal stress that are applied on it.

Keywords: Aluminum, copper, Friction-stir welding (FSW), mechanical pressure, thermal stress.

INTRODUCTION:

Friction-stir welding (FSW) is a solid-state joining process (meaning the metal is not melted during the process) and is used for applications where the original metal

characteristics must remain unchanged as far as possible. This process is primarily used on aluminum, and most often on large pieces which cannot be easily heat treated post weld to recover temper characteristics.

PRINCIPLE OF OPERATION

Schematic diagram of the FSW process: (A) Two discrete metal work pieces butted together, along with the tool (with a probe). The progress of the tool through the joint, also showing the weld zone and the region affected by the tool shoulder. In FSW, a cylindrical-shouldered tool, with a profiled threaded/unthreaded probe (nib or pin) is rotated at a constant speed and fed at a constant traverse rate into the joint line between two pieces of sheet or plate material, which are butted together. The parts have to be clamped rigidly onto a backing bar in a manner that prevents the abutting joint faces from being forced apart. The length of the nib is slightly less than the weld depth required and the tool shoulder should be in intimate contact with the work surface. The nib is then moved against the work, or vice versa. Frictional heat is generated between the wear-resistant welding tool shoulder and nib, and the material of the work pieces. This heat, along with the heat generated by the mechanical mixing process and the adiabatic heat within the material, cause the stirred materials to soften without reaching the melting point (hence cited a solid-state process), allowing the traversing of the tool along the weld line in a plasticized tubular shaft of metal. As the pin is moved in the direction of welding, the leading face of the pin, assisted by a special pin profile, forces plasticized material to the back of the pin while applying a substantial forging force to consolidate the weld metal. The welding of the material is facilitated by severe plastic deformation in the solid state, involving dynamic recrystallization of the base material.
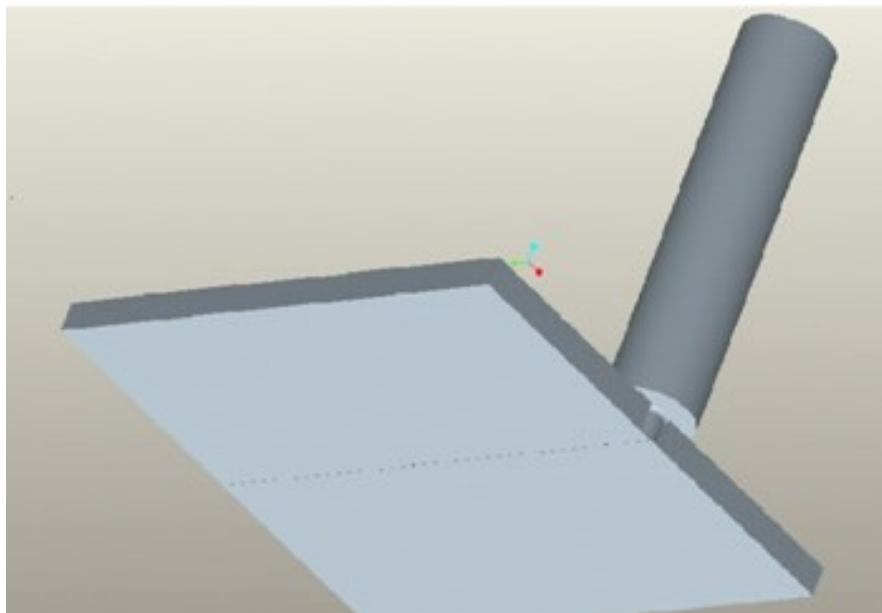
Figure 1: 3-D Model of Friction Surfacing

FSW is used as the main engine for the calculation of stresses and temperatures. The model does not consider the transient variations of variables during the initial tool insertion period or the final tool withdrawal period. The model solves the equations of conservation of mass, momentum and energy in steady-state, three-dimensional Cartesian coordinate considering incompressible single phase flow. It calculates three dimensional heat generation

rates, temperature and velocity fields, viscosity, flow stress, strain rate and torque for various welding conditions and tool and work piece materials. Since the details of the model are already available in the literature,6-12 these are not repeated here. Instead, only the extension of the heat transfer and materials flow model to calculate the bending and maximum shear stresses are discussed here.

$$\frac{da}{dN} = A\Delta K^m \tag{1}$$

$$\Delta K = \Delta\sigma(\pi a)^{1/2} \tag{2}$$

$$N_f = [a_f^{(1-m/2)} - a_0^{(1-m/2)}]/[A(1-m/2)\Delta\sigma^m\pi^{0.5m}] \tag{3}$$

$$a_f = [K_I/(1.12\tau_b)]^2/\pi \tag{4}$$

$$\sigma_B = \frac{4\cos\theta}{\pi r^3}\int_{z_1}^{L} z\,q(z)\,dz \tag{5}$$

$$\tau_T = \frac{M_T}{\pi r^3/2} \tag{6}$$

$$M_T = \oint_A r_A \times (1-\delta)\,\tau \times dA \tag{7}$$

Where MT is the sticking torque, rA is the distance of any infinitesimal area element, dA, from the tool axis, ' is the spatial fractional slip, % is the temperature dependent shear strength. The shear stress, %B, at point A due to bending can now be computed as

$$\tau_B = \frac{4}{3}\frac{\sin^2\theta}{\pi r^2}\int_{z_1}^{L} q(z)\,dz \tag{8}$$

$$\tau_{max} = \sqrt{\left(\frac{\sigma_B}{2}\right)^2 + (\tau_B + \tau_T \sin\theta)^2 + (\tau_T \cos\theta)^2} \qquad (9)$$

TOOL ROTATION AND TRAVERSE SPEEDS

There are two tool speeds to be considered in friction-stir welding; how fast the tool rotates and how quickly it traverses the interface. These two parameters have considerable importance and must be chosen with care to ensure a successful and efficient welding cycle. The relationship between the welding speeds and the heat input during welding is complex but, in general, it can be said that increasing the rotation speed or decreasing the traverse speed will result in a hotter weld. In order to produce a successful weld it is necessary that the material surrounding the tool is hot enough to enable the extensive plastic flow required and minimize the forces acting on the tool. If the material is too cool then voids or other flaws may be present in the stir zone and in extreme cases the tool may break. At the other end of the scale excessively high heat input may be detrimental to the final properties of the weld. Theoretically, this could even result in defects due to the liquation of low-melting-point phases (similar to liquation cracking in fusion welds). These competing demands lead onto the concept of a 'processing window': the range of processing parameters that will produce a good quality weld. Within this window the resulting weld will have a sufficiently high heat input to ensure adequate material plasticity but not so high that the weld properties are excessively reduced.

TOOL TILT AND PLUNGE DEPTH
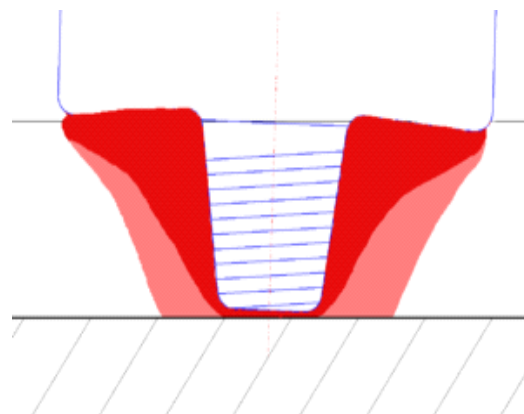
Figure 2: A drawing showing the plunge depth and tilt of the tool

The tool is moving to the left.

International Journal of Research

Available at https://edupediapublications.org/journals

p-ISSN: 2348-6848
e-ISSN: 2348-795X
Volume 03 Issue 11
July 2016

The plunge depth is defined as the depth of the lowest point of the shoulder below the surface of the welded plate and has been found to be a critical parameter for ensuring weld quality. Plunging the shoulder below the plate surface increases the pressure below the tool and helps ensure adequate forging of the material at the rear of the tool. Tilting the tool by 2-4 degrees, such that the rear of the tool is lower than the front, has been found to assist this forging process. The plunge depth needs to be correctly set, both to ensure the necessary downward pressure is achieved and to ensure that the tool fully penetrates the weld. Given the high loads required the welding machine may deflect and so reduce the plunge depth compared to the nominal setting, which may result in flaws in the weld. On the other hand an excessive plunge depth may result in the pin rubbing on the backing plate surface or a significant under match of the weld thickness compared to the base material. Variable load welders have been developed to automatically compensate for changes in the tool displacement while TWI have demonstrated a roller system that maintains the tool position above the weld plate.

TOOL DESIGN

The design of the tool is a critical factor as a good tool can improve both the quality of the weld and the maximum possible welding speed. It is desirable that the tool material is sufficiently strong, tough and hard wearing, at the welding temperature. Further it should have a good oxidation resistance and a low

thermal conductivity to minimize heat loss and thermal damage to the machinery further up the drive train. Hot-worked tool steel such as AISI H13 has proven perfectly acceptable for welding aluminium alloys within thickness ranges of 0.5 – 50 mm but more advanced tool materials are necessary for more demanding applications such as highly abrasive metal matrix composites or higher melting point materials such as steel or titanium.

Improvements in tool design have been shown to cause substantial improvements in productivity and quality. TWI has developed tools specifically designed to increase the depth of penetration and so increase the plate thickness that can be successfully welded. An example is the 'whorl' design that uses a tapered pin with re-entrant features or a variable pitch thread in order to improve the downwards flow of material. Additional designs include the Triflute and Trivex series. The Triflute design has a complex system of three tapering, threaded re-entrant flutes that appear to increase material movement around the tool. The Trivex tools use a simpler, non-cylindrical, pin and have been found to reduce the forces acting on the tool during welding. The majority of tools have a concave shoulder profile which acts as an escape volume for the material displaced by the pin, prevents material from extruding out of the sides of the shoulder and maintains downwards pressure and hence good forging of the material behind the tool. The Triflute tool uses an alternative system with a series of concentric grooves machined into the

surface which are intended to produce additional movement of material in the upper layers of the weld.

GENERATION AND FLOW OF HEAT

For any welding process it is, in general, desirable to increase the travel speed and minimize the heat input as this will increase productivity and possibly reduce the impact of welding on the mechanical properties of the weld. At the same time it is necessary to ensure that the temperature around the tool is sufficiently high to permit adequate material flow and prevent flaws or tool fracture. When the traverse speed is increased, for a given heat input, there is less time for heat to conduct ahead of the tool and the thermal gradients are larger. At some point the speed will be so high that the material ahead of the tool will be too cold and the flow stress too high, to permit adequate material movement, resulting in flaws or tool fracture. If the 'hot zone' is too large then there is scope to increase the traverse speed and hence productivity.

The welding cycle can be split into several stages during which the heat flow and thermal profile will be different:

- **Dwell**. The material is preheated by a stationary, rotating tool in order to achieve a sufficient temperature ahead of the tool to allow the traverse. This period may also include the plunge of the tool into the work piece.

- **Transient heating**. When the tool begins to move there will be a transient period where the heat production and temperature around the tool will alter in a complex manner until an essentially steady-state is reached.

- **Pseudo steady-state**. Although fluctuations in heat generation will occur the thermal field around the tool remains effectively constant, at least on the macroscopic scale.

- **Post steady-state**. Near the end of the weld heat may 'reflect' from the end of the plate leading to additional heating around the tool.

Heat generation during friction-stir welding arises from two main sources: friction at the surface of the tool and the deformation of the material around the tool. The heat generation is often assumed to occur predominantly under the shoulder, due to its greater surface area, and to be equal to the power required to overcome the contact forces between the tool and the workpiece. The contact condition under the shoulder can be described by sliding friction, using a friction coefficient μ and interfacial pressure P, or sticking friction, based on the interfacial shear strength &tor; at an appropriate temperature and strain rate. Mathematical approximations for the total heat generated by the tool shoulder Q_{total} have been developed using both sliding and sticking friction models:

$$Q_{total} = \frac{2}{3}\pi P \mu \omega \left(R_{shoulder}^3 - R_{pin}^3 \right) \text{(Sliding)}$$

$$Q_{total} = \frac{2}{3}\pi \tau \omega \left(R_{shoulder}^3 - R_{pin}^3 \right) \text{(Sticking)}$$

Where ω is the angular velocity of the tool, $R_{shoulder}$ is the radius of the tool shoulder and R_{pin} that of the pin. Several other equations have been proposed to account for factors such as the pin but the general approach remains the same.

A major difficulty in applying these equations is determining suitable values for the friction coefficient or the interfacial shear stress. The conditions under the tool are both extreme and very difficult to measure. To date, these parameters have been used as 'fitting parameters' where the model works back from measured thermal data to obtain a reasonable simulated thermal field. While this approach is useful for creating process models to predict, for

- 2000 series aluminium (Al-Cu)

- 5000 series aluminium (Al-Mg)

- 6000 series aluminium (Al-Mg-Si)

- 7000 series aluminium (Al-Zn)

- 8000 series aluminium (Al-Li)

example, residual stresses it is less useful for providing insights into the process itself.

MATERIALS AND THICKNESSES

Friction stir welding can be used for joining many types of materials and material combinations, if tool materials and designs can be found which operate at the forging temperature of the work pieces.

For aluminium alloys, the following alloys are easily welded. Maximum thickness in a single pass is dependent on machine power, but values ≥50mm are achievable. TWI has welded 75mm 6xxx material in a single pass, and larger thicknesses are possible.
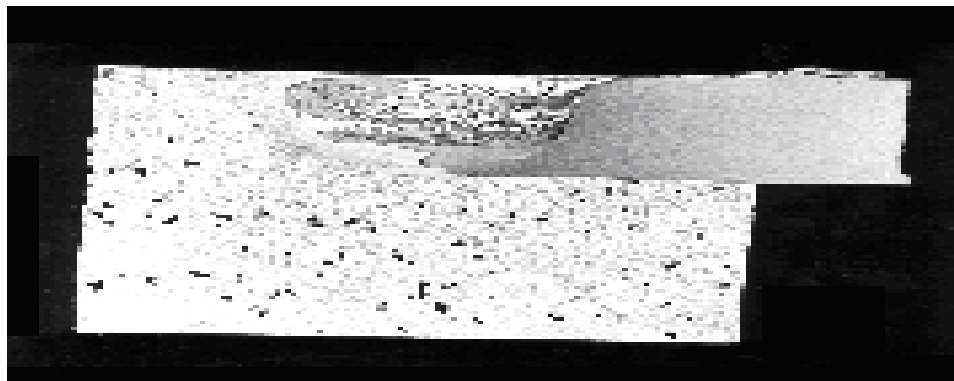
MMCs based on aluminum (metal matrix composites) Other aluminum alloys of the 1000 (commercially pure), 3000 (Al-Mn) and 4000 (Al-Si) series, aluminum castings.

Other materials successfully welded include:

- Copper and its alloys (up to 50mm in one pass)
- Lead
- Titanium and its alloys
- Magnesium alloys
- Zinc
- Plastics
- Mild and C-Mn steels
- Stainless steel (austenitic, martensitic and duplex)
- Nickel alloys

FRICTION STIR WELDING OF CAST ALUMINIUM ALLOY

The most popular aluminum casting-alloy contains about 8 wt% of silicon. It therefore solidifies to primary aluminum-rich dendrites and a eutectic mixture of aluminum solid-solution and almost pure silicon. The latter occurs as coarse silicon particles which tend to be brittle. The cast alloy usually has some porosity. Friction stir welding has the advantage that it breaks up the coarse silicon particles and heals any pores by the mechanical processing, as illustrated below.
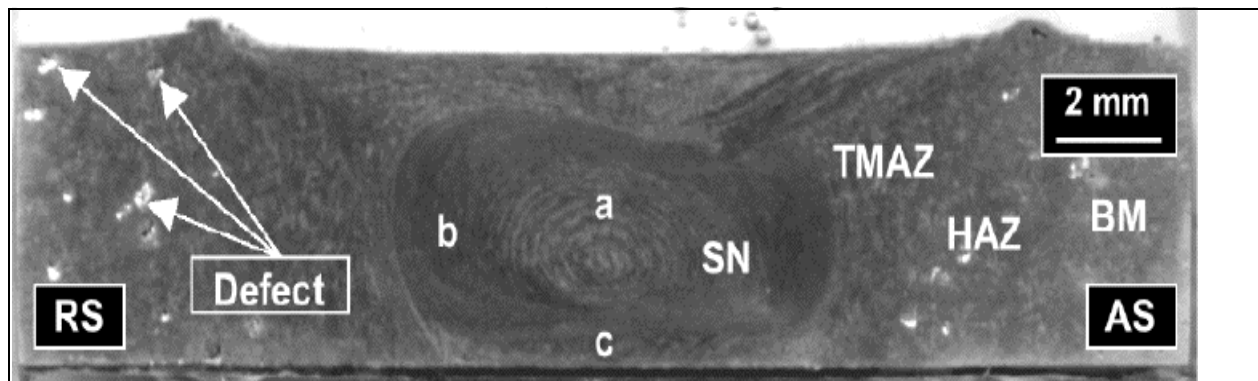
A section through a friction stir weld made in an Al-Si casting alloy. There are pores indicated in the base metal (BM). HAZ represents the heat affected zone, TMAZ the thermo mechanically affected zone, and SN the stir nugget. The photographs in this section have kindly been provided by Professor H. Fujii of JWRI, Japan.
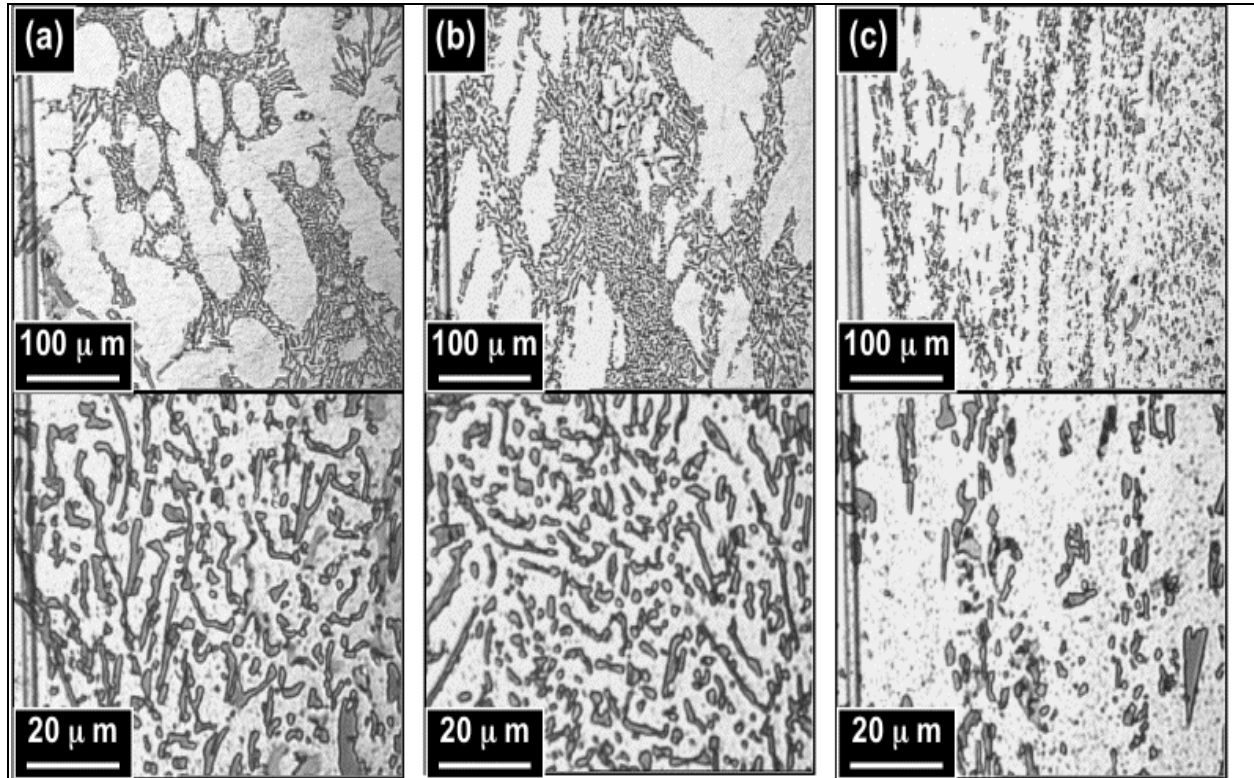
Optical micrographs showing the microstructure in (a) the base metal; (b) heat-affected zone; (c) the thermomechanically affected zone, where considerable refinement of the silicon has occurred.
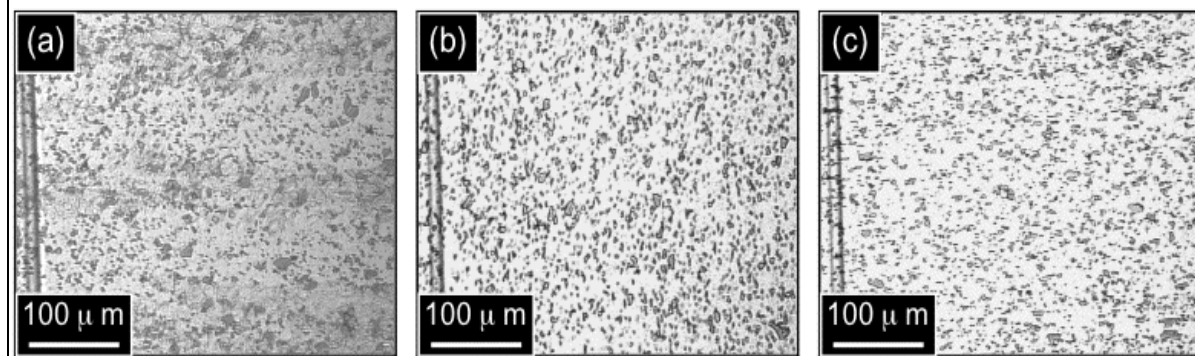
Optical micrographs of regions (a), (b) and (c) of the stir nugget. The location of these regions is identified in macroscopic section presented above.

	Tensile strength (MPa)	Proof stress (MPa)	Elongation (%)	Fracture location
Joint	150	85	1.6	BM
Weld	179	87	5.3	TMAZ
SN	251	96	14.4	SN

The refinement of silicon and elimination of porosity leads to better mechanically properties in the weld than in the base plates.

MODELS OF CUTTING TOOLS
ROUND TOOL

PLATE1
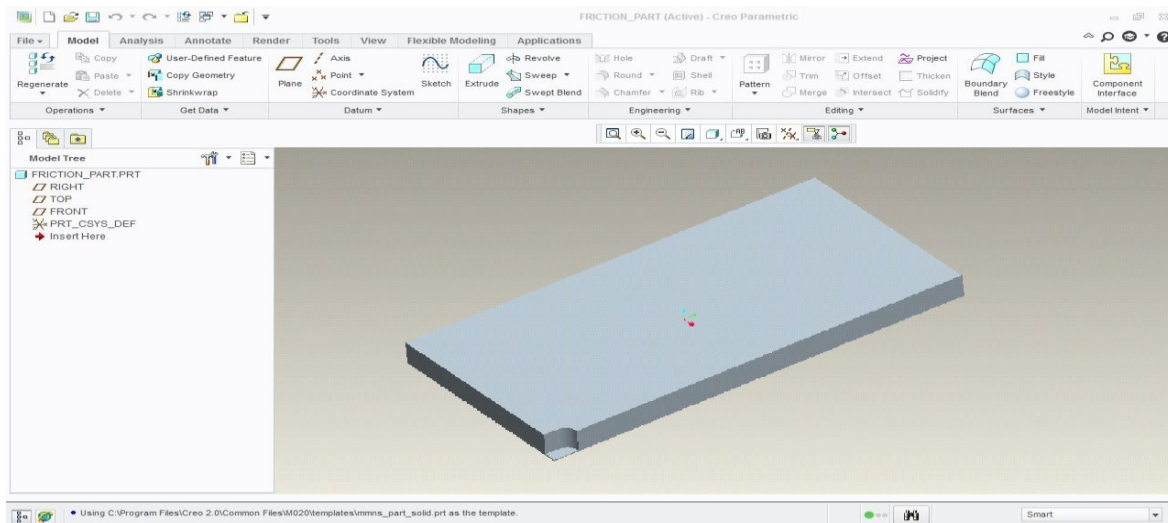
PLATE2
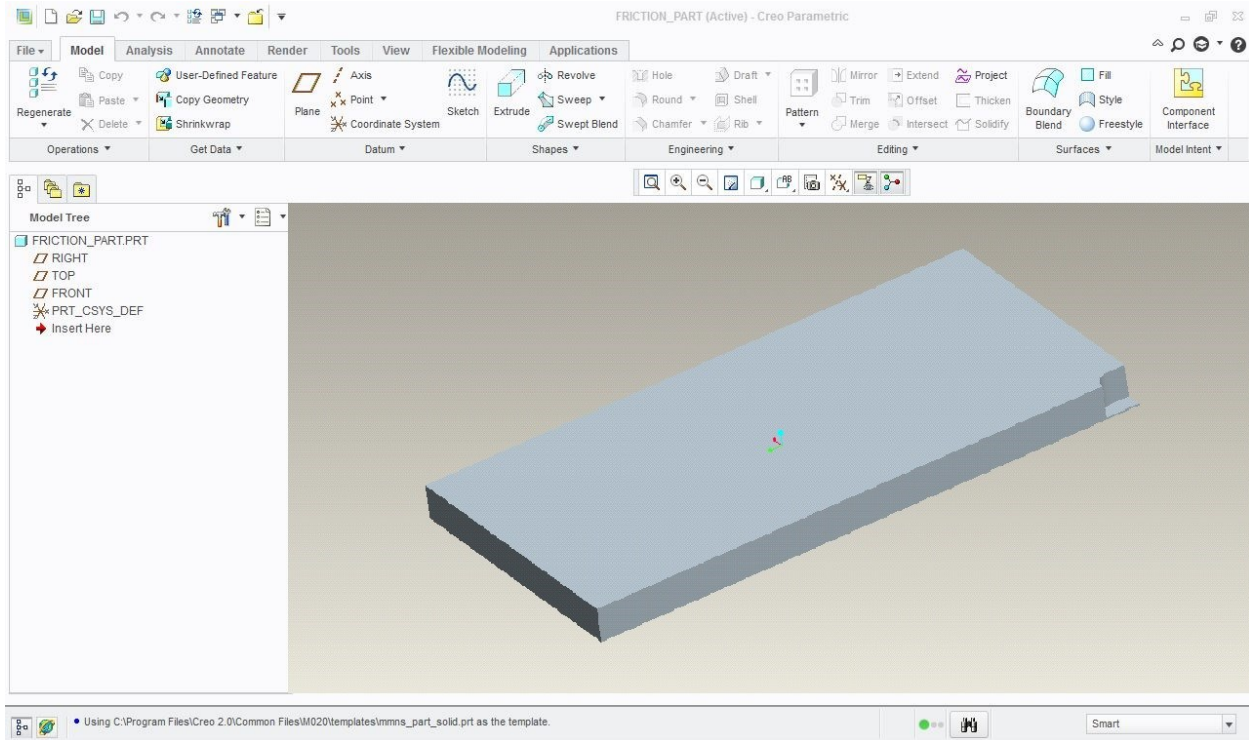
ROUND TOOL
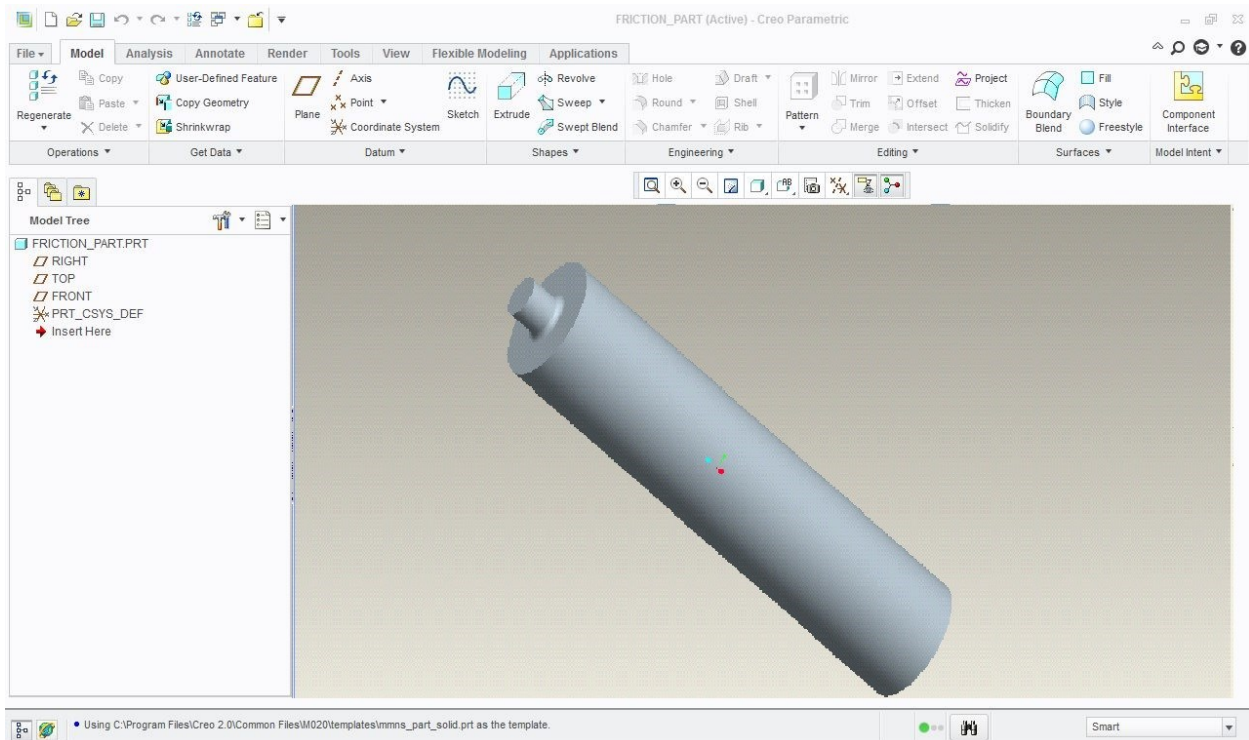
ROUND TOOL ASSM
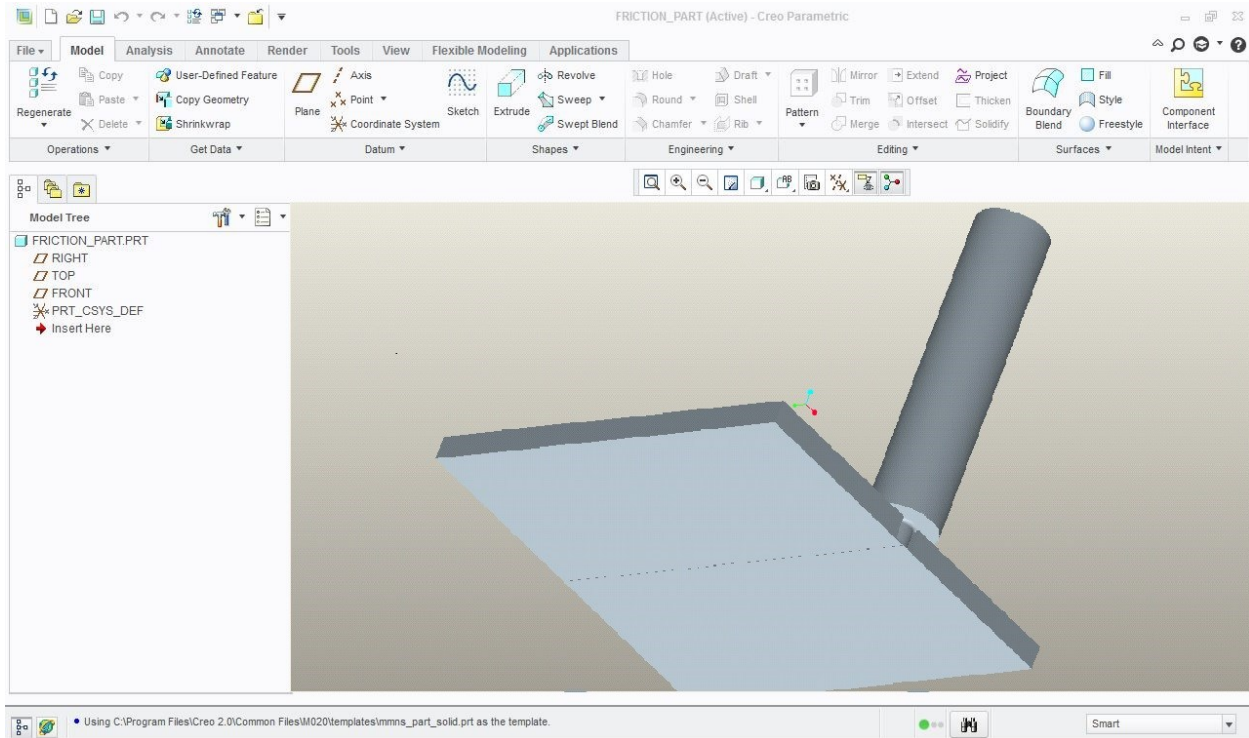
SQUARE TOOL

PLATE1
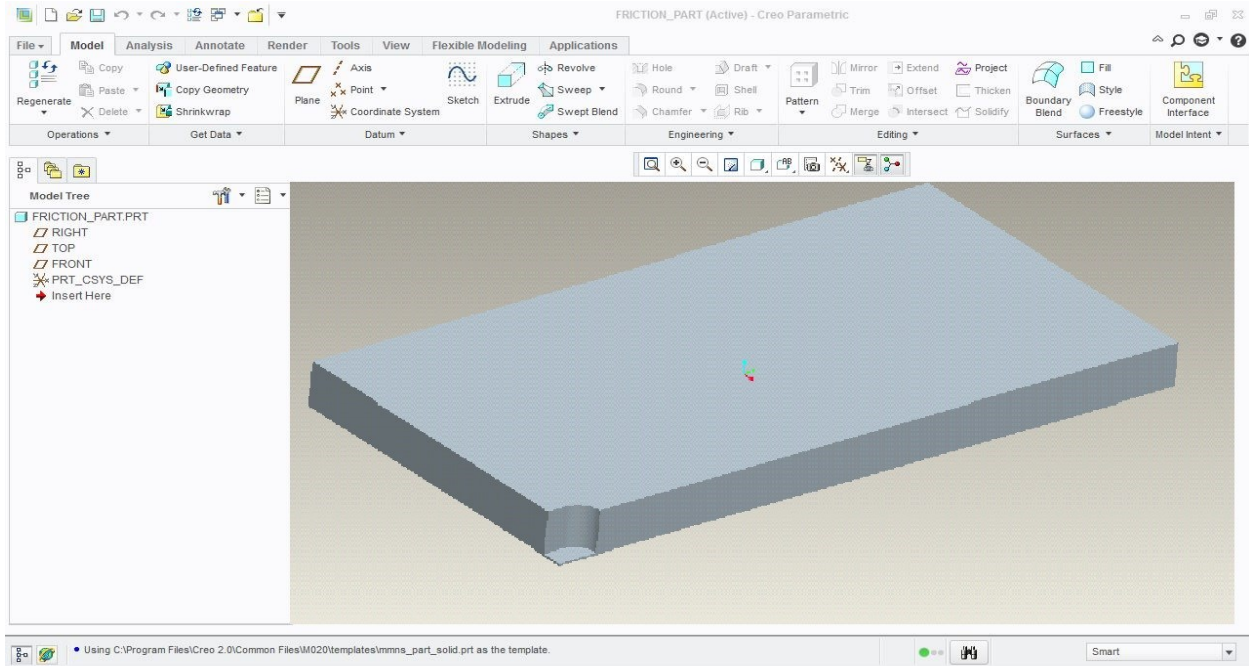
PLATE2
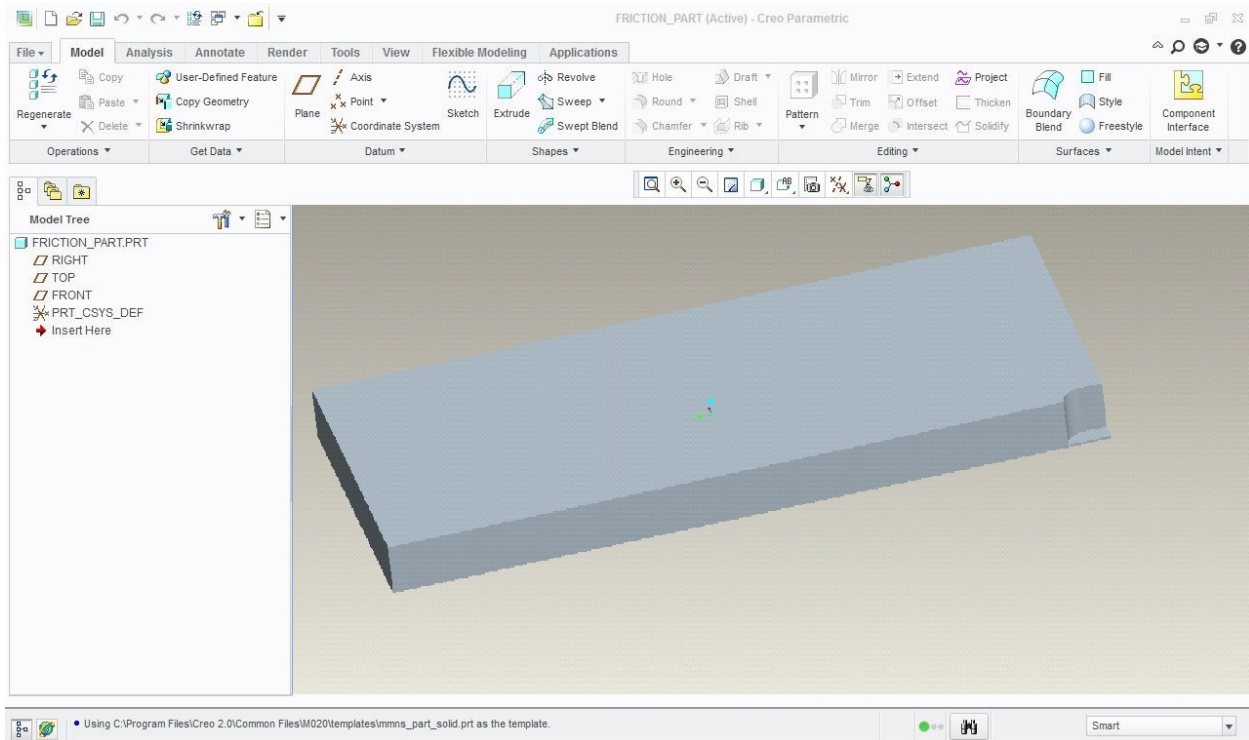
SQUARE TOOL
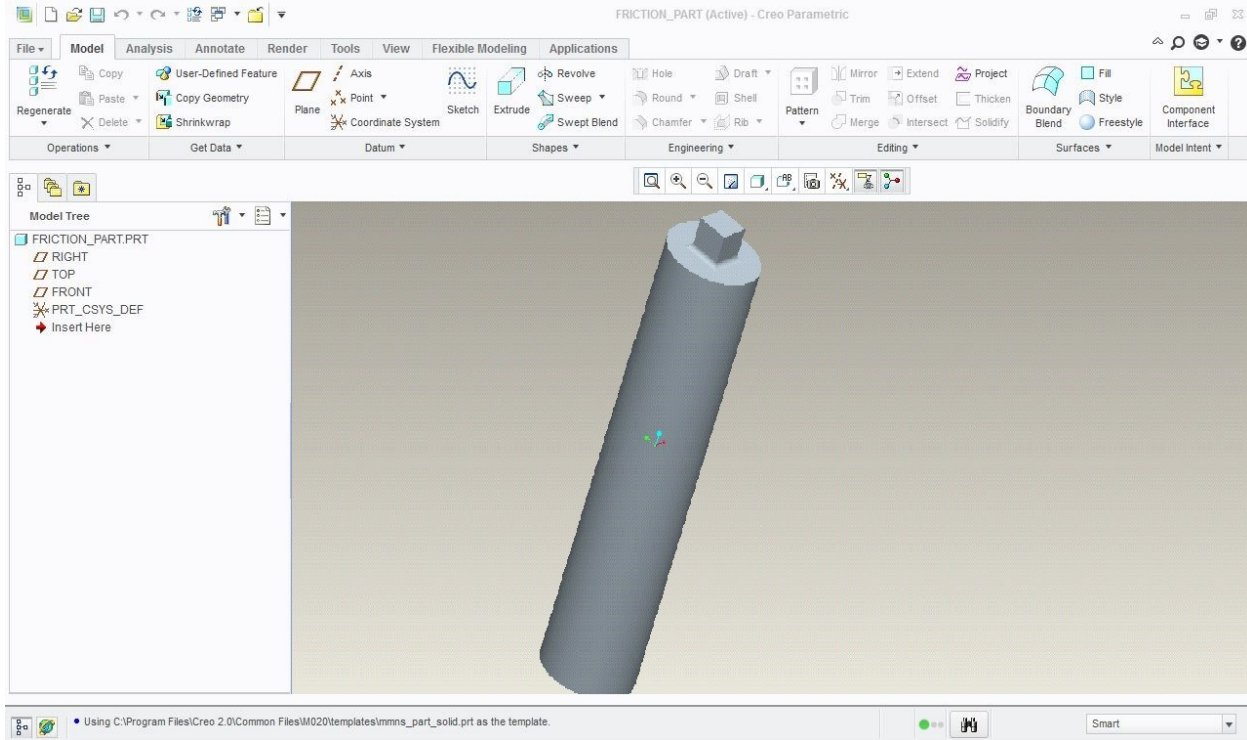
SQUARE TOOL ASSMEMBLY
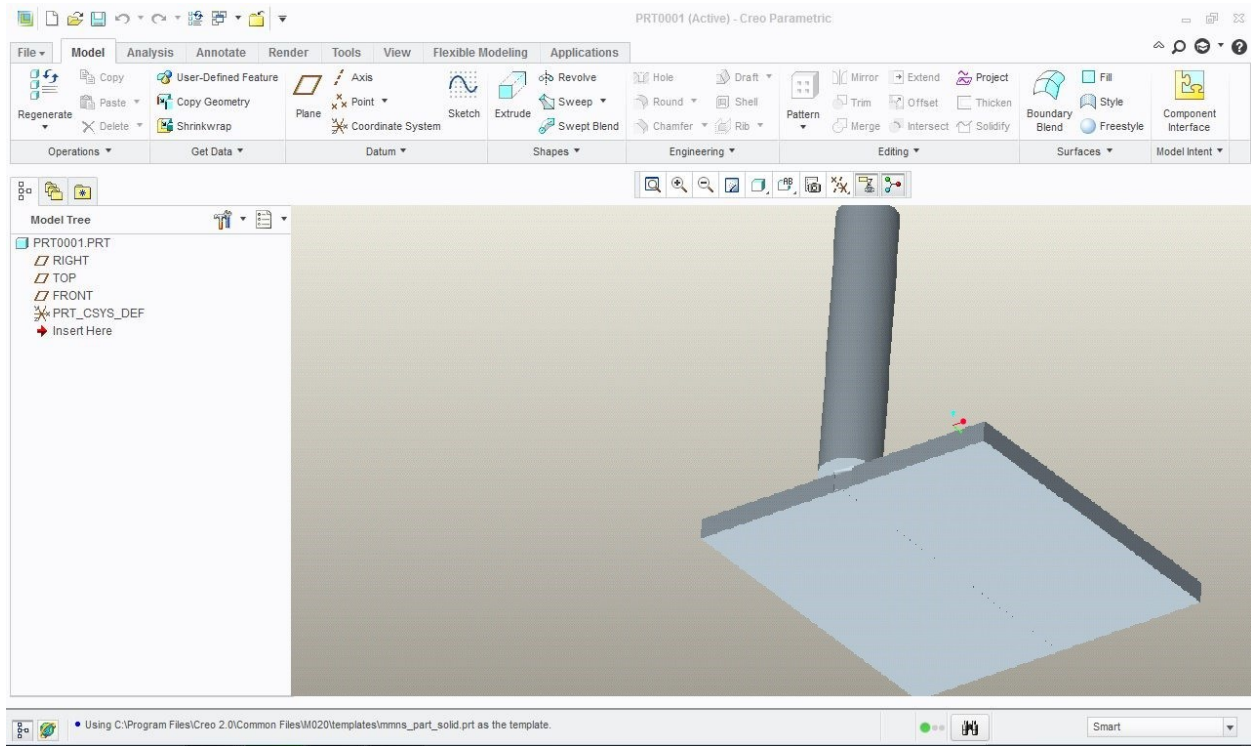
COUPLED FIELD ANALYSIS OF ALUMINUM ALLOY 6061 AND CAST COPPER

1000 rpm

ROUND TOOL

Software used is ANSYS10

Type of analysis done- Couple field analysis

Enter units-/units,si,mm,kg,sec,k

Set working directory

Change job name

Select Preference select thermal

Select element type as a solid brick 20 node 90

Enter material properties as a thermal conductivity 0.18 W/mm. K

Enter material properties as a specific heat 896 J/Kg-^{0}K
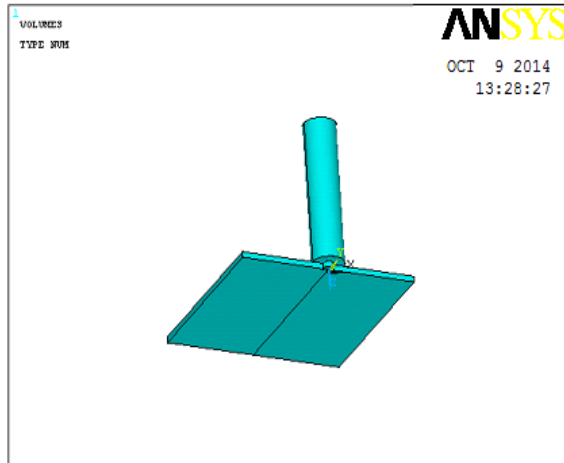
Import IGES model   Meshed model
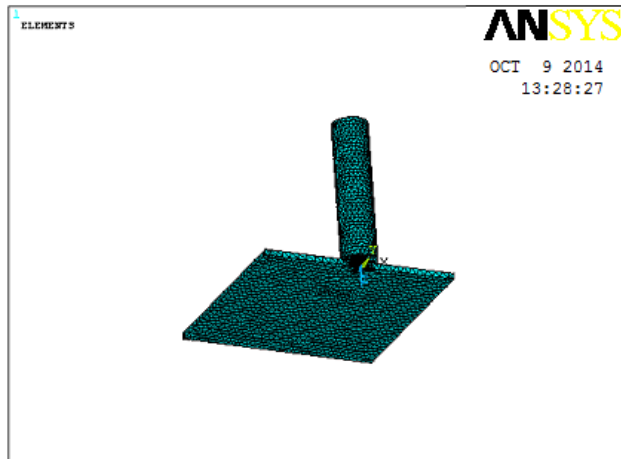
RESULTS OF THERMAL FIELD IN FRICTION SURFACING
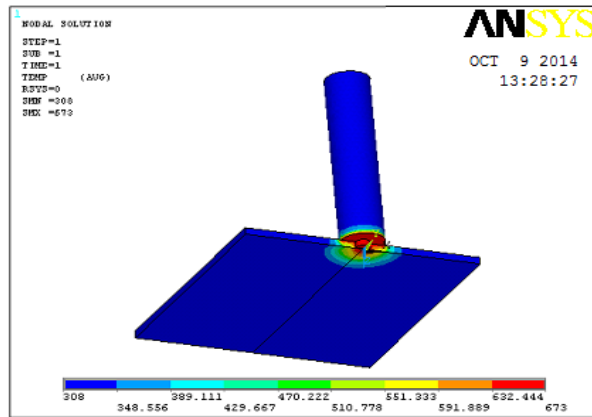
Temperature distribution   Thermal flux
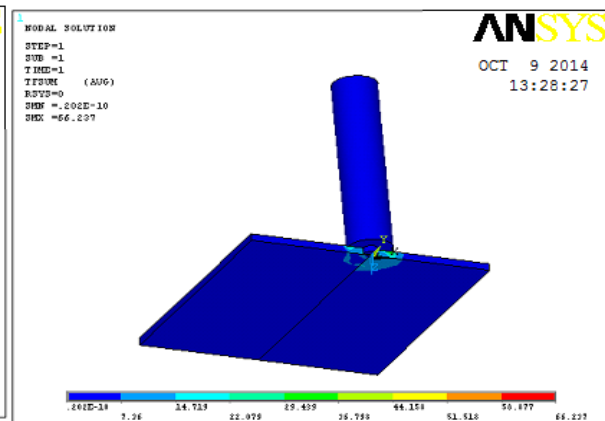
Thermal gradient   Displacement
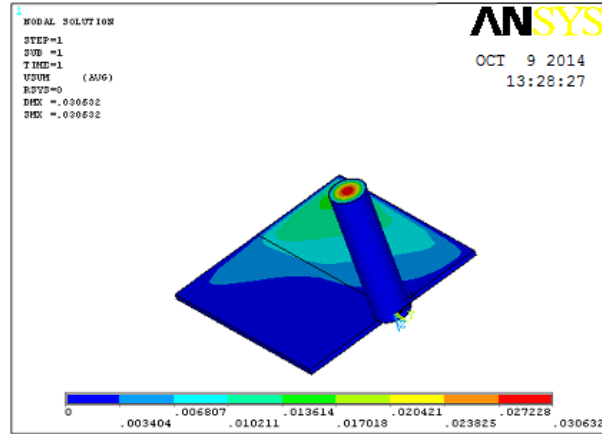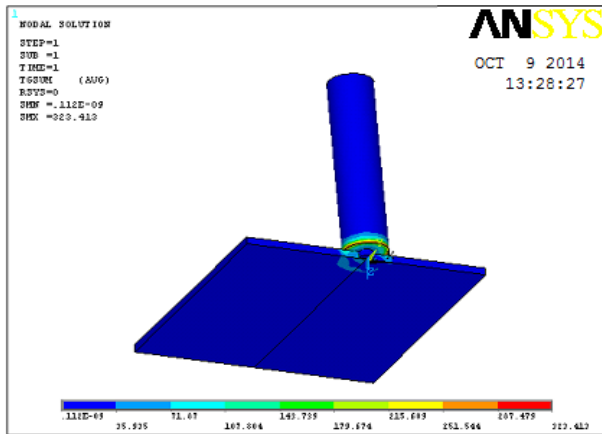
Vonmises stress Strain
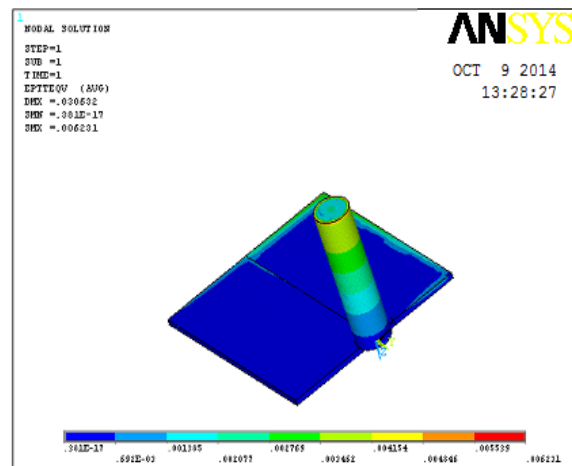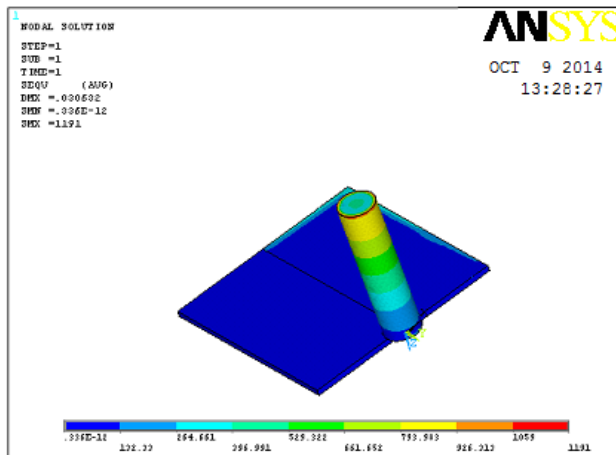
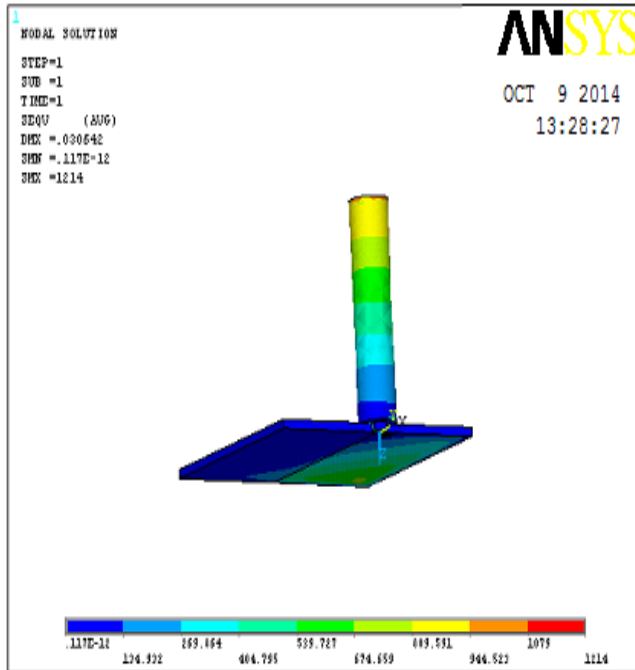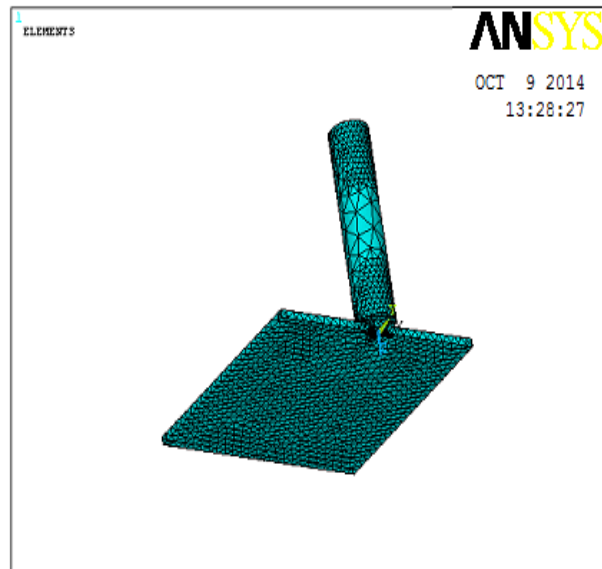SQUARE TOOL

Imported Model Meshed model
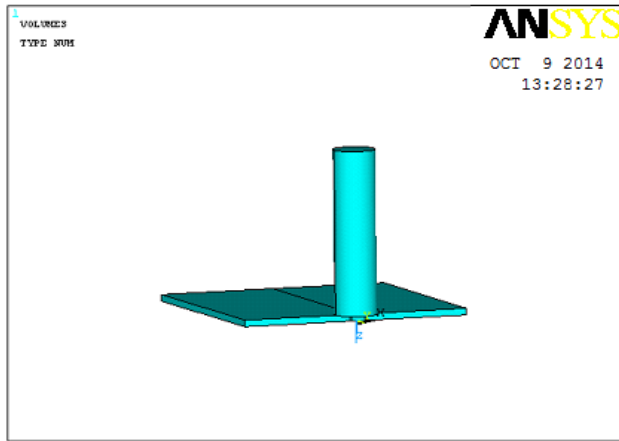
Temperature
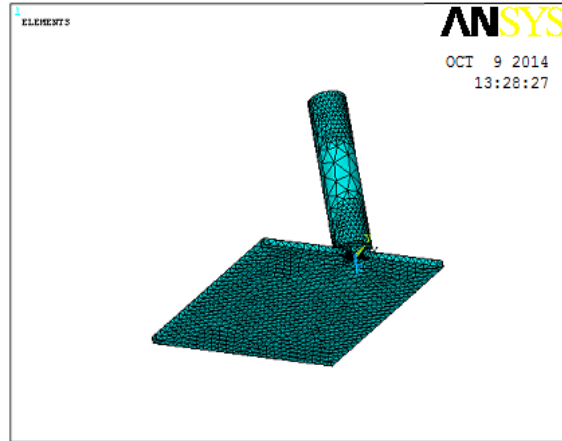
Thermal gradient
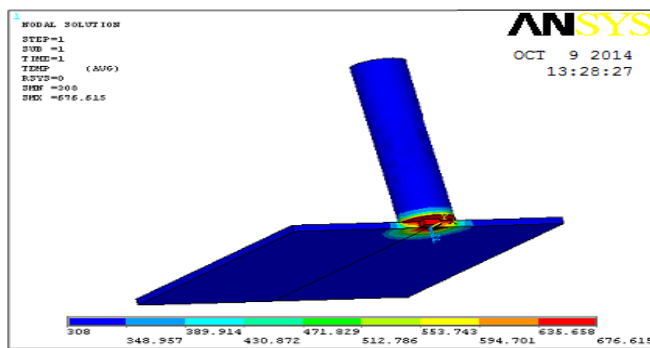
Thermal flux

Displacement
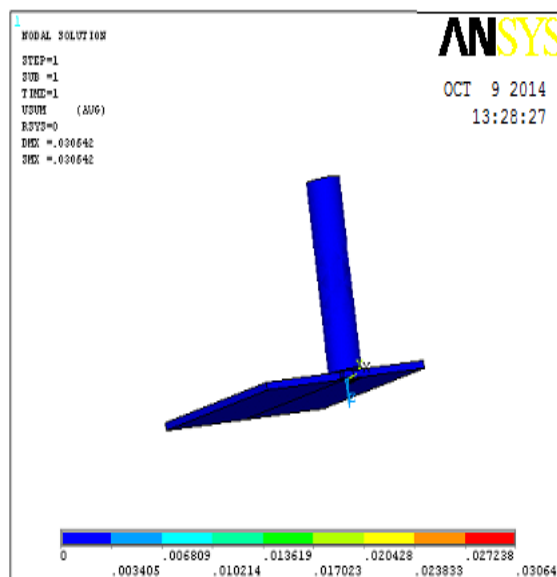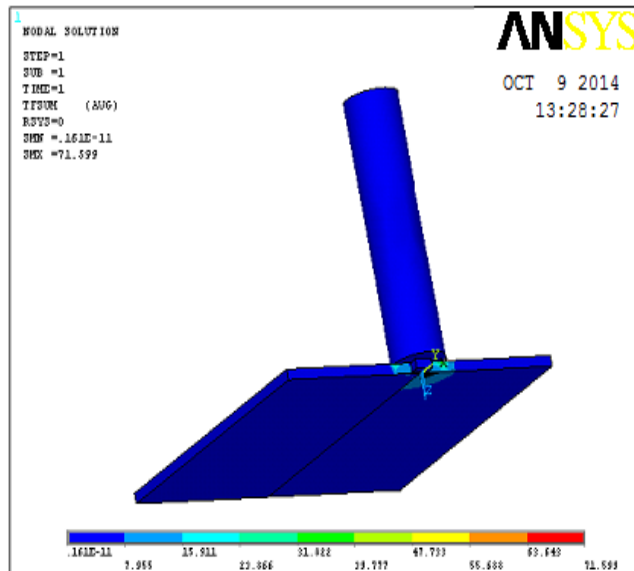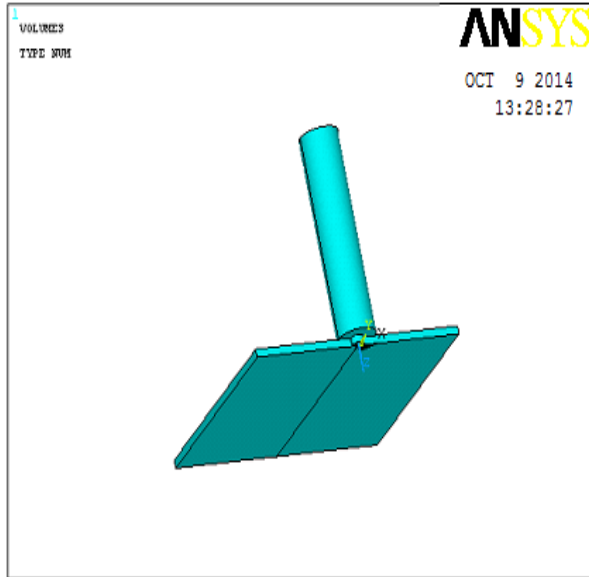
Von misses stress   Strain
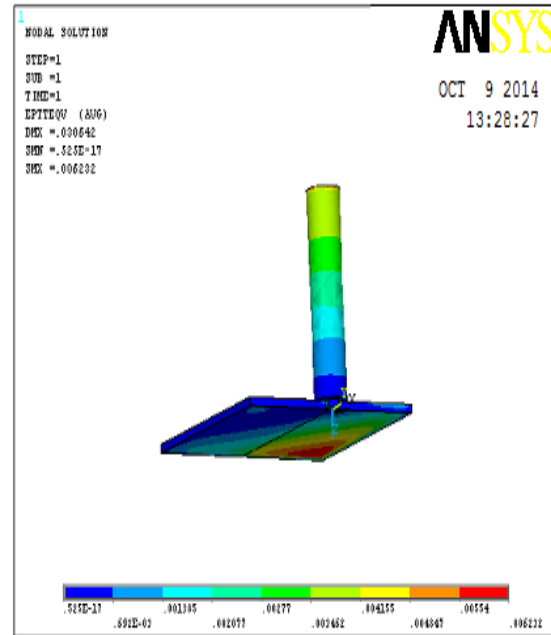
STRUCTURAL ANALYSIS OF ALUMINUM ALLOY 6061 AND CAST COPPER

1000 rpm
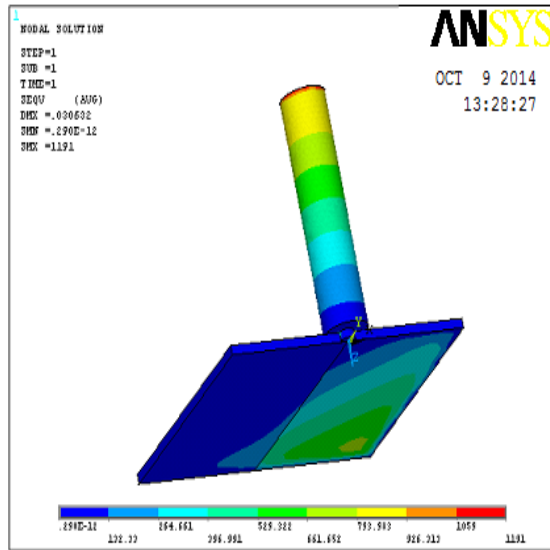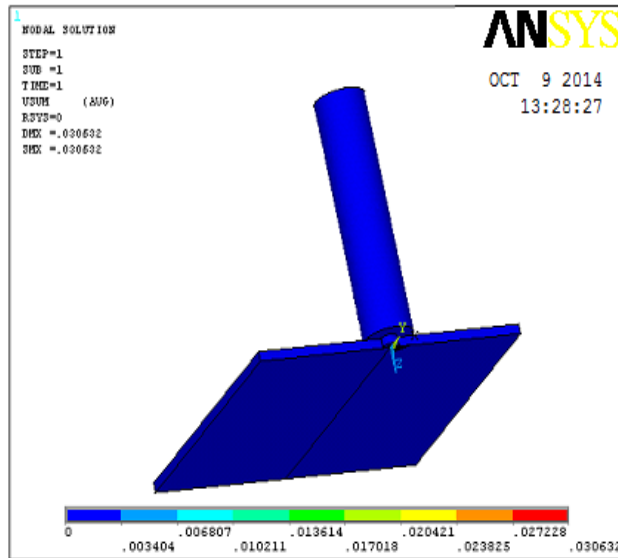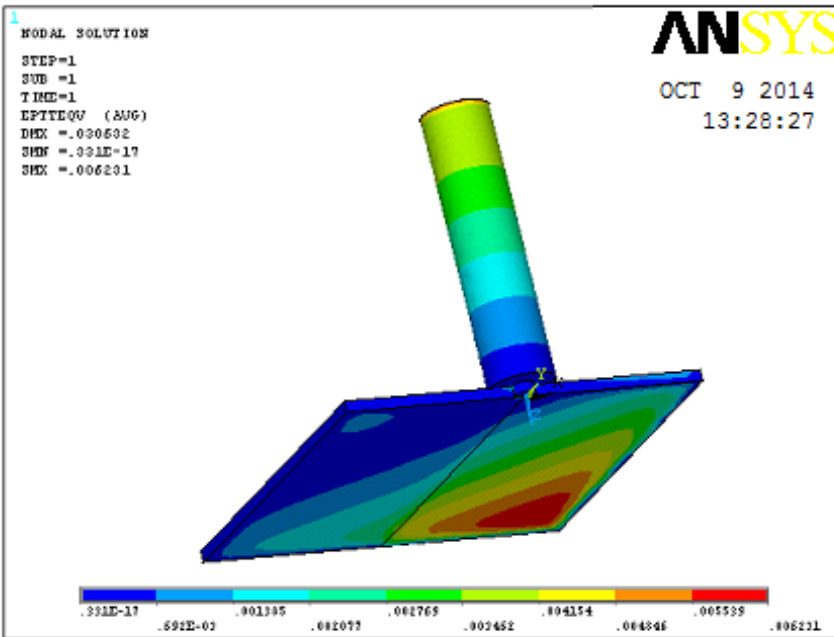
ROUND TOOL
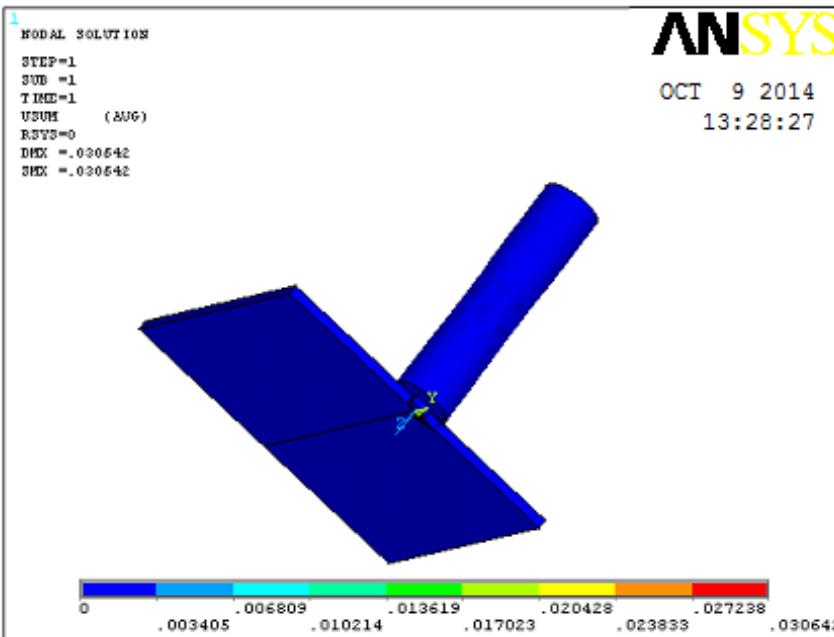
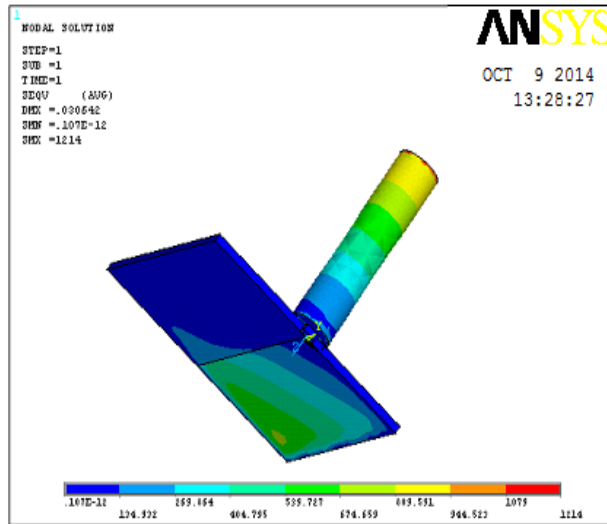Imported Model   Meshed Model

Displacement Stress

SQUARE TOOL

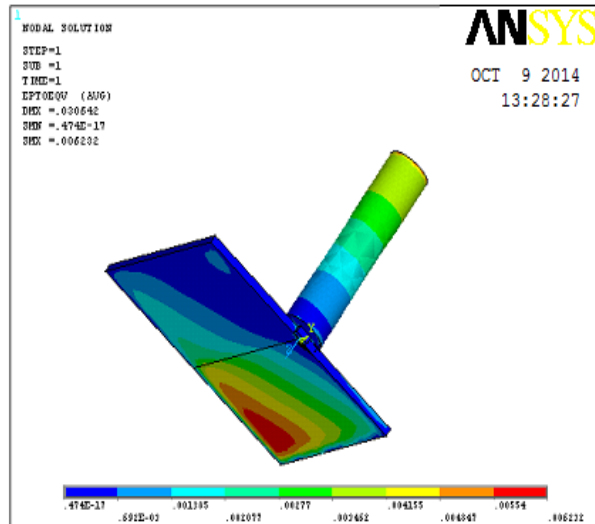Displacement

Stress   Strain

ANALYSIS RESULTS SUMMERY

THERMAL RESULT

	Temperature (K)	Thermal Gradient (K/mm)	Thermal Flux (W/mm²)
Round Tool	673	323.413	66.237
Square Tool	676.615	330.034	71.599

STRUCTURAL ANALYSIS RESULT

	Displacement (mm)	Stress (N/mm²)	Strain

| Round Tool | 0.030632 | 1191 | 0.006231 |
| Square Tool | 0.030642 | 1214 | 0.006232 |

CONCLUSION

In our project we have designed 2 types of cutting tools Round and Square for doing Friction Stir Welding of two dissimilar materials Aluminum alloy 6061 and Copper running at speed of 1000rpm. We have conducted FEA process coupled field and structural analysis on tools Round, Round taper, square, triangle and thread tool to verify the temperature distribution, thermal flux, gradient and stresses. By observing the results, thermal flux and thermal gradient are more for square tool but the stresses produced are more than round tool. Temperature is also produced for required melting point of plates. So for using Friction Stir Welding, round cutting tool is more effective than square tool from FEA results.

BIBILOGRAPHY

1. W. M. Thomas, E. D. Nicholas, J. C. Needham, M. G. Murch, P. Temple smith and C. J. Dawes: 'Friction stir butt welding', US Patent 5460317, 1995.

2. C. J. Dawes and W. M. Thomas: 'Friction stir process welds aluminum alloys', Weld. J., 1996, 75, (3), 41–45.

3. G. Cam: 'Friction stir welded structural materials: beyond Alloys', Int. Mater. Rev., 2011, 56, (1), 1–48.

4. R. S. Mishra and Z. Y. Ma: 'Friction stir welding and processing', Mater. Sci. Eng. A, 2005, 50, (1–2), 1–78.

Tensile strength of galvanized iron glass fiber sandwich panel.

Gurustal Somnath Swamy[1], Srikanth Rangdal[2], Mohammed Ghufran Uddin[3], Mahantesh Katagi[4].

[1](Department of Mechanical Engineering, Aurora Scientific Technological and Research Academy, JNTUH, Telangana, India)
[2](Department of Mechanical Engineering, Nishitha College of Engineering and Technology, Peeran Cheru, Himayat Sagar Road, Hyderabad, Telangana , India)
[3](Department of Mechanical Engineering, Shadan College of Engineering and Technology, On Srisailam Highway, Near International Airport, Hyderabad, Telangana , India)
[4](Department of Mechanical Engineering, Aurora Scientific Technological and Research Academy, JNTUH, Telangana, India)

Abstract: *The composite materials are replacing the traditional materials, because of its superior properties such as high tensile strength, low thermal expansion, high strength to weight ratio. The developments of new materials are on the anvil and are growing day by day. The recent need to develop a new range of materials has resulted in the development of high performance lightweight composites with excellent properties. Mixing of metals with Glass-Fiber Reinforced Polymers (GFRPs) is finding increased applications. Metal–composite systems consist of alternating layers of metal and fiber-reinforced polymer composites which are bonded by an adhesive. In this study, a galvanized iron glass fiber reinforced plastic sandwich panel composite is developed and their tensile strength is evaluated. Experimental results were in good agreement with predictions from simple models. On an overall basis, the sandwich panel exhibited better tensile strength performance than the monolithic galvanized iron.*

I   Introduction

The term composite can be defined as a material composed of two or more different materials, with the properties of the resultant material being superior to the properties of the individual materials being superior to the properties of individual material that make up the composite.

Glass Fiber Reinforced Polymers (GFRPs) is a fiber reinforced polymer made of a plastic matrix reinforced by fine fibers of glass. Fiber glass is a lightweight, strong, and robust material used in different industries due to their excellent properties. Although strength properties are somewhat lower than carbon fiber and it is less stiff, the material is typically far less brittle, and the raw materials are much less expensive. Its bulk strength and weight properties are very favorable when compared to metals, and it can be easily formed using molding processes several researches have been taken place in this direction.

Sandwich structured composites are a special class of composite materials which have become very popular due to high specific strength and bending stiffness. Low density of these materials makes them especially suitable for use in aeronautical, space and marine applications Sandwich composites primarily have two components namely, skin and core. If an adhesive is used to bind skins with the core, the adhesive layer can also be considered as an additional component in the structure. The thickness of the adhesive layer is generally neglected because it is much smaller than the thickness of skins or the core. The properties of sandwich composites depend upon properties of the core and skins, their relative thickness and the bonding characteristics between them. Other advantages offered by sandwich construction are elimination of welding, superior insulating qualities and design versatility. Even if the concept of sandwich construction is not very new, it has primarily been adopted for non-strength part of structures in the last decade. This is because there are a variety of problem areas to be overcome when the sandwich construction is applied to design of dynamically loaded structures. To enhance the attractiveness of sandwich construction, it is thus essential to better understand the local strength characteristic of sandwich panel/beam members.

The main objective of this study is to prepare a galvanized iron-glass fiber sandwich panel and test for the tensile test properties of the sandwich panel using universal testing machine.

## II   Material Used

2.1. Galvanized Iron

Galvanization, or galvanization, (or galvanizing as it is most commonly called in that industry), is the process of applying a protective zinc coating to steel or iron, to prevent rusting. The most common method is hot-dip galvanizing, in which parts are submerged in a bath of molten zinc. It forms a coating of corrosion-

resistant zinc which prevents corrosive substances from reaching the more delicate part of the metal. The zinc serves as a sacrificial anode so that even if the coating is scratched, the exposed steel will still be protected by the remaining zinc. The zinc protects its base metal by corroding before iron, for better results application of chromates over zinc is also seen as an industrial trend.

2.2. Glass Fiber

Fiberglass (or fiberglass) is a type of fiber reinforced plastic where the reinforcement fiber is specifically glass fiber. The glass fiber may be randomly arranged, flattened into a sheet (called a chopped strand mat), or woven into a fabric. The plastic matrix may be a thermosetting plastic – most often epoxy, polyester resin – or vinyl ester, or thermoplastic. The glass fibers are made of various types of glass depending upon the fiberglass use. These glasses all contain silica or silicate, with varying amounts of oxides of calcium, magnesium, and sometimes boron. To be used in fiberglass, glass fibers have to be made with very low levels of defects. Fiber glass is a strong lightweight material and is used for many products. Although it is not as strong and stiff as composites based on carbon fiber, it is less brittle, and its raw materials are much cheaper. Applications of fiberglass include aircraft, boats, automobiles, bath tubs and enclosures, swimming pools, hot tubs, septic tanks, water tanks, roofing, pipes, cladding, casts, surfboards, and external door skins.
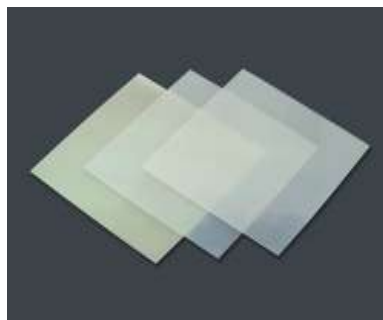
2.3. Copped Strand Mat

Chopped strand mat or CSM is a form of reinforcement used in fiberglass. It consists of glass fibers laid randomly across each other and held together by a binder. It is typically processed using the hand lay-up technique, where sheets of material are placed in a mould and brushed with resin. Because the binder dissolves in resin, the material easily conforms to different shapes when wetted out. After the resin cures, the hardened product can be taken from the mould and finished. Using chopped strand mat gives a fiberglass with isotropic in-plane material properties

2.4. Resin and Hardener

In polymer chemistry and materials science, resin is a "solid or highly viscous substance," which is typically convertible into polymers. Such viscous substances can be plant-derived or synthetic in origin. They are often mixtures of organic compounds. The resin produced by most plants is composed mainly of terpenes and derivatives. The most common terpenes in resin are the bicyclic, delta-3 carene, and sabinene, themonocyclicterpenes limonene and terpinolene,andtricyclic sesquiterpenes, longifolene, caryophyllene and del ta-cadinene. Some resins also contain a high proportion of resin acids. The individual components of resin can be separated by fractional distillation. Rosins on the other hand are less volatile and consist, inter alia, of diterpenes.

Hardener is the one that hardens; especially a substance added (as to a paint or varnish) to harden the film. Both resin and hardener are mixed together and the mixed part is used to join the two surfaces

III   Experimental Setup

3.1. Preparation of composite specimen

The surface of the Galvanized iron sheet and the inner surface of the mould cavity were coated with wax. The Galvanized iron sheet was placed inside the mould with the roughened surface facing up. A coating of the resin-hardener mixture was applied over the Galvanized iron surface followed by placing the CSM over the above coating. Two layers of unidirectional (UD) fibers wetted with resin hardener mixture were then placed over the CSM. A CSM layer was again placed over which the outer Galvanized iron sheet was placed. The mould cavity was closed by a wax coated acrylic sheet. Weights were placed over the sheet in such a way that uniform pressure was obtained. The set up was left for curing for 6 hours at room temperature.
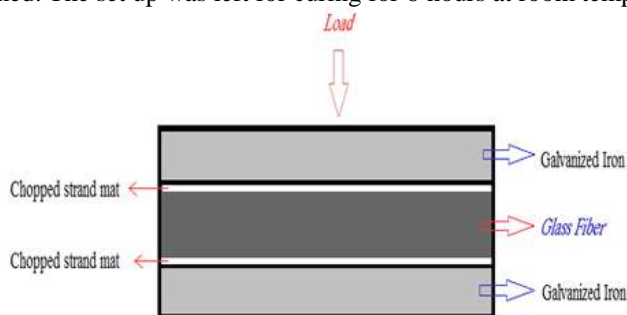
IV.   Results and Discussion

4.4. Tensile properties

The hybrid composite material fabricated is cut into required dimension using a saw cutter and the edges finished by using emery paper for mechanical testing. The tensile test specimen is prepared according to the ASTM D638 standard. The dimensions, gauge length and cross-head speeds are chosen according to the ASTM D638 standard. A tensile test involves mounting the specimen in a machine and subjecting it to the tension. The testing process involves placing the test specimen in the testing machine and applying tension to it until it fractures. The tensile force is recorded as a function of the increase in gauge length. During the application of tension, the elongation of the gauge section is recorded against the applied force. Below given details are the length, width and thickness of the specimen.

Below figure shows the tensile testing of the specimen conducted on universal testing machine (UTM). Photo has been taken after testing specimen breaks into two parts.

Length = 250mm, width = 20.84mm, thick = 3.78mm

Specimen during testing   Below figure shows the specimen after tensile testing. It shows that it has been broke into two parts.


Tested Specimen The sample graph of flexural strength observed for the Galvanized iron-glass fiber composites. The result indicated that the

Maximum applied load up to around	200 KN,
Maximum elongation	200 mm,
Specimen cross section area	78.73 mm^2 and
Final gauge length	64.84mm

Output Data

Load at yield	5.87 mm,
Yield stress	74.516 N/mm^2,
Load at peak	7.170 KN,
Tensile strength	91.018 N/mm^2 and
% Elongation	29.68 %.
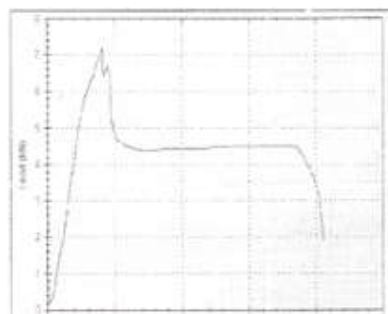
Tensile testing graph Below figure shows the certificate of testing taken from Raghavendra Spectro Metallurgical Laboratory. Certificate shows the complete details about specimen before testing and after testing.

V   CONCLUSION

Tensile test is conducted on the galvanized iron alloy glass fiber sandwich panel and it is observed that galvanized iron alloy glass fiber sandwich panel has more strength to weight ratio compared to uniform galvanized iron. From tensile test on the specimen it was observed that the start of plastic deformation could be delayed, resulting in increase of ultimate strength. From tensile test of composite material, tensile strength capacity of sandwich panel is more compare to monolithic materials. Hence sandwich panel composite material is acceptable in Automobile, Aerospace, and Marine engineering. The experimental tests have demonstrated that the light weight Galvanized iron panels have good properties of energy dissipation and the amount of energy absorption under tensile test can be highly improved by reinforcing them by means of Glass fiber sheets, which can be designed according to the application of the sandwich. Tensile analysis is done on galvanized iron alloy glass fiber sandwich panel and there will be scope for study on square, TPS (flat walls) and TPS (corrugated walls) panels. In addition to the importance of reinforcement and matrix in polymer composites, the tensile strength between the sheets is key issue for overall metal fiber laminate performance. An adequate surface treatment of the metallic layer is required to assure a good mechanical and adhesive bond between the sheets.

Reference

[1].   Gurustal Somnath Swamy.et al. Bending moment of galvanized iron glass fiber sandwich panel, Int. Journal of Engineering Research and Applications, ISSN: 2248-9622, Vol. 6, Issue 5, (Part - 5) May 2016, pp.47-51.
[2].   K.Alagarraja.et al. Fabrication and testing of fiber reinforced Polymer composites material, IOSR Journal of Mechanical and Civil Engineering (IOSR-JMCE) e- ISSN: 2278-1684, p-ISSN: 2320–334X *PP 27 34 www.iosrjournals.org.*
[3].   Gurustal Somnath Swamy.et al. Bending Moment of Aluminium Alloy Glass Fiber Sandwich Panel, International Journal of Innovative Research in Science, Engineering and Technology, ISSN (Online): 2319-8753 ISSN (Print): 2347-6710, (An ISO 3297: 2007 Certified Organization) Vol. 5, Issue 5, May 2016.
[4].   Isaac M. Daniel, Jandro. L, Abot. J. (2000). Fabrication, testing and analysis of composite sandwich beams
[5].   Herranen. H, Pabut. O, Eerme. M, Majak. J, Pohlak. M, Kers. J & Aruniit. A (2012). Design and testing of sandwich structures with different core materials. Materials Science.
[6].   Kaveh Kabir, Tania Vodenitcharova, Mark Hoffman, "Response of galvanized iron foamcored sandwich panels to bending load"Elsevier, Composites: Part B 64 (2014).
[7].   Fakhrurrazi b ab karim have studied on experimental and finite element evaluation of bending for Galvanized iron, Jan 2013, universiti malaysia pahang.
[8].   V. Crupi, G. Epasto, E. Guglielmino, "Comparison of galvanized iron sandwiches for lightweight ship structures: Honeycomb vs. foam", Elsevier, Marine Structures 30 (2013).